NMR- und impedanzspektroskopische Untersuchungen zur Dynamik und lokalen Struktur in mechanochemisch dargestellten Nichtgleichgewichtsphasen

Von der Naturwissenschaftlichen Fakultät der

Gottfried Wilhelm Leibniz Universität Hannover

zur Erlangung des Grades

DOKTOR DER NATURWISSENSCHAFTEN

Dr. rer. nat.

genehmigte Dissertation

von

Dipl.-Chem. Andre Düvel

geboren am 28. Oktober 1981, in Hannover

2014

Referent: Prof. Dr. Paul Heitjans

Korreferent: Prof. Dr. Jürgen Caro

2. Korreferent: Prof. Dr. K.-D. Becker

Tag der Promotion: 14.02.2014

Für Theo.

Contents

1 Abstract 6

2 Zusammenfassung 6

3 Introduction 8

4 Mechanochemistry 9

4.1 History of mechanochemistry: a brief overview 9

4.2 Mechanochemistry: implementation and observations 9

4.3 High-energy ball milling 11

4.4 Mechanisms and models 12

5 X-ray scattering 15

6 Diffusion in solids 18

7 Impedance spectroscopy 20

8 NMR 21

8.1 The nuclear spin 21

8.2 Nuclear magnetic resonance spectroscopy 22

9 Increase of the fluoride ion conductivity due to cation-mixing: mechanosynthesis and characterization of metastable $\mathrm{Ba}_{1-x}\mathrm{Ca}_x\mathrm{F}_2$ 28

9.1 Introduction 28

9.2 Experimental details 31

9.3 Results and discussion 32

  9.3.1 Characterization by X-ray diffraction 32

  9.3.2 Characterization by ^{19}F NMR spectroscopy 51

  9.3.3 Pair distribution function 67

  9.3.4 Ionic conductivity of the compounds 69

  9.3.5 Static ^{19}F NMR 75

9.4 Conclusions and Outlook 77

10 Mechanosynthesis and characterization of the fluoride ion conductor $\mathrm{Ba}_{1-x}\mathrm{La}_x\mathrm{F}_{2+x}$ 92

11 Mechanosynthesis and characterization of BaLiF_3 and $\mathrm{Ba}_{1-x}\mathrm{Sr}_x\mathrm{LiF}_3$ 107

12 Mechanosynthesis of BaMgF_4, BaZnF_4 and $\mathrm{BaMg}_{0.5}\mathrm{Zn}_{0.5}\mathrm{F}_4$ 148

12.1 Introduction 148

12.2 Experimental 149

12.3 Results and Discussion 149

  12.3.1 X-ray powder diffraction 149

  12.3.2 ^{19}F MAS NMR spectroscopy 152

12.4 Conclusions and Outlook 156

13 The fast fluoride ion conducting system LaF_3-SnF_2 and first investigations of the electrochemical stability of mechanosynthesized fluorides 160

14 Mechanosynthesis of a new polymorph of SnF_2? 167

15 Mechanosynthesis and characterization of the garnet-type fast Li ion conductor Al-doped $Li_7La_3Zr_2O_{12}$ 173

16 Investigations of the mechanically induced phase transformation of γ-Al_2O_3 to α-Al_2O_3 189

1 Abstract

The systems $Ba_{1-x}Ca_xF_2$, $Ba_{1-x}Sr_xF_2$, $Ca_{1-x}Sr_xF_2$, $Ba_{1-x}La_xF_{2+x}$, LaF_3-SnF_2, SnF_2, $BaMgF_4$-$BaZnF_4$, $Ba_{1-x}Sr_xLiF_3$, $BaLiF_3$ and Al-doped $Li_7La_3Zr_2O_{12}$ (LLZ) were synthesized by high-energy ball milling and investigated for their structures and ionic conductivities. Furthermore the mechanically induced phase transformation of γ-Al_2O_3 to α-Al_2O_3 was examined. All these systems are characterized by compounds being in a non-equilibrium energetic state. The system $Ba_{1-x}Ca_xF_2$, which is characterized by a broad miscibility gap that was closed by employing a mechanochemical synthesis routine, exhibits a fluoride ion conductivity maximum for compositions $x \approx 0.50$. Indications for such a maximum were also found for microcrystalline $Ba_{1-x}Sr_xF_2$ within this study. This conductivity behavior was already reported for single crystalline $Ca_{1-x}Sr_xF_2$ and $Pb_{1-x}Cd_xF_2$ in the literature. Therefore, the increase of the fluoride ion conductivity could be a general effect in fluorides crystallizing in the fluorite structure caused by the isovalent substitution of cations. The miscibility gap known for the system $Ba_{1-x}La_xF_{2+x}$ in the compositional range $0.55 \leq x \leq 0.85$ was closed by a mechanosynthesis routine. Evidence for a smooth transition from the fluorite structure of BaF_2 to the tysonite-structure of LaF_3 was found. The increased conductivity in the compositional range $0 < x \leq 0.4$ could be ascribed to a very high ratio of highly mobile fluoride ions to non-mobile or slow-moving fluoride ions while the conductivity as well as this ratio decreases from $x = 0.40$ to $x = 0.75$.

The system LaF_3-SnF_2 exhibited a maximum fluoride ion conductivity being only about one order of magnitude smaller than the one of the fastest known fluoride ion conductor, $PbSnF_4$, which was ascribed to the very small size of the SnF_2 crystallites of about 2 nm exhibiting a large amount of probably highly conducting grain boundaries. Solely milling SnF_2 seems to lead to the formation of a yet unknown polymorph of SnF_2. It was found that nano-crystalline $BaMgF_4$ and $BaZnF_4$, being ferroelectrics, can be prepared by high-energy ball milling equimolar mixtures of the binary fluorides. Furthermore, an intermediate compound, $BaMg_{0.5}Zn_{0.5}F_4$, could be prepared this way. Mechanosynthesized, nano-crystalline $BaLiF_3$ exhibited an increased ionic conductivity but a lower jump rate for the ions compared to single- or polycrystalline material. Indications were found that in case of the mechanosynthesized, nano-crystalline $BaLiF_3$, both, Li and F ions are mobile while in case of the single or polycrystalline material probably only one of them is mobile. $Ba_{1-x}Sr_xLiF_3$ showed similar ionic conductivities as $BaLiF_3$ but, as indicated by NMR experiments, seems to be characterized by a different conductivity mechanism.

A systematic study on the influence of Al-doping on cubic LLZ, being a very fast Li ion conductor, was performed. This was enabled by the development of a low-temperature synthesis routine allowing a very accurate adjustment of the stoichiometry. Indications for a substitution of La and Zr ions by Al were found which seems to alter the structure and probably lowers the jump barriers for the Li ions.

The smaller the initial crystallite size the slower the mechanically induced phase transformation of γ-Al_2O_3 to stable α-Al_2O_3. This is probably caused by the, in comparison to α-Al_2O_3, lower surface energy of γ-Al_2O_3. The, in the progress of the ball milling formed, pentagonally by oxygen coordinated, Al ions play a crucial role for the phase transformation as was already reported in the literature for the thermally induced $\gamma \rightarrow \alpha$ phase transformation. The large and adjustable amount of these pentagonally coordinated Al enables a very fine dispersion of small clusters of catalytically active substances, binding at these sites, on the surface of the mechanically treated γ-Al_2O_3, leading to a high catalytic performance as was verified for V_2O_5 by the Leibniz Institute for Catalysis.

Keywords: Mechanochemistry, fluoride ion dynamics, solid state NMR spectroscopy

2 Zusammenfassung

Die Systeme $Ba_{1-x}Ca_xF_2$, $Ba_{1-x}Sr_xF_2$, $Ca_{1-x}Sr_xF_2$, $Ba_{1-x}La_xF_{2+x}$, LaF_3-SnF_2, SnF_2, $BaMgF_4$-$BaZnF_4$, $Ba_{1-x}Sr_xLiF_3$, $BaLiF_3$ und Al-dotiertes $Li_7La_3Zr_2O_{12}$ (LLZ) wurden mittels Hochenergiekugelmahlens synthetisiert und deren Struktur und ionische Leitfähigkeit untersucht. Darüber hinaus wurde die mechanisch induzierte Phasenumwandlung von γ-Al_2O_3 zu α-Al_2O_3 erkundet. All diese Systeme sind durch Verbindungen, welche sich in einem energetischen Nichtgleichgewichtszustand befinden, charakterisiert. Das System $Ba_{1-x}Ca_xF_2$, welches eine breite Mischungslücke aufweist, die durch eine mechanochemische Syntheseroute geschlossen werden konnte, weist ein F^- Leitfähigkeitsmaximum im Bereich von Zusammensetzungen nahe $x \approx 0.50$ auf. Hinweise auf ein derartiges Leitfähigkeitsmaximum für $x \approx 0.5$ wurden auch für mikrokristallines $Ba_{1-x}Sr_xF_2$ innerhalb dieser Studie gefunden. Dieses Leitfähigkeitsverhalten wurde bereits für einkristallines $Ca_{1-x}Sr_xF_2$ sowie $Pb_{1-x}Cd_xF_2$ in der Literatur beschrieben. Somit scheint es denkbar, dass es sich um ein grundsätzliches, durch die isovalente Substitution der Kationen verursachtes Phänomen handelt, welches bei Fluoriden, die in der Fluoritstruktur kristallisieren, auftritt. Die für das System $Ba_{1-x}La_xF_{2+x}$ bekannte Mischungslücke im Bereich $0.55 \leq x \leq 0.85$ konnte mittels einer mechanochemischen Syntheseroute geschlossen werden. Es wurden Hinweise für einen kontinuierlichen Übergang von der Fluoritstruktur des BaF_2 zur Tysonitstruktur des LaF_3 gefunden. Die im Zusam-

mensetzungsbereich $0 < x \leq 0.4$ beobachtete Erhöhung der Leitfähigkeit geht einher mit einem sehr großen Verhältnis von hochmobilen Fluor-Ionen zu nicht-mobilen oder langsamen Fluor-Ionen, während sowohl die Leitfähigkeit als auch dieses Verhältnis für Zusammensetzungen im Bereich $x = 0.40$ bis $x = 0.75$ abnehmen.

Das System LaF_3-SnF_2 weist eine maximale Fluorionenleitfähigkeit auf, die nur etwa eine Größ-enordnung kleiner als die des schnellsten bekannten Fluorionenleiters, $PbSnF_4$, ist. Die hohe Leitfähigkeit wurde auf die geringe Kristallitgröße des SnF_2 von nur etwa 2 nm zurückgeführt, die zu einem großen Anteil von vermutlich hochleitfähigen Korngrenzbereichen führt. Wird SnF_2 allein gemahlen, so scheint dies zur Bildung eines bisher unbekannten Polymorphs des SnF_2 zu führen. Es konnte gezeigt werden, dass die Synthese von nanokristallinem $BaMgF_4$ und $BaZnF_4$, welche Ferroelektrika sind, mittels Hochenergiekugelmahlens äquimolarer Mischungen der binären Fluoride möglich ist. Darüber hinaus konnte eine Übergangsverbindung, $BaMg_{0.5}Zn_{0.5}F_4$, hergestellt werden. Mechanosynthetisiertes, nanokristallines $BaLiF_3$ wies eine im Vergleich zum einkristallinen oder polykristallinem Material erhöhte ionische Leitfähigkeit aber gleichzeitig verringerte Sprungrate der Ionen auf. Es ergaben sich Hinweise darauf, daß im Fall des mechanosynthetisierten, nanokristallinen $BaLiF_3$ beide Ionenspezies, also Li- und F-Ionen, mobil sind, während im Falle von einkristallinem oder polykristallinem Material wahrscheinlich nur eine Ionenspezies mobil ist. $Ba_{1-x}Sr_xLiF_3$ zeigte ähnliche ionische Leitfähigkeiten wie das $BaLiF_3$, allerdings, wie NMR Experimente zeigen konnten, scheint es durch einen anderen Leitungsmechanismus charakterisiert zu sein.

Es wurde eine systematische Studie über den Einfluss der Al-Dotierung von kubischem LLZ, das ein sehr schneller Lithiumionenleiter ist, durchgeführt. Diese wurde durch die Entwicklung einer Tieftemperatur-Syntheseroute ermöglicht, da so eine sehr genaue Einstellung der Stöchiometrie erreicht werden konnte. Es zeigten sich Hinweise für die Substitution von La und Zr-Ionen durch Al-Ionen, die zu einer Veränderung der Struktur und wahrscheinlich einer Herabsenkung der Sprungbarrieren für die Li-Ionen führt.

Je kleiner die initiale Kristallitgröße, desto langsamer findet die mechanisch induzierte Phasen-umwandlung von γ-Al_2O_3 zum stabilen α-Al_2O_3 statt. Dies ist wahrscheinlich auf die im Vergleich zum α-Al_2O_3 kleinere Oberflächenenergie des γ-Al_2O_3 zurückzuführen. Die im Verlauf des Kugelmahlprozesses gebildeten fünffach mit Sauerstoff koordinierten Al-Ionen spielen eine wesentliche Rolle für die Phasenumwandlung, so wie es in der Literatur für die thermisch induzierte $\gamma \rightarrow \alpha$ Phasenumwandlung bereits berichtet wurde. Der große und einstellbare Anteil der fünffach mit Sauerstoff koordinierten Al-Ionen erlaubt eine sehr feine Verteilung von, an diesen sich bindenden, Clustern katalytisch aktiver Materialien auf der Oberfläche des mechanisch behandelten γ-Al_2O_3, was zu einer sehr guten katalytischen Wirksamkeit führt, wie im Falle von V_2O_5 im Leibniz Institut für Katalyse gezeigt werden konnte.

Stichworte: Mechanochemie, Fluor-Ionen Dymamik, Festkörper NMR Spektroskopie

3 Introduction

The synthesis and characterization of yet unknown compounds is an important source for the development of new technologies and progress in science. A popular example is the synthesis of high-temperature superconductors. The synthesis of a material that could conduct an electric current without resistance at ambient temperature would be of high benefit in many technological sectors. There are countless other examples of materials with desired properties in the areas of heterogeneous catalysis, ion conductors and electrode materials for secondary batteries, magnetic materials (e. g., for generators), materials for construction or tools (hardness, stiffness, stability against corrosion etc. Science fiction example: a material with a tensile strength large enough for a space elevator), phosphorescent materials, dyestuffs and many more. Also the substitution of rare (thus very expensive) or toxic substances used in important applications is of large interest. Hence, there are two main tasks:

- the prediction of structure and properties from the chemical composition
- the synthesis of potentially interesting materials

Since not even the structure-property relationships are understood for many systems, the first task is most probably out of reach for the near (and probably also for the more remote) future.

Essentially, the studies shown within this work address the synthesis of compounds not yet known and their characterization. Thereby a main focus lies on the investigation of possible relations between the ionic conductivity and the micro-structure of the compounds. Especially in case of $Ba_{1-x}Ca_xF_2$ and isostructured fluorides this is a main task.

The synthesis technique used is mechanosynthesis, i. e., the synthesis of compounds by high-energy ball milling of mixtures of starting materials. This technique allows the synthesis of non-equilibrium compounds which are hardly or not at all accessible by conventional solid state synthesis routines. Accordingly, another task of these studies is to add some information to gain a better understanding of this highly complex synthesis routine.

In addition to the synthesis of a fast Li ion conductor and a study dealing with the phase transformation of γ-Al_2O_3 the studies shown in the following address the synthesis and characterization of fluorides exhibiting a high fluoride ion conductivity. Such materials may be of some interest for fluoride ion batteries which in principle should have electric capacities even larger than high capacity Li ion batteries and, moreover, are assumed to be more secure. However, for several reasons that will be discussed later, the development of such battery systems did not turn out to be of large success so far.

The characterization of the structure of compounds was accomplished by X-ray scattering and, being of high importance for this work, nuclear magnetic resonance (NMR) spectroscopy. While the first technique mainly gives information about the long-range structure, NMR spectroscopy delivers information about the micro-structure of the compounds. For some of the systems additional information was gained by X-ray total scattering analysis to calculate their pair distribution functions. The dynamic properties are primarily investigated by impedance spectroscopy and line shape analysis of NMR spectra.

4 Mechanochemistry

4.1 History of mechanochemistry: a brief overview

Mechanochemistry was defined as a "branch of chemistry which is concerned with chemical and physico-chemical transformations of substances in all states of aggregation produced by the effect of mechanical energy" by Heinicke[1]. Therefore, it can be said that the history of this branch of chemistry started several thousand years ago. In the stone age tools were created from stones skilfully struck against each other. Thus, the ignition of fire by hitting pyrite (from greek $\pi\upsilon\rho$ = fire, FeS_2) with a quartz (SiO_2) or flint (SiO_2 x n H_2O, being the typical material from which tools were made in the stone age), leading to the exothermic reaction $2\ FeS_2 + 5.5\ O_2 \rightarrow Fe_2O_3 + 4\ SO_2$, may have been the first chemical reaction initiated by man. The resulting sparks of burning pyrite were used to ignite highly flammable substances like, e. g., tinder fungus. As stated by the South Tyrol Museum of Archaeology pyrite and tinder fungus were also found in the about 5000 years old pouch of the so called Iceman. In the following times instead of pyrite also fire steel, which is a brittle, carbon rich steel, was used in the same way. In modern lighters the sparks igniting the flammable gas are generated by the friction of steel on a cerium iron alloy.[2] More convenient types of lighters use a piezoelectric to generate a large potential difference, by hitting the piezoelectric with a hammer pin when pressing the button of the lighter (producing a clicking noise). The generated discharge spark ignites the flammable gas. The ignition of a match which is based on the reaction of $KClO_3$, sulfur and red phosphor, is also initiated mechanically.[3] Thus, the common ways to ignite a fire are still based on the introduction of mechanical energy into the system.

Although mechanochemical reactions were and are used in several areas (e. g., grinding of materials for the preparation of paints, balms, pharmaceuticals) and were already common for the people in the stone age, there are not many publications dealing with a mechanochemical reactions before the 19th century.[4] The probably oldest one known is from 315 B.C.E. in which Theophrastus of Eresus reported on the mechanically initiated reduction of cinnabar (HgS) to mercury by grinding it in a copper mortar with a copper pestle.[5] The next well known publication was about the reduction of silver chloride by grinding it with other metals in a mortar reported by Michael Faraday.[6] Some systematic studies were done in the 1880s by Walthére Spring and Matthew Carey Lea, see ref. 4 for more details. In 1918 Wilhelm Ostwald introduced mechanically initiated chemical reactions into the chemical systematics in addition to thermally, electrochemically and photochemically initiated reactions.[7] The term "mechanochemistry" however, was already introduced by Crismer six years earlier[8]. In the first half of the 20th century mechanochemical studies were a rather exotic area of chemistry. This changed in the 1960s when more and more research groups worked in this field mainly in the Soviet Union and Eastern Europe where it still resides. Over the last years the mechanochemistry also found slowly increasing attention in the so called western countries.

4.2 Mechanochemistry: implementation and observations

Although the use of pestle and mortar are in principle sufficient to perform mechanochemical reactions, today mainly ball mills are used for this purpose. However, it should be noted that even in a mortar at least very high pressures of about 1.5 GPa can easily be reached as shown by Dachille and Roy[9]. In general, the effect of common mechanical actions on material should not be underestimated, see e. g., ref. 10 where the change of aragonite to calcite accompanied by an enrichment of ^{18}O by drilling is reported. Without knowledge of this change the obtained drill cores from geological layers produced by ancient corals would give wrong information about the temperature at the time the corals lived.[10]

Small mechanical force can initiate chemical reactions. A good example are initial explosives like, for instance, mercury fulminate ($(CNO)_2Hg$). Its explosive decomposition to CO, N_2 and Hg can be initiated by very weak mechanical force.[11] Just recently, another interesting result, which was at first assumed to be a mechanochemical reaction initiated by very weak force was published. Instead of the explosive decomposition of a high energetic compound, Dreger et al. reported on the fast and easy synthesis of nano-crystalline alkaline earth metal fluorides just by shaking the starting materials NH_4F and the respective metalhydroxides in a plastic container.[12] In a subsequent study, done in cooperation with the author, however, it was found that the reaction also occurs if the starting materials are simply brought into contact[13], as it is also known for, e. g., the oxidation of glycerin by $KMnO_4$.[14]

Mechanical energy can easily be transformed into heat. Thus, one may argue that mechanochemistry is just thermochemistry but with an inconvenient way of heating the powders. However, if the same mixtures of starting materials are treated by a mechanochemical synthesis routine and by a conventional thermal synthesis routine, the reaction products will differ in many cases.[15] Furthermore, many compounds accessible by a mechanosynthesis routine cannot be prepared by a conventional solid state synthesis[15], as will also be shown in the following chapters. A good example for the different products of thermal and mechanical treatment was already discussed by M. Carey Lea in 1893[16]. He reported on the decomposition of silver chloride and mercuric chloride due to grinding in a mortar. Heating of these compounds, however, leads to an undecomposed melting and sublimation, respectively.[4]

An observation for most mechanochemical reactions of ceramic materials, be it the synthesis of a compound from a mixture of starting materials or the treatment of a single compound in a high-energy ball mill, is the formation of nano-crystalline materials, while the formation of nano-particles is not a particular strength of the mechanochemical processing. The nanosized crystallites mechanically prepared often consist of a quite well ordered core and a more or less disordered grain boundary.[15] The crystallites are commonly agglomerated forming sometimes quite large particles. One would expect the formation of nano-crystalline material by high-energy ball milling of amorphous materials due to the high energies introduced. However, in case of alloys amorphous materials can be prepared by high-energy ball milling.[17] The introduction of impurities like oxygen in such alloys, however, shall result in crystallization as reported by Birol[18]. This leads to the crystallization behavior of ceramics. Milling a ceramic can result in materials with quite large amounts of amorphous material. But can a glass (partially) be crystallized by high-energy ball milling? An interesting example is a study dealing with the change of properties of glassy β-spodumene ($LiAlSi_2O_6$) due to high-energy ball milling conducted by Kuhn et al.[19,20] They found, that the Li ion mobility of the glassy β-spodumene is reduced due to high-energy ball milling exhibiting values very similar to the ones of high-energy ball milled crystalline β-spodumene. In contrast to the nano-crystalline material prepared from poly-crystalline β-spodumene, the high-energy ball milled glass exhibited an XRPD pattern with only a few peaks of very low intensity. Therefore, the milled glass was denominated as "nano-glass". The reduction of the Li ion mobility was assumed to be due to a structural relaxation of the glass. Thus, it would be interesting to increase the milling time (or change the milling conditions) to test if the structural relaxation eventually results in a crystallization of the β-spodumene or if the nano-glassy condition of the material turns out to be stable under (certain) high-energy ball milling conditions.

In addition the synthesis of compounds in the course of the milling process, high-energy ball milling is also used to reduce reaction temperatures for thermal synthesis routines. This is called mechanical activation.[21] The effect is due to the formation of large amounts of nanosized crystallites exhibiting fresh and, thus, reactive surfaces. Additionally, the good intermixing of the starting materials increases the reactivity of the mixture. For conventional solid state synthesis the starting materials are often also high-energy ball milled in solvents (high-energy ball milling for mechanosynthesis is generally done without solvents) for good intermixing and grain size reduction, see e. g. ref. 22.

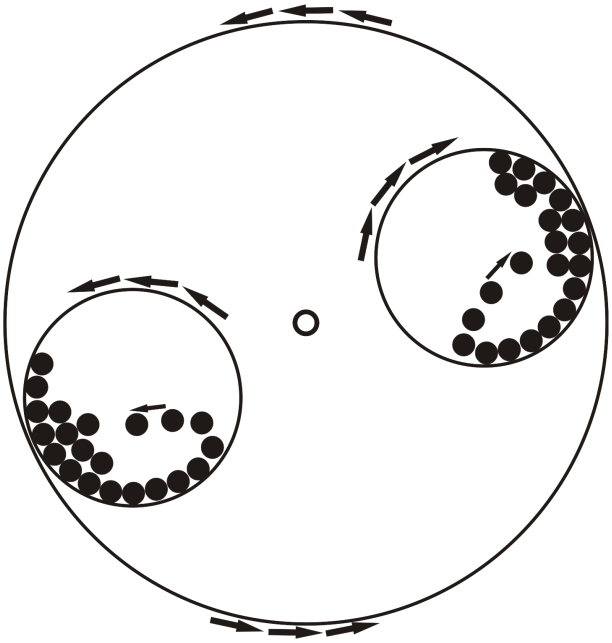

Figure 1: Sketch of a planetary mill in action at a rotational speed leading to a cataract motion of the milling balls.

4.3 High-energy ball milling

Typical ball mill types used in laboratories are shaker or vibro mills and planetary mills. In the first type of mill a single milling ball is put into a beaker made from a very hard material like for instance stabilized ZrO_2 together with the material to be milled. Now the beaker is closed and shaken such that the ball hits the walls of the beaker. Thus, the energy is introduced by impact. Although a SPEX 8000 shaker mill was used for a few experiments most of the work presented in this study is executed with a planetary mill. In a planetary mill two or four milling beakers are placed onto a main disc opposing each other. The main disc as well as the beakers themselves can be rotated in the same plane. In the case of the planetary mill used here, which is a P7 premium line (Fritsch), a full revolution of the main disc leads to a full rotation of the two beakers whereby the beakers and the main disc rotate in opposite directions. Inside the beakers several milling balls, commonly smaller than in case of a shaker mill, are present. For the work presented here amounts of 100 or 140 milling balls with diameters of about 5 mm were used. According to Fritsch the contrarotating disc and beakers cause complex trajectories of the milling balls. At a certain rotational speed the geometry of the mill shall lead to the detachment of some of the milling balls from the beaker walls. These balls are accelerated away from the axis of the main disc leading to impact events at the other milling balls and, thus, the material milled, as illustrated in Fig. 1. This is called cataract motion. At first view this seems unexpected since the forces acting on the milling balls always lead away from the axis of the main disc such that they should stay at the beaker wall farthest away from the axis of the main disc. However, due to friction (roll friction as well as sliding friction) the milling balls cannot follow the forces acting upon them instantaneous. Starting at a certain speed of the mill the balls cannot roll to the place of maximum centrifugal force due to frictional resistance fast enough such that they follow the rotation of the beaker until they are almost opposed to the place of maximum centrifugal force, see Fig. 1. At that position they detach from the wall and fall towards the place of maximum centrifugal force. While they fall the beaker is still rotating leading to a complex trajectory of the falling milling balls. A correct mathematical description of the process and, thus, the movement of the milling balls, is highly complex. A distribution of kinetic energies of the milling balls can be assumed. This can be tested very easily by putting the milling balls into a sieve which is gently shaken, being, however, a clearly less complex motion than inside the milling beaker. Most of the time the milling balls will follow the movement of the sieve close to its ground. Sometimes a milling ball will detach from the others and fall back onto them. But if the sieve is shaken for a sufficiently long time, a milling ball will gain a large impulse and jump out the sieve. However, a simplified estimation of the movement of one ball in the beaker shall be done here.

4.4 Mechanisms and models

The largest distance between the axis of the main disc and the wall of the milling beaker is about 9.1 cm. The inside radius of the beakers is approximately 2.35 cm. The milling balls have a diameter of around 5 mm. The centrifugal acceleration a can be calculated by

$$a = \frac{v^2}{r} \tag{1}$$

with v being the velocity of the milling ball and r its distance from the axis of the main disc. At the rotational speed used, which was 600 rounds per minute (rpm) = 10 rounds per second (rps), $v = 20\pi r$. The point where the milling ball detaches from the beaker wall is not known as well as its velocity relative to the beaker. Therefore, the starting velocity is assumed to be 0 m/s. As starting point the point of maximum centrifugal force rotated by 180° is taken. This leads to a distance of approximately 4.65 cm of free fall for the milling ball. Thus, the milling ball is accelerated from r_1 = 9.1 cm - 4.7 cm = 4.4 cm to r_2 = 9.1 cm - 0.025 cm = 9.075 cm. The acceleration a is a function of r. This leads to

$$a = (20\pi r)^2/r \tag{2}$$

$$\mathrm{d}a/\mathrm{d}r = \mathrm{d}(20\pi r)^2/\mathrm{d}r = 400\pi^2 2r \tag{3}$$

$$\int_{r_1}^{r_2} 800\pi^2 r = 400\pi^2((0.09075\text{ m})^2 - (0.044\text{ m})^2) \approx 24.87\text{ m/s}^2 \tag{4}$$

$$s = at^2 \approx 0.0465\text{ m} \tag{5}$$

$$t = \sqrt{s/a} \approx 0.043\text{ s} \tag{6}$$

$$v = at \approx 1.075\text{ m/s.} \tag{7}$$

Thus, in case of a milling ball made of stabilized ZrO_2 with a diameter of 5 mm and a specific density of $\rho \approx 5.9$ g/cm^3 (given by Fritsch) the milling ball has an kinetic energy of $E_{\text{kin}} = 0.5 \cdot 3.86 \cdot 10^{-4}$ kg $\cdot$ (1.075 m/s)$^2 \approx 2.23$ x 10^{-4} J (5.66 x 10^{-4} J in case of a milling ball made of tungsten carbide with ρ = 14.95 g/cm^3 (given by Fritsch)). This energy may appear to be rather small. However, if we assume that the milling ball fell onto a spherical BaF_2 crystallite with a diameter of 10 nm the energy is distributed over about 26363 ions and, thus, 4.377 x 10^{-20} mol. This leads to an energy of approximately 5 x 10^{12} kJ/mol (1.3 x 10^{13} kJ/mol) being introduced into the crystallite. The lattice energy of BaF_2 is 2.352 x 10^3 kJ/mol[23]. The sum of the first and second ionisation energies of Ba is about 22 MJ/mol[24]. The ionisation energy of fluorine is approximately 25 MJ/mol[25]. Therefore, if in fact all the energy is transmitted into the crystallite, it will not just be decomposed completely, but it will become a plasma. Even if only a small part of the energy of the impacting milling ball (a large part of the energy will be transferred to other milling balls and the beaker wall) is distributed over the ions forming a small crystal it would be enough to generate high-energetic states. The small area in which the plasma or another high energetic state of the material is generated should cool very fast until it reaches (almost) ambient temperature again. In the 1960s the "magma-plasma model" was developed to describe the processes happening in the course of a mechanochemical reaction. According to this model an impact event at a particle transforms a part of that particle to a plasma. From this plasma the product forms at the residual surface of the particle.[26] Therefore, it seems plausible to assume that high-energetic states may be frozen this way. Thus, high-energy ball milling might exhibit some similarities with molecular beam epitaxy (MBE) at cool surfaces. See ref. 27 for a report on the synthesis of a compound by MBE.

However that be, it should be noted that there are several models dealing with the mechanisms and reactions taking place in the course of a mechanochemical synthesis reaction.[28] However, it seems plausible that the formation of the products takes place in the surface regions of the milled starting materials. The mechanical treatment introduces high pressures, shear forces and high temperatures into the materials treated. Furthermore, discharge sparks due to the mechanical cracking of grains may be generated which could affect the reactivity. However, Calka and Wexler[29] showed that the additional introduction of electric discharges while milling enabled reactions which did not occur in case of a mechanical treatment without these artificially introduced discharge events. Radiation may also be produced while ball milling due to the discharge sparks in some cases which may influence the reaction path, see e. g., ref. 30. The generation of radiation by mechanically breaking chemical bonds is known as triboluminescence, a long known phenomenon, see ref. 31. It may be mentioned that the fast unrolling of a scotch tape in vacuum leads to the generation of X-rays.[32] Thus, high energetic radiation might be produced in the course of milling of specific materials. Nonetheless, due to the large amount of potential influencing variables, it is very likely that different mechanically induced reactions follow different reaction paths and mechanisms.[28]

Mechanochemical synthesis strategies can be used for the synthesis of organic and inorganic compounds, for catalysis or extraction of elements from minerals.[28] Thus, mechanochemistry should not be seen as an exotic technique but as the common, efficient and easy to use tool for the chemist it is and always was.

References

[1] G. Heinicke, "Tribochemistry", Akademie-Verlag, Berlin, 1986.

[2] M. Binnewies, M. Jäckel, H. Willner, G. Rayner-Canham, "Allgemeine und Anorganische Chemie", Spektrum Akademischer Verlage Heidelberg - Berlin, 2004, p. 708.

[3] M. Binnewies, M. Jäckel, H. Willner, G. Rayner-Canham, "Allgemeine und Anorganische Chemie", Spektrum Akademischer Verlage Heidelberg - Berlin, 2004, p. 479.

[4] K. Takacs, Chem. Soc. Rev. 42 (2013) 7649.

[5] L. Takacs, J. Met. 52 (2000) 12.

[6] M. Faraday, Q. J. Sci., Lit., Arts, 8 (1820) 374.

[7] W. Ostwald, "Die chemische Literatur und die Organisation der Wissenschaft", in "Handbuch der allgemeinen Chemie", ed. W. Ostwald and C. Drucker, Akademische Verlagsgesellschaft m. b. H., Leipzig, 1919, pp. 70 and 77.

[8] L. Crismer, Bull. Soc. Chim. Belg. 26 (1912) 41.

[9] F. Dachille, R. Roy, Nature 186 (1960) 34.

[10] I. Gill, J. J. Olson, D. K. Hubbard, Geology 4 (1995) 333.

[11] R. Biedermann, "Die Sprengstoffe", Teubner, Leipzig, Berlin 1917, p. 120.

[12] M. Dreger, G. Scholz, E. Kemnitz, Solid State Sci. 14 (2012) 528.

[13] G. Scholz, K. Meyer, A. Düvel, P. Heitjans, E. Kemnitz, Z. Anorg. Allg. Chem. 639 (2013) 960.

[14] F. R. Kreißel, O Krätz, "Feuer und Flamme, Schall und Rauch", Wiley-VCH Weinheim, 2. Aufl. 2008, S. 123.

[15] V. Šepelák, A. Düvel, M. Wilkening, K.-D. Becker, P. Heitjans, Chem. Soc. Rev. 42 (2013) 7507.

[16] M. C. Lea, Am. J. Sci., 46 (1893) 413.

[17] C. C. Koch, O. B. Cavin, C. G. McKamey, J. O. Scarbrough, Appl. Phys. Lett. 43 (1983) 1017.

[18] Y. Birol, Scripta Mater. 34 (1996) 1081.

[19] A. Kuhn, E. Tobschall, P. Heitjans, Z. Phys. Chem. 223 (2009) 1359.

[20] A. Kuhn, M. Wilkening, P. Heitjans, Solid State Ionics 180 (2009) 302.

[21] L. L. Shaw, Mater. Manuf. Process. 16 (2001) 405.

[22] R. Murugan, V. Thangadurai, W. Weppner, Angew. Chem. Int. Ed. 46 (2007) 7778.

[23] D. W. Smith, "Inorganic Substances: A Prelude to the Study of Descriptive Inorganic Chemistry", Cambridge University Press, 1990, p. 145.

[24] E. Riedel, "Anorganische Chemie", 5. Auflage, Walter de Gruyter, Berlin, New York, 2002, p. 592.

[25] E. Riedel, "Anorganische Chemie", 5. Auflage, Walter de Gruyter, Berlin, New York, 2002, p. 399.

[26] P. A. Thiessen, K. Meyer and G. Heinicke, Grundlagen der Tribochemie, Akademie-Verlag, Berlin, 1967.

[27] D. Fischer, M. Jansen, J. Am. Chem. Soc. 124 (2002) 3488.

[28] P. Baláž, M. Achimovičová, M. Baláž, P. Billik, Z. Cherkezova-Zheleva, J. M. Criado, F. Delogu, E. Dutková, E. Gaffet, F. J. Gotor, R. Kumar, I. Mitov, T. Rojac, M. Senna, A. Streletskii, K. Wieczorek-Ciurowa, Chem. Soc. Rev. 42 (2013) 7571.

[29] A. Calka, D. Wexler, Nature 419 (2002) 147.

[30] P. G. Fox, J. Mater. Sci. 10 (1975) 340.

[31] T. L. Dawson, Color. Technol. 126 (2010) 177.

[32] C. G. Camara, J. V. Escobar, J. R. Hird, S. J. Putterman, Nature 455 (2008) 1089.

5 X-ray scattering

To investigate the structure of a crystalline compound, scattering techniques are the methods of choice. In addition to neutron and electron scattering the most common technique is X-ray scattering. It is based on the interaction of monochromatic X-ray radiation with the electrons of the atoms or ions forming the crystal. Since distances between ions or atoms in a crystal, which are in the range of about one angstrom, have the same magnitude as the wavelength of the X-rays, the scattering at the equally spaced atoms or ions in a crystal lattice leads to constructive and destructive interference depending on the angle in which the X-rays incide at the atomic planes created by the atoms or ions. The relation of the distance between the atomic planes d and the angle of incidence on them, denominated as θ, is given by the Bragg equation,

$$n\lambda = 2d\sin\theta \tag{8}$$

with $n \in \mathbb{N}$ and λ being the wavelength of the X-rays used. Thus, for constructive interference between the X-rays, the difference of the path lengths of the X-rays scattered at the parallel atomic planes, $2d\sin\theta$, have to be an integer multiple of the wavelength of the X-rays used.

In the case of a powder diffraction measurement as done with the samples investigated within this study, a powdered sample is put onto a sample holder and pressed to a flat plane. From this pellet the inciding x-rays are reflected towards a detector counting the intensity of the radiation. The X-ray source and the detector move around the sample in one plane in a forficate way. The movement is done in steps of a certain angle (in the order of 0.01°). Hence, for a certain amount of angles it is tested if the Bragg condition is satisfied. If this is the case, there will be constructive interference between the rays scattered at a certain regiment of atomic planes, leading to a high intensity of the radiation. Consequently, a peak at a certain angle θ is obtained. If the intensity of the radiation recorded by the detector is plotted as a function of 2θ the powder diffraction pattern of the sample is obtained. Since each peak can be associated with a certain distance d between atomic planes, the powder pattern in principle allows the identification of the structure of the compound investigated. To gain a 'reflection' of the x-rays at the atomic planes, it is obvious that θ can be varied in a range between slightly above 0° and slightly beneath 90°. For 0° no reflection is possible and for $\theta > 90°$ the pattern is mirrored. In the range from 0° to 90° $\sin\theta$ increases from ≈ 0 to ≈ 1 which means that a large d is connected with a small angle of incidence θ. Furthermore, with decreasing wavelength of the X-ray radiation used, the angle of incidence for a constructive interference for a certain distance d between atomic planes decreases.

If the compound is found to crystallize in a cubic structure the lattice parameter a can easily be calculated:

$$a = d(h^2 + k^2 + l^2)^{\frac{1}{2}} \tag{9}$$

With h, k and l being the Miller-Indices. To understand the meaning of the Miller-Indices we have to look at a unit cell of a crystal. The unit cell is defined by its three vectors $\vec{a}$, $\vec{b}$ and $\vec{c}$ and the angles between them. Each point in the lattice can therefore be described by a vector $\vec{g}$ being a sum of the three vectors:

$$\vec{g} = u\vec{a} + v\vec{b} + w\vec{c} \tag{10}$$

The triple of numbers uvw describes a point in the lattice. Two points can define a line in the lattice. Since all the lines can be parallel shifted such that one of the points becomes 000, a line can therefore be defined by one triple giving the direction of the line which is denoted as $[uvw]$. Thus, the triple $[uvw]$ describes a regiment of lines orientated in one direction in the lattice. To define a plane in the lattice, again three numbers are necessary that describe the points at which this plane subtends the coordination axis, thus, the *a* (m00), *b* (0n0) and *c* (00p) axis. The Miller indices are the inverse of these numbers. Therefore, a plane subtending the axis at (214) is described by the Miller indices ($\frac{1}{2}\frac{1}{1}\frac{1}{4}$). To get integer numbers the least common multiple of the denominator has to be found. This leads to the Miller-Indice (241).[1]

According to the Bragg equation one might expect the diffractogram to consist of single bars with no extent in the 2θ dimension. This is, of course, not the case since there is still constructive interference for $2d\sin(\theta \pm \delta\theta)$. Furthermore there is a small phase shift of the X-ray radiation when passing through an atomic plane due to thermal motion of the atoms. Scattering at multiple atomic planes leads to an accumulation of these phase shifts. Thus, the diffractogram consists of peaks with a narrow top and broad base. The peak width, or to be more exact the full width at half maximum (FWHM), is influenced by several factors which can be separated into instrumental broadening due to imperfections of the diffractometer as well as general effects of the measuring principle, and broadening caused by properties of the sample. The latter ones are primarily a small crystallite size and heterogeneous strain. The sharpness of the peaks is connected to the number N of scattering centers for the X-rays. The more parallel atomic planes formed by the atoms or ions scattering the X-rays, the sharper the peak becomes. Thereby the phase difference δ between the rays interfering has to satisfy the condition $\delta = 360°/N$ for destructive interference. Hence, for small crystallites with diameters smaller than about 1 μm an increase of the peak width can be observed due to the reduced number of scattering centers in these crystallites. If the crystallite size becomes too small, there will be no peaks visible at all and the sample is denominated as non-crystalline or amorphous. So the transition from nano-crystalline to amorphous materials is not easy to define by XRPD measurements.

To calculate the average crystallite size or the lattice strain from the FWHM of the XRPD peaks the FWHM has to be decreased by the instrumental broadening effects. For that purpose the diffractogram of a single crystalline material is recorded. From that pattern the FWHM of the peaks is determined. The difference of the two widths gives the width of the peaks caused by the properties of the sample itself, denominated as β. With this information the equation introduced by Scherrer can give the average crystallite size, i. e., the average diameter of the crystallites $\langle d \rangle$:

$$\langle d \rangle = \frac{K\lambda 360°}{2\pi\beta[°2\theta]cos\theta} \tag{11}$$

Thereby, K is a geometric factor which is 0.89 in case of spherical crystallites. However, since the crystallite size is not the only value influencing the FWHM of the XRPD peaks, the values obtained from the Scherrer equation commonly underestimates the average crystallite size. As already mentioned, a main source for peak broadening is heterogeneous strain or microstrain ε. Microstrain means a local change of d due to structural disorder. It is defined as follows[2]:

$$\varepsilon = \frac{d_{\text{hkl}} - d_{\text{hkl,0}}}{d_{\text{hkl,0}}} \tag{12}$$

Thereby, d_{hkl} is a distance between atomic planes in the strained system and $d_{\text{hkl,0}}$ the same in the non-strained system. Thus, ε gives the deviation-width of d_{hkl} from $d_{\text{hkl,0}}$. To calculate both, the average crystallite size and the microstrain, in 1953 Williamson and Hall introduced the following equation[3]:

$$\frac{\beta\cos\theta}{\lambda} = 4\varepsilon\frac{\sin\theta}{\lambda} + \frac{1}{\langle d \rangle} \tag{13}$$

A plot of $\frac{\beta\cos\theta}{\lambda}$ as a function of $4\frac{\sin\theta}{\lambda}$ gives points which can be fitted with a line. The slope of this line gives ε and the intercept with the ordinate the inverse average crystallite size. Expectedly, the crystallite sizes calculated this way are larger than the ones calculated with Scherrer's equation.

However, the correct estimation of the average crystallite size of a compound remains a non-trivial task. In principle it can also be done by transmission electron microscopy, but several thousands of crystallites have to be analyzed to get a hardly significant statistics. Another way is the simulation of the XRPD pattern by assuming the crystallite size and microstrain. The average crystallite size can also be estimated from the pair distribution function of a sample gained from scattering experiments as shown in this work for the system $\mathrm{Ba}_{1-x}\mathrm{La}_x\mathrm{F}_{2+x}$.

As already discussed the scattering angle θ at which a peak occurs in the diffractogram depends on the wavelength of the X-ray radiation used. This makes a comparison of patterns difficult. To avoid this problem the scattering vector $\vec{q}$ can be used which is the vector difference between the vectors of the incoming radiation $\vec{k_0}$ and the scattered radiation $\vec{k_0'}$: $\vec{q} = \vec{K'} - \vec{k'}$ with $|\vec{k_0'}| = |\vec{k'}| = 2\pi/\lambda$. The connection between the scattering angle θ and the absolute value of the scattering vector $\vec{q}$ is given in the following equation (for elastic scattering)[4]:

$$q = 2k_0 \sin(\theta) = 4\pi \sin(\theta)/\lambda \tag{14}$$

As commonly known the diffraction pattern of a compound represents the arrangement of the scattering objects in reciprocal space. Where $\vec{r}$ is the position vector of an atom or ion in normal space, $\vec{q}$ is the position vector of them in reciprocal space. Thus, a Fourier transformation of the diffraction pattern should lead to a pattern being a function of $\vec{r}$. For this purpose the XRPD pattern in which the intensity I_e of the elastically scattered radiation can be found as a function of q has to be converted to the structure factor $S(q)$[5]:

$$S(q) = 1 + \frac{I_e(q) - \left[\sum_{i=1}^{n} c_i f_i^2(q)\right]}{\left[\sum_{i=1}^{n} c_i f_i(q)\right]^2} \tag{15}$$

Thereby, c_i and f_i are the atomic concentration and scattering factors of the atomic species in the sample. To get I_e the diffraction pattern has to be corrected for absorption, fluorescence and inelastic Compton scattering.

From the structure factor the total reduced pair distribution function, $G(r)$, can be calculated by a Fourier transformation[4,5]:

$$G(r) = 4\pi r[\rho(r) - \rho_0] = \frac{2}{\pi} \int_0^{q_{\max}} q(S(q) - 1)\sin(rq)dq \tag{16}$$

Thereby, $\rho(r)$ and ρ_0 are the local and average atomic number densities, respectively. r is the radial distance. This function gives the probability to find an atom or ion in a certain distance r from each other. Thus, information about the microstructure of a compound can be obtained which is of particular interest in case of disordered materials. However, as can be seen from equation (16) an integration from $q = 0$ to a maximum value of q is done. Hence, the larger q, the better the resolution of $r(q)$. Commonly a q-value of at least 15 Å^{-1} should be used. Nonetheless, in case of Cu-Kα radiation with λ = 0.154 nm $q_{\max}$ would be about 7 Å^{-1}. Ergo X-rays with smaller wavelengths should be used. Furthermore, the radiation should be highly monochromatic and of high intensity. Therefore, synchrotron radiation is commonly used for this purpose.

References

[1] W. Borchardt-Ott, "Kristallographie - Eine Einführung für Naturwissenschaftler", Springer-Verlag Berlin Heidelberg, 7. überarbeitete und erweiterte Auflage, 2009, pp. 9.

[2] T. Saito, N. Minakawa, Y. Morii, Z. Xiao, T. Sasaki, Y. Hirose, Adv. X Ray Anal. 47 (2004) 181.

[3] G. K. Williamson and W. H. Hall, Acta Metall. 1 (1953) 22.

[4] Th. Proffen, S. J. L. Billinge, T. Egami, D. Louca, Z. Kristallogr. 218 (2003) 132.

[5] W.-C. Pilgrim, J. R. Stellhorn, S. Hosokawa, Bunsenmagazin 3 (2013) 131.

6 Diffusion in solids

Diffusion is the random movement of particles in space. In case of particles of different species A and B which are at the time $t = 0$ separated from each other, diffusion leads to an intermixing of these particle species exhibiting a transport of species A to the spatial region of species B and of species B to the spatial region of species A. Thus, the diffusion of particles equalizes an initial concentration gradient by creating a flux of particles $\boldsymbol{j}$:

$$j = -\boldsymbol{D}^{\mathrm{tr}} \nabla c. \tag{17}$$

Thereby, $\boldsymbol{D}^{\mathrm{tr}}$ is the tracer diffusion coefficient tensor and ∇c the concentration gradient. This is known as Fick's first law. If the number of particles is constant, the following equation describes the change of the concentration of the species due to the diffusion:

$$\frac{\delta c}{\delta t} = \nabla(\boldsymbol{D}^{\mathrm{tr}} \nabla c) \tag{18}$$

This is Fick's second law. If $\boldsymbol{D}^{\mathrm{tr}}$ is independent of the concentration, the following equation is obtained:

$$\frac{\delta c}{\delta t} = \boldsymbol{D}^{\mathrm{tr}} \Delta c \tag{19}$$

Since the temperature of a system is given by the energy of its particles the diffusion can be assumed to be dependent on temperature. This dependency can be described by an empiric Arrhenius law:

$$\boldsymbol{D}^{\mathrm{tr}}(T) = \boldsymbol{D}_0^{\mathrm{tr}} \exp\left(-\frac{\Delta H}{RT}\right) \tag{20}$$

Thereby, ΔH is the activation enthalpy of the diffusion and D_0^{tr} a pre-exponential factor. In a solid, the activation enthalpy consists of two parts. The first part is the migration enthalpy which is the energy the atom or ion needs to jump from its position to a vacant site. For a jump the ion has to overcome a potential barrier created by the neighboring ions. In the case that there are many vacant sites for instance due to doping with a heterovalent ion species or a structure with inherently partly occupied sites the activation enthalpy can be understood as migration enthalpy. If, however, defects have to be created thermally, the activation enthalpy is in the most simple case the sum of the migration enthalpy and a fraction of the defect formation enthalpy (depending on the defect formation mechanism).

If the diffusivity of an ion species in a solid shall be investigated, there is commonly no concentration gradient (although it can be created, vide infra). Thus, the self diffusion is investigated. While the diffusion equalizing a concentration gradient can often very easily be observed (e. g., the diffusion of MnO_4^- in water by dropping a small amount of $KMnO_4$ into the water and following the expansion of the violet color), the investigation of the self diffusion is more difficult. This problem can be circumvented by using tracers. A tracer is an isotope of the diffusing species. The tracer is put into the material of which the diffusion coefficient shall be investigated at a certain position. Thus, a concentration gradient is created. After a definite time the material is cooled down to stop or slow down the diffusion and cut into thin slices. If the tracer is radioactive the diffusion coefficient can directly be determined from the radioactivity profile using a suitable solution of the diffusion equation (eq. (19)). Also a non-radioactive isotope of the ion diffusing in the solid can be used for the experiment. The amount of this species at a certain position in the solid can then be estimated by vaporizing the material after the diffusion experiment and analyzing the resulting gas by mass spectrometry. However, the diffusion behavior of that isotope may differ from the one of the most abundant isotope diffusing in the solid (in case of isotopes with small atomic numbers). Furthermore, the extraction or production of isotopes is often elaborate and expensive. In addition to that, in some cases the half-life of the available isotopes is too short for diffusion experiments. Therefore, methods which do not need tracers are needed. There are several methods available like for instance neutron scattering, impedance spectroscopy and several NMR methods. These methods allow the investigation of the diffusion processes on different time scales. Very slow diffusion processes can be investigated by neutron scattering[1] and NMR techniques like spin-alignment-echo (SAE) NMR[2] or 2D NMR[3]. Faster processes are inter alia accessible by impedance spectroscopy, motional narrowing of NMR lines, spin lattice relaxation at low magnetic field strengths and β-NMR[4]. Very fast diffusion processes can be measured by field gradient NMR, β-NMR and spin lattice relaxation experiments at high magnetic field strengths.

The self diffusion is characterized by the self diffusion coefficient D^{sd} which according to Einstein and Smoluchowski can be described as follows:

$$D^{\mathrm{sd}} = \lim_{t\to\infty} \frac{1}{2dt} \langle \vec{R}^2 \rangle \tag{21}$$

Thereby, d is the dimensionality of the diffusion and $\langle \vec{R}^2 \rangle$ the mean squared displacement of the particle observed. In case of a cubic lattice and jumps between neighboring sites D^{sd} can be described as:

$$D^{\mathrm{sd}} = \frac{l^2}{2d\tau} \tag{22}$$

with l being the jump length and τ the mean dwelling time of the ion at a site. This equation is correct in case of uncorrelated jumps of the ions. In real systems jumps of the ions are often at least partly correlated. The jump of an ion from site A to site B creates a vacancy at site A to which the ion can jump back. Obviously, this jump process does not add to the transport of ions in the solid which reduces the mean square displacement of the ions to $\langle R^2_{\mathrm{corr}} \rangle < \langle R^2 \rangle$ and, therefore, the diffusion coefficient. This can be described by a correlation factor f_c:

$$f_{\mathrm{c}} = \lim_{t \to \infty} \frac{\langle \vec{R}^2_{\mathrm{corr}} \rangle}{\langle \vec{R}^2 \rangle} \tag{23}$$

Thus, $0 \leq f_{\mathrm{c}} \leq 1$. Since correlated back and forth jumps do not contribute to the ionic transport but to the spin lattice relaxation or motional narrowing from which the jump rates of the ions can in principle be calculated or estimated, the from equation (22) obtained self diffusion coefficient is larger than the tracer diffusion coefficient in case of correlated jumps:

$$D^{\mathrm{tr}} = f_{\mathrm{c}} D^{\mathrm{sd}} \tag{24}$$

The tracer diffusion coefficient can in principle also be calculated from the direct current conductivity σ_{dc} of a material by the Nernst-Einstein equation (eq. (26)):

$$D^{\mathrm{tr}} = D^{\mathrm{NE}} H_{\mathrm{V}} \tag{25}$$

$$D^{\mathrm{NE}} = \frac{\sigma_{\mathrm{dc}} k_{\mathrm{B}} T}{n q^2} \tag{26}$$

Thereby, H_{V} is the Haven ratio, with $H_{\mathrm{V}} = 1$ for uncorrelated movement of the ions, k_{B} is the Boltzmann constant, n is the effective density of mobile ions and q the charge of the ions.

References

[1] Y. Zhang, M. Tyagi, E. Mamontov, S.-H. Chen, J. Phys.: Condens. Matter 24 (2012) 064112.

[2] B. Ruprecht, M. Wilkening, R. Uecker, P. Heitjans, Phys. Chem. Chem. Phys. 14 (2012) 11974.

[3] P. Bottke, D. Freude, M. Wilkening, J. Phys. Chem. C 117 (2013) 8114.

[4] P. Heitjans, Solid State Ionics 18 & 19 (1986) 50.

7 Impedance spectroscopy

The conductivities of the samples investigated within this study were measured by impedance spectroscopy. The impedance Z is the electric resistance to an alternating voltage $V(t) = V_0 \exp(i\omega t)$ with the angular frequency $\omega = 2\pi f$ resulting in an alternating current $I(t) = I_0 \exp(i(\omega t - \theta))$ with θ being the phase angle between current and voltage and $i = \sqrt{-1}$ the imaginary unit. Thereby, the amplitude of the voltage used is in the order of 20 mV for a nearly linear response of the system.[1] It should be noted that a phase angle $\theta \neq 0$ is only observed if the sample has a capacitative or inductive resistance causing a delayed response of the system[1]. In case of an ohmic resistor $\theta = 0$.

The complex impedance Z^* can be calculated similarly to the resistance $R = V/I$ of an ohmic system:

$$Z^* = \frac{V(t)}{I(t)} = \frac{V_0 \exp[i(\omega t)]}{I_0 \exp[i(\omega t - \theta)]} = Z_0 \exp(i\theta) \tag{27}$$

The inverse of the complex impedance is denominated as admittance $Y^* = 1/Z^*$.[1] The normalized quantity of the admittance is the conductivity σ^*. In the case that the measurements are done at a sample with plane parallel electrodes (as (in approximation) done in the case of the conducted experiments), then

$$\sigma^* = Y^* d/A \tag{28}$$

with d being the thickness of the sample and A being the surface of an electrode (in approximation both electrodes have identical surfaces).

The complex values like impedance, admittance and, thus, conductivity can be separated into a real (Z') and a complex part (Z'').[1]

$$Z^* = Z' + Z'' \tag{29}$$

$$Y^* = Y' + Y'' \tag{30}$$

$$\sigma^* = \sigma' + \sigma'' \tag{31}$$

In an admittance spectra as shown in several of the following chapters the real part is plotted as a function of frequency. From the frequency independent plateau the direct current (DC) admittance is estimated which is then transformed into the real part of the conductivity σ', being the dc conductivity.

The impedance is usually measured as a function of frequency and temperature. Time-response-measurements (dc) and Impedance Spectroscopy are connected via Fourier Transformation. For practical reasons, impedance spectroscopy is used for fast processes (ionic hopping) while slow processes (polarization) are investigated by time-response measurements.

References

[1] E. Barsoukov, J. R. Macdonald, editors, "Impedance Spectroscopy", John Wiley & Sons, Inc. Hoboken, New Jersey, 2005.

8 NMR

8.1 The nuclear spin

Fermions like protons, electrons and neutrons are characterized by a half-integer spin s = 1/2, while bosons are characterized by an integer spin s = 1. The spin is the quantum-mechanical analogon to the classical angular momentum creating a magnetic dipole. The spin of the electron is the origin of paramagnetism of atoms and molecules due to unpaired electrons (the spins of paired electron cancel out each other). The spins of the nucleons in a nuclei couple and, thus, give the nucleus a combined spin: the nuclear spin $I = \frac{1}{2}n$ with $n \in \mathbb{N}$. In case of odd mass numbers of the nuclei a half-integer nuclear spin is obtained as observed for, e. g., ^{1}H ($I = 1/2$), ^{7}Li ($I = 3/2$), ^{19}F ($I = 1/2$) or ^{27}Al ($I = 5/2$)[1]. If the number of protons and the number of neutrons forming a nucleus are both even this leads to a canceling of the spins[1]. Examples are ^{12}C ($I = 0$), ^{16}O ($I = 0$) or ^{40}Ca ($I = 0$). Integer spins are observed for nuclei with odd numbers of protons and neutrons like it is the case for ^{6}Li ($I = 1$), ^{14}N ($I = 1$) or ^{138}La ($I = 5$). This is valid for the nuclei in their ground-state. The spin of a nucleus can be changed by the absorption or emission of a high-energetic photon. For example, $I = 1/2$ for ^{57}Fe. If it absorbs a γ-quant of the right energy (14.4 keV) its spin changes to 3/2.[2]

The absolute value of the nuclear spin is given by $|\vec{I}| = \sqrt{I(I+1)}\hbar$, with $\hbar = h/2\pi$ and h being the Planck constant. Thus, $\vec{I}$ is quantized. If we define the direction of the magnetic field as the z-axis, then

$$|\vec{I_z}| = m\hbar \tag{32}$$

$$m = I, I-1, ..., -1 \tag{33}$$

with m being the magnetic quantum number.

8.2 Nuclear magnetic resonance spectroscopy

The nuclear spin is connected to its magnetic moment by

$$\vec{\mu} = \gamma\vec{I} \tag{34}$$

with γ being the gyromagnetic ratio which can be calculated as follows:

$$\gamma = \frac{g_I \cdot \mu_N}{\hbar} \tag{35}$$

$$\mu_N = \frac{e \cdot \hbar}{2m_{\text{proton}}} \tag{36}$$

with g_I being the empirical and nuclear specific Landé g-factor, e the charge of the electron, m_{proton} the mass of the proton and μ_N the nuclear magneton. If nuclei with $I \neq 0$ are brought into an external magnetic field B_0 the magnetic moments connected with their spins will interact with the magnetic field. The sum of the magnetic moments aligned in the magnetic field gives the measurable quantity, the so called magnetization

$$\vec{M} = \sum_i \vec{\mu}_i. \tag{37}$$

The potential energy of the nucleus with $I \neq 0$ depends on its alignment in the magnetic field:

$$E = -\vec{\mu}\vec{B_0} \tag{38}$$

giving combined with equations (32) and (34):

$$E = -\gamma m\hbar B_0. \tag{39}$$

Thus, in case of a nucleus with $I = 1/2$, when brought into a magnetic field, there are two possible energetic states distinguishable with $m = +1/2$ and $m = -1/2$, in case of a nucleus with $I = 3/2$ there are four energetic states due to four possible values for m: $m = +3/2$, $m = +1/2$, $m = -1/2$ and $m = -3/2$. They are called Zeeman levels named after Pieter Zeeman (1865-1943). In general the number of different Zeeman levels is $m = 2I+1$. As can be seen from equation (38), the energy difference between these states is equal. Thereby the +1/2 level has a lower energy than the -1/2 level (cf. equation (38)). This leads to a preference of the +1/2 level creating a magnetization $\vec{M}$ in direction of the field, thus, along the z-axis.

Transitions between the Zeeman levels can be initiated by the absorption or stimulated emission of a photon with its spin being $s = 1$ (spontaneous emission is a rather rare event here[3]). Due to the conservation of angular momentum only transitions between neighboring levels are possible. Thus, for a transition the change of energy is:

$$\Delta E = h\nu = \hbar\gamma B_0 = \hbar\omega_0 \tag{40}$$

with ω_0 being the Larmor precession of the magnetic moments. The Larmor precession is caused by the angular momentum $\vec{T}$ acting upon the magnetic moments, created by the magnetic field B_0:

$$\vec{T} = \vec{\mu} \times \vec{B_0} = \mu B_0 \sin\theta \tag{41}$$

Thus, the magnetic moments of the nuclei precess around the z-axis in a cone-shaped fashion.

The occupation ratio of the Zeeman levels can be calculated as exemplarily shown in the following for ^{19}F situated in a magnet with the magnetic field strength of 14.1 T at a temperature of 293 K.

$$\frac{N_{+1/2}}{N_{-1/2}} = \exp(-\Delta E/kT) = \exp(-\hbar\gamma B_0/kT) \tag{42}$$

$$\approx \exp(-6.626x10^{-34}/2\pi \cdot 2.52x10^{8} \cdot 14.1/1.380x10^{-23} \cdot 293) = 0.9991 \tag{43}$$

Thus, in this case the ratio is about 1111 nuclei situated at the lower energetic Zeeman level to 1110 nuclei situated at the higher energetic Zeeman level.

If a photon with the Larmor frequency $\omega_0/2\pi = \nu_0$ of a nucleus interacts with that nucleus in the magnetic field it comes into resonance with it and the nucleus can attain the next higher energetic level (absorption) or the next lower energetic level (stimulated emission).

For an NMR experiment the sample is put into a coil and placed in the magnetic field. The magnetic moments of the nuclei will align to the direction of the magnetic field, thus, to the z-axis. An NMR signal can be measured if the magnetization $\vec{M}$ precesses in the xy-plane since this movement induces an electric current in the coil. To get the magnetization into the xy-plane another magnetic field is necessary. As already shown, the magnetic field $\vec{B_0}$ induces an angular momentum $\vec{T}$ to the magnetic dipoles. Thus, applying an alternating electric current with an angular frequency being the Larmor frequency ω_0 at the coil comprising the sample, a magnetic field $\vec{B_1}$ in the xy-plane is induced. This generates an angular momentum which leads to a precession ω_1 of the magnetization around the x or y-axis. However, two magnetic fields are now acting upon the magnetic moments. This makes the treatment of the system complex. Therefore, the coordinate system is rotated with the Larmor precession ω_0. This eliminates the effect of $\vec{B_0}$ such that the resulting magnetic field acting upon the magnetic moments is $\vec{B_1}$. In case of a $\vec{B_1}$ in direction of the x-axis follows:

$$\vec{\omega}_1(\omega_0) = -\gamma\vec{B}_1(\omega_0) = \frac{\mathrm{d}\theta(\omega_0)}{\mathrm{d}t}\vec{e}_x \tag{44}$$

Thereby, θ is the angle the magnetization is rotated around the x-axis. By varying the field strength of $\vec{B_1}$ or the beam time t, θ can be adjusted:

$$\theta = \omega_1 t \tag{45}$$

Hence, the simplest experiment is the use of a $\pi/2$ pulse to bring the magnetization into the xy-plane. A decaying, sinusoidal signal results, which is, therefore, denominated as free induction decay (FID). The decay is due to the spin-spin relaxation, i. e., a dephasing of the magnetic dipoles. The dephasing is caused by small differences of the local magnetic fields the nuclei experience. These differences are due to inhomogeneities of the magnetic field $\vec{B_0}$ and interactions between the nuclei. Thus, if there are strong interactions, the signal will decay fast. The spin-spin relaxation can be described by an exponential time-law:

$$M(t) = M_0\exp(-\frac{t}{T_2^*}) \tag{46}$$

with T_2^* being the spin-spin relaxation time. As already mentioned it has different origins which can be separated into microscopic variations of the magnetic field due to spin-spin interactions, different electronic environments of the nuclei (= different chemical shifts), dipolar interactions, diffusion et cetera and macroscopic variations of the magnetic field, thus external field inhomogeneities. The latter one means that the magnetic field strength of the applied field B_0 differs at different regions of the sample which has a large impact on T_2^*. To get rid of this part (and other static effects) a Hahn echo (or spin echo) experiment can be performed. For this purpose a $\pi/2$-pulse is applied followed by an π-pulse after an evolution time τ in which the spins dephase. The π-pulse leads to a refocussing of the spins creating an Gaussian shaped signal with a maximum intensity after 2τ. However, only the spins which did not change their precession frequency during the waiting time will be refocussed. Therefore, the exponential decay of the echo-amplitude with increasing waiting time τ is solely due to irreversible spin-spin relaxation characterized by the time constant T_2 instead of T_2^* in eq. (46).

The FID can be transformed from the time-domain into the frequency-domain by a Fourier transform giving the NMR spectrum. It consists of one or several NMR lines situated at different frequencies reflecting the magnetic environments of the nuclei. If a compound which has only one chemical environment for the nuclei observed is measured, the frequency of this signal, ν_{ref}, can be used as a reference. The difference of the frequency of the NMR line of other compounds and the frequency of the reference is the chemical shift $\delta = \frac{\nu-\nu_{\text{ref}}}{\nu_{\text{ref}}}$. It is commonly given in parts per million (ppm) of the spectrometer frequency to compare chemical shifts measured with different spectrometer frequencies. In case of a spectrum recorded with ν_0 = 400 MHz 10 ppm would be 10 ppm x 400 MHz = 4 kHz, in case of ν_0 = 800 MHz it would be 8 kHz. Thus, the higher the spectrometer frequency, the larger the distances between two NMR lines spaced by a certain chemical shift which leads to an increased resolution since the dipolar broadening of the NMR lines is not a function of magnetic field strength, cf. eq. (49).

In case of a fast decay of the signal, the Fourier transform leads to broad NMR lines since the line width of the NMR lines $\Delta\nu$ is given by:

$$\Delta\nu = \frac{1}{T_2^*}. \tag{47}$$

Thus, if the interactions between the nuclei are weak or if they are averaged out due to a fast movement of the nuclei to each other, the decay-time of the FID will be quite long giving narrow NMR lines. This effect can be rationalized by going back to the FID. The FID consists of a superposition of sinusoidal signals with slightly different frequencies caused by the precession of the magnetic moments situated in different magnetic environments of the sample leading to slightly different precession frequencies. The larger the interactions between the nuclei, the larger the differences between the precession frequencies and, therefore, the faster the dephasing of the magnetic moments. If, however, the nuclei change their sites fast, they also change their precession frequency often. If this change is that fast that the phase shift between the different precession frequencies leading to the dephasing cannot build up, an average precession frequency is obtained. Fourier transform of this FID gives a narrow NMR line. This process is called motional narrowing. This is the reason why NMR lines of liquids are much narrower than NMR lines of solids. In the extreme case that all interactions between the nuclei are averaged out, the FID is dominated by the inhomogeneities of the magnetic field which is called extreme narrowing regime. Motional narrowing sets in if the jump rate of the nuclei investigated or the one of its interacting, surrounding nuclei is larger than the full width at half maximum (fwhm) of the non narrowed NMR line. That way the jump rate of the nuclei observed or the one of its surrounding particles can be estimated.

Another important relaxation mechanism is the spin lattice relaxation (SLR). While the spin-spin relaxation is an entropic phenomenon, the SLR is accompanied by a change of the energy of the system. The SLR causes the magnetization $\vec{M}$ to relax towards the z-axis in time t. This process can be described by a single-exponential time-law:

$$M(t) = M_0[1 - \exp(-\frac{t}{T_1})] \tag{48}$$

T_1 is called the spin lattice relaxation time. For the measurements the magnetization is brought into the xy-plane by applying a $\pi/2$-pulse. After a waiting time t the towards the z-axis relaxed magnetization is brought into the xy-plane by applying another $\pi/2$-pulse. Like in case of the measurement of T_2 the variation of the waiting time allows the determination of T_1 by plotting $M(t)$ as a function of t.

SLR is caused by a fast change of the magnitude and direction of magnetic interactions like dipolar coupling, being the most important kind or interaction in this process, between the nuclei creating fluctuating magnetic fields. These induce the nuclei to flip amongst their spin states.[3] The fast change of the interactions is caused by motions of the nuclei to each other since the dipolar coupling depends on the internuclear distance and angular arrangement of the nuclei[3]:

$$K_{\mathrm{AX}} = \left(\frac{\mu_0}{4\pi}\right)\frac{\hbar\gamma_{\mathrm{A}}\gamma_{\mathrm{X}}}{r_{\mathrm{AX}}^3}(2\pi)^{-1} \tag{49}$$

Thereby, A and X are the two different nuclei, μ_0 is the permeability of vacuum and $K_{\mathrm{AX}}(3\cos^2\theta - 1)$ is the splitting of the NMR lines in Hz which, according to the equation, is a function of the distance r_{AX} of the two nuclei and the angle between their connecting line and the z-axis.

The probability that the fluctuations of these local fields have a component oscillating at ω_0 satisfying the resonance condition for an interaction with the respective nucleus gives the rate T_1^{-1} of the relaxation process. This probability is given by the spectral density function:

$$J(\omega) \propto \frac{2\tau_c}{1 + \omega^2\tau_c^2} \tag{50}$$

Thereby τ_c is the correlation time, thus, the time over which two conditions of a system (in this case regarding the magnetic interactions) are still correlated to each other. It can be seen as memory of the system. Therefore, it is closely related to the kind and velocities of the motions of the nuclei. ω is the angular frequency of the oscillation of the magnetic fields acting upon the nuclei observed. Expectedly, J(ω_0) becomes maximal in the case that $\tau_c^{-1} \approx \omega_0$. This can be used to estimate the jump rate of an ion in a solid. If the change of the inter-nuclear interactions is solely due to translational ionic motion, their jump rate is τ_c^{-1}.

To find τ_c the SLR rate T_1^{-1} of a sample is measured at different temperatures (assuming that the mobility of the ion is thermally activated). The temperature at which the rate becomes maximal gives $\tau_c^{-1} \approx \omega_0$. According to the BPP model[4], the dependence of τ_c on temperature can be described by an Arrhenius term:

$$\tau_c^{-1} = \tau_\infty^{-1}\exp\left(\frac{E_A}{kT}\right) \tag{51}$$

τ_∞ is the jump frequency at infinite temperature, E_A the activation energy of the motion of the ions and k is Boltzmann's constant. If this equation is introduced into equation (50) two limiting cases are obtained. For high temperatures, thus, for $\omega\tau_c \ll 1$, T_1 is correlated directly to τ_c, since for this case $\frac{\tau_c}{1+\omega^2\tau_c^2} \approx \frac{\tau_c}{1} = \tau_c$:

$$T_1^{-1} \propto \tau_c \propto \exp\left(\frac{E_a}{kT}\right) \tag{52}$$

$$\ln(T_1^{-1}) \propto \frac{E_A}{kT} \tag{53}$$

while in case of low temperatures, thus, $\omega\tau_c \gg 1$ the following relation is obtained:

$$T_1^{-1} \propto \frac{1}{\omega^2\tau_c} \propto \omega^{-2}\exp\left(\frac{E_A}{kT}\right) \tag{54}$$

$$\ln(T_1^{-1}) \propto -2\ln(\omega) - \frac{E_A}{kT} \tag{55}$$

Thus, an Arrhenius-plot of the SLR rate as a function of the inverse temperature gives the activation energy for the ionic motion observed. In case of low temperatures, thus, for the so called low temperature flank, commonly a smaller activation energy is observed than for the so called high temperature flank since in this regime only short range motion of the ions is observed, while the high-temperature regime (high temperature flank) exhibits the long-range motion processes of the ions. Furthermore, changing ω_0 leads to a shift of the low temperature flank in the Arrhenius plot in the direction of $\ln(T_1^{-1})$.

A technique used for many of the systems investigated in this study is magic angle spinning (MAS) NMR. This technique is used to get rid of the line broadening caused by dipolar interactions between the nuclei and chemical shift anisotropy (CSA). The CSA is due to an anisotropic environment of the nuclei observed such that crystallites with different orientations towards the z-axis and, thus, $\vec{B}_0$, show different chemical shifts. As was already shown in equation (49) the dipolar interactions are a function of the angle between the connecting line between the interacting nuclei and the z-axis. Hence, if the term $(3\cos^2\theta - 1) = 0$, there would be no dipolar interactions. This is the case if $\theta \approx 54.7°$. Since in a powdered sample not all connecting lines between the nuclei will be situated in that angle, and since the chemical shift anisotropy is not affected this way, the sample has to be rotated around this angle. In time-wise average that way all connecting lines of the interacting nuclei form an angle $\theta \approx 54.7°$ with the z-axis. Also the CSA is averaged this way. To achieve this time-wise average the sample has to be spun with a frequency larger than the fwhm of the NMR line to be narrowed. Since the ^{19}F spectra exhibit NMR lines with a broadness in the order of 30 kHz (due to the large gyromagnetic moment of ^{19}F) in case of this nucleus, spinning rates ν_{rot} clearly larger than 30 kHz are necessary. The ^{19}F MAS NMR spectra shown in the following studies were recorded at a spinning rate of 60 kHz. In most cases additional NMR lines can be seen in an MAS NMR spectrum which change their chemical shift with spinning frequency (that way they can be identified in complex spectra). They are called spinning sidebands. They surround the central NMR lines in distances of $n\nu_{\mathrm{rot}}$ with $n \in \mathbb{N}$. The origin of this lines is the fact that the spacial orientations of the connecting lines between the nuclei in relation to $\vec{B}_0$ are the same every $1/\nu_{\mathrm{rot}}$ s. Hence, every $1/\nu_{\mathrm{rot}}$ s the FID contains the signal of the unchanged spectra. Fourier transformation leads to the respective NMR lines.

In case of the ^{27}Al MAS NMR spectra, shown in some of the studies in this work, smaller spinning speeds can be used due to the smaller gyromagnetic ratio of ^{27}Al compared to the one of ^{19}F. However, since this nucleus has a spin $I = 5/2$, it has a nuclear quadrupole moment Q (as all nuclei with $I > 1/2$). The nuclear quadrupole moment leads to a change of the energies of the Zeeman levels in case the nucleus is situated in an electric field gradient, e. g., if it is coordinated by atoms in a non-axial symmetric fashion. Thus, the equidistant Zeeman energy levels are changed to non-equidistant energy levels, such that additional NMR lines are generated. The perturbations of the Zeeman levels can be calculated as shown in the following:

$$E = E^{(0)} + E^{(1)} + E^{(2)} \tag{56}$$

Thereby $E^{(0)}$ is the energy level without perturbation and $E^{(1)}$ and $E^{(2)}$ are the first-order and the second-order perturbations to the Zeeman levels. According to ref. 5 they can be calculated as shown in the following:

$$E^{(0)} = -\gamma m \hbar B_0 \tag{57}$$

$$E^{(1)} = \frac{e^2qQ}{4I(2I-1)}(3m^2 - I(I+1))\frac{1}{2}[3\cos^2\theta - 1) + \eta_Q \cos 2\phi \sin^2\theta] \tag{58}$$

$$E^{(2)} = -\left(\frac{e^2qQ}{4I(2I-1)}\right)^2 \frac{m}{\omega_0} \times \left\{ -\frac{1}{5}(I(I+1) - 3m^2)(3+\eta_Q^2) \right. \tag{59}$$

$$+\frac{1}{28}(8I(I+1) - 12m^2 - 3)[(\eta_Q^2 - 3)(3\cos^2\theta - 1) + 6\eta_Q \sin^2\theta \cos 2\phi] \tag{60}$$

$$+\frac{1}{8}(18I(I+1) - 34m^2 - 5)\left[\frac{1}{140}(18+\eta_Q^2)(35\cos^4\theta - 30\cos^2\theta + 3) \right. \tag{61}$$

$$\left.\left. +\frac{3}{7}\eta_Q \sin^2\theta(7\cos^2\theta - 1)\cos^2\phi + \frac{1}{4}\eta_Q^2 \sin^4\theta \cos^4\phi \right]\right\} \tag{62}$$

Thereby $eq = V_{zz}$ is the anisotropy of the electric field gradient (EFG) $\mathbf{V}$, which is a second rank tensor, $\eta_Q = \frac{V_{xx}-V_{yy}}{V_{zz}}$ is the asymmetry parameter of the EFG (which is zero in case of an axially symmetric electric field gradient), ϕ and θ are the angles emerging from the orientation of the coordination polyhedron surrounding the nucleus with respect to the z-axis. The angular dependence of the perturbation leads to the emergence of a large number of additional NMR lines slightly differing in their chemical shift and, thus, line broadening. The first order perturbation shows a dependence on $3\cos^2\theta - 1$ and, therefore, the first order perturbation can be decreased by magic angle spinning. The second order perturbation, however, does not show such a dependence but exhibits a proportionality to ω_0^{-1} and, thus, to the magnetic field strength. Hence, the second order perturbation decreases with increasing field strength. Thus, to record well separated, narrow NMR lines with chemical shifts close to the ones which would be obtained without the perturbations, the measurements should be done under MAS conditions at a high magnetic field strength. However, the available field strength for a magnet is limited and MAS spinning cannot remove the whole first order perturbation (cf. eq. (58)). Therefore, other techniques like multiple quantum MAS NMR (which will not be treated in this short introduction to NMR spectroscopy) have to be used to get unperturbed spectra of nuclei with $I > 1/2$.

References

[1] M. H. Levitt, "spin dynamics" John Wiley & Sons, Ltd., England, 2008.

[2] P. Gütlich, Chem. unserer Zeit 4 (2004) 133.

[3] P. J. Hore, "Nuclear Magnetic Resonance", Oxford University Press Inc., New York, 1995.

[4] N. Bloembergen, E. M. Purcell, R. V. Pound, Phys. Rev. 73 (1948) 379.

[5] M. J. Duer, "Solid-State NMR Spectroscopy", Blackwell Publishing Ltd., 2004.

9 Increase of the fluoride ion conductivity due to cation-mixing: mechanosynthesis and characterization of metastable $Ba_{1-x}Ca_xF_2$

9.1 Introduction

The synthesis of metastable materials with new or enhanced catalytic, mechanical, optical, magnetical or electrical properties is a mainspring for progress in science and technology.[1–14] Although many materials with potentially interesting properties are predicted to be able to exist, they remain in a theoretical state since the synthesis of these phases is often difficult, see e. g. refs. 1, 15 and 16. Some non-equilibrium materials hardly accessible by thermal synthesis routines were found to be accessible by employing molecular beam epitaxy (MBE) and the use of low temperature substrates.[17–22] Unfortunately, this technique comes along with some disadvantages. For instance, MBE is restricted to the synthesis of small amounts of the metastable material, i. e. thin films with a thickness of about a micrometer or less. Additionally the experimental efforts (temperature, deposition rate, and pressure have to be carefully adjusted to find conditions allowing the deposition of metastable phases on a suitable substrate[1,19,20]) as well as the financial costs are rather high. However, in addition to other techniques being more or less laborious, mechanosynthesis, which is performed by high-energy ball milling, has proven to be a very simple method for the preparation of rather large quantities (at least some grams) of several metastable phases.[11,23–25]

One of the properties most desired for ceramic materials these days is a high ion conductivity. While fast Li ion conductors are in the focus of research also ceramic fast fluoride ion conductors are of interest, for instance for chemical sensors[26,27], but also for high capacity secondary batteries used in particular for high temperature applications[28–39].

There are several basic principles to facilitate fast ion conduction in ceramics which are, e. g., the reduction of the crystallite size[40], doping with aliovalent ions[26] or stabilizing fast ion conducting structures[41]. Another interesting example is the generation of highly conducting interfaces between materials exhibiting moderate ionic conduction. For instance, Sata et al. reported on the preparation of heterolayered films consisting of BaF_2 and CaF_2 by MBE which showed an anionic conductivity parallel to the layers exceeding the ones of the binary fluorides by several orders of magnitude.[42] They assumed that, due to the different standard chemical potentials of fluoride ion interstitials and vacancies in BaF_2 and CaF_2, a certain amount of fluoride ions occupy interstitial sites in CaF_2 close to the interfaces of the layers creating fluoride ion vacancies in the BaF_2 layer. That way space charge regions between the layers are generated.[43] The conductivity increases with decreasing thickness of the layers until the whole bulk material becomes part of the charged and, thus, defective region which exhibits an increased ionic diffusivity.

Another way to increase the ionic conductivity of ceramics is the partial substitution of cations. This has been shown for many oxygen ion conductors but also for fluoride ion conductors.[26,44] For instance, the substitution of Ba ions in BaF_2 by heterovalent ions like rare earth elements (RE) leads to $Ba_{1-x}RE_xF_{2+x}$ compounds with an increased fluoride ion conductivity compared to pure BaF_2.[26] But also in case of isovalent cation substitution ionic conduction can be facilitated. This was, e. g., found for $Ca_{1-x}Sr_xF_2$, crystallizing in the fluorite structure, which in addition exhibit an increased hardness compared to the binary fluorides.[45–48] An even more pronounced effect was found for $Pb_{1-x}Cd_xF_2$ which also crystallizes in the fluorite structure.[49] Therefore, one may assume that $Ba_{1-x}Ca_xF_2$ should also present an increased fluoride ion conductivity. In addition to that, $Ba_{1-x}Ca_xF_2$ may be of some interest for optical applications as it was found for $Ca_{1-x}Sr_xF_2$ and $Ba_{1-x}Sr_xF_2$.[50] Materials with a cubic structure like the fluorite structure do not show birefringence at wavelengths larger than approximately 400 nm. For smaller wavelengths, however, intrinsic birefringence with values of $n_{\langle 110\rangle} - n_{\langle 001\rangle} = \Delta n$ of approximately 10^{-7} can also be observed in materials with cubic structure which decreases the possible resolution of lenses made of these materials.[51,52]

It was found that $\Delta n_{\mathrm{CaF_2}} < 0$, while $\Delta n_{\mathrm{BaF_2}}$ as well as $\Delta n_{\mathrm{SrF_2}} > 0$. Thus, an appropriately composed solid solution of SrF_2 and CaF_2 or BaF_2 and CaF_2 is assumed to show no birefringence at short wavelengths which would ease the use of these fluorides as lens-material for vacuum ultraviolet (VUV) lithography with wavelengths down to 157 nm[51,53]. In this context it should be noted that it is also possible, but tricky, to significantly reduce birefringence in pure CaF_2, see e. g. ref. 54.

However, while CaF_2 and SrF_2 as well as BaF_2 and SrF_2 form end-to-end solid solutions accessible by thermal synthesis[52,55,56] as well as, e. g., by high energy ball milling[23] this is not known for the system BaF_2-CaF_2[55,57] probably due to the large gap between the ionic radii of barium and calcium ions of about 37 pm[58] or approximately 30 pm when the more accurate values of Shannon and Prewitt are used[59]. Although BaF_2 and CaF_2 form solid solutions at elevated temperatures to a large degree, i. e., from $x = 0$ to $x = 0.62(5)$ (α-phase) and from $x = 0.92(2)$ to $x = 1$ (β-phase), they decompose while cooling, see Fig. 2.[60]

Recently, Sorokin et al.[61] tried to synthesize $Ba_{0.30}Ca_{0.70}F_2$ by conventional solid state synthesis and quenching techniques ($\approx$ 250 K/s). They were not able to synthesize the intended compound but a mixture of a Ba-rich ($x = 0.04$) and a Ca-rich ($x = 0.97$) phase was obtained. The different phases are lamellar ordered which is typical for the solidification of an eutectic system. Thereby, a seed-crystal forms at a grain boundary. This is beneficial since by that the surface energy of the seed crystal is reduced. The seed crystal grows, fed by the cations diffusing perpendicular to the growth direction.[62] Thus, the grain boundary moves with the growth front of the crystal through the grain, see Fig. 3 for a simple sketch of the process. Thereby, the space around the crystal is depleted in one species primarily forming the crystal and enriched in the other species. Thus, a concentration gradient forms, leading to a flow of the abundant species away from the growing crystal and, therefore, the growth of a neighboring crystal of the other phase is facilitated. The spatial extent of the crystals is limited by the diffusivity of the cations. A fast cooling reduces the diameter of the layers, while slow cooling should result in thick layers. Thus, it seems plausible that a very fast cooling could prevent the decomposition. It should be noted that two geometries are observed in most cases of eutectic growth which are layers like observed in this case or rods. Which one of these geometries is realized by the system mainly depends on the interface surface energies.[63] Since this structure is resemblant to the one prepared by Sata et al.[42] employing MBE, Sorokin et al. ascribed the enhanced dc conductivity found for their system to the emergence of space charge regions between the lamellae.[61]

Nevertheless, already in 1982 Sullivan et al. reported on the preparation of $Ba_{0.20}Ca_{0.80}F_2$ (by assuming Vegard's law to be applicable in this case) using MBE with a relatively low substrate temperature of about 613 K.[17] They assumed that (Ba,Ca)F_2 compounds should be accessible over the whole range of composition using MBE, see also ref. 18.

In contrast, Schumann et al.[64] found a mixture of $Ba_{0.01}Ca_{0.99}F_2$ and $Ba_{0.92}Ca_{0.08}F_2$ as a result of deposition of a mixture to give $Ba_{0.23}Ca_{0.77}F_2$ using flash evaporation technique. In 1995 Hidaka et al.[65] found some evidence for the formation of metastable $Ba_{1-x}Ca_xF_2$ solid solutions with $x = 0.30$, $x = 0.50$ and $x = 0.70$ grown by MBE on Si doped InP substrates. They used X-ray photoelectron spectroscopy (XPS) for the analysis of the phases prepared.[65] Thus, as already shown for several other metastable phases[1,19–22], also metastable $Ba_{1-x}Ca_xF_2$ solid solutions can most probably be obtained by employing MBE at sufficiently low substrate temperatures[18].

Recently, Ruprecht et al.[66] reported on the preparation of a nanostructured composite of a Ba-rich and a Ca-rich $Ba_{1-x}Ca_xF_2$ phase by high-energy ball milling which exhibited an unexpectedly high fluoride ion diffusivity. For some of these mixtures direct current (dc) conductivities two orders of magnitude higher than the ones observed by Sata et al.[42] for the BaF_2-CaF_2 heterolayers were measured. It should be mentioned that the dc conductivities measured are almost completely due to fluoride ion transport, while the electronic contribution is negligible.[66] Small crystallites of the Ca-rich phase next to even smaller crystallites of the Ba-rich phase were found in these sam-

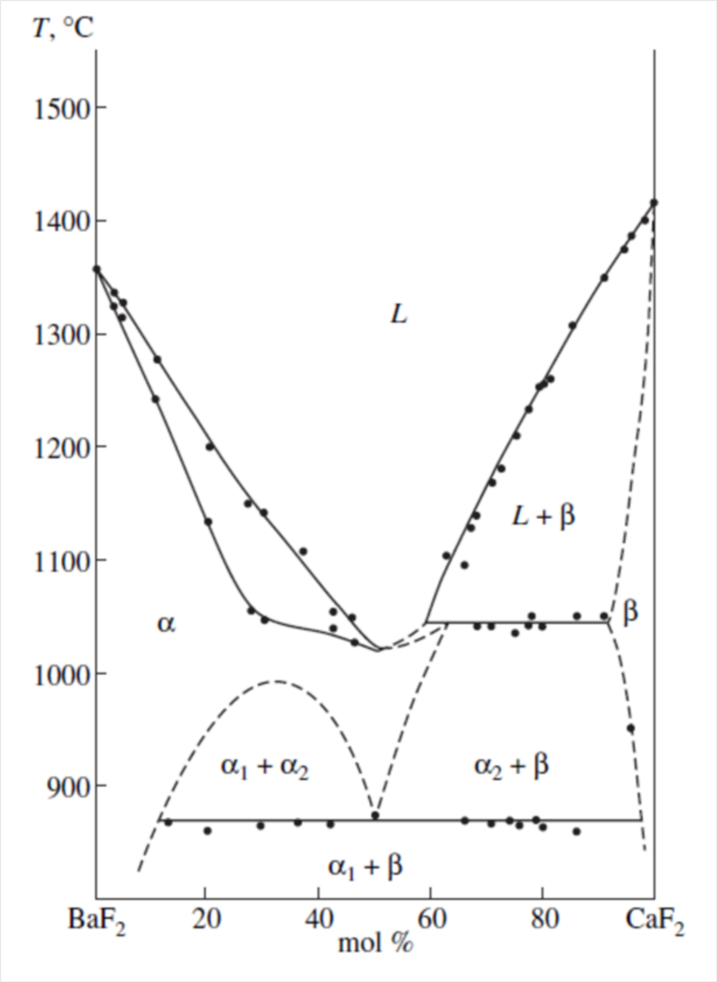

Figure 2: Phase diagram of the BaF_2-CaF_2 system taken from ref. 60. While both components are miscible in the liquid (L) phase they exsolve while cooling, forming a BaF_2-rich (α) and a CaF_2-rich (β) phase.

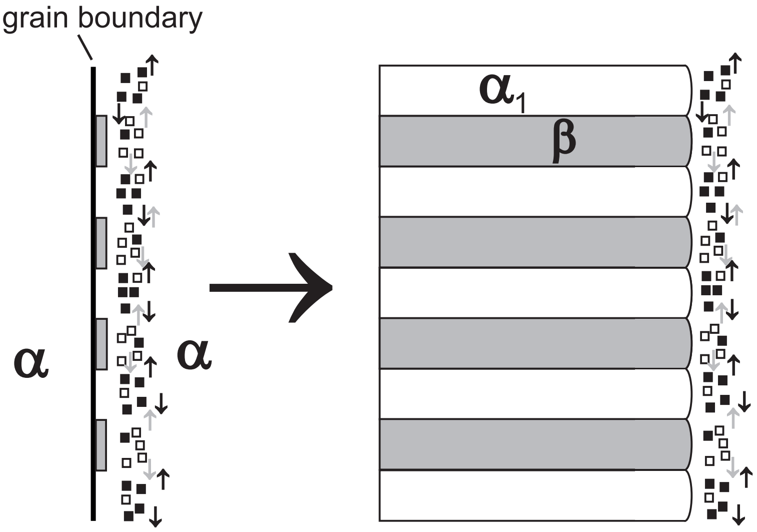

Figure 3: Formation of a lamellar structure starting from a grain boundary between two grains of the α-phase. From the β-phase rejected Ba ions (empty squares) diffuse to the α_1-phase while the abundant Ca ions (black squares) move to the β-phase.

ples by employing transmission electron microscopy (TEM) as analytical tool. This indicates the possibility of a 3D network of space charge regions between these crystallites which may be the origin of the enhanced ionic conductivity. However, some evidence for a "mixed cation effect" being the main reason for the enhanced ionic conductivity rather than space charge regions between the two phases was found.[66] Of course it has to be distinguished between the effect found for $Ca_{1-x}Sr_xF_2$[45–47], $Pb_{1-x}Cd_xF_2$[49] and for $Ba_{1-x}Ca_xF_2$ in which the diffusivity of the anions is increased, and the so called mixed cation effect found in glasses in which mixing of two different mobile cation species leads to a decrease of the cationic conductivity.[67] Therefore, the effect was named as "mixed alkaline-earth effect" in the short publication dealing briefly with the mechanosynthesis, first ^{19}F MAS NMR spectra and conductivity measurements on $Ba_{1-x}Ca_xF_2$, published in 2011 in J. Phys. Chem. C.[68] However, since a very similar effect was also found for $Pb_{1-x}Cd_xF_2$ this name is not appropriate. Hence, the effect will simply be named "enhancement of anion mobility by isovalent cation substitution" effect (abbreviated as EAMICS) in the following. The main focus of this chapter lies on investigations regarding the formation, decomposition and the microstructure of the mechanosynthesized $Ba_{1-x}Ca_xF_2$. Furthermore, some results regarding the structure and ionic conductivity gained for mechanosynthesized $Ca_{1-x}Sr_xF_2$ and mechanosynthesized, annealed and single crystalline $Ba_{1-x}Sr_xF_2$ were added for comparison. The reaction process as well as the structure of the $Ba_{1-x}Ca_xF_2$ compounds were investigated by X-ray powder diffraction (XRPD) (for two samples up to the high q-range to calculate their pair distribution functions) and ^{19}F MAS NMR spectroscopy at a spinning speed of 60 kHz. This combination of techniques allows insight into the macro- as well as the microstructure of the powders obtained. Impedance spectroscopy and static ^{19}F NMR were used to determine the fluoride ion diffusivity in the samples.

9.2 Experimental details

A series of samples with compositions $Ba_{1-x}Ca_xF_2$ with $0 \leq x \leq 1$ were prepared by joint milling of μm-sized pure BaF_2 (99.99%, Sigma Aldrich) and CaF_2 (99.95%, Alfa Aesar). The synthesis was carried out using a Fritsch P7 premium line planetary mill employing a ZrO_2 milling vial set (45 mL) in combination with 140 milling balls (5 mm in diameter) of the same material. The total mass of each mixture was about 2 g. Milling times t_{mill} used reached up to 99 h. Some compositions were also prepared by milling in a vial set made of tungsten carbide with 100 milling balls while keeping all other parameters unchanged. The temperature of the milling beakers did not exceed 350 K while milling. The temperature was measured inside the beaker using a pyrometer directly after the longest milling period applied.

Some of the samples were investigated by high resolution transmission electron microscopy (HR-TEM). Except for the $Ba_{1-x}Ca_xF_2$ sample with x = 0.10, which was investigated by Dr. Andriy Lotnyk at the TEM center of the Christian Albrecht Universität (CAU) Kiel, the samples were investigated by Prof. Dr. Armin Feldhoff in Hannover. The measurements were done with a JEOL 2100F in Hannover and with different devices in the TEM center of the CAU Kiel.

The obtained powders were characterized by XRPD using a Bruker (D8 Advance) diffractometer operating with Cu-Kα radiation at 40 kV which corresponds to a wavelength of $\lambda \approx 0.154$ nm. For four samples PDFs were calculated from diffractograms obtained at the High-Resolution Powder Diffraction (HRPD) beamline P02.1 of the PETRA III electron storage ring at DESY (Hamburg, Germany) in transmission mode by Dr. Jozef Bednarcik. The energy of the synchrotron radiation was set to 59.81 keV, which corresponds to a wavelength of λ = 0.02073 nm. Two-dimensional XRD patterns were collected using a fast image plate detector Perkin Elmer 1621 (2048x2048 pixels, 200x200 μm^2 pixel size) carefully mounted orthogonal to the X-ray beam. The samples were illuminated for 10 s by the X-ray beam. For each sample measurements were done with different distances between sample and detector to obtain the best resolution in the low as well as the high

q-range. The two dimensional XRPD patterns were integrated to the q-space by Dr. J. Bednarcik by employing the software package FIT2D[69] giving several one dimensional XRPD patterns for different ranges of q. These patterns were merged to a single pattern for each sample. The obtained diffractograms were corrected (absorption, fluorescence, Compton scattering etc.) and eventually Fourier transformed to PDF patterns by employing the software PDFgetX2[70].

For the impedance measurements the powders were pressed to pellets with a diameter of 8 mm and approximately 1 mm in thickness (measured with a vernier caliper for each pellet) at an uniaxial pressure of circa 1 GPa. Electrodes were applied by Au evaporation employing an Edwards 306 evaporator. The conductivity measurements were carried out with an HP 4192 A analyzer connected to a home-built cell, which allows measurements in adjustable atmospheres, with a four-terminal configuration in the frequency range from 5 Hz to 13 kHz. For the measurements the pellets were heated in a constant flow of dry nitrogen gas (99.999%) to prevent incorporation of oxygen and to work with samples free of water which would increase the dc conductivity due to proton conductivity. A Eurotherm controller was used to monitor and adjust the temperature.

^{19}F MAS NMR spectra were recorded with two different Bruker Avance III spectrometers operating at 471 MHz and 565 MHz, respectively. The NMR spectra were acquired using a single excitation pulse of approximately 2 μs, and an accumulation number of 32 scans. The spinning speed was ν_{rot} = 60 kHz using room-temperature bearing gas. Static ^{19}F NMR spectra were recorded with an MSL 400 spectrometer connected to a shimmed cryomagnet with a nominal magnetic field of 9.4 T corresponding to a ^{19}F NMR resonance frequency of 376 MHz. For the static ^{19}F NMR measurements the powders were dried at 473 K and vacuum-sealed in glass ampullae.

9.3 Results and discussion

9.3.1 Characterization by X-ray diffraction

In Fig. 4a) the XRPD patterns of $Ba_{1-x}Ca_xF_2$ are shown for $0 \leq x \leq 1$. All samples shown in Fig. 4a) crystallize in the cubic fluorite structure (space group $Fm\bar{3}m$). Starting from pure BaF_2 the peaks shift to larger diffraction angles 2θ with increasing amount of CaF_2 which indicates lattice contraction. The lattice parameter a, calculated according to

$$a = \frac{\lambda}{2 \cdot sin(\theta)} \cdot \sqrt{(h^2 + k^2 + l^2)} \tag{63}$$

as a function of composition x is shown in Fig. 4b). Thereby, λ = 0.154 nm is the average wavelength of the X-ray radiation used, and h, k and l are the Miller indices of BaF_2. With increasing x the lattice parameter a decreases in accordance with Vegard's law as it is also observed for $Ba_{1-x}Sr_xF_2$, and, with decreasing x, for $Ca_{1-x}Sr_xF_2$, see Fig. 4b).

The average crystallite size $\langle d \rangle$ as well as the lattice strain $\varepsilon = (d_{\mathrm{hkl}} - d_{\mathrm{hkl,0}})/d_{\mathrm{hkl,0}}$, whereby $d_{\mathrm{hkl,0}}$ is a distance between atomic planes in the non-strained system, and d_{hkl} the respective one in the strained system, were estimated by employing the equation introduced by Williamson and Hall[71]:

$$\frac{\beta_r cos(\theta)}{\lambda_{\mathrm{XRD}}} = 4\varepsilon \frac{sin(\theta)}{\lambda_{\mathrm{XRD}}} + \frac{1}{\langle d \rangle}. \tag{64}$$

Thereby, β_r denotes the difference of the full linewidth at half maximum (fwhm) of the XRPD peaks measured and the instrumental peak broadening (which is assumed to be 0.1°2θ, estimated from the XRPD pattern of a $BaLiF_3$ single crystal). The $\langle d \rangle$ values were in the range from 19 to 46 nm for the samples shown in Fig. 4a) while the lattice strain ε varied in a range from 0.002 to 0.008, see Fig. 5. The lattice strain is largest for the samples with $0.30 \leq x \leq 0.80$ reflecting the mismatch of

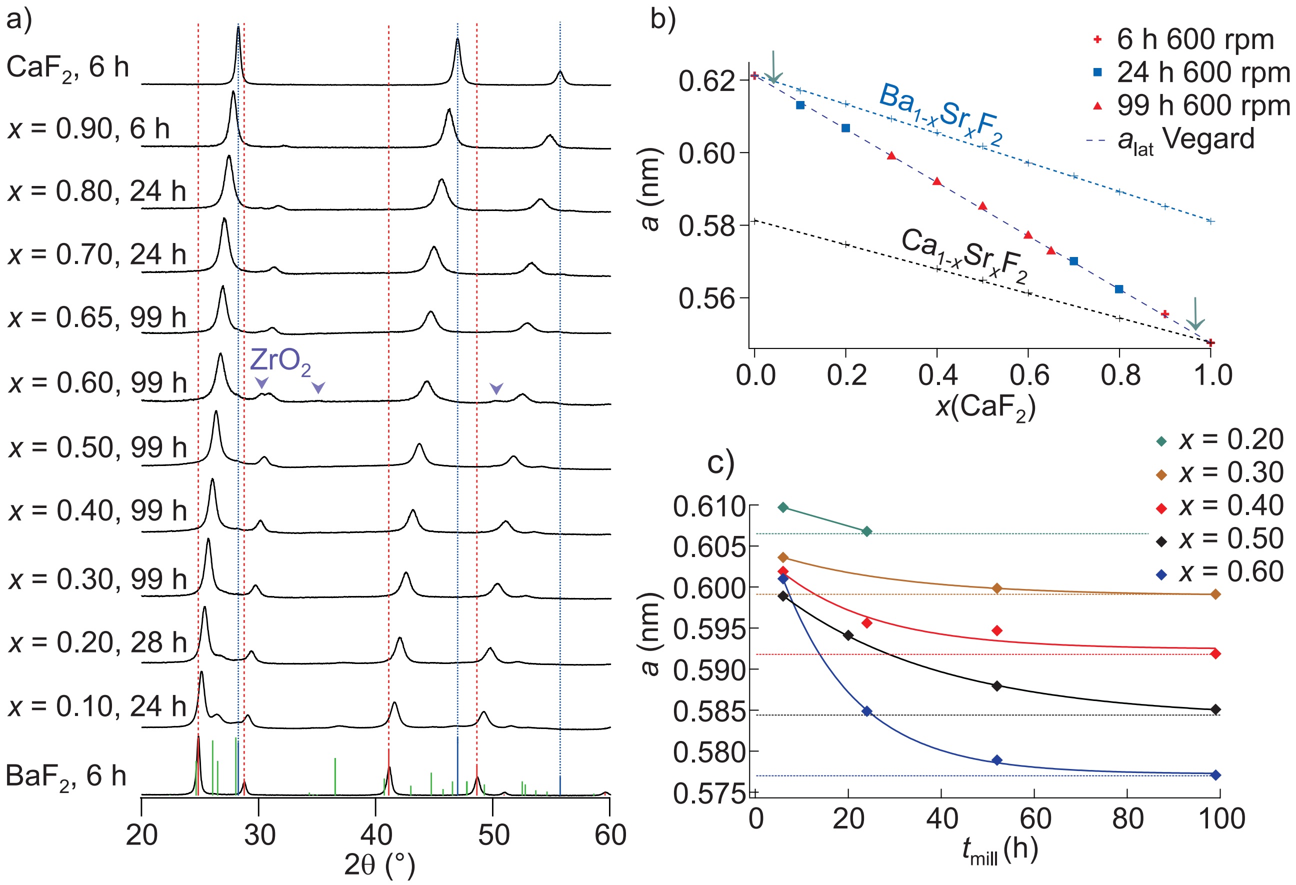

Figure 4: a) XRPD patterns of the different $Ba_{1-x}Ca_xF_2$ samples. With decreasing amount of BaF_2 (red dotted lines) the corresponding peaks shift to larger 2θ values indicating lattice contraction until CaF_2 (blue dotted lines) is reached. For small x also orthorhombic BaF_2 is visible (green bars). In case of the sample with $x = 0.60$ abraded ZrO_2 (violet arrows) shows up. b) lattice parameter a of the synthesized solid solutions as a function of composition. The green arrows mark the compositions reached by thermal synthesis taken from refs. 61,60. For comparison the lattice parameters of several $Ba_{1-x}Sr_xF_2$ and $Ca_{1-x}Sr_xF_2$ samples are also shown. c) dependence of the lattice parameter on t_{mill} for some of the samples. For $Ba_{1-x}Ca_xF_2$ solid solutions in the range from $x = 0.30$ to $x = 0.65$ milling times of 99 h were necessary to reach lattice parameters in accordance with Vegard's law. The lattice parameters in accordance with Vegard's law are indicated by horizontal lines. In case of the samples with $0.30 \leq x \leq 0.60$ the approach to these lines seems to follow an exponential law in the timescale reviewed (see text for further details).

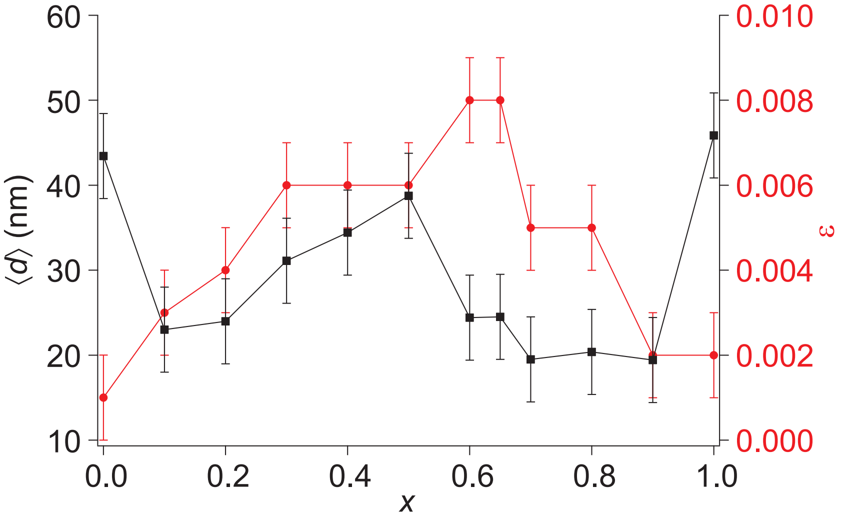

Figure 5: Average crystallite size $\langle d\rangle$ and lattice strain ε as a function of composition x of the $Ba_{1-x}Ca_xF_2$ samples.

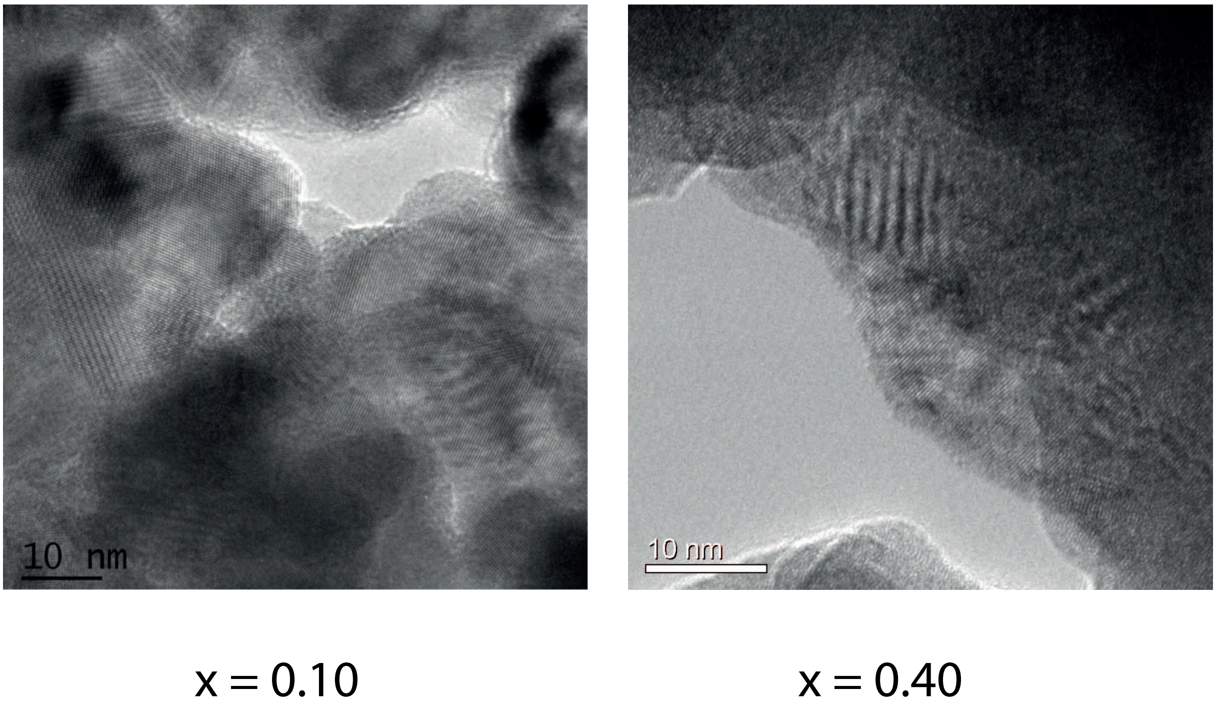

Figure 6: HR TEM micrograph of $Ba_{0.10}Ca_{0.90}F_2$ (left) and $Ba_{0.60}Ca_{0.40}F_2$ (right).

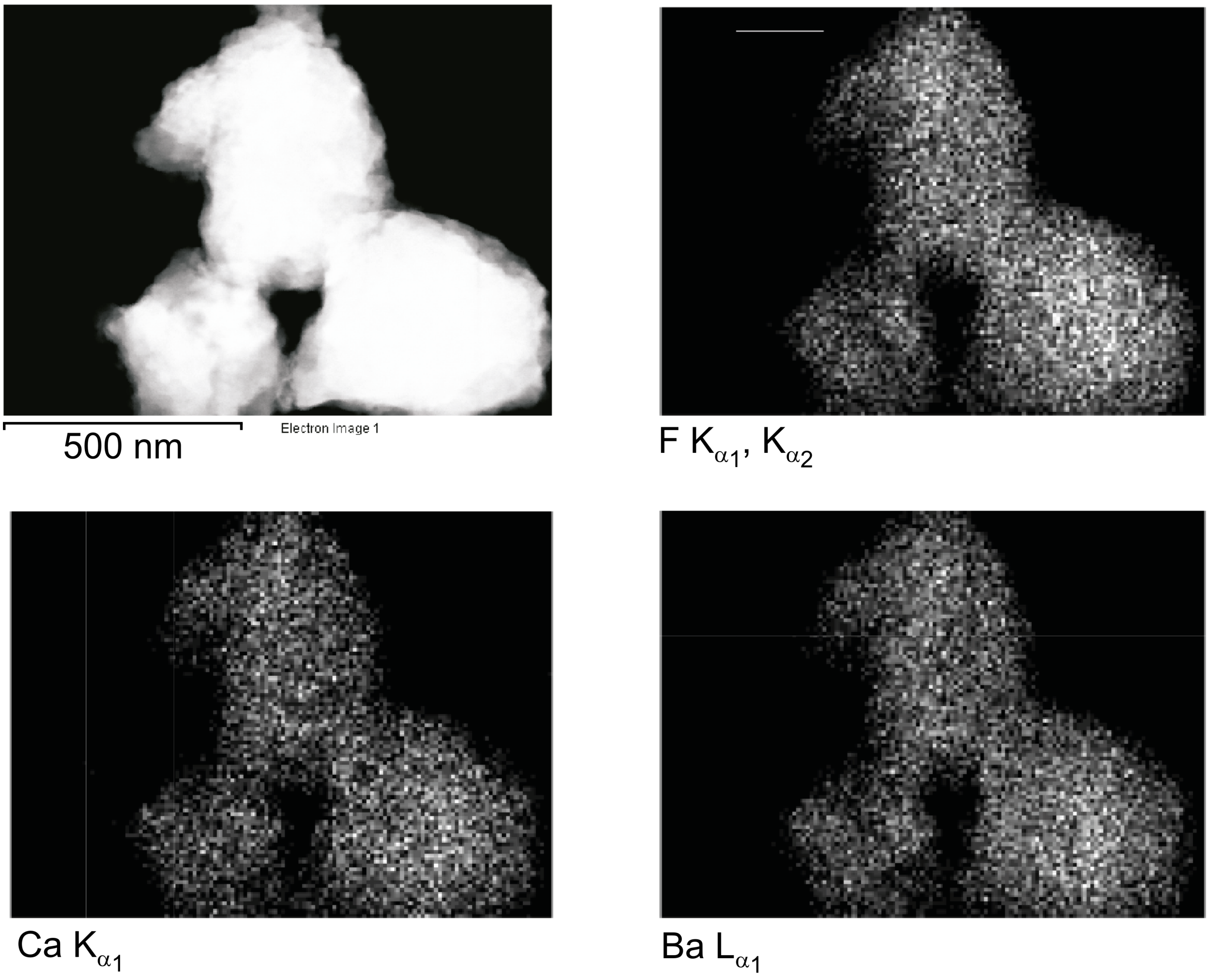
500 nm
Electron Image 1
F K_{α_1}, K_{α_2}
Ca K_{α_1}
Ba L_{α_1}

Figure 7: TEM micrograph of an agglomerate of crystallites of $Ba_{0.60}Ca_{0.40}F_2$ (a) and the spatial distribution of fluorine (b), Ca (c) and Ba (d) in it.

the ionic radii of the Ba and Ca ions leading to a highly distorted lattice. The average crystallite size of the samples increases from $x = 0.10$ to $x = 0.50$ and decreases significantly for $x > 0.50$, see Fig. 5. Therefore, it seems possible that the formation mechanism changes with x resulting in different crystallite sizes of the $Ba_{1-x}Ca_xF_2$. The formation mechanism will be discussed in more detail later. It should be noted, that increasing the milling time for the binary fluorides did not lead to a further decrease of the crystallite size.

In Fig. 6 a HR-TEM micrograph of $Ba_{0.10}Ca_{0.90}F_2$ (measured in Kiel), prepared by 24 h of milling, and a HR-TEM micrograph of $Ba_{0.60}Ca_{0.40}F_2$ (measured in Hannover), prepared by milling for 99 h, are shown. Different nano-crystalline grains can be clearly distinguished by the differently orientated atomic plane regiments. The crystallite sizes are in good agreement with the ones obtained from the XRPD patterns with equation (64). Furthermore, for the sample with $x = 0.40$, the spatial distribution of the elements was investigated by energy dispersive X-ray spectroscopy (EDXS) which was also done in Hannover. As can be seen in Fig. 7 the fluoride ions, the Ca ions and the Ba ions can be found homogeneously distributed in the crystallites which supports the assumption that $Ba_{1-x}Ca_xF_2$ with the intended composition was formed.

For the samples with $x = 0.10$ and $x = 0.20$ a small amount of orthorhombic BaF_2 (space group *Pnam*[72]) can be observed. See Fig. 8 for a magnification of the XRPD patterns of the sample with $x = 0.20$. The behavior of the sample with $x = 0.10$ is very similar to the one of the sample with $x = 0.20$ and, thus, not shown here. The peaks are very broad which points to very small crystallite sizes and especially a distorted lattice since the peaks in the XRPD patterns of nano-crystalline orthorhombic BaF_2 reported by Xie et al.[73] (vide infra) were clearly narrower.

Orthorhombic BaF_2 and phase transformations induced by grinding or milling Orthorhombic BaF_2 is a high pressure polymorph of BaF_2. The high pressure phase transformation from the fluorite structure to the orthorhombic $PbCl_2$ (cotunnite) structure is inter alia also known for CaF_2 and SrF_2.[72,74–76] Orthorhombic BaF_2 (as well as SrF_2 and CaF_2) is metastable at ambient conditions.[72,74] It can be preserved by quenching, i. e., by a fast release of the hydrostatic pressure in the anvil cell.[74] The transition pressure necessary at ambient temperature for the transformation increases with decreasing atomic number. The values reported are: between 2.5 GPa and 3 GPa for BaF_2[72,74,76], 5 GPa for SrF_2[72] and 9 GPa for CaF_2[72]. If large shear forces are introduced into the sample while quenching the amount of orthorhombic BaF_2 which can be preserved at standard pressure is decreased due to the fact that shear forces increase the rate of the phase transformation (in both directions, vide infra).[74] Thus, pressure transmitting media like NaCl[72,74] or other materials with a low shear strength at high pressures[76,77] are used to minimize the shear forces.

Orthorhombic BaF_2 retransforms into the cubic fluorite modification if it is annealed at temperatures ≥ 473 K[74,75]. Seifert[74,75] reported that orthorhombic BaF_2 cannot be obtained at temperatures higher than 773 K even at a pressure of 5 GPa. Samara[78], however reported on a decrease of the transformation pressure with increasing temperature which is assumed to be due to a high activation energy of the phase transformation.

While in the fluorite structure the cations are coordinated by 8 anions, in the cotunnite structure the coordination number is 9 (whereby not all of the distances between F^- and Ba^{2+} are equal).[74] Interestingly, also PbF_2 crystallizes in the cotunnite structure and transforms to the more symmetric fluorite-structure at temperatures beyond 588 K which is metastable at ambient temperature.[74,79] The fluorite-type PbF_2 transforms to the stable cotunnite-type PbF_2 at pressures of approximately 0.4 GPa.[80] The ionic radius of the cation seems to play a decisive role concerning the transition pressures and stabilities of the polymorphs of several binary fluorides as shown by Dorfman et al.[72] Thus, it seems unexpected that PbF_2 ($r(Pb^{2+}) = 0.132$ nm[58] (0.129 nm[59]) is stable in the cotunnite-structure, while the stable modification of BaF_2 ($r(Ba^{2+}) = 0.143$ nm[58] (0.142 nm[59]) is reported to be the fluorite-structure. However, Pb and Ba present different electronegativities

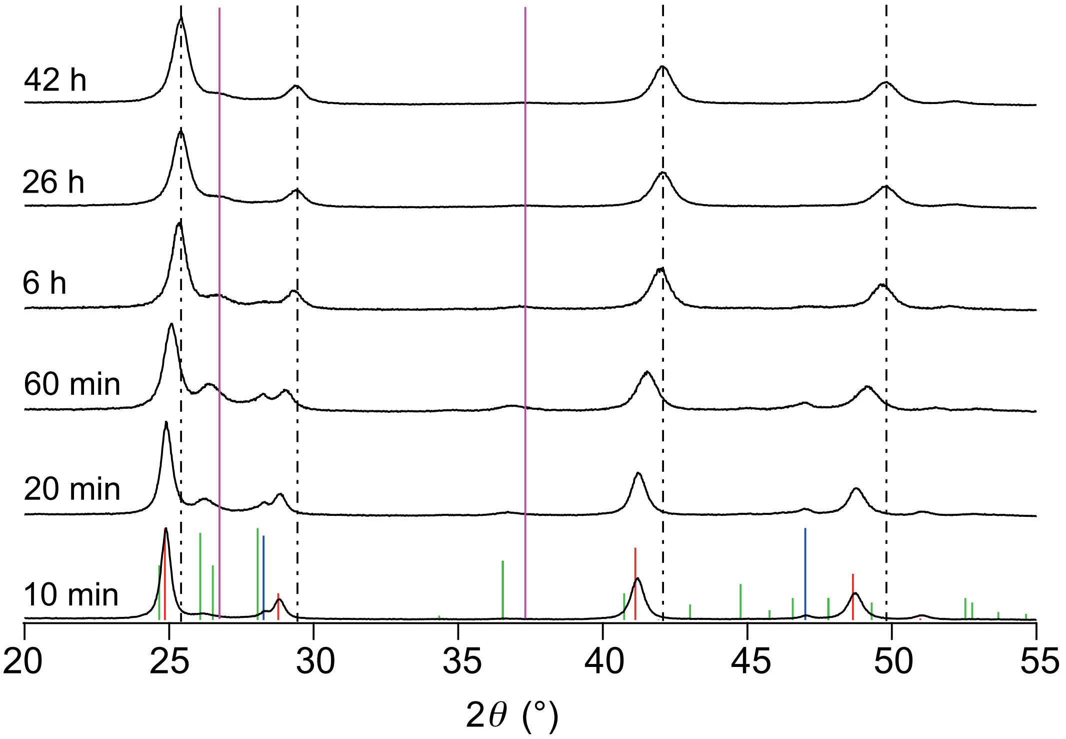

Figure 8: XRPD patterns of a mixture to give $Ba_{0.80}Ca_{0.20}F_2$ milled for different times. With increasing milling time the peaks of BaF_2 shift to larger diffraction angles which indicates lattice contraction due to incorporation of Ca ions. A small amount of orthorhombic BaF_2 (green bars) can be observed whose peaks are increasingly shifted to higher values of 2θ with increasing t_{mill} (magenta bars), which indicates the formation of orthorhombic $(Ba,Ca)F_2$. For milling times of about six hours and longer the amount of the orthorhombic phase decreases compared to the sample milled for 60 minutes.

(Pb: 2.33, Ba: 0.89, by using the values introduced by Pauling) which leads to different covalent characters of the M-F bonds in PbF_2 (Δ_{EN} = 1.67) and BaF_2 (Δ_{EN} = 3.11) which influences the stability of a crystal structure.

The fluorite → cotunnite phase transformation in PbF_2 is reported to be reconstructive[81] while Seifert[74] assumed the transformation of fluorite-type BaF_2 to cotunnite-type BaF_2 to be dilatational, i. e., that the cotunnite structure is obtained by a deformation of coordination polyhedra in the fluorite structure and not due to a reconstructive process. However, regarding the evidences found for a high activation energy for the phase transformation found by Samara[78] a dilatational process seems not to be very likely.[82] A reconstructive phase transformation of cubic BaF_2 to orthorhombic BaF_2 would also be in accordance to the observation of Smith et al.[83] They found a very sluggish phase transformation when treating cubic BaF_2 with hydrostatic pressure in contrast to a rather fast transition in a non-hydrostatic pressure experiment. Seifert[74], however, reported on a fast phase transformation of cubic BaF_2 to orthorhombic BaF_2. This contradiction may be solved if the role of shear stress is regarded.[83–86] Shear stress leads to the rupture of bonds which probably ease and, by this accelerates a reconstructive process which, therefore, seems to be the more probable phase transformation process, here. However, the true nature of the mechanism of the phase transformation of cubic BaF_2 to orthorhombic BaF_2 remains, as far as the literature known to the author is regarded, to be clarified.

If the pressure acting upon the BaF_2 is increased further, the cotunnite structure transforms to the Ni_2In structure in which the cations are coordinated by 11 anions.[76] The pressures needed for this transformation are 14 GPa, 29 GPa, and 72 GPa for BaF_2, SrF_2 and CaF_2, respectively.[72] In contrast to the cotunnite structure the Ni_2In structure is probably not metastable at ambient conditions.[72]

Orthorhombic BaF_2 often forms if cubic BaF_2 is high-energy ball milled.[23,66] It should be noted that it was not possible to produce orthorhombic SrF_2 or orthorhombic CaF_2 by high-energy ball milling within this study (even after 2 h at 1000 rpm in a tungsten carbide vial set no orthorhombic SrF_2 was observable). Interestingly, large amounts of metastable orthorhombic BaF_2 can be obtained if BaF_2 is milled together with NaCl, KF, CaO or BaO (NaCl-structure, space group $Fm\overline{3}m$[87]) or, less pronounced, with compounds like SiO_2 (space group $P3221$[88,89]) or yttrium stabilized ZrO_2 (space group $Fm\overline{3}m$[90]) in a molar ratio of 9 (BaF_2) to 1 ensuring a high probability of a contact between the two compounds. The mechanical treatment of BaF_2 with γ-Al_2O_3 crystallizing in a highly complex structure which is assumed to be a kind of defect spinel structure (γ-phase)[91], respectively, also leads to the formation of large amounts of orthorhombic BaF_2. Thus, it seems that the mechanically induced formation of orthorhombic BaF_2 can be clearly facilitated by joint milling of BaF_2 with a compound BaF_2 does not react with to a new non-binary phase (unlike, e. g., BaF_2 + LiF → $BaLiF_3$) while milling. XRPD patterns and some ^{19}F MAS NMR spectra of these composites are shown in the supplement to this chapter.

If the maximal pressure of one ball at the wall of the beaker under the milling conditions used is calculated by employing the formula introduced by Hertz[92]

$$p_{max} = \frac{1}{\pi} \cdot \sqrt[3]{\frac{1.5FE^2}{r_b^2(1-\nu^2)^2}} \tag{65}$$

$$F = \frac{mv^2}{r} \tag{66}$$

(ZrO_2 milling balls with a diameter $d = 2r_b = 5$ mm, radius of the sun gear $r_{sg} = 9.1$ cm, radius of the milling beaker $r_{mb} = 2.35$ cm, rotational speed set to 600 rpm, Young's modulus $E = 205$ GPa and Poisson's ratio $\nu = 0.3$[93], $\rho = 6.06$ g cm^{-1} (declared by Fritsch)), a maximum pressure of about 0.40 GPa is found. Thus, the pressure is too low for the transformation by almost a factor of 10.

However, it has to be considered that, in addition to friction between the balls and the wall and in-between the balls, energy is also introduced by impacts of balls at the beaker walls and other balls.[94,95] Furthermore, the interactions between the milling balls is highly chaotic but nevertheless a distribution of kinetic energy of the milling balls can be assumed. This can easily be exemplified by putting the milling balls into a sieve which is gently shaken. The positions of most of the milling balls do not change in a pronounced way. However, over time a few of the milling balls gain so much kinetic energy that they can leave the sieve. Thus, it seems plausible to assume that a broad distribution of pressures is introduced into the material. Anyhow, already in the 1950s the formation of high pressure polymorphs just by grinding the low pressure polymorphs was observed.[84,96,97] A popular example is PbO_2. It transforms at pressures as high as 10 GPa from the rutile to an orthorhombic structure[98] which can already be achieved by grinding in a mortar or milling in a shaker mill.[84] It was shown that the reaction is only due to hydrostatic pressure since shear stress does not alter the hydrostatic pressure needed for the phase transformation but only the transformation rate (vide supra)[83–86]. Thus, the formation of at ambient conditions metastable high pressure polymorphs by milling may deliver information about the maximum pressures occurring while milling in a specific (ball) mill under specific conditions (material of the vial set, speed, ball to powder ratio).

For BaF_2 the transformation to the cotunnite phase was observed after treatment of a powdered sample in a roller mill.[74,75] It should be mentioned, that the orthorhombic BaF_2 obtained from the roller mill showed broad XRPD peaks[74,75] as also observed for the orthorhombic BaF_2 prepared by ball milling in this study (vide supra). Thus, the orthorhombic BaF_2 prepared by high-energy ball milling in this study seems to become stabilized due to a quenching process. Interestingly, orthorhombic SrF_2 as well as orthorhombic CaF_2 were, although in clearly smaller amounts than in case of BaF_2, accessible by employing a roller mill[74] which is in contrast to the results obtained with the planetary mill used in this study (vide supra). Thus, the pressures introduced in the roller mill seems to be higher than in the planetary mill or the temperatures occurring while milling in the planetary mill are too high or the cooling process is slower so that a complete retransformation is initiated.

Orthorhombic BaF_2 is reported to slowly retransform to the cubic phase if the sample is not phase pure orthorhombic BaF_2 but a mixture of the orthorhombic and the cubic phase[74] which was also observed in this study.

Since the phase transformation seems to be solely due to the introduced pressure it seems likely that by an increase of the density of the milling balls the transformation should be facilitated (more events with a sufficient high pressure in the same time compared to the situation in a milling vial set made of a material with a lower density). In fact, changing the milling vial set from the one made of stabilized ZrO_2 to one made of tungsten carbide which has a larger Young's modulus ($E_{300\,\mathrm{K}} \approx$ 700 GPa, $\nu \approx 0.2$)[99] and a higher density (14.95 g cm^{-1}, declared by Fritsch) than ZrO_2 (vide supra) leads to a faster phase transformation (tested for a milling period of 20 min). The pressure estimated by using equation (65) leads to $p_{\mathrm{max}} = 1.13$ GPa. However, if the milling time is increased, the amount of the orthorhombic BaF_2 prepared does not increase to clearly higher values than obtained after the 20 min of milling or by milling in the ZrO_2 vial set. Thus, the orthorhombic BaF_2 retransforms to the cubic phase leading to a dynamic equilibrium while milling between the two phases. This was also observed for ball milled PbF_2.[100] Thus, the origin of the increased amount of the orthorhombic BaF_2 in case of joint milling cubic BaF_2 with an inert phase (vide supra) is most probably a decreased retransformation rate since an increase in pressure, as just shown for the mechanical treatment in the WC vial set, which may also occur if a small grain of the inert phase is hit by a ball and transfers the force to an even smaller area, does not increase the total amount of the orthorhombic BaF_2 prepared.

The retransformation is probably due to the shear stress introduced which increases the transformation rate significantly as already shown (vide supra). The shear force dissipates into heat which probably, especially in the tip of a crack[101], creates temperatures high enough ($>$ 473 K, vide supra) for a (fast) thermally induced relaxation of the structure. Furthermore, as already mentioned the orthorhombic phase retransforms to the cubic phase if it is contaminated by the cubic phase even when stored at ambient conditions. It seems plausible to assume that this retransformation rate can be increased by thermal treatment. Thus, a suppression of the retransformation should be possible if the shear forces introduced into the material are reduced. As already mentioned the shear forces introduced into the grains at high pressures generated in anvil cells can be strongly reduced by the use of pressure transmitting media which encloses the grains of the material to be investigated. Therefore, they enable a more (in case of liquids which stay liquid even at high pressures like mixtures of ethanol and methanol) or less (solids) hydrostatic pressure acting upon these grains.[77] Thus, perhaps the joint milling of BaF_2 with inert compounds leads to a similar effect. BaF_2 grains become enclosed by the inert material which leads to a more uniform pressure introduced into the material. Thus, the direct retransformation after the occurrence of a for a transformation sufficient pressure would be reduced as well as the introduction of shear stress into already formed orthorhombic BaF_2 hit by a milling ball.

It should be noted, that Bocker et al. observed nano-crystalline orthorhombic BaF_2 in annealed glasses which they ascribed to high pressures building up due to the crystallization of the glass[102]. The formation of orthorhombic BaF_2 was observed in only two of three glasses while in the other glass solely cubic BaF_2 was observed. In contrast to the glass exhibiting only cubic BaF_2 after the heat treatment the two other glasses contained small amounts of KF which also facilitates the formation of orthorhombic BaF_2 initiated by high-energy ball milling as already mentioned above. Bocker et al. did not suggest an explanation for the role of KF. It seems plausible to assume that also in this case the KF acted as a pressure transmitting medium reducing shear forces acting on the BaF_2.

Interestingly, orthorhombic BaF_2 can also be obtained from aqueous solution, as shown by Kolar et al.[103] and Xie et al.[73]. Kolar et al. found orthorhombic BaF_2 to form in the first minute after the start of the reaction of $Ba(NO_3)_2(aq)$ with $NH_4F(aq)$ with a maximum ratio of 91% after a reaction time of 30 s. The formation of orthorhombic BaF_2 was ascribed to the Ostwald step rule[104] by Kolar et al.[103] The orthorhombic BaF_2 transforms to the cubic phase when the reaction progresses until, after 1200 s, no orthorhombic BaF_2 can be observed. They found evidence that orthorhombic BaF_2 is more soluble in water than cubic BaF_2 which leads to a transformation of the orthorhombic phase to the cubic phase. Interestingly, the orthorhombic BaF_2 prepared this way was stable for months as "dry powder"[103] (although it was not phase pure) which is in contrast to the orthorhombic BaF_2 prepared by joint ball milling of BaF_2 and KF whose amount clearly decreases within some weeks of storage in ambient air, and to the results reported by Seifert[74] for orthorhombic BaF_2 obtained at high pressures. Although Kolar et al. did not specify the storage conditions and, thus, the decomposition observed for the sample prepared by high-energy ball milling may be solely due to air moisture (KF is highly hygroscopic), one may assume that the orthorhombic BaF_2 prepared by milling differs in reactivity which may be due to the distorted character of the mechanosynthesized orthorhombic BaF_2.

Xie et al.[73] reported on the preparation of orthorhombic BaF_2 by solvothermal synthesis. They observed the formation of nanorods in case of orthorhombic BaF_2 (synthesis temperature 433 K, reaction time 4 h to 12 h) and nanocubes in case of cubic BaF_2 (synthesis temperature 453 K, reaction time 12 h to 48 h).[73] In the first stage, the cubic BaF_2 is found as spherical particles with diameters of about 4 nm. When the reaction progresses these particles grow to rectangular nanoparticles of 5(1) nm x 6(1) nm after 48 h. For the orthorhombic BaF_2 the rods observed exhibited diameters of 1.5(1) nm and lengths of about 5(0.5) nm after 4 h and 3.5(1) nm and lengths of more than 300 nm after 12 h.[73]

The stabilization of a metastable polymorph by a drastic reduction of the size of the crystallites is inter alia known for Al_2O_3. It is a matter of common knowledge that in the micro- or single crystalline regime α-Al_2O_3 is the thermodynamically stable phase. However, for Al_2O_3 crystallites with surface areas larger than about 125 m^2g^{-1} the γ-modification becomes the thermodynamically stable phase due to the lower surface energy of γ-Al_2O_3 compared to α-Al_2O_3.[105,106]

The surface to volume ratio in case of the orthorhombic phase is 2.66 after 4 h and finally, after 12 h at 433 K, 1.14. In case of the cubic phase when assuming a spherical shape a value of 1.5 is found after 12 h, and after 48 h in case of a cuboid of 5 nm x 5 nm x 6 nm a value of 1.13 or even smaller is obtained if the one dimension of the cuboid which is not observable is even larger than 5 nm. The orthorhombic BaF_2 transforms to cubic BaF_2 when heat treated at 433 K for more than 12 h or at higher temperatures. This transformation goes along with an aggregation of the nanorods[73]. Since the surface to volume ratio of the orthorhombic BaF_2 is larger than the one found for the cubic phase a stabilization of the orthorhombic phase due to a smaller surface energy of this polymorph seems possible. However, after long heat treatment the surface to volume ratios of both modifications are very similar. So the formation of larger crystals of the orthorhombic phase may be fostered by the already formed crystals of orthorhombic BaF_2 serving as seed crystals. It should be mentioned that the larger solubility of the orthorhombic BaF_2 observed by Kolar et al. seems to be in contradiction with the results of Xie et al. However, the solubility of compounds at hydrothermal conditions is different from the ones at ambient conditions, which might explain this difference.

One may also assume that, like found for PbF_2, the orthorhombic BaF_2 is in fact the stable phase at low temperatures as also suggested by Xie et al.[73]. However, the results of Dreger et al.[107] describing low temperature solid state synthesis routines leading to cubic BaF_2 and even more striking the results of Bach et al.[108] who found cubic BaF_2 forming directly from amorphous BaF_2 at 253 K by employing MBE render this assumption rather improbable. Thus, the cause for the formation of orthorhombic BaF_2 under solvothermal conditions at low temperatures remains unexplained.

TEM measurements on a mixture of BaF_2 and KF (molar ratio 9 :1) milled for six hours, which exhibited a large amount of orthorhombic BaF_2, revealed crystallite sizes in a range of 6 nm to 15 nm for the orthorhombic phase while the crystallites of the cubic phase showed crystallite sizes between 8 and 26 nm (unfortunately the images are lost due to the loss of a storage device). Thus, although a rough tendency for smaller crystallites in case of the orthorhombic BaF_2 can be observed here, a stabilization due to a larger surface to volume ratio of the orthorhombic BaF_2 compared to the cubic phase seems rather unlikely. For completeness, it should be mentioned that it is possible that the necessary pressure needed for the phase transformation from cubic to orthorhombic BaF_2 is largely reduced in case of nano-crystalline BaF_2 compared to larger crystallites of cubic BaF_2. However, for many materials it was found that the transition pressure increases with decreasing crystallite size, see e. g. ref. 109. Hence, further investigations are necessary to understand this and other phase transformations introduced by mechanical treatment in more detail.

Orthorhombic $Ba_{1-x}Ca_xF_2$ As can be seen in Fig. 8 the peaks of the orthorhombic phase are shifted to larger diffraction angles which indicates lattice contraction. The larger t_{mill} or x, the larger the shift of the peaks of the orthorhombic phase. Therefore, it seems plausible to assume that Ca ions are successively incorporated into the lattice of the orthorhombic BaF_2 and, thus, orthorhombic $Ba_{1-x}Ca_xF_2$ is formed. The amount of the orthorhombic phase also depends on t_{mill}. After 10 minutes only a small amount is formed which increases with increasing milling time up to t_{mill} = 60 min. For larger milling times the amount of the orthorhombic phases decreases most probably due to the formation of the cubic solid solution presumably being the energetically favored phase.

The formation of orthorhombic $Ba_{1-x}Ca_xF_2$ was, as far as the author knows, not yet reported in the literature. Neither orthorhombic $Ba_{1-x}Sr_xF_2$ nor orthorhombic $Ca_{1-x}Sr_xF_2$ were found in the literature. It would be interesting to investigate the high pressure transformation of these ternary fluorides. In case of $Ca_{0.75}Y_{0.25}F_2$ the formation of the high pressure modification is not observed even at a pressure of 11.2 GPa and, thus, if possible at all, shifted to higher pressures than found to be necessary for pure CaF_2.[72,74] There was no mixture of BaF_2 and SrF_2 which was high-energy ball milled in ZrO_2 vial sets that exhibited any other phase than cubic $Ba_{1-x}Sr_xF_2$. Maybe this phase can be observed in case of short milling times or by using WC vial sets (higher pressures). However, since $Ba_{1-x}Sr_xF_2$ is a more stable phase its energetic minimum is probably clearly smaller than the one of metastable orthorhombic $Ba_{1-x}Sr_xF_2$. In case of the $Ba_{1-x}Ca_xF_2$ in which the cubic (vide supra) as well as the orthorhombic phase are metastable the energetic difference between these structures could be smaller such that both structures can coexist.

Formation of $Ba_{1-x}Ca_xF_2$ with $x \lesssim 0.75$ In the range from $x = 0.30$ to $x = 0.65$ a very long milling time of about 99 h (when employing the ZrO_2 vial set) is necessary to reach lattice parameters in accordance with Vegard's law. For $x = 0.50$ (less pronounced also for $x = 0.40$, not shown here) a small amount of residual CaF_2 can be seen in the XRPD pattern even after 99 h of milling, see Fig. 10. Expectedly, for the sample with $x = 0.50$ a small deviation from Vegard's law towards a slightly larger a can be observed.

The amount of CaF_2 introduced into BaF_2 and, thus, the decrease of the lattice parameter a of the $Ba_{1-x}Ca_xF_2$, depends on t_{mill}, see Fig. 4. The decrease of the lattice parameter of the cubic solid solutions seems to follow an exponential law (Fig. 4). As already mentioned above, the orthorhombic phase also shows lattice contraction with the increase of t_{mill}. In Fig. 9 XRPD patterns of mixtures to yield the samples with $x = 0.60$, $x = 0.65$ and $x = 0.70$ milled for six hours, respectively, are shown. The amount of Ca ions incorporated into the BaF_2 lattice increases with increasing deviation of the composition from $x = 0.50$. This is expected since the probability for a contact of a BaF_2 unit with a CaF_2 unit, necessary to substitute Ba ions by Ca ions in BaF_2 or Ca ions by Ba ions in CaF_2, increases the larger the overspill of one of the binary fluorides becomes. Accordingly, after six hours of milling the reaction is more advanced in case of the sample with $x = 0.70$ than for the sample with $x = 0.65$. In turn, the latter sample shows a larger amount of Ca ions incorporated than the sample with $x = 0.60$ (see Fig. 9). Thus, Ba ions are consecutively substituted by Ca ions in the BaF_2 lattice and, expectedly, to a smaller degree Ca ions by Ba ions in the CaF_2 lattice during milling. Expectedly, since CaF_2 has the smaller lattice parameter and a higher hardness such that the CaF_2-crystallites are less destroyed during milling than the ones of BaF_2 which makes it harder for the Ba ions to get into the CaF_2 lattice. This is in agreement with the slope found for the decrease of a with t_{mill} since an exponential decrease is expected due to $a = \mathrm{f}(x(CaF_2))$ and $x_0(CaF_2)$-$x(CaF_2) = \mathrm{f}(t_{\mathrm{mill}}) = x_0(CaF_2)\exp(-kt_{\mathrm{mill}})$ where $x(CaF_2)$ is the amount of CaF_2 introduced into the BaF_2. The lattice parameter gives the composition x of $Ba_{1-x}Ca_xF_2$ by employing Vegard's law. In Fig. 11 a) a logarithmic plot of $x_0(CaF_2)$-$x(CaF_2)$ as a function of milling time t_{mill} is shown. Expectedly, a linear decrease is observed for the samples (admittedly, in the case of the sample with $x = 0.30$ there is a large deviation of one of the points from a linear decrease). The slope of these lines give the velocity constants k which are shown as a function of x in Fig. 11 b). In accordance with the previous deliberations, the smallest reaction velocity constant is found for the mixture to give $Ba_{0.50}Ca_{0.50}F_2$ and the largest one for the mixture to give $Ba_{0.80}Ca_{0.20}F_2$.

Interestingly, the reaction progress can be accelerated by changing the vial set material. Exemplarily, an XRPD pattern of a mixture to give $Ba_{0.50}Ca_{0.50}F_2$ milled in a vial set made of tungsten carbide, being a stiffer, harder and much denser material than ZrO_2 (WC: Young's modulus $E_{300\,\mathrm{K}} \approx 700$ GPa, Poisson's ratio $\nu \approx 0.2$[99], $\rho = 14.95$ g cm^{-3} (declared by Fritsch); ZrO_2: $E = 205$ GPa and $\nu = 0.3$[93], $\rho = 5.9$ g cm^{-3} (declared by Fritsch)), for only 30 h at 600 rpm with 100 balls (5 mm in diameter) made of the same material is also shown in Fig. 10. The lattice constant of this sample is in good agreement with Vegard's law. In contrast to the sample milled for 99 h in the ZrO_2 vial set no peaks of residual CaF_2 can be observed. Thus, in addition to a small amount of abraded WC, phase pure $Ba_{0.50}Ca_{0.50}F_2$ is obtained. For completeness, also the XRPD patterns of the samples with $x = 0.40$, $x = 0.50$ and $x = 0.60$ prepared by milling in a tungsten carbide vial set

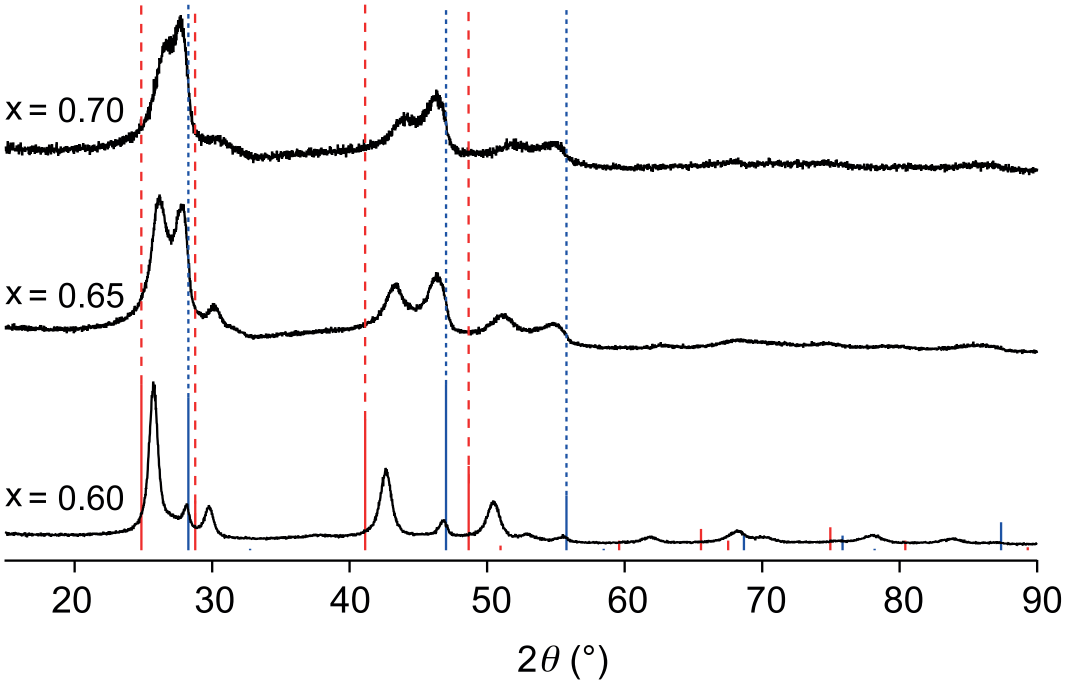

Figure 9: XRPD patterns of the $Ba_{1-x}Ca_xF_2$ compounds from $x = 0.60$ to $x = 0.70$ milled for 6 h, respectively. The sample with x = 0.65 shows two peaks with similar intensities, exhibiting a Ba-rich and a Ca-rich mixed phase, easily spotted by comparing the peak positions to the ones of BaF_2 (red dotted lines) and CaF_2 (blue dotted lines). A similar XRPD pattern is obtained for the sample with $x = 0.70$.

for only 30 h are shown in Fig. 12 and compared to the samples milled for 99 h in ZrO_2. For all these samples the synthesis in the WC vial set seems to be beneficial compared to the synthesis in the ZrO_2 vial set regarding the completeness of the reaction. The synthesis process probably can be further improved concerning the reduction of t_{mill} and abrasion by systematically varying the milling parameters. However that be, the introduction of larger mechanical force and, thus, higher energies into the mixture accelerates the reaction. Hence, the reaction seems to need high energies to take place.

Formation of $Ba_{1-x}Ca_xF_2$, $x \gtrsim 0.75$ Interestingly, in case of $Ba_{1-x}Ca_xF_2$ with $x = 0.75$, $x = 0.80$ and $x = 0.90$, thus, probably for all mixed fluoride samples with $x \gtrsim 0.75$, the $Ba_{1-x}Ca_xF_2$ compounds seem to be formed directly from the binary fluorides since no shift of the CaF_2 and BaF_2 XRPD peaks can be observed but the emergence of the XRPD peaks of the final phase next to the XRPD peaks of the binary fluorides as exemplarily shown for the sample with $x = 0.80$ in Fig. 13. A comparable, but not identical, result is found for a sample with $x = 0.70$ after 3 h of milling, see Fig. 14. The binary fluorides are still almost phase pure while the peak of a mixed phase (which is not $Ba_{0.30}Ca_{0.70}F_2$) embedded by amorphous material or a broad distribution of compositions of x is observed in between the peaks of the binary fluorides. However, after 6 h of milling no binary fluorides can be observed anymore. Thus, this composition lies in the transition area of compositions of the two regimes of formation behavior.

Already after 10 min of milling an XRPD peak of small intensity representing a small amount of $Ba_{0.20}Ca_{0.80}F_2$ can be seen at a diffraction angle 2θ of about 27.45°. Thus, the reaction is faster than in case of the samples with $x < 0.75$ but restricted to a smaller amount of the milled material at the same time. After 6 h of milling also the (002) peak which in case of pure CaF_2 has a vanishing intensity becomes visible at about 31.7° 2θ. This is due to the larger atomic form factor of the Ba

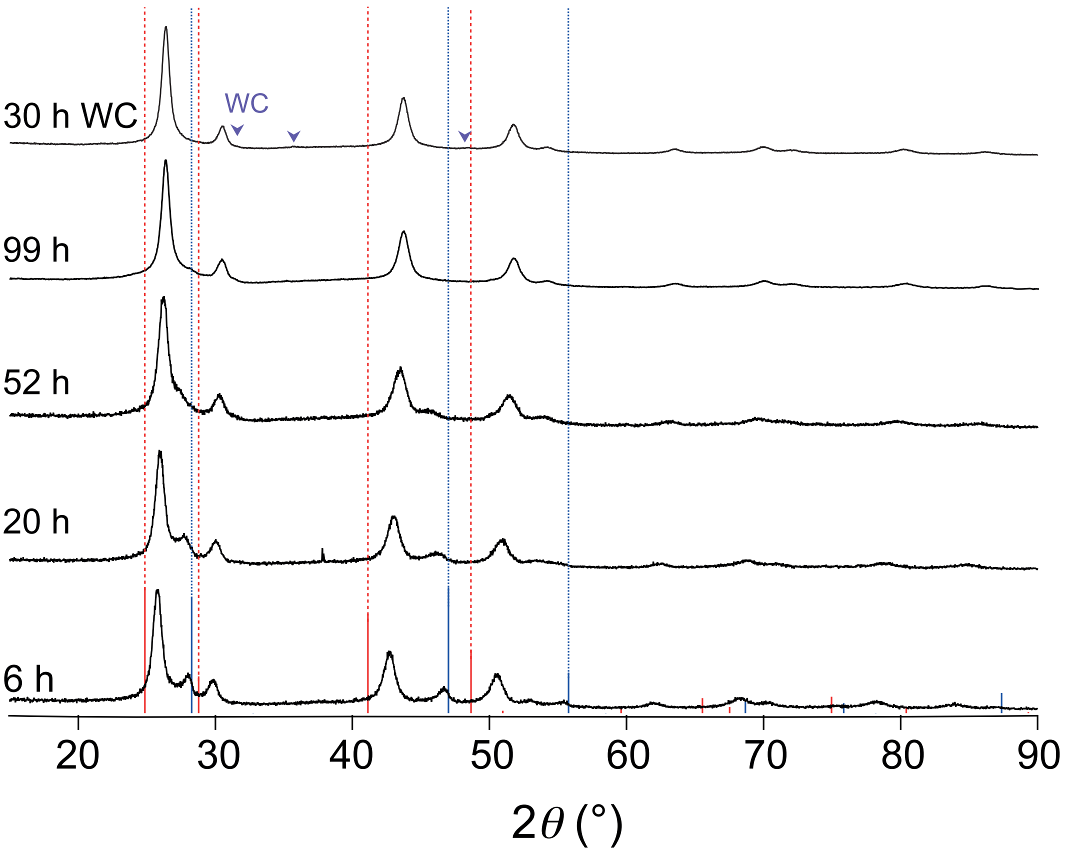

Figure 10: XRPD patterns of a mixture to give $Ba_{0.50}Ca_{0.50}F_2$ milled for different t_{mill}. For the sample milled for six hours residual CaF_2 (blue bars) is visible. After 20 h of milling the CaF_2 is converted to a Ca-rich mixed phase of $(Ba,Ca)F_2$. Finally, milling for 99 h leads to a shift to larger diffraction angles 2θ once more, exhibiting, in addition to a very small amount of residual CaF_2, nearly pure $Ba_{0.50}Ca_{0.50}F_2$. Milling for 30 h in a tungsten carbide (WC) vial set leads to phase pure $Ba_{050}Ca_{0.50}F_2$.

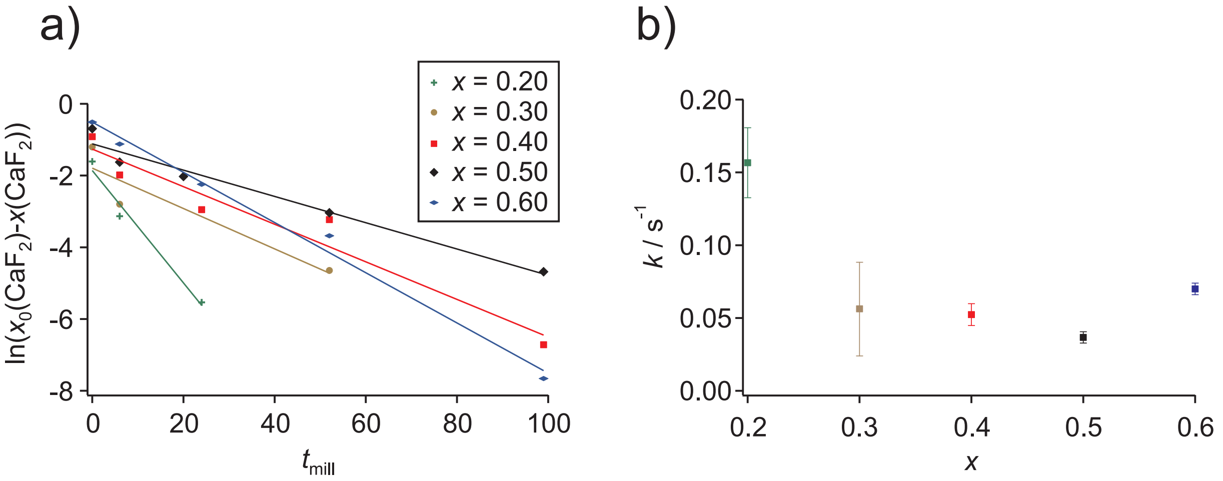

Figure 11: a) plot of $\ln(x_0(CaF_2)-x(CaF_2))$ vs. t_{mill} to give the reaction velocity constants k which are shown in b) as a function of x.

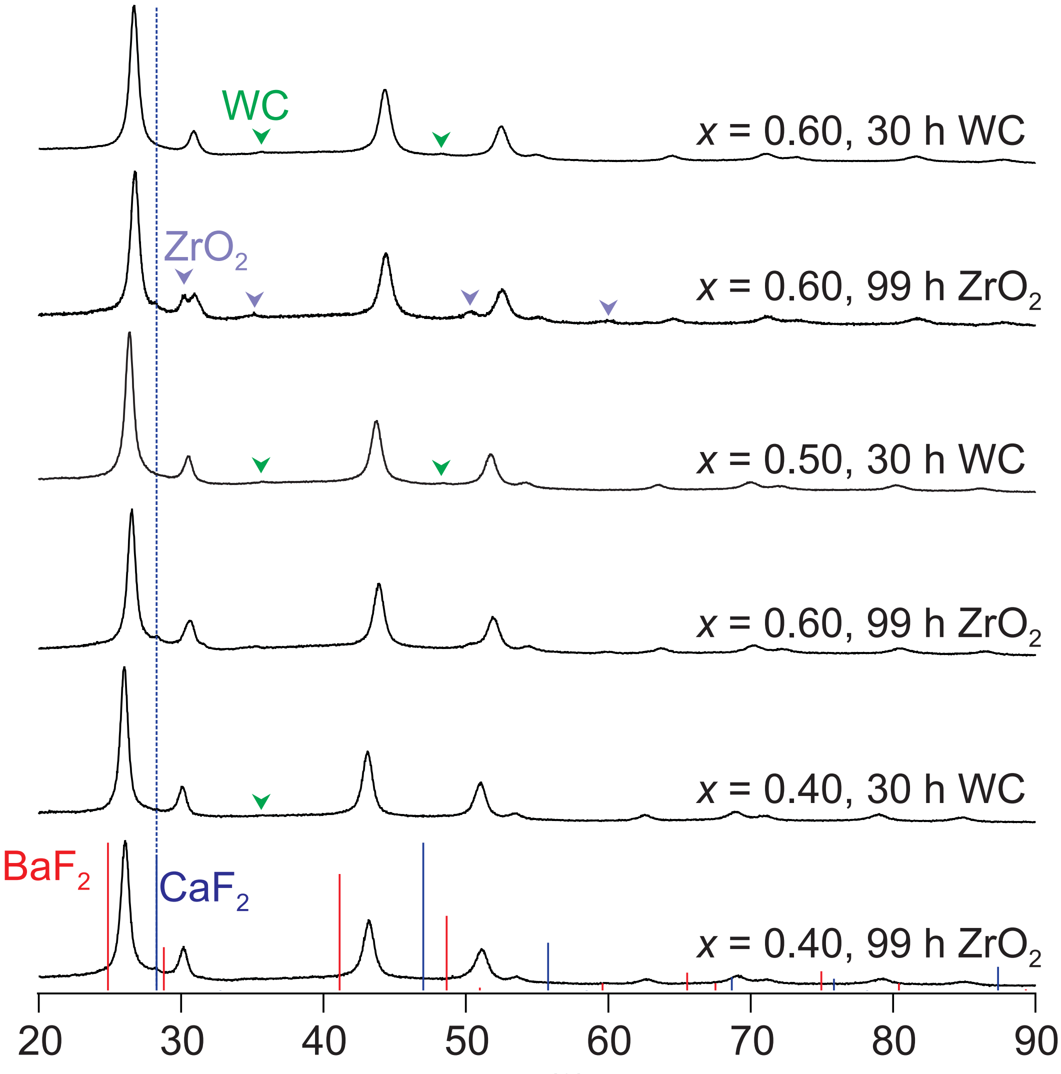

Figure 12: XRPD patterns of compositions to yield $Ba_{0.40}Ca_{0.60}F_2$, $Ba_{0.50}Ca_{0.50}F_2$ and $Ba_{0.60}Ca_{0.40}F_2$ milled in the ZrO_2 vial set for 99 h in comparison to samples of the same composition milled in WC vial sets for 30 h.

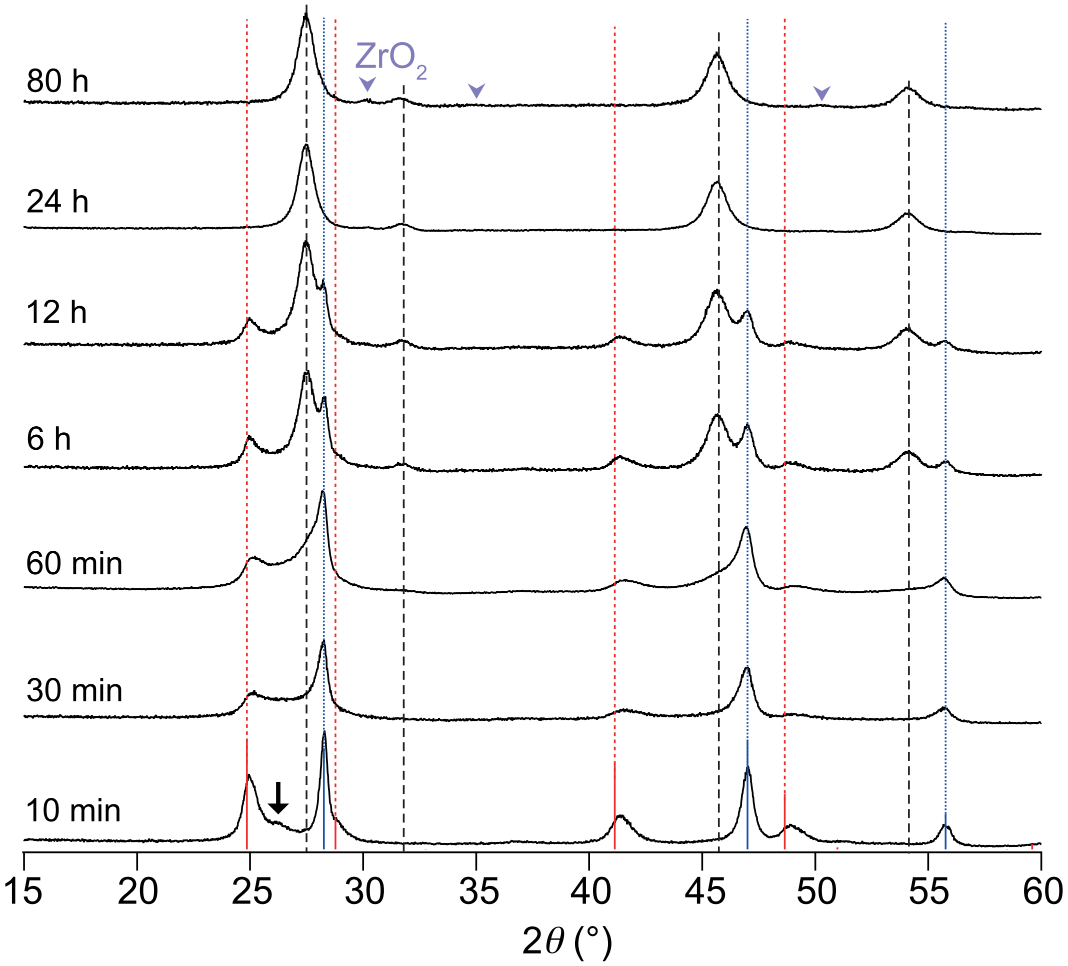

Figure 13: XRPD patterns of a composition to yield $Ba_{0.20}Ca_{0.80}F_2$ milled for the times indicated. After 10 min of milling an intermediate phase is observed which can also be seen after 12 h of milling (black arrows). After 24 h of milling no residual starting materials can be observed anymore. No further change but a small amount of abraded ZrO_2 (violet arrows) can be observed in the pattern after milling for 80 h.

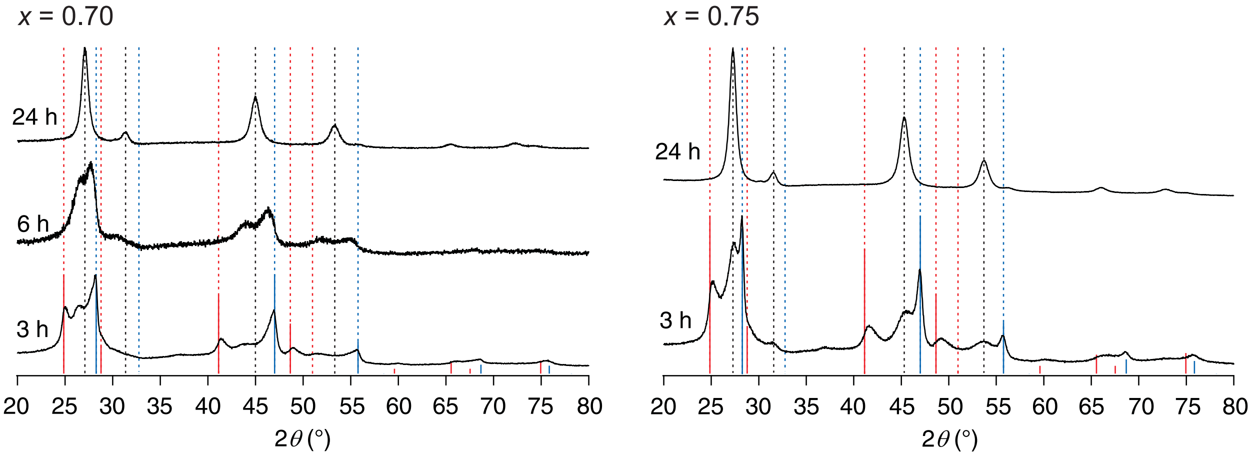

Figure 14: Left: XRPD patterns of a composition to give $Ba_{0.30}Ca_{0.70}F_2$ milled for the times indicated. After 3 h of milling still almost phase pure binary fluorides can be observed in addition to mixed phases. After 6 h of milling no BaF_2 or CaF_2 can be detected. Right: XRPD patterns of a composition to give $Ba_{0.25}Ca_{0.75}F_2$ milled for the times indicated. After 3 h the binary fluorides in addition to $Ba_{0.25}Ca_{0.75}F_2$ can be observed.

ions incorporated into CaF_2 increasing the scattering ability of the atomic planes.

If the XRPD patterns are examined in more detail, it can be seen that there is some intensity between the (111) peaks of the binary fluorides (at about 24.85° and 28.27° 2θ) pointing to (i) amorphous material or (ii) a broad distribution of compositions x. The arrow in Fig. 13 marks a rather well resolved broad intensity. It can be observed after 10 min of milling. For larger milling times it is masked by the overall increased intensity between the (111) peaks of the binary fluorides. Thus, it is questionable if this is a singular intermediate phase or just a snapshot of the beginning of the formation of the manifold of phases with compositions $0 < x < 1$.

It should be mentioned that in case of the samples with $x = 0.10$, $x = 0.15$ and $x = 0.20$ (as for all other compositions with $x < 0.75$ investigated (vide supra)) no fast quasi single step reaction can be observed. Instead a time dependent behavior of the lattice parameter is obtained as already shown for the sample with $x = 0.20$, see Fig. 8.

Possible formation mechanisms For the samples with $x < 0.70$ no residual pure binary fluorides in addition to a crystalline solid solution can be seen even after short reaction times. Thus, the reaction progresses in steps to the final composition. A stepwise progress of the reaction is only possible if in approximation every BaF_2 (CaF_2) unit comes into reactive contact with a CaF_2 (BaF_2) unit within a rather narrow time window.

Obviously, a reactive contact is only possible at the surfaces of the crystallites. Thus, the reaction may be imagined in the following way: a BaF_2 crystallite comes into contact with a CaF_2 crystallite. Into this region energy is introduced by friction or impact while milling. This leads to a mixing of the cations in a small volume in the interfacial region between the two crystallites. Ca substitutes Ba in the BaF_2 crystallite, and Ba substitutes Ca in the CaF_2 crystallite. Thus, two phases, one rich in Ca the other rich in Ba are generated as was observed experimentally in case of the samples with $x < 0.70$. It seems plausible to assume that the small Ca ions will substitute Ba in BaF_2 easier than the large Ba ions Ca in CaF_2. Therefore, more Ba ions will be substituted by Ca in BaF_2 than Ca ions by Ba in CaF_2 which is in agreement with the experimental findings.

Furthermore, after the reaction it seems plausible to assume that the mixed phases are probably enclosed by the two crystallites consisting of BaF_2 and CaF_2. Thus, it seems feasible to assume that

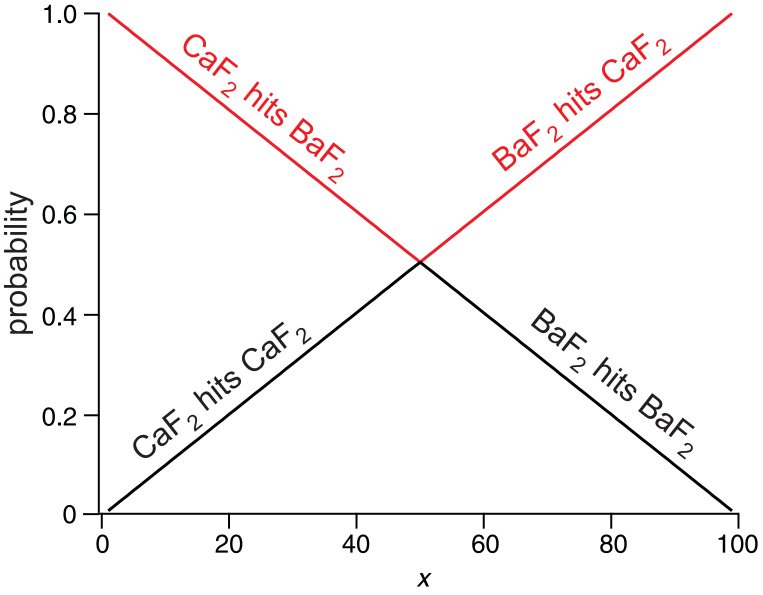

Figure 15: Probability of a contact between the binary fluorides in an ideal mixture of the binary fluorides as a function of x.

first the residual binary fluorides presenting free surfaces will react with each other until the mixed phases will exhibit free surfaces and by this become accessible for other crystallites due to crushing of the crystallites enclosing the mixed phases. It also seems possible that in case of a repetitive introduction of energy into the connected crystallites the reaction between them will progress, i. e., the amount of substituted cations increases in both crystallites. The concentration gradient of the two different cation-species in the crystallite may, at the same time, initiate diffusion over short periods of time (when energy is introduced by mechanical force) inside the due to the mechanical treatment defective crystallites leading to a homogenization of the concentration of the introduced cation species. This would lead to a composition of at maximum $x = 0.50$ (starting from an x close to 1 and an x with a value close to 0) in the interfacial regions.

However, a mixing of cations has to be initiated by a contact between crystallites. The formation of the mixed phases starts in the interfacial regions. Diffusion of Ca ions into the BaF_2 crystallite and of Ba ions into the CaF_2 crystallite might play a role for the progress of the mixing process, thus, the reaction may not be limited to the surface assigned regions of the crystallites.

However, as already shown, the whole material in the milling beaker reacts within a small time window in case of the samples with $x < 0.70$. Therefore, either all material is in a rather short period of time part of a surface or diffusion of cations inside the crystallites has to play an important role. Obviously, for both mechanisms small (and defective) crystallites would be beneficial regarding a fast process which is necessary for a quasi homogeneous reaction rate at all times in the whole material.

In case of the samples with $x \geq 0.75$ only a rather small fraction of the material reacts at one time. Thus, for long periods of time a large part of the BaF_2 (CaF_2) does not come into contact with CaF_2 (BaF_2). The small part of the binary fluorides reacting, however, is transformed very fast to the $Ba_{1-x}Ca_xF_2$ with the respective composition x intended to be prepared. Thus, there seems to be a limited number of reaction centers which are fed from the binary fluorides. In these reaction centers all compositions x are passed until the material is homogenized and the solid solution reflecting the overall BaF_2 to CaF_2 ratio is formed. Thus, the compositions in these small reaction volumes becomes very similar to the overall composition and, in case of the mixtures to give solid solutions with $x = 0.80$, after milling times larger than 1 h the amount of the solid $Ba_{1-x}Ca_xF_2$ with the stoichiometry representing the overall composition became larger than the ones of the $Ba_{1-x}Ca_xF_2$ compounds with other compositions.

Since in case of the samples with $x \leq 0.25$ a stepwise reaction progress is observed this difference cannot be explained by the contact probabilities due to the BaF_2 to CaF_2 ratio. As shown in Fig. 15 the probability of a contact between CaF_2 and BaF_2 (in an ideal mixture of the BaF_2 and CaF_2 units) increases with increasing deviation of the composition from $x = 0.50$. Thereby, $p(CaF_2\text{-}CaF_2) = x(CaF_2)$ is the probability of a contact between a CaF_2 unit and another CaF_2 unit, $p(BaF_2\text{-}BaF_2) = x(BaF_2)$ is the probability for a contact between a BaF_2 unit and another BaF_2 unit, $p(BaF_2\text{-}CaF_2) = x(BaF_2)$ is the probability for a contact between a BaF_2 unit and a CaF_2 unit (for $x \leq 0.50$) and $p(CaF_2\text{-}BaF_2) = x(CaF_2)$ is the probability for a contact between a CaF_2 unit and a BaF_2 unit (for $x \geq 0.50$).

One may assume a size effect causing the different reaction behaviors in the two compositional regimes such that, e. g., the crystallites of one of the binary fluorides are much larger than the crystallites of the other binary fluoride. In the recent study of Ruprecht et al.[66] dealing with the mechanosynthesis of $(Ba,Ca)F_2$ mixed phases the BaF_2 crystallites were found to be clearly smaller than the CaF_2 crystallites while the reaction progresses.

If the CaF_2 crystallites are much larger than the BaF_2 crystallites the surface of the CaF_2 crystallites will probably be occupied rapidly by the small BaF_2 crystallites. Depending on the BaF_2 to CaF_2 ratio and the difference in size and, thus, specific surface area of the crystallites of the two binary fluorides there will be residual BaF_2 crystallites which from this moment cannot come into contact with CaF_2. Thus, the reaction will take place on the rather small surface of the CaF_2 crystallites while a more or less large ratio of the BaF_2 as well as of the CaF_2 will be quasi inert until fresh CaF_2 surfaces are generated by crushing the crystallites. Certainly, the obtained result may also be explained if both binary fluorides consisted of large crystallites.

If the CaF_2 crystallites are clearly larger than the BaF_2 crystallites the effect should be more pronounced in case of small x (if the crystallite size differences are not changed) since there is more BaF_2 and less CaF_2 offering surface areas for reaction. Thus, perhaps the crystallite sizes differ with x which may be due to the different hardness of CaF_2 and BaF_2[57] or a different behavior concerning agglomeration. If for instance CaF_2 crystallites tend to bond with other CaF_2 crystallites more tightly than it is true for BaF_2 crystallites, a mixing of the two binary fluorides would be easier in case of a mixture with a large BaF_2 to CaF_2 ratio, thus, for mixtures leading to $Ba_{1-x}Ca_xF_2$ with a rather small x. In case of mixtures with large amounts of CaF_2 the amount of BaF_2 may not be sufficient to prevent the CaF_2 crystallites to agglomerate and, therefore, the accessible surface area of CaF_2 would be strongly reduced.

In general it can be said that in case of the samples with $x \geq 0.75$ the reaction of the fluorides seems to be restricted to the surface of large crystallites while in case of the samples with $x < 0.75$ the reaction takes place in almost the whole material at the same time. This seems to be in agreement with the results obtained for the sample with $x = 0.70$. At first the reaction would be restricted to the surface of the large CaF_2 crystallites or agglomerates. While the reaction progresses the size of the crystallites is reduced and/or the CaF_2 agglomerates are destroyed, the CaF_2 crystallites became separated by BaF_2 crystallites and the whole material starts to react with each other within a small time window. Furthermore, since the reaction seems to be restricted to small volumes over long time scales diffusion does not seem to play an important role. So in case of $x > 0.70$ the reaction seems to take place in volumes close to the surface of the crystallites.

Thus, the distribution of sizes of the two binary fluorides as a function of x in the time regime the reaction progresses needs to be examined, e. g., by TEM.

Thermal stability The thermal stability of some of the $Ba_{1-x}Ca_xF_2$ prepared was tested. As can be seen in Fig. 16, $Ba_{0.50}Ca_{0.50}F_2$ decomposes to the binary fluorides at elevated temperatures.

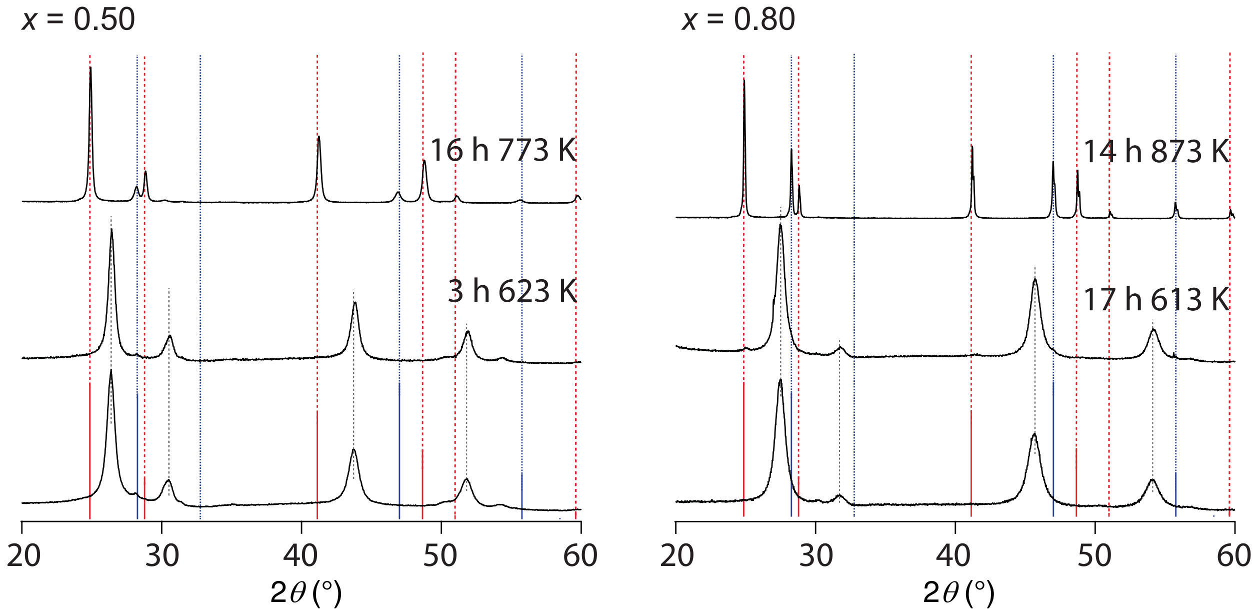

Figure 16: Left: XRPD patterns of $Ba_{0.50}Ca_{0.50}F_2$ milled for 99 h and the same sample after heat treatment. After three hours at 623 K the pattern is almost unchanged apart from a slight narrowing of the peaks. The $Ba_{0.50}Ca_{0.50}F_2$ is completely decomposed to the binary fluorides BaF_2 (red lines) and CaF_2 (blue lines) after 16 hours at 773 K. Right: XRPD patterns of $Ba_{0.20}Ca_{0.80}F_2$ after milling for 24 h and after heat treatment. After 17 h at 613 K small peaks of the binary fluorides become visible while the positions of the peaks of the solid solutions remain unchanged. After14 h at 873 K a complete decomposition of the solid solution to the binary fluorides is observed.

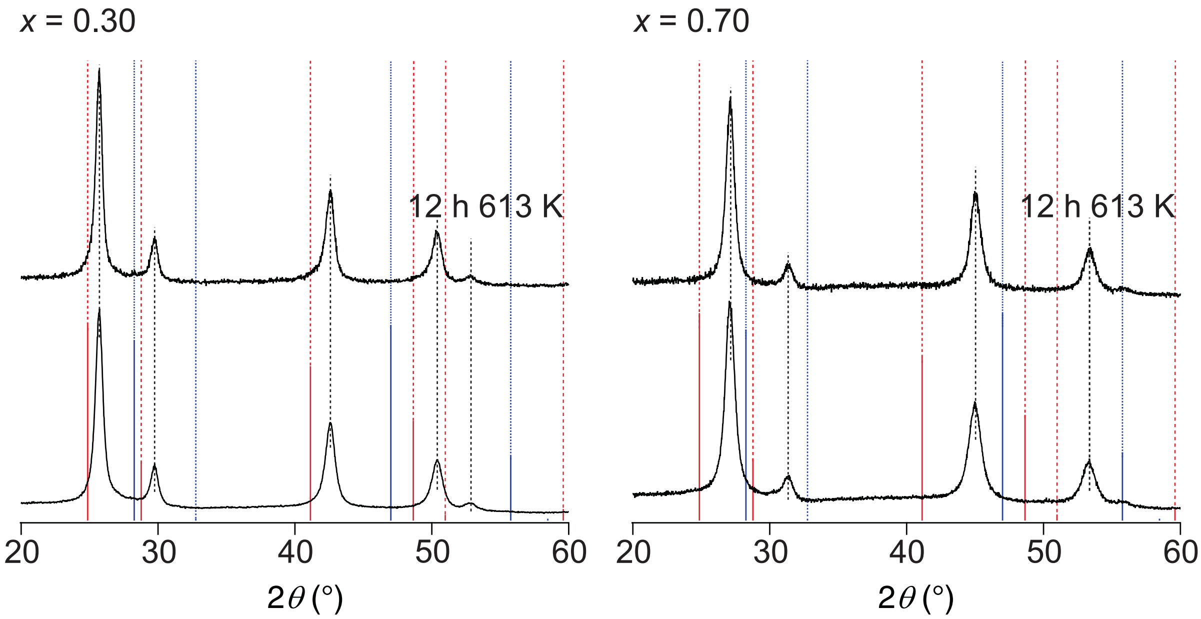

Figure 17: Left: XRPD patterns of $Ba_{0.70}Ca_{0.30}F_2$ after 99 h of milling and after heat treatment. After 12 h at 613 K the pattern is almost unchanged apart from a slight narrowing of the peaks. Right: XRPD patterns of $Ba_{0.30}Ca_{0.70}F_2$ after milling for 99 h and after heat treatment. After 12 h at 613 K the pattern is almost unchanged apart from a slight narrowing of the peaks.

However, the solid solution is stable at 623 K for at least three hours. Since $Ba_{0.20}Ca_{0.80}F_2$ formed unintentionally by employing MBE[17] (vide supra) one may assume a larger stability of this phase. However, it was not possible to prepare micro-crystalline $Ba_{0.20}Ca_{0.80}F_2$ by heating the sample milled for 24 hours for several hours at 873 K. Also in this case the only products obtained are BaF_2 and CaF_2, see Fig. 16. Already after 17 h at 613 K small peaks of CaF_2 became visible. As shown in Fig. 17, the XRPD pattern of $Ba_{0.70}Ca_{0.30}F_2$ and $Ba_{0.30}Ca_{0.70}F_2$ remain almost unchanged after annealing at 613 K for 12 h apart from a slight narrowing of the peaks probably due to grain growth or reduction of substitutional disorder. Thus, $Ba_{1-x}Ca_xF_2$ compounds seem to be relatively stable even at 613 K. It may be noted, that Sullivan et al. used a substrate temperature of 613 K for deposition of $Ba_{0.20}Ca_{0.80}F_2$ [17] (vide supra).

For the mixture of a Ca-rich and a Ba-rich phase reported about by Ruprecht et al. a partial decomposition to the binary fluorides as well as the formation of oxides and carbonates after storage under air at ambient temperature for more than ten months was observed. However, at least $Ba_{0.50}Ca_{0.50}F_2$ prepared in this study (t_{mill} = 99 h, ZrO_2) which was exemplarily tested seems to be stable for at minimum nine months and remains phase pure under the same conditions.

It is assumed that the generation of non-equilibrium phases by high-energy ball milling is due to the 'freezing' of impact-induced high energetic states.[110–112] Therefore, it should be tested if $Ba_{1-x}Ca_xF_2$ solid solutions are accessible by faster quenching techniques[113–115] than employed by inter alia Sorokin et al.[61] who threw the crucible with the liquid BaF_2-CaF_2 mixture into liquid nitrogen. However, it should be emphasized, that the mechanosynthesis of compounds is not yet understood in detail.[112]

9.3.2 Characterization by ^{19}F NMR spectroscopy

Local environments of the fluoride ions To investigate the microscopic structure of the prepared solid solutions, ^{19}F MAS NMR spectra were recorded for some of the samples. In Fig. 18 the ^{19}F MAS NMR spectra of six samples ($x = 0.20$, $x = 0.40$, $x = 0.50$, $x = 0.65$, $x = 0.70$ and $x = 0.80$) are shown. Interestingly, there are up to five NMR lines ($x = 0.50$) visible. The isotropic chemical shifts δ_{iso} of the NMR lines recorded exhibit a clear correlation with the different contents of CaF_2 in the samples, i. e., a small CaF_2 content leads to NMR lines near the chemical shift of pure BaF_2 (153 ppm)[116] whereas a large amount of CaF_2 induces NMR lines near the chemical shift of pure CaF_2 (58 ppm).[116] The NMR lines of the samples with intermediate values of x expectedly show up between the NMR lines of the pure binary fluorides.

It is reasonable to assign the different NMR lines to the different cationic environments of the fluoride ions. Since all of the $Ba_{1-x}Ca_xF_2$ compounds prepared crystallize in the fluorite structure and show lattice parameters in accordance with Vegard's law, it seems appropriate to assume that only the cation sites of the fluorite structure (of course disregarding disorder like Frenkel defects) are occupied by the two cation species. In the fluorite structure each fluoride ion is coordinated by four cations in this case thus, Ca or Ba. Therefore, the fluoride ions can be situated in five different environments which are $[Ba]_4$, $[Ba]_3[Ca]$, $[Ba]_2[Ca]_2$, $[Ba][Ca]_3$ and $[Ca]_4$ (see Fig. 19 for an idealized crystal structure of $Ba_{0.50}Ca_{0.50}F_2$).

In Fig. 20 the ^{19}F MAS NMR spectra of $Ca_{1-x}Sr_xF_2$ (left), prepared by high-energy ball milling for 6 h under the same conditions as used for $Ba_{1-x}Ca_xF_2$, and $Ba_{1-x}Sr_xF_2$ (right) prepared the same way are shown for several compositions x. As can be seen, also for this samples up to five NMR lines are visible which, however, are separated more clearly from each other, especially in case of $Ba_{1-x}Sr_xF_2$. The reasons for this will be discussed later. In case of these samples the five NMR lines can also be ascribed to the five different chemical environments of the fluoride ions.

As can be clearly seen in Fig. 18 five NMR lines show up for the $Ba_{1-x}Ca_xF_2$ samples with $x = 0.50$ and $x = 0.65$. In Tab. 1 the chemical shifts of the NMR lines recorded from the six samples are listed. It is plausible to assign the NMR lines at about 55 ppm to a $[Ca]_4$ environment. Going

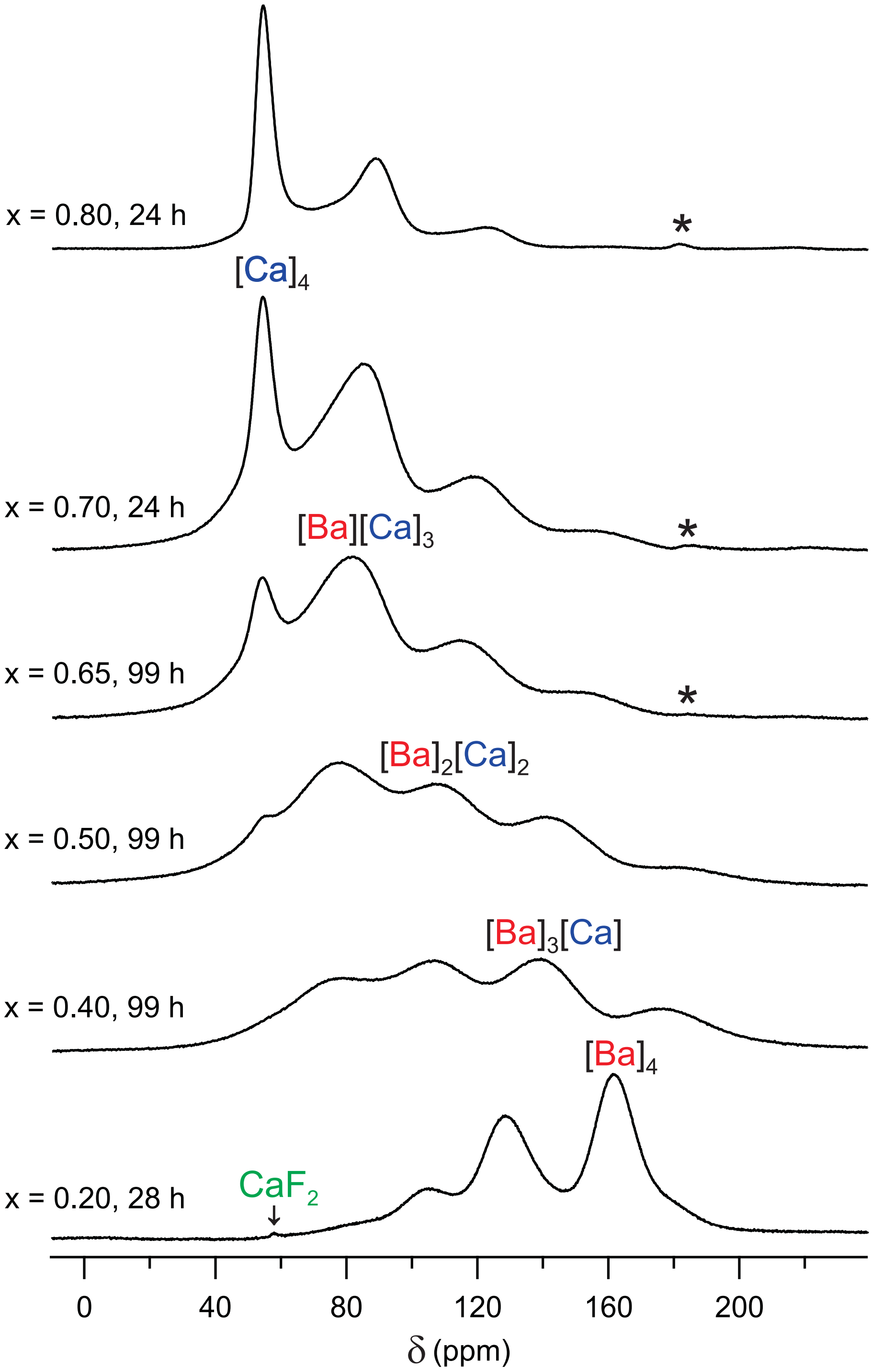

Figure 18: ^{19}F MAS NMR spectra recorded at 471 MHz and a spinning speed of 60 kHz. The samples show up to five different NMR lines (see text for further explanations). The asterisks mark spinning side-bands. The sample with $x = 0.20$ shows a very small amount of residual CaF_2.

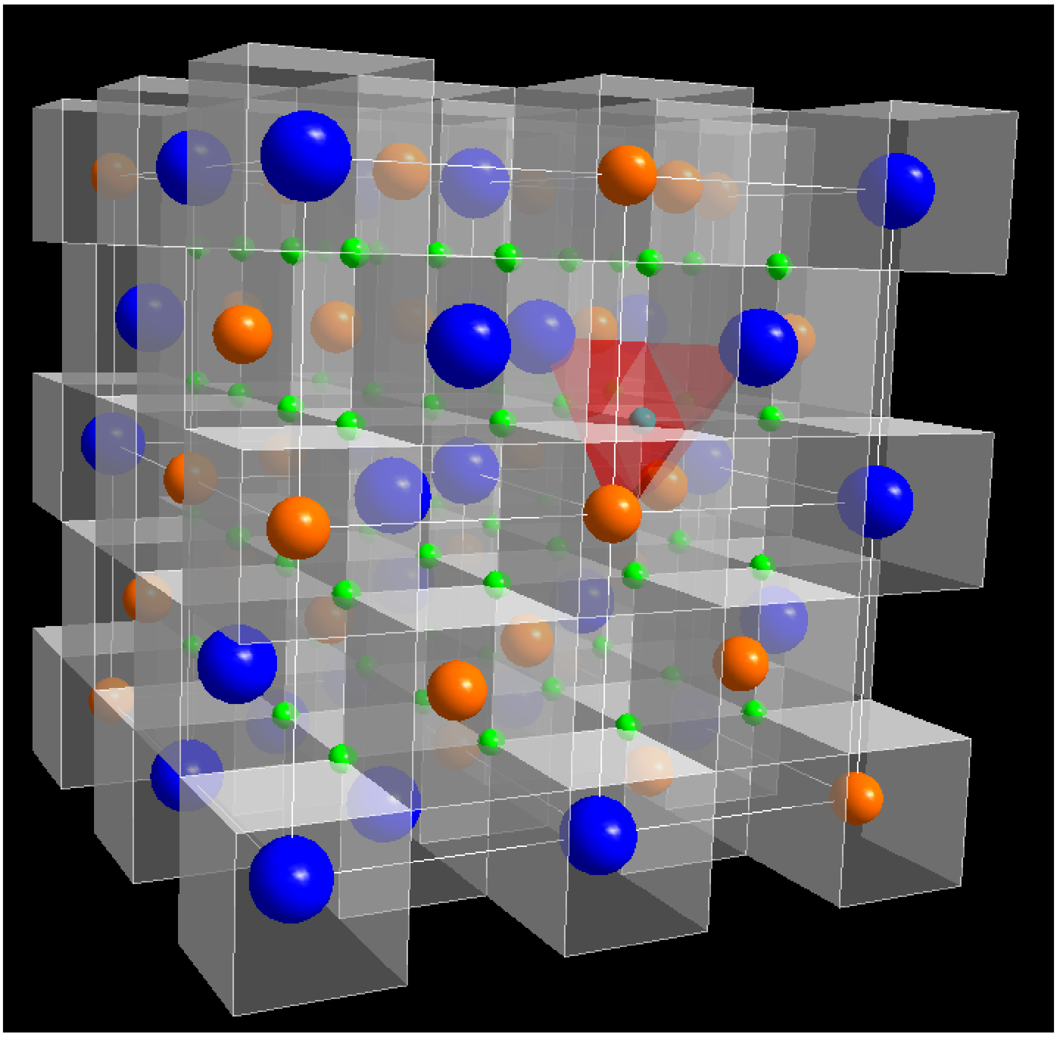

Figure 19: Idealized structure of $Ba_{0.50}Ca_{0.50}F_2$. The large blue balls represent Ba ion while the Ca ions are displayed as smaller, orange balls. The green balls represent fluoride ions. The fluoride ions themselves are coordinated tetrahedrally by the cations. The cations are cubically coordinated by fluoride ions. The fluoride ion cubes share all their edges with other cubes.

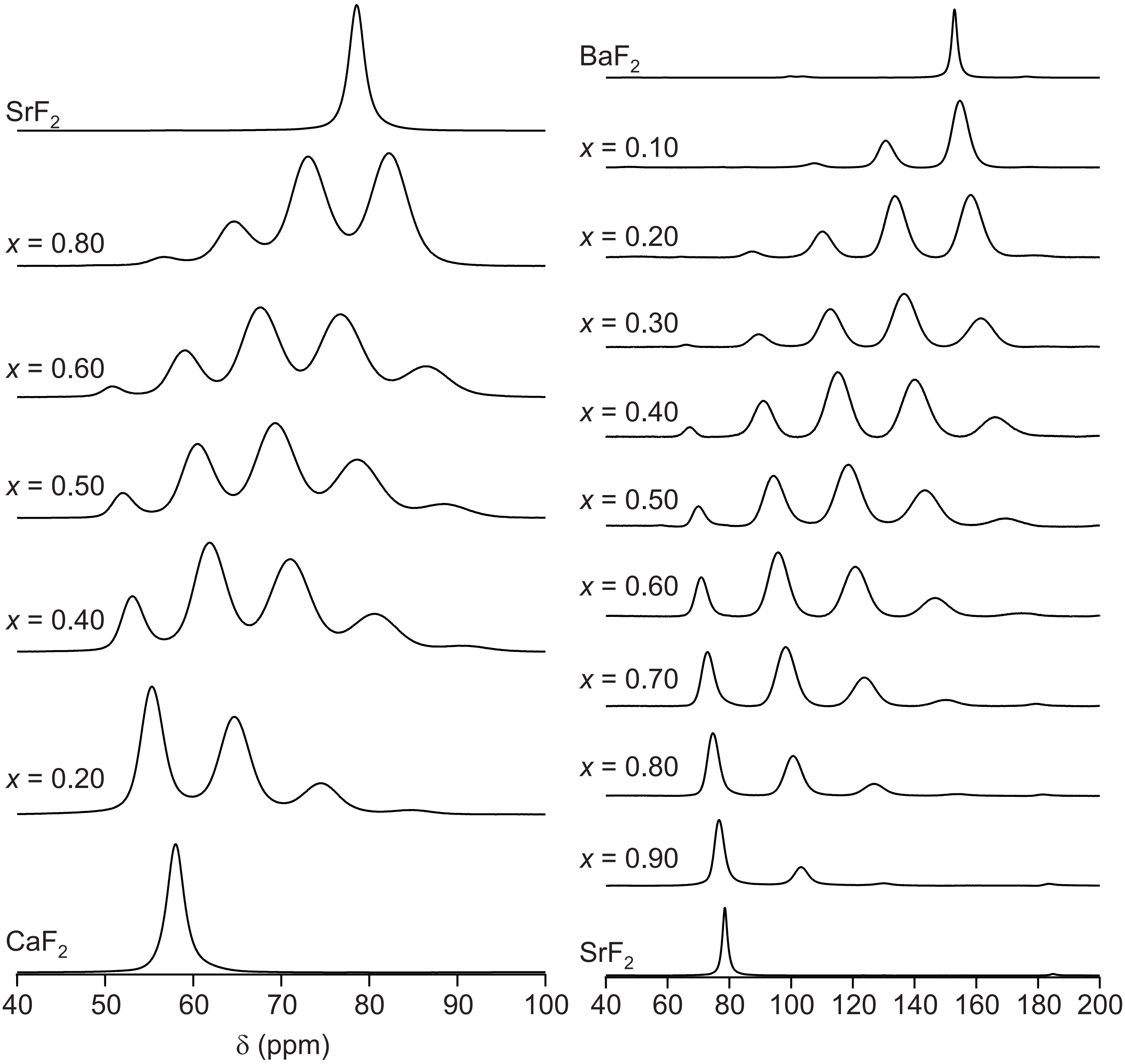

Figure 20: ^{19}F MAS NMR spectra of $Ca_{1-x}Sr_xF_2$ (left) and $Ba_{1-x}Sr_xF_2$ recorded at 565 MHz and a spinning speed of 60 kHz. All the samples were prepared by high-energy ball milling for 6 h. The samples show up to five different NMR lines clearly separated from each other (see text for further explanations). The asterisks mark spinning side-bands.

to larger chemical shift values the ratio of Ba cations increases until the $[\mathrm{Ba}]_4$ environment can be found at around 162 ppm in case of the sample with $x = 0.20$. This assignment is also reasonable if the empirical superposition model of Bureau et al. is considered[116] as shown in the following.

Table 1: δ_{iso} (in ppm) of the six samples of $\mathrm{Ba}_{1-x}\mathrm{Ca}_x\mathrm{F}_2$.

$x = 0.20$	$x = 0.40$	$x = 0.50$	$x = 0.65$	$x = 0.70$	$x = 0.80$	
		55	55	55	55	$[\mathrm{Ca}]_4$
76	77	78	82	86	89	$[\mathrm{Ba}][\mathrm{Ca}]_3$
105	107	108	115	120	124	$[\mathrm{Ba}]_2[\mathrm{Ca}]_2$
129	139	141	151	158		$[\mathrm{Ba}]_3[\mathrm{Ca}]$
162	177	182	187			$[\mathrm{Ba}]_4$

According to this model it is possible to estimate the chemical shift of complex or mixed fluorides in a qualitative manner by using the experimental chemical shift values of the binary fluorides forming the complex or mixed fluoride. In this case, only the first shell of neighbors of the fluoride ions is taken into account, since the cations farther away have only a small direct effect on the chemical shift which is smaller than the expected error of this method. Furthermore, the calculations would become more and more complex if all the possible next nearest cationic neighbors are regarded.

The shift of the resonance frequency is due to the electrons surrounding the nucleus. The resonance frequency of a nucleus not surrounded by electrons would be

$$\nu_0 = \frac{\gamma B_0}{2\pi} \tag{67}$$

with γ being the gyromagnetic ratio of the nucleus and B_0 the magnetic field applied. In case of a nucleus surrounded by electrons the magnetic field will induce a circular movement of the electrons around the magnetic field lines due to the Lorentz force. The circular movement creates a magnetic field in opposite direction to $\vec{B_0}$ which reduces the field strength the nucleus experiences and is, therefore, called diamagnetic shielding.

The diamagnetic shielding of the nucleus is not the only effect which changes the local magnetic field the nucleus experiences. The external magnetic field distorts the electron distribution around the nucleus which can be described by a mixing of the ground state with excited states of the electron wave function. Some of these excited states may possess paramagnetic properties which leads to paramagnetic deshielding of the nucleus. Thus, a shielding constant σ changing the magnetic field to $B = B_0(1-\sigma)$ can be described as the sum of a diamagnetic and a paramagnetic contribution

$$\sigma = \sigma^d + \sigma^p. \tag{68}$$

Therefore, the resonance frequency of a nucleus surrounded by electrons is

$$\nu = \frac{\gamma B_0(1-\sigma)}{2\pi} \tag{69}$$

whereby the change of the resonance frequency is very small and, thus, given in parts per million (ppm) of the Larmor frequency ν_0. Instead of the absolute value for the difference between ν_0 and ν of the respective nucleus a shift of its resonance frequency relative to the resonance frequency of this nucleus in a reference substance ν_{ref} is measured which is the chemical shift δ:

$$\delta = 10^6 \frac{\nu - \nu_{\mathrm{ref}}}{\nu_{\mathrm{ref}}} \tag{70}$$

With respect to (69) equation (70) can be formulated as

$$\delta = 10^6 \frac{\sigma_{\mathrm{ref}} - \sigma}{1 - \sigma_{\mathrm{ref}}} \tag{71}$$

and since $1 \gg \sigma_{\mathrm{ref}}$ (71) can be simplified to

$$\delta \approx \sigma_{\mathrm{ref}} - \sigma \tag{72}$$

when δ is given in ppm.

At this point we should note that the shielding of the nucleus is described by a tensor of second order, thus, a 3 x 3 matrix

$$\boldsymbol{\sigma} = \begin{pmatrix} \sigma_{xx} & \sigma_{xy} & \sigma_{xz} \\ \sigma_{yx} & \sigma_{yy} & \sigma_{yz} \\ \sigma_{zx} & \sigma_{zy} & \sigma_{zz} \end{pmatrix} \tag{73}$$

It is possible to choose the axis frame such that the shielding tensor is diagonal. This can be done when the surrounding electron distribution, thus, the surrounding atoms (in a molecule or crystal) of the nucleus in question is used to define the axis frame. The obtained axis frame is called the principal axis frame (PAF). In case of molecules in a liquid state the orientation of this PAF with respect to B_0 changes very fast, such that in average an isotropic shielding of the nucleus is obtained which is $\sigma_{iso} = \frac{1}{3}(\sigma_{xx} + \sigma_{yy} + \sigma_{zz})$. The same is true under MAS conditions. Therefore, here the isotropic chemical shift is measured.

$$\delta_{\mathrm{iso}} = \frac{\sigma_{\mathrm{iso,ref}} - \sigma_{\mathrm{iso}}}{1 - \sigma_{\mathrm{iso,ref}}} \approx \sigma_{\mathrm{iso,ref}} - \sigma_{\mathrm{iso}} \tag{74}$$

The isotropic chemical shift can in principle be calculated if the shielding tensor is known. The components of the shielding tensor can be calculated using the following equations:

$$\sigma^{d}_{\gamma\gamma} = \frac{\mu_0 e^2}{4\pi 2 m_e} \langle \Psi_0 | \sum_i \frac{\alpha_i^2 + \beta_i^2}{r_i^3} | \Psi_0 \rangle \tag{75}$$

$$\sigma^{p}_{\alpha\beta} = -\frac{\mu_0 e^2}{4\pi 2 m_e} \sum_{k \neq 0} \left[\frac{\langle \Psi_0 | \sum_i \hat{l}_{i\alpha} | \Psi_k \rangle \langle \Psi_k | \sum_i \frac{\hat{l}_{i\beta}}{r_i^3} | \Psi_0 \rangle + \langle \Psi_0 | \sum_i \frac{\hat{l}_{i\beta}}{r_i^3} | \Psi_k \langle \Psi_k | \sum_i \hat{l}_{i\alpha} | \Psi_0 \rangle \rangle}{E_k - E_0} \right] \tag{76}$$

Thereby μ_0 is the vacuum permeability, e is the charge of the electron and m_e its mass, α, β, γ are Cartesian coordinates, r_i is the distance of the ith electron from the nucleus in question while $\hat{l}_{i\alpha}$ and $\hat{l}_{i\beta}$ are the α and β components of the angular momentum of the ith electron, respectively. Ψ_0 is the wave function in the ground state, while Ψ_k is the wave function in an excited state of the system (vide supra). $E_k - E_0$ is the energy difference between the excited state and the ground state of the electron system. Thus, the wavefunctions Ψ_0 and Ψ_k of the system have to be known which is in case of the excited state only possible by the use of approximations.

The shielding depends on r_i which means that only the inner electrons will have a pronounced effect on the chemical shift. The effect of the surrounding atoms on the local magnetic field of the nucleus in question is negligible in case of diamagnetic shielding but has a pronounced effect on the paramagnetic shielding. $\sigma^{p}_{\mathrm{iso}}$ for ^{19}F was calculated by Bureau et. al.[116] by summarizing the squares of overlap integrals S_{l} (l = ligand) of the atomic orbitals of the nucleus in question and the ones of the surrounding atoms (see ref. 116). For $\sigma^{d}_{\mathrm{iso}}$ they calculated a value of 480 ppm. Based on the absolute scale of Hindermann and Cornwell[117] C_6F_6 has a shift of 352.9 ppm. In accordance with (12) it follows that

$$\delta_{\text{iso}} = \sigma_{\text{ref}} - \sigma^d - \sigma^p = 352.9\text{ ppm} - 480\text{ ppm} - \sigma^p = -127.1 - \sigma^p\ (\text{ppm}) = -127.1 - \frac{\sum\limits_l S_l}{\Delta}(\text{ppm}). \tag{77}$$

whereby the average value $\Delta > 0$ replaces $E_k - E_0 > 0$[116]. However, Bureau et al. showed that the chemical shift of a fluorine atom in a defined environment can be approximated by a very simple method which they named superposition model. As already mentioned σ^p can be calculated as a sum of the deshielding contributions of the different atoms surrounding the fluorine atom in question, thus, $\sigma^p = \sum\limits_{\text{l}} \sigma_{\text{l}}$. According to Bureau et al. these values can be estimated in the following way:

$$\sigma_{\text{l}} = \sigma_{\text{l}0}\exp[-\alpha_{\text{l}}(d - d_0)] \tag{78}$$
$$\sigma_{\text{l},0} = (\delta_{\text{iso,exp}} + 127.1)/cn \tag{79}$$
$$\alpha_{\text{l}} = -0.806 r_{\text{l}} + 4.048 \tag{80}$$
$$\delta_{\text{iso,calc}} = -127.1 - \sum_{\text{l}} \sigma_{\text{l}}. \tag{81}$$

Here $\delta_{\text{iso,exp}}$ is the chemical shift and d_0 is d(M-F) of the corresponding binary (basic) fluoride which would be BaF_2 if the contribution of a Ba ion to the chemical shift of fluorine shall be estimated or LiF in case of a Li ion etc. cn is the coordination number of the fluoride ion in question. Thus, $\sigma_{l,0} = (153 + 127.1)/4 = 70.025$ ppm in case of BaF_2. r_l is the ionic radius of the ligand cation, d is d(M-F) in the compound whose chemical shift shall be calculated. As can be seen from the information given above, the distance of the cation to the fluoride ion d(M-F) in the solid solutions plays a crucial role in the calculation. Small variations of d have a large effect on the chemical shift due to the exponential character of equation (78).

If d(M-F) is calculated based on the lattice parameters a calculated from the XRPD patterns of the different solid solutions, the chemical shifts calculated strongly deviates from the ones found experimentally and listed in Tab. 1. Exemplarily, for the sample with $x = 0.40$ the following values are calculated: 270 ppm, 196 ppm, 121 ppm, 47 ppm and -28 ppm. Since the lattice parameter a obtained from the XRPD pattern is an average value it seems appropriate to assume that d(Ba-F) differs from d(Ca-F) in the mixed phases since the cations have different ionic radii (112 pm and 142 pm for eightfold coordinated Ca^{2+} and Ba^{2+}, respectively[59]). If the cation-fluorine distances are taken from the pure fluorides BaF_2 and CaF_2 the following values are obtained: 152 ppm, 129 ppm, 105 ppm, 82 ppm and 58 ppm which are in fair agreement with the values measured. Since for the $[Ca]_4$ environment a value of 55 ppm is found, d(Ca-F) should be slightly larger than in pure CaF_2 which is reasonable due to the strain introduced by the larger Ba ions. If the value of d(Ca-F) is increased by about 0.2%, a chemical shift of 55 ppm is obtained.

The distances d between the cation and the fluoride ion in the solid solutions can be directly calculated from the chemical shift using equation (78):

$$\sigma_{\text{l}} = \sigma_{\text{l}0}\exp[-\alpha_{\text{l}}(d - d_0)] \tag{82}$$
$$d = \frac{ln\frac{\sigma_{\text{l}}}{\sigma_{\text{l}0}}}{-\alpha_{\text{l}}} + d_0 \tag{83}$$
$$\sigma_{\text{l}} = \frac{-127.1 + \delta_{\text{iso,exp}}}{N} \tag{84}$$

Where N is the number of cations of the same species coordinated to the fluoride ion. In case of the mixed cationic environments σ_{l} can be found when the σ_{l}-values obtained for $N = cn$ are used, here named as $\sigma_{\mathrm{l,par}}$:

$$\sigma_{\mathrm{l}} = \frac{-127.1 - N\sigma_{\mathrm{l,par}} - \delta_{\mathrm{iso,exp}}}{cn - N} \tag{85}$$

Thus, if d(Ba-F) in the $[\mathrm{Ca}]_3[\mathrm{Ba}]$ environment of $\mathrm{Ba}_{1-x}\mathrm{Ca}_x\mathrm{F}_2$ with a certain x and a respective $\delta_{\mathrm{iso,exp}}$ of the NMR line representing this environment shall be calculated, equation (85) will be

$$\begin{aligned}\sigma_{\mathrm{l}} &= \frac{-127.1 - 3\sigma_{\mathrm{l,[Ca]_4}} - \delta_{\mathrm{iso,exp}}}{4-3} &(86)\\ &= -127.1 - 3\sigma_{\mathrm{l,[Ca]_4}} - \delta_{\mathrm{iso,exp}}. &(87)\end{aligned}$$

To calculate d(Ca-F) in the same environment equation (85) will be:

$$\begin{aligned}\sigma_{\mathrm{l}} &= \frac{-127.1 - \sigma_{\mathrm{l,[Ba]_4}} - \delta_{\mathrm{iso,exp}}}{4-1} &(88)\\ &= \frac{-127.1 - \sigma_{\mathrm{l,[Ba]_4}} - \delta_{\mathrm{iso,exp}}}{3} &(89)\end{aligned}$$

The values calculated this way are probably fraud with a systematic error since it is not clear if the deshielding σ_{l} in a mixed coordination sphere does not differ from the one in the $[\mathrm{Ba}]_4$ or the $[\mathrm{Ca}]_4$ environment, $\sigma_{\mathrm{l,par}}$, since d(Ba-F) and d(Ca-F) could be smaller or larger in a mixed cationic environment than in the $[\mathrm{Ba}]_4$ or the $[\mathrm{Ca}]_4$ environment. Furthermore, it is assumed that in one coordination shell all cations of the same species have the same distance to the fluoride ion which might not be the case since it seems likely that the type of MF_8 cubes, i. e. the cation species centering these cubes, surrounding the MF_8 cubes which are part of the $[\mathrm{Ba}]_{4-z}[\mathrm{Ca}]_z$ environment in question, influences d(M-F) in this environment. Thus, there could be a distribution of distances d(M-F) with M = Ca^{2+} or Ba^{2+} in the respective $[\mathrm{Ba}]_{4-z}[\mathrm{Ca}]_z$ environments for each composition x of the $\mathrm{Ba}_{1-x}\mathrm{Ca}_x\mathrm{F}_2$ compounds. However, it should be noted that due to the exponential connection between d(M-F) and σ_l such a distribution should be rather narrow.

The values obtained for d(M-F) as a function of compositions show a plausible trend for the systems $\mathrm{Ba}_{1-x}\mathrm{Sr}_x\mathrm{F}_2$ and $\mathrm{Ca}_{1-x}\mathrm{Sr}_x\mathrm{F}_2$, i. e. the lattice parameter a decreases with decreasing d(M-F), while the situation is less clear for $\mathrm{Ba}_{1-x}\mathrm{Ca}_x\mathrm{F}_2$, as shown in Fig. 21. Especially for d(Ca-F) no clear change with x is visible. Intuitively one would assume an increased distance d(M-F) in case of the smaller cation and a decreased distance d(M-F) for the larger cations to reduce the mismatch between the MF_8 cubes. Interestingly, d(Ba-F) as well as d(Ca-F) in the mixed cationic environments are found to be larger than in the $[\mathrm{Ba}]_4$ and $[\mathrm{Ca}]_4$ environments, respectively. This is, less pronounced, also the case for $\mathrm{Ca}_{1-x}\mathrm{Sr}_x\mathrm{F}_2$ and $\mathrm{Ba}_{1-x}\mathrm{Sr}_x\mathrm{F}_2$. One may assume that this difference is due to the errors of the calculation by employing equation (85). But, if d(Ca-F) is smaller than calculated, d(Ba-F) would necessarily be larger than d(Ba-F) in the $[\mathrm{Ba}]_4$ environment. If d(Ba-F) is smaller than calculated, d(Ca-F) would necessarily be larger than d(Ca-F) in the $[\mathrm{Ca}]_4$ environment. Thus, it seems that in fact the MF_8 cubes neighboring each other expand in case that their centers are not occupied with the same cation species. Since the chemical shifts do not lead to unique possible arrangements of the cations around the fluoride ion another possibility seems to be the assumption of heterogeneous distances d(Ba-F) and d(Ca-F) in the mixed cationic environments which would lead to distorted MF_8 cubes. In case of $\mathrm{Ba}_{1-x}\mathrm{Ca}_x\mathrm{F}_2$ with $x = 0.50$ for the $[\mathrm{Ca}]_3[\mathrm{Ba}]$ coordination sphere a value of d(Ba-F) even larger than d(Ba-F) in BaF_2 is calculated which supports the assumption of distorted MF_8 cubes. Furthermore, we have to consider the broadness of the NMR lines especially in case of $\mathrm{Ba}_{1-x}\mathrm{Ca}_x\mathrm{F}_2$ which is most probably due to a distribution of d(M-F) values as will be shown in more detail later. It should also be considered, that a decrease of d(Ba-F) should be energetically less favorable than an expansion since for the ionic bond the attractive term scales with $1/d$ but the repulsive part scales with $1/d^x$ with $x \geq 10$. Thus, the repulsive force increases with d^{10} or even a higher power while the attractive force increases only with d.[118]

In Fig. 22 the coordination of one fluoride ion by the four cations is shown. As can be seen in this figure the fluoride ions (colored green) are cubically arranged around the cations in the fluorite structure. Some edges of these cubes are shared between the coordination spheres illustrated by red balls. As already shown, the chemical shifts of the NMR lines recorded for the $Ba_{1-x}Ca_xF_2$ solid solution show strong evidence that d(Ba-F) $\neq$ d(Ca-F). Therefore, the fluoride ion cubes surrounding the Ca ions have to be smaller than the cubes around the Ba ions which would lead to a mismatch between neighboring cubes with different cation: d(F-F) = d(M-F)/$\sqrt{3}$ which would lead to a mismatch in the order of 0.03 nm ([Ba][Ca]$_3$) to 0.0235 nm ([Ba]$_3$[Ca]) in case of $Ba_{1-x}Ca_xF_2$, 0.013 nm for $Ba_{1-x}Sr_xF_2$ and 0.012 nm for $Ca_{1-x}Sr_xF_2$ (according to the d(M-F) values shown in Fig. 21).

Finally, we should note that the superposition model gives only a rough trend and no exact chemical shift values, for which much more elaborate calculations are necessary, see, e. g., ref. 119. However, to test the quality of the d(M-F) values calculated from the ^{19}F MAS NMR spectra these values can be averaged by $\sum_{i=1}^{4} d_i(\text{M-F}) b_i$ with b_i being the abundance of the respective distance in the compound. Example: d(Ca-F) in the [Ca]$_3$[Ba] environment shall be d_2(Ca-F). Then, b_2(Ca-F) = c_2(Ca-F)/(c_1(Ca-F)+c_2(Ca-F)+c_3(Ca-F)+c_4(Ca-F))) with c_i being the integrals of the NMR lines assigned to the four $[Ba]_{1-z}[Ca]_z$ environments in which Ca occurs (see also next chapter). If the d(M-F) values calculated from the ^{19}F MAS NMR spectra are accurate, the averaged d(M-F) values should be very similar to the ones calculated from the respective XRPD patterns since the X-ray diffraction technique provides the over a large scale averaged distances in the system. For a better comparison with the values obtained from the XRPD patterns the d(M-F) values are used to calculate the average lattice parameter a_{av} by employing the following formulas (exemplarily for the $Ba_{1-x}Ca_xF_2$ system):

$$a_{\text{Ca-F}} = \frac{d(\text{Ca-F})}{(0.25^2 + 0.25^2 + 0.25^2)^{0.5}} \tag{90}$$

$$a_{\text{Ba-F}} = \frac{d(\text{Ba-F})}{(0.25^2 + 0.25^2 + 0.25^2)^{0.5}} \tag{91}$$

$$a_{\text{av}} = a_{\text{Ca-F}} \cdot x(\text{CaF}_2) + a_{\text{Ba-F}} \cdot (1 - x(\text{CaF}_2)) \tag{92}$$

In table 2 the lattice parameters calculated are shown for the samples for which all necessary data (distances of all environments) is available (cf. Fig 21). The values obtained are in surprisingly good agreement with the ones calculated from the respective XRPD patterns. While in case of $Ca_{1-x}Sr_xF_2$ and $Ba_{1-x}Sr_xF_2$ almost no differences can be seen, in case of $Ba_{1-x}Ca_xF_2$ the differences between the lattice parameters calculated from the ^{19}F MAS NMR spectra and the ones calculated from the XRPD patterns are a bit larger. This is probably due to the less accurate estimation of the amounts of the respective environments b_i (see next chapter) or due to the larger distribution of distances d(M-F) in this compound.

Cation distribution Expectedly, an NMR line representing the [Ca]$_4$ environment does not show up for the sample with x = 0.20 due to the small CaF_2 content and, thus, the negligible quantity of this environment in this sample (vide supra). In the sample with x = 0.40 this NMR line is partly covered by the shoulder of the NMR line of the [Ca]$_3$[Ba] environment and, thus, this coordination sphere is almost not detectable in the sample. Accordingly, an NMR line for the [Ba]$_4$ environment cannot be found for the sample with x = 0.80. Even the [Ba]$_3$[Ca] environment does not show up.

In Fig. 23 on the left side the amount of fluoride ions located in the five different environments with composition x is shown. The lines show the fractions of the different environments expected

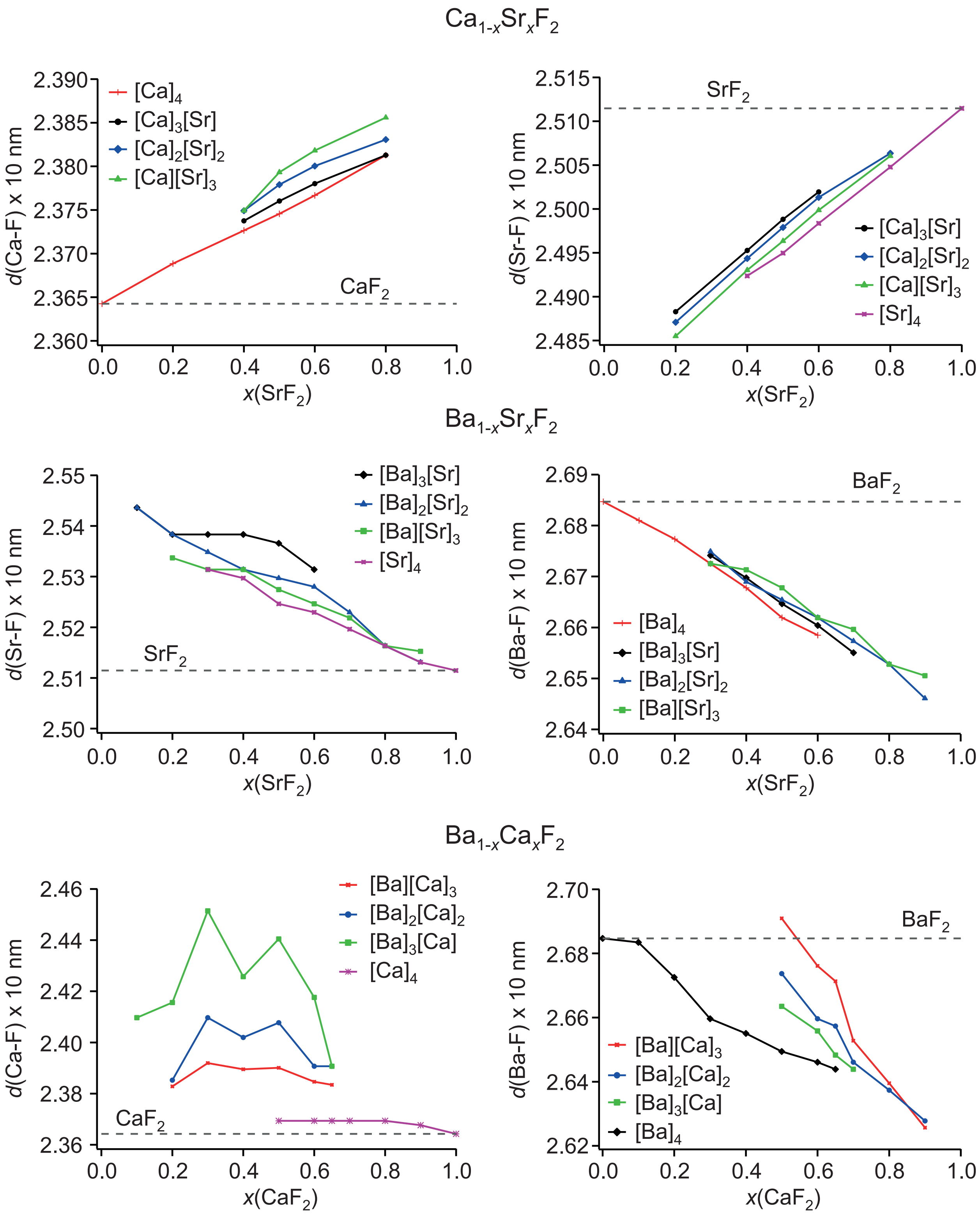

Figure 21: d(M-F) calculated for $Ca_{1-x}Sr_xF_2$, $Ba_{1-x}Sr_xF_2$ and $Ba_{1-x}Ca_xF_2$.

Table 2: Average distances in the solid solutions calculated from ^{19}F MAS NMR chemical shift values

$Ca_{1-x}Sr_xF_2$	x	d_{av}(Ca-F) in nm	d_{av}(Sr-F) in nm	a_{av} in nm	a_{XRPD} in nm
	0.40	0.2374	0.2494	0.5594	0.5597
	0.50	0.2378	0.2498	0.5629	0.5631
	0.60	0.2380	0.2500	0.5664	0.5665

$Ba_{1-x}Sr_xF_2$	x	d_{av}(Sr-F) in nm	d_{av}(Ba-F) in nm	a_{av} in nm	a_{XRPD} in nm
	0.30	0.2536	0.2674	0.6080	0.6080
	0.40	0.2534	0.2669	0.6040	0.6040
	0.50	0.2531	0.2666	0.6000	0.6000
	0.60	0.2526	0.2662	0.5959	0.5960

$Ba_{1-x}Ca_xF_2$	x	d_{av}(Ca-F) in nm	d_{av}(Ba-F) in nm	a_{av} in nm	a_{XRPD} in nm
	0.50	0.2401	0.2666	0.5851	0.5831
	0.60	0.2386	0.2657	0.5760	0.5757
	0.65	0.2383	0.2650	0.5718	0.5721

if the two different cation species are distributed randomly over the lattice sites. To calculate these values a cubical lattice consisting of 1.5625 x 10^{10} cations was simulated with a program which algorithm was designed by Dr. Benjamin Ruprecht and the author and written by Dipl.-Ing. Malte B. Rücker. For the random distribution of the cations over the lattice sites the Mersenne Twister algorithm was used.[120] Expectedly, a highly symmetric distribution is obtained.

While in case of $Ba_{1-x}Sr_xF_2$ and $Ca_{1-x}Sr_xF_2$[56] a random distribution of the cations was observed this is not true for $Ba_{1-x}Ca_xF_2$. As can be seen in Fig. 23 on the left side, only the $[Ca]_4$ and $[Ba]_4$ environments follow the predicted values for a random distribution of the cations in case of $Ba_{1-x}Ca_xF_2$, roughly. The amount of fluoride ions in the mixed cationic environments clearly differ from the amounts expected in case of a random distribution. This is partly due to the badly separated NMR lines which made a fit of them difficult which can also be seen if the stoichiometry of the samples is tested by adding the integrals of the NMR lines and weighting them by their Ba- or Ca-content. This leads to x values close to the ones expected for x = 0.40 (0.41), x = 0.70 (0.71) and x = 0.80 (0.83) but shows rather large differences in case of the samples with x = 0.50 (0.59), x = 0.60 (0.66) and x = 0.65 (0.71), thus for the samples exhibiting the NMR spectra with the broadest and most overlapping NMR lines, see Table 3. The $[Ba][Ca]_3$ environment, however, seems to be clearly overrepresented while the $[Ba]_2[Ca]_2$ and the $[Ba]_3[Ca]$ environments are underrepresented, which can already be seen in Fig. 18.

One may assume that this could be a kinetic effect, i. e., that initially the different environments are not in equilibrium. Hence, with increasing t_{mill} the cations should become more and more randomly distributed over the lattice sites. The relative amounts of the different coordination spheres were also found to be a function of t_{mill} in $Ba_{1-x}Sr_xLiF_3$.[23]

However, as shown in Fig. 24 no pronounced change of the amounts of the different fluoride ion environments was found for a sample with x = 0.30 milled for 99 h compared to the one milled for 52 h as well as for a sample with x = 0.80 milled for 24 h and 80 h, respectively. Therefore, it seems unlikely that a kinetic effect is the reason for the deviation from a random distribution of the cations.

The deficiency in Ba-rich environments for larger x might simply be explained by the overall decrease of d(M-F) with increasing x which also leads to a decreasing lattice parameter. The larger x the larger should be the strain introduced by Ba-rich environments and, thus, Ca-rich environments will be preferred. As already mentioned, it is energetically favorable to substitute a Ba ion in a $[Ca]_4$

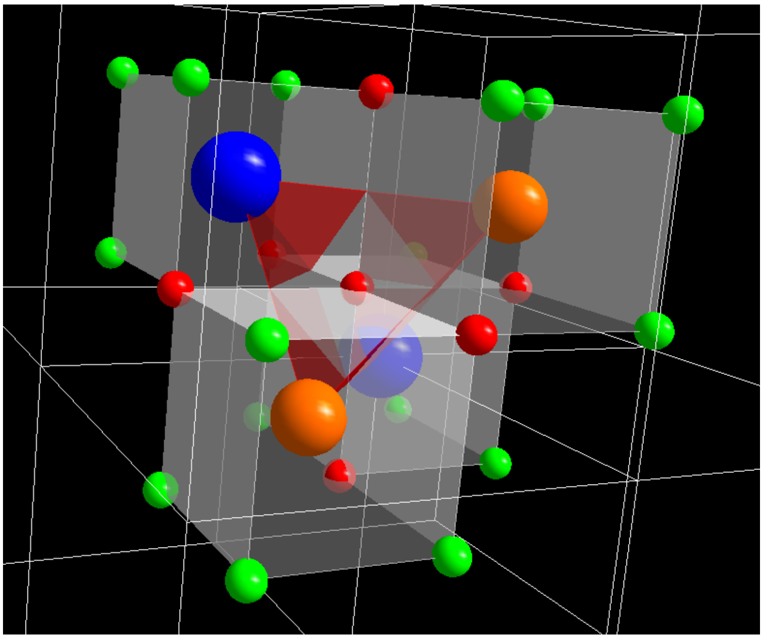

Figure 22: Coordination sphere of a fluoride ion in $Ba_{1-x}Ca_xF_2$ where Ba ions are portrayed as blue balls and Ca ions as orange balls. The balls colored red mark the fluoride ions shared by the four cation associated MF_8 cubes.

environment for a Ca ion and increase the average M-F distance, than to substitute a Ca ion in a $[Ba]_4$ environment for a Ba ion and decrease the average M-F distance. This is in good agreement with the results shown in Fig. 23 for $x \geq 0.50$ especially for the $[Ba]_2[Ca]_2$ environment. For this environment it also has to be considered that there are four shared edges of the MF_8 cubes centered by non-similar cation species while in case of $[Ba]_3[Ca]$ and $[Ba][Ca]_3$ three edges of the MF_8 cubes centered by non-similar cation species are shared which presumably should result in a reduced tension of these environments compared to the $[Ba]_2[Ca]_2$ environment.

In Fig. 23 on the right side, δ_{iso} measured for the different cation coordination spheres in the systems $Ca_{1-x}Sr_xF_2$, $Ba_{1-x}Sr_xF_2$ and $Ba_{1-x}Ca_xF_2$ as a function of composition are shown. An almost perfect linear slope is obtained for $Ca_{1-x}Sr_xF_2$ and $Ba_{1-x}Sr_xF_2$ which was also found for $Ca_{1-x}Sr_xF_2$ by Youngman et al.[121] and Ponader et al.[56] and for $Ba_{1-x}Sr_xLiF_3$[23], while the slope is only in approximation linear in case of $Ba_{1-x}Ca_xF_2$. This linear dependence of δ_{iso} is, as already discussed before, most probably due to the change of d(M-F). Expectedly, no change is observed for the chemical shift of the $[Ca]_4$ environment in $Ba_{1-x}Ca_xF_2$ for $x = 0.50$ to $x = 0.80$. Thus, as already shown in Fig. 21 d(Ca-F) seems to be constant in this coordination sphere in this compositional range. It should be noted that if the $[Ca]_4$ environments were segregated from the other environments, this would imply the presence of (small clusters of) CaF_2 which was not observed by XRPD or ^{19}F MAS NMR. Therefore, the reason for the fixed d(Ca-F) has to be found on a microscopic level. At first glance one might think that the further environment of the $[Ca]_4$ coordination sphere for all compositions is very similar which could also explain the deviation from a statistical distribution of the five coordination environments of the fluoride ions. However, it seems more likely that the Ca-F distances in the $[Ca]_4$ environment, in contrast to the Ba-F distances in the $[Ba]_4$ environment, are hardly influenced by the ions surrounding it apart from an increase of d(Ca-F) compared to d(Ca-F) in CaF_2. This would mean that the small $[Ca]_4$ environment can be placed in every $[Ba]_z[Ca]_{4-z}$ neighborhood without creating sufficient amounts of strain to force the Ca ions or fluoride ions in this environment to change their place while the larger $[Ba]_4$ environment as well as the other environments occupying more space than the $[Ca]_4$ environment have to change their distances to fit into

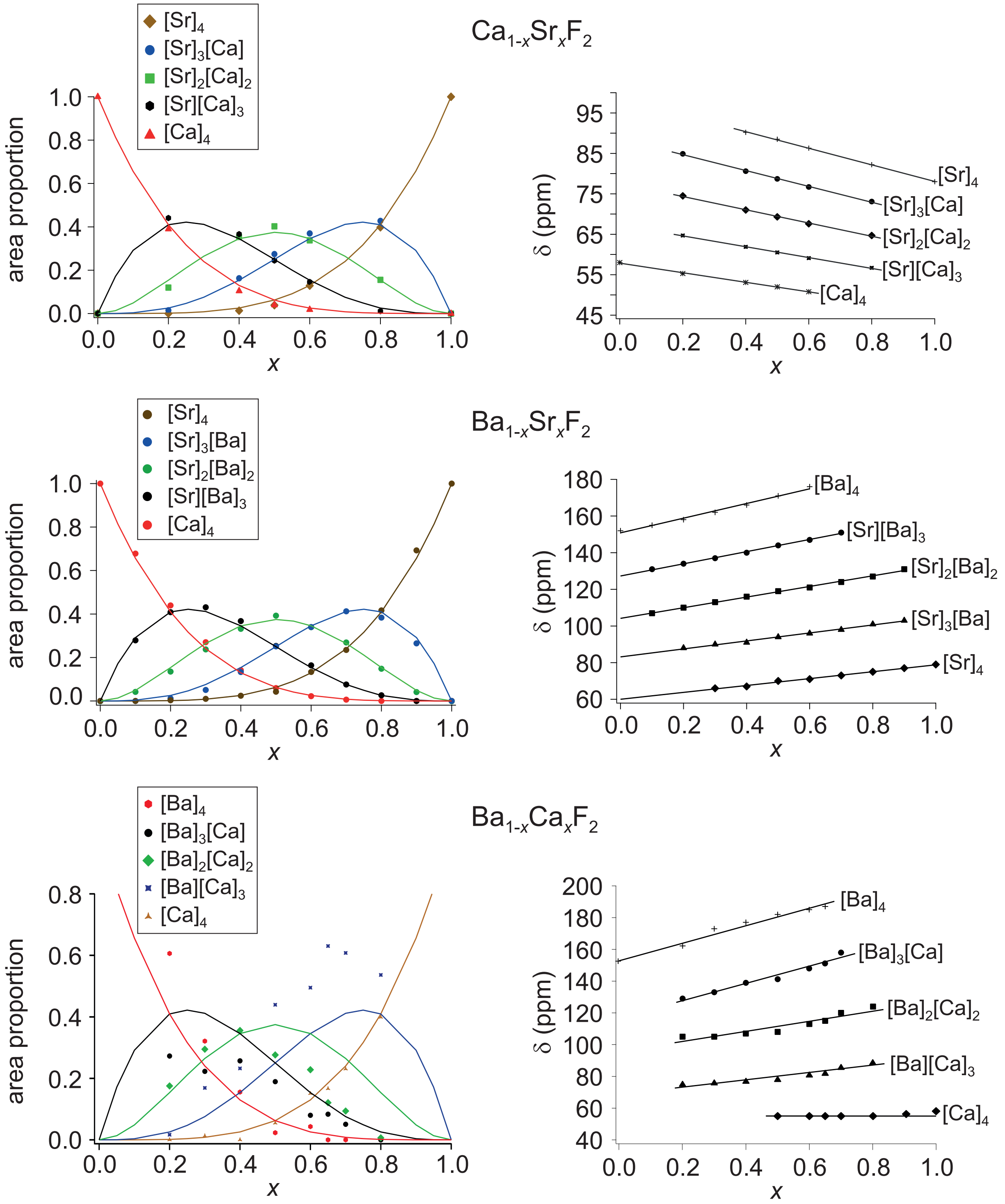

Figure 23: Left: change of the areas of the NMR lines of the different $[Ba]_z[Ca]_{4-z}$, $0 \leq z \leq 4$, environments in dependence of x. Right: shift of δ_{iso} in dependence of x. With increasing x the NMR lines are shifted to higher ppm values except for the $[Ca]_4$ coordination sphere.

Table 3: Stoichiometries of the samples estimated from the integrals of the NMR lines

x real	x calculated
0.20	0.16
0.30	0.36
0.40	0.41
0.50	0.59
0.60	0.66
0.65	0.71
0.70	0.72
0.80	0.83

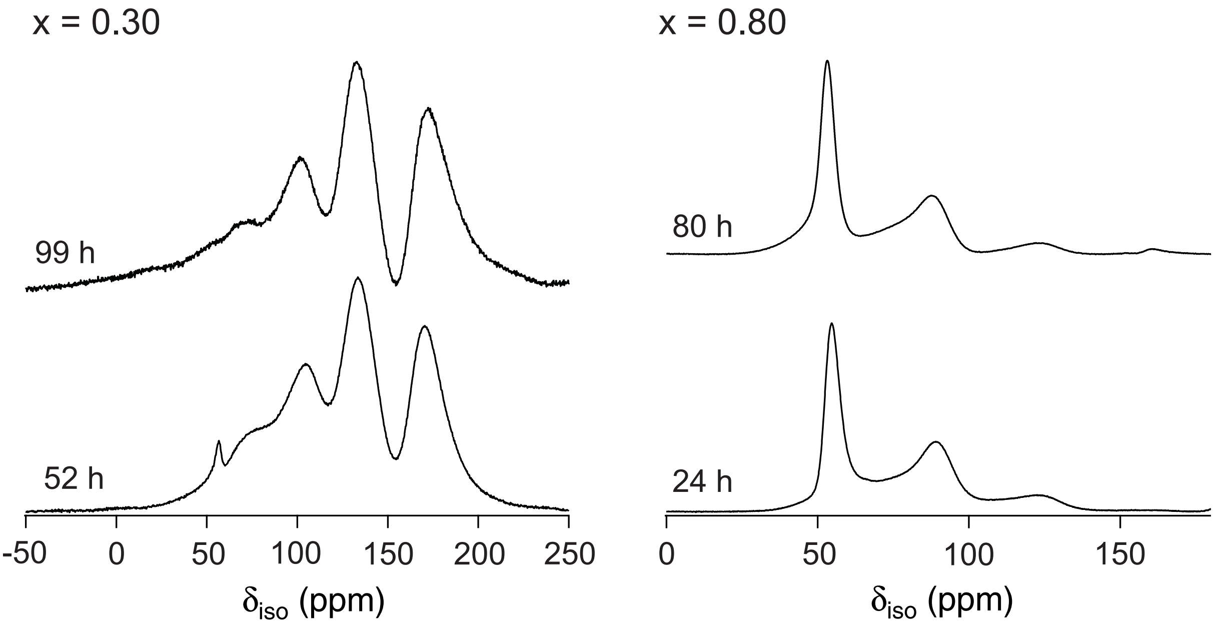

Figure 24: Left: ^{19}F MAS NMR spectra of a sample with x = 0.30 after 52 h and 99 h of milling. Right: ^{19}F MAS NMR spectra of a sample with x = 0.80 after 24 h and 80 h of milling.

the different $[Ba]_z[Ca]_{4-z}$ neighborhoods.

It should be mentioned that the chemical shift in a solid can be used to estimate the temperature of a sample in the probe coil very precisely due to d(N'-N") = f(T) with N' and N" being nuclei of which one or both are NMR active.[122] The high spinning frequency of the rotor as well as the necessary small diameter of the rotor lead to an increase of the sample temperature in the order of 40 to 60 K.[123] Thus, the absolute values of the positions of the NMR lines measured are different from the ones at 293 K. Since all the NMR lines are referenced to C_6F_6 and were measured at the same spinning frequency the chemical shifts should not be much different from the ones which would be measured at ambient temperatures although the change of d(M-F) with T is material specific. Thus, if chemical shifts recorded at different spinning speeds are compared this potential source of error should not be ignored.

Substitutional disorder As mentioned above, the NMR lines reflecting the different $[Ba]_z[Ca]_{4-z}$, $z \leq 4$, environments are very broad which is probably due to a variety of slightly different magnetic environments for each fluoride ion located in one of the cationic environments. This is probably

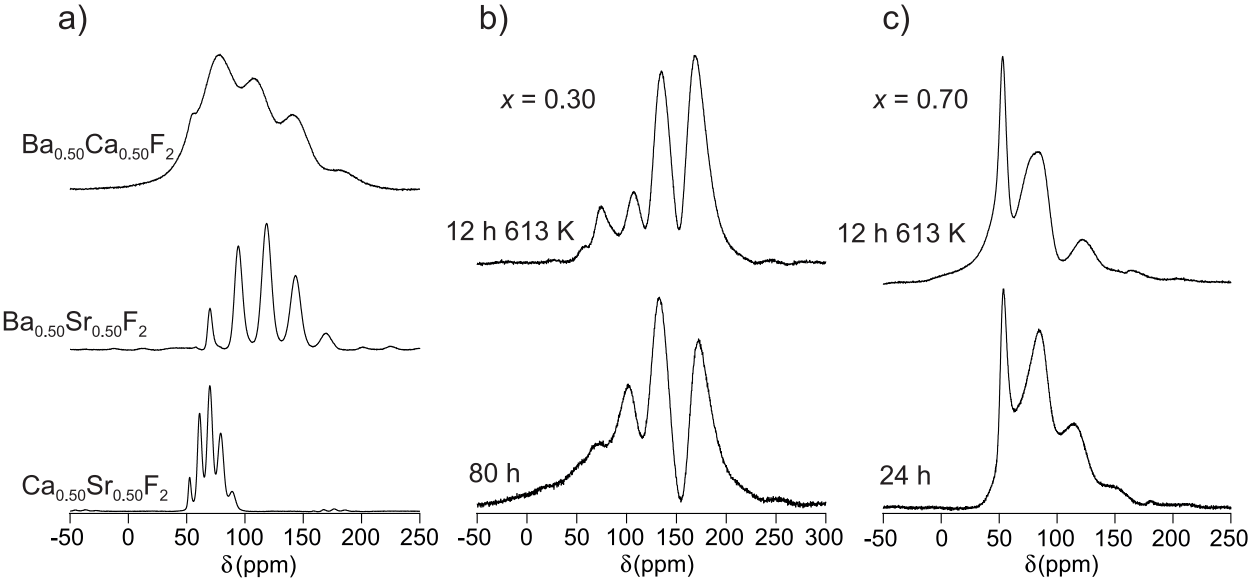

Figure 25: a) ^{19}F MAS NMR spectra of $Ca_{0.5}Sr_{0.5}F_2$, $Ba_{0.5}Sr_{0.5}F_2$ after 10 h and $Ba_{0.5}Ca_{0.5}F_2$ after 99 h of milling, respectively. For all samples five NMR lines are visible which clearly deviate in position and fwhm. b) ^{19}F MAS NMR spectra of a sample with x = 0.30 milled for 80 h and of the same sample after annealing for 12 h at 613 K. c) ^{19}F MAS NMR spectra of a sample with x = 0.70 milled for 24 h and of the same sample after annealing for 12 h at 613 K.

due to different distributions of the cations in the higher coordination spheres of the respective $[Ba]_z[Ca]_{4-z}F$ unit. Therefore, slightly different distortions of the lattice next to this unit emerge which change d(Ba-F) and d(Ca-F) in this unit and, thus, unequal magnetic environments for the fluoride ions, although located in the same type of $[Ba]_z[Ca]_{4-z}$ environment, are established. Thus, the broad NMR lines are superpositions of NMR lines with slightly different chemical shifts.

Interestingly, the full width at half maximum (fwhm) of the ^{19}F NMR line of the $[Ca]_4$ environment is considerably smaller than the ones of the other $[Ba]_z[Ca]_{4-z}$ environments. As already shown, the chemical shift of the $[Ca]_4$ environment does not change with x over a broad compositional range and, thus, d(Ca-F) is considered to be constant in this environment for the compositions with $x = 0.50$ to $x = 0.80$. Therefore, this environment experiences only the outer changes of the cation-anion distance as well as the different deshielding[23,116] due to the different kind of cations enclosing this unit in the farther neighborhood which leads to a narrower NMR line. Accordingly, the fwhm of the ^{19}F MAS NMR line of the $[Ca]_4$ environment in the solid solutions is still more than about a factor of two larger than the fwhm of the ^{19}F MAS NMR line of milled pure CaF_2. This is also true for the NMR lines of the other binary fluorides when compared to the respective isocationic environments $[Ba]_4$, $[Sr]_4$ and $[Ca]_4$ in $Ba_{1-x}Ca_xF_2$, $Ba_{1-x}Sr_xF_2$ as well as in $Ca_{1-x}Sr_xF_2$.

In Fig. 25 a) ^{19}F MAS NMR spectra of $Ca_{0.50}Sr_{0.50}F_2$, $Ba_{0.50}Sr_{0.50}F_2$ both milled for 10 h and of $Ba_{0.50}Ca_{0.50}F_2$ milled for 99 h are shown. The spectrum of $Ca_{0.50}Sr_{0.50}F_2$ consists of five narrow NMR lines with only slightly different chemical shifts. In comparison the clearly broader NMR lines of $Ba_{0.50}Sr_{0.50}F_2$ are distributed over a much wider range of chemical shifts reflecting the large deshielding of the fluoride ions due of the large number of electrons of the Ba ions compared to Sr and Ca ions.[116] While the chemical shift range of $Ba_{0.50}Ca_{0.50}F_2$ is only a little wider, the NMR lines are much broader than the ones of $Ba_{0.50}Sr_{0.50}F_2$ which is probably due to the large difference of the ionic radii of the Ba and Ca ions leading to a larger variability of d(M-F) in this compound and probably also due to differences of the microstructure of the $Ba_{1-x}Ca_xF_2$ and the microstructure of $Ba_{1-x}Sr_xF_2$ and $Ca_{1-x}Sr_xF_2$ as discussed before.

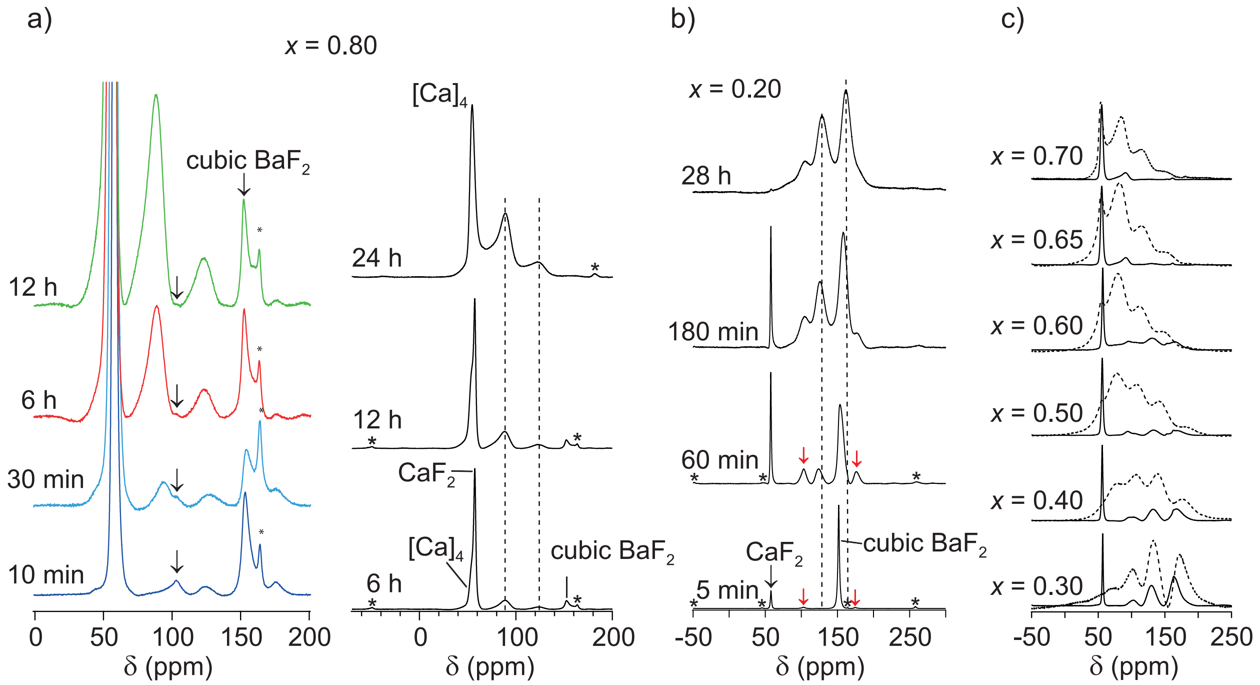

Figure 26: a) ^{19}F MAS NMR spectra of the sample with $x = 0.80$ after mechanical treatment for different t_{mill}. An additional NMR line is visible (black arrows). Spinning sidebands are marked by asterisks. The different position of the sidebands for the sample milled for 24 h is due to the smaller field strength (^{19}F resonance frequency = 471 MHz) at which this spectrum was recorded. b) ^{19}F MAS NMR spectra of the sample with $x = 0.20$ recorded at 565 MHz after mechanical treatment for the periods shown. After five minutes of milling the NMR line of cubic BaF_2 dominates the spectrum. Small amounts of orthorhombic BaF_2 show up (red arrows). c) Spectra of the mixtures to give $Ba_{1-x}Ca_xF_2$ with $x = 0.30$, $x = 0.40$, $x = 0.50$, $x = 0.60$, $x = 0.65$ and $x = 0.70$ after six hours of milling. For comparison the spectra (dotted lines) of the same samples after 99 h ($x = 0.30$, $x = 0.40$, $x = 0.50$, $x = 0.60$ and $x = 0.65$) and 24 h ($x = 0.70$) of milling, respectively, are shown.

Thermal stability and formation In Fig. 25 also ^{19}F MAS NMR spectra of the soft annealed (12 h at 613 K) samples $Ba_{0.70}Ca_{0.30}F_2$ (b) and $Ba_{0.30}Ca_{0.70}F_2$ (c) are shown. Although there were no signs of decomposition visible in the XRPD patterns of these compounds after heat treatment (vide supra), the spectra exhibit a change of the amounts of the fluoride ions in the different cationic environments. For $Ba_{0.70}Ca_{0.30}F_2$ the amounts of fluoride ions in the Ba rich environments increased, while the amounts of fluoride ions in the Ca rich environments decreased. Accordingly, in case of $Ba_{0.30}Ca_{0.70}F_2$ a change towards the Ca rich environments is observed. However, in both cases no NMR lines of the binary fluorides emerge. Therefore, the narrowing of the XRPD peaks after soft annealing of the $Ba_{1-x}Ca_xF_2$ discussed in section 9.3.1 is at least partly due to a reduced substitutional disorder.

In Fig. 26 a) the change of the ^{19}F MAS NMR spectra of the sample with $x = 0.80$ with increasing t_{mill} is shown. After six hours of milling the narrow NMR line of CaF_2 is still clearly visible and also the NMR line of cubic BaF_2 exhibiting a smaller intensity is resolved. Next to the NMR line of CaF_2 the broader NMR line of the $[Ca]_4$ environment shows up increasing in intensity with increasing milling time. The NMR lines of the $[Ca]_3[Ba]$ and $[Ca]_2[Ba]_2$ environments are clearly visible already after six hours of milling. The chemical shifts of these NMR lines show no dependence on t_{mill}. This is in accordance with the observation of a (pseudo-)single step reaction by XRPD already discussed before (see Fig. 13). For short milling times an additional NMR line emerges (Fig. 26 d)) which probably can be assigned to the intermediate phase found in the XRPD pattern after 10 min of milling. This NMR line decreases in intensity with increasing t_{mill} and, thus, progressing reaction to the solid solution. In Fig. 26 b) the formation of the sample with $x = 0.20$ is shown. After five minutes of milling the spectrum is dominated by the NMR line of BaF_2. In addition to the smaller NMR line of CaF_2 reflecting the much smaller amount of this fluoride in this mixture NMR lines of orthorhombic BaF_2 show up at 103 and 176 ppm (red arrows)[66]. In accordance with the results obtained by XRPD the amount of orthorhombic BaF_2 is clearly increased after 60 minutes of milling. After 28 hours of milling no orthorhombic BaF_2 can be detected by ^{19}F MAS NMR due to the broad NMR lines of the $[Ba]_4$ and $[Ba]_2[Ca]_2$ environments masking the residual small amount of the orthorhombic phase (compare Fig. 8). The shift of the NMR lines representing the different cationic environments of the fluoride ions with t_{mill} can be clearly seen (dotted lines). This is in accordance with the observation in Fig. 8 showing a decrease of the lattice parameter a with increasing milling time. Interestingly, the NMR line of BaF_2 has changed to the one of the $[Ba]_4$ environment after 60 minutes of milling, i. e., it is broadened and lost a lot of intensity, while the NMR line of the CaF_2 remained unchanged. Thus, as already deduced from the XRPDs the BaF_2 reacts much faster than the CaF_2 which is probably due to the larger lattice parameter of the BaF_2 which should ease the introduction of the small Ca ions into it and the larger hardness of the CaF_2 which should lead to a stronger decrease of the BaF_2 crystallite size compared to the one of the CaF_2 which also should accelerate the reaction of the BaF_2.

In Fig. 26 c) spectra of the samples with compositions in the range $x = 0.30$ to $x = 0.70$ after mechanical treatment for six hours are shown. The $[Ba]_4$, $[Ba]_3[Ca]$ and $[Ba]_2[Ca]_2$ environments are already clearly visible except for the samples with $x = 0.65$ and $x = 0.70$. For the samples with $x = 0.30$ to $x = 0.60$ a very similar chemical shift for each of the coordination spheres can be observed, which is in accordance with their very similar lattice parameter (see Fig. 4) indicating a similar formation mechanism for these samples, as shown before. As already discussed above the NMR lines of the different coordination spheres shift to larger ppm values with increasing t_{mill}.

9.3.3 Pair distribution function

For $Ba_{0.50}Ca_{0.50}F_2$, $Ba_{0.60}Ca_{0.40}F_2$, $Ba_{0.50}Sr_{0.50}F_2$ and $Ca_{0.50}Sr_{0.50}F_2$ XRPD patterns were recorded using synchrotron radiation which enabled the measurement of diffractograms with q-values of up to 20 Å^{-1}. This allowed the calculation of pair distribution functions (PDF) of the samples by

Fourier transformation of the diffractograms. While the XRPD patterns allow the determination of the average positions of the atoms the PDF pattern exhibits the actual distances between the atoms. In Fig. 27 the PDF patterns of the samples are shown. The q-range used for the Fourier transform was 18 $Å^{-1}$ for all samples since the quality of the diffractograms is drastically decreased for larger values of q due to instrumental effects. Since all the samples crystallize in the cubic fluorite structure the PDF patterns of the samples are very similar. The distances between the ions increase in the order $Ca_{0.50}Sr_{0.50}F$, $Ba_{0.50}Sr_{0.50}F_2$, $Ba_{0.60}Ca_{0.40}F_2$, and $Ba_{0.50}Sr_{0.50}F_2$ which is in agreement with the lattice parameters obtained from the XRPD patterns. In the same order the width of the peaks in the PDF patterns increase indicating an increase of the distribution width of the distances of the ions in the compounds. The lattice parameters can also be seen in the PDF patterns (the second M-M distance, which are marked with a ‡) and are in good agreement with the values form the XRPD patterns. With increasing distance only the metal-metal distances can be seen due to the larger structure factors of the metal ions compared to the one of the fluoride ion. The shortest metal-fluoride distances (which are marked with a #) in the compounds are slightly smaller (about 0.002 nm) than the d(M-F) values calculated from the ^{19}F MAS NMR chemical shifts with M being the metal ion with the larger atomic number and, thus, larger structure factor. Expectedly, the slightly different distances calculated from the ^{19}F MAS NMR spectra are not resolved in the PDF pattern but a broad peak is visible which is most probably a superposition of the several distances d(M-F). An increase of q could increase the resolution such that some of the different M-F distances may become visible. Interestingly, the PDF pattern of the samples $Ca_{0.50}Sr_{0.50}F$ and $Ba_{0.50}Sr_{0.50}F_2$ show one, the samples $Ba_{0.60}Ca_{0.40}F_2$ and $Ba_{0.50}Ca_{0.50}F_2$ two additional peaks which cannot be assigned to a distance in the fluorite lattice, see the black arrows in Fig. 27. For the $Ba_{0.50}Sr_{0.50}F_2$ the peak can be found at 0.36 nm, while in case of the $Ca_{0.50}Sr_{0.50}F_2$ just a broad shoulder is observable in this region. In case of $Ba_{0.60}Ca_{0.40}F_2$ the peak is located at 0.33 nm and for the sample with the composition $Ba_{0.50}Ca_{0.50}F_2$ it can be found at 0.305 nm. Thus, this distance is correlated with the lattice parameter of the compounds. These distances seem too large for a M-F distance and too short for a M-M distance in the fluorite lattice (the smallest d(Ca-Ca) in CaF_2 is 0.386 nm). The second peak in case of the two $Ba_{1-x}Ca_xF_2$ samples shows up at 0.228 nm for the sample with $x = 0.40$ and at 0.226 nm for the sample with $x = 0.50$. These distances are shorter than the shortest distance in CaF_2 (d(Ca-F) = 0.236 nm). There was also no additional ^{19}F NMR line in the spectra of these samples visible which can be assigned to such a short M-F distance. In case of a d(Ca-F) smaller than 0.236 nm the ^{19}F NMR line should be located at a higher ppm value than the one of the $[Ca]_4$. In fact the NMR lines of the $[Ca]_3[Ba]$ environments seem to be a bit asymmetric. Thus, maybe the NMR line which can be assigned to this short Ca-F distance is overlaid by the other NMR lines. This could also explain the too high abundance of the $[Ca]_3[Ba]$ environment. Perhaps it is a F-F distance although the ionic radii of 0.133 nm and the fact that they would repel each other make this assumption rather improbable. By all means, this distance seems to represent the distortion of the fluorite structure due to the different ionic radii of the two different cation species building up the structure. Therefore, the larger distance might be caused by a cation-cation distance which is decreased due to these distortions. On the other hand, the small distance is not visible in case of the $Ca_{0.50}Sr_{0.50}F_2$ and the $Ba_{0.50}Sr_{0.50}F_2$ but only the larger distance can be observed. Thus, there seems to be no direct connection between the two additional distances. However, without a reliable simulation of the lattice the true nature of these distances cannot be revealed. Another way to assign these peaks is to measure the Extended-X-ray-Fine Structure (EXAFS) which allows to distinguish between the elements being part of a pair of the pair distribution function. Such measurements were done in October at Diamond Light Source in Oxfordshire. The measurement results are currently processed. Furthermore, after these measurements a simulation of the microstructure will be initiated using all the information gained with the different techniques as a reference.

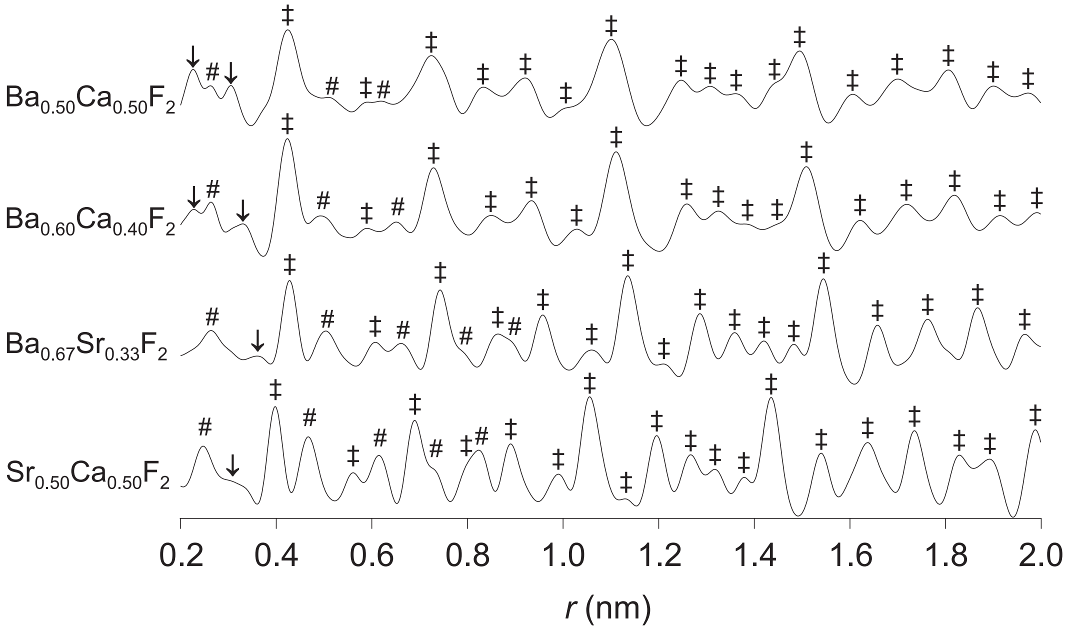

Figure 27: PDF patterns of $Ba_{0.50}Ca_{0.50}F_2$, $Ba_{0.60}Ca_{0.40}F_2$, $Ba_{0.50}Sr_{0.50}F_2$ and $Ca_{0.50}Sr_{0.50}F_2$. Metal-metal distances are marked with a ‡ while metal-fluoride distances are marked with a #.

9.3.4 Ionic conductivity of the compounds

In Fig. 28 the temperature dependence of the dc conductivity of a selection of $Ba_{1-x}Ca_xF_2$ samples is shown in an Arrhenius representation according to

$$\sigma_{\mathrm{dc}}T = \sigma_0 \exp(-E_{\mathrm{a}}/(k_{\mathrm{B}}T)) \tag{93}$$

where E_a denotes the activation enthalpy, σ_0 is the pre-exponential factor and k_B is Boltzmann's constant.

As already shown by Ruprecht et al.[66] the dc conductivity of a mixture of 0.40 parts BaF_2 and 0.60 parts CaF_2 mechanically treated in a high-energy ball mill is higher than the ones of the mechanically treated binary fluorides. With an ionic conductivity of about $3x10^{-3}$ S/cm observed for $Ba_{0.50}Ca_{0.50}F_2$ at 588 K this fluoride ion conductor is comparable to the well known fast ion conductor $Ba_{0.50}La_{0.50}F_{2.5}$ for which a dc conductivity of $2.5x10^{-3}$ S/cm was found at that temperature.[124] The dc conductivity of $Ba_{0.50}Ca_{0.50}F_2$ is about 2 orders of magnitude higher than the one of pure BaF_2 milled for 6 h. Thus, it is very similar to the value found in the study of Ruprecht et al. for their BaF_2-CaF_2 mixture milled 3 hours in a tungsten carbide vial set.[66] In turn, the dc conductivity of milled BaF_2 is about two orders of magnitude higher than that of untreated BaF_2 (cf. ref. 66) and even about three orders of magnitude higher than found for single-crystalline BaF_2[124]. The dc conductivity of single-crystalline CaF_2 (not shown in Fig. 28) is even lower than the one of single-crystalline BaF_2 with a dc conductivity of about 1.75 x 10^{-10} S/cm at 572 K[45]. A micro-crystalline sample of CaF_2 was not measured due to persistent problems to press a pellet which survives the measurements in a sufficiently broad temperature range. Mechanical treatment of the binary fluorides for $t_{\mathrm{mill}} > 6$ h does not lead to a further increase of their dc conductivity.

The increased conductivity of the binary fluorides after milling can be ascribed to the formation of large amounts of highly conductive grain boundaries.[66,125] Since the $Ba_{1-x}Ca_xF_2$ samples do not clearly differ in crystallite size (cf. Fig. 5) this effect cannot explain the increased ionic conductivity found for $Ba_{1-x}Ca_xF_2$. In case of $Ca_{1-x}Sr_xF_2$ and $Ba_{1-x}Sr_xF_2$ prepared by mechanical treatment only the expected increase of the conductivity from CaF_2 to SrF_2 and SrF_2 to BaF_2 can be observed,

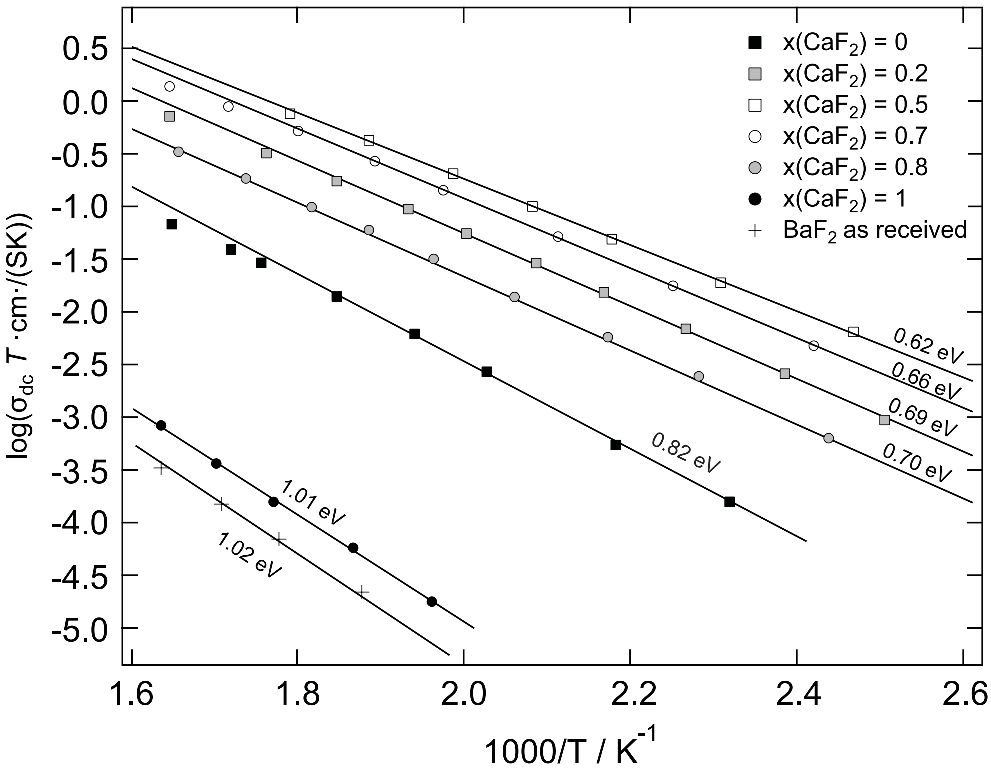

Figure 28: Arrhenius plot of the dc conductivities of some of the samples prepared by 6 hours of milling. The sample with $x = 0.50$ shows the highest dc conductivity, while milled CaF_2 shows a by 4 orders of magnitude smaller conductivity. At high temperatures the dc conductivity is not increasing linearly anymore probably due to decomposition of the compounds or grain growth in case of the binary fluorides.

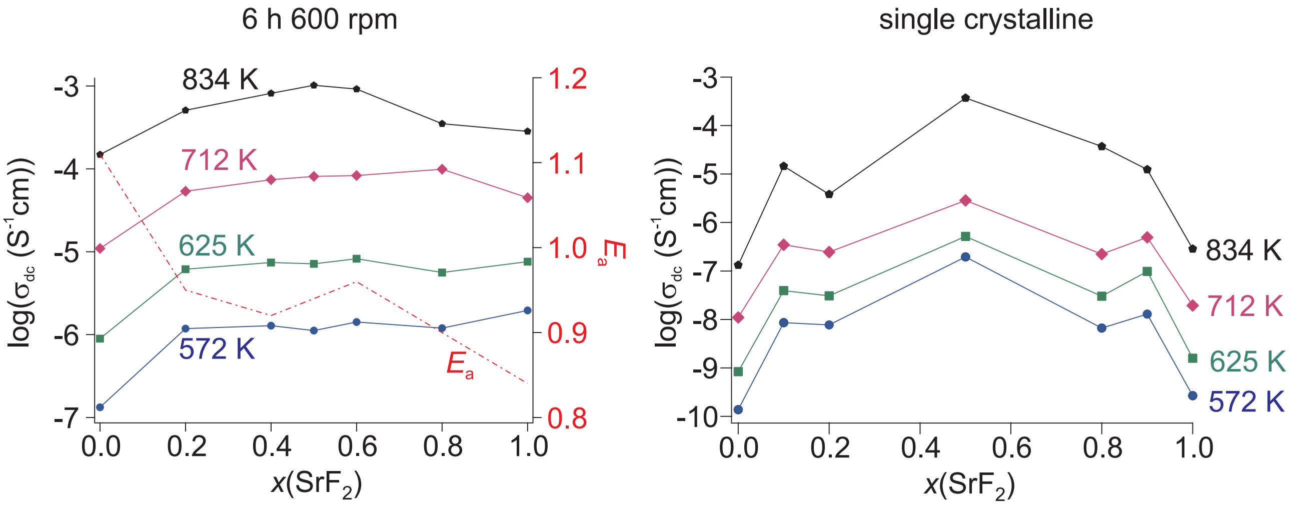

Figure 29: Dc conductivities at different temperatures as a function of composition x for $Ca_{1-x}Sr_xF_2$ prepared by high-energy ball milling (left), and of single crystalline $Ca_{1-x}Sr_xF_2$ (data taken from ref. 45).

see Figs. 29 (left) and 30 (top). In case of single crystalline $Ca_{1-x}Sr_xF_2$, however, a maximum of the conductivity for $x \approx 0.50$ was observed by Subrahmanya Sarma et al.[45], see Fig. 29 (right) for which the data of Subrahmanya Sarma et al.[45] was used. Interestingly, as can be seen in Fig. 29, the nanostructured $Ca_{1-x}Sr_xF_2$ exhibits an overall higher dc conductivity than the single-crystalline material[45,47] most probably due to the defects introduced by high-energy ball milling masking the EAMICS effect. The preparation of and conductivity measurements on the $Ca_{1-x}Sr_xF_2$ (as well as of $Ba_{1-x}Sr_xF_2$) were done by E. Merzlyakova in the frame of her bachelor thesis under my guidance.

To test if the EAMICS effect is also present in the $Ba_{1-x}Sr_xF_2$ system (the author found no such work in the literature) the mechanosynthesized material was heat treated to get rid of the defects and highly conducting grain boundaries probably responsible for the high conductivities observed. Furthermore, two single crystals with the compositions $Ba_{0.67}Sr_{0.33}F_2$ and $Ba_{0.50}Sr_{0.50}F_2$ were obtained from Dr. Reinhard Uecker from the Leibniz Institut für Kristallzüchtung in Berlin. From these crystals discs were sawed out and used for the impedance measurements. Furthermore, a small amount of the material was investigated by XRPD to confirm their stoichiometry and purity. It was found that both crystals have lattice parameters which are in good agreement with the intended stoichiometries. No impurities were found in the diffraction patterns. For comparison, disk shaped crystals of BaF_2 and SrF_2 were bought from Korth Kristalle GmbH. The conductivity measurements on these materials were done by A.-T. Duong in the frame of her bachelor thesis under my guidance. As can be seen in Fig. 30, the heat treatment of the $Ba_{1-x}Sr_xF_2$ leads to an overall decrease of the dc conductivity and there seems to be a conductivity maximum at a composition of $x = 0.50$ which indicates the existence of the EAMICS effect. However, in case of the single crystalline material there is no clear effect visible. Thus, in case of this material investigations of more compositions are necessary to decide if there is an effect or not.

In case of $Ba_{1-x}Ca_xF_2$ a pronounced conductivity maximum can be observed in a range from $x = 0.30$ to $x = 0.70$, see Fig. 31 a). In this range the dc conductivity of the samples does not change in a very distinct way. A drastic increase of the dc conductivity by more than two orders of magnitude to a value which is very similar to that of milled BaF_2 was observed at $T = 554$ K (for lower temperatures the conductivity of the CaF_2 was out of the accessible measuring range of the impedance spectrometer used) when x was decreased from 1 to 0.90. However, with increasing amount of fluoride ions in the $[Ba]_4$ and $[Ca]_4$ environments the ionic conductivity converges to the one of the respective binary fluoride.

It should be mentioned that for comparison BaF_2 and CaF_2 were milled separately for 3 h at 600 rpm. After milling, similar volumes (the respective masses were calculated from their densities given in the literature) of the binary fluorides were put into a round-bottomed flask filled with isopropyl alcohol and stirred for a day. Then the solvent was evaporated by heating. From the obtained powder an XRPD pattern was recorded which showed CaF_2, cubic BaF_2 and a small amount of orthorhombic BaF_2. A crystallite size of about 146(5) nm for the BaF_2 and 136(5) nm for the CaF_2 was calculated from the diffractogram of the mixture by employing the formula of Williamson and Hall[71]. The conductivity of this sample at a temperature of about 554 K is shown in Fig. 31 a), marked by an arrow. It is much smaller than the conductivity of the $Ba_{1-x}Ca_xF_2$ and slightly higher than found by Sata et al. for BaF_2-CaF_2 layers with a layer-thickness of 103 nm. In case of a 3D network of space charge regions between the CaF_2 and BaF_2 crystallites the amount of highly conducting grain boundary regions should be higher than in case of a layered system. Therefore, the conductivity observed for the mixed sample might be explained by a space charge model. However, it was not investigated if both fluorides were thoroughly intermixed. Even if they were, the grains are probably less dense packed than in the layered system prepared by Sata et al.[42] by employing MBE. Hence, the conductivity of the non-intermixed binary fluorides, milled for 3 h and subsequently stirred 24 h in isopropyl alcohol should be measured, too. In the case that an effect of the intermixing can be observed the intermixed sample needs to be investigated in more detail, e. g., by TEM before reliable conclusions are possible. This will be done in the future.

It should also be mentioned that Sata et al.[126] ruled out a mixed cation effect being the reason for the increased ionic conductivity found for their epitaxial layers of BaF_2 and CaF_2 (vide supra). To do this they prepared a sample by simultaneous deposition of CaF_2 and BaF_2 which they assumed to lead to a maximum mixing of BaF_2 and CaF_2.[126] Interestingly, they found only a slight increase of the conductivity compared to the binary fluorides being clearly smaller than the conductivity found in the epitaxial layers. Therefore, and since they used substrate-temperatures of about 773 K for deposition it seems very likely that no metastable $Ba_{1-x}Ca_xF_2$ was formed but a mixture of small grains of a Ba-rich and a Ca-rich phase with compositions comparable to the ones prepared by Sorokin et al. by conventional solid state synthesis[61] (vide supra). As mentioned above $Ba_{0.50}Ca_{0.50}F_2$ is completely decomposed to the binary fluorides after annealing this sample at 773 K for several hours.

Zahn et al.[127] calculated the qualitative effect of a single Ba ion introduced into a CaF_2 lattice and of a single Ca ion introduced into a BaF_2 lattice on the ionic conductivity. They assumed that the mixing of the cations in the fluorite lattice can be approximated by the use of the space charge model which explained the increase of the fluoride ion conductivity in a layered BaF_2-CaF_2 system very well.[43,128] According to their calculations vacancies shall be trapped close to the Ba ions introduced. The introduction of Ca ions into BaF_2 shall stabilize fluoride ions on the interstitial position in the center of the unit cell of the fluorite lattice, octahedrally coordinated by six cations, due to the smaller ionic radius of the Ca ion compared to the one of the Ba ion. By this means vacancies shall be created in the lattice which should increase the fluoride ion conductivity of the material. The introduction of Ba ions into the CaF_2 on the other hand shall decrease the ionic conductivity. The last prediction is not in agreement with the results shown here since the strongest increase of the conductivity can be observed when going from pure CaF_2 to $Ba_{0.10}Ca_{0.90}F_2$, see Fig. 31. Furthermore, Zahn et al.[127] did not mention structural relaxation caused by the substitution of Ba ions by Ca ions (or Ca ions by Ba ions) in BaF_2 (CaF_2).

Expectedly, since the cations are substituted by isovalent cations, for all samples a rather similar pre-exponential factor σ_0 being in the range of 10^5 to 10^6 $S{\cdot}cm^{-1}K$ was found, see Fig. 32. For the samples in the range of $x = 0.30$ to $x = 0.70$ the range is even narrower: 2.4 x 10^5 to 4.5 x 10^5 $S{\cdot}cm^{-1}K$. The prefactor σ_0 can be described by the following equation:

$$\sigma_0 = \frac{Nq^2fa^2}{H_r k_B 6\tau_0} \tag{94}$$

$$\tau_0^{-1} = \tau^{-1} e^{E_a/(k_B T)} \tag{95}$$

Thereby, E_a denotes the activation energy, N is the mobile ion concentration, a is the average jump distance of the mobile ions, q is the electric charge of the mobile ions, f is the correlation factor, H_r is the Haven ratio, τ^{-1} is the average jump rate of the mobile ion, τ_0 is a pre-exponential factor which can be understood as attempt frequency and k_B is Boltzmann's constant.[129] Thus, an increase of σ_0 could mean an increase of the mobile ion concentration. Thus, if the number of vacancies would increase with x, σ_0 should also increase until a saturation value is reached. Since there is no clear increase visible, it seems plausible to assume that there is no increase of the mobile ion concentration in the $Ba_{1-x}Ca_xF_2$ compounds.

The activation energies obtained, shown in Fig. 31, reflect the dc conductivities pretty good since a high dc conductivity goes along with a small activation energy. The plateau found for the dc conductivities in the range from $x = 0.30$ to $x = 0.70$ is mirrored by the activation enthalpies. The activation enthalpy for the ionic conductivity consists of two parts, which is (i) the energy necessary for the ion to leave its potential well and (ii) the defect-formation enthalpy. Thus, the migration potential barrier may be decreased as well as defects may be formed more easily due to the distortion

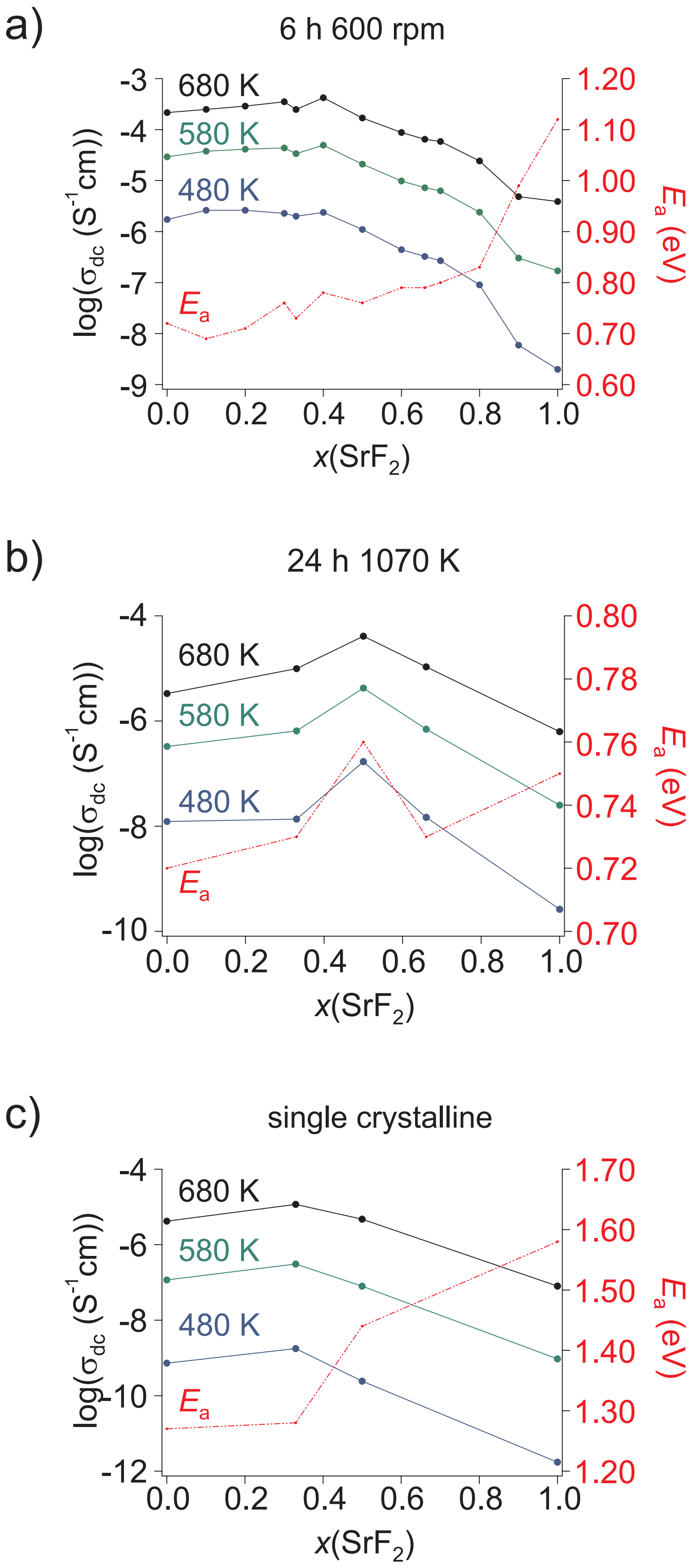

Figure 30: Dc conductivities at different temperatures as a function of composition x for a) $Ba_{1-x}Sr_xF_2$ prepared by high energy ball milling, b) the mechanosynthesized material after annealing at 1070 K for 24 h (at center), and of single crystalline $Ba_{1-x}Sr_xF_2$, c).

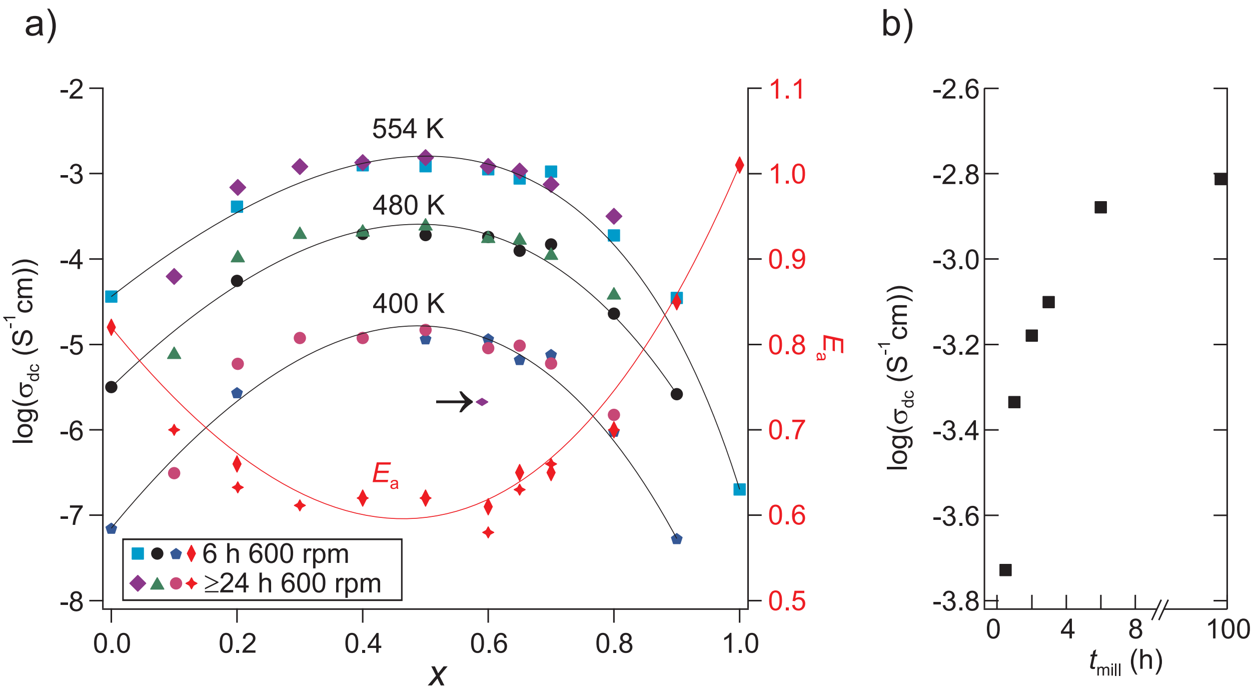

Figure 31: a) Dc conductivities of $Ba_{1-x}Ca_xF_2$ in dependence of x at three different temperatures. A broad maximum from around $x = 0.30$ to $x = 0.70$ shows up. Milling the mixtures for 24 h or even longer (see Fig. 4 for respective t_{mill}) does not change their dc conductivity in a pronounced way. Also the activation energies in dependence of x are shown. The arrow marks the conductivity of a mixture of nano-crystalline BaF_2 and CaF_2 at a temperature of 554 K. See text for further explanations. b) Change of the dc conductivity of $Ba_{0.50}Ca_{0.50}F_2$ as a function of the milling time.

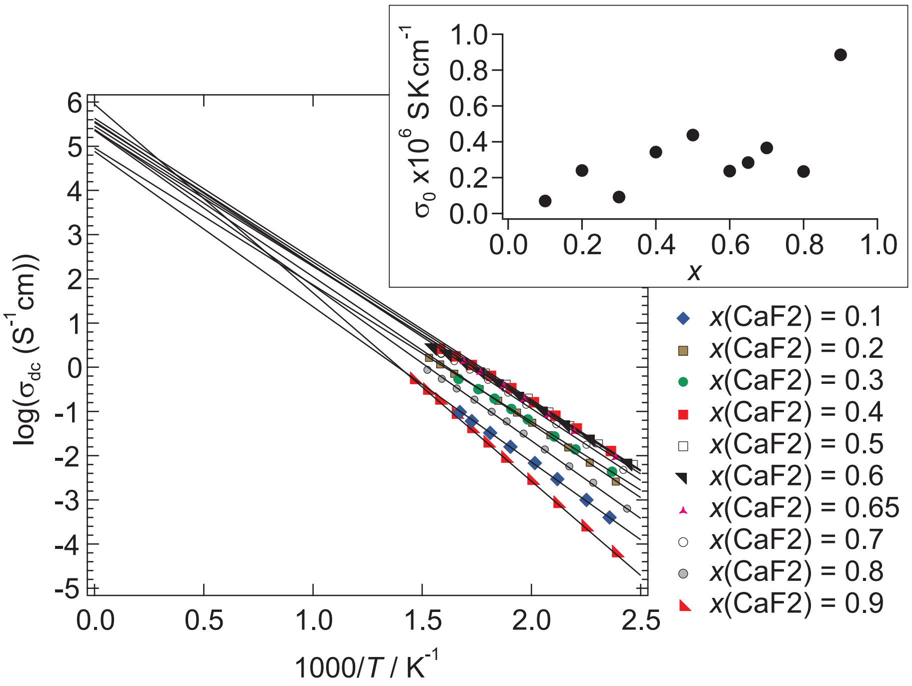

Figure 32: Arrhenius plot of the conductivities of the $Ba_{1-x}Ca_xF_2$ samples. The inset shows the pre-exponential factor σ_0 as a function of composition x.

of the lattice reflected by the different $[\mathrm{Ba}]_z[\mathrm{Ca}]_{4-z}$ environments of the fluoride ions. Combining the fact that N is roughly constant as a function of x and that there is a minimum of activation energy for compositions in the range $0.30 \leq x \leq 0.70$ it seems plausible to assume decreased migration potential barriers being responsible for the increased dc conductivity observed.

As can be seen in Fig. 31 b) the dc conductivity increases with increasing milling time. Interestingly, the milling time has almost no influence on the dc conductivity if $t_{\mathrm{mill}} \geq 6$ h are considered, see Fig. 31 b), although the macrostructure of the mixtures changes in a pronounced way with t_{mill} as already shown before. However, as shown in Fig. 4 the lattice parameter of the samples with x = 0.30 to x = 0.65 after six hours of milling are very similar. Thus, the cationic environments of the fluoride ions should be very similar in all these samples as actually found for the samples with x = 0.30, x = 0.40, x = 0.50 and x = 0.60, see Fig. 26. In fact, all these samples show the $[\mathrm{Ba}]_3[\mathrm{Ca}]$ and the $[\mathrm{Ba}]_2[\mathrm{Ca}]_2$ environments which probably enable the fluoride ions to be highly mobile. The large amount of residual $\mathrm{CaF_2}$ as well as the lattice parameter and, accordingly, d(Ba-F) within this coordination spheres seem to have almost no effect on the ionic conductivity, see Fig. 31. However, as already shown also for the samples with x = 0.90 and x = 0.10 the dc conductivity is clearly enhanced. Therefore, also the $[\mathrm{Ba}][\mathrm{Ca}]_3$ as well as the $[\mathrm{Ba}]_3[\mathrm{Ca}]$ facilitates a high mobility of the fluoride ions compared to the $[\mathrm{Ba}]_4$ along with the $[\mathrm{Ca}]_4$ coordination spheres in the binary fluorides.

Thus, the mixed cationic environments which enable a high diffusivity of the fluoride ions most likely create highly conducting percolation paths through the bulk material. After only six hours of milling the amount of this mixed cationic environments enabling a high mobility of the fluoride ions is already clearly beyond the percolation threshold. Thus, most of the possible direct paths between the electrodes consisting of the highly conducting environments are already formed. Therefore, if the amount of the mixed phase is increased further, the amount of direct paths is not increased in a pronounced way. Instead of this, the interconnection between the paths increases which will not noteworthy contribute to the dc conductivity but affects the mobility in the short range regime as will be shown in the next paragraph. Hence, if the reaction progresses the ionic conductivity is only very slightly increased. This result is in accordance with the observation obtained by Ruprecht et al.[66] In that study the ionic conductivity increased with increasing milling time until a saturation conductivity was reached, although no phase pure $\mathrm{Ba}_{1-x}\mathrm{Ca}_x\mathrm{F}_2$ was investigated.

9.3.5 Static ^{19}F NMR

For some of the samples static ^{19}F NMR spectra were recorded at temperatures between 293 K and 473 K. Exemplarily, in Fig. 33 a) the NMR spectra of the sample with x = 0.50 after 6 h and 99 h of milling, respectively, are shown. The sample milled for 6 h exhibits three NMR lines at all temperatures measured while the one milled for 99 h shows only a single line at high temperatures (see Fig. 33) which is also true for the other samples investigated. The narrow NMR line in the middle is caused by chemical exchange of fluoride ions between their different cationic environments. If the exchange rate between these different cationic environments exceeds the distance between the respective NMR lines the discrete NMR lines coalesce to a single NMR line.[130] The chemical shift of that NMR line will be an average of the chemical shifts (δ_i) of the fluoride ions in the different cationic environments participating on the exchange weighted by the relative populations (p_i) of these environments. Thus, the two residual, broad NMR lines visible at high temperatures for the sample obtained after only 6 h of milling represent fluoride ions which do not participate in a fast exchange. Accordingly, these NMR lines can be ascribed to residual reactants, i. e., the binary fluorides or compositions of $\mathrm{Ba}_{1-x}\mathrm{Ca}_x\mathrm{F}_2$ with very large or very small x. In case of the single phase $\mathrm{Ba}_{1-x}\mathrm{Ca}_x\mathrm{F}_2$ almost every fluoride ion participates in the fast exchange between the different chemical environments and, thus, only a single NMR line is visible at high temperatures.

In Fig. 33 b) the chemical shifts of the narrow NMR lines (δ_c) of some compositions are shown. The chemical shift values are in tolerable agreement with the expected chemical shift values if a

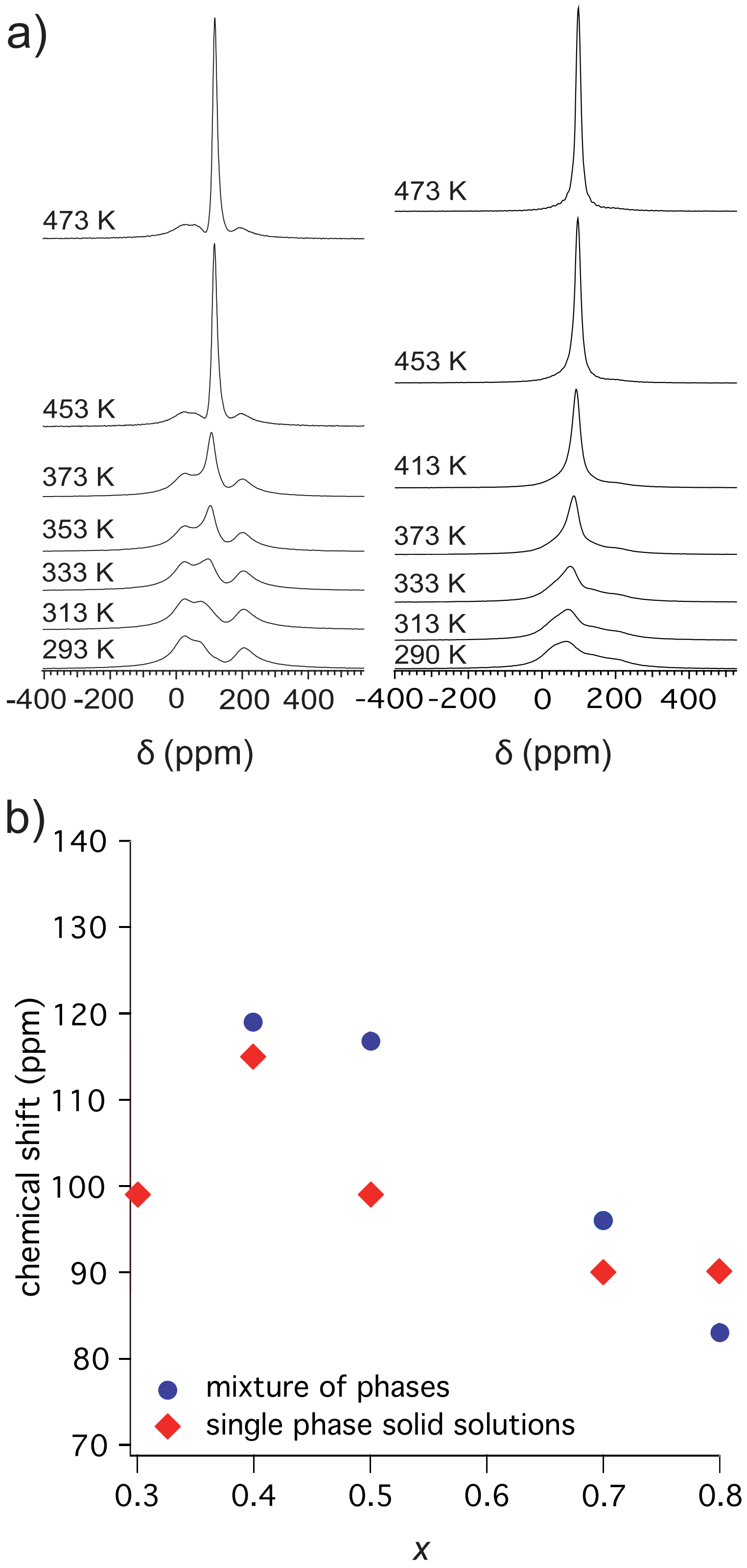

Figure 33: a) Static ^{19}F NMR lines of the sample with x = 0.50 after 6 h and 99 h of milling. b) Chemical shift of the narrow line for the different compositions after 6 h of milling and for the solid solution (with t_{mill} as specified in Fig. 4).

chemical exchange of fluoride ions between some of the cationic environments is assumed. If the $[Ba]_2[Ca]_2$ environment is examined, a chemical shift of about 100 ppm is calculated ($\sum p_i \delta_i = \delta_c$) for the sample with x = 0.50 taking into account the possible environments in direct neighborhood of this cationic environment which are $[Ba]_4$, $[Ba]_3[Ca]$, $[Ba]_2[Ca]_2$ and $[Ba][Ca]_3$. In case of the sample with x = 0.40 a chemical shift of about 120 ppm is found that way which is in good agreement with the chemical shift found experimentally. In case of the sample with x = 0.80 an exchange between the $[Ba][Ca]_3$ environment with its possible direct neighbors $[Ba]_3[Ca]$, $[Ba]_2[Ca]_2$, $[Ba][Ca]_3$ and $[Ca]_4$ has to be assumed to get a value of about 90 ppm being in good agreement with the value found.

9.4 Conclusions and Outlook

Metastable $Ba_{1-x}Ca_xF_2$ compounds with $0 \leq x \leq 1$ are accessible by high-energy ball milling. The lattice parameter a of the samples prepared was found to be in agreement with Vegard's law. Accordingly, all lattice parameters between the ones of BaF_2 and CaF_2 are accessible by joint milling of mixtures of the binary fluorides. Except for the samples with x = 0.10 and x = 0.20 in which small amounts of orthorhombic $Ba_{1-x}Ca_xF_2$ were found, the compounds prepared are single phase materials. Furthermore, only in a few samples prepared by using very long milling times small amounts of abraded ZrO_2 or WC were observed.

^{19}F MAS NMR measurements expectedly exhibit five different chemical environments of the fluoride ions as it was also found for $Ca_{1-x}Sr_xF_2$[121], $Ba_{1-x}Sr_xF_2$ and $Ba_{1-x}Sr_xLiF_3$.[23] This supports the assumption of the formation of metastable $Ba_{1-x}Ca_xF_2$ also from an atomic point of view since these results can hardly be explained by the perfect mixing of very small nano-crystals of BaF_2 and CaF_2 which would likewise result in average lattice parameters in accordance to Vegard's law. Furthermore, from the chemical shifts of the respective NMR lines in the ^{19}F MAS NMR spectra the distances d(M-F) between the respective cations and fluoride ions were calculated. The average distances d_{av} calculated from these d(M-F) were in almost perfect agreement with the values obtained from the XRPD patterns which exhibit the capability of ^{19}F MAS NMR spectroscopy to get information about the microstructure of a complex fluoride. From this data it was concluded that the fluorite structure the $Ba_{1-x}Ca_xF_2$ compounds (as well as the $Ca_{1-x}Sr_xF_2$ and $Ba_{1-x}Sr_xF_2$ compounds) crystallize in, is most probably highly distorted. These results were corroborated by the pair distribution functions of $Ba_{0.50}Ca_{0.50}F_2$ and $Ba_{0.60}Ca_{0.40}F_2$ which showed distances which cannot be assigned to distances in the ideal fluorite lattice. In addition also in case of the stable compounds $Ca_{0.50}Sr_{0.50}F_2$ and $Ba_{0.50}Sr_{0.50}F_2$ evidence for structural distortions was found this way.

The very first stages of the reaction of BaF_2 and CaF_2 to $Ba_{1-x}Ca_xF_2$ were investigated by XRPD and ^{19}F MAS NMR. The formation of the solid solutions by mechanical treatment turned out to be due to a consecutive introduction of CaF_2 into the BaF_2 lattice and BaF_2 into the CaF_2 lattice, except for the compounds with $x \geq 0.75$, which means that in a short period of time the whole material comes into reactive contact. The compositions with $x \geq 0.75$ were formed in a pseudo-single step reaction directly from the binary fluorides which indicates that only a small amount of the binary fluorides comes into reactive contact in time. This reacting material then forms the final composition very fast. During, or after this process some new reaction spheres of the binary fluorides are created keeping the majority of the binary fluorides untouched over long milling times. This can be explained by the assumption of a variation of the agglomeration behavior and the crystallite sizes of the binary fluorides with composition x of the mixtures when mechanically treated in a high-energy ball mill.

The prepared mixed phase with x = 0.50 exhibits an about two orders of magnitude higher dc conductivity than found for mechanically treated BaF_2. This maximum is embedded in an slightly curved plateau from x = 0.30 to x = 0.70. The dc conductivities of $Ba_{1-x}Ca_xF_2$ seem to be solely dependent on E_a. A similar behavior is already known for single crystalline $Ca_{1-x}Sr_xF_2$

and $Pb_{1-x}Cd_xF_2$ from the literature[45,49]. The results obtained for $Ba_{1-x}Sr_xF_2$ regarding its conductivity behavior as a function of x are to this moment still inconclusive although some preliminary results indicate the existence of a conductivity maximum at $x = 0.50$ and, thus, the existence of a EAMICS effect for all three compounds.

The enhanced dc conductivity of $Ba_{1-x}Ca_xF_2$ is assumed to be due to ion conduction in the bulk material. The mixed fluoride ion coordination spheres observed by ^{19}F MAS NMR are probably characterized by decreased migration potential barriers, probably caused by structural disorder, compared with the ones of the fluoride ion coordination spheres in the pure binary fluorides. This result is corroborated by temperature dependent static ^{19}F NMR measurements.

Further investigations to reveal the microstructure of the mixed fluorides are necessary to understand the properties of these systems. EXAFS measurements, which were done in October 2013, will contribute to a better understanding of the microstructure. The information gained from these measurements, the PDF patterns (which will be fitted in the future by employing the software DISCUS) and the results from the ^{19}F MAS NMR measurements will allow a well-founded simulation of the lattice. The knowledge of the microstructure will allow the determination of pathways for the fluoride ions and general insight into the origins of the enhanced fluoride ion conductivity of the mixed earth alkaline fluoride compounds.

According to the literature, $Ba_{1-x}Ca_xF_2$ compounds with $0 \leq x \leq 1$ are probably also accessibly by MBE[17,18,65] if the temperature of the substrate is low. Therefore, metastable $Ba_{1-x}Ca_xF_2$ seems to be accessible by both, a fast quenching process speculated to happen in the course of mechanochemical reactions[111,112], as well as low temperature deposition techniques. Therefore, a comparison of the properties of $Ba_{1-x}Ca_xF_2$ or mixed phases prepared by both techniques would be interesting also for a comparison of the reaction mechanisms of the two techniques.

In general, it should be tested if other metastable phases which are to this time only accessible by deposition techniques can also be prepared by high-energy ball milling which would allow the preparation of larger amounts of these phases.

Acknowledgement. The author thanks J. Bednarcik for the measurements at DESY, B. Ruprecht and M. B. Rücker for their help to set up the algorithm of the lattice simulator and M. B. Rücker for programming it, S. Wegner (Bruker Biospin) for some of the ^{19}F MAS NMR measurements, R. Uecker for the preparation of single crystals of $Ba_{0.50}Sr_{0.50}F_2$ and $Ba_{0.67}Sr_{0.33}F_2$, K. Partovi for his contribution to several impedance measurements as well as E. Merzlyakova and A.-T. Duong for their support in preparation of some of the samples. Financial support by the Deutsche Forschungsgemeinschaft (DFG) within the frame of the Priority Program 1415, Kristalline Nichtgleichgewichtsphasen, is highly appreciated.

References

[1] M. J. Rosseinsky, Angew. Chem. Int. Ed. 47 (2008) 8778.

[2] N. Dubrovinskaia, L. Dubrovinsky, W. Crichton, F. Langenhorst, A. Richter, Appl. Phys. Lett. 87 (2005) 083106.

[3] Z. Pan, H. Sun, Y. Zhang, C. Chen, Phys. Rev. Lett. 102 (2009) 055503.

[4] A. Misra, P. K. Tyagi, B. S. Yadav, P. Rai, D. S. Misra, V. Pancholi, I. D. Samajdar, Appl. Phys. Lett. 89 (2006) 071911.

[5] W. Lubeigt, G. M. Bonner, J. E. Hastie, M. D. Dawson, D. Burns, A. J. Kemp, Opt. Express 18 (2010) 16765.

[6] L. Zheng, Y. Xu, D. Jin, Y. Xie, Chem. Mater. 21 (2009) 5681.

[7] M. E. Norako, R. L. Brutchey, Chem. Mater. 22 (2010) 1613.

[8] Z.-P. Yang, L. Ci, J. A. Bur, S.-Y. Lin, P. M. Ajayan, Nano Lett. 8 (2008) 446.

[9] M. Jansen, J. C. Schön, Nature Mater. 3 (2004) 838.

[10] W.-H. Xie, Y.-Q. Xu, B.-G. Liu, Phys. Rev. Lett. 91 (2003) 037204.

[11] V, Šepelák, A. Feldhoff, P. Heitjans, F. Krumeich, D. Menzel, F. J. Litterst, I. Bergmann, K. D. Becker, Chem. Mater. 18 (2006) 3057.

[12] E. Montanari, L. Righi, G. Calestani, A. Migliori, E. Gilioli, F. Bolzoni, Chem. Mater. 17 (2005) 1765.

[13] A. Kuhn, P. Sreeraj, R. Pöttgen, H.-D. Wiemhöfer, M. Wilkening, P. Heitjans, J. Am. Chem. Soc. 133 (2011) 11018.

[14] A. Kuhn, P. Sreeraj, R. Pöttgen, H.-D. Wiemhöfer, M. Wilkening, P. Heitjans, Angew. Chem. Int. Ed. 50 (2011) 12099.

[15] M. Jansen, K. Doll, J. C. Schön, Acta Cryst. A66 (2010) 518.

[16] M. A. C. Wevers, J. C. Schön, M. Jansen, J. Phys.: Condens. Matter 11 (1999) 6487.

[17] P. W. Sullivan, R. F. C. Farrow and G. R. Jones, J. Crystal Growth 60 (1982) 403.

[18] R. F. C. Farrow, J. Vac. Sci. Technol. B 1 (2) (1983) 222.

[19] Ž. P. Čančarević, J. C. Schön, D. Fischer, M. Jansen, Mater. Sci. Forum 494 (2005) 61.

[20] Y. Liebold-Ribeiro, D. Fischer, M. Jansen, Angew. Chem. Int. Ed. 47 (2008) 4428.

[21] D. Fischer, A. Müller, M. Jansen, Z. Anorg. Allg. Chem. 630 (2004) 2697.

[22] A. Bach, D. Fischer, X. Mu, W. Sigle, P. E. van Aken, M. Jansen, Inorg. Chem. 50 (2011) 1563.

[23] A. Düvel, S. Wegner, K. Efimov, A. Feldhoff, P. Heitjans, M. Wilkening, J. Mater. Chem. 21 (2011) 6238.

[24] V. Šepelák, L. Wilde, U. Steinike, K. D. Becker, Mater. Sci. Eng. A 375-377 (2004) 865.

[25] K. L. Da Silva, D. Menzel, A. Feldhoff, C. Kübel, M. Bruns, A. Paesano, A. Düvel, M. Wilkening, M. Ghafari, H. Hahn, F. J. Litterst, P. Heitjans, K. D. Becker, V. Šepelák, J. Phys. Chem. C 115 (2011) 7209.

[26] N. I. Sorokin, B. P. Sobolev, Crystallogr. Rep. 52 (2007) 842.

[27] N. I. Sorokin, J. Electrochem. 42 (2006) 744.

[28] J. G. Kennedy, C. Hunter, J. Electrochem. Soc., 1976, 123, 10-14.

[29] J. Schoonman, J. Electrochem. Soc., 1976, 123, 1772-1775.

[30] Y. Danto, G. Punjade, J. D. Pistré, C. Lucat, J. Salardenne, Thin Solid Films, 1978, 55, 347-354.

[31] J. Schoonman, K. E. D. Wapenaar, G. Oversluizen, G. J. Dirksen, J. Electrochem. Soc., 1979, 126, 709-713.

[32] P. Hagenmuller, J.-M. Réau, C. Lucat, S. Matar, G. Villeneuve, Solid State Ionics, 1981, 3/4, 341-345.

[33] J. Schoonman, A. Wolfert, Solid State Ionics, 1981, 3/4, 373-379.

[34] I. Kosacki, Appl. Phys. A, 1989, 49, 413-424.

[35] M. Shareefuddin, M. Jamal,. M. N. Chary, J. Phys. D: Appl. Phys., 1995, 28, 440-442.

[36] N. I. Sorokin, Russ. J. Electrochem., 2006, 42, 744-759.

[37] G. G. Amatucci, N. Prereira, J. Fluorine Chem., 2006, 128, 243-262.

[38] W. West, J. Whitacre and L. Del Castillo, "Solid State Fluoride Battery for High Temperature Applications", Electrochemical Society Meeting Proceedings, May 2007, Chicago, IL.

[39] M. Anji Reddy, M. Fichtner, J. Mater. Chem. 21 (2011) 17059.

[40] P. Heitjans, M. Wilkening, Def. Diff. Forum 283-286 (2009) 705.

[41] H. Yugami, A. Koike, M. Shigame, T. Suemoto, Phys. Rev. B 44 (1991) 9214.

[42] N. Sata, K. Ebermann, K. Eberl and J. Maier, Nature 408 (2000) 946.

[43] D. Zahn, O. Hochrein, X. Guo, J. Maier, J. Phys. Chem. C 113 (2009) 1315.

[44] A. Orera, P. R. Slater, Chem. Mater. 22 (2010) 675.

[45] M. V. Subrahmanya Sarma, S. V. Suryanarayana, Solid State Ionics 42 (1990) 227.

[46] M. V. Subrahmanya Sarma, S. V. Suryanarayana, J. Mater. Sci. Let. 5 (1986) 1277.

[47] N. I. Sorokin, D. N. Karimov, E. A. Krivandina, Z. I. Zhmurova, O. N. Komar'kova, Crystallogr. Rep. 53 (2008) 271.

[48] D. N. Karimov, O. N. Komar'kova, N. I. Sorokin, V. A. Bezhanov, S. P. Chernov, P. A. Popov, B. P Sobolev, Crystallogr. Rep. 55 (2010) 556.

[49] I. Kosacki, Appl. Phys. A 49 (1989) 413.

[50] J. T. Mouchovski, K. A. Temelkov, N. K. Vuchkov, Prog. Cryst. Growth Charact. Mater. 57 (2011) 1.

[51] J. H. Burnett, Z. H. Levine, E. L. Shirley, Phys. Rev. B 64 (2001) 241102(R).

[52] D. Klimm, M. Rabe, R. Bertram, R. Uecker, L. Parthier, J. Cryst. Growth 310 (2007) 310.

[53] A. G. Serebryakov, F. Bociort, J. Braat, J. Opt. Technol. 70 (2003) 566.

[54] A. Serebriakov, F. Bociort, J. Braat, Proc. of SPIE 5754 (2005) 1780.

[55] É. G. Chernevskaya and G. V. Anan'eva, Soviet Physics-Solid State 8 (1966) 169.

[56] C. W. Ponader, R. E. Youngman, C. M. Smith, J. Am. Ceram. Soc. 88 (2005) 2447.

[57] D. L. Deadmore, H. E. Sliney, NASA-TM-88979 (1987).

[58] V. M. Goldschmidt, Skr. Norske Vidensk.-Akad., Mat.-Naturv. Kl. 2 (1926).

[59] R. D. Shannon and C. T. Prewitt, Acta Cryst. B25 (1969) 925.

[60] P. P. Fedorov, I. I. Buchinskaya, N. A. Ivanovskaya, V. V. Konovalova, S. V. Lavrishchev and B. P. Sobolev, Doklady Phys. Chem. 401 (2005) 53.

[61] N. I. Sorokin, I. I. Buchinskaya, P. P. Fedorov and B. P. Sobolev, Inorg. Mater. 44 (2008) 189.

[62] W. Kurz, D. J. Fisher, "Fundamentals of Solidification", Trans Tech Publications, 1984, Switzerland, Germany, UK, USA, ch. 5, pp. 97-106.

[63] D. J. S. Cooksey, D. Munson, M. P. Wilkinson, A. Hellawell, Philos. Mag. 10 (1964) 745.

[64] B. Schumann, G. Kühn, G. Wagner, Cryst. Res. Technol. 21 (1986) 1139.

[65] A. Hidaka and H. Ikoma, Jpn. J. Appl. Phys. 34 (1995) 4641.

[66] B. Ruprecht, M. Wilkening, A. Feldhoff, S. Steuernagel and P. Heitjans, Phys. Chem. Chem. Phys. 11 (2009) 3071.

[67] J. O. Isard, J. Non-Cryst. Solids 1 (1969) 235.

[68] A. Düvel, B. Ruprecht, P. Heitjans, M. Wilkening, J. Phys. Chem. C 115 (2011) 23784.

[69] A. P. Hammersley, S. O. Svensson, M. Hanfland, A. N. Fitch, D. Häusermann, High Press. Res. 1996, 14, 235.

[70] X. Qiu, J. W. Thompson, S. J. L. Billinge, J. Appl. Cryst. 2004, 32, 678-678.

[71] G. K. Williamson and W. H. Hall, Acta Metall. 1 (1953) 22.

[72] S. M. Dorfman, F. Jiang, Z. Mao, A. Kubo, Y. Meng, V. B. Prakapenka, T. S Duffy, Phys. Rev. B 81 (2010) 174121.

[73] T. Xie, S. Li, Q. Peng, Y. Li, Angew. Chem. Int. Ed. 48 (2009) 196.

[74] K. F. Seifert, Fortschr. Miner. 45 (1968) 214.

[75] K. F. Seifert, Chem.-Ing.-Tech. 38 (1966) 1100.

[76] J. M. Leger, J. Haines, A. Atouf, O. Schulte, S. Hull, Phys. Rev. B: Condens. Matter 52 (1995) 13247.

[77] G. J. Piermarini, S. Block, J. D. Barnett, J. Appl. Phys. 44 (1973) 5377.

[78] G. A. Samara, Phys. Rev. B 2 (1970) 4194.

[79] E. D. D. Schmidt, K. Vedam, J. Phys. Chem. Solids 27 (1966) 1563.

[80] A. Costales, M. A. Blanco, R. Pandey, J. M. Recio, Phys. Rev. B 61 (2000) 11359.

[81] G. A. Samara, Phys. Rev. B 13 (1976) 4529.

[82] C. N. R. Rao, Bull. Mater. Sci. 3 (1981) 75.

[83] J. S. Smith, S. Desgreniers, J. S. Tse, J. Sun, D. D. Klug, Y. Ohishi, Phys. Rev. B 79 (2009) 134104.

[84] F. Dachille, R. Roy, Nature 4718 (1960) 70.

[85] F. Dachille, R. Roy, "The Physics and Chemistry of High Pressures" Society for Chemical Industry, London, England (1962).

[86] R. Roy, J. Solid State Chem. 111 (1994) 11.

[87] Swanson, Fuyat., Natl. Bur. Stand. (U.S.), Circ. 539, II, (1953), 41.

[88] A. Kern, W. Eysel, Mineralogisch-Petrograph. Inst., Univ. Heidelberg, Germany., ICDD Grant-in-Aid, (1993).

[89] Swanson, Fuyat., Natl. Bur. Stand. (U.S.), Circ. 539, 3, (1954), 24.

[90] Pfoertsch, McCarthy, Penn State University, University Park, Pennsylvania, USA., ICDD Grant-in-Aid, (1977).

[91] E. Menéndez-Proupin, G. Gutiérrez, Phys. Rev. B 72 (2005) 035116.

[92] H. Hertz, J. Reine Angew. Math. 92 (1881) 156.

[93] W. Papst, G. Tichá, E. Gregorová, Ceramics-Silikáty 48 (2004) 41.

[94] P. P. Chattopadhyay, I. Manna, S. Talapatra, S. K. Pabi, Mater. Chem. Phys. 68 (2001) 85.

[95] C. Suryanarayana, Prog. Mater. Sci. 46 (2001) 1.

[96] A. I. Zaslavsky, Y. A. Kondrashov, S. S. Tolkachev, Doklady Akad. Nauk. 75 (1950) 559.

[97] H. Bode, E. Voss, Z. Elektrochem. 60 (1956) 1053.

[98] W. B. White, F. Dachille, R. Roy, J. Am. Ceram. Soc. 44 (1961) 170.

[99] R. R. Reeber, K. Wang, J. Am. Ceram. Soc. 82 (1999) 129.

[100] G. Dénés, M. C. Madamba, MRS Proceedings 481 (1998) 673.

[101] P. G. Fox, J. Mater. Sci. 10 (1975) 340.

[102] C. Bocker, I. Avramov, C. Rüssel, Scripta Mater. 62 (2010) 814.

[103] Z. Kolar, J. J. M. Binsma, B. Subotić, J. Cryst. Growth. 76 (1986) 408.

[104] W. Ostwald, Z. Phys. Chem. 22 (1897) 290.

[105] J. M. McHale, A. Auroux, A. J. Perrotta, A. Navrotsky, Science 277 (1997) 788.

[106] A. Düvel, E. Romanova, , M. Sharifi, D. Freude, M. Wark, P. Heitjans, M. Wilkening, J. Phys. Chem. C 115 (2011) 22770.

[107] M. Dreger, G. Scholz, E. Kemnitz, Solid State Sci. 14 (2012) 528.

[108] A. Bach, D. Fischer, X. Mu, W. Sigle, N. Toto, S. Neelamraju, J. C. Schön, P. A. van Aken, M. Jansen, poster presentation at "1. Berichtskolloquium" in the frame of the priority project SPP 1415 in Boppard (05.10.11 - 07.10.11).

[109] H. Zhu, Y. Ma, H. Yang, C. Ji, D. Hou, L. Guo, J. Phys. Chem. Solids. 71 (2010) 1183.

[110] A. E. Ermakov, Fiz. Met. Metalloved. 20 (1991) 5.

[111] F. Kh. Urakaev in High-energy ball milling - Mechanochemical processing of nanopowders, ed. M. Sopicka-Lizer, Woodhead Publishing Limited, 2010, chap. 2, pp. 9-44.

[112] V. Šepelák, I. Bergmann, S. Indris, A. Feldhoff, H. Hahn, K. D. Becker, C. P. Grey, P. Heitjans, J. Mater. Chem. 21 (2011) 8332.

[113] H. S. Chen, C. E. Miller, Rev. Sci. Instrum. 41 (1970) 1237.

[114] R. Roberge, H. Herman, Mater. Sci. Eng. 3 (1968/69) 62.

[115] M. Moss, D. L. Smith, R. A. Lefever, Appl. Phys. Lett. 5 (1964) 120.

[116] B. Bureau, G. Silly, J. Y. Buzaré and J. Emery, Chem. Phys. 249 (1999) 89.

[117] D. K. Hindermann, C. D. Cornwell, J. Chem. Phys. 48 (1968) 4148.

[118] A. F. Hollemann, E. Wibert, "Lehrbuch der Anorganischen Chemie", 101. Auflage, W. de Gruyter, New York - Berlin 1995, p.121.

[119] A. Zheng, S.-B. Liu, and F. Deng, J. Phys. Chem. C 113 (2009) 15018.

[120] M. Matsumoto, T. Nishimura, ACM T. Model. Comput. S. 8 (1998) 3.

[121] R. E. Youngman and C. M. Smith, Phys. Rev. B 78 (2008) 014112.

[122] T. Takahashi, H. Kawashima, H. Sugisawa, T. Baba, Solid State Nucl. Mag. 15 (1999) 119.

[123] J.-P. Demers, V. Chevelkov, A. Lange, Solid State Nucl. Magn. Reson. 40 (2011) 101.

[124] N. I. Sorokin, M. W. Breiter, Solid State Ionics 99 (1997) 241.

[125] W. Puin. S. Rodewald, R. Ramlau, P. Heitjans, J. Maier, Solid State Ionics 131(2000) 159.

[126] N. Sata, N. Y. Jin-Phillipp, K. Eberl, J. Maier, Solid State Ion. 154 (2002) 497.

[127] D. Zahn, P. Heitjans, J. Maier, Chem. Eur. J. 18 (2012) 6225.

[128] X. Guo, J. Maier, Adv. Funct. Mater. 19 (2009) 96.

[129] P. Heitjans, S. Indris, J. Phys.: Condens. Matter, 2003, 15, R1257-R1289.

[130] M. J. Duerr, "Introduction to Solid-State NMR Spectroscopy", Blackwell Publishing Ltd., 2004, p. 295ff.

Appendix: orthorhombic BaF_2

All powders were treated in a Fritsch Pulverisette 7 premium line. The overall mass of the powders to be milled was 2 g. All XRPD patterns were recorded with a D8 Advance diffractometer (Bruker). The ZrO_2 milling vial sets were equipped with 140 milling balls (5 mm in diameter) made of the same material, while the WC milling vial set was equipped with 100 milling balls (5 mm in diameter) made of the same material.

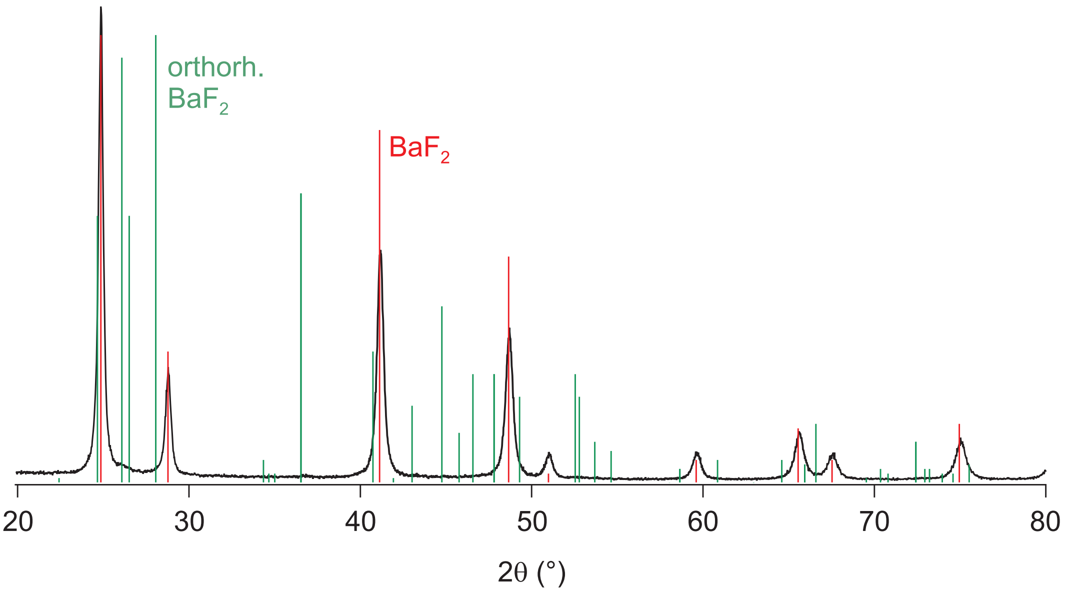

Figure 34: XRPD pattern of BaF_2 milled for 6 h at 600 rpm in a ZrO_2 milling vial set.

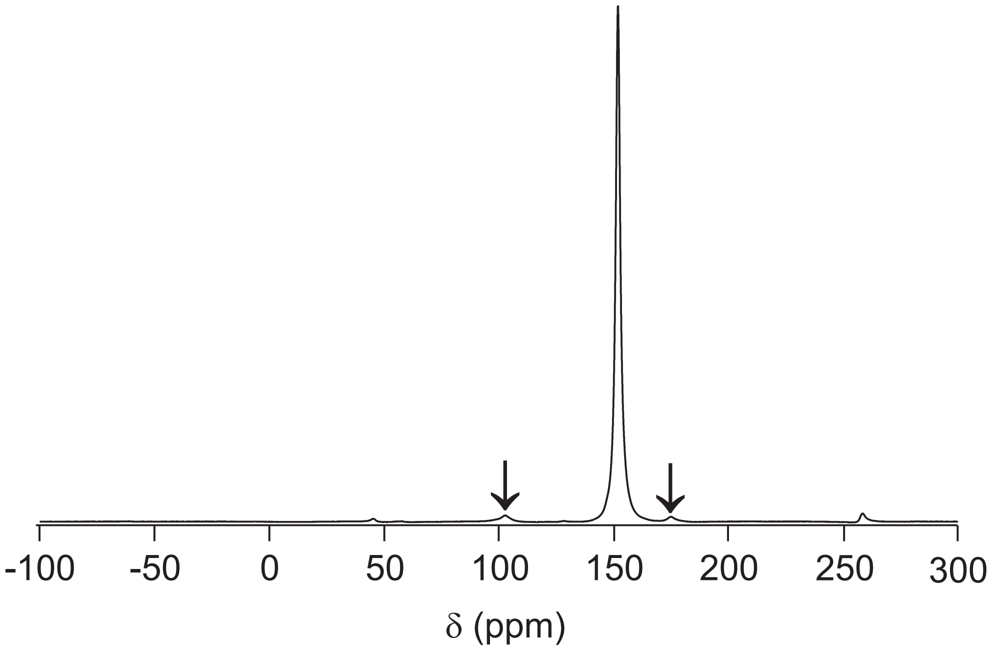

Figure 35: ^{19}F MAS NMR spectrum of BaF_2 milled for 6 h at 600 rpm in a ZrO_2 milling vial set. The spectrum was recorded with ν_0 = 565 MHz and ν_{rot} = 60 kHz. The NMR lines associated with the orthorhombic BaF_2 at 103 ppm and 176 ppm are marked with arrows. The main NMR line at 152 ppm represents the cubic BaF_2.

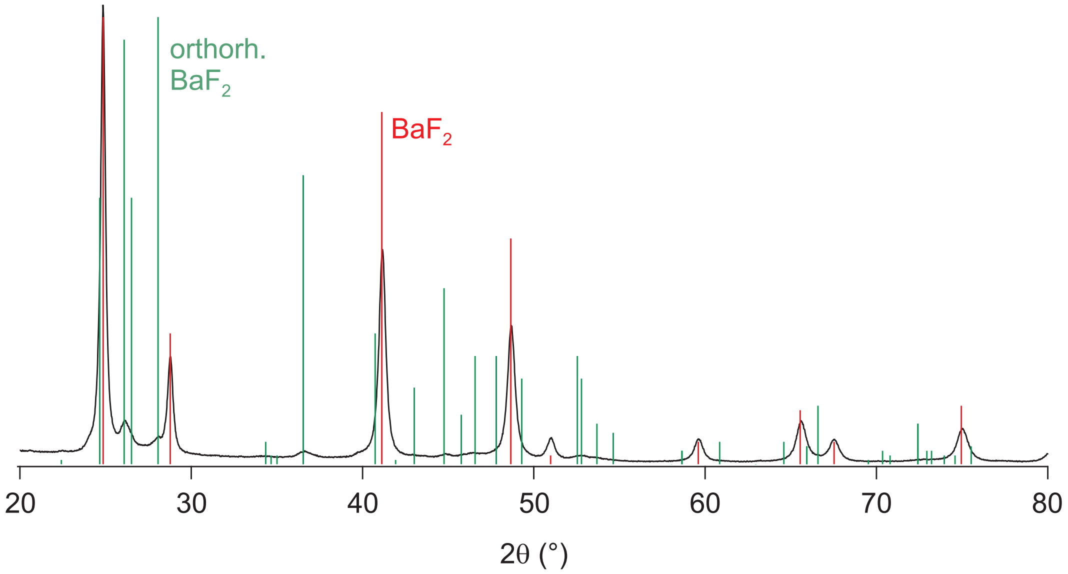

Figure 36: XRPD pattern of BaF_2 milled for 4 h at 600 rpm in a WC vial set. The amount of orthorhombic BaF_2 is a bit larger than in case of the BaF_2 milled for 6 h in a ZrO_2 milling vial set.

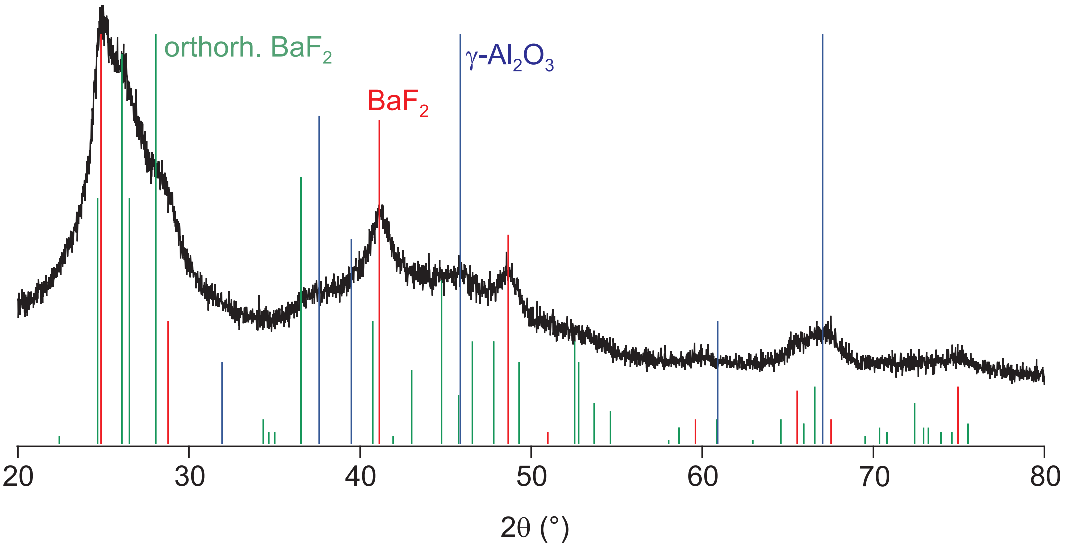

Figure 37: XRPD pattern of a mixture consisting of similar volumes of BaF$_2$ and γ-Al$_2$O$_3$ milled for 6 h at 600 rpm in a ZrO$_2$ milling vial set. A large amount of orthorhombic BaF$_2$ can be observed.

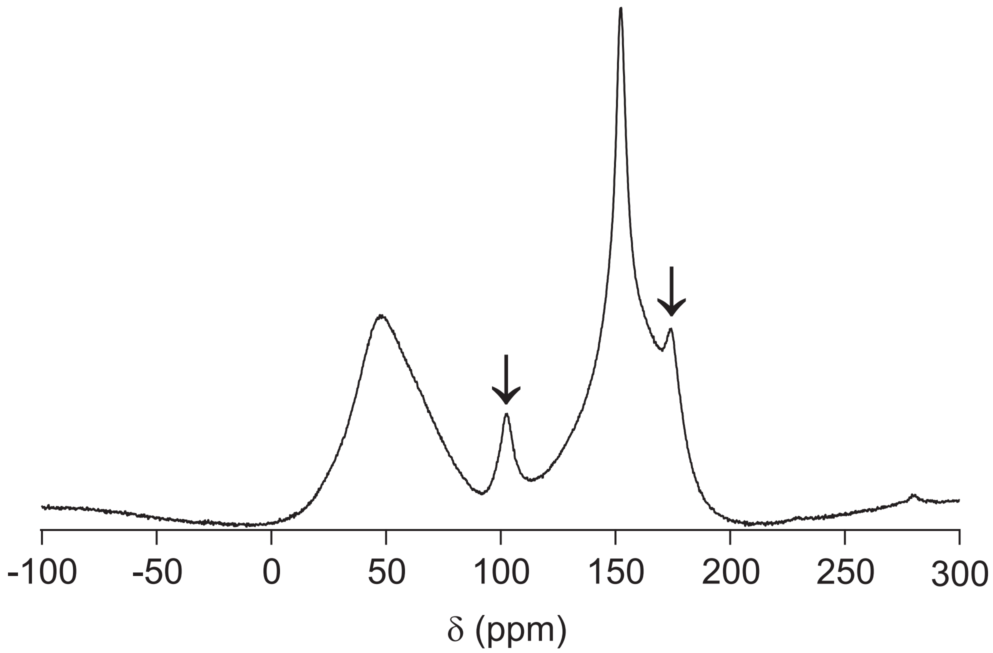

Figure 38: ^{19}F MAS NMR spectrum of the mixture of BaF$_2$ and γ-Al$_2$O$_3$ milled for 6 h at 600 rpm in a ZrO$_2$ milling vial set. The spectrum was recorded with ν_0 = 565 MHz and ν_{rot} = 60 kHz. The NMR lines associated with the orthorhombic BaF$_2$ at 103 ppm and 176 ppm are marked with arrows. The main NMR line at 152 ppm represents the cubic BaF$_2$. The broad NMR line peaked at about 46 ppm is most probably due to fluoride ions residing at the surfaces of γ-Al$_2$O$_3$ crystallites.

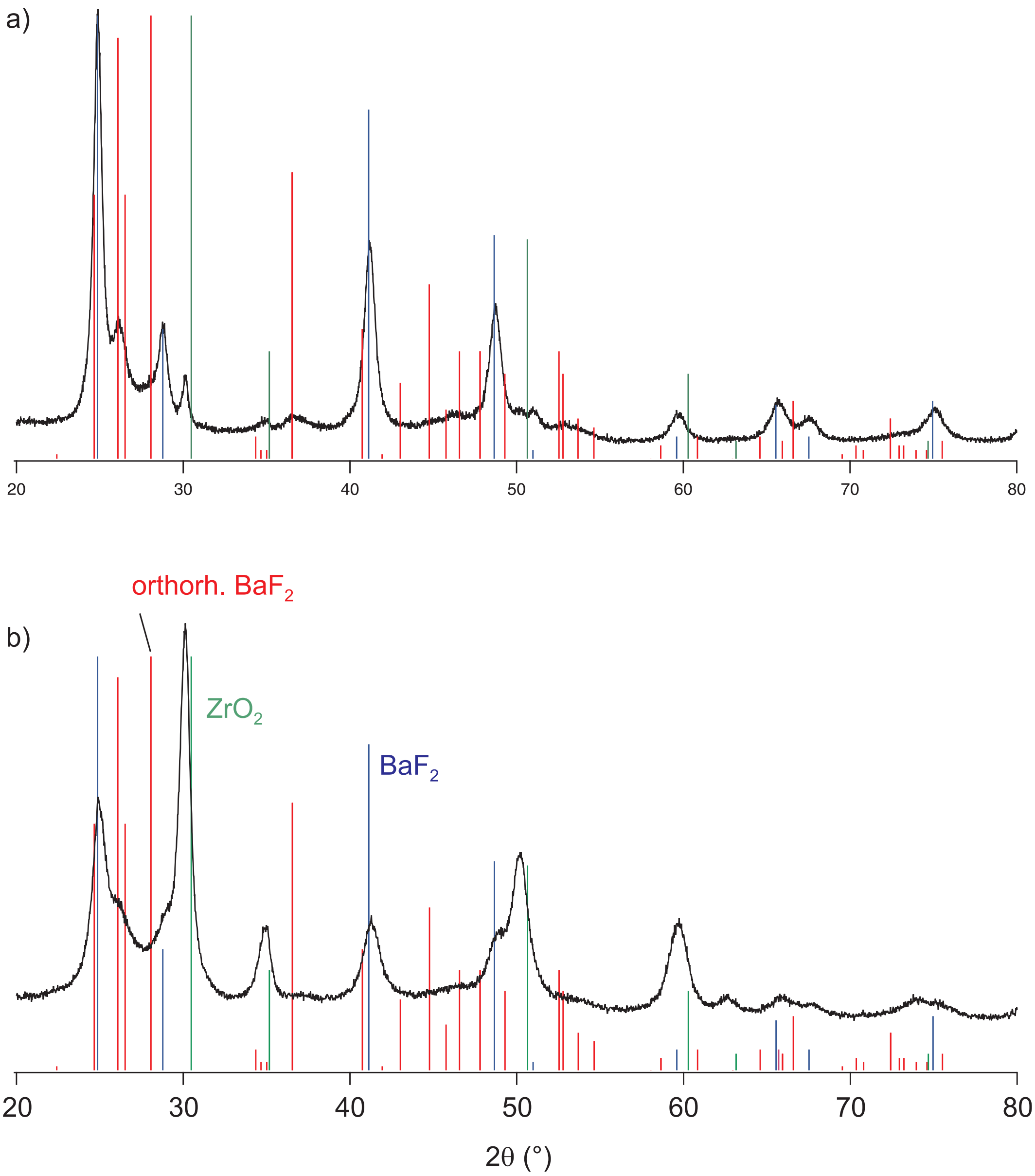

Figure 39: a) XRPD pattern of a mixture of 9 BaF_2 and 1 yttria stabilized ZrO_2 milled for 6 h at 600 rpm in a WC milling vial set. The shift of the peaks associated with the stabilized ZrO_2 are shifted to smaller scattering angles due to the substitution of some of the Zr ions by the larger Y ions. b) XRPD pattern of a mixture of similar volumes of BaF_2 and yttria stabilized ZrO_2 milled for 6 h at 600 rpm in a WC milling vial set.

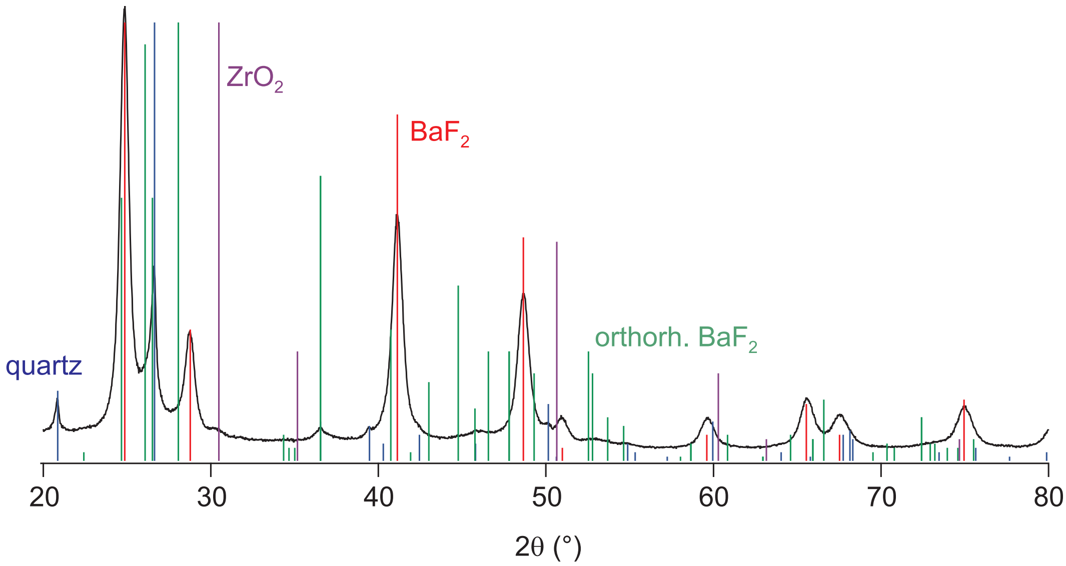

Figure 40: XRPD pattern of a mixture of similar volumes of BaF_2 and quartz milled for 6 h at 600 rpm in a ZrO_2 milling vial set.

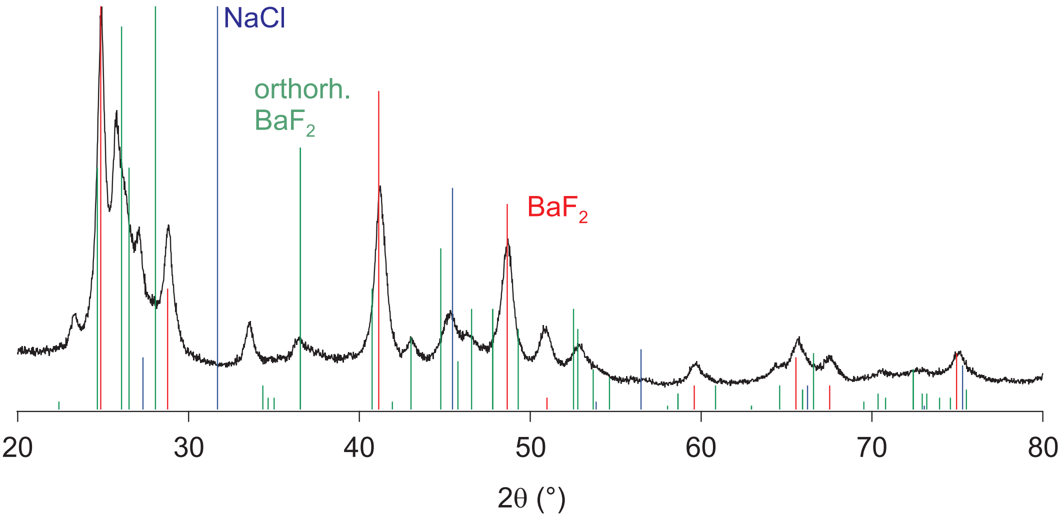

Figure 41: XRPD pattern of a mixture of 9 BaF_2 and 1 NaCl milled for 6 h at 600 rpm in a ZrO_2 milling vial set. The two additional peaks at about 23°2θ and 34°2θ could not be assigned (neither peaks NaF nor peaks of $BaCl_2$ being obvious candidates of compounds to form could be found in the pattern).

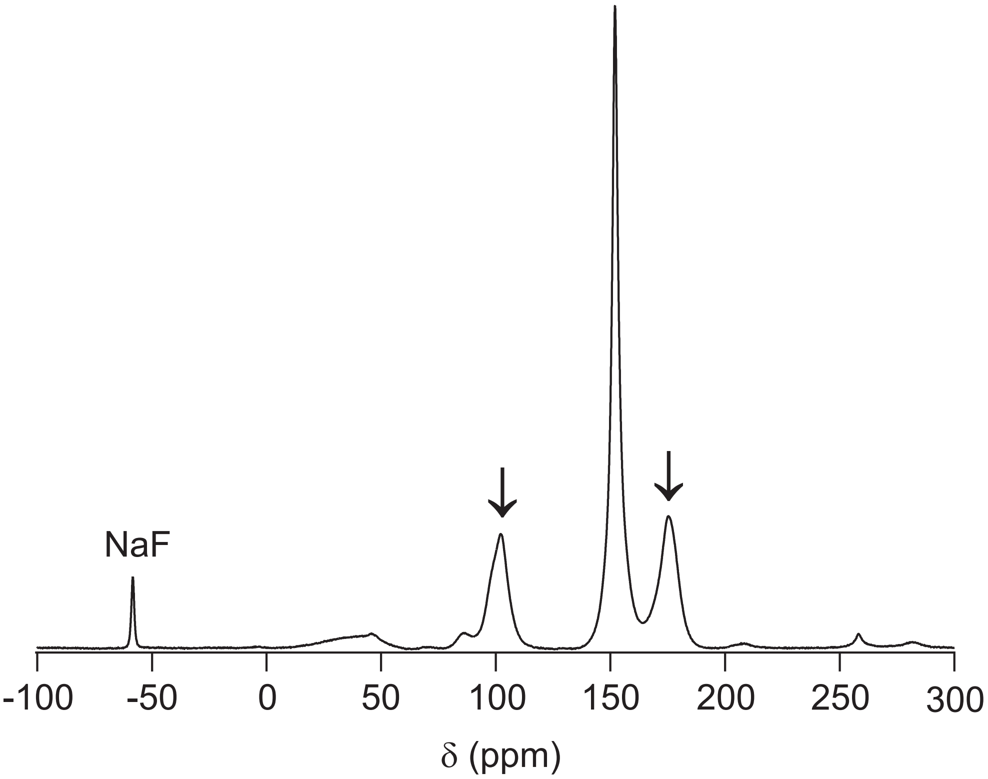

Figure 42: ^{19}F MAS NMR spectrum of the mixture of 9 BaF_2 and 1 NaCl milled for 6 h at 600 rpm in a ZrO_2 milling vial set. The spectrum was recorded with ν_0 = 565 MHz and ν_{rot} = 60 kHz. The NMR lines associated with the orthorhombic BaF_2 at 103 ppm and 176 ppm are marked with arrows. The main NMR line at 152 ppm represents the cubic BaF_2. A small amount of X-ray amorphous NaF can be observed at δ = -52 ppm. The other NMR lines could not be assigned to a compound, yet.

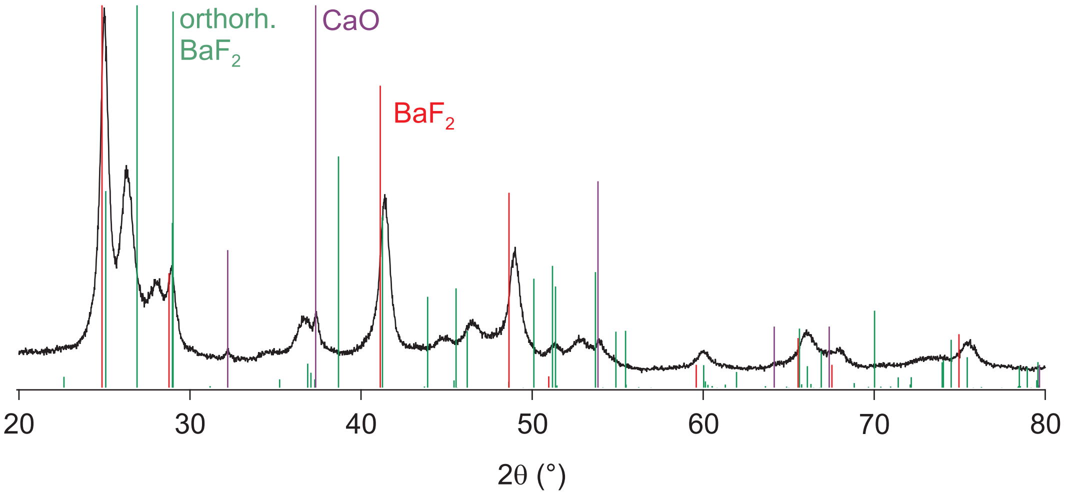

Figure 43: XRPD pattern of a mixture of 9 BaF_2 and 1 CaO milled for 6 h at 600 rpm in a ZrO_2 milling vial set. The peaks of the cubic BaF_2 are shifted to slightly larger angles 2θ probably due to the formation of $Ba_{1-x}Ca_xF_2$ while the peaks of the orthorhombic BaF_2 are shifted to smaller angles 2θ probably due to the formation of orthorhombic $Ba_{1-x}Ca_xF_2$.

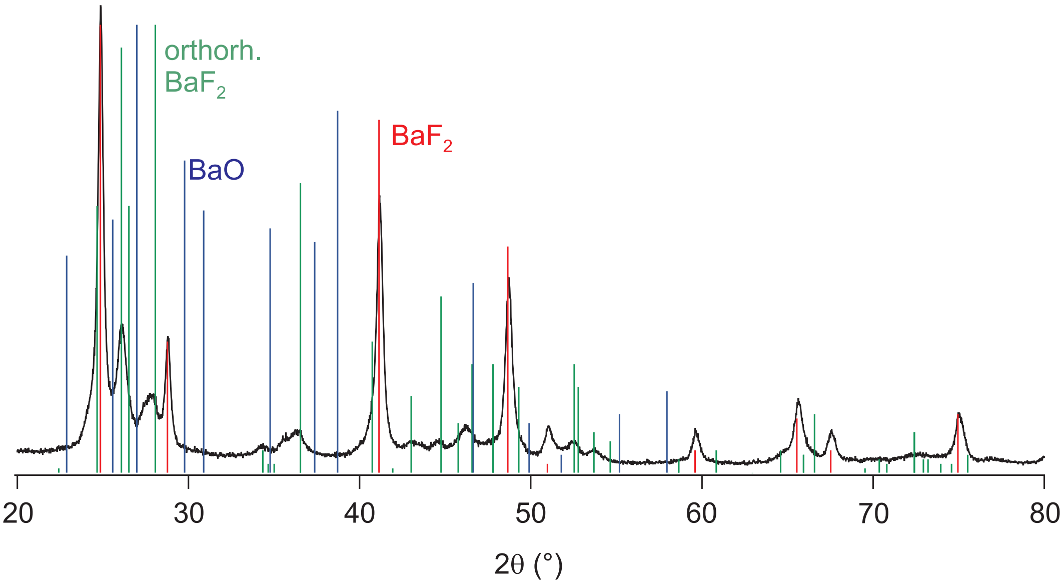

Figure 44: XRPD pattern of a mixture of 9 BaF_2 and 1 BaO milled for 6 h at 600 rpm in a ZrO_2 vial set.

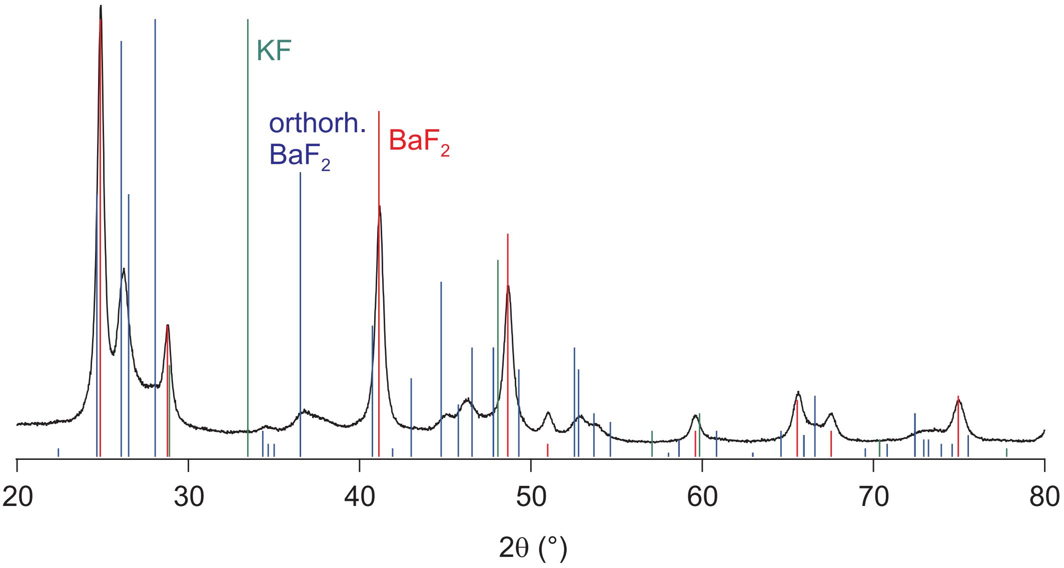

Figure 45: XRPD pattern of a mixture of 9 BaF_2 and 1 KF milled for 6 h at 600 rpm in a ZrO_2 vial set.

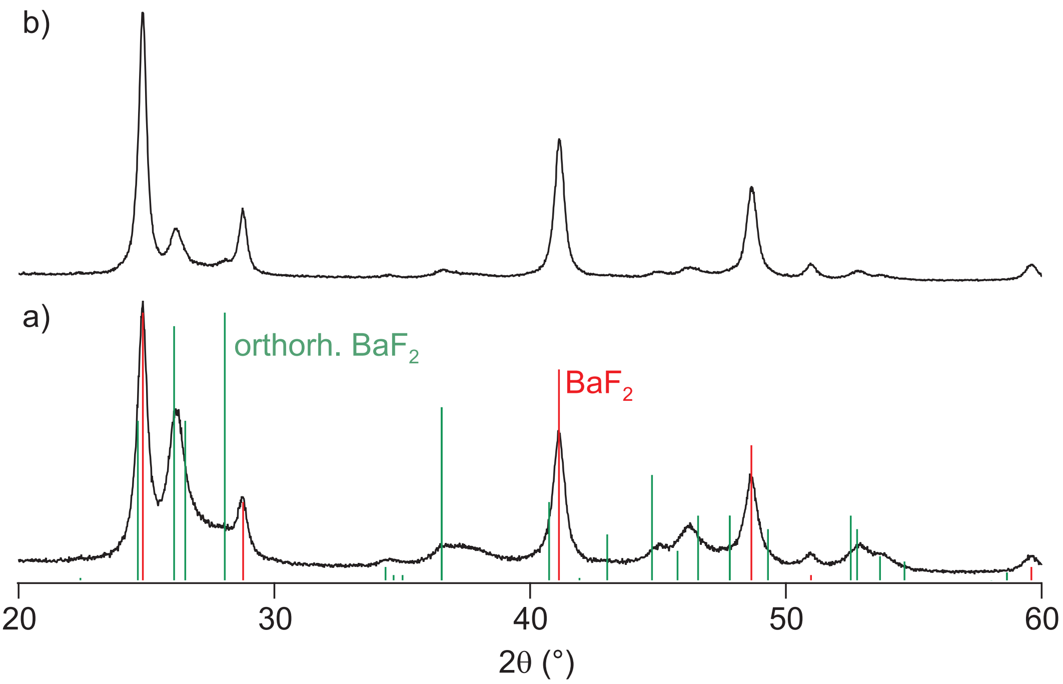

Figure 46: a) XRPD pattern of the mixture of 9 BaF_2 and 1 KF milled for 6 h at 600 rpm in a ZrO_2 vial set. b) XRPD pattern of the same sample after four months of storage in air.

10 Mechanosynthesis and characterization of the fluoride ion conductor $Ba_{1-x}La_xF_{2+x}$

The system $Ba_{1-x}La_xF_{2+x}$ as well as related systems of alkaline earth fluorides crystallizing in the fluorite or tysonite structure (heavily) doped with rare earth fluorides were investigated for some decades regarding their high fluoride ion conductivity[1] of which its origin is still not satisfactory clarified. A sophisticated and popular model is the enhanced ionic motion model created by Wapenaar and Schoonman in 1979.[2] According to this model the increased ionic conductivity is due to a distribution of jump enthalpies for the fluoride ions. This distribution is caused by the structural relaxation of the fluorite lattice close to so called 2:2:2 defect clusters (caused by the incorporation of LaF_3) creating percolation paths for the fluoride ions.[3] According to this model it is assumed that the fluoride ions in this clusters are non-mobile.[3] Some years later Andersen et al., however, found evidence that at least some of the fluoride ions in these clusters are mobile.[4]

Another interesting aspect of this system is its structure. The assumption of the formation of 2:2:2 clusters and related defect clusters is based on the interpretation of neutron scattering data.[5] However, eight years later Chernov et al.[6] argued that these defect clusters are structurally very similar to parts of the tysonite structure. Hence, it seems likely, that starting from the fluorite structure and increasing the amount of incorporated LaF_3 the structure of the formed $Ba_{1-x}La_xF_{2+x}$ should slowly change to the one of the tysonite structure. However, BaF_2 and LaF_3 are immiscible from $x \sim 0.55$ to $x \sim 0.85$[7,8] such that this theory could not be tested.

In the following manuscript entitled "Mechanosynthesis of the fast fluoride ion conductor $Ba_{1-x}La_xF_{2+x}$ - from the fluorite to the tysonite structure" (written mainly by the author and Prof. P. Heitjans) which will be published in J. Phys. Chem. C the mechanosynthesis of $Ba_{1-x}La_xF_{2+x}$ over the whole range of compositions is reported. By employing XRPD, Synchrotron measurements carried out at Deutsches Elektronen Synchrotron (DESY) by Dr. Jozef Bednarcik which were used to calculate pair distributions functions of some of the samples prepared and ^{19}F MAS NMR measurements evidence was found for a continuous change from the fluorite to the tysonite structure. The XRPD patterns can be assigned to the fluorite structure for compositions x up to 0.775 while ^{19}F MAS NMR spectra reveal structural aspects of the tysonite structure for the samples with $x \gtrsim 0.70$.

Regarding the ionic conductivity differences to the results observed for single crystalline material were found. The dc conductivities of the mechanosynthesized fluorite-type $Ba_{1-x}La_xF_{2+x}$ compounds are larger than the ones reported for the single crystalline material, except for the sample with $x = 0.50$ for which very similar values were found. A broad conductivity maximum was observed for the samples with x between $\sim$0.30 and $\sim$0.40 followed by a conductivity minimum at about $x = 0.75$. In case of the, judging from the XRPD patterns, tysonite structured compounds the conductivities of the mechanosynthesized samples are clearly smaller than the one of the single crystalline material. Another clear difference is the increase of the pre-exponential factor with increasing x in the range $0 \leq x \leq 0.80$ while in case of the single crystalline material no correlation between the composition and the pre-exponential factor was observed. Static ^{19}F NMR measurements were done to reveal the fluoride ion diffusivity from a microscopic point of view. Interestingly, it was found that at temperatures beyond 433 K all the fluoride ions seem to be highly mobile in case of the samples with $0.10 \leq x \leq 0.50$. Combined with indications found for the formation of 2:2:2 clusters in the mechanosynthesized material this means that the fluoride ions in the 2:2:2 cluster are not non-mobile. Hence, there are no percolating highly ion conducting paths. Instead of this the whole material became fast fluoride ion conducting. The decrease of the dc conductivity observed for the samples with $0.50 < x < 0.80$ is accompanied by the observation of non-mobile fluoride ions visible in the static ^{19}F NMR spectra. Furthermore, the motional narrowed NMR lines are broadened compared to the ones observed for the samples with ≤ 0.50. Thus, there seems to be an exchange of fluoride ions between several magnetically and, thus, chemically different fluorine sites leading to a superposition of several coalesced NMR lines. The chemical shifts of the narrowed NMR lines increase with x in a continuous fashion which also supports the assumption of a continuous transition from the fluorite to the tysonite structure.

In the future also single crystalline $Ba_{1-x}La_xF_{2+x}$ should be investigated with static ^{19}F NMR to test if also for this samples all fluoride ions are mobile at moderate temperature. Furthermore, it should be tested if there are microstructural differences between the single-crystalline and the mechanosynthesized samples.

References

[1] N. I. Sorokin and B. P. Sobolev, Chrystallogr. Rep., **2007**, 52, 842-863.

[2] K. E. D. Wapenaar, J. Schoonman, J. Electrochem. Soc., **1979**,126, 667-672.

[3] K. E. D. Wapenaar, J. L. van Koesveld, J. Schoonman, Solide State Ionics, **1981**, 2, 145-154.

[4] N. H. Andersen, K. N. Clausen, J. K. Kjems, J. Schoonman, J. Phys. C: Solid State Phys., **1986**, 19, 2377-2389.

[5] J. K. Kjems, N. H. Andersen, J. Schoonman, K. Clausen, Physica B&C, **1983**, 120, 357-361.

[6] S. V. Chernov, W. Gunßer, I. V. Murin, Solid State Ionics, **1991**, 47, 67-70.

[7] S. V. Kuznetsov, P. P. Fedorov, Inorg. Mater. **2008**, 44, 1434-1458.

[8] B. P. Sobolev, N. L. Tkachenko, J. Less Common Met. **1982**, 85, 155-170.

Reproduced with permission from The Journal of Physical Chemistry C, in press.
Unpublished work copyright 2014 American Chemical Society.

THE JOURNAL OF PHYSICAL CHEMISTRY C
Article
pubs.acs.org/JPCC

Mechanosynthesis of the Fast Fluoride Ion Conductor $Ba_{1-x}La_xF_{2+x}$: From the Fluorite to the Tysonite Structure

A. Düvel,*[†] J. Bednarcik,[‡] V. Šepelák,[§] and P. Heitjans*[†]

[†]Institute of Physical Chemistry and Electrochemistry, and ZFM − Center for Solid State Chemistry and New Materials, Leibniz University Hannover, Callinstr. 3-3a, 30167 Hannover, Germany

[‡]Deutsches Elektronensynchrotron DESY, Notkestr. 85, 22607 Hamburg, Germany

[§]Institute of Nanotechnology, Karlsruhe Institute of Technology (KIT), Hermann-von-Helmholtz-Platz 1, D-76344 Eggenstein-Leopoldshafen, Germany

Supporting Information

ABSTRACT: $Ba_{1-x}La_xF_{2+x}$ covering the whole range of compositions was synthesized by high-energy ball milling of mixtures of BaF_2 and LaF_3 at ambient temperature. The compounds obtained in this way crystallize in the cubic fluorite structure in the range from $0 \leq x \lesssim 0.775$ which extends the range for the fluorite-type $Ba_{1-x}La_xF_{2+x}$ covered up to now ($0 \leq x \leq 0.55$) considerably. By employing ^{19}F NMR spectroscopy and X-ray (total) scattering, indications for a continuous change from the fluorite (BaF_2) to the tysonite structure (LaF_3) were found. The mechanosynthesized samples showed slightly higher fluoride ion conductivities for the samples with $x \leq 0.40$ and clearly smaller conductivities in the case of the samples with $x \geq 0.85$ than reported for their monocrystalline counterparts. Two conductivity maxima at $x \approx 0.40$ and $x \approx 0.85$ and a conductivity minimum at $x \approx 0.75$ were observed for the mechanosynthesized $Ba_{1-x}La_xF_{2+x}$. For the samples with $0.10 \leq x \leq 0.50$, exhibiting a dc conductivity in the order of 10^{-5} S/cm at 400 K, all fluoride ions seem to be highly mobile at temperatures beyond 453 K. The decrease of the ionic conductivity observed for $Ba_{1-x}La_xF_{2+x}$ with increasing x in the range from $x \approx 0.50$ to $x \approx 0.75$ is accompanied by a change of the diffusion behavior and a decrease of the ratio of highly mobile to nonmobile or slow fluoride ions.

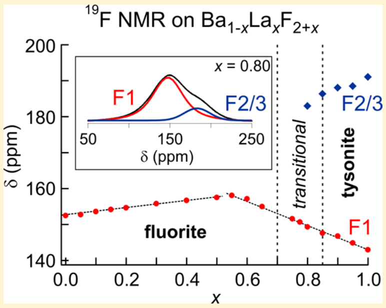

I. INTRODUCTION

Over the last years it has become apparent that compounds ground or synthesized by high-energy ball milling often show a change in their properties, e.g., an enhanced ionic conductivity, compared to their micro- or monocrystalline counterparts prepared by conventional solid state synthesis routines.[1−5] Furthermore, the synthesis of compounds conducted by mechanical treatment of the starting materials, the so-called mechanosynthesis, is known to be a very efficient technique for the preparation of metastable, partly new, compounds.[5−7] A well-known specialty of this technique is the preparation of solid solutions of normally immiscible or hardly miscible phases.[5−9] In this respect, the BaF_2−LaF_3 system is of particular interest. $Ba_{1-x}La_xF_{2+x}$ crystallizes in the fluorite structure (space group $Fm\bar{3}m$) for compositions $x \lesssim 0.55$[10,11] and in the tysonite structure (space group $P\bar{3}c1$) for $x \gtrsim 0.85$[10,11]. In the intermediate composition range from $x \approx 0.55$ to $x \approx 0.85$, the system is characterized by a miscibility gap.[10,11]

The microstructure, or more specifically the fluoride ion sublattice of fluorite-type $Ba_{1-x}La_xF_{2+x}$, turned out to be quite complex. By neutron scattering experiments some indications for the formation of so-called 2:2:2 clusters were found for the fluorite-type $Ba_{1-x}La_xF_{2+x}$ with $x \gtrsim 0.05$.[12,13] These 2:2:2 clusters consist of two fluoride ion interstitials (x = 0.5, y = 0.32, z = 0.32)[14] denoted as F′, two fluoride ion interstitials (x = 0.46, y = 0.46, z = 0.46)[14] denoted as F″ and two F^- vacancies (x = 0.25, y = 0.25, z = 0.25).[14] Chernov et al.[15] argued that the structure of these clusters resembles structural elements of the tysonite structure. This assumption was corroborated by results of Kadlec et al.[16] who found vibration modes in $Ba_{1-x}La_xF_{2+x}$ similar to those in LaF_3. Hence, an investigation of the transition of $Ba_{1-x}La_xF_{2+x}$ from the fluorite structure to the tysonite structure seems tempting. In addition, the 2:2:2 clusters are assumed to be responsible for the enhanced ionic conductivity observed for the compounds with $0.05 \lesssim x \lesssim 0.50$.[16−20] According to the enhanced ionic motion model,[18,21] the structural relaxation of the BaF_2 lattice close to the clusters leads to a decrease of the migration barriers of the fluoride ions. As a consequence, percolation paths for the fluoride ions should be formed in the interface regions of the moderate fluoride ion conductor BaF_2 and the presumed nonconducting 2:2:2 clusters.[18,21] It should be noted that in contradiction to the latter assumption, which is based on calculations regarding the stability of the 2:2:2 clusters,[18,22] the results of Andersen et al.[13] indicate that at least some of the fluoride ions in the 2:2:2 clusters are mobile.

Due to its high ionic conductivity $Ba_{1-x}La_xF_{2+x}$ was already used as a solid fluoride ion conductor in a chemical sensor[23]

Received: October 8, 2013
Revised: January 17, 2014

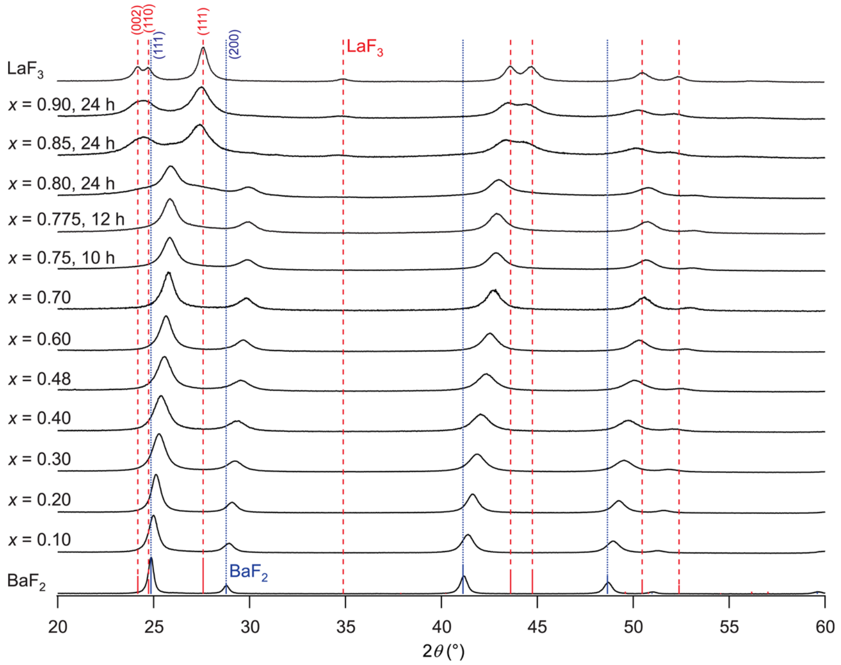

Figure 1. XRPD patterns of the different $Ba_{1-x}La_xF_{2+x}$ compounds. If not stated otherwise all compositions were milled for six hours. With a decreasing amount of BaF_2 (blue bars) the corresponding peaks shift to larger 2θ values in the case of the compounds which crystallize in the fluorite structure. For $x > 0.80$ the samples show the typical XRPD pattern of LaF_3 (red bars) shifted to smaller values of 2θ. See text for further explanations.

and as an electrolyte in a fluoride ion battery.[24] Fluoride ion batteries have found some attention in the past and present since they promise a large inherent safety and very high capacities.[23−34] For this kind of batteries, in which a reaction of the type $MF_y + M' \rightleftharpoons M + M'F_y$ (M = metal) takes place, only ceramic electrolytes have been tested, yet. Therefore, the fluoride ion battery systems exhibiting a high specific energy investigated up to now can only be operated at elevated temperatures due to the rather low ionic conductivity of the electrolytes being stable in a sufficiently broad potential range. The latter criterion most probably excludes the usage of the very fast known fluoride ion conductors containing lead or tin[35] like PbF_2,[36] $PbSnF_4$,[37] and presumably also $BaSnF_4$. Thus, other fast fluoride ion conductors have to be found. $Ba_{1-x}La_xF_{2+x}$ seems to offer a high electrochemical stability[38] but in comparison with, e.g., $PbSnF_4$ a rather low ionic conductivity.[20,37] As already mentioned, the ionic conductivity of several ceramic compounds could be increased by mechanical treatment or mechanosynthesis. Furthermore, as stated above, the miscibility gap of BaF_2 and LaF_3 may be closed by employing a mechanosynthesis routine.[6] Hence, mechanosynthesis may open up a path to the preparation of $Ba_{1-x}La_xF_{2+x}$ compounds which exhibit higher ion conductivities than observed so far for this system.

Therefore, in this study the ionic conductivity of mechanosynthesized $Ba_{1-x}La_xF_{2+x}$ with $0 \leq x \leq 1$ was investigated by impedance spectroscopy. Further insight regarding the fluoride ion diffusion in the prepared materials was gained by ^{19}F nuclear magnetic resonance (NMR) spectroscopy. The structure and microstructure of the samples were investigated by X-ray powder diffraction (XRPD), transmission electron microscopy (TEM), and ^{19}F magic angle spinning (MAS) NMR spectroscopy. For some samples X-ray scattering experiments were done up to large q-values to calculate their pair distribution functions (PDFs), $G(r)$.

II. EXPERIMENTAL DETAILS

A series of samples with compositions $Ba_{1-x}La_xF_{2+x}$ with $0 \leq x \leq 1$ were prepared by joint milling of micrometer-sized pure BaF_2 (99.99%, Sigma Aldrich) and LaF_3 (99.9%, Fluka). The synthesis was carried out using a Fritsch P7 premium line planetary mill employing a ZrO_2 milling vial set (45 mL) in combination with 140 milling balls (5 mm in diameter) of the same material. The total mass of each mixture was 2.0000(5) g. Milling times t_{mill} used reached from 6 to 24 h. The temperature of the milling beaker was measured with a pyrometer in the inside of the beaker directly after milling. It did not exceed 343 K.

The obtained powders were characterized by XRPD using a D8 Advance diffractometer (Bruker) operating with Cu−K_α radiation at 40 kV which corresponds to a wavelength $\lambda \approx 0.154$ nm. For some of the samples PDFs were calculated from X-ray diffractograms obtained at the High-Resolution Powder Diffraction (HRPD) beamline P02.1 of the PETRA III electron storage ring at DESY (Hamburg, Germany) in transmission mode. The energy of the synchrotron radiation was set to 59.81 keV, which corresponds to a wavelength of $\lambda = 0.02073$ nm. Two-dimensional XRD patterns were collected using a Perkin-Elmer 1621 fast image plate detector (2048 × 2048 pixels, 200 × 200 μm^2 pixel size) carefully mounted orthogonal to the X-ray beam. The samples were illuminated for 10 s by the X-ray beam. For each sample measurements were done with different distances between the sample and detector to obtain the best resolution in the low as well as the high q-range. The two-dimensional XRPD patterns were integrated to the q-space by employing the software package FIT2D.[39] This results in several one-dimensional XRPD patterns for different ranges of q which were merged to a single pattern for each sample. The obtained diffractograms were corrected (absorption, fluorescence, Compton scattering, etc.) and eventually Fourier transformed to PDFs by employing the software PDFgetX2.[40]

For TEM investigations, the powdered sample was dispersed in isopropyl alcohol. A drop of approximately 10 μL of this suspension was dried on a copper-supported holey carbon film. (S)TEM was done at 200 kV on a field-emission instrument of the type JEOL JEM-2100F-UHR.

The impedance measurements were done on cylindrical pellets with a diameter of 8 mm and approximately 1 mm thickness (measured with a vernier caliper for each pellet). The pellets were produced by cold-pressing the powders at a uniaxial pressure of about 1 GPa. Electrodes were applied by coating the plane parallel sides of the pellets with an alcohol-based graphite conductive adhesive (Alfa Aesar). The measurements were done with an HP 4192 A analyzer connected to a home-built cell with a four-terminal configuration in the frequency range from 5 Hz to 13 MHz. The cell is designed to be operated under controlled atmospheres. Here, a constant flow of dry argon gas (99.999%) was applied. A Eurotherm controller was used to monitor and adjust the temperature.

For the temperature-variable static ^{19}F NMR measurements the powdered samples were put into glass ampullae, dried in vacuum at 380 K for at least 24 h, and then heat sealed. The measurements were done with an MSL 400 spectrometer (Bruker) connected to a shimmed Oxford cryomagnet with a nominal field of 9.4 T which corresponds to an ^{19}F resonance frequency of $\nu_0 = 376.5$ MHz. A modified 7 mm MAS NMR probe (Bruker Biospin) was used for the measurements. The duration of the $\pi/2$ excitation pulse applied was 3.3 μs. For all measurements the saturation recovery pulse sequence was used, followed by an adjustable waiting time and a single $\pi/2$ pulse.[41,42] For each spectrum 32 scans were accumulated. To obtain fully relaxed spectra the waiting time was chosen to be five times the relaxation time T_1 at the respective temperature.

The ^{19}F MAS NMR spectra were recorded with an Avance III spectrometer (Bruker) operating at $\nu_0 = 564.7$ MHz by employing a 1.3 mm MAS probe (Bruker) and using room-temperature bearing gas. The NMR spectra were acquired by applying a single $\pi/2$ excitation pulse with a length of approximately 2 μs. For each spectrum 32 scans were accumulated with a recycle delay of 5 s and a spinning speed of $\nu_{\mathrm{rot}} = 60$ kHz. All ^{19}F NMR spectra were referenced to C_6F_6 (which has a chemical shift $\delta = -162.9$ ppm when referenced to CCl_3F[43]).

III. RESULTS AND DISCUSSION

A. Characterization by X-ray Diffraction. Starting from pure BaF_2 all XRPD peaks of the $Ba_{1-x}La_xF_{2+x}$ show the typical pattern of the fluorite structure in a range from $0 \leq x \leq 0.775$ (see Figure 1). The positions of the peaks are shifted toward larger 2θ values with increasing amounts of LaF_3 which indicates lattice contraction. Even the sample with $x = 0.80$ shows the typical pattern of the fluorite structure, but there are also some very broad peaks of weak intensity exhibiting the XRPD pattern (particularly the (002), (110), and (111) peaks) of LaF_3 crystallizing in the tysonite structure which seem to be shifted toward smaller values of 2θ. It should be noted that an increase of the milling time from 24 to 60 h or the change of the milling vial set does not lead to the disappearance of the XRPD peaks of the tysonite phase in the case of the sample with $x = 0.80$ (see Figure S1, Supporting Information). In the case of the sample with $x = 0.85$, the shifted (111) and (200) peaks of the BaF_2 pattern can still be detected at approximately 26° 2θ and 30.1° 2θ besides the typical pattern of LaF_3 (space group $P\bar{3}cl$) shifted toward smaller values of 2θ. Thus, these two samples seem to be mixtures of $Ba_{1-x}La_xF_{2+x}$ crystallites of which a part crystallizes in the fluorite and the other ones in the tysonite structure. The width of the small peaks in the case of the sample with $x = 0.80$ makes a clear assignment to a phase difficult. Thus, judging from the XRPD pattern it cannot be excluded that just residual pure LaF_3 or amorphous material is present. However, it should be noted that both structures should be highly distorted in this range of compositions as will be discussed later. Thus, one might assume that the samples with $x = 0.80$ and $x = 0.85$ may be transitional phases combining structural aspects of both structures and are not mixtures of differently structured crystallites of $Ba_{1-x}La_xF_{2+x}$, which is essentially in agreement with the deliberations of Chernov et al.[15] (vide supra). The samples with $x > 0.85$ show the XRPD pattern of LaF_3 in which the peaks are shifted toward smaller diffraction angles which indicates lattice expansion.

The PDFs, i.e., G as a function of r, of the samples with $x = 0.20$, $x = 0.50$, $x = 0.70$, $x = 0.80$, and $x = 0.85$, shown in Figure 2, exhibit the average distances r of the ions in real space or, to be more exact, the probability to find ions in a certain distance from each other (by integration of $G(r)$ from r_1 to r_2).[44] At first view the patterns of all the samples are very similar. Even in the case of the sample with $x = 0.85$ exhibiting an XRPD pattern typical of the tysonite structure (see Figure 1), almost all of the peaks visible in the PDFs of the other samples crystallizing in the fluorite structure still show up. Starting from the sample with $x = 0.20$ the distances between the ions decrease with increasing x as was already observed in the XRPD patterns in Figure 1. The lattice parameters a of the fluorite type $Ba_{1-x}La_xF_{2+x}$ can easily be recognized in the PDFs of the samples as the second from left of the M−M (M = Ba^{2+}, La^{3+}) peaks, which are marked with an ‡. They are in good agreement with the ones obtained directly from the XRPD patterns (vide infra).

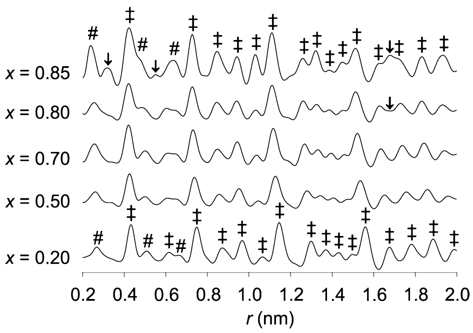

Figure 2. Pair distribution functions of several $Ba_{1-x}La_xF_{2+x}$ compounds. ‡ marks M−M distances, while # shows the distances between M and F. See text for further explanations.

Going from $x = 0.80$ to $x = 0.85$ the change of the structures can be observed by the disappearance of the peak representing the lattice parameter a of the fluorite lattice, the emergence of three new peaks (arrows in Figure 2), and a change of the height of some of the peaks already present in the PDFs of the other samples. Furthermore, the first peak is clearly shifted to smaller r (0.24 nm) and shows a higher intensity compared to the peak representing the shortest M−F distance in the case of the sample with $x = 0.80$. It can be attributed to the shortest distance between La^{3+} and F^- in the tysonite structure. The new peak at 0.32 nm probably represents a cation−fluoride ion

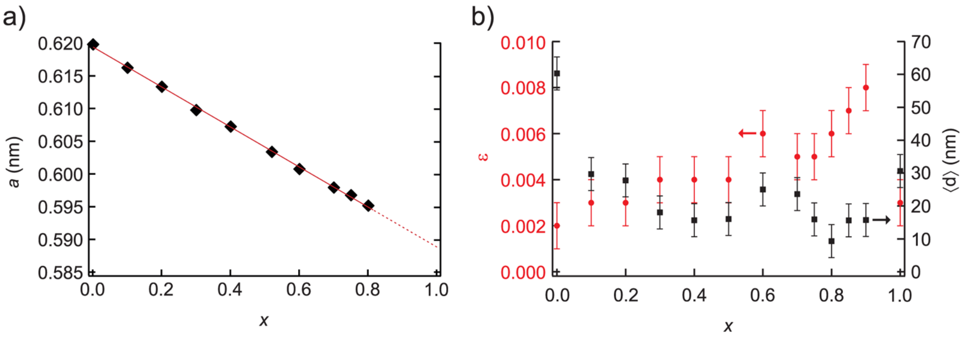

Figure 3. (a) Lattice parameter *a* of the $Ba_{1-x}La_xF_{2+x}$ compounds exhibiting the fluorite structure, whose XRPD patterns are shown in Figure 1, as a function of composition *x*. (b) Average crystallite size ⟨*d*⟩ (black squares) and lattice strain *ε* (red circles) as a function of *x*.

distance in the tysonite structure since it is too small for a cation−cation distance. Thus, this peak is probably associated with a Ba−F distance in the tysonite structure. The other new peak at 0.55 nm probably shows a Ba−Ba distance of Ba ions neighboring each other in the tysonite structure. This assumption is in good agreement with the assumed Ba−F distance of about 0.32 nm and the low intensity of the peak, representing the expected low abundance of this pair. The last new peak in the shown distance regime at 1.68 nm can probably be attributed to a La−La distance in the tysonite structure. A similarly positioned peak seems to exist also in the sample with $x = 0.80$ (marked by an arrow). Apart from these three peaks, the La−F peak at 0.24 nm, and several changes in the intensity of some of the cation−cation peaks due to different coordination numbers, the PDF of the tysonite structured $Ba_{0.15}La_{0.85}F_{2.85}$ is similar to the ones of the fluorite structured samples.

There are no peaks in the PDFs which can clearly be associated with the M−F distances in the 2:2:2 clusters (the M−M distances are the same as in the undistorted fluorite structure). These distances are, however, rather close to the ones in the undistorted fluorite structure and, therefore, difficult to separate from each other. However, there should be a peak between the first two peaks in the PDFs of the samples with $x = 0.20$ up to $x = 0.80$ corresponding to the distances between the cations and the fluoride ions at F′ and F″ sites. In fact, a broad shoulder can be seen in this range in the case of the samples with $x = 0.20$, $x = 0.50$, and $x = 0.80$ but not for the sample with $x = 0.70$. Whereas the sample with $x = 0.70$ lacks such a shoulder, its first M−F peak is clearly broader and larger than observed for the other samples. Thus, one might assume a change of the cluster structure for this sample. Furthermore, it should be noted that the position of the second smallest *d*(M−F) peak changed in a pronounced way: from about $r = 0.50$ nm in the case of the sample with $x = 0.70$ to $r = 0.48$ nm for the sample with $x = 0.80$. Therefore, the shoulder in the case of the sample with $x = 0.80$ is probably not due to the 2:2:2 clusters but may rather be related with the peak at 0.32 nm appearing in the PDF of the sample with $x = 0.85$ which probably represents the shortest Ba−F distance in the tysonite structure (vide supra).

Although the PDFs of the samples with $x = 0.80$ and $x = 0.85$ seem to be quite similar, the PDF of the sample with $x = 0.80$ is still more similar to the PDFs of the samples with $x = 0.20$, $x = 0.50$, and $x = 0.70$. Coming back to the question regarding the actual structure of the sample with $x = 0.80$, it can be seen that the PDF of this sample indeed combines aspects of the PDFs of the samples with $x = 0.70$ and $x = 0.85$ without showing identical peaks. There are also no peaks in the PDF of the sample with $x = 0.80$ which can clearly be matched with distances in pure LaF_3 (which admittedly does not rule out the possibility of the presence of a small amount of LaF_3 in this sample). Therefore, it seems reasonable to assume that the sample with $x = 0.80$ is not a mixture of $Ba_{1-x}La_xF_{2+x}$ crystallizing in the fluorite and $Ba_{1-x}La_xF_{2+x}$ crystallizing in the tysonite structure. Instead of this, it seems to crystallize in a structure in between these structures.

In Figure 3a the lattice parameter *a* of the $Ba_{1-x}La_xF_{2+x}$ crystallizing in the (structurally distorted) cubic fluorite structure, calculated according to

$$a = \frac{\lambda_{XRD}}{2 \cdot \sin \theta} \cdot \sqrt{(h^2 + k^2 + l^2)} \tag{1}$$

is shown as a function of *x*. Here $\lambda_{XRD} = 0.154$ nm is the average wavelength of the X-ray radiation used, and *h*, *k*, and *l* are the Miller indices of BaF_2. The positions of the maxima of the first ten peaks were used for the calculations. With increasing amount of LaF_3 the lattice parameters *a* of the compounds decrease linearly in the range $0 \leq x \leq 0.80$. The slope of the line is 0.0306(4) and, thus, very similar to the one reported by Sobolev et al. for monocrystalline $Ba_{1-x}La_xF_{2+x}$[11] which is 0.03033. This indicates that the intended amounts of LaF_3 were introduced into the BaF_2 lattice for $x \leq 0.80$.

The XRPD peaks of the $Ba_{1-x}La_xF_{2+x}$ are very broad. This can inter alia be caused by a reduced number of scattering centers (atomic planes) due to size reduction of the crystallites or by lattice strain which leads to a distribution of distances between the atomic planes. Interestingly, the peaks of the binary fluorides are less broad than the ones of the $Ba_{1-x}La_xF_{2+x}$ products. This is probably mainly due to an enhanced size reduction caused by the mechanical interaction of the $Ba_{1-x}La_xF_{2+x}$ crystallites with each other or with the starting materials which seems to be more effective than in the case of the pure binary fluorides.

This is indicated by the results obtained by employing the procedure introduced by Williamson and Hall[45] using the full width at half-maximum (fwhm) of the XRPD peaks corrected for instrumental broadening effects (see ref 4 for more details). Values of the average crystallite size ⟨*d*⟩ in a range from 9(5) nm ($x = 0.80$) to 29(5) nm ($x = 0.10$) were found for $Ba_{1-x}La_xF_{2+x}$ without a continuous trend when plotted as a function of *x* (see Figure 3b). The lattice strain *ε* varies from 0.002(1) to 0.008(1) and increases with *x* (Figure 3b) which indicates increasing structural disorder with rising *x*. In the case of the ball-milled binary fluoride, values of 60(5) nm ($\varepsilon = 0.002$) for BaF_2 and 31(5) nm ($\varepsilon = 0.003$) for LaF_3 were determined. The average crystallite size can also be estimated from the PDFs as the distance r at which $G(r)$ cannot be separated from noise anymore (see Figure S2, Supporting Information). The values obtained that way are in quite good agreement with the values obtained by the Williamson and Hall approach.

In Figure 4 a high-resolution (HR)TEM micrograph of the sample with $x = 0.80$ is shown. The crystallites were found in agglomerates and exhibit diameters of approximately 10 nm which is in good agreement with the value calculated from the XRPD and the PDF. They show a well-ordered structure even at their boundaries.

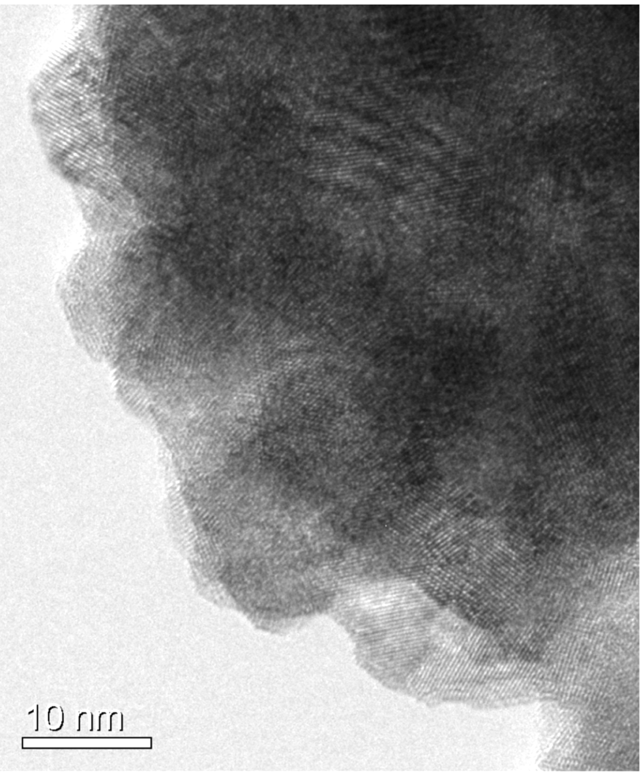

Figure 4. HRTEM micrograph of the sample with $x = 0.80$.

The thermal stability of $Ba_{1-x}La_xF_{2+x}$ was tested for the samples with $x = 0.80$ and $x = 0.65$. After heat treatment for 6 h at 873 K in air the XRPD patterns exhibit the formation of LaF_3 besides $Ba_{1-x}La_xF_{2+x}$ (see Figure 5). The XRPD peaks of the $Ba_{1-x}La_xF_{2+x}$ are narrowed which is due to grain growth or decreased lattice strain, and they are shifted to smaller values of 2θ. Thus, the $Ba_{1-x}La_xF_{2+x}$ compounds were depleted in LaF_3 by thermal treatment. Several additional peaks of weak intensity are also visible which we were not able to attribute to a known phase. Since the lattice parameter a of the $Ba_{1-x}La_xF_{2+x}$ crystallizing in the fluorite structure changes linearly with x it was possible to calculate the compositions of the annealed samples. They changed from $x = 0.80$ to $x = 0.66$ and from $x = 0.65$ to $x = 0.57$, respectively. Thus, the higher the LaF_3 content of the thermally treated $Ba_{1-x}La_xF_{2+x}$, the more pronounced is the depletion of LaF_3. Hence, as already expected, the fluorite-type $Ba_{1-x}La_xF_{2+x}$ with $0.55 \lesssim x \lesssim 0.80$ is metastable at room temperature and most probably cannot be prepared by conventional solid state synthesis.

B. ^{19}F MAS NMR Spectroscopy. For several mixed fluoridic systems it was possible to receive an impression of the unequal cationic environments of the fluoride ions and, thus, of the microstructure of the materials by ^{19}F MAS NMR spectroscopy using high spinning speeds.[6,7,46] However, the spectra obtained for the $Ba_{1-x}La_xF_{2+x}$ do not allow a separation of the different cationic environments of the fluoride ions (see Figure 6). Whereas in the case of solid solutions of BaF_2 and CaF_2[6], BaF_2 and SrF_2,[6] or CaF_2 and SrF_2,[6,46] which crystallize in the fluorite structure, up to five NMR lines, representing the five possible cationic environments of the tetrahedrally coordinated fluoride ions, were observed, here at maximum two NMR lines can be separated (see Figure 6). This is due to several characteristics of this system. First, the isotropic chemical shifts δ_{iso} of the ^{19}F NMR lines of BaF_2 (152 ppm) and LaF_3 (143 and 192 ppm) are close to each other. Furthermore, the mechanical treatment of the pure binary fluorides leads to a broadening of their NMR lines (see Figure 6). The high defect concentration in the mechanically treated materials, especially in the grain boundary affected regions of the crystallites, leads to a large amount of fluoride ions situated in slightly different chemical environments. Hence, these fluoride ions experience slightly different magnetic field strengths leading to a manifold of NMR lines with similar chemical shifts which merge into a broad NMR line. This line broadening eases the superposition of NMR lines which are separated in the case of well-ordered materials. However, the presumably most important aspect is the fact that the excess positive charge of the La ions substituting the Ba ions in the BaF_2 has to be compensated by fluoride ions sitting on interstitial sites which leads to the formation of a structurally distorted lattice. For instance, in the case of $Ba_{0.5}La_{0.5}F_{2.5}$ in theory 1/5 of the fluoride ions have to occupy interstitial sites. As already mentioned before, indications for the formation of 2:2:2 clusters, hosting the additional fluoride ions in monocrystalline $Ba_{1-x}La_xF_{2+x}$, were found by neutron scattering.[13] Since the slope of the lattice parameter as a function of x is very similar to the one found for single crystals and judging from the PDFs (vide supra), it seems likely that also for the mechanosynthesized $Ba_{1-x}La_xF_{2+x}$ these (or similar) cluster structures are formed at least for the samples with $x < 0.70$. Especially in the case of large x many fluoride ions should be situated in slightly different chemical environments, e.g., fluoride ions at the different sites in the 2:2:2 clusters, fluoride ions on regular sites close to displaced fluoride ion sites, fluoride ions coordinated by different cation species, or fluoride ions experiencing strain in the fluorite structure for instance close to the 2:2:2 clusters. Thus, there should be many NMR lines with slightly different chemical shifts which apparently cannot be resolved anymore. As a consequence very broad NMR lines emerge.

The fluoride ions at some of the sites associated with the 2:2:2 clusters might be represented by the NMR line with an isotropic chemical shift of about 170 ppm in the spectrum of the sample with $x = 0.05$ (see Figure 6), which was also reported by Rongeat et al.[47] This NMR line increases in intensity with increasing x and, thus, increasing amount of excess fluoride ions until it overlaps with the central NMR line. That way an increasingly broad NMR line with a fwhm of up to 57 ppm for the sample with $x = 0.775$ is obtained. Thus, when sticking to this hypothesis the 2:2:2 clusters and the fluorite-type structure cannot be distinguished in the case of $Ba_{1-x}La_xF_{2+x}$ with $x > 0.40$ which implies that the whole material is strongly affected by the 2:2:2 clusters in that compositional range.

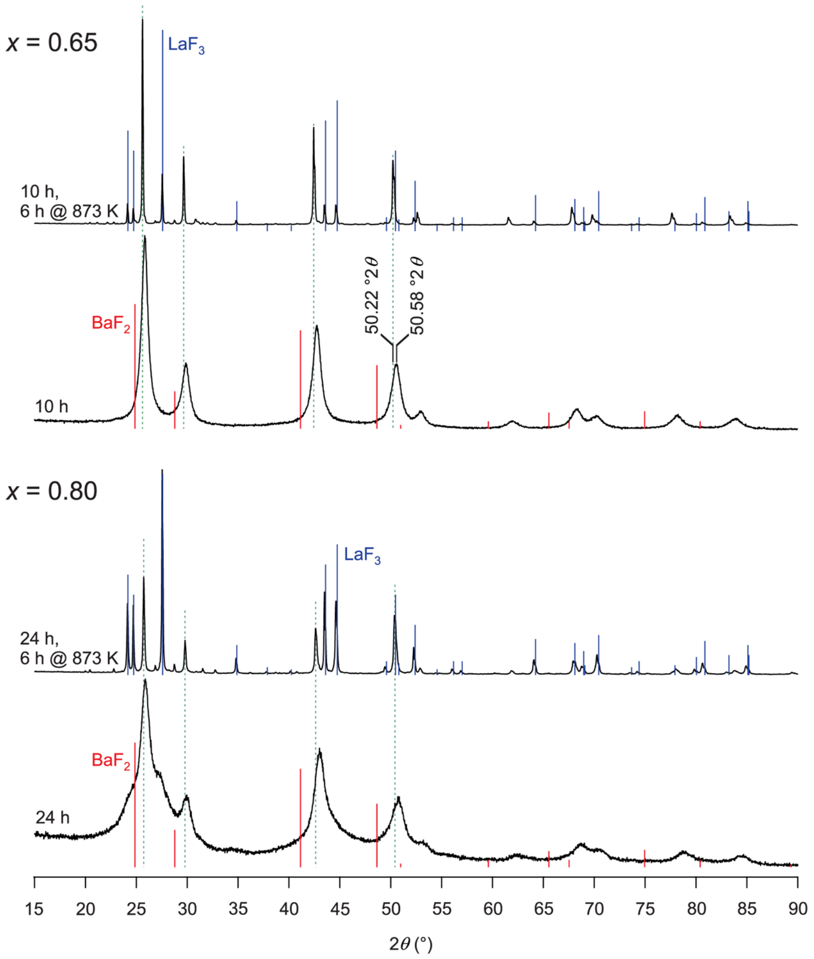

Figure 5. XRPD patterns of $Ba_{0.35}La_{0.65}F_{2.65}$ (top) and $Ba_{0.20}La_{0.80}F_{2.80}$ (bottom) after annealing for 6 h at 873 K in comparison to the XRPD patterns of the mechanosynthesized samples with the milling times 10 and 24 h, respectively, before annealing. The green dotted lines show the positions of the XRPD peaks of the $Ba_{1-x}La_xF_{2+x}$ after annealing. The red bars indicate the positions of the XRPD peaks of BaF_2 and the blue bars the ones of LaF_3.

In the spectra of milled BaF_2 and of the sample with $x = 0.05$ also the NMR lines representing orthorhombic BaF_2[3] (black arrows in Figure 6) can be found. Orthorhombic BaF_2 is a high-pressure phase of BaF_2[48,49] and known to form while milling.[3,7,48] For LaF_3, which crystallizes in the tysonite structure, three NMR lines in the case of monocrystalline material were observed.[50] These three NMR lines can be attributed to the three different sites of the fluoride ions, F1, F2, and F3, in the LaF_3 lattice (see ref 50). The fluoride ions on the F1 sites exhibit a chemical shift of approximately 143 ppm, while the ones on F2 and F3 sites (which do not differ that much from each other regarding their local cationic environments) can be found at around 192 ppm (see Figure 6). The fluoride ions on the F1 sites are coordinated by 4 La^{3+} which differ in distance d(La−F): 0.246, 0.248, 0.264, and 0.300 nm.[51] The fluoride ions on the F2 and F3 sites are coordinated by 3 La^{3+} with a distance d(La−F) of approximately 0.242 and 0.244 nm, respectively.[51] These short distances lead to the large chemical shifts observed compared to the one representing the fluoride ions on the F1 sites with clearly larger cation−fluoride ion distances.[52]

The NMR lines representing the fluoride ions on the F2 and F3 sites cannot be separated in the ^{19}F MAS NMR spectra of high-energy ball-milled LaF_3. With decreasing x the two NMR lines representing the fluoride ions on F1 sites or fluoride ion sites in the structurally distorted fluorite lattice and the fluoride ions on F2/3 sites converge until for the sample with $x = 0.75$ the two NMR lines can hardly be separated and eventually for the sample with $x = 0.65$ only a single NMR line is observed. Thus, with decreasing x the chemical environments of the fluoride ions on the F2 and F3 sites become more and more similar to the ones of the fluoride ions on the F1 sites or the ones located in the fluorite-type $Ba_{1-x}La_xF_{2+x}$. Hence, the microstructure seems to become more homogeneous. Furthermore, this means that for the sample with $x = 0.75$ clearly and solely showing the XRPD pattern of the fluorite structure an NMR line of considerable intensity representing fluoride ions in distorted F2/3 sites can be seen (see the two fit-lines in the spectra in Figure 6), which is in agreement with the deliberations of Chernov et al.[15] and the results of Kadlec et al.[16] (see Section I). It should be kept in mind that the TEM micrographs as well as the XRPD patterns show no hints for noteworthy amounts of amorphous material. Hence, it seems that the structure of the crystalline material is homogenized regarding the fluoride ion coordination spheres. These results indicate a continuous transition from the fluorite to the tysonite structure.

As observed for the lattice parameter (see Figure 3a), also in the case of the chemical shift a linear dependence on x is observed as shown in Figure 7. The change of the chemical shift

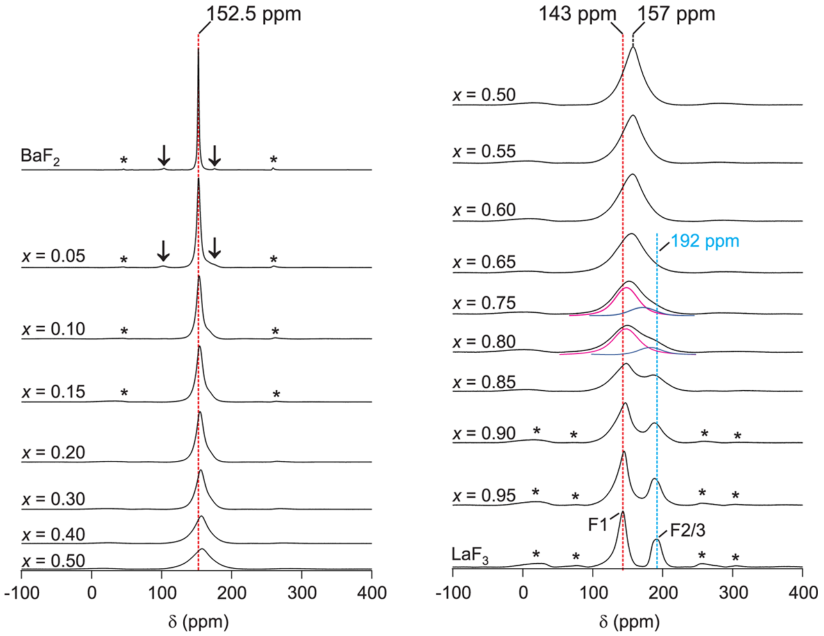

Figure 6. ^{19}F MAS NMR spectra of $Ba_{1-x}La_xF_{2+x}$ with the compositions x as indicated, recorded at $\nu_0 = 565$ MHz with $\nu_{rot} = 60$ kHz. For comparison also the spectra of the milled binary fluorides are shown. The spectra of the samples with $x = 0.75$ and $x = 0.80$ were fitted by two lines (see text for further explanations). The arrows show the NMR lines representing orthorhombic BaF_2. Spinning sidebands are marked by asterisks.

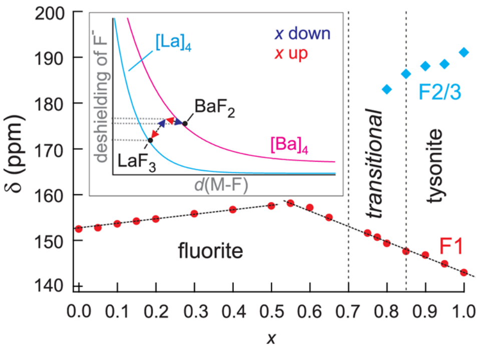

Figure 7. Variation of the chemical shift of ^{19}F in $Ba_{1-x}La_xF_{2+x}$ with x. The red points denote the maxima of the main NMR lines in Figure 6 corresponding to F^- on their sites in the fluorite structure and F1 sites in the tysonite structure. The blue rhombi denote the maxima of the less intense NMR lines clearly visible for the samples with $x \geq 0.80$ corresponding to F^- on F2 and F3 sites in the tysonite structure. The inset shows the deshielding of the F1 fluoride ions and the ones in the fluorite structure by the two cation species as a function of the distance between cation and fluoride ion d(M−F). See text for further explanations.

is associated with d(M−F), as was already discussed in refs 6 and 7. However, the NMR line representing the fluoride ions on the F1 sites shifts toward larger chemical shift values with increasing amounts of BaF_2 and, thus, increasing lattice parameter. At first glance this seems unexpected since an expanding lattice, and thus expanding distances d(La/Ba−F), should lead to a decrease of the isotropic ^{19}F NMR chemical shift.[6,7,52] In fact such a behavior can be seen for the NMR line representing the fluoride ions on F2/3 sites (see Figure 7). Therefore, the increase of the chemical shift is most probably due to a larger deshielding of the fluoride ions by the Ba ions introduced with respect to the La ions. Simply put, the value of the isotropic ^{19}F NMR chemical shift can be treated as the sum of the diamagnetic shielding and the paramagnetic deshielding of the fluoride ions. The diamagnetic shielding is caused by the electrons of the fluoride ion and is not affected by its chemical environment. The paramagnetic deshielding, however, is caused by the electrons of the atoms or ions surrounding the fluoride ion. Its value can be determined by simply summing up the respective contributions of these atoms or ions.[52,53] Of course the separation of the diamagnetic shielding from the paramagnetic deshielding is rather hypothetical. The paramagnetic deshielding of the fluoride ion strongly depends on the distance d(M−F) in an exponential way.[52] Thus, the smaller the initial distance between the cation and the fluoride ion the larger the change of the isotropic chemical shift when d(M−F) is varied. Therefore, the fluoride ions on F2 sites can be distinguished from the fluoride ions at the almost identical F3 sites in polycrystalline LaF_3[50] despite that $\Delta(d(M-F)) = d(M-F3) - d(M-F2) = 0.002$ nm. In BaF_2 a distance of 0.268 nm between the fluoride ion and the four Ba^{2+} leads to a chemical shift of 152 ppm. Although the distances d(La−F) of three of the four cations coordinating the fluorine on the F1 site in LaF_3 are clearly smaller than 0.268 nm, its chemical shift is only 143 ppm. Therefore, as may already be estimated from their different ionic radii, the deshielding of the La ions is smaller for this distance regime than the one of the Ba ions. Thus, the increase of the distances between the ions which should lead to a decrease of the chemical shift is overcompensated by the deshielding of the fluoride ions by the Ba ions. This leads to an increase of the isotropic chemical shift with decreasing x. However, when x is decreased below a certain value the expansion of the lattice should overcompensate the higher deshielding of the Ba ions due to the exponential decline of the deshielding with increasing d(M−F), as illustrated in the inset of Figure 7. Hence, the chemical shift should not increase anymore but start to decrease toward the chemical shift value of BaF_2. In fact, this is observed: starting at a composition of x = 0.55 the chemical shift value decreases with decreasing x (Figure 7).

The decrease of the chemical shift of the NMR line representing the fluoride ions on the F2/3 sites with increasing BaF_2 content is also due to the substitution of the La ions coordinating these fluoride ions by Ba ions since the fluoride ions on F1 sites share their cationic neighbors with the fluoride ions on F2 and F3 sites. The increase of the, in this case initially very small, cation−fluoride ion distances (vide supra) causes a decrease of the chemical shift. This eventually leads to an averaging of the distances between fluoride ions and cations in the three coordinations spheres of the fluoride ions as already described before.

Interestingly, the change of the chemical shift with x in a range from $x = 0.55$ to $x = 1$ seems to be linear although in this range the macroscopic structure of $Ba_{1-x}La_xF_{2+x}$ changes from fluorite to tysonite. This means that the change of the chemical environment of the fluoride ions situated in $Ba_{1-x}La_xF_{2+x}$ crystallizing in the structurally distorted fluorite lattice to the one of the F1 sites in the $Ba_{1-x}La_xF_{2+x}$ crystallizing in the distorted tysonite structure is continuous.

It should be noted that the ^{19}F MAS NMR spectra of annealed samples (18 h at 823 K) of the stable compounds ($x \leq 0.55$), which are not shown here, do not differ in chemical shift or shape when compared with their mechanosynthesized counterparts but show just a slight decrease of the fwhm. Thus, the microstructure of the mechanosynthesized, nanocrystalline $Ba_{1-x}La_xF_{2+x}$ with $x \leq 0.55$ seems to be similar to the one of the microcrystalline $Ba_{1-x}La_xF_{2+x}$.

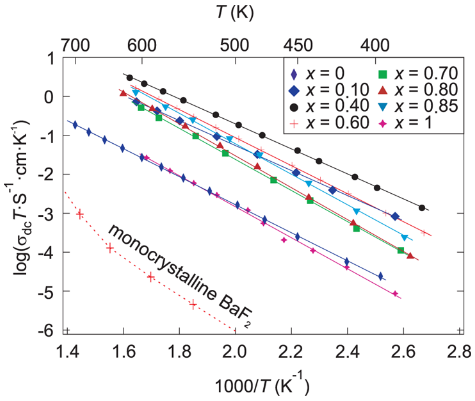

Figure 8. Logarithmic plot of the dc conductivities of some of the mechanosynthesized $Ba_{1-x}La_xF_{2+x}$ samples as a function of inverse temperature fitted by using the Arrhenius eq 2. For comparison also the dc conductivities of a BaF_2 single crystal taken from ref 19 are shown.

C. Ionic Conductivity of the Compounds. In Figure 8 the temperature dependence of the dc conductivity taken from the frequency-independent plateaus of the conductivity spectra (σ as a function of frequency) of a selection of samples is shown in an Arrhenius representation according to

$$\sigma_{dc}T = A_0 e^{-E_a/(k_B T)} \tag{2}$$

with

$$A_0 = \frac{Nq^2 f b^2}{H_r k_B 6\tau_0} \tag{3}$$

$$\tau_0^{-1} = \tau^{-1} e^{E_a/(k_B T)} \tag{4}$$

where E_a denotes the activation energy; N is the particle density of the charge carriers; b is the average jump distance of the mobile ions; q is the electric charge of the mobile ions; $0 \leq f \leq 1$ gives the degree of correlation of the ion jumps (f = 1: uncorrelated jumps); H_r is the Haven ratio; τ^{-1} is the average jump rate of the mobile ion; τ_0 is the pre-exponential factor; and k_B is Boltzmann's constant (see, e.g., ref 54). The milling times are the same as shown in Figure 1.

The ionic conductivities of the $Ba_{1-x}La_xF_{2+x}$ compounds are clearly larger than the ones found for the binary fluorides. Compared to the dc conductivity of monocrystalline BaF_2 reported by Sorokin et al.[19] the dc conductivity of the BaF_2 was also increased by approximately 3 orders of magnitude by high-energy ball milling (see also Figure 9a and refs 3 and 55). Interestingly, in the case of the LaF_3 the mechanical treatment shows no effect on the dc conductivity as can be seen by comparison with the ionic conductivity of a single crystal investigated by Sinitsyn et al.[56]

If the negative imaginary part of the impedance ($-Z''$) is plotted versus its real part (Z'), a single depressed semicircle is observed for all samples investigated in this study (see Figure S3, Supporting Information). Therefore, the conductivity in the grains cannot be distinguished from the one in the grain boundaries which makes an elucidation of the processes leading to the dc conductivities measured difficult.

The dc conductivity of the $Ba_{1-x}La_xF_{2+x}$ compounds varies with x in a range of approximately 0.6 orders of magnitude at a temperature of 588 K as shown in Figure 9a. Starting from pure ball-milled BaF_2 the conductivity increases by about 1 order of magnitude when going to $Ba_{0.90}La_{0.10}F_{2.1}$. A maximum of conductivity is observed for the sample with $x = 0.40$ which is in good agreement with the results of Rongeat et al.[47] for mechanosynthesized $Ba_{1-x}La_xF_{2+x}$ with $x \leq 0.55$. From $x = 0.40$ on, the dc conductivity decreases with increasing x until a minimum of the dc conductivity for the sample with $x = 0.75$ is reached. If x is increased further a second maximum occurs at $x = 0.85$. This behavior can be observed in a range from 350 to 588 K, although the positions of the maxima change from $x = 0.30$ and $x = 0.90$ at 350 K to $x = 0.40$ and $x = 0.85$ at 588 K, respectively (see Figure 9a).

In the range from $x = 0.10$ to $x = 0.40$ the dc conductivities at 588 K of the samples prepared are approximately 0.5 orders of magnitude larger than the ones reported for monocrystalline $Ba_{1-x}La_xF_{2+x}$ by Sorokin et al.[19] In the case of the sample with $x = 0.50$ the conductivities of the mechanosynthesized and the monocrystalline material are very similar (see Figure 9a). Sorokin et al.[19] as well as Wapenaar et al.[18] reported increasing conductivities and decreasing activation energies with increasing LaF_3 content from $x = 0$ to $x = 0.50$. Andersen et al., however, found no decrease of the activation energy going from $x = 0.209$ to $x = 0.492$ but a slight increase from 0.54 to 0.57 eV.[13] In the case of the $Ba_{1-x}La_xF_{2+x}$ samples prepared here the conductivities increase from $x = 0$ to $x = 0.40$, and the activation energies decrease between $x = 0$ and $x = 0.20$. However, it should be noted that the latter vary by only 0.05 eV in the range from $x = 0.10$ to $x = 0.50$ (see Figure 9b).

In Figure 9b also the pre-exponential factors A_0 of the mechanosynthesized samples are shown as a function of x. It can be seen that the pre-exponential factors of the binary fluorides are clearly smaller than the ones found for $Ba_{1-x}La_xF_{2+x}$. Interestingly, A_0 increases almost linearly from $x = 0.10$ to $x = 0.80$ where a maximum of A_0 is reached (see Figure 9b). Since A_0 depends on several parameters (cf. eq 3),

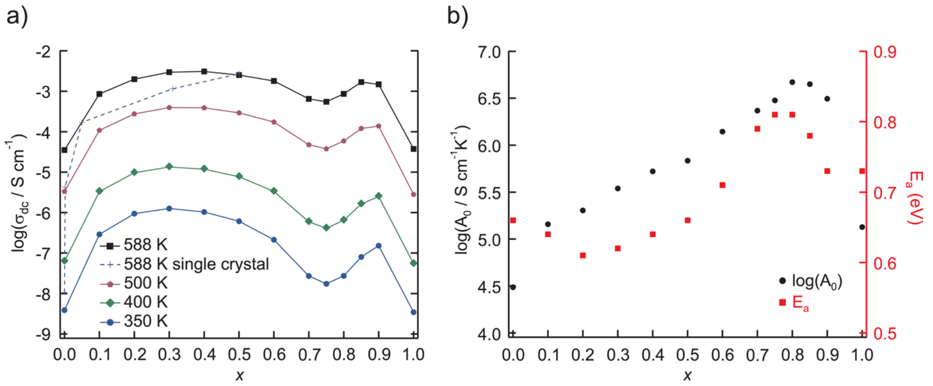

Figure 9. (a) Isothermes of the dc conductivities of mechanosynthesized $Ba_{1-x}La_xF_{2+x}$ as a function of x at the temperatures indicated. The lines are meant to guide the eye. For comparison also the isotherm of the dc conductivity of monocrystalline $Ba_{1-x}La_xF_{2+x}$ at 588 K taken from ref 19 is shown (dotted line). (b) Activation energies E_a and pre-exponential factors A_0 of the samples as a function of x. See text for further explanations.

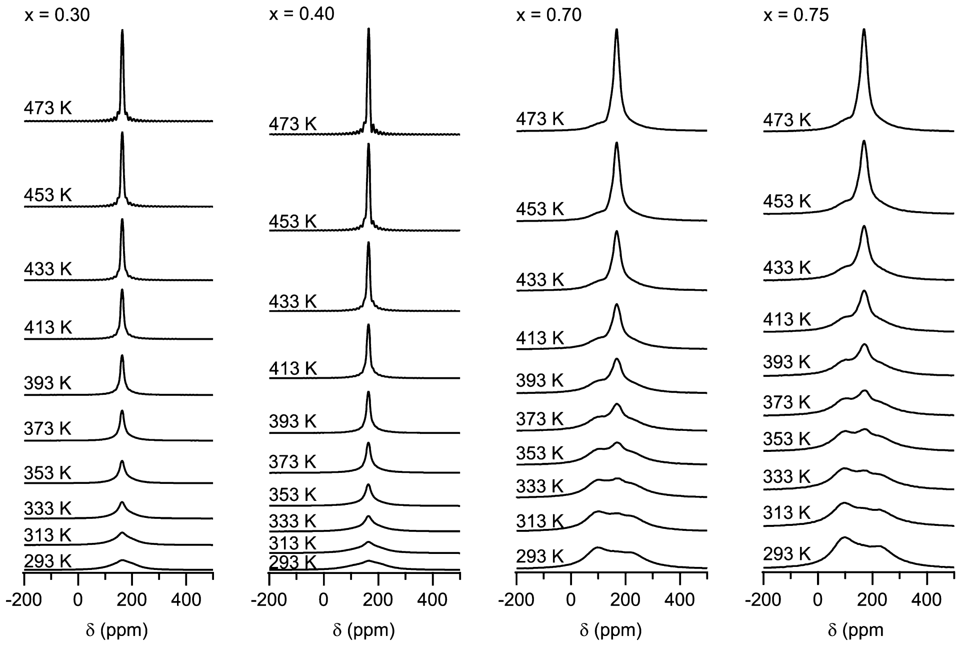

Figure 10. ^{19}F NMR spectra of the $Ba_{1-x}La_xF_{2+x}$ samples with x = 0.30, x = 0.40, x = 0.70, and x = 0.75 recorded at ν_0 = 376 MHz at different temperatures.

it is hard to say which is the origin of this increase. However, due to the linear increase of A_0 it seems plausible to assume an increase of the particle density of mobile fluoride ions N with increasing x. No continuous change of the pre-exponential factor with x was observed for monocrystalline $Ba_{1-x}La_xF_{2+x}$ with $x \leq 0.50$ by Sorokin et al.[19] It should be noted that by keeping the value of the pre-exponential factor fixed to the value found for the sample with x = 0.50 the quality of the fittings of the Arrhenius plots is clearly reduced, and the behavior of the activation energy as a function of x is not changed significantly (not shown). Thus, the different conductivity behavior of the monocrystalline and the mechanosynthesized $Ba_{1-x}La_xF_{2+x}$ seems to be real.

The different conductivity behaviors of the mechanosynthesized $Ba_{1-x}La_xF_{2+x}$ and the monocrystalline material might be due to grain boundary effects as assumed by Rongeat et al.[47] In fact, the positions of the dc conductivity maxima seem to be in quite good agreement with the minima of the average crystallite size shown in Figure 3b. We will come back to this in the next section. To find an alternative explanation, it should be recalled that the PDF of the sample with x = 0.70 lacks a typical distance of the 2:2:2 clusters which, however, was observed in the PDFs of the samples with x = 0.20 and x = 0.50 (see section A). Hence, the decrease of the ionic conductivity between x = 0.40 and x = 0.75 might be due to a change of the microstructure of the grains or grain boundaries with x such that the migration enthalpy or defect formation enthalpy increases. Differing microstructures are often found for mechanically treated or synthesized compounds and their micro- or monocrystalline counterparts.[5] However, if the formation of percolation paths consisting of the distorted fluorite lattice close to the 2:2:2 clusters is assumed, a decrease of the conductivity is expected if the number of the presumed non- or badly conducting 2:2:2 clusters is increased beyond a certain number such that more and more paths are blocked by these clusters. Such behavior was, e.g., found for mixtures of the poor Li ion conductor Li_2O and the insulator B_2O_3.[57] In this context it should be recalled that the ^{19}F MAS NMR spectra showed a coalescence of the NMR line probably representing the fluoride ions in the 2:2:2 clusters for the samples with x >

0.40 (see chapter B). However, a decrease of the ionic conductivity was not observed for monocrystalline $Ba_{1-x}La_xF_{2+x}$ up to $x \approx 0.50$. Kadlec et al.[16] assumed that this behavior may be explained by the assumption that the clusters formed are fragments of the tysonite structured fast fluoride ion conductor LaF_3 (see also ref 15) such that networks of these clusters should also show a good ionic conductivity. As already mentioned, Andersen et al.[13] found evidence that at least some of the fluoride ions in the 2:2:2 clusters are mobile.

Interestingly, the dc conductivity measured for the samples with $x = 0.90$ and $x = 0.85$ is approximately 1 order of magnitude smaller than reported by Reddy et al.[24] They also prepared $Ba_{1-x}La_xF_{2+x}$ with $1 \geq x \geq 0.85$ by high-energy ball milling. However, their compounds were prepared by milling in argon atmosphere and by using silicon nitride as a vial set material. Thus, the atmosphere, the mechanical energy, or the amount or kind of abraded material of the milling vial set introduced into the mixture seems to have an influence on the ion conductivity of tysonite-type $Ba_{1-x}La_xF_{2+x}$. Interestingly, the ionic conductivity of single crystals of $Ba_{1-x}La_xF_{2+x}$ crystallizing in the tysonite structure is even higher than reported by Reddy et al. for their mechanosynthesized samples.[24,58] They assumed that the decrease of the ionic conductivity is due to blocking grain boundaries.[47] In this context it might also be recapitulated that high-energy ball milling of LaF_3 did not increase its ionic conductivity compared to monocrystalline LaF_3. Thus, the introduction of defects or grain boundaries into tysonite structured $Ba_{1-x}La_xF_{2+x}$ due to mechanical stressing seems to impede the fluoride ion conductivity.

D. Static ^{19}F NMR. To gain information on the fluoride ion diffusion in $Ba_{1-x}La_xF_{2+x}$ from a microscopic point of view and to find answers to some of the questions raised by the results of the conductivity measurements, temperature-variable static ^{19}F NMR measurements were performed on all samples. In Figure 10 the ^{19}F NMR spectra of the $Ba_{1-x}La_xF_{2+x}$ samples with the highest ($x = 0.30$ and $x = 0.40$) and lowest ion conductivity ($x = 0.70$ and $x = 0.75$), in a temperature range from 293 to 473 K, are shown. The NMR lines of the samples with $x = 0.30$ and $x = 0.40$ consist of a single Lorentzian-shaped NMR line at 293 K, while the ones of the samples with $x = 0.70$ and $x = 0.75$ seem to be composed of at least two NMR lines. Furthermore, the NMR lines of the latter samples are much broader than those of the samples with $x = 0.30$ and $x = 0.40$. It should be mentioned that, expectedly, all the NMR lines are much broader than the NMR lines recorded under MAS conditions due to dipolar interactions of the fluoride ions. Moreover, it should be noted that the spectra of the samples investigated in a compositional range of $0.10 \leq x \leq 0.50$ are very similar to each other as well as the spectra of the samples with $0.60 \leq x \leq 0.80$ (see Figure S1, Supporting Information). The latter ones, however, show an increase of the line width with increasing x.

At a temperature of 313 K the spectra of the four samples shown in Figure 10 exhibit the emergence of a narrow NMR line atop the broad NMR line. This phenomenon is called motional narrowing in the case of the narrowing of a single NMR line and coalescence if two or more separated NMR lines fuse to a single, narrow NMR line. The origin of this effect is in both cases the same: the ions change their positions in the structure so fast that they lose their identity regarding their magnetic environment. Therefore, these ions experience an averaged magnetic environment and, thus, are represented by a single, narrow NMR line.[59] Motional narrowing can be observed if the jump frequency of the ion species investigated, or of the ions surrounding that species, becomes larger than the fwhm of the non-narrowed NMR line (Δ_{RL}). In the case of coalescence the jump rate has to be larger than the distance between the NMR lines which fuse to a single NMR line due to the exchange of fluoride ions between the sites represented by the initially separated NMR lines.[59] Thus, for the samples with $x = 0.30$ and $x = 0.40$ a jump rate of some of the fluoride ions exceeding $\Delta_{RL} = 46$ kHz at 313 K can be deduced from the spectra. For the narrow NMR line visible at $T \geq 313$ K in the spectra of the samples with $x = 0.70$ and $x = 0.75$ the calculation cannot be done since it is not clear which and how many NMR lines coalesce. The larger width of the narrow NMR line in the case of the samples with $0.60 \leq x \leq 0.80$ (fwhm ≈ 30 ppm at 473 K) compared to the ones of the samples with $x < 0.60$ (fwhm ≈ 10 ppm at 473 K) is probably due to a superposition of several narrow NMR lines with slightly different chemical shifts, thus originating from different NMR lines coalescing. This would mean that there is fast exchange of fluoride ions between more than one pair of chemically different fluoride ion sites. For comparison and completeness it should be noted that the NMR spectrum of BaF_2 consists of a single broad NMR line, and no change of the spectra with temperature up to 473 K was observed (not shown). The spectrum of LaF_3 (not shown) consists of two NMR lines at ambient temperature, exhibiting a narrow NMR line at temperatures larger than 333 K which is clearly narrower than the ones observed for the samples with $0.60 \leq x \leq 0.80$.

While for the samples with $x = 0.30$ and $x = 0.40$ a narrowing of the entire NMR line with increasing temperature can be observed until at a temperature of about 453 K only the narrow NMR line is left, in the case of the spectra of the other two samples shown in Figure 10, a broad NMR line is still visible beneath the narrow NMR line even at 473 K. Thus, the ratio of mobile fluoride ions to nonmobile or slow fluoride ions is clearly larger in the case of the samples with $x = 0.30$ and $x = 0.40$ than for the samples with $x = 0.70$ and $x = 0.75$ which may explain the decreased conductivity of the latter samples. Furthermore, there seem to be no nonmobile or even slow fluoride ions in the samples with $0.10 \leq x \leq 0.50$ at temperatures larger 453 K, although the fluoride ions in the 2:2:2 clusters, which seem to be present also in the mechanosynthesized $Ba_{1-x}La_xF_{2+x}$ (see sections A and B), were expected to be nonmobile at these temperatures.[18,21] In the case of percolation pathways between the fluorite-type structured material and the 2:2:2 clusters not all fluoride ions should be highly mobile but only the fluoride ions in the regions close to the 2:2:2 clusters. In that case a narrow line atop a broad NMR line would be observed even at 473 K (see, e.g., ref 60). However, also for the sample with $x = 0.10$ in which only a part of the material should be affected by the clusters a single narrow NMR line is obtained at 473 K (see Figure S4, Supporting Information). Thus, the percolation model outlined above seems inappropriate to describe the fluoride ion conductivity of the mechanosynthesized $Ba_{1-x}La_xF_{2+x}$ since the whole material seems to be highly conductive for the samples investigated with $x \leq 0.50$. Moreover, fluoride ions in the bulk and fluoride ions in the grain boundaries cannot be separated by their diffusivity for the samples with $x \leq 0.50$. If the increased ionic conductivity was caused by highly conducting grain boundaries, a narrow NMR line atop a broad NMR line representing the less good conducting bulk material should be observed. For the samples with $0.60 \leq x \leq 0.80$, however, the broad part of the NMR line might be associated with slow fluoride ions in the bulk and the narrow NMR line with fast fluoride ions in the grain boundaries. However, since the crystallite sizes for all $Ba_{1-x}La_xF_{2+x}$ samples investigated are quite similar it seems more likely that a change of the microstructure is responsible for the emergence of a broad NMR line beneath the narrow NMR line for the samples with $0.60 \leq x \leq 0.80$. This is also in accordance with the broadening of the narrow NMR line (vide supra) and the results discussed in section A. Wang et al.[50] reported that the mobility of the fluoride ions in the F1 sublattice of LaF_3 starts at lower temperatures and has a lower activation energy than the ones in the F2 and F3 sublattices. Therefore, the steady change of the character of the fluoride ion environments from the one at the fluorite and F1 sites toward the one of the F2/3 sites with increasing x might explain the decrease of the fluoride ion mobility.

In Figure 11 the chemical shifts of the maxima of the narrow NMR lines as a function of x are shown. The chemical shift increases with x in an approximately linear fashion from x = 0.10 to x = 0.75. In the case of the tysonite structured $Ba_{1-x}La_xF_{2+x}$ the chemical shift values of the narrow NMR lines are very similar to the chemical shift value of the narrow NMR line in LaF_3, indicating similar transport mechanisms in these samples. Interestingly, the values of the chemical shifts of the narrow NMR lines of the samples with x = 0.75, x = 0.775, and x = 0.80 lie in-between the values of the chemical shifts of the narrow NMR lines of the samples with x = 0.70 (167 ppm) and x = 0.85 (177 ppm) (see Figure 11). Thus, there seems to be a smooth transition regarding the dynamic behavior of the fluoride ions when going from the fluorite to the tysonite structured $Ba_{1-x}La_xF_{2+x}$ reflecting the assumed continuous change from the fluorite to the tysonite structure.

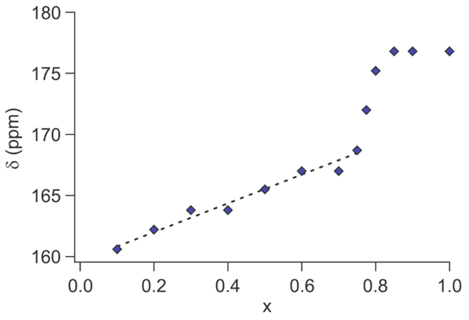

Figure 11. Change of the ^{19}F NMR istropic chemical shift of the narrow NMR line of the $Ba_{1-x}La_xF_{2+x}$ samples at 473 K, recorded at ν_0 = 376 MHz.

IV. CONCLUSIONS

$Ba_{1-x}La_xF_{2+x}$ crystallizing in the cubic fluorite structure in the large range of $0 \leq x \leq 0.775$ was prepared by high-energy ball milling. A linear change of the lattice parameter a is observed for the samples in a range of $0 \leq x \leq 0.80$. $Ba_{1-x}La_xF_{2+x}$ with $0.55 < x < 0.80$ turned out to be metastable at ambient conditions and is, as already reported in different studies, most probably not accessible by conventional solid state synthesis.

By employing ^{19}F NMR, TEM, and X-ray total scattering, several indications for a continuous change from the fluorite to the tysonite structure by passing a structurally distorted crystalline phase were obtained. This transitional phase, found within a range from $x \approx 0.70$ to $x \approx 0.85$, combines structural aspects of both crystal structures.

The mechanosynthesized fluorite-type $Ba_{1-x}La_xF_{2+x}$ compounds show slightly higher dc conductivities for $x \leq 0.40$ than observed for the monocrystalline $Ba_{1-x}La_xF_{2+x}$ reported in the literature. In the case of the tysonite-type $Ba_{1-x}La_xF_{2+x}$ a pronounced decrease of the ionic conductivity with respect to the monocrystalline material was observed. A conductivity maximum for the fluorite-type material was found for $x \approx 0.40$. For compositions with $x > 0.40$ the ionic conductivity decreases until a conductivity minimum is reached for the sample with x = 0.75. The decrease of the ionic conductivity is accompanied by a change of the microstructure and diffusion behavior of the fluoride ions as well as a decrease of the ratio of highly mobile fluoride ions to nonmobile or slow moving fluoride ions.

For the samples with $0.10 \leq x \leq 0.50$ a high mobility of all fluoride ions at temperatures beyond 453 K in the $Ba_{1-x}La_xF_{2+x}$ was observed which means that (i) also the fluoride ions in the 2:2:2 clusters which seem to be present in the mechanosynthesized $Ba_{1-x}La_xF_{2+x}$ are highly mobile and (ii) the fluoride ion diffusivities in the bulk and the grain boundaries do not differ in a pronounced way. Thus, the enhanced ionic conductivity of the mechanosynthesized fluorite-type $Ba_{1-x}La_xF_{2+x}$ seems to be caused by the distorted fluorite lattice decreasing the migration or defect formation enthalpies for the fluoride ions in the whole material.

■ ASSOCIATED CONTENT

Supporting Information

Additional XRPD patterns, the PDFs plotted up to large r-values, Cole−Cole plots, and static ^{19}F NMR spectra of some of the samples. This material is available free of charge via the Internet at http://pubs.acs.org.

■ AUTHOR INFORMATION

Corresponding Authors

*Tel.: +49 511 7623187. E-mail: heitjans@pci.uni-hannover.de (P.H.).
*Tel: +49 511 7623273. E-mail: duevel@pci.uni-hannover.de (A.D.).

Notes

The authors declare no competing financial interest.

■ ACKNOWLEDGMENTS

We thank A. Feldhoff for the TEM measurements and E. Merzlyakova, W.-Y. Tsang, and A.-T. Duong for their support in sample preparation. We thank J. Caro for access to the Bruker Advance D8 diffractometer. We would like to thank I. Hanzu and M. Wilkening for valuable discussions and general help. Financial support by the Deutsche Forschungsgemeinschaft (DFG) within the frame of the Priority Program SPP 1415 is highly appreciated.

■ REFERENCES

(1) Heitjans, P.; Indris, S. Fast Diffusion in Nanocrystalline Ceramics Prepared by Ball Milling. *J. Mater. Sci.* **2004**, *39*, 5091−5096.

(2) Wilkening, M.; Epp, V.; Feldhoff, A.; Heitjans, P. Tuning the Li Diffusivity of Poor Ionic Conductors by Mechanical Treatment: High Li Conductivity of Strongly Defective $LiTaO_3$ Nanoparticles. *J. Phys. Chem. C* **2008**, *112*, 9291−9300.

(3) Ruprecht, B.; Wilkening, M.; Feldhoff, A.; Steuernagel, S.; Heitjans, P. High Anion Conductivity in a Ternary Non-Equilibrium Phase of BaF_2 and CaF_2 with Mixed Cations. *Phys. Chem. Chem. Phys.* **2009**, *11*, 3071−3081.

(4) Düvel, A.; Wilkening, M.; Uecker, R.; Wegner, S.; Šepelák, V.; Heitjans, P. Mechanosynthesized Nanocrystalline $BaLiF_3$: The Impact of Grain Boundaries and Structural Disorder on Ionic Transport. *Phys. Chem. Chem. Phys.* **2010**, *12*, 11251−11262.

(5) Šepelák, V.; Düvel, A.; Wilkening, M.; Becker, K.-D.; Heitjans, P. Mechanochemical Reactions and Syntheses of Oxides. *Chem. Soc. Rev.* **2013**, *42*, 7507−7520.

(6) Düvel, A.; Ruprecht, B.; Heitjans, P.; Wilkening, M. Mixed Alkaline-Earth Effect in the Metastable Anion Conductor $Ba_{1-x}Ca_xF_2$ ($0 \leq x \leq 1$): Correlating Long-Range Ion Transport with Local Structures Revealed by Ultrafast ^{19}F MAS NMR. *J. Phys. Chem. C* **2011**, *115*, 23784−23789.

(7) Düvel, A.; Wegner, S.; Efimov, K.; Feldhoff, A.; Heitjans, P.; Wilkening, M. Access to Metastable Complex Ion Conductors via Mechanosynthesis: Preparation, Microstructure and Conductivity of $(Ba,Sr)LiF_3$ with Inverse Perovskite Structure. *J. Mater. Chem.* **2011**, *21*, 6238−6250.

(8) Lyakhov, N.; Grigorieva, T.; Barinova, A.; Lomayeva, S.; Yelsukov, E.; Ulyanov, A. Nanosized Mechanocomposites and Solid Solution in Immiscible Metal Systems. *J. Mater. Sci.* **2004**, *39*, 5421−5423.

(9) Šepelák, V.; Becker, K.-D. Mechanochemistry: From Mechanical Degradation to Novel Materials Properties. *J. Korean Ceram. Soc.* **2012**, *49*, 19−28.

(10) Kuznetsov, S. V.; Fedorov, P. P. Morphological Stability of Solid-Liquid Interface During Melt Crystallization of $M_{1-x}R_xF_{2+x}$ Solid Solutions. *Inorg. Mater.* **2008**, *44*, 1434−1458.

(11) Sobolev, B. P.; Tkachenko, N. L. Phase Diagrams of BaF_2-(Y, Ln)F_3 Systems. *J. Less Common Met.* **1982**, *85*, 155−170.

(12) Kjems, J. K.; Andersen, N. H.; Schoonman, J.; Clausen, K. Structure and Dynamics of Disordered Solids - a Neutron-Scattering Study of $Ba_{1-x}La_xF_{2+x}$. *Phys. B&C* **1983**, *120*, 357−361.

(13) Andersen, N. H.; Clausen, K. N.; Kjems, J. K.; Schoonman, J. A Study of the Disorder in Heavily Doped $Ba_{1-x}La_xF_{2+x}$ by Neutron-Scattering, Ionic Conductivity and Specific-Heat Measurements. *J. Phys. C: Solid State Phys.* **1986**, *19*, 2377−2389.

(14) Cheetham, A. K.; Fender, B. E. F.; Steele, D.; Taylor, R. I.; Willis, B. T. M. Defect Structure of Fluorite Compounds Containing Excess Anions. *Solid State Commun.* **1970**, *8*, 171−173.

(15) Chernov, S. V.; Gunßer, W.; Murin, I. V. On Rare-Earth Clustering in Fluorite Type Solid Solutions MF_2-REF_3. *Solid State Ionics* **1991**, *47*, 67−70.

(16) Kadlec, F.; Simon, P.; Raimboux, N. J. Vibrational Spectra of Superionic Crystals $(BaF_2)_{1-x}(LaF_3)_x$. *Phys. Chem. Solids* **1999**, *60*, 861−866.

(17) Ivanov-Shits, A. K.; Sorokin, N. I.; Fedorov, P. P.; Sobolev, B. P. Specific Features of Ion Transport in Nonstoichiometric Fluorite-Type $Ba_{1-x}R_xF_{2+x}$ (R=La-Lu) Phases. *Solid State Ionics* **1989**, *31*, 269−280.

(18) Wapenaar, K. E. D.; van Koesveld, J. L.; Schoonman, J. Conductivity Enhancement in Fluorite-Structured $Ba_{1-x}La_xF_{2+x}$ Solid Solutions. *Solid State Ionics* **1981**, *2*, 145−154.

(19) Sorokin, N. I.; Breiter, M. W. Anionic Conductivity and Thermal Stability of Single Crystals of Solid Solutions Based on Barium Fluoride. *Solid State Ionics* **1997**, *99*, 241−250.

(20) Sorokin, N. I.; Sobolev, B. P. Nonstoichiometric Fluorides - Solid Electrolytes for Electrochemical Devices: A Review. *Crystallogr. Rep.* **2007**, *52*, 842−863.

(21) Wapenaar, K. E. D.; Schoonman, J. The Ionic Conductivity of Fluorite-Structured Solid Solutions of Composition: MF_2: UF_4: CeF_3 (M = Ca, Sr, Ba). *J. Electrochem. Soc.* **1979**, *126*, 667−672.

(22) Catlow, C. R. A. The Defect Properties of Anion-Excess Alkaline-Earth Fluorides. II. Intermediate and High Dopant Concentrations. *J. Phys. C* **1976**, *9*, 1859.

(23) Sorokin, N. I. Superionic Transport in Solid Fluoride Solutions with a Fluorite Structure. *Russ. J. Electrochem.* **2006**, *42*, 744−759.

(24) Anji Reddy, M.; Fichtner, M. Batteries Based on Fluoride Shuttle. *J. Mater. Chem.* **2011**, *21*, 17059−17062.

(25) Kennedy, J. H.; Hunter, J. C. Thin-Film Galvanic Cell $Pb/PbF_2/PbF_2$, CuF_2/Cu. *J. Electrochem. Soc.* **1976**, *123*, 10−14.

(26) Schoonman, J. A Solid-State Galvanic Cell with Fluoride-Conducting Electrolytes. *J. Electrochem. Soc.* **1976**, *123*, 1772−1775.

(27) Danto, Y.; Punjade, G.; Pistré, J. D.; Lucat, C.; Salardenne, J. A $Pb/PbF_2/BiF_3/Bi$ Thin Solid Film Reversible Galvanic Cell. *Thin Solid Films* **1978**, *55*, 347−354.

(28) Schoonman, J.; Wapenaar, K. E. D.; Oversluizen, G.; Dirksen, G. J. Fluoride-Conducting Solid Electrolytes in Galvanic Cells. *J. Electrochem. Soc.* **1979**, *126*, 709−713.

(29) Hagenmuller, P.; Réau, J.-M.; Lucat, C.; Matar, S.; Villeneuve, G. Ionic Conductivity of Fluorite-Type Fluorides. *Solid State Ionics* **1981**, *3/4*, 341−345.

(30) Schoonman, J.; Wolfert, A. Solid-State Galvanic Cells with Fast Fluoride Conducting Electrolytes. *Solid State Ionics* **1981**, *3/4*, 373−379.

(31) Kosacki, I. Physical Properties and Applications of $Cd_{1-x}Pb_xF_2$ Superionic Crystals. *Appl. Phys. A: Mater. Sci. Process.* **1989**, *49*, 413−424.

(32) Shareefuddin, M.; Jamal, M.; Narashima Chary, M. Solid State Battery with Pure and Doped Sodium Yttrium Fluoride as the Solid Electrolyte. *J. Phys. D: Appl. Phys.* **1995**, *28*, 440−442.

(33) Amatucci, G. G.; Prereira, N. Fluoride Based Electrode Materials for Advanced Energy Storage Devices. *J. Fluorine Chem.* **2006**, *128*, 243−262.

(34) West, W.; Whitacre, J.; Del Castillo, L. Solid State Fluoride Battery for High Temperature Applications. *Electrochemical Society Meeting*, May 2007, Chicago, IL.

(35) Bouazza, S.; Saberi, A.; Willert-Porada, M. Preparation and Electrochemical Properties of Nano-Sized SnF_2 as Negative Electrode for Lithium-Ion Batteries. *Mater. Lett.* **2011**, *65*, 1334−1336.

(36) Bonne, R. W.; Schoonman, J. Electrode Processes of Lead Halides: Part 2: β-PbF_2. *J. Electrochem. Soc.* **1978**, *125*, 1628−1632.

(37) Stefan, I. C.; Jacobson, C. P.; Visco, S. J.; De Jonghe, L. C. Solid-State Electrochemistry of Fluoride Ionic Conductive Materials. *Electrochemical Society Meeting*, October 2004, Honolulu, HI.

(38) Hanzu, I.; Düvel, A.; Preishuber-Pflügel, F.; Heitjans, P.; Wilkening, M. unpublished results.

(39) Hammersley, A. P.; Svensson, S. O.; Hanfland, M.; Fitch, A. N.; Häusermann, D. Two-Dimensional Detector Software: From Real Detector to Idealised Image or Two Theta Scan. *High Press. Res.* **1996**, *14*, 235.

(40) Qiu, X.; Thompson, J. W.; Billinge, S. J. L. PDFgetX2: A GUI-Driven Program to Obtain the Pair Distribution Function from X-Ray Powder Diffraction Data. *J. Appl. Crystallogr.* **2004**, *37*, 678−678.

(41) *Diffusion in Condensed Matter - Methods, Materials, Models*; Heitjans, P., Kärger, J., Eds.; Springer: Berlin, 2005.

(42) Fukushima, E.; Roeder, S. B. W. *Experimental Pulse NMR*; Addison-Wesley: Reading, MA, 1981.

(43) Stanley, P. D. *Organofluorines*; Neilson, A. H., Ed.; Springer-Verlag: Berlin Heidelberg, 2002; p 12.

(44) Bednarcik, J.; Michalik, S.; Kolesar, V.; Rütt, U.; Franz, H. In Situ XRD Studies of Nanocrystallization of Fe-Based Metallic Glass: A Comparative Study by Reciprocal and Direct Space Methods. *Phys. Chem. Chem. Phys.* **2013**, *15*, 8470−8479.

(45) Williamson, G. K.; Hall, W. H. X-Ray Line Broadening from Filed Aluminium and Wolfram. *Acta Metall.* **1953**, *1*, 22−31.

(46) Youngman, R. E.; Smith, C. M. Multinuclear NMR Studies of Mixed $Ca_{1-x}Sr_xF_2$ Crystals. *Phys. Rev. B* **2008**, *78*, 014112−1−014112−6.

(47) Rongeat, C.; Anji Reddy, M.; Witter, R.; Fichtner, M. Nanostructured Fluorite-Type Fluorides as Electrolytes for Fluoride Ion Batteries. *J. Phys. Chem. C* **2013**, *117*, 4943−4950.

(48) Seifert, K.-F. Untersuchungen zur Druck-Kristallchemie der AX_2-Verbindungen. *Fortschr. Miner.* **1968**, *45*, 214−280.

(49) Leger, J. M.; Haines, J.; Atouf, A.; Schulte, O. High-Pressure X-Ray and Neutron-Diffraction Studies of BaF_2: An Example of a Coordination Number of 11 in AX_2 Compounds. *Phys. Rev. B* **1995**, *52*, 13247−13256.

(50) Wang, F.; Grey, C. P. Probing the Mechanism of Fluoride-Ion Conduction in LaF_3 and Strontium-Doped LaF_3 with High-Resolution ^{19}F MAS NMR. *Chem. Mater.* **1997**, *9*, 1068−1070.

(51) Maximov, B.; Schulz, H. Space Group, Crystal Structure and Twinning of Lanthanum Trifluoride. *Acta Crystallogr.* **1985**, *B41*, 88−91.

(52) Bureau, B.; Silly, G.; Buzaré, J. Y.; Emery, J. Superposition Model for ^{19}F Isotropic Chemical Shift in Ionic Fluorides: From Basic Metal Fluorides to Transition Metal Fluoride Glasses. *Chem. Phys.* **1999**, *249*, 89−104.

(53) Duer, M. J. *Introduction to Solid-State NMR Spectroscopy*; Blackwell Publishing Ltd.: U.K., 2004; p 116ff.

(54) Heitjans, P.; Indris, S. Diffusion and Ionic Conduction in Nanocrystalline Ceramics. *J. Phys.: Condens. Matter* **2003**, *15*, R1257−R1289.

(55) Puin, W.; Rodewald, S.; Ramlau, R.; Heitjans, P.; Maier, J. Local and Overall Ionic Conductivity in Nanocrystalline CaF_2. *Solid State Ionics* **2000**, *131*, 159−164.

(56) Sinitsyn, V. V.; Lips, O.; Privalov, A. F.; Fujara, F.; Murin, I. V. Transport Properties of LaF_3 Fast Ionic Conductor Studied by Field Gradient NMR and Impedance Spectroscopy. *J. Phys. Chem. Solids* **2003**, *64*, 1201−1205.

(57) Indris, S.; Heitjans, P.; Roman, H. E.; Bunde, A. Nanocrystalline versus Microcrystalline $Li_2O:B_2O_3$ Composites: Anomalous Ionic Conductivities and Percolation Theory. *Phys. Rev. Lett.* **2000**, *84*, 2889−2892.

(58) Roos, A.; Schoonman, J. Electronic Conductivity in $La_{1-x}Ba_xF_{3-x}$ Crystals. *Solid State Ionics* **1984**, *13*, 205−211.

(59) Duer, M. J. *Introduction to Solid-State NMR Spectroscopy*; Blackwell Publishing Ltd.: U.K., 2004; p 295ff.

(60) Heitjans, P.; Indris, S.; Wilkening, M. In *Nanocomposites: Ionic Conducting Materials and Structural Spectroscopies*; Knauth, P., Schoonman, J., Eds.; Springer: Berlin, 2008, pp 227−246.

11 Mechanosynthesis and characterization of $BaLiF_3$ and $Ba_{1-x}Sr_xLiF_3$

$BaLiF_3$ (or $LiBaF_3$) is one of the rare compounds crystallizing in the inverse perovskite structure. The typical formula for the perovskite is ABX_3 where A has a lower valence than B.[1] In the cubic perovskite A forms the edges of a cube, B is in the center of this cube and X can be found at the face centers. Thus, in the cubic perovskite, Li should be located at the A-position, Ba at the B-position and F at the X-position. Whether a compound crystallizes in the cubic perovskite structure can be calculated by employing the formula introduced by Goldschmidt:

$$t = \frac{r_A + r_X}{\sqrt{2}(r_B + r_X)} \tag{96}$$

Thereby r_A, r_B and r_X are the ionic radii of the ions. Thus, t is the ratio of the diagonal of a site $(2(r_A + r_X)$ of the cube and the lattice parameter multiplied by $\sqrt{2}$ (from the Pythagorean theorem: $c^2 = a^2 + a^2 = 2a^2$ leading to $c = \sqrt{2}a)$, i. e. $2\sqrt{2}(r_B + r_X)$. If both values are equal, thus t = 1, the conditions for a cube are satisfied. However, even in case of a small deviation the cubic perovskite structure is obtained. The limits are about $0.89 \leq t \leq 1$ according to ref. 2. The A site is coordinated by 12 anions, the B-site by 6 anions and the anions by 2+4 cations. In order to calculate which cation will occupy which site in the perovskite structure, the ionic radii are needed. The ionic radius is a concept treating ions as hard spheres, which they are not. However, for the calculations this concept is used by employing the ionic radii calculated by Shannon and Prewitt[3] being the commonly accepted values regarding ionic radii at the moment. The ionic radii change with coordination number. Expectedly, for the small Li ion a coordination number of 12 is not known. Thus, for the calculations the ionic radii of the sixfold coordinated Li is used. Therefore, these calculations can only give a rough trend. The following values are obtained: $t(LiBaF_3) = 0.54$ and $t(BaLiF_3) = 1.00$ (= perfect cube). Thus, this compound crystallizes in the inverse perovskite structure and is written as $BaLiF_3$.[4,5] See Fig. 47 for a sketch of the structure of $BaLiF_3$.

However, there seems to be some confusion in the literature about the terminology. Ludekens and Welch named the perovskite in which the A and B positions are exchanged an "inverted" perovskite. This term is also used by Boumriche et al.[1]. In crystallography the term inverted means the structure after the symmetry operation "inversion". Since the cubic perovskite structure is centrosymmetric the inversion would lead to the very same structure. This might be the reason why Luaña et al.[6] used the terms inverse perovskite and anti-perovskite. However, these denominations are commonly used for perovskite-type structures in which cations and anions have exchanged their positions, see e. g. ref. 7. Furthermore, if the chemical formula is written as $BaLiF_3$ and then named inverse perovskite, this would suggest that Ba is the ion at the B site and Li the ion at the A site. Thus an appropriate name needs to be found for these compounds. Maybe "cation-inverse perovskite" (here: cation-inverse perovskite $LiBaF_3$) and "anion-cation inverse perovskite" could be a solution. However, in accordance with the three papers attached to this introduction the compound will be named $BaLiF_3$ in the following.

The first paper published in Phys. Chem. Chem. Phys., mainly written by Prof. M. Wilkening, deals with the mechanosynthesis of $BaLiF_3$ and its characterization by XRPD and impedance measurements. It was found that $BaLiF_3$ can be prepared by high-energy ball milling of an equimolar mixture of LiF and BaF_3. The mechanosynthesized $BaLiF_3$ showed an ionic conductivity three orders of magnitude higher than $BaLiF_3$ prepared by a conventional solid state synthesis. After heat treatment of the mechanosynthesized $BaLiF_3$ its conductivity decreased by about two orders of magnitude being very similar to the intrinsic conductivity of a $BaLiF_3$ single crystal which was delivered by Dr. Reinhard Uecker from the Leibniz Institut für Kristallzüchtung in Berlin. It should be noted that for the intrinsic conductivity of the single crystalline $BaLiF_3$ an activation energy of about 1

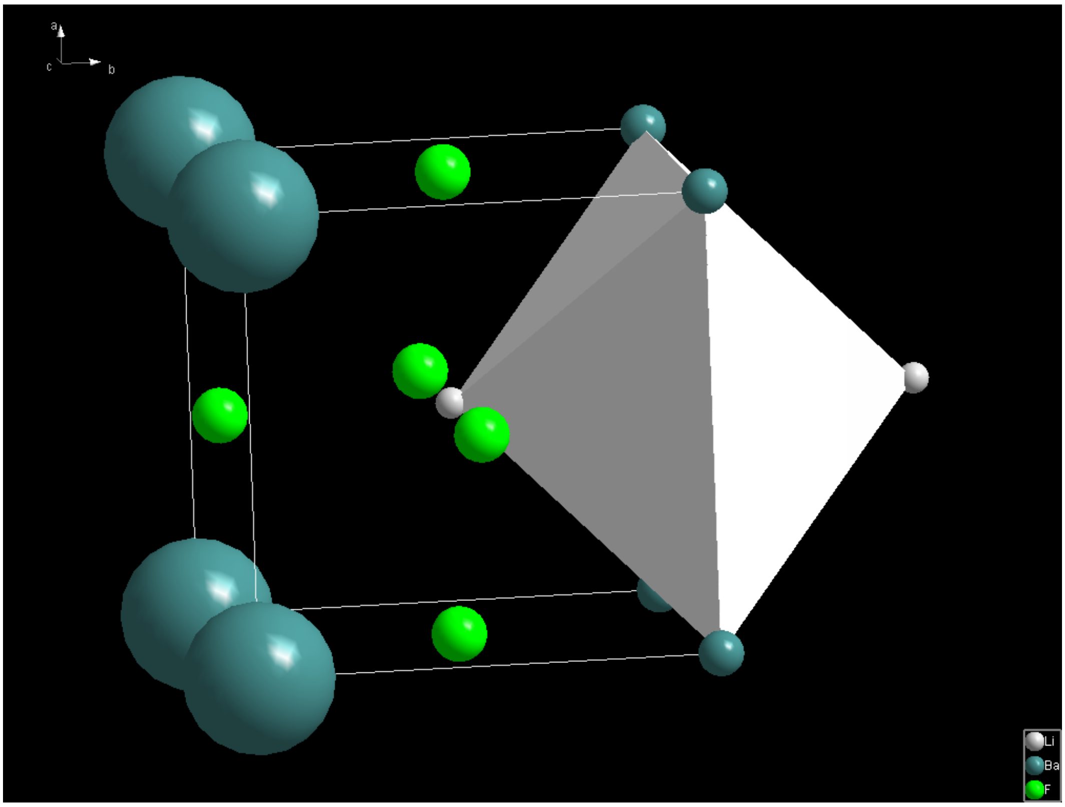

Figure 47: Structure of $BaLiF_3$.

eV was found while its extrinsic conductivity was characterized by half that activation energy, thus 0.5 eV, which is a common ratio observed for ion conductors.[8] Furthermore it was shown that the conductivity of the single crystal can be largely decreased by grinding and pressing a new pellet from the obtained powder. Thus, the grain boundaries of the micro-crystalline material block the ion transport while in case of the nano-crystalline $BaLiF_3$ the ion transport seems to be facilitated. Therefore, the structure of the grain boundaries in the nano-crystalline $BaLiF_3$ is probably different from that in the micro-crystalline samples.

In the second paper, written by Prof. M. Wilkening and the author, temperature dependent ^7Li NMR measurements were shown. The ^7Li NMR spectra of the mechanosynthesized, the annealed and the conventionally synthesized $BaLiF_3$ differ at elevated temperatures as shown in the paper. The $BaLiF_3$ prepared by solid state synthesis and in a more pronounced way also the annealed mechanosynthesized $BaLiF_3$ showed a motional narrowing of the NMR line. The narrowing is due to a fast change of the chemical environment of the Li ions averaging the dipolar interactions of the Li ions with the other ions. The dipolar interactions scale with the gyromagnetic ratio of the ions interacting.[9] Since the gyromagnetic ratio of Ba is much smaller than the one of fluorine and lithium the Li-Ba interaction leads to the smallest line broadening. Thus, the Li-Li as well as the Li-F interactions are the main sources for line broadening. Therefore, by this means it cannot be determined which of these ion species is moving since in both cases a line narrowing is expected.

Interestingly, the mechanosynthesized sample showed only a small amount of highly mobile ions although exhibiting a much higher ionic conductivity than the heat-treated samples. Thus, it seems reasonable that in case of the mechanosynthesized sample more ions are mobile than in case of the heat-treated $BaLiF_3$ but that they move slower. This might be explained by the assumption that in the mechanosynthesized $BaLiF_3$ fluoride ions as well as Li ions are mobile while in the polycrystalline $BaLiF_3$ only the fluoride ions are mobile. It should be mentioned that a molecular dynamics study of

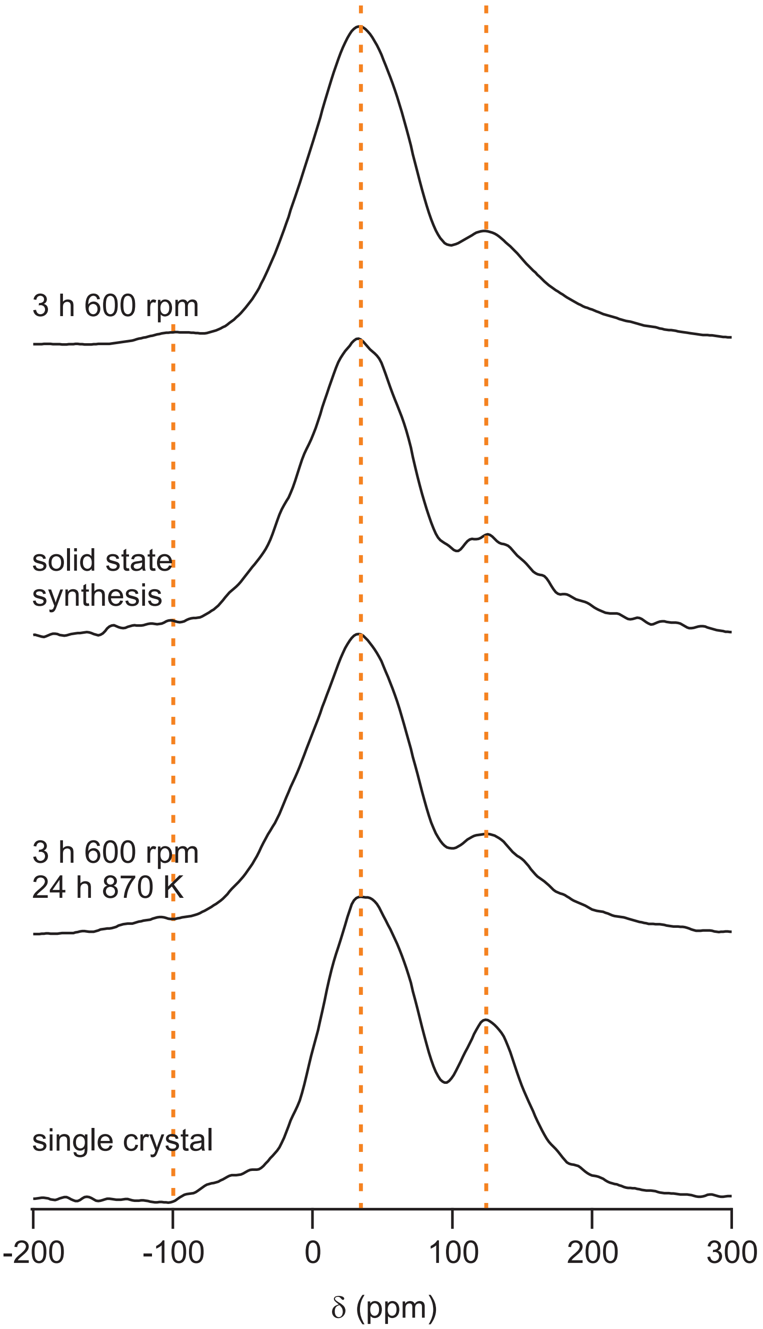

Figure 48: Static ^{19} NMR spectra of different samples of BaLiF$_3$. The measurements were done with a Larmor-frequency of 376 MHz. All samples exhibit a very similar spectrum.

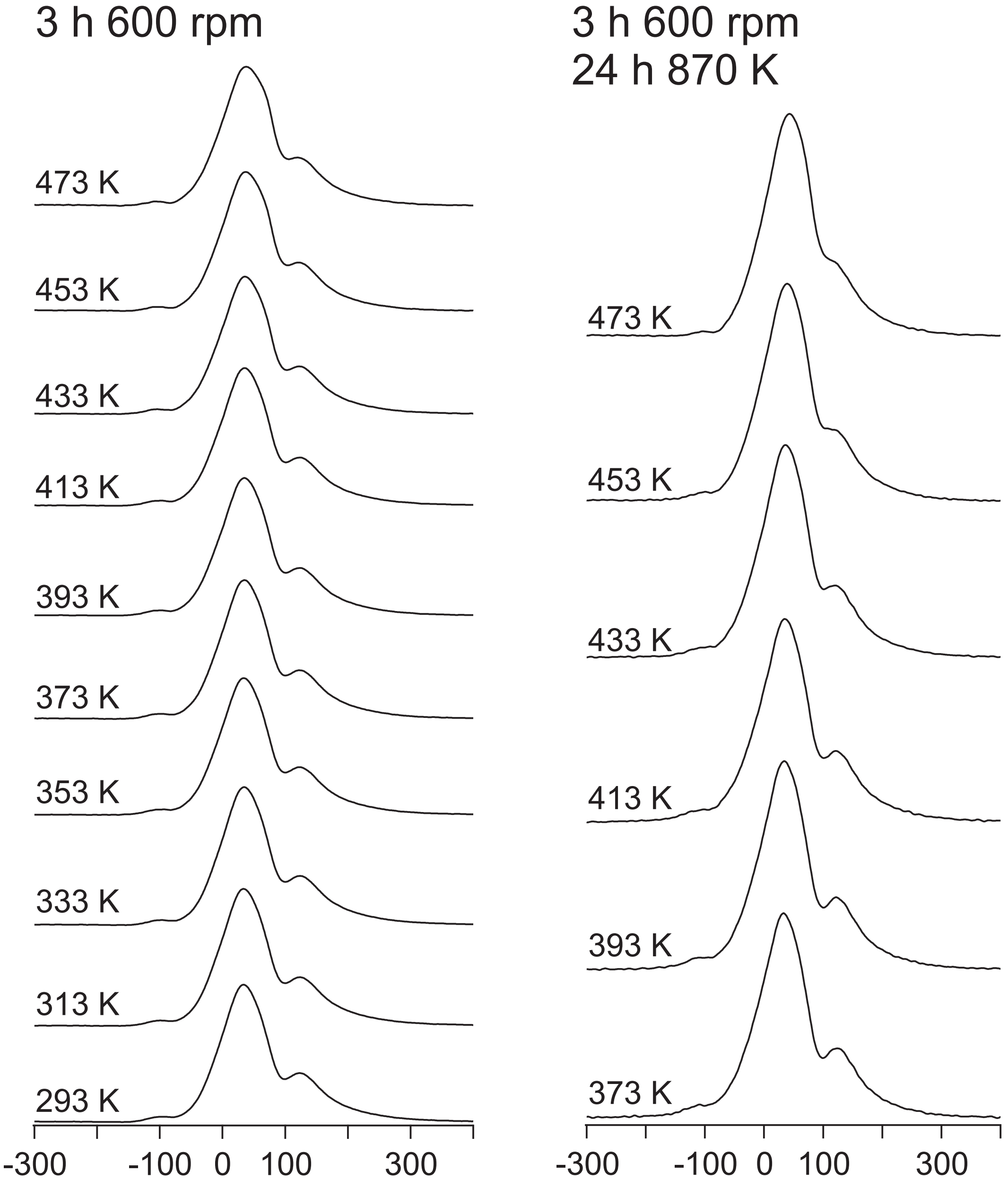

Figure 49: Static ^{19} NMR spectra of mechanosynthesized $BaLiF_3$ (left) and of the same material after annealing at 870 K for 24 h. The measurements were done with a Larmor-frequency of 376 MHz.

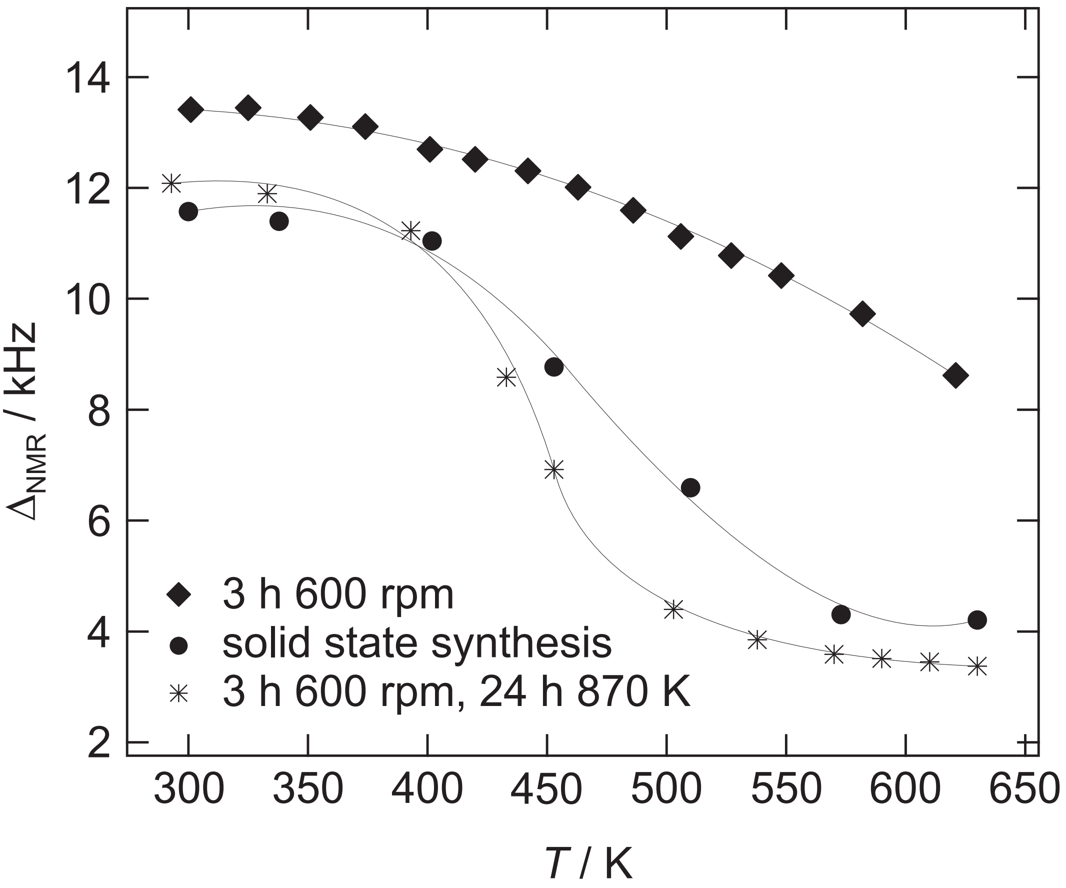

Figure 50: Change of the fwhm of the ^{7}Li NMR lines of the $BaLiF_3$ samples denoted.

Zahn et al.[10] showed that both ion species are mobile in case of amorphous $BaLiF_3$. Amorphous, or at least highly distorted $BaLiF_3$ can be assumed to be present in the grain boundary-regions of the mechanosynthesized $BaLiF_3$. However, this assumption still needs to be tested which will be done in the future. For this purpose the conductivity of the three $BaLiF_3$ samples by using Li electrodes and applying a dc voltage will be measured in order to determine their Li transference numbers. When compared to the dc conductivity as well as to the electronic conductivity the transport numbers of the three species would be gained.

For completeness temperature-variable ^{19}F NMR spectra of the mechanosynthesized sample and of the mechanosynthesized $BaLiF_3$ after heat treatment at 870 K for 24 h are shown in Fig. 49. The measurements were done with a modified 7 mm MAS probe (Bruker) without spinning the sample. Interestingly, three NMR lines seem to be visible in the static NMR spectra, see Fig. 48. The line shape is very similar to the ones reported for single crystalline $RbCaF_3$[11] (t = 0.93) and $RbPbF_3$[12] (t = 0.86). Kaliaperumal et al. stated that three NMR lines are expected in case of the $RbCaF_3$ due to chemical shift anisotropy. The fluoride ion in the cubic perovskite $RbCaF_3$ is coordinated by two Ca ions in one direction and four Rb ions in the two other directions of the lattice (see Fig. 47 for the situation in $BaLiF_3$ in which Li assumes the role Ca has in $RbCaF_3$). Therefore $\sigma_{xx} = \sigma_{yy} \neq \sigma_{zz}$ if the Ca ions are located in the z-direction of the fluoride ion. As can be seen in Fig. 48 three NMR lines were found for single crystalline $BaLiF_3$. The orientation of the crystal to the magnetic field was not adjusted or determined since the sample was simply thrown into the feed line of the coil of the MAS probe for this first measurements. The integrals of the two main NMR lines give a ratio of 0.75(1) to 0.25(1) for the line centered at about 38 ppm to the NMR line centered at about 125 ppm. Interestingly, except for the NMR line centered at about -60 ppm which seems to shift to about -100 pm and the decrease of the intensity of the NMR line centered at approximately 125 ppm, the line shapes of the polycrystalline as well as of the nano-crystalline $BaLiF_3$ are very similar to the one of the single crystalline $BaLiF_3$. This is unexpected since the chemical shift anisotropy depends on the orientation of a crystal in the magnetic field. In case of a powdered sample the crystallites will have all possible orientations in the magnetic field. Since every orientation of a crystallite should have the same probability (at least there is no reason, like, for instance, magnetism of the crystallites which would align the crystals to the external magnetic field, why they should not) there should not be distinct lines but a superposition of all possible NMR lines generating a broad NMR line with sharp edges at highest and lowest chemical shift. The NMR lines of the powdered samples are broadened and the intensity of the NMR line located at about 125 ppm is decreased compared to the NMR lines of the single crystal. However, the two NMR lines are still separated. Thus, it seems that, for a reason unknown, there is a discontinuity in the orientational dependence of the shielding of the fluoride ion. Or a (potentially dynamic) distortion of the structure has to be assumed. However, there is evidence for a cubic perovskite structure gained by XRPD as well as by elastic neutron scattering.[1] Therefore, the investigation of the dependence of the chemical shift from the orientation of a single crystal in the magnetic field would be interesting. There already exists a study, but the authors do not show the ^{19}F NMR spectra but solely the change of the fwhm as function of the orientation of the crystal in the magnetic field without mentioning the emergence of extra-NMR lines[13]. However, a probe enabling such an experiment was not available. Furthermore, powdered $RbCaF_3$ as well as $RbPbF_3$ should be investigated by static ^{19}F NMR in the future.

The ^{19}F NMR lines of the mechanosynthesized sample do not change with increasing temperature. Even the NMR line of the heat treated $BaLiF_3$ changes only slightly at temperatures larger than 433 K where an additional NMR line seems to emerge at around 99 ppm. This NMR line probably indicates the presence of highly mobile ions as already indicated by the motional narrowing of the ^{7}Li NMR lines of this sample. See Fig. 50 for the change of the full width at half maximum (fwhm) of the ^{7}Li NMR lines with temperature for the three $BaLiF_3$ samples investigated. Motional narrowing can be observed if the jump frequency of the observed ion (or its surrounding) exceeds the width

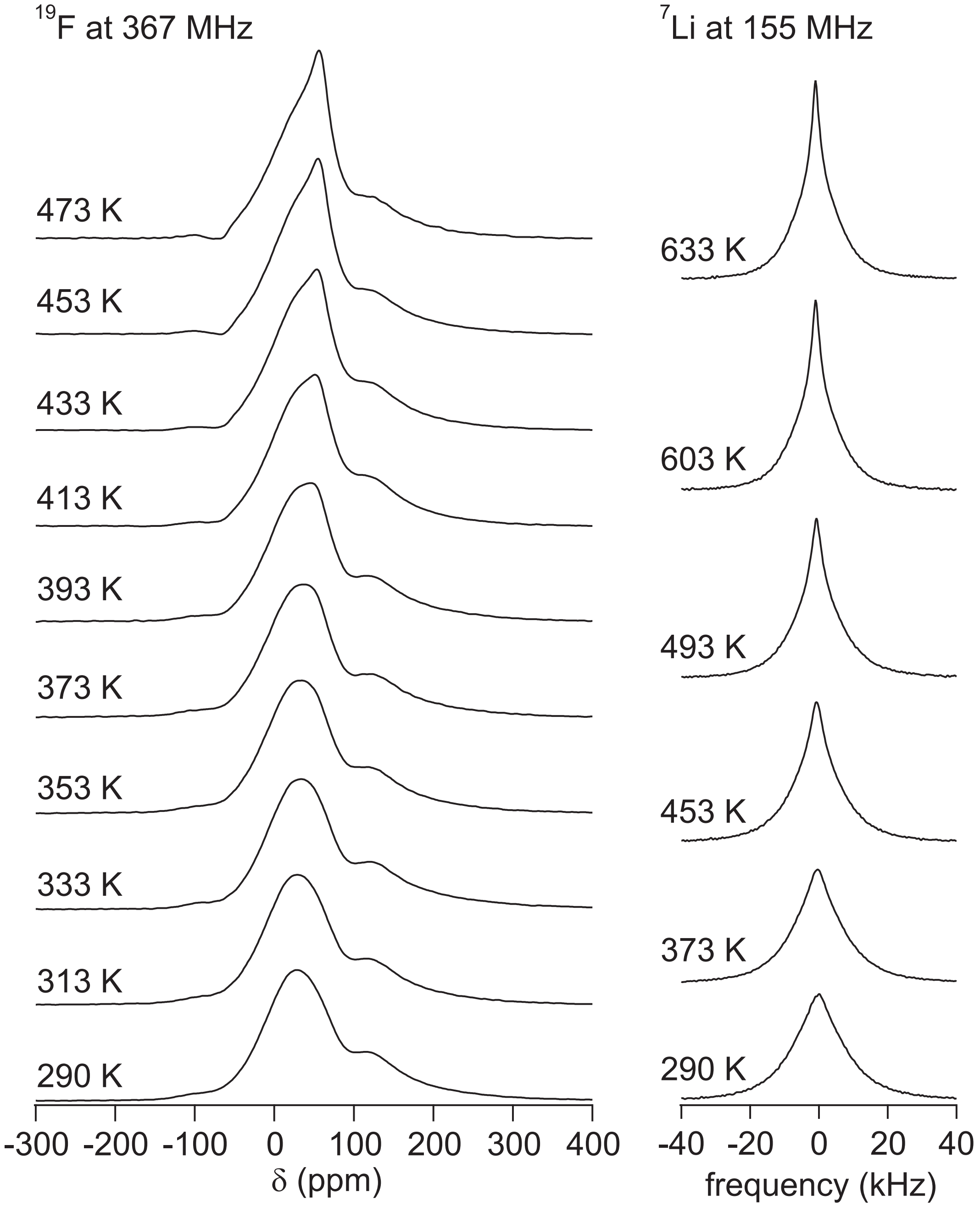

Figure 51: Left: static ^{19}F NMR spectra of mechanosynthesized $Ba_{0.74}Sr_{0.26}LiF_3$ recorded at the temperatures indicated. The measurements were done with a Larmor-frequency of 376 MHz. Right: static ^{7}Li NMR spectra of the same sample recorded at the temperatures denoted. The measurements were done at a Larmor-frequency of 155 MHz.

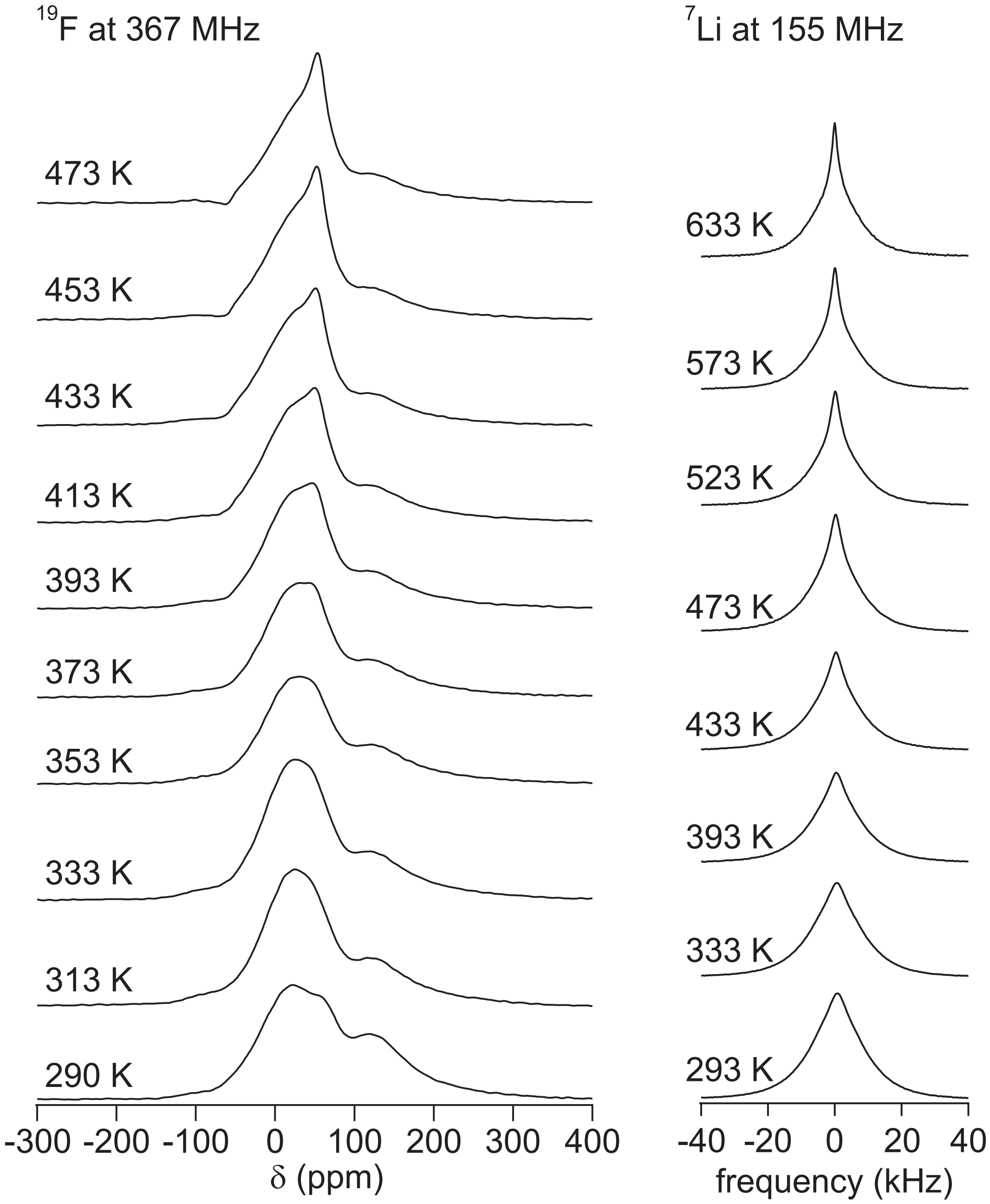

Figure 52: Left: static ^{19}F NMR spectra of mechanosynthesized $Ba_{0.60}Sr_{0.40}LiF_3$ recorded at the temperatures indicated. The measurements were done with a Larmor-frequency of 376 MHz. Right: static ^{7}Li NMR spectra of the same sample recorded at the temperatures denoted. The measurements were done at a Larmor-frequency of 155 MHz.

of the non-narrowed NMR line, thus, in this case for jump frequencies larger than 12 kHz. The ^{19}F NMR lines, however, are much broader than the ^{7}Li NMR lines such that a higher jump frequency is necessary for a motional narrowing. Since the ^{19}F NMR spectrum consists of more than one line also a coalescence is possible. This means that two or more NMR lines converge to one narrow line due to exchange of the fluorine between the different sites in the lattice. This happens if the jump frequency exceeds the distance between the NMR lines converging. However, in both cases jump frequencies clearly larger than about 30 kHz are needed for the emergence of a narrow NMR line in the ^{19}F NMR spectra.

The preparation of $SrLiF_3$ as well as $CaLiF_3$ was not reported in the literature, yet. However, Roy assumed that these compounds could form at low temperatures[5]. According to the calculations of Luaña et al.[6] $CaLiF_3$ and $SrLiF_3$ shall be more stable than a mixture of the binary fluorides as well as for perovskite-type $LiCaF_3$ and $LiSrF_3$. Both compounds should crystallize in the cubic cation inverted perovskite structure[2]: $t(SrLiF_3) = 0.95$, $t(LiSrF_3) = 0.59$, $t(CaLiF_3) = 0.92$, $t(LiCaF_3) = 0.63$. All attempts to prepare these compounds by high-energy ball milling failed. In all cases no reaction of the two binary fluorides was observed. However, an exchange of a part of the Ba ions by Sr ions is possible as shown in the third paper dealing with the synthesis and characterization of $Ba_{1-x}Sr_xLiF_3$ published in Journal of Material Chemistry (written by the author and Prof. M. Wilkening). It was found that single phase material crystallizing in the inverse perovskite structure can be obtained by high-energy ball milling for compositions up to $x = 0.40$. $Ba_{1-x}Sr_xLiF_3$ turned out to be not accessible by conventional solid state synthesis since it starts to slowly decomposed to $BaLiF_3$ (or $Ba_{1-x}Sr_xLiF_3$ with very small x), $Ba_{1-x}Sr_xF_2$ and LiF when heat-treated at temperature above 393 K.

^{19}F MAS NMR spectra of $Ba_{1-x}Sr_xLiF_3$ consisted of five NMR lines which can be assigned to the five different possible environments of the fluoride ions. The fluoride ion is coordinated by two Li and four Ba ions in the $BaLiF_3$ structure. If only the Ba ions are substituted by Sr ions (which seems to be the case judging from the ^{19}F MAS NMR spectra) the following environments will be formed: $[Ba]_4[Li]_2$, $[Ba]_3[Sr][Li]_2$, $[Ba]_2[Sr]_2[Li]_2$, $[Ba][Sr]_3[Li]_2$ and $[Sr]_4[Li]_2$. Also the formation behavior was studied by employing ^{19}F MAS NMR. It turned out that initially $BaLiF_3$ was formed and subsequently SrF_2 was introduced into the $BaLiF_3$ to eventually form $Ba_{1-x}Sr_xLiF_3$. Furthermore, $Ba_{1-x}Sr_xF_2$ seemed to be a competing product of the reaction of mixtures of LiF, BaF_2 and SrF_2.

Interestingly, the dc conductivities found for the mechanosynthesized $Ba_{1-x}Sr_xLiF_3$ samples are similar to the dc conductivities found for the mechanosynthesized $BaLiF_3$. However, the temperature-variable static NMR spectra of $Ba_{1-x}Sr_xLiF_3$ and $BaLiF_3$ differ as shown in Figs. 51 and 52 where the ^{19}F NMR spectra as well as the ^{7}Li NMR spectra of $Ba_{0.74}Sr_{0.26}LiF_3$ and $Ba_{0.60}Sr_{0.40}LiF_3$ are shown. Note that the ^{19}F NMR spectra recorded at ambient temperature are similar to the ^{19}F NMR spectra of $BaLiF_3$ at this temperature corroborating the assumption that the interaction of the fluoride ions with the Li ions is the origin of the three NMR lines in the static spectra of $BaLiF_3$. As mentioned before, in case of the mechanosynthesized $BaLiF_3$ almost no motional narrowing is visible in case of the ^{7}Li NMR spectra even at 630 K and no change at all of the ^{19}F NMR lines can be observed. However, in case of these two $Ba_{1-x}Sr_xLiF_3$ samples the ^{7}Li NMR spectra as well as the ^{19}F NMR spectra exhibit the emergence of narrow NMR lines. For both samples the ^{7}Li NMR lines exhibit a narrow NMR line atop a broader NMR line. The ^{19}F NMR spectra of $Ba_{0.74}Sr_{0.26}LiF_3$ and $Ba_{0.60}Sr_{0.40}LiF_3$ reveal the emergence of an additional narrow line at temperatures larger than 373 K with a chemical shift of 56 ppm and 54 ppm (at 473 K), respectively. Thus, only a part of the ions are highly mobile and their jump frequencies seem to be clearly higher than even in case of the heat treated $BaLiF_3$ discussed before.

Since the ionic conductivities of the $Ba_{1-x}Sr_xLiF_3$ samples investigated and the one of mechanosynthesized $BaLiF_3$ are similar, the transport mechanism for the ions change when Ba ions are substituted by Sr ions in $BaLiF_3$. If in mechanosynthesized $BaLiF_3$ fluoride as well as Li ions are mobile, this seems to decrease the jump rate of both ions. Thus, it seems plausible that in case of $Ba_{1-x}Sr_xLiF_3$ only one ion species is mobile. This could be due to the structural distortions introduced into the perovskite structure by the introduction of the smaller Sr ions ($r(Sr^{2+}(XII) = 0.144$ nm, $r(Ba^{2+}(XII) = 0.160$ nm[3]) facilitating the mobility of one ion species and reducing it for the other ion species. However, the fast ionic motions observed may also be due to the decomposition of the $Ba_{1-x}Sr_xLiF_3$ which was observed for temperatures larger than 373 K. This would also agree with the observation of a more pronounced motional narrowing in case of $Ba_{0.60}Sr_{0.40}LiF_3$. On the other hand, the increase of the SrF_2 amount should also lead to an increase of the ionic motion if a decrease of the jump barriers due to structural distortions is assumed to be the origin of the enhanced ionic motion. The origin of the different ionic transport behaviors of $BaLiF_3$ and $Ba_{1-x}Sr_xLiF_3$ will be evaluated in the future, starting by separating the fluoride ion from the Li ion conductivity the same way as already discussed for the $BaLiF_3$ samples (vide supra). Furthermore, the mechanosynthesis of $Ba_{1-x}Ca_xLiF_3$ will be tested.

References

[1] A. Boumriche, J. Y. Gesland, A. Bulou, M. Rousseau, J. L. Fourquet, B. Hennion, Solid State Commun. 91 (1994) 125.

[2] U. Müller, Inorganic Structural Chemistry, Second Edition, John Wiley & Sons Ltd, England, 2006, p. 203.

[3] R. D. Shannon, Acta Cryst. A32 (1976) 751.

[4] W. L. W. Ludekens and A. J. E. Welch, Acta Cryst. 5 (1952) 841.

[5] R. Roy, J. Am. Ceram. Soc. 37 (1954) 581.

[6] V. Luaña, A. Costales, A. Martin Pendás, M- Flórez, V. M. Garcia Fernández, Solid State Commun. 104 (1997) 47.

[7] S. V. Krivovichev, Z. Kristallogr. 223 (2008) 109.

[8] S. Flügge, Handbuch der Physik, Band XX, Springer Berlin - Göttingen - Heidelberg 1957, "Ionic Conductivity" A. B. Lidiard, p. 280.

[9] J. H. Van Vleck, Phys. Rev. 74 (1948) 1168.

[10] D. Zahn, S. Hermann, P. Heitjans, Phys. Chem. Chem. Phys. 13 (2011) 21492.

[11] R. Kaliaperumal, R. E. J. Sears, C. B. Finch, J. Chem. Phys. 87 (1987) 68.

[12] Y. Yamane, K. Yamada, K. Inoue, Solid State Ionics 179 (2008) 605.

[13] A. Goto, R. Miyabe, T. Shimizu, H. Kitazawa, K. Hashi, H. Abe, G. Kido, K. Shimamura, T. Fukuda, Physica B 298 (2001) 585.

A. Düvel, M. Wilkening, R. Uecker, S. Wegner, V. Sepelak, Phys. Chem. Chem. Phys. 12 (2010) 11251 - Reproduced by permission of the PCCP Owner Societies. http://pubs.rsc.org/en/content/articlelanding/2010/cp/c004530f#!divAbstract

View Article Online / Journal Homepage / Table of Contents for this issue

PCCP

Physical Chemistry Chemical Physics

www.rsc.org/pccp

Volume 12 | Number 37 | 7 October 2010 | Pages 11153–11796

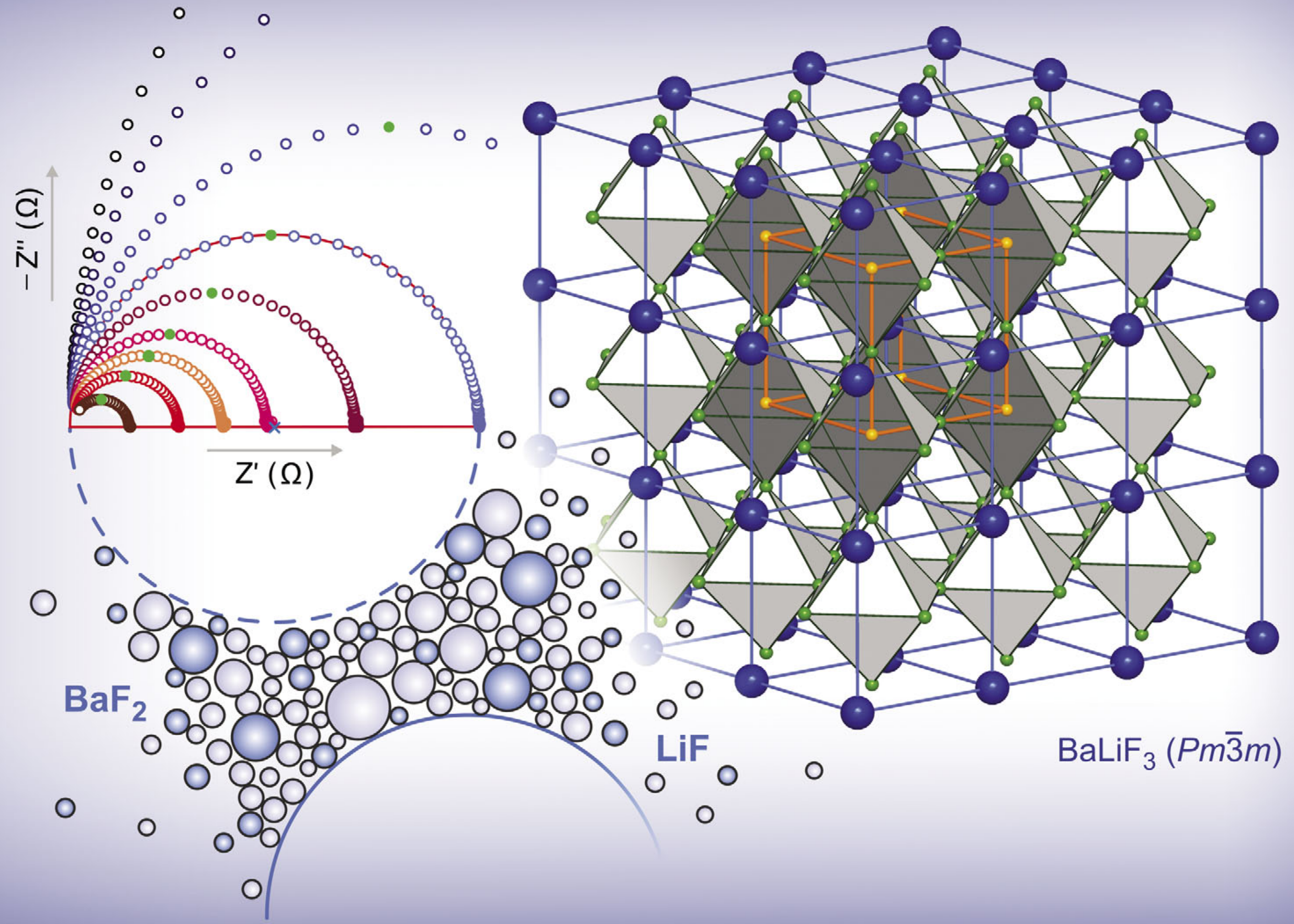

ISSN 1463-9076

COVER ARTICLE
Wilkening *et al.*
Mechanosynthesized nanocrystalline $BaLiF_3$: The impact of grain boundaries and structural disorder on ionic transport

PERSPECTIVE
Compton *et al.*
Nanoparticle-modified electrodes

Published on 16 August 2010. Downloaded by TIB und Universitaetsbibliothek Hannover on 24/03/2014 19:26:35.

Mechanosynthesized nanocrystalline $BaLiF_3$: The impact of grain boundaries and structural disorder on ionic transport

Andre Düvel,[ab] Martin Wilkening,*[ab] Reinhard Uecker,[c] Sebastian Wegner,[d] Vladimir Šepelák†[be] and Paul Heitjans[ab]

Received 22nd March 2010, Accepted 14th July 2010
DOI: 10.1039/c004530f

The mechanosynthesis of highly pure nanocrystalline $BaLiF_3$ is reported. The product with mean crystallite diameter of about 30 nm was prepared by joint high-energy ball-milling of the two binary fluorides LiF and BaF_2 at ambient temperature. Compared to coarse-grained $BaLiF_3$ with µm-sized crystallites, which is available *via* conventional solid-state synthesis at much higher temperatures, the mechanosynthesized product exhibits a drastic increase of ionic conductivity by several orders of magnitude. This is presumably due to structural disorder introduced during milling and to the presence of a large volume fraction of interfacial regions in the nanocrystalline form of $BaLiF_3$ providing fast diffusion pathways for the charge carriers. Starting from mechanosynthesized nanocrystalline $BaLiF_3$ it is possible to tune the transport parameters in a well defined way by subsequent annealing. Changes of the electrical response of mechanosynthesized $BaLiF_3$ during annealing are studied *in situ* by impedance spectroscopy. The results are compared with those of a structurally well-ordered single crystal which clearly shows extrinsic and intrinsic regions of ionic conduction.

I. Introduction

Fast-ion conductors play a crucial role in materials science.[1–7] In particular, they are needed to develop sustainable energy storage systems, chemical sensors or advanced electrochromic devices.[8–17] Currently, there are two main strategies to find (ceramic) materials showing high ionic conductivity. One is to synthesize new bulk materials with improved transport properties, the other is to modify the microstructure of known (single- or multi-phase) materials and, thus, to take advantage of nano-size and interface effects.[18,19] In a simplified view nanocrystalline ion conductors can be regarded as structurally heterogeneous materials consisting of nm-sized crystalline grains and a large fraction of interfacial regions[4] which in many cases dominate the overall ionic transport behaviour. The interfacial regions may also show structural disorder and can provide fast diffusion pathways for the ions.[20] Recently, we observed a large increase of the Li ion conductivity of lithium tantalate, $LiTaO_3$, when the microcrystalline source material with a mean crystallite diameter in the µm range was high-energy ball-milled for several hours in a shaker mill in order to produce its nanocrystalline, structurally disordered but chemically identical counterpart.[21] Subsequent annealing of the so obtained nanocrystalline sample allowed us to adjust the Li dc-conductivity in a controlled way. $LiTaO_3$ as well as nanocrystalline $LiNbO_3$ investigated before[20,22–25] served as a model substance to study the influence of crystallite size and structural disorder on the ionic conductivity.

In the present paper we extend our investigations to a ternary Li containing fluoride *viz* $BaLiF_3$. In particular, the paper is aimed at the fundamental question how and to which extent interfaces and grain boundaries affect the overall charge transport in ion conductors. $BaLiF_3$ turned out to be a suitable model system for this purpose. It is one of the rare examples and the only known ternary fluoride which crystallizes with the cubic inverse perovskite-type structure[26–28] (space group $Pm\bar{3}m$, a = 0.3996 nm (polycrystalline powder, see ref. 26), a = 0.3994(7) nm (single crystal, see ref. 29). Presumably, two mobile charge carriers, Li^+ and F^-, are present in $BaLiF_3$. This is in contrast to $LiTaO_3$ where Li cations dominate ionic conductivity.[21] It is presently not clear whether one of the two is dominant; this is subject to future work in our laboratory. While nanocrystalline $LiTaO_3$ was prepared by reducing the particle size of coarse-grained lithium tantalate by ball milling (top–down approach, see ref. 21), phase pure nanocrystalline $BaLiF_3$ can be easily mechanosynthesized by high-energy ball milling a stoichiometric mixture of LiF and BaF_2 at ambient temperature as is shown here. Mechanosynthesis by high-energy ball-milling inducing a heterogeneous reaction has been used in recent years to produce quite a number of compounds not easily accessible by conventional routes (see, *e.g.*, ref. 30–33). To our knowledge, the mechanosynthesis route has not been reported for $BaLiF_3$ in the literature so far. The mean crystallite size of the product obtained ranges from 11 to 30 nm. Let us note that

---

[a] *Institute of Physical Chemistry and Electrochemistry, Leibniz University Hannover, Callinstr. 3a, D-30167 Hannover, Germany. E-mail: wilkening@pci.uni-hannover.de*
[b] *Center for Solid State Chemistry and New Materials, Leibniz University Hannover, Callinstr. 3a, D-30167 Hannover, Germany*
[c] *Leibniz Institute of Crystal Growth, Max-Born-Str. 2, D-12489 Berlin, Germany*
[d] *Bruker BioSpin GmbH, D-76287 Silberstreifen, Germany*
[e] *Institute of Nanotechnology, Karlsruhe Institute of Technology, Herrmann-von-Helmholtz-Platz 1, D-76344 Eggenstein-Leopoldshafen, Germany*
† On leave from the Slovak Academy of Sciences, Košice, Slovakia.

Published on 16 August 2010. Downloaded by TIB und Universitaetsbibliothek Hannover on 24/03/2014 19:26:35.

in its single crystalline form $BaLiF_3$ is considered to be a promising window material in the ultra-violet and vacuum-ultra-violet region.[29] Moreover, it is of interest as a potential laser-active medium when doped with suitable transition metals[34–37] and discussed as possible candidate for quantum computing devices.[38]

The ionic transport parameters and diffusion properties of as prepared and annealed mechanosynthesized $BaLiF_3$, which was characterized by X-ray diffraction, ultra-fast ^{19}F MAS NMR spectroscopy as well as preliminary TEM micrographs, were investigated by impedance spectroscopy. The results are compared with those of a Czochralski grown $BaLiF_3$ single crystal, see, *e.g.*, ref. 39, as well as with those of a micro-crystalline powder sample. The latter was prepared by conventional solid-state synthesis[40] and is characterized by a mean crystallite size with a diameter of about 0.8 μm.

II. Experiment

A Preparation of $BaLiF_3$

Nanocrystalline $BaLiF_3$ was prepared by high-energy ball milling of BaF_2 (99.99%, Sigma Aldrich) together with an equimolar amount of LiF (99.99%, Alfa Aesar) in a Fritsch Pulverisette 7 (premium line) planetary mill. The total mass of the mixture was about 2 g. A grinding beaker made of stabilized ZrO_2 with a volume of 45 mL was employed. The mixture was mechanically treated for times between 30 and 180 min using 140 milling balls (ZrO_2, 5 mm in diameter) at 600 rpm. One sample, which was prepared by milling of BaF_2 and LiF in an equimolar ratio for three hours, was annealed at 870 K for 24 h as well as 50 h in air.

Single crystalline $BaLiF_3$ was prepared by the following procedure. First, the starting materials of the crystal growth processes BaF_2 (crystal pieces) and LiF (GFI "optical grade") were purified by a pre-treatment,[34] *i.e.*, the source materials were treated with HF at elevated temperatures. Afterwards they were mixed in the required ratio and subjected to a zone melting procedure under HF. Since $BaLiF_3$ melts incongruently at about 1100 K the composition of the starting melt has to deviate from the crystal composition. According to the peritectic point of the binary phase diagram BaF_2-LiF the chosen composition was $Ba_{0.86}Li_{1.14}F_{2.86}$. The crystal was grown in a platinum crucible by conventional Czochralski technique with RF-heating and automatic diameter control. In order to suppress oxidation of the melt the growth atmosphere consisted of an Ar-CF_4 mixture. The growth rate was 2 mm h^{-1} and the rotation varied from 10 to 25 min^{-1}. The so obtained colorless crystal was 70 mm in length and 18 mm in diameter.

For comparison, polycrystalline $BaLiF_3$ was also prepared by conventional solid-state (high-temperature) synthesis following the procedure being described in detail in ref. 40. According to that preparation route an equimolar mixture of BaF_2 and LiF, which was initially mixed for 10 min in a planetary mill at 600 rpm, was heated for about two hours in nitrogen atmosphere at 620 K for drying purposes and then fired at 1020 K for 5 h. After that it was left to cool down to room temperature. It has to be mentioned that synthesizing $BaLiF_3$ *via* ceramic synthesis routes has some disadvantages compared to one-step mechanochemical preparation. In particular, vaporization of Li at high temperatures leads to less pure and non-stoichiometric products.

B XRD, impedance and NMR measurements

Sample characterization of the powders was carried out at room temperature using X-ray diffraction (XRD) with a Philips PW 1800 operating with Cu-Kα radiation at 40 kV. For the impedance spectroscopy measurements an HP 4192 A analyzer (frequency range 5 Hz to 13 MHz) connected to a home-built cell was employed. Conductivity jigs with a four terminal configuration were used. The powdered samples were pressed to cylindrical pellets (8 mm in diameter and 1 mm in thickness) at room temperature. If not stated otherwise this was done by applying an uniaxial pressure of about 1 GPa. Electrodes were applied either by Au sputtering or by subsequent pressing the uncoated pellet between Pt powder. During the measurements the impedance samples were strictly kept under inert gas atmosphere by using a stream of dry nitrogen (99.999%). Temperatures ranged from 298 K to about 800 K.

^{19}F MAS (magic angle spinning) NMR spectra were acquired with a Bruker Avance III spectrometer operating at 471 MHz. The NMR spectra were recorded using a single excitation pulse at an ultra-fast spinning speed of ν_{rot} = 60 kHz with room-temperature bearing gas. The $\pi/2$ pulse length was about 2 μs.

III. Results and discussion

A Sample characterization by XRD and ^{19}F MAS NMR

In Fig. 1 X-ray diffraction (XRD) powder patterns of equimolar mixtures of BaF_2 and LiF treated in the planetary mill for t_{mill} = 30, 60 and 180 min, respectively, are shown. Already after 30 min of milling, the XRD powder pattern of $BaLiF_3$ with its inverse cubic perovskite structure (see Fig. 1) dominates the diffractogram. After milling the mixture for one hour the conversion of LiF and BaF_2 to $BaLiF_3$ seems to be close to 100% since there are no peaks visible pointing to residual LiF or BaF_2. The latter are highlighted in Fig. 1(a) by asterisks and filled circles, respectively. The XRD peak positions found for $BaLiF_3$ are in perfect agreement with those reported in the literature.[41] For comparison, in Fig. 1 the XRD pattern of a sample prepared by conventional solid-state synthesis as well as that of mechanosynthesized $BaLiF_3$, which was annealed at 870 K for 24 h, are also shown.

In Fig. 2 magnifications of some of the XRD patterns displayed in Fig. 1 are shown in order to verify the phase purity of the mechanosynthesized products with respect to residual LiF and BaF_2. In contrast to the conventionally prepared sample where a small amount of residual BaF_2 is found, after 1 h of mechanical activation of the LiF : BaF_2-mixture, the XRD peaks of the two binary starting materials cannot be detected any longer. Furthermore, it can be clearly seen that $BaLiF_3$ ($Pm\bar{3}m$) is the only phase which is formed under the milling conditions described above. This is fully corroborated by ^{19}F MAS NMR (*vide infra*).

This journal is © the Owner Societies 2010

View Article Online

Published on 16 August 2010. Downloaded by TIB und Universitaetsbibliothek Hannover on 24/03/2014 19:26:35.

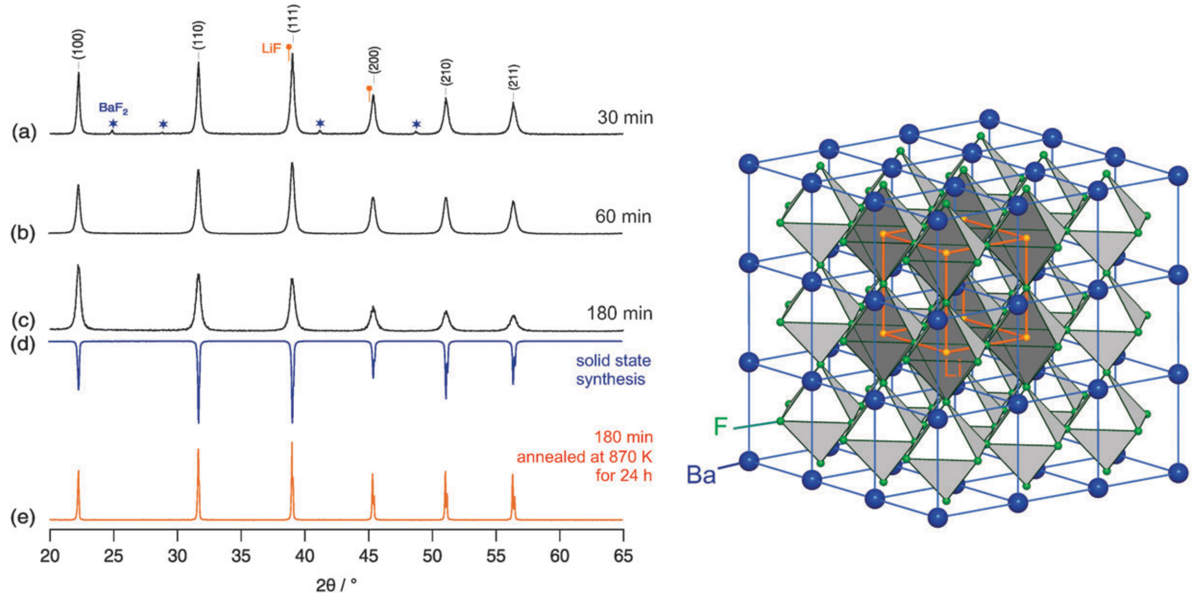

Fig. 1 Left: X-ray powder diffraction patterns of nanocrystalline $BaLiF_3$ prepared by mechanical treatment of BaF_2 and LiF (molar ratio of 1 : 1) in a planetary mill at 600 rpm and for different milling times t_{mill} (a) 30 min, (b) 60 min and (c) 180 min. (d) For comparison, the corresponding XRD pattern of conventionally prepared $BaLiF_3$ is shown, too. (e) XRD pattern of mechanosynthesized $BaLiF_3$ (t_{mill}) which was annealed at 870 K for 24 h. Right: Crystal structure of $BaLiF_3$ (space group $Pm\bar{3}m$). Large blue spheres denote Ba cations, orange and green spheres represent Li cations and F anions.

Compared to the XRD peak widths of conventionally prepared $BaLiF_3$, those of the ball-milled product are broadened due to both much smaller crystallite sizes and effects of lattice strain ε. In a first approximation we have used the equation introduced by Scherrer[42] (1) to determine the mean crystallite size $\langle d\rangle$, which is related to the broadening of the peak *via*

$$\langle d\rangle = \frac{K\cdot\lambda_{\mathrm{XRD}}\cdot 360^\circ}{2\pi\cdot\beta_{f(\theta,hkl)}[^\circ 2\theta]\cdot\cos\theta} \qquad (1)$$

θ denotes the angle between the surface of the sample and the incident X-ray beam. $K = 0.89$ is chosen assuming a spherical shape of the crystallites. λ_{XRD} is the average wavelength of the X-ray source. For a Cu anode λ_{XRD} of the $K\alpha_1$ line equals 0.154 nm. In the case of Lorentzian-shaped XRD peaks, which is the case here, the width (fwhm, full width at half maximum) $\beta_{f(\theta,hkl)}$ is given by $\beta_{f(\theta)} = \beta_{r(\theta)} - \beta_{g(\theta)}$ taking into account instrumental broadening effects. $\beta_{r(\theta)}$ is the measured peak width and $\beta_{g(\theta)}$ is the width of a reference material such as microcrystalline CaF_2 or coarse-grained $BaLiF_3$ produced from $BaLiF_3$ single crystals. Expectedly, the mechanosynthesized $BaLiF_3$ samples show mean crystallite sizes in the nm-range. As an example, mechanosynthesized $BaLiF_3$ obtained after $t_{\mathrm{mill}} = 180$ min is characterized by $\langle d\rangle \approx 30$ nm. Reducing the milling time leads to an increase of $\langle d\rangle$ (see Table 1). The sample which was prepared by solid-state synthesis at a much higher temperature has a crystallite size of 0.8 µm. Interestingly, the XRD peak widths of the mechanosynthesized material, which was additionally annealed at 870 K, are less broadened than those of the conventionally prepared one which was calcined at much higher T (see Fig. 2(b) for comparisons). Most likely, this is due to a larger mean crystallite size indicating that the microstructure of a ball-milled powder favours grain growth. In order to quantify to which degree lattice strain ε affects the $\langle d\rangle$ values listed in Table 1, we have analyzed the XRD patterns according to the procedure of Williamson and Hall.[43]

$$\frac{\beta_{f(\theta,hkl)}\cos\theta}{\lambda_{\mathrm{XRD}}} = 4\varepsilon\frac{\sin\theta}{\lambda} + \frac{1}{\langle d\rangle} \qquad (2)$$

Except for the mixture milled for 30 min, the values obtained by eqn (2) for $\langle d\rangle$ are twice as large as those estimated *via* eqn (1), see Table 1. This indicates that the values obtained by the Scherrer equation should be regarded as a rough estimate for the crystalline size.

Apart from an almost negligible impurity, which might be identified with orthorhombic BaF_2 (chemical shifts δ amount to 102 and 176 ppm, see ref. 44) or another metastable intermediate, the phase purity of mechanosynthesized $BaLiF_3$ probed by X-ray powder diffraction is clearly confirmed by the room temperature ^{19}F MAS NMR spectrum shown in Fig. 3. Orthorhombic BaF_2 is a known high pressure modification of BaF_2.[45,46] In a previous study we have shown that it is formed to a small extent during mechanical treatment of cubic BaF_2 for 3 h in a planetary mill.[44,47] Increasing the milling time to about 6 h increases the amount of orthorhombic BaF_2 formed. Thus, one might suppose that during the initial stages of milling an LiF : BaF_2 mixture, orthorhombic BaF_2 is formed first which transforms into $BaLiF_3$ shortly after.

In agreement with the crystal structure of $BaLiF_3$ a single and Lorentzian-shaped ^{19}F NMR resonance line is observed under high-speed MAS conditions. It shows up at $\delta = 66$ ppm when referenced to C_6F_6. The measured chemical shift is identical to that recently reported in the literature for a powdered sample of $BaLiF_3$.[48] Here, the same δ-values are found for the other samples investigated within this study.

View Article Online

Published on 16 August 2010. Downloaded by TIB und Universitaetsbibliothek Hannover on 24/03/2014 19:26:35.

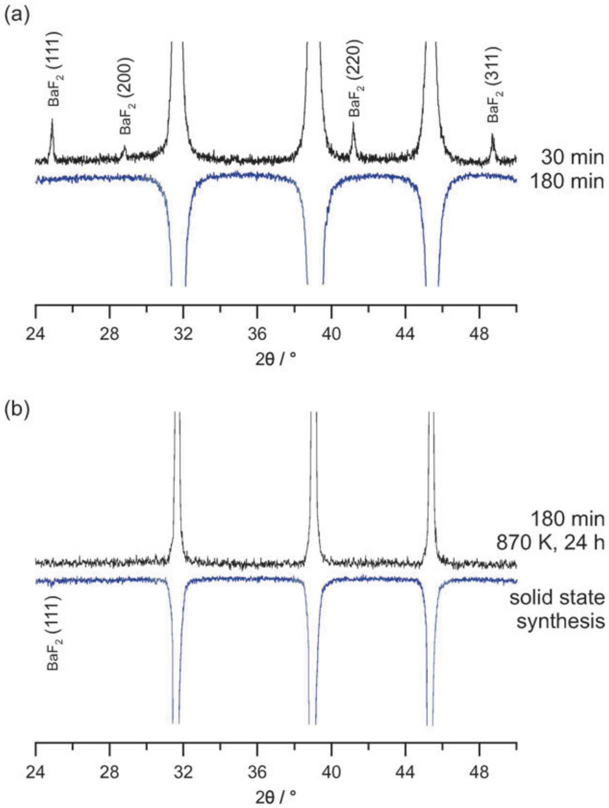

Fig. 2 Magnifications of the XRD powder patterns shown in Fig. 1. The XRD peaks of residual BaF_2 are indicated. After $t_{\text{mill}} = 60$ min the formation of $BaLiF_3$ is completed. The diffractogram of a sample treated for 180 min in the planetary mill verifies the phase purity of mechanosynthesized $BaLiF_3$. For comparison, the XRD diffractograms of the two coarse-grained samples are also shown. The peak at about 25° 2θ, which is of very low intensity, reveals a very small amount of residual BaF_2 owing to weighing errors.

Table 1 $\langle d \rangle$ and ε values of $BaLiF_3$ prepared *via* different ways. The mean crystallite sizes were estimated *via* XRD peak broadening. The error of $\langle d \rangle$ is at least of the order of ±5 nm

t_{mill}	$\langle d \rangle$ (eqn (1))	ε	$\langle d \rangle$ (eqn (2))
30 min	50 nm	0.003	340 nm
60 min	40 nm	0.002	80 nm
180 min	30 nm	0.002	60 nm

However, the NMR line width of the mechanically synthesized nanocrystalline product is by more than a factor of two larger than that of microcrystalline $BaLiF_3$ (Fig. 3). Since the spectra are recorded with the same spinning speed ν_{rot} of approximately 60 kHz, the larger line width can be attributed to a distribution of chemical shifts present in the mechanically prepared product. This clearly reflects microstructural disorder such as distortions of the F^- octahedra or deviations from ideal bond lengths.

B Impedance spectroscopy studies on structurally different forms of $BaLiF_3$

1. Mechanosynthesized, nanocrystalline $BaLiF_3$

a Basics. Impedance spectroscopy is a simple but important method to study the electrical processes occurring in a system on applying an ac signal across the sample pellet.[49,50] The technique is based on analyzing the electrical response of the system usually after a sinusoidal perturbation. The impedance is generally calculated as a function of the frequency of this perturbation. Conventionally, the output response, which comprises both resistive (real part) and reactive (imaginary part) components, is either displayed in a complex plane plot (Nyquist plot or Cole–Cole diagram) or in form of impedance spectra, *i.e.*, the real part σ' of the complex conductivity $\hat{\sigma}(\omega)$ is plotted *vs.* frequency. Here, $\omega(= f{\cdot}2\pi)$ denotes the angular frequency. In a Cole–Cole plot the negative imaginary part $-Z''$ of the impedance (ω) is plotted *vs.* the real part Z' and appears in succeeding semicircles representing the contributions to the electrical properties due to the bulk material, grain boundary effects and, if there are any, interfacial polarization phenomena.[4] The impedance $\hat{Z}(\omega)$ is given by

$$\hat{Z}(\omega) = Z' - iZ'' = R - \frac{i}{\omega C} \quad \text{and} \quad \frac{Z'}{Z''} = \frac{\varepsilon''}{\varepsilon'} = \tan\delta \qquad (3)$$

where R and C are the resistance and capacitance, respectively. $i = (-1)^{1/2}$ is the imaginary unit, ε' and ε'' denote the real and imaginary parts of the complex dielectric permittivity. δ is the loss angle. The peaks of the different semicircles are characterized by their individual time constants according to the relation

$$\omega_{\max}\tau = \omega_{\max}RC = 1 \qquad (4)$$

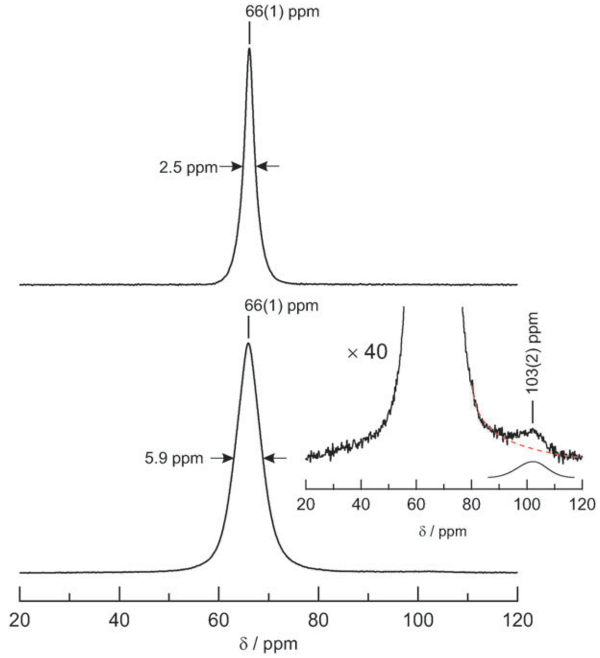

Fig. 3 ^{19}F MAS NMR spectra of 'single crystalline' (top) and mechanosynthesized (nanocrystalline) $BaLiF_3$ (bottom) which were recorded at a spinning speed of 60 kHz using ambient bearing gas pressure. A small piece of the single crystal was ground in an agate mortar for the MAS NMR measurements. The different line widths (fwhm) are 2.5 and 5.9 ppm, respectively. Inset: magnification of the NMR spectrum of nanocrystalline $BaLiF_3$. Most likely, the signal of very low intensity which shows up at about 103 ppm can be attributed to orthorhombic BaF_2.

This journal is © the Owner Societies 2010

Published on 16 August 2010. Downloaded by TIB und Universitaetsbibliothek Hannover on 24/03/2014 19:26:35.

Thus, the relaxation frequency is given by $f_{\max} = 1/(2\pi RC)$. Alternatively, other representations, *e.g.*, the complex modulus $\hat{M}(\omega) = M' + iM''$ can be used to highlight a particular aspect of the electrical response of a sample. For example, the modulus representation is useful when measurements are affected by high capacitance effects, such as those due to inter-granular impedances and electrode polarization effects.[51,52] $\hat{M}(\omega)$ is related to the complex impedance *via* the equation

$$M' + iM'' = i\omega C_0\hat{Z} \tag{5}$$

where $C_0 = (\varepsilon_0 A)/d$. A and d are area and thickness of the pellet and ε_0 is the permittivity of free space.

b Complex plane plots and impedance spectra. The first part of this section is concerned with nanocrystalline $BaLiF_3$ synthesized by high-energy ball milling (see above). We have started to characterize the sample by impedance spectroscopy measurements at temperatures $T > 385$ K. The temperature was continually increased in order to detect any changes of the electrical response of the sample. In Fig. 4(a) the complex impedance spectra of mechanosynthesized $BaLiF_3$ are shown which were measured at the temperatures indicated. Partly, the corresponding peak frequencies, *i.e.*, the frequencies where the imaginary part passes through the maximum, are given.

As often observed for structurally disordered materials, the arcs of mechanically prepared $BaLiF_3$ can be described by depressed semicircles, *i.e.*, the respective centers lie below the Z' axis. In particular, this holds for low temperatures when the data of $BaLiF_3$ is regarded. These shifts clearly reveal that the curves are composed of a range of semicircular arcs pointing to a large distribution of relaxation frequencies being characteristic of the electrical response of the sample. With increasing temperature the shape of the arcs progressively become more semicircular and their centers shift towards the origin of the complex plane plot. Most likely, these observations are due to slight structural changes of the sample. At low frequencies spikes are clearly visible which originate from electrode polarization effects.

The same features also govern the corresponding impedance spectra which are shown in Fig. 4(b). At both low T and low frequencies they clearly show a distinct dc-conductivity plateau. The dc-conductivity σ_{dc} is identical to the value which can be determined from the corresponding resistance of the low-frequency intercept of the complex impedance arcs on the real axis. With increasing frequency the dispersive region of the impedance spectra shows up. Once again, the frequency dependence of σ' changes with temperature. Up to frequencies of about $f = 1$ MHz the spectra can be roughly described by a power law behaviour according to $\sigma' = \sigma'_{dc} + A_0\omega^s$ with A_0 being the dispersion parameter and s the power law exponent usually ranging between 0 and 1. Here, s turns out to be depending on temperature. It is approximately 0.63 at low and reaches 0.40 at high temperatures.

In Fig. 4(c) the temperature dependence of the dc-conductivity is shown in an Arrhenius representation according to

$$\sigma_{dc}T = \sigma_0\exp(-E_a/(k_BT)) \tag{6}$$

where E_a denotes the activation energy and k_B Boltzmann's constant. E_a turns out to be 0.74(1) eV. Very similar results were obtained for a sample which was prepared by mechanical treatment of LiF and BaF_2 for $t_{mill} = 20$ h under the same preparation conditions. For that sample a mean crystallite diameter of about 11 nm can be estimated from XRD peak broadening (see section III A). For comparison with the $\sigma_{dc}T$ data, the temperature dependance of the so-called characteristic frequency ω_c, being a measure of the onset of conductivity dispersion according to $\sigma'(\omega_c) = 2\sigma'(\text{dc})$, is shown in Fig. 4(c), too. $\omega_c(T)$ also follows Arrhenius behaviour with an activation energy being similar to that deduced from $\sigma_{dc}T$ (*cf.* Fig. 4(c)). Plotting $\sigma_{dc}T$ *vs.* ω_c in a log-log plot should result in a straight line with a slope of unity. This is only roughly fulfilled below 465 K. At higher T deviations show up and the slope is reduced to about 0.8

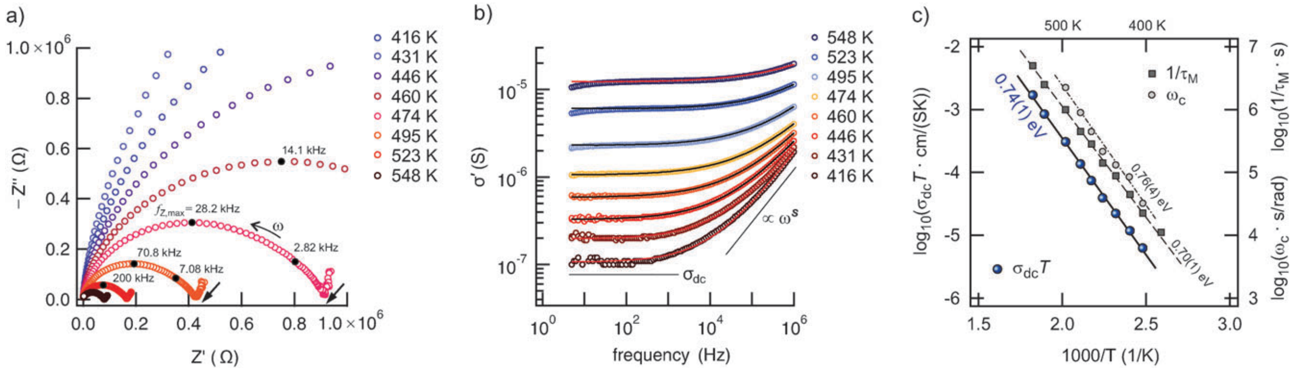

Fig. 4 (a) Cole–Cole plots of mechanosynthesized $BaLiF_3$ which was produced by joint milling of LiF and BaF_2 in a planetary mill for 3 h. The frequencies $f_{Z,\max}$ indicated follow Arrhenius behaviour. From the intercepts at low frequencies (marked exemplarily by two arrows) the resistance is obtained showing the same temperature dependence as the dc-conductivity (see Fig. 4(b)). (b) Corresponding impedance spectra of mechanosynthesized $BaLiF_3$, *i.e.*, the real part of $\hat{\sigma}$ is plotted *vs.* frequency $f = \omega/2\pi$. The dc-conductivities can be directly read out from the low-frequency plateau where σ' is independent of frequency. Solid lines represent fits according to Jonscher's power law: $\sigma' = \sigma_{dc} + A_0\omega^s$ (see text for further explanation). (c) Electrical dc-conductivity of mechanosynthesized nanocrystalline $BaLiF_3$ as a function of temperature (plotted as $\sigma_{dc}T$ *vs.* $1000/T$). Solid lines represent fits according to an Arrhenius law. The activation energy turns out to be 0.74(1) eV characterizing long-range transport of the charge carriers in the ternary fluoride. For comparison, the electrical relaxation rate τ_M^{-1} deduced from the M'' maxima and the characteristic frequency ω_c are also included.

Published on 16 August 2010. Downloaded by TIB und Universitaetsbibliothek Hannover on 24/03/2014 19:26:35.

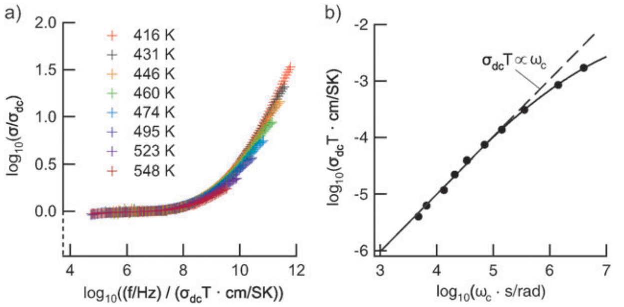

Fig. 5 (a) Conductivity master curve of mechanosynthesized $BaLiF_3$. The scaled spectra were recorded at the temperatures indicated. (b) $\sigma_{dc}T$ *vs.* ω_c. Note the deviation from a linear relation of the two quantities indicated by the dashed line.

indicating that the electrical relaxation behaviour depends on temperature. The fact that a linear relationship between σ_{dc} and ω_c is not fully observed is also seen when the well-known time-temperature scaling[53,54] σ/σ_{dc} *vs* $f/(\sigma_{dc}T)$ or the modulus representation is used to characterize the conduction processes in mechanosynthesized $BaLiF_3$. In order to obtain a conductivity master curve (see Fig. 5), σ_{dc} and $\sigma_{dc}T$ are used to scale the conductivity spectra which collapse into a single curve if $\sigma_{dc} \propto \omega_c$ holds. It can be seen from Fig. 5 that the scaled impedance spectra do not coincide. This is in agreement with the features observed when M'' is plotted *vs.* frequency for different temperatures (Fig. 6).

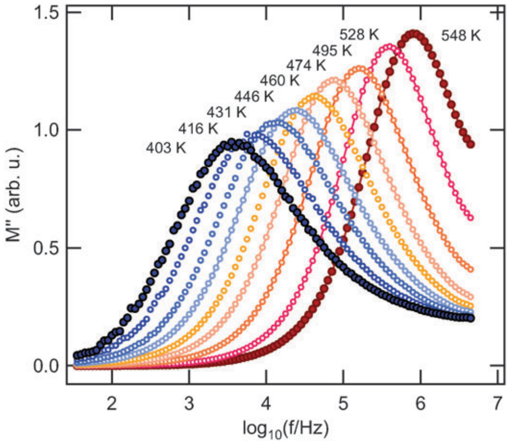

Fig. 6 Frequency dependence of the imaginary part of the electric modulus of mechanosynthesized $BaLiF_3$ at various temperatures. The relaxation rates τ_M^{-1}, which can be deduced from the peak maxima, are shown in Fig. 5. The temperature was continuously increased and the curves were measured beginning from the lowest temperature.

c Comparison with the modulus representation. The peak maxima of $M''(\omega/2\pi)$ increase with increasing T. This is accompanied by a reduction of the peak widths. Simultaneously, the asymmetry of the modulus curves, which shows up at the best at low T, continuously decreases leading to more symmetric peaks at higher temperatures. Altogether, these findings clearly reflect that particularly at low T highly non-Debye behaviour is observed which is also expressed by the depressed semicircles of Fig. 4(a). Moreover, the non-Debye response observed depends clearly on temperature. Generally, a (normalised) Kohlrausch-Williams-Watts (KWW) correlation function,[54–59]

$$\phi(t) = \exp(-(t/\tau')^{\beta'}) \qquad 0 < \beta' \leqslant 1 \qquad (7)$$

considering a distribution of electrical relaxation times, τ' by the exponent $\beta' < 1$, is simply assumed in an empirical manner to explain (asymmetric) modulus curves. Ideal Debye behaviour is obtained when β' equals 1. It is worth mentioning that eqn (7) fits $M''(\omega/2\pi)$ well except at large frequencies. However, this has negligible effect on the electrical relaxation rate $1/\tau_M$, which can be deduced from the peak maxima of M'' (see below). Moynihan *et al.* proposed

$$\hat{M}(\omega) = (1/\varepsilon_\infty)\{1 - L(-\mathrm{d}\phi/\mathrm{d}t)\} \qquad (8)$$

with $\lim_{\omega\to\infty}\hat{M}(\omega) = 1/\varepsilon_\infty$ and where $L(x)$ is the Laplace transform of x.[59] Numerical simulations[59] of $\hat{M}(\omega)$ for given β' values can be used to relate the full width at half maximum Γ of the $M''(\omega)$-curves with β'. In Fig. 7 β' $(1/T)$ of the M''-curves of Fig. 6 is shown ranging from approximately 0.5 ($T \approx 400$ K) to about 0.64 ($T \approx 530$ K). Let us note that the use of M'' to analyze impedance data is often criticized[50,60] because M'' represents a tangled combination of both the conductivity σ' and the permittivity ε' which, in contrast to M'', can be measured directly. However, here the M'' representation is just used to highlight changes of the electrical response of the samples during heat treatment and to compare these results with those obtained when σ' is analyzed directly. With this in mind we have additionally parameterized the M'' data of as prepared mechanosynthesized $BaLiF_3$ on the frequency scale directly with Lorentzian-shaped fits according to

$$M'' \propto \frac{\omega\tau_M}{1 + (\omega\tau_M)^{2-n_\sigma}} \qquad (9)$$

Once again, such an analysis, which is used here simply to illustrate the deviations from ideal Debye behaviour, yields temperature dependent stretching factors $\beta = 1 - n_\sigma$ ranging from 0.31 at about 385 K to *ca.* 0.5 when the temperature is raised to about 550 K (see Fig. 7). The peak maxima of Fig. 6 mark the crossover from long-range to short-range motions of the charge carriers. The frequencies $f_{M,\max}$ associated can be roughly transformed into electrical relaxation rates $1/\tau_M$ *via* $f_{M,\max}2\pi\cdot\tau_M = 1$. The temperature dependence of $1/\tau_M$ obtained this way is shown in Fig. 7 together with that of $1-n_\sigma$. Taking into account non-exponential KWW-correlation functions (eqn (7)), the rates obtained *via* eqn (9) slightly differ from those shown in Fig. 4(c) yielding an activation energy (0.75(2) eV) which is very similar to that obtained when $\sigma_{dc}T$ is analyzed (0.74(1) eV, see Fig. 4(c)). The corresponding pre-exponential factor $\tau_{M,0}^{-1}$ of the underlying Arrhenius law

$$\tau_M^{-1} = \tau_{M,0}^{-1}\exp(-E_{a,M}/(k_B T)) \qquad (10)$$

turns out to be about 2.2×10^{13} s^{-1} and, thus, lies in the typical range of phonon frequencies.

The deviation from Debye behavior manifests itself also in the absolute widths of the modulus spectra. At low temperatures the peak width Γ (fwhm) is about 2.1 decades (on the frequency scale). The spectrum measured at the highest T (see Fig. 6) reveals a peak width of only 1.7 decades. Ideal

Published on 16 August 2010. Downloaded by TIB und Universitaetsbibliothek Hannover on 24/03/2014 19:26:35.

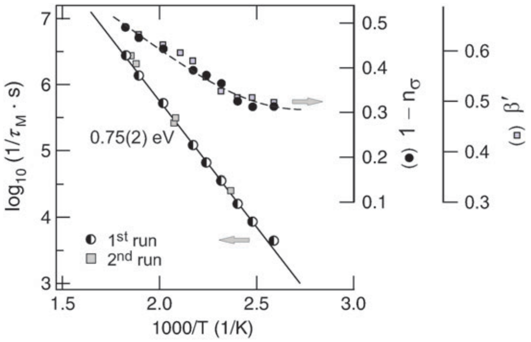

Fig. 7 Temperature dependence of (i) the most probable electrical relaxation time τ_M in nanocrystalline BaLiF$_3$ as obtained from eqn (9) and (ii) the stretching exponent β' of the underlying KWW correlation function (eqn (7)) as well as $1 - n_\sigma$ obtained from eqn (9). The solid line shows a fit according to an Arrhenius relation, $\tau_M^{-1} = \tau_{M,0}^{-1}\exp(-E_{a,M}/(k_BT))$, with $E_{a,M} = 0.75(2)$ eV and $\tau_{M,0}^{-1} = 2.2 \times 10^{13}$ s^{-1}. Squares show the relaxation rates deduced from the complex modulus spectra of Fig. 8.

Debye response is characterized by a width of about 1.14 decades. As we will show below, such a behaviour is exactly found when structurally well-ordered, single crystalline BaLiF$_3$ is investigated by impedance spectroscopy.

d Influence of annealing on σ' and M''. After the last measurement performed at 548 K the sample was let to cool down to room temperature. Then a second run of measurements was started. The corresponding modulus spectra are shown in Fig. 8. It can be seen that after annealing, the shape of $M''(\omega)$ turns out to be nearly independent of temperature. The peaks are all characterized by almost the same width which equals that of the spectrum measured at 548 K of the first run. Interestingly, the positions of the peak maxima did not change. Therefore, analyzing the data of the second run according to eqn (9) yields electrical relaxation rates τ_M^{-1} being very similar to those measured before (see Fig. 7). A third run of measurements did not lead to any further changes of the data. Obviously, the sample was brought into a stable structural state. The changes observed for the first and second run should also show up in the corresponding impedance spectra. For comparison, in Fig. 9(a) the spectra of the second run are compared with those displayed in Fig. 4(b). Note that the respective temperatures of the two runs slightly differ. Whereas at high temperatures the spectra coincide, a remarkable difference shows up at low T when the dispersive regime is regarded. In contrast to the first run, the spectra of the sample exposed to 550 K, can be scaled such that an almost ideal master curve is obtained, *i.e.*, the linear relationship $\sigma_{dc}T \propto \omega_c$ is more and more fulfilled. The spectra can be fitted with power laws characterized by $s \approx 0.4$ depending only slightly on T. This is in fair agreement with $\beta' \approx 0.64$ which can be very roughly related to s *via* $\beta' = 1 - s$.[55]

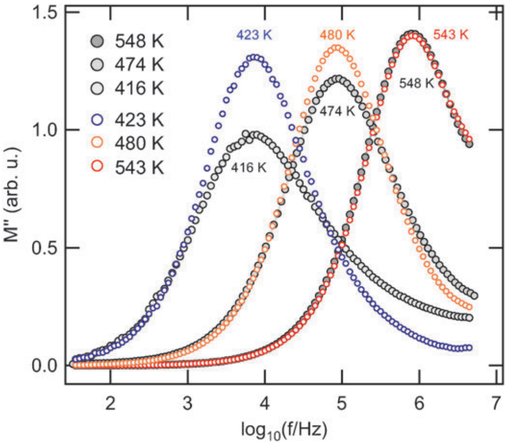

Fig. 8 Repetition of the complex modulus measurements shown in Fig. 6 after the sample was exposed to about 550 K. The curves were recorded at 423 K, 480 K, and 543 K (2nd run). For comparison, some of the curves of Fig. 6, whose peak height depends on T are shown, too. The corresponding relaxation rates τ_M^{-1} are shown in Fig. 7.

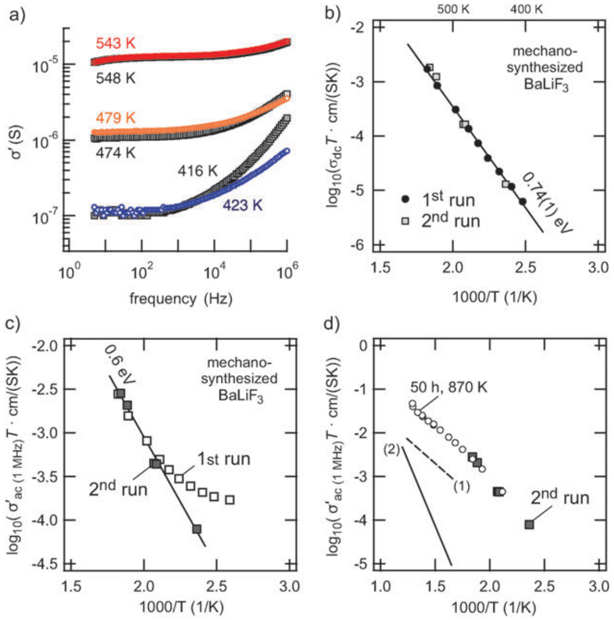

Fig. 9 (a) Impedance spectra of mechanosynthesized BaLiF$_3$ after the sample was exposed to about 500 K. Spectra recorded at 416, 474 and 548 K are those already shown in Fig. 4(b). (b) dc-conductivity of the spectra displayed on the left. For comparison, the data of Fig. 4(c) are shown, too. (c) ac-conductivity ($\sigma'_{\mathrm{ac(1\,MHz)}}T$), read out at 1 MHz, of mechanosynthesized BaLiF$_3$ (1st and 2nd run). (d) Comparison of the ac-conductivity of Fig. 9(c) with that of a mechanosynthesized BaLiF$_3$ sample which was annealed for 50 h at 870 K. For further comparison, $\sigma'_{\mathrm{ac(1\,MHz)}}$ (1) and σ_{dc} (2) of BaLiF$_3$ prepared by solid-state synthesis are also shown. See text for further details.

Expectedly, the scaling behaviour observed for σ' holds also for the corresponding modulus spectra of the second run of measurements. The soft annealing process carried out at 550 K and under N_2 atmosphere does not influence the dc-plateaus. Instead, the thermally induced structural relaxation of the sample mainly affects short-range motions of the charge carriers rather than long-range transport parameters. This can be clearly illustrated when the ac-conductivity σ' is read out at a frequency of 1 MHz and plotted as $\sigma'T$ *vs.* the inverse temperature (Fig. 9(c)). Before annealing at 550 K $\sigma'_{\mathrm{ac(1\,MHz)}}T$ exhibits non-Arrhenius behaviour. This is in contrast to the situation after the sample was exposed to 550 K. The data of the annealed sample follow an Arrhenius law with an

Published on 16 August 2010. Downloaded by TIB und Universitaetsbibliothek Hannover on 24/03/2014 19:26:35.

activation energy of approximately 0.6 eV. It is worth noting in this context that grain growth is not observed when nanocrystalline $BaLiF_3$ is exposed to 550 K for several hours. Most likely, internal strain is released and/or the structure of the material is locally relaxed at elevated temperatures. Interestingly, the effect observed here is less pronounced when t_{mill} is increased from 3 to 20 h. Internal strain seems to be generated in the early stages of milling and is still preserved even after 3 h of mechanical treatment. Obviously, at larger milling times structural relaxation can be induced also mechanically. Recently, such a process was reported for mechanically treated $LiAlSi_2O_6$ glass samples.[61]

Nevertheless, the modulus peaks of structurally disordered, nanocrystalline $BaLiF_3$ prepared by ball milling remain asymmetric in shape. The non-Debye behaviour observed is a clear indication of non-random correlated motions of interacting charge carriers. As shown in the next subsection, this is in contrast to a perfectly ordered single crystal of $BaLiF_3$ where the ions move randomly from site to site.

2. $BaLiF_3$ single crystal—comparison with mechanosynthesized (nanocrystalline) and microcrystalline $BaLiF_3$

a Comparison of σ' *and* M''. Provided the ions do not interact with each other or with their surrounding matrix, $\sigma(\omega)$ will be constant. Indeed, exactly this electrical behaviour is observed for the $BaLiF_3$ single crystal. In Fig. 10 and 11 the data from impedance spectroscopy are shown which were recorded at temperatures ranging from *ca.* 450 K to 720 K. The shape of the complex modulus $M''(\omega)$ (Fig. 11) is independent of temperature and the peak width turned out to be about 1.15 which is in agreement with the expected value for Debye behaviour. Fitting eqn (9) to the $M''(\omega)$ data yields $n_\sigma = 0$ reflecting fully symmetric modulus peaks which clearly indicates that ion hopping in the $BaLiF_3$ crystal is governed by an exponential correlation function which is characteristic of random hopping processes *via* point defects. The same features show up in the corresponding Cole–Cole plots (Fig. 10(a)) and impedance spectra (see Fig. 10(b)). The complex plane representation reveals (perfect) semicircles whose centers lie on the Z'-axis, *i.e.* they can be represented with a single *RC* unit. Expectedly, any dispersive regimes are absent in the impedance spectra at least in the frequency range covered here.

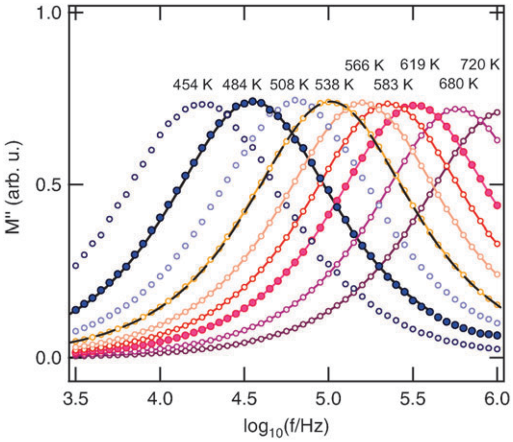

Fig. 11 Frequency dependence of the imaginary part of the electric modulus of single crystalline $BaLiF_3$. The complex modulus curves were recorded at the temperatures indicated. The corresponding relaxation rates τ_M^{-1} are shown in Fig. 10(c). The dashed line shows a fit according to eqn (9). The peaks are fully symmetric leading to an exponent $n_\sigma = 0$.

b dc-conductivity of single crystalline $BaLiF_3$. In Fig. 10(c) $\sigma_{dc}T$ of the single crystal is plotted *vs.* the inverse temperature. The data were recorded starting from the lowest temperature. Interestingly, below 625 K single crystalline $BaLiF_3$ shows a rather high ionic conductivity following an Arrhenius law with an activation energy of only 0.5 eV (Fig. 10(c)). A similar value (see also Fig. 10(c)) is found when the modulus peaks of Fig. 11 are analyzed. For comparison, in Fig. 10(c) the corresponding conductivity relaxation rates $1/\tau_M$ are also included.

Below 660 K σ_{dc} of single crystalline $BaLiF_3$ can be attributed to extrinsic ion conduction. Above 660 K the $\sigma_{dc}T$ values sharply increase. Obviously, the ionic dc-conductivity at higher T is of intrinsic nature with an activation energy of 0.98 eV. Although this behaviour was not observed by the impedance measurements on single crystalline $BaLiF_3$ carried out earlier by Rush *et al.*,[62] it is expected for an undoped, *i.e.*,

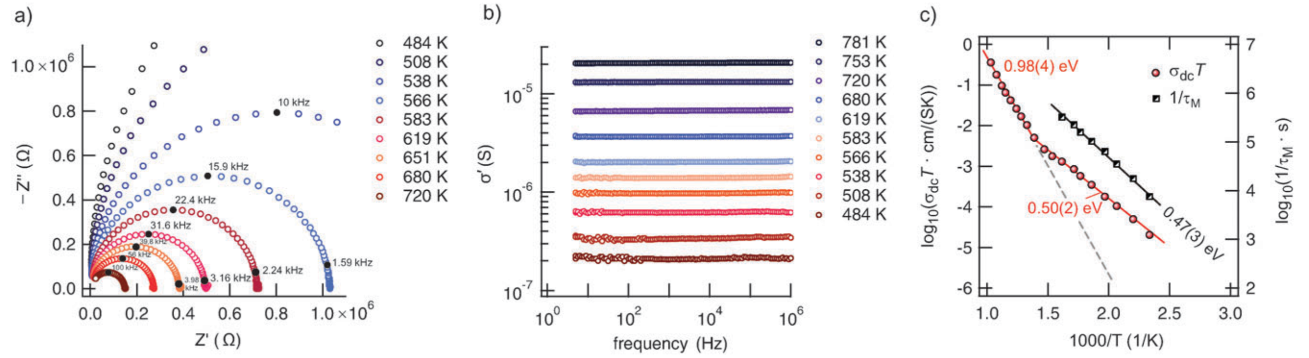

Fig. 10 (a) Cole–Cole plots of single crystalline $BaLiF_3$. The centers of the semicircles lie on the real axis reflecting ideal Debye behavior. From the intercepts at low frequencies (see the arrows in Fig. 4(a)) the resistances can be read out which show the same temperature dependence as the dc-conductivity (see Fig. 10(c)). (b) Corresponding impedance spectra which are, up to a frequency of 1 MHz, composed of dc plateaus, only. (c) $\sigma_{dc}T$ *vs.* $1000/T$. Solid lines represent fits according to $\sigma_{dc}T = \sigma_0\exp(-E_a/(k_BT))$ with the activation energies indicated. For comparison, the electrical relaxation rate τ_M^{-1} deduced from the M'' maxima are shown, too.

Published on 16 August 2010. Downloaded by TIB und Universitaetsbibliothek Hannover on 24/03/2014 19:26:35.

nominally pure ionic crystal. Halide crystals, in particular, may contain heterovalent cations and other impurities leading in the case of $BaLiF_3$ to a variety of impurity-related defects. The two activation energies probed represent the migration (0.50 eV) and the total activation energy (0.98 eV) of the charge carriers, respectively. The latter comprises both the formation activation energy as well as the migration activation energy of the ions due to the permanent lattice defects. Rush *et al.* have shown that doping of $BaLiF_3$ with oxygen anions causes an increase of the ionic conductivity suggesting that the mobile defects are F^- vacancies.[62] They reported an activation energy of 0.50 eV for F^- vacancy migration and 0.55 eV for F^- interstitial migration. The latter was deduced from $BaLiF_3$ crystals doped with Ce^{3+}, which most likely produces F^- interstitials at large Ce^{3+} concentrations. Li vacancies are reported to be formed at low Ce^{3+} concentrations.[63] One might suppose that ion conductivity in the extrinsic region is due to F^- vacancy migration. However, it is worth noting that preliminary ^7Li NMR line shape measurements give evidence that the Li cations are mobile, too. Certainly, it cannot be excluded that F^- vacancies are particularly formed during the crystal-growth process described above. Hence, the observation of an extrinsic dc-conductivity region is not surprising at all. We have observed a slight shift of the extrinsic dc-conductivities towards larger values when the single crystal, which was kept under inert gas atmosphere inside the impedance cell, was exposed to very high temperatures of about 1000 K. Presumably, point defects formed at high T are responsible for the enhanced conductivity in the extrinsic region pointing out that the thermal history of the sample is relevant for its transport behaviour.

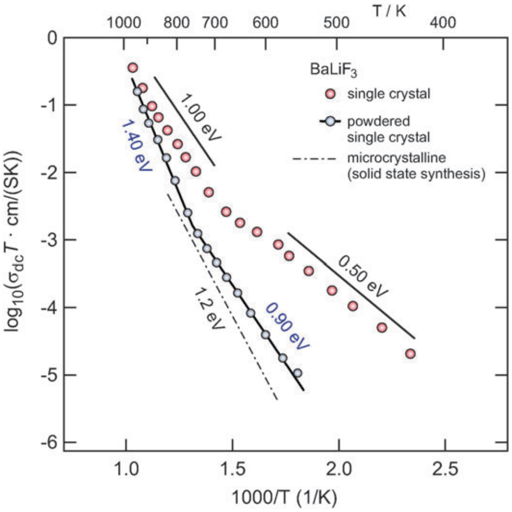

Fig. 12 Temperature dependence of the dc-conductivity of a $BaLiF_3$ sample which was obtained by grinding a small piece of the $BaLiF_3$ single-crystal (*cf.* Fig. 10). For comparison, $\sigma_{dc}(1/T)$ of the single crystal and of a microcrystalline sample, which was prepared by solid-state reaction (see above and Fig. 14), is indicated, too (dashed-dotted line).

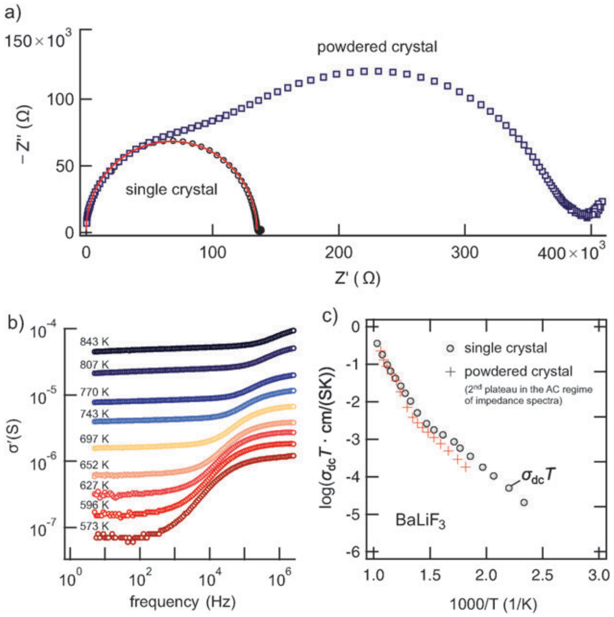

Fig. 13 (a) Cole–Cole (complex plane) plot ($-Z''$ *vs.* Z') of the electrical response of $BaLiF_3$ which was obtained after grinding the single crystal. For comparison, the data of the single crystal is shown, too. The measurement was carried out at 720 K. Whereas the contribution in the low impedance range is due to ion transport in the bulk, the depressed one showing up at larger impedance values can be attributed to blocking grain boundary regions. (b) Impedance spectra of the powdered crystal. (c) Comparison of σ_{dc} with σ' determined from the second frequency-independent plateau of the impedance spectra shown in (b).

c Influence of grain boundaries on ion transport. When the single crystal was ground by hand using an agate mortar and the resulting powder was pressed into a pellet for impedance measurements afterwards, the dc-conductivity clearly decreased as is shown in Fig. 12. Obviously, grain boundaries introduced have a pronounced blocking effect on long-range ionic transport and mask the observation of the fast transport processes in the bulk. The activation energies of both the intrinsic and extrinsic conduction processes increase by about 0.4 eV. From the corresponding complex plane plots as well as the impedance spectra the electrical response resulting from grain boundaries can be clearly differentiated from that which is attributed to ion transport taking place in the bulk material. As an example, in Fig. 13 the Cole–Cole plot of the powdered $BaLiF_3$ crystal is compared with that of the intact single crystal recorded at the same temperature and corrected for the different sample thickness and diameter. In accordance with this plot, the corresponding impedance spectra show another plateau at frequencies larger than 10^5 Hz. The corresponding conductivities σ' of the second plateau are in good agreement with those of the single crystal (see Fig. 10(b)).

Consistently, below 650 K the modulus peaks of the powdered sample exhibit a shallow shoulder located on the low frequency side of $M''(\omega)$. This might be attributed to ions located near the grain boundary regions showing electrical relaxation frequencies in the kHz range. In contrast, the electrical response of the microcrystalline sample which was conventionally prepared by solid-state synthesis (see above, *cf.* Fig. 1(d)) seems to be fully determined by grain boundary effects which drastically limit long-range transport in $BaLiF_3$

Published on 16 August 2010. Downloaded by TIB und Universitaetsbibliothek Hannover on 24/03/2014 19:26:35.

at least below 750 K. The corresponding activation E_a energy turns out to be about 1.2 eV.

d Ionic dc-conductivity of structurally different forms of BaLiF$_3$. For comparison, the temperature dependencies of σ_{dc} of single crystalline BaLiF$_3$, the conventionally prepared counterpart as well as of the mechanosynthesized material are shown in Fig. 14. Although the mechanosynthesized, nanocrystalline material can be characterized by a large volume fraction of grain boundaries, its dc-conductivity is comparable to that of the extrinsic one of the single crystal (450 K $<$ T $<$ 500 K). Obviously, the increased defect concentration in nanocrystalline BaLiF$_3$ introduced by ball milling compensates for the effect of blocking grain boundaries so that long-range transport can occur resulting in an overall high ionic dc-conductivity. Above 500 K the dc-conductivity of the nanocrystalline material even starts to exceed that of the single crystalline material. Compared to the activation energy characterizing intrinsic ion conduction in the single crystal, E_a of the mechanosynthesized sample is by a factor of about 3/4 lower. However, it is worth noting that in many cases the microstructure of the grain boundaries of mechanically treated materials is expected to differ from that of coarse-grained and even structurally well-ordered nanocrystalline materials. Recently, this was shown using LiNbO$_3$ which can be prepared in structurally different forms, too.[20] The dc-conductivity of ball-milled LiNbO$_3$ ($\langle d \rangle$ = 20 nm) is by many orders of magnitude higher than that of the single crystalline LiNbO$_3$ counterpart. Moreover, it is comparable to that of fully X-ray amorphous LiNbO$_3$. High-resolution (HR) TEM and EXAFS measurements gave direct evidence for an amorphous grain boundary structure of the nanocrystalline material which was prepared using a high-energy shaker mill.[20] This is in contrast to a nanocrystalline sample obtained by partial calcination of amorphous LiNbO$_3$. No indications could be found for a large volume fraction of amorphous LiNbO$_3$ in such a sample.[20] In contrast to that result, preliminary HR-TEM images of mechanosynthesized BaLiF$_3$ show that the nm-sized crystallites are covered by a thin amorphous layer of about 2 nm in thickness. Thus, one might assume that once again structurally disordered interfacial regions have to be considered when discussing the observed trends of σ_{dc} presented in Fig. 14.

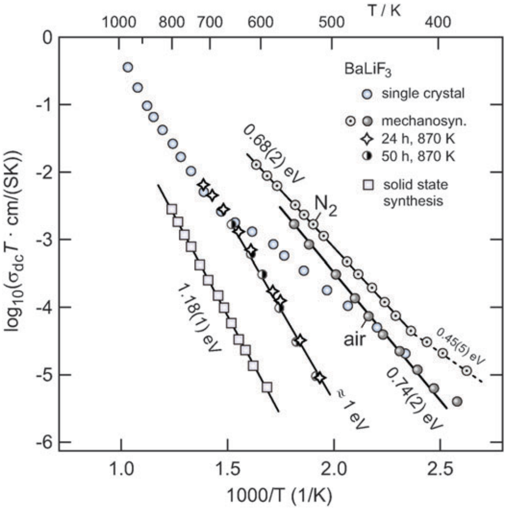

Fig. 14 Temperature dependence of σ_{dc} of single-crystalline, conventionally prepared microcrystalline and mechanosynthesized BaLiF$_3$. For comparison, the σ_{dc} values of mechanically synthesized BaLiF$_3$ which was annealed for 24 and 50 h, respectively, are also shown. Solid lines show fits according to an Arrhenius law (*cf.* eqn (6)).

For the sake of completeness, the dc-conductivity values of mechanosynthesized BaLiF$_3$ which was annealed for some tens of hours at elevated temperature are included in Fig. 14, too. The samples annealed at 870 K for 24 h and 50 h, respectively, have average crystallite diameters with values in the μm range (see the corresponding XRD-pattern of the sample annealed for 24 h in Fig. 1). The activation energies E_a found are very similar and amount to be about 1.0 eV, thus, almost identical with that one of intrinsic conduction in single crystalline BaLiF$_3$. Preliminary TEM micrographs reveal that the annealed samples consist of μm-sized particles which are sintered together forming relatively large interconnected cluster assembled agglomerates.

Annealing a mechanosynthesized sample at 1020 K for 5 h resulted in an additional decrease of σ_{dc} finally reaching the ionic conductivity of the microcrystalline material as expected. It is worth mentioning that an increase of the uniaxial pressure applied to prepare dense impedance pellets by about a factor of four does not lead to any changes of the conductivity results of the annealed samples. Thus, the lower conductivity found for the annealed samples cannot be interpreted in terms of the samples' package densities.

Interestingly, ac-conductivities read out at 1 MHz, see Fig. 9, reveal that short range ion motions in the nanocrystalline as prepared sample are very similar to those of the annealed one which was heated at, *e.g.*, for 50 h at 870 K. This indicates a comparable and relatively high bulk conductivity of the two samples which is characterized by an activation energy of about 0.6 eV (see above).

Note that both ball milling and annealing of the materials were carried out in air atmosphere. As mentioned above, one might expect that if oxygen incorporation occurs this would lead to an increase of the dc-conductivity presumably due to the formation of vacant fluorine positions. To explore this, we have mechanosynthesized BaLiF$_3$ under inert gas atmosphere, too. Remarkably, a slight enhancement of σ_{dc} by a factor of approximately two is found (see Fig. 14) rather than a decrease. Accordingly, the activation energy is reduced to 0.68 eV. Careful inspection of the σ_{dc} values of the sample prepared under inert gas atmosphere reveals a slight deviation from Arrhenius behaviour below 410 K (see dotted line in Fig. 14). It has still to be checked if this is caused by extrinsic ion conduction. For comparison with the data of the single crystal, the activation energy corresponding to the dashed line in Fig. 14 turns out to be 0.45(5) eV. In order to confirm or rule out such a contribution, an impedance analyzer being able to detect dc-conductivities smaller than 10^{-7} S will be employed.

Finally, preliminary impedance measurements show that by appropriate doping of mechanosynthesized BaLiF$_3$ with Sr^{2+}, which can be easily carried out by milling a mixture consisting of BaF$_2$, SrF$_2$, and LiF, the electric conductivity can be further

Published on 16 August 2010. Downloaded by TIB und Universitaetsbibliothek Hannover on 24/03/2014 19:26:35.

increased by one order of magnitude. Details about $BaLiF_3$ samples modified in such a way will be reported in a subsequent paper.

IV. Summary and conclusion

$BaLiF_3$ served as an interesting model system to study the effects of nanostructuring and structural disorder on long-range as well as short-range ion motions in solids. It belongs to one of the rare fluorides which crystallize with the *anti*-perovskite structure. Nanocrystalline samples can be prepared with high purity by high-energy ball milling of a stoichiometric mixture of LiF and BaF_2. Mechanical treatment of the binary source materials for 3 h in a planetary mill at 600 rpm yields $BaLiF_3$ nano-crystallites with a mean diameter of approximately 30 nm. Interestingly, the Arrhenius-type dc-conductivity of the mechanosynthesized product is by four orders of magnitude higher than that of conventionally prepared $BaLiF_3$ with µm-sized crystallites. Accordingly, the activation energy E_a of the nanocrystalline sample is much smaller than that of the coarse-grained counterparts including also samples which were obtained by appropriate heat-treatment of the as prepared mechanosynthesized material. It was shown that both ball-milling and subsequent annealing allow the adjustment of desired transport parameters over a dynamic range of some decades. Such a knowledge-based controlling of transport properties is essential for the design of new functional materials.

The influence of grain boundary regions on ion transport was studied by comparing with a single crystal, which shows a relatively high extrinsic ionic conductivity from the outset. Single crystalline $BaLiF_3$ shows two conductivity regions which can be ascribed to intrinsic and extrinsic ionic transport. As expected, the respective activation energies differ by about a factor of two reflecting the migration activation energy and the total activation energy. The latter comprises both the migration as well as the formation activation energy of the charge carriers. In the powdered sample the extrinsic conductivity region starts to be masked by grain boundary effects obviously limiting ion transport in the inverse perowskite structure of $BaLiF_3$. These seem to have a non-blocking character in the case of mechanically prepared, nanocrystalline $BaLiF_3$ with a large amount of interfacial regions and grain boundaries. The blocking character reappears when the nanocrystalline sample is annealed at higher temperatures. It became obvious that the microstructure of a material with a given chemical composition can have a drastic effect on its ionic transport parameters, see also ref. 21,64–67.

It will be a challenge to study the structural details of the different samples from a microscopic point of view. For this purpose NMR measurements, see, *e.g.*, ref. 21,68–72, are underway which are suitable to study Li and F diffusion parameters separately from each other.

Acknowledgements

We are very grateful to S.L. Baldochi and I.M. Ranieri, Center for Laser and Applications of IPEN in São Paulo (Brazil) for the pre-treatment of the starting material for the crystal growth process. We thank A. Feldhoff and F. Steinbach (Leibniz University Hannover) for preliminary TEM investigations. Financial support by the Deutsche Forschungsgemeinschaft (DFG) within the frame of the Priority Program SPP 1415 is highly acknowledged.

References

1 J. C. Boivin and G. Mairesse, *Chem. Mater.*, 1998, **10**, 2870.
2 D. A. Keen, *J. Phys.: Condens. Matter*, 2002, **14**, R819.
3 S. Stølen, E. Bakken and C. E. Mohn, *Phys. Chem. Chem. Phys.*, 2006, **8**, 429.
4 P. Heitjans and S. Indris, *J. Phys.: Condens. Matter*, 2003, **15**, R1257.
5 V. Thangadurai and W. Weppner, *Ionics*, 2006, **12**, 81.
6 S. Hull, *Rep. Prog. Phys.*, 2004, **67**, 1233.
7 V. V. Kharton, F. M. B. Marques and A. Atkinson, *Solid State Ionics*, 2004, **174**, 135.
8 A. S. Aricò, P. G. Bruce, B. Scrosati, J.-M. Tarascon and W. V. Schalkwijk, *Nat. Mater.*, 2005, **4**, 366.
9 P. G. Bruce, B. Scrosati and J.-M. Tarascon, *Angew. Chem., Int. Ed.*, 2008, **47**, 2930.
10 S. Chandra, *Superionic Solids, Principles and Applications*, North-Holland, Amsterdam, 1981.
11 *Lithium Ion Batteries*, ed. M. Wakihara and O. Yamamoto, Wiley-VCH, Weinheim, 1998.
12 M. Whittingham, *Chem. Rev.*, 2004, **104**, 4271.
13 J.-M. Tarascon and M. Armand, *Nature*, 2001, **414**, 359.
14 M. Armand and J.-M. Tarascon, *Nature*, 2008, **451**, 652.
15 C. Xu, J. Tamaki, N. Miura and N. Yamazoe, *Sens. Actuators, B*, 1991, **3**, 147.
16 S. Davis, A. V. Chadwick and J. D. Wright, *J. Mater. Chem.*, 1998, **8**, 2065.
17 G. A. Niklasson and C. G. Granqvist, *J. Mater. Chem.*, 2007, **17**, 127.
18 J. Maier, *Nat. Mater.*, 2005, **4**, 805.
19 J. Maier, *J. Electroceram.*, 2004, **13**, 593.
20 P. Heitjans, M. Masoud, A. Feldhoff and M. Wilkening, *Faraday Discuss.*, 2007, **134**, 67.
21 M. Wilkening, V. Epp, A. Feldhoff and P. Heitjans, *J. Phys. Chem. C*, 2008, **112**, 9291.
22 M. Masoud and P. Heitjans, *Defect Diffus. Forum*, 2005, **237–240**, 1016.
23 M. Wilkening, D. Bork, S. Indris and P. Heitjans, *Phys. Chem. Chem. Phys.*, 2002, **4**, 3246.
24 D. Bork and P. Heitjans, *J. Phys. Chem. B*, 2001, **105**, 9162.
25 D. Bork and P. Heitjans, *J. Phys. Chem. B*, 1998, **102**, 7303.
26 A. Boumriche, J. Y. Gesland, A. Bulou, M. Rousseau, J. L. Fourquet and B. Hennion, *Solid State Commun.*, 1994, **91**, 125.
27 S. A. Korba, H. Meradji, S. Ghemid and B. Bouhafs, *Comput. Mater. Sci.*, 2009, **44**, 1265.
28 V. Luaña, A. Costales, M. Pendãs, M. Flórez and V. M. G. Fernàndez, *Solid State Commun.*, 1997, **104**, 47.
29 A. Bensalah, K. Shimamura, T. Fujita, H. Sato, M. Nikl and T. Fukuda, *J. Alloys Compd.*, 2003, **348**, 258.
30 B. Kubias, M. J. G. Fait and R. Schlögl, *Mechanochemical Methods*, in *Handbook of Heterogeneous Catalysis*, ed. G. Ertl, H. Knözinger, F. Schüth and J. Weitkamp, Wiley-VCH, Weinheim, 2008, vol. 1.
31 E. Avvakumov, M. Senna and N. Kosova, *Soft Mechanochemical Synthesis: A Basis for New Chemical Technologies*, Kluwer Academic Publishers, Boston, 2001.
32 V. Šepelák, I. Bergmann, A. Feldhoff, P. Heitjans, F. Krumeich, D. Menzel, F. J. Litterst, S. J. Campbell and K. D. Becker, *J. Phys. Chem. C*, 2007, **111**, 5026.
33 V. Šepelák, K. D. Becker, I. Bergmann, S. Suzuki, S. Indris, A. Feldhoff, P. Heitjans and C. P. Grey, *Chem. Mater.*, 2009, **21**, 2518.
34 S. Baldochi, A. Santo, E. Martins, M. Duarte, M. Vieira, N. Vieira and S. Morato, *J. Cryst. Growth*, 1996, **166**, 375.
35 S. Baldochi, K. Shimamura, K. Nakano, N. Mujilatu and T. Fukuda, *J. Cryst. Growth*, 1999, **200**, 521.

Published on 16 August 2010. Downloaded by TIB und Universitaetsbibliothek Hannover on 24/03/2014 19:26:35.

36 M. Mortier, J. Gesland, M. Rousseau, F. Auzel and D. Meichenin, *Rad. Eff. Def. Solids*, 1995, **136**, 975.

37 A. Santo, S. Morato and S. Baldochi, *J. Cryst. Growth*, 1999, **203**, 156.

38 A. Goto, T. Shimizu, R. Miyabe, K. Hashi, H. Kitazawa, G. Kido, K. Shimamura and T. Fukuda, *Appl. Phys. A: Mater. Sci. Process.*, 2002, **74**, 73.

39 S. Baldochi, V. Mazzocchi, C. Parente and S. Morato, *Mater. Res. Bull.*, 1994, **29**, 1321.

40 Y. Tan and C. Shi, *J. Solid State Chem.*, 2000, **150**, 178.

41 H. Swanson, H. McMurdie, M. Morris and E. Evans, *Natl. Bur. Stand.;(U.S.), Monogr.*, 1967, **25**, 35.

42 P. Scherrer, *Göttinger Nachrichten*, 1918, **2**, 98.

43 G. K. Williamson and W. H. Hall, *Acta Metall.*, 1953, **1**, 22.

44 B. Ruprecht, M. Wilkening, S. Steuernagel and P. Heitjans, *J. Mater. Chem.*, 2008, **18**, 5412.

45 J. M. Leger, J. Haines, A. Atouf, O. Schulte and S. Hull, *Phys. Rev. B: Condens. Matter*, 1995, **52**, 13247.

46 V. Kanchana, G. Vaitheeswaran and M. Rajagopalan, *J. Alloys Compd.*, 2003, **359**, 66.

47 B. Ruprecht, M. Wilkening, A. Feldhoff, S. Steuernagel and P. Heitjans, *Phys. Chem. Chem. Phys.*, 2009, **11**, 3071.

48 M. Body, G. Silly, C. Legein and J. Buzaré, *J. Phys. Chem. B*, 2005, **109**, 10270.

49 *Impedance Spectroscopy—Theory, Experiment and Applications*, ed. E. Barsoukov and J. R. MacDonald, Wiley & Sons Hoboken, New Jersey, 2005.

50 D. L. Sidebottom, *Rev. Mod. Phys.*, 2009, **81**, 999.

51 I. Hodge, M. Ingram and R. West, *J. Electroanal. Chem.*, 1976, **74**, 125.

52 P. Macedo, C. Moynihan and R. Bose, *Phys. Chem. Glasses*, 1972, **13**, 171.

53 B. Roling, A. Happe, K. Funke and M. D. Ingram, *Phys. Rev. Lett.*, 1997, **78**, 2160.

54 K. Funke, C. Cramer and D. Wilmer, in *Diffusion in Condensed Matter—Methods, Materials, Models*, ed. P. Heitjans and J. Kärger, Springer, Berlin, 2005, ch. 9, pp. 857–893.

55 D. Sidebottom, P. Green and R. Brow, *J. Non-Cryst. Solids*, 1995, **183**, 151.

56 K. Ngai and O. Kanert, *Solid State Ionics*, 1992, **53–56**, 936.

57 C. Moynihan, *J. Non-Cryst. Solids*, 1994, **172–174**, 1395.

58 K. Ngai, *Solid State Ionics*, 1981, **5**, 27.

59 C. Moynihan, L. Boesch and N. Laberge, *Phys. Chem. Glasses*, 1973, **14**, 122.

60 I. Hodge, K. Ngai and C. Moynihan, *J. Non-Cryst. Solids*, 2005, **351**, 104.

61 A. Kuhn, M. Wilkening and P. Heitjans, *Solid State Ionics*, 2009, **180**, 302.

62 G. Rush, A. Chadwick, R. Jackson, M. Valerio and J. De Lima, *Radiat. Eff. Defects Solids*, 2001, **155**, 393.

63 Y. Tan and C. Shi, *J. Solid State Chem.*, 2000, **150**, 178.

64 M. Wilkening, A. Kuhn and P. Heitjans, *Phys. Rev. B: Condens. Matter Mater. Phys.*, 2008, **78**, 054303.

65 A. V. Chadwick and S. Savin, *Solid State Ionics*, 2006, **177**, 3001.

66 M. Pooley and A. Chadwick, *Radiat. Eff. Defects Solids*, 2003, **158**, 197.

67 D. T. Shane, R. L. Corey, R. C. Bowman, Jr., R. Zidan, A. C. Stowe, S.-J. Hwang, C. Kim and M. S. Conradi, *J. Phys. Chem. C*, 2009, **113**, 18414.

68 M. Wilkening, C. Lyness, A. R. Armstrong and P. G. Bruce, *J. Phys. Chem. C*, 2009, **113**, 4741.

69 M. Wilkening, J. Heine, C. Lyness, A. R. Armstrong and P. G. Bruce, *Phys. Rev. B: Condens. Matter Mater. Phys.*, 2009, **80**, 064302.

70 P. Heitjans and M. Wilkening, *Mat. Res. Soc. Bull.*, 2009, **34**, 915.

71 M. Wilkening, S. Indris and P. Heitjans, *Phys. Chem. Chem. Phys.*, 2003, **5**, 2225.

72 M. Wilkening, C. Mühle, M. Jansen and P. Heitjans, *J. Phys. Chem. B*, 2007, **111**, 8691.

This journal is © the Owner Societies 2010

Solid State Ionics 184 (2011) 65–69

Contents lists available at ScienceDirect

Solid State Ionics

journal homepage: www.elsevier.com/locate/ssi

Ion conduction and dynamics in mechanosynthesized nanocrystalline $BaLiF_3$

A. Düvel [a,b,*], M. Wilkening [a,b,*], S. Wegner [c], A. Feldhoff [a,b], V. Šepelák [b,d], P. Heitjans [a,b]

[a] *Institute of Physical Chemistry and Electrochemistry, Leibniz University Hannover, Callinstr. 3a, D-30167 Hannover, Germany*
[b] *Center for Solid State Chemistry and New Materials (ZFM), Leibniz University Hannover, Germany*
[c] *Bruker BioSpin GmbH, D-76287 Silberstreifen, Germany*
[d] *Institute of Nanotechnology, Karlsruhe Institute of Technology, Herrmann-von-Helmholtz-Platz 1, D-76344 Eggenstein-Leopoldshafen, Germany*

ARTICLE INFO

Article history:
Received 17 May 2010
Received in revised form 18 May 2010
Accepted 27 August 2010
Available online 28 September 2010

Keywords:
Mechanochemistry
Milling
Nanocrystalline
Impedance spectroscopy
Conductivity
Solid state NMR

ABSTRACT

Highly pure nanocrystalline $BaLiF_3$ (space group $Pm\bar{3}m$, inverse perovskite structure) with a mean crystallite size of the order of 30 nm was mechanosynthesized from the binary fluorides LiF and BaF_2. The source materials with µm-sized crystallites were treated in a planetary mill for several hours at ambient temperature. The product is characterized by X-ray diffraction and transmission electron microscopy. Its ionic conductivity was probed by solid state impedance spectroscopy. For comparison, a coarse-grained sample of $BaLiF_3$ with a mean crystallite diameter in the µm range was synthesized by conventional high-temperature ceramic synthesis. The ionic conductivity (dc) of the mechanosynthesized nanocrystalline sample, which is characterized by a large fraction of interfacial regions, is by about three orders of magnitude ($T=570$ K) larger than that of the conventionally prepared one. Preliminary temperature-variable ^{7}Li NMR spectra provide first insights into the Li dynamics of the samples studied.

© 2010 Elsevier B.V. All rights reserved.

1. Introduction

Nanocrystalline ceramics [1,2], which show fast ionic conduction, increasingly play an important role in the development of sustainable energy storage systems, chemical sensors or advanced electrochromic devices [3–7]. The investigation of ion transport in materials with the same chemical composition but different crystallite sizes and microstructures might inter alia help to understand the influence of interfacial effects on dynamic properties [8–11]. Such a knowledge is crucial for the development of new functional materials.

Recently, it has been shown that the Li ion conductivity in lithium tantalate ($LiTaO_3$), which was used as a model substance to study the influence of structural disorder on ionic transport, can be increased by several orders of magnitude when the coarse-grained source material is treated for several hours in a high-energy ball mill [8]. Similar results are obtained for other materials such as lithium niobate ($LiNbO_3$) [9,10] or the binary fluorides BaF_2 and CaF_2 which form a highly defective nanocrystalline mixed phase (Ba, Ca)F_2 when milled together [12,13].

The ternary fluoride $BaLiF_3$ crystallizing with the space group $Pm\bar{3}m$ (inverse perovskite structure) [14] is another interesting model system to study ionic transport in a ceramic which can be prepared in a nano- and microcrystalline as well as single crystalline form [15]. In the present study nanocrystalline $BaLiF_3$ was mechanosynthesized from LiF and BaF_2 using a high-energy planetary mill at ambient temperature. Its ionic conductivity (dc), which was measured by impedance spectroscopy, exceeds that of the microcrystalline counterpart by nearly three orders of magnitude. This might be ascribed to the large fraction of interfacial regions providing fast diffusion pathways of the ions as well as the large amount of defects introduced by ball milling. Remarkably, the material is relatively stable against grain growth up to approximately 550 K so that the high ion conductivity is preserved even at elevated temperatures.

2. Experimental

2.1. Preparation of $BaLiF_3$

Nanocrystalline $BaLiF_3$ was prepared by high-energy ball milling of an equimolar mixture of LiF (99.99%, Alfa Aesar) and BaF_2 (99.99%, Sigma Aldrich) in a Fritsch Pulverisette 7 (premium line). A grinding beaker made of stabilized ZrO_2 (45 mL) and 140 balls (5 mm in diameter) of the same material were used. The mixture was milled for $t_{mix}=180$ min with 600 rpm under ambient atmosphere. A part of the so obtained material was pressed to pellets with a diameter of 8 mm by applying a uniaxial pressure of 1 GPa. After that these pellets were annealed at 870 K in air for 24 h.

For comparison, a sample of $BaLiF_3$ was prepared by conventional solid state synthesis [16]. To this end an equimolar mixture of BaF_2 and LiF was initially milled for 10 min at 600 rpm under air. After heating the mixture for 3 h at 620 K for drying purpose it was fired at 1020 K for 5 h. The complete synthesis was strictly done under N_2

---

* Corresponding authors. Institute of Physical Chemistry and Electrochemistry, Leibniz University Hannover, Callinstr. 3a, D-30167 Hannover, Germany. Tel.: +49 511 762 5293; fax: +49 511 762 19121.
E-mail addresses: duevel@pci.uni-hannover.de (A. Düvel), wilkening@pci.uni-hannover.de (M. Wilkening).

0167-2738/$ – see front matter © 2010 Elsevier B.V. All rights reserved.
doi:10.1016/j.ssi.2010.08.025

atmosphere. It has to be mentioned that the conventional synthesis is disadvantageous compared to the one-step mechanochemical routine. Since Li starts to evaporate at high temperatures it needed several attempts to find a tolerable mixing ratio close to LiF:BaF_2. Nevertheless this synthesis route leads to a less pure and less stoichiometric product.

2.2. XRD, TEM, impedance and NMR measurements

The characterization of the samples was carried out at room temperature using X-ray diffraction (XRD) with a Philips PW 1800 operating with Cu-Kα radiation at 40 kV. An HP 4192 A analyzer connected to a home-built cell was employed to record the impedance data. Frequencies investigated ranged from 5 Hz to 13 MHz. Conductivity jigs with a four terminal configuration were used. The samples were pressed to cylindrical pellets (8 mm in diameter, about 1 mm in thickness) with a uniaxial pressure of about 1 GPa. Electrodes were applied by subsequent pressing the uncoated pellet between Pt powder. During the measurements the pellet was kept under inert gas atmosphere by using a constant flow of dry nitrogen (99.999%).

^{19}F magic angle spinning (MAS) NMR spectra were acquired with a Bruker Avance III 500 wideband spectrometer operating at a radio frequency of 471 MHz. The spectra were recorded using a single excitation pulse (pulse length $\pi/2 = 2$ µs) at an ultra-fast spinning speed of 60 kHz. Static ^{7}Li NMR spectra were recorded with a Bruker MSL 400 spectrometer connected to a shimmed Oxford cryomagnet with a fixed field of 9.4 T corresponding to a ^{7}Li resonance frequency of 155 MHz. The $\pi/2$ pulse length was about 3 µs.

For transmission electron microscope (TEM) investigations, a powder specimen was dispersed in ethanol, and a drop of 10 µL of suspension was dried on a copper-supported holey carbon film. (Scanning) transmission electron microscopy (S)TEM was made at 200 kV on a field-emission instrument of the type JEOL JEM-2100F-UHR in bright-field, dark-field, and phase contrasts.

3. Results and discussion

In Fig. 1 the XRD patterns of the samples investigated are shown. $BaLiF_3$ is the only phase which is formed by high-energy ball milling a stoichiometric mixture of LiF and BaF_2. Compared to the sample prepared by solid state synthesis, which shows a small amount of residual BaF_2 [17], the mechanosynthesized product is remarkably pure. As expected, the XRD peaks of the nanocrystalline material are broadened due to size effects and strain. Disregarding the latter, a mean crystallite size of approximately 30 nm can be roughly estimated using the equation introduced by Scherrer [18]. Details for such an estimation in a similar system can be found elsewhere [12]. Annealing the nanocrystalline material at 870 K for 24 h causes a decrease of the diffraction peak widths leading to crystallites with diameters in the µm range. Interestingly, the XRD peak widths of this annealed sample are even smaller than those of the material which was prepared by solid state synthesis, i.e., fired for 5 h at about 1020 K.

The particle sizes determined from TEM micrographs (see Fig. 2) are in fair agreement with the values deduced from XRD peak broadening. The nanocrystalline sample consists of cluster-assembled particles whose diameters range from 50 to 100 nm. A significant amount of amorphous material is not observed. However, the particles seem to be covered with an amorphous-like layer with a thickness of only 1 nm, see the high-resolution (HR) TEM micrograph in Fig. 3. In contrast to that, the TEM image of the annealed sample reveals a homogenous material consisting of µm-sized particles being interconnected to each other, while those of the sample prepared by solid state synthesis are characterized by a large distribution of different sizes ranging from some tens of nanometer to some µm. However, the volume fraction of µm-sized particles clearly dominates as compared to that of the nano-particles. The presence of very small crystallites next to larger ones points to an unfinished Ostwald ripening process, i.e., larger particles grow on expense of the smaller ones in order to minimize the energy of the system [19]. Let us mention that it is known for some materials that annealing of a metal or ceramic powder consisting of particles with diameters in the range of some nanometers leads to microcrystalline materials with improved properties such as hardness and ductility [20–22]. Here, annealing of mechanosynthesized nanocrystalline $BaLiF_3$ seems to represent an interesting synthesis route to obtain µm-sized and uniformly shaped crystallites.

Further characterization of the samples was carried out by ^{19}F MAS NMR. Corresponding spectra are shown in Fig. 4. Expectedly, $BaLiF_3$ shows only a single NMR line whose isotropic chemical shift δ is 66 ppm when referenced to C_6F_6. This is in perfect agreement with the value reported in the literature [23]. Compared to the sample which

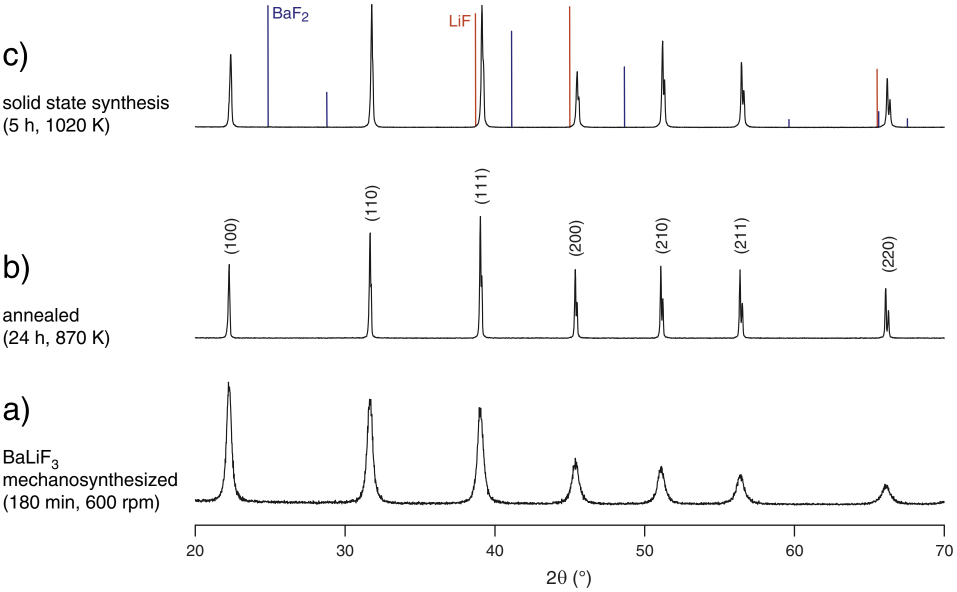

Fig. 1. X-ray powder diffraction patterns of a) mechanosynthesized nanocrystalline $BaLiF_3$, b) the mechanosynthesized sample after annealing for 24 h at 870 K and c) the sample prepared by solid state synthesis at higher temperature. Vertical lines indicate the positions and intensities of the XRD peaks of the source materials BaF_2 and LiF, respectively.

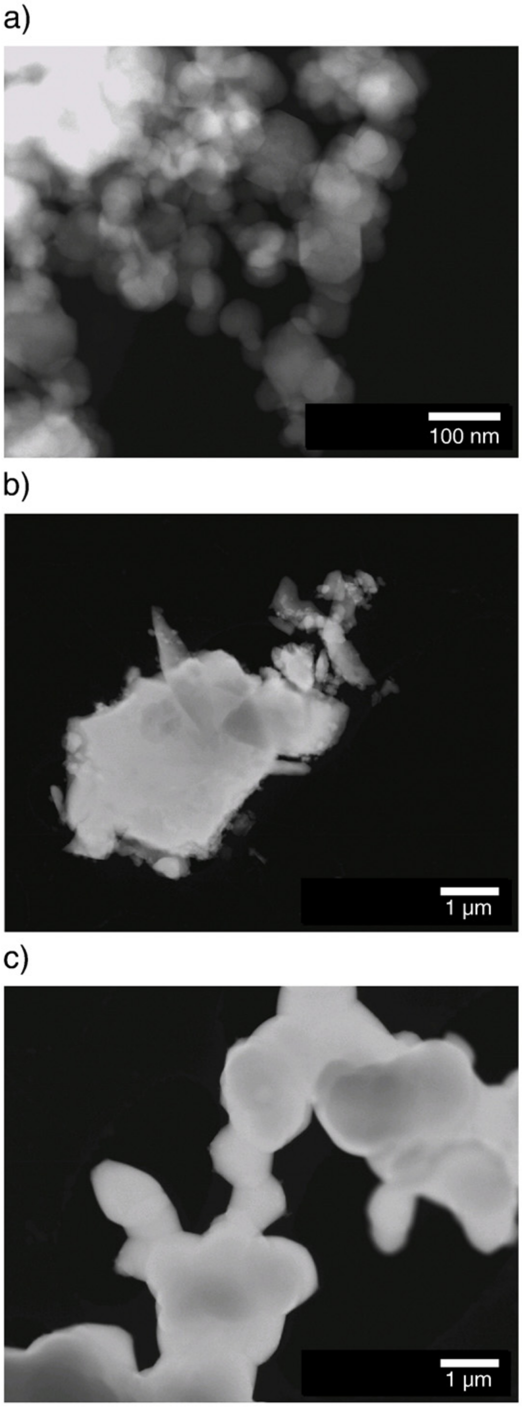

Fig. 2. STEM micrographs of a) mechanosynthesized $BaLiF_3$, b) a sample prepared by solid state synthesis at 1020 K and c) the annealed material.

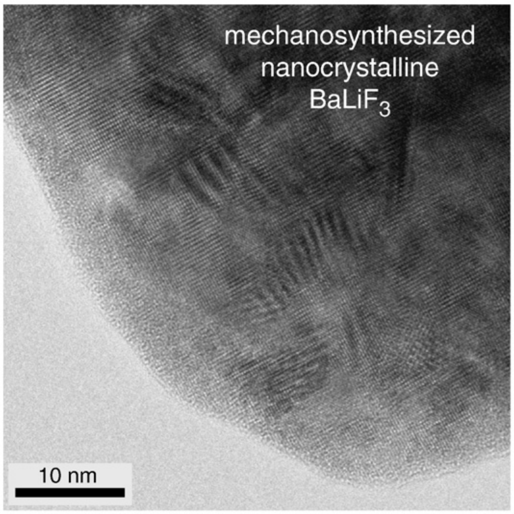

Fig. 3. HR-TEM micrograph of nanocrystalline $BaLiF_3$ which was prepared in a planetary mill from a stoichiometric mixture of LiF and BaF_2.

was annealed for 24 h, the ^{19}F MAS NMR line width of the nanocrystalline material is broadened indicating a large distribution of slightly different chemical environments of the F ions. This unequivocally points to a material with a large number density of structural defects.

In Fig. 5 the temperature dependence of the dc conductivity σ_{dc} of mechanosynthesized $BaLiF_3$, its annealed counterpart as well as that prepared by conventional solid state synthesis are shown in an Arrhenius plot. σ_{dc} values were determined from the frequency independent plateau of the corresponding impedance spectra. The mechanosynthesized sample shows the highest dc conductivity with an activation energy E_a of 0.74(1) eV. After annealing, σ_{dc} decreases by about 1.5 orders of magnitude and E_a increases to 1.04(3) eV. The sample prepared by solid state synthesis exhibits a dc conductivity which is about three orders of magnitude ($T = 560$ K) lower than that of the sample prepared by ball milling. Accordingly, it shows the highest activation energy ($E_a = 1.18(1)$ eV). Regarding the TEM micrographs presented above, it seems reasonable that the lower dc conductivity of the conventionally prepared material is caused by grain boundaries blocking long-range ionic transport (see also Ref. [17]). Let us note that annealing the mechanosynthesized sample for 5 h at 1020 K leads to a microcrystalline material whose σ_{dc} values are very similar to those obtained for the material prepared conventionally.

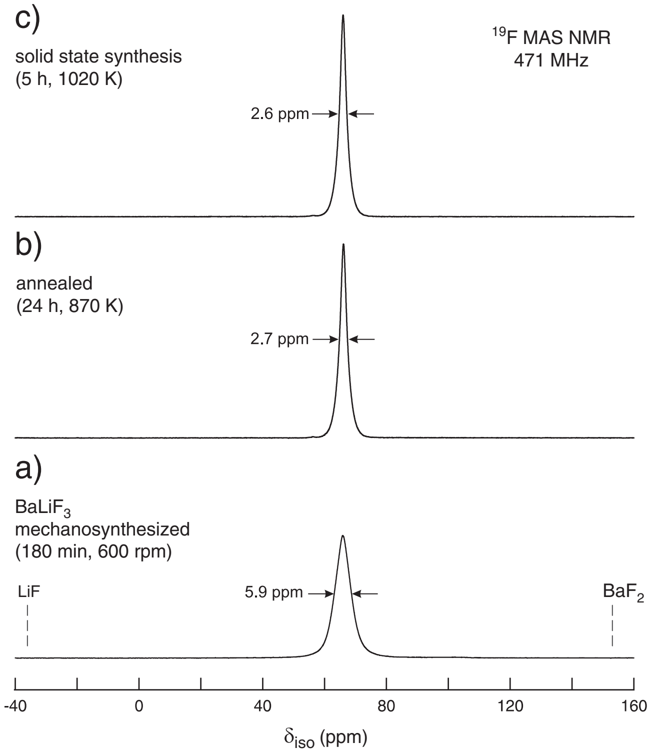

Fig. 4. ^{19}F MAS NMR spectra of the three samples investigated. Spectra were recorded at 471 MHz and a spinning speed of 60 kHz. Only a single NMR line shows up at $\delta_{iso} = 66$ ppm proving the high purity of the samples prepared. Dashed lines indicate chemical shifts of the starting materials BaF_2 and LiF, respectively. See text for further details.

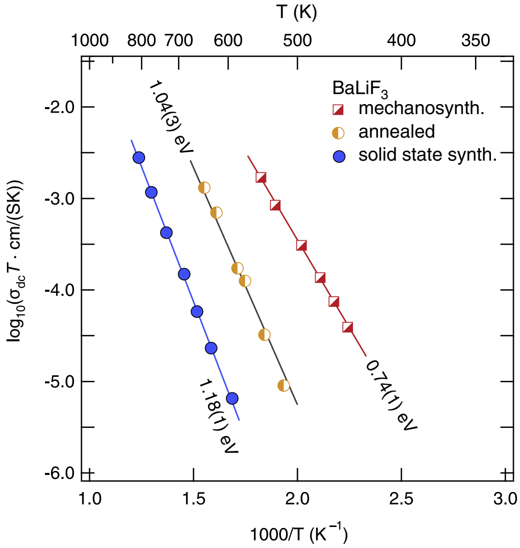

Fig. 5. Arrhenius diagram of the dc conductivity plotted as $\sigma_{dc}T$ vs. the inverse temperature of mechanosynthesized $BaLiF_3$ as well as its annealed counterpart. For comparison, data of the sample synthesized via a ceramic route is also shown.

Although the mechanosynthesized sample is characterized by a large volume fraction of grain boundaries and interfacial regions its dc conductivity is higher than those found for the other two samples. Therefore, it seems reasonable that the interfacial regions, in contrast to those of the samples with μm-sized crystallites, provide pathways for fast ion transport. Most likely, these regions are characterized by a large number fraction of defects introduced by mechanical treatment.

In Fig. 6 temperature-variable ^{7}Li NMR spectra recorded at a resonance frequency of 155 MHz are shown. The spectra were obtained by Fourier transformation of the free induction decay which is obtained after excitation of the sample with a single radio frequency pulse. Due to the cubic symmetry of $BaLiF_3$ quadrupole intensities are absent although ^{7}Li is a spin-3/2 nucleus. In the case of the mechanosynthesized sample NMR echo techniques may be helpful to detect Li ions residing in distorted polyeder with lower symmetry. Presumably, such quadrupole intensities are expected for those Li ions residing near or in the interfacial regions of the nanocrystalline sample. Here, we will restrict ourselves to discuss the central transition only. At low temperatures the NMR lines of all three samples are dipolarly broadened due to ^{7}Li–^{7}Li as well as ^{7}Li–^{19}F interactions. In the so-called rigid-lattice regime the line width Δ (full width at half maximum) is of the order of 8 kHz. It is worth mentioning that the NMR line shape of a powder sample of $BaLiF_3$ significantly deviates from a pure Gaussian. This can be explained regarding the investigation of Goto et al. who recorded NMR line widths of a $BaLiF_3$ single crystal as a function of its orientation in the static magnetic field [24]. The observed line shape here for a powder sample is the superposition of the NMR lines shown by Goto et al [24].

In general, with increasing temperature Li diffusivity increases and the mean jump rate reaches the order of the rigid-lattice value of Δ. Consequently, Δ decreases due to averaging of dipole–dipole interactions [25]. Therefore, the NMR line shows the typical motional narrowing due to Li jumps with rates of the order of $10^{-4}\,s^{-1}$ [26]. Finally, at sufficiently high temperatures the line width is solely determined by the inhomogeneity of the static magnetic field used (extreme narrowing regime). Motional line narrowing is clearly seen for the sample prepared conventionally (Fig. 6c) as well as for that which was mechanosynthesized but annealed at higher temperatures (Fig. 6b). More precisely, the conventionally prepared sample exhibits a so-called heterogeneous motional narrowing. For comparison, it shows a heterogeneous distribution of crystallite sizes. For example, at $T = 510$ K the ^{7}Li NMR line is composed of a broad and narrow contribution (Fig. 6c). The latter increases with increasing T reaching an area fraction of about 45% at 630 K. In contrast, the NMR line of the annealed sample is composed of only a single Lorentzian shaped NMR line at this temperature. Motional narrowing of this sample seems to

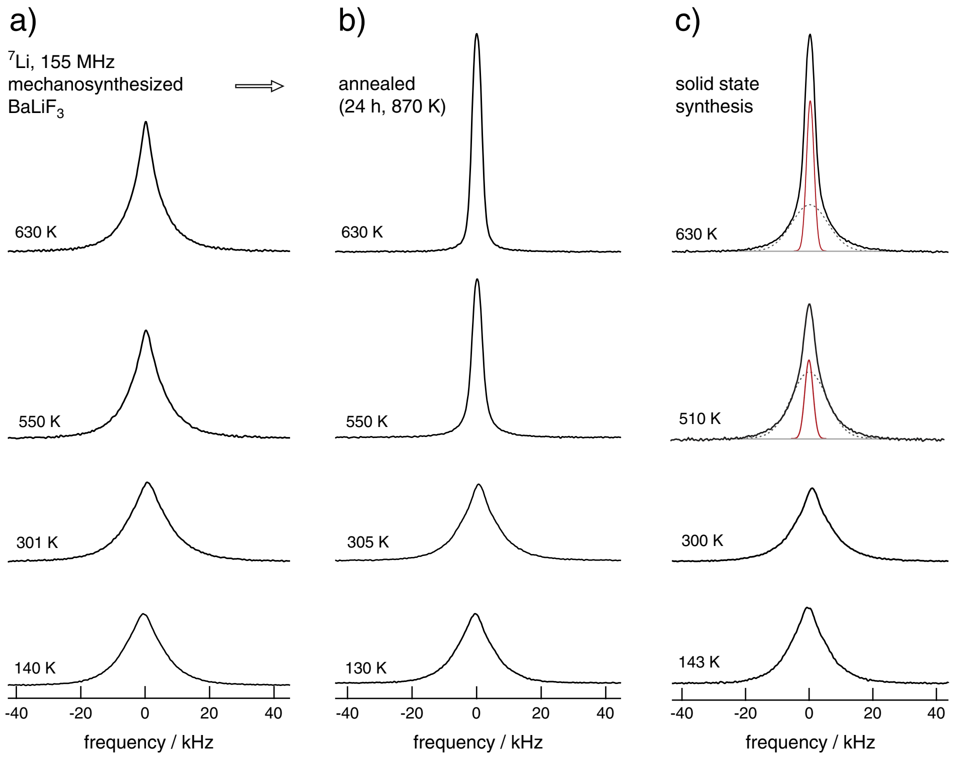

Fig. 6. a) Temperature-variable ^{7}Li NMR spectra of mechanosynthesized $BaLiF_3$ which were recorded at a resonance frequency of 155 MHz. b) ^{7}Li NMR spectra obtained after the nanocrystalline sample (see (a)) was exposed to 870 K for 24 h. c) Corresponding NMR spectra of $BaLiF_3$ prepared using a ceramic synthesis route.

be more homogenous which might be related to the microstructure observed by TEM, see above.

Surprisingly, up to $T = 630\,K$ no such significant motional narrowing of the ^{7}Li NMR line is observed for the mechanosynthesized sample (Fig. 6a), which, in contrast to the μm-sized samples, shows the highest dc conductivity (Fig. 5). So far, preliminary ^{19}F NMR spectra at temperatures up to 473 K do not indicate a large amount of highly mobile F anions overcompensating the apparently low Li diffusivity observed (Fig. 6a). It is worth noting that dc conductivity measurements are sensitive to long-range Li transport rather than to short range motions which also affects NMR line shapes. Thus, the observed motional narrowing of the coarse-grained samples might be caused by fast Li motions within a crystallite but grain boundaries might block long-range motions of the Li ions. Interestingly, these fast Li ions cannot be clearly resolved in the case of the mechanosynthesized sample. The enhanced dc conductivity of the nanocrystalline material might be explained by a small number fraction of highly mobile Li (and/or F anions) located in the interfacial regions which are different in microstructure when compared to those of the annealed counterpart. Possibly, these regions form a network of fast diffusion pathways for the ions. A rather small number fraction of mobile ions might be hardly detectable by recording NMR line shapes.

Certainly, further ^{7}Li NMR and ^{19}F NMR measurements including spin-lattice relaxation techniques[2,25] are necessary to figure out the different diffusivities of the two charge carriers in $BaLiF_3$. However, already now the NMR results indicate that ionic conduction in nanocrystalline $BaLiF_3$ seems to be quite different from that observed for the microcrystalline counterpart.

4. Conclusion

Nanocrystalline $BaLiF_3$ can be easily prepared and in high purity by high-energy ball milling from BaF_2 and LiF at ambient temperature. The dc conductivity (at $T = 560$ K) is about three orders of magnitude higher than that of a sample obtained by conventional solid state synthesis carried out at high temperature. Probably, in the coarse-grained material blocking grain boundaries affect charge carrier transport over long distances. A similar situation is found for a sample which was obtained by annealing the as-prepared nanocrystalline material. However, ^{7}Li NMR line shape measurements indicate fast Li motion in the microcrystalline materials. Although a higher dc conductivity and lower activation energy is found for the mechanosynthesized sample, a significant motional narrowing of the ^{7}Li NMR line is not observed. However, the enhanced transport properties might be explained by a fast interfacial diffusion process.

Acknowledgement

We gratefully acknowledge financial support by the Deutsche Forschungsgemeinschaft (SPP 1415).

References

[1] P. Heitjans, S. Indris, J. Phys. Condens. Matter 15 (2003) R1257.
[2] P. Heitjans, M. Wilkening, MRS Bull. 34 (2009) 915.
[3] M. Armand, J.-M. Tarascon, Nature 451 (2008) 652.
[4] P.G. Bruce, B. Scrosati, J.-M. Tarascon, Angew. Chem. - Intern. Ed. 47 (2008) 2930.
[5] A.S. Aricó, P.G. Bruce, B. Scrosati, J.-M. Tarascon, W.V. Schalkwijk, Nature 4 (2005) 366.
[6] S. Davis, A.V. Chadwick, J.D. Wright, J. Mater. Chem. 8 (1998) 2065.
[7] G.A. Niklasson, C.G. Granqvist, J. Mater. Chem. 17 (2007) 127.
[8] M. Wilkening, V. Epp, A. Feldhoff, P. Heitjans, J. Phys. Chem. C 112 (2008) 9291.
[9] P. Heitjans, M. Masoud, A. Feldhoff, M. Wilkening, Faraday Discuss. 134 (2007) 67.
[10] M. Masoud, P. Heitjans, Def. Diff. Forum 237–240 (2005) 1061.
[11] T. Matsuo, M. Shibasaki, T. Katsumata, Y. Onoda, Jpn. J. Appl. Phys. 33 (1994) 3913.
[12] B. Ruprecht, M. Wilkening, A. Feldhoff, S. Steuernagel, P. Heitjans, Phys. Chem. Chem. Phys. 11 (2009) 3071.
[13] B. Ruprecht, M. Wilkening, S. Steuernagel, P. Heitjans, J. Mater. Chem. 18 (2008) 5412.
[14] A. Boumriche, J.Y. Gesland, A. Bulou, M. Rousseau, J.L. Fourquet, B. Hennion, Solid State Commun. 91 (1994) 125.
[15] A. Düvel, M. Wilkening, P. Heitjans, Diffusion Fundamentals 11 (2009) 46 (open-access online journal, www.diffusion-fundamentals.org).
[16] Y. Tan, C. Shi, J. Solid State Chem. 150 (2000) 178.
[17] A. Düvel, M. Wilkening, R. Uecker, S. Wegner, V. Šepelák, P. Heitjans, Phys. Chem. Chem. Phys. 12 (2010) 11251.
[18] P. Scherrer, Göttinger Nachrichten 2 (1918) 89.
[19] W. Ostwald, Z. Phys. Chem. 34 (1900) 495.
[20] G.E. Fougere, J.R. Weertman, R.W. Siegel, Nanostruct. Mater. 5 (1995) 127.
[21] M.J. Mayo, Nanostruct. Mater. 9 (1997) 717.
[22] A. Ghosh, A.K. Suri, B.T. Rao, T.R. Ramamohan, J. Am. Ceram. Soc. 90 (2007) 2015.
[23] B. Bureau, G. Silly, J.Y. Buzaré, J. Emery, Chem. Phys. 249 (1999) 89.
[24] A. Goto, R. Miyabe, T. Shimizu, H. Kitazawa, K. Hashi, H. Abe, G. Kido, K. Shimamura, T. Fukuda, Phys. B 298 (2001) 585.
[25] P. Heitjans, A. Schirmer, S. Indris, in: P. Heitjans, J. Kärger (Eds.), Diffusion in Condensed Matter — Methods, Materials, Models, Springer, Berlin, 2005.
[26] P. Heitjans, S. Indris, M. Wilkening, Diffusion Fundamentals 2 (2005) 45 (open-access online journal, www.diffusion-fundamentals.org).

Reprinted from Solid State Ionics, 184, A. Düvel, M. Wilkening, S. Wegner, A. Feldhoff, V. Sepelak, P. Heitjans,
Ion conduction and dynamics in mechanosynthesized nanocrystalline BaLiF3, 65, Copyright 2011, with permission from Elsevier.
http://www.sciencedirect.com/science/article/pii/S0167273810004893

View Article Online / Journal Homepage / Table of Contents for this issue
Dynamic Article Links

Journal of
Materials Chemistry

Cite this: *J. Mater. Chem.*, 2011, **21**, 6238

www.rsc.org/materials

A. Düvel, S. Wegner, K. Efimov, A. Feldhoff, P. Heitjans, M. Wilkening,
J. Mater. Chem. 21 (2011) 6238 - Reproduced by permission of The Royal Society of Chemistry.
http://pubs.rsc.org/en/content/articlelanding/2011/jm/c0jm03439h#!divAbstract

Published on 24 March 2011. Downloaded by TIB und Universitaetsbibliothek Hannover on 24/03/2014 19:27:28.

PAPER

Access to metastable complex ion conductors *via* mechanosynthesis: preparation, microstructure and conductivity of (Ba,Sr)LiF_3 with inverse perovskite structure†

A. Düvel,[a] S. Wegner,[b] K. Efimov,[a] A. Feldhoff,[a] P. Heitjans[a] and M. Wilkening*[a]

Received 12th October 2010, Accepted 17th February 2011
DOI: 10.1039/c0jm03439h

Highly metastable $Ba_{1-x}Sr_xLiF_3$ ($0 < x \leq x_{max} \approx 0.4$) with an inverse perovskite structure analogous to that of $BaLiF_3$ was synthesized by soft mechanical treatment of BaF_2 and LiF together with SrF_2 at ambient temperature. *Ex* as well as *in situ* X-ray powder diffraction (XRPD) measurements show that heat treatment at 393 K initiates the decomposition of the mixed phase into $BaLiF_3$, LiF and $(Sr,Ba)F_2$. Structural details of the metastable compound $(Ba,Sr)LiF_3$ were investigated by ultrafast ^{19}F magic angle spinning (MAS) nuclear magnetic resonance (NMR) spectroscopy. Interestingly, five magnetically inequivalent F sites were identified which correspond to fluorine anions coordinated by a variable number of Ba and Sr cations, respectively. Details from XRPD and NMR spectroscopy are discussed with respect to the formation mechanisms and thermal stability of the as prepared fluorides. Impedance spectroscopy is used to characterize (long-range) ionic transport properties. Results are compared with those obtained recently on mechanosynthesized $BaLiF_3$.

I. Introduction

For many years much effort has been spent on developing new ion conductors[1–10] being vital for the successful design of, for instance, high-energy batteries,[8,11–13] fuel cells,[1,2,13] electrochromic devices,[1,2,13] and sensors.[1,2] To at least the same extent, many attempts have been undertaken focussing on the improvement of transport parameters of known ion conductors by, *e.g.* interface engineering.[14–19] In many cases this is done following essentially two routes, *viz* either by (i) varying chemical compositions of, for example, non-stoichiometric compounds or (ii) *via* directed modification of local microstructures in order to take advantage of, *e.g.*, nano-size or interfacial effects while the overall chemical composition roughly remains untouched.[14–18,20–22]

The playground of suitable materials being helpful in the field of interesting ion conductors might be further extended when thermodynamically metastable compounds are made available, see, *e.g.* ref. 23–25. Often, such materials are predicted theoretically,[26–28] however, their synthesis is difficult if not even impossible by employing standard preparation techniques commonly requiring high temperatures. A number of studies exist where metastable compounds have been successfully synthesized by mechanosynthesis (high-energy ball milling) carried out at room temperature by the use of shaker or planetary mills.[29–33] Conspicuously often, the so obtained compounds reveal new structural and electric, as well as magnetic, properties which can be systematically controlled by varying the numerous milling conditions such as the milling time, the kind of vial set used, the ball-to-powder weight ratio, *etc.*[34,35] Therefore, the mechanosynthesis of solids[36,37] is being increasingly considered in the preparation of new functional materials whose properties have to be directed in a specific way.

So far, diffusion properties of metastable crystalline ion conductors prepared by ball milling have been less intensively studied.[23–25,38] In the present paper we will show how mechanosynthesis can be used to prepare a non-equilibrium ion conductor, which is not or only hardly available by high-temperature ceramic synthesis. Structural details are revealed and the formation as well as decomposition mechanisms are studied by both X-ray powder diffraction (XRPD) and ultrafast ^{19}F magic angle spinning (MAS) nuclear magnetic resonance (NMR) spectroscopy. Additionally, the overall ionic conductivity of the highly metastable mechanosynthesized product is investigated by electrical impedance spectroscopy.

The inverse perovskite $BaLiF_3$, see, *e.g.*, ref. 39, can easily be prepared by treating BaF_2 with the same amount of LiF in a high-energy ball mill.[40] Since the product is single phase and of very high purity, it is an ideal model substance to investigate to which degree Sr can be substituted for isovalent Ba in the cubic structure. Here, it turned out that the resulting quaternary fluoride $Ba_{1-x}Sr_xLiF_3$ is very sensitive to heat-treatment.

---

[a] *Institute of Physical Chemistry and Electrochemistry, and Center for Solid State Chemistry and New Materials (ZFM), Leibniz University Hannover, Callinstr. 3a, D-30167 Hannover, Germany*
[b] *Bruker BioSpin GmbH, Silberstreifen, D-76287 Rheinstetten, Germany. E-mail: wilkening@pci.uni-hannover.de*

† Electronic supplementary information (ESI) available. See DOI: 10.1039/c0jm03439h

This journal is © The Royal Society of Chemistry 2011

Published on 24 March 2011. Downloaded by TIB und Universitaetsbibliothek Hannover on 24/03/2014 19:27:28.

At sufficiently high temperature it decomposes leaving over the almost Sr-free $BaLiF_3$ which is much more stable than the quaternary compound. Thus, it is expected that the mixed phase with a large Sr content cannot be prepared by conventional high-temperature solid-state synthesis without taking advantage of, *e.g.*, a well elaborated quenching technique. Even by ball milling carried out below 350 K the upper limit of x reached is approximately 0.3 if $t_{\mathrm{mill}} \leq 3$ h. For $t_{\mathrm{mill}} > 3$ h larger x values of up to 0.4 are accessible. Let us note that the synthesis of $SrLiF_3$ as well as that of $CaLiF_3$ crystallizing with (distorted) perovskite structure have not been reported in the literature yet.

II. Experimental details

A series of samples with the composition $Ba_{1-x}Sr_xLiF_3$ (Fig. 1) was prepared by joint milling of highly pure BaF_2 (99.99%, Sigma Aldrich), SrF_2 (99.99%, Alfa Aesar), and LiF (99.99%, Alfa Aesar) at ambient temperature. The synthesis was carried out in air using a planetary mill (Fritsch, P7 premium line) operated at a rotational speed of 600 rpm, see also ref. 40. The mill was equipped with a ZrO_2 vial set in combination with 140 milling balls (ZrO_2, 5 mm in diameter). The total mass of each mixture was about 2 g. If not stated otherwise the milling time t_{mill} was set to 3 h. The samples obtained after milling were characterised by X-ray powder diffraction using a Philips PW 1800 as well as a Bruker (D8 Advance) diffractometer both operating with Cu Kα radiation at 40 kV. For transmission electron microscope (TEM) investigations, a powder specimen was dispersed in ethanol, and a drop of 10 μL of suspension was dried on a copper-supported holey carbon film. (Scanning) transmission electron microscopy (S)TEM was made at 200 kV on a field-emission instrument of the type JEOL JEM-2100F-UHR in bright-field, dark-field, and phase contrast.

In order to study the decomposition process of the quaternary fluorides prepared, some *in situ* XRPD measurements (see Fig. S1, ESI†) were carried out using the D8 Advance in combination with a high-temperature cell HTK-1200N (Anton-Paar) flushed with air. Temperatures ranged from 298 K to 973 K. The equilibration time before each scan was 60 min. Heating and cooling rates were set to 12 K min^{-1}.

For the alternating current (ac) conductivity measurements an HP 4192 A analyzer as well as a Novocontrol Concept 80 broadband dielectric spectrometer were employed. The HP impedance analyzer, working at frequencies from 5 Hz to 13 MHz, is connected to a home-built cell with a four-terminal-configuration. The cell is designed such that conductivities can be measured under inert gas atmosphere. Here, the impedance samples were strictly kept under dry nitrogen gas (99.999%). A Eurotherm controller was used to adjust and monitor the temperature (385 K–730 K) near the sample. The Novocontrol impedance spectrometer is equipped with a BDS 1200 sample cell and a BETA analyzer which is capable to measure impedances down to 10^{-14} S at frequencies ranging from a few μHz to 20 MHz. Temperature regulation and controlling within an

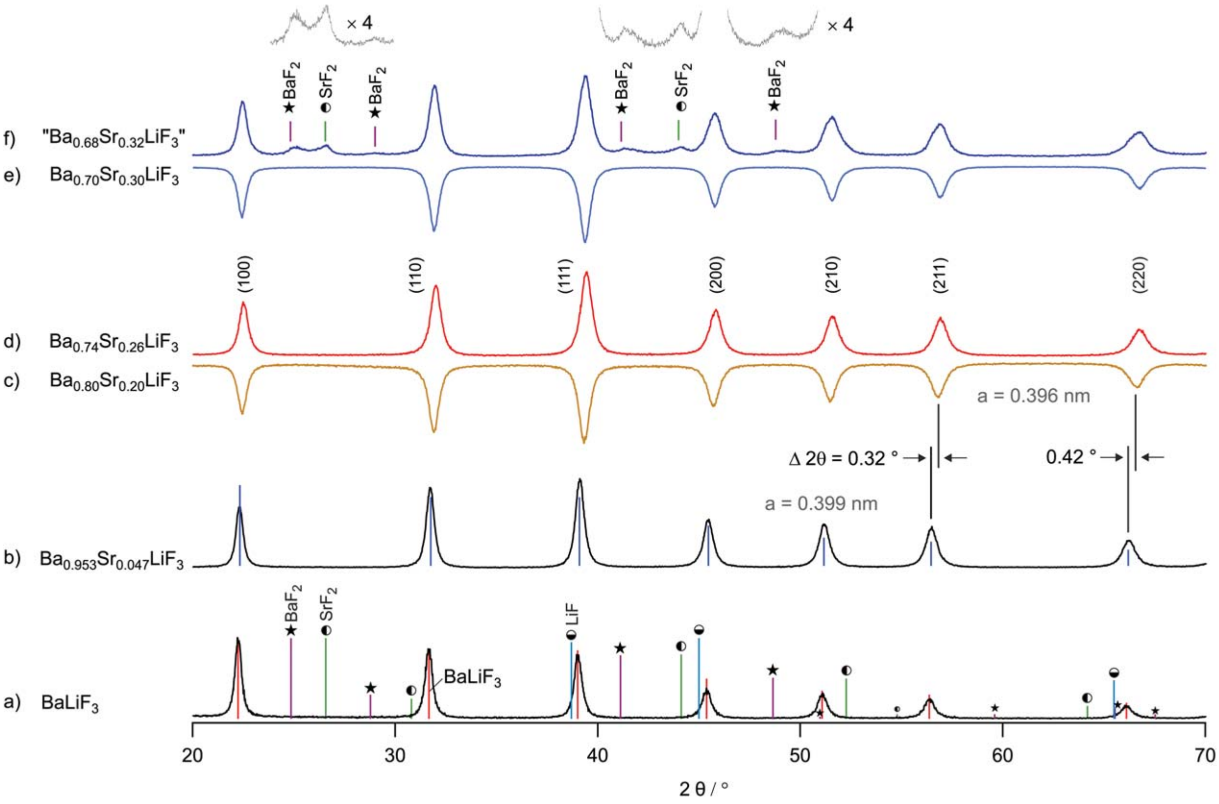

Fig. 1 (a) XRPD of mechanosynthesized $BaLiF_3$ prepared by mechanical treatment of BaF_2 and LiF (molar ratio of 1 : 1) in a planetary mill at 600 rpm (b)–(e) XRPD patterns of $Ba_{1-x}Sr_xLiF_3$ with different compositions x. The peaks slightly shift towards larger diffraction angles (shown for $x = 0.047$ and $x = 0.2$) clearly indicating lattice contraction, *i.e.*, a decrease of a, due to the incorporation of Sr^{2+}. (f) At $x \geq 0.32$ the maximum Sr^{2+} level is exceeded when t_{mill} is set to 3 h. Besides $(Ba,Sr)LiF_3$ the binary fluorides SrF_2 and BaF_2 show up.

Published on 24 March 2011. Downloaded by TIB und Universitaetsbibliothek Hannover on 24/03/2014 19:27:28.

accuracy of about 0.5 K was carried out with a Quattro cryosystem (Novocontrol) using dry nitrogen gas. The root mean square ac voltage was typically 0.1 to 1.0 V. Prior to the measurements the powder samples were uniaxially cold-pressed at 1 GPa to cylindrical pellets which were 8 mm in diameter and approximately 1 mm in thickness. The thickness of each pellet was measured with a vernier calliper. Electrodes were applied either by Au evaporation using an Edwards 306 or by pressing the uncoated pellet between Pt powder. It turned out that the kind of electrodes have no effect on the electrical impedance response measured.

^{19}F MAS NMR spectra were recorded with a Bruker Avance III spectrometer operating at 471 MHz. The NMR spectra were acquired using a single excitation pulse whose length was approximately 2 µs. The spinning speed was $\nu_{\mathrm{rot}} = 60$ kHz with room-temperature bearing gas leading to a temperature in the sample chamber of approximately 340 K. Such an ultrafast rotation frequency ensures a sufficiently high resolution of the MAS NMR spectra even in a structurally disordered sample with nm-sized crystallites. Usually, in those materials the ^{19}F MAS NMR line widths exhibit a broader distribution of chemical shifts[23,38,40] than it is observed in their chemically identical but structurally well-ordered counterparts with a much larger mean crystallite size. ^{6}Li MAS NMR spectra of $Ba_{0.74}Sr_{0.26}LiF_3$ were recorded at magnetic fields of 17.6 T and 14.1 T corresponding to the resonance frequencies of 107 MHz and 88 MHz, respectively. The rotation frequency was either 12 kHz (17.6 T) or 30 kHz (14.1 T).

III. Results and discussion

A. Sample characterization by XRD and ^{19}F MAS NMR

1. X-Ray diffraction patterns and TEM micrographs. Mechanical treatment of BaF_2 together with LiF at ambient temperature results in the formation of the inverse perovskite $BaLiF_3$ (space group $Pm\bar{3}m$, $a = 0.3996$ nm, see also ref. 39). In Fig. 1 the corresponding XRPD pattern is shown. Vertical lines indicate the position and intensity of the diffraction peaks which can be found in the literature.[41] Substitution of SrF_2 for BaF_2 leads to the formation of a mixed fluoride while the cubic symmetry of $BaLiF_3$ is retained. Additional diffraction peaks which would indicate the formation of new phases do not show up. With increasing Sr content x the XRPD peaks of $Ba_{1-x}Sr_xLiF_3$ shift towards larger angles 2θ. Thus, the lattice contracts when Ba^{2+} cations (ionic radius of 143 pm)[42] are continuously replaced with the smaller Sr^{2+} ions (127 pm).[42] The mean lattice parameter a can be calculated according to $a = [\lambda/(2\sin\theta)]\sqrt{h^2+k^2+l^2}$ where $\lambda = 0.154$ nm is the average wavelength of the Cu Kα radiation used and h, k and l denote Miller's indices of $BaLiF_3$ (see the XRPD pattern of Fig. 1d). In Fig. 2 the parameter a is shown as a function of x. Beginning from $a = 0.3996$ nm ($x = 0$) it decreases to approximately 0.396 nm when the composition reaches $x = 0.3$. The values shown refer to a milling time of 20 h and 10 h, respectively. Similar results are found for shorter milling times if $x < 0.3$. For $t_{\mathrm{mill}} = 20$ h the upper composition limit which can be reached by mechanical treatment is about 0.4. For larger values of x the diffraction peaks of SrF_2 and BaF_2 show up in the corresponding XRPD pattern. ^{19}F MAS NMR also revealed the formation of a very small amount of $(Ba,Sr)F_2$ (see below).

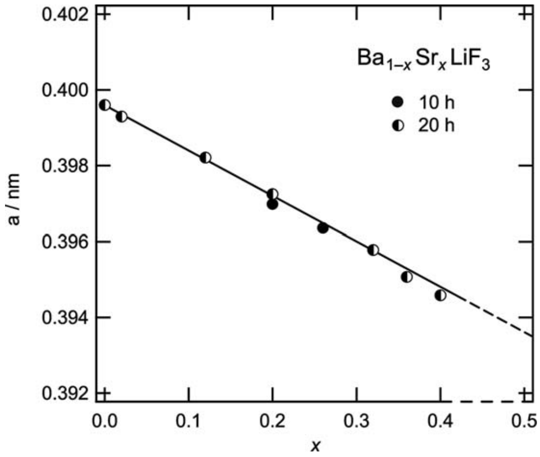

Fig. 2 Lattice constant a of mechanosynthesized $Ba_{1-x}Sr_xLiF_3$ as a function of composition x. The decrease of a indicates the incorporation of the smaller Sr^{2+} ions (ionic radius 127 pm) into $BaLiF_3$. The radius of Ba^{2+} is about 143 pm. See text for further details.

Provided the linear relationship found between a and x (Fig. 2) is valid over the whole composition range, by extrapolating the fit $a(x)$ to $x = 1.0$ the lattice constant of not-yet-synthesized "$SrLiF_3$" can be roughly estimated to $a = 0.3875$ nm. For comparison, the value calculated by Ouenzerfi *et al.*[43] for single crystalline perovskite-type "$SrLiF_3$" is only 0.376 nm.

A rough analysis of the XRPD peak widths $\delta_{2\theta}$ (fwhm, full width at half maximum) of Sr-free $BaLiF_3$ using the formalism introduced by Scherrer[44] (see ref. 23,38 for details of a similar analysis) yields a mean crystallite size $\langle d_c \rangle$ of approximately 25 nm for $t_{\mathrm{mill}} = 3$ h. Of course, the Scherrer equation does not consider internal strain ε additionally leading to XRPD peak broadening. Interestingly, with incorporation of Sr, *i.e.*, with increasing x, the peak widths of $Ba_{1-x}Sr_xLiF_3$, which was prepared under the same milling conditions as $BaLiF_3$, increase. This can be clearly seen when the XRPD pattern of a sample with $x = 0.2$ is compared with that of $BaLiF_3$ (Fig. 3). Irrespective of the indices $h\,k\,l$ the width $\delta_{2\theta}$ increases by about 37% when going from $x = 0$ to $x = 0.2$. Additionally, we have analyzed the XRPD peaks of a series of samples prepared by milling for 20 h: according to the method by Williamson and Hall[45] which takes peak broadening by strain (see also ref. 23,40) into account, the mean crystallite size $\langle d_c \rangle$ of a sample with $x = 0.26$ turns out to be about 36 nm and ε is of the order of 3.8×10^{-3}. From the corresponding Williamson and Hall plots it is deduced that for this series the crystallite size $\langle d_c \rangle$ decreases from approximately 46 nm at $x = 0.02$ to *ca.* 28 nm when $x = 0.4$ is reached. This increase of the peak width might be either due to a combination of both (i) a smaller mean crystallite size and the additional introduction of internal strain, or (ii) simply due to a larger distribution of diffraction angles in the phase with mixed cations, *i.e.*, due to small variations of a. The first assumption might be explained by the larger hardness of SrF_2, ref. 46, compared to BaF_2, see also ref. 38,23 for a similar comparison. However, our analysis shows that the ε values exhibit a decrease rather than an increase with increasing x. Thus, most likely there is a distribution of lattice

This journal is © The Royal Society of Chemistry 2011

Published on 24 March 2011. Downloaded by TIB und Universitaetsbibliothek Hannover on 24/03/2014 19:27:28.

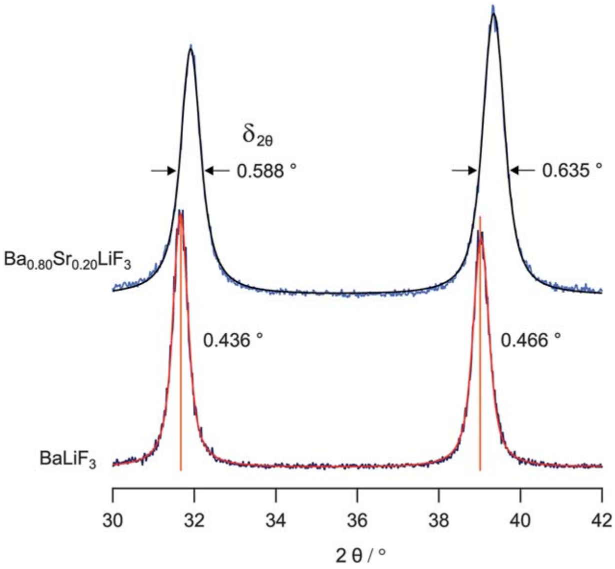

Fig. 3 Magnification of the XRPD patterns of $BaLiF_3$ and $Ba_{0.8}Sr_{0.2}LiF_3$ (t_{mill} = 3 h) in the range from $2\theta = 32°$ to 42°. Solid lines represent fits with a combination of Gaussian and Lorentzian lines to obtain the peak widths $\delta_{2\theta}$ indicated.

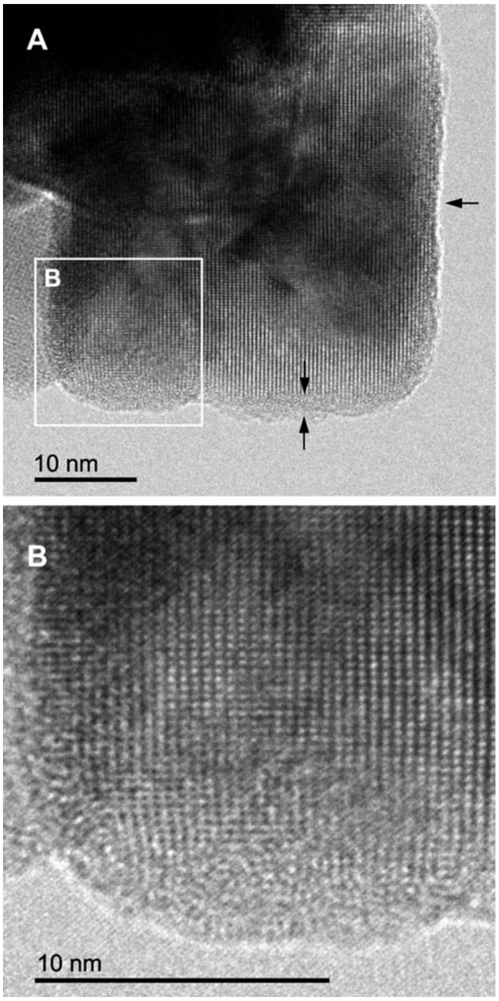

Fig. 4 Typical TEM micrograph of mechanochemically synthesized $Ba_{0.74}Sr_{0.26}LiF_3$ which was treated in a planetary mill for 20 h. The lower image (B) shows the magnification of the rectangular area highlighted in the upper one (A). See text for further discussion.

constants present. This is in agreement with the results from ^{19}F MAS NMR spectroscopy (*vide infra*) revealing a series of different local environments for the F anions. A very similar observation concerning XRPD peak broadening (and ^{19}F MAS NMR) was made for $(Ba,Ca)F_2$ which was also prepared by mechanical treatment of the binary source materials BaF_2 and CaF_2 in a shaker mill, see ref. 23,38.

TEM micrographs roughly confirm the crystallite sizes estimated from XRPD peak broadening. Several micrographs of a sample with the composition $Ba_{0.74}Sr_{0.26}LiF_3$ which was milled for 20 h show crystallites with diameters ranging from 10 to 50 nm. As an example, in Fig. 4 a TEM image of a crystallite is shown characterised by a mean diameter of approximately 45 nm. Defects in the inner regions of the crystallite are difficult to be seen by TEM. While some of the grain boundary regions reveal only a small area fraction showing dislocations being located on the surface of the crystallites (see arrow on the right hand side), there are also regions visible exhibiting structural disorder (see arrows in the lower part of micrograph A in Fig. 4). In these regions, which are characterised by a thickness of only 1 to 2 nm, no long-range order as in the inner part of crystallites is present. However, large amounts of amorphous $(Ba,Sr)LiF_3$, which might additionally influence the transport parameters (see below), are absent. This is similar to mechanosynthesized $BaLiF_3$ investigated by TEM recently.[47]

2. ^{19}F MAS NMR spectra. The ^{19}F MAS NMR spectrum of $Ba_{0.74}Sr_{0.26}LiF_3$ is composed of five signals which can be well resolved using a spinning speed of 60 kHz (Fig. 5). This observation is similar to that made in ref. 48,49. ^{19}F NMR chemical shifts of $Ba_{0.74}Sr_{0.26}LiF_3$, when referenced to C_6F_6, range from 70 to 32 ppm. The NMR line at 70 ppm can be attributed to F anions with four Ba cations as next nearest neighbours ($[Ba]_4$-configuration). For comparison, in $BaLiF_3$ a single NMR line shows up at 66 ppm. The slight shift towards more positive ppm values might be explained by the lattice contraction observed for $(Ba,Sr)LiF_3$. The fact that in the case of $(Ba,Sr)LiF_3$ no signal is observed at 66 ppm clearly shows that no large amounts of a separate $BaLiF_3$ phase are present. Moreover, neither SrF_2 (δ_{iso} = 78 ppm), BaF_2 (153 ppm) nor LiF (−37 ppm) are detected. Thus, there are no hints pointing to any residual non-reacted source materials. For comparison, the ^6Li MAS spectra, which were recorded at 107 MHz and 88 MHz, respectively, are composed of a single resonance line. The spinning speed was 12 and 30 kHz, respectively.

The successive replacement of Ba with Sr leads to the configurations $[Sr][Ba]_3$, $[Sr]_2[Ba]_2$, $[Sr]_3[Ba]$ and $[Sr]_4$. Analogous structural units were recently found in $(Ca,Sr)F_2$ single crystals with the fluorite structure, *i.e.*, cubic symmetry.[49] According to the assignment of the five ^{19}F NMR lines shown in Fig. 5 the isotropic chemical shift δ_{iso} decreases the more Ba cations are replaced with Sr ions. Thus, the ^{19}F NMR signal of pure "$SrLiF_3$" would show up at δ_{iso} values comparable to that of $[Sr]_4$. The proposed assignment is also reasonable when the

Published on 24 March 2011. Downloaded by TIB und Universitaetsbibliothek Hannover on 24/03/2014 19:27:28.

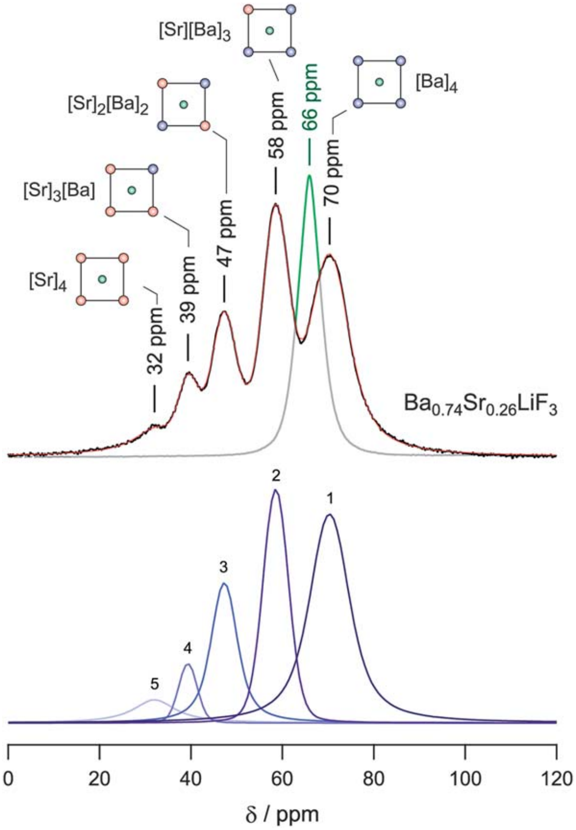

Fig. 5 Solid-state ^{19}F MAS NMR spectrum of mechanosynthesized $Ba_{0.74}Sr_{0.26}LiF_3$ recorded at 471 MHz and a spinning speed of 60 kHz. The spectrum is referenced to C_6F_6. It is composed of five NMR lines with distinct chemical shifts δ_{iso} ranging from 70 to 32 ppm. For comparison, the ^{19}F MAS NMR spectrum of mechanosynthesized $BaLiF_3$ is also shown which consists of a single line at 66 ppm (green line). The red line shows a fit composed of a combination of suitable Voigt functions which are separately shown in the lower part of the figure. Let us note that fitting the spectrum with Gaussian functions leads to a fit of a very similar quality. See text for further details.

NMR intensities and areas under the signals are regarded. Most probably, $[Ba]_4$ as well as $[Sr][Ba]_3$ are formed when the Sr concentration is kept much smaller than that of Ba^{2+} (see also Fig. 6). Indeed, the signals at 70 and 58 ppm dominate the ^{19}F MAS NMR spectrum of Fig. 5. Both the NMR signal at 70 ppm and that located at 32 ppm, which are assigned to $[Ba]_4$ and $[Sr]_4$ units, respectively, show larger intensities as expected for, *e.g.*, a binominal distribution of Ba and Sr on the available lattice sites. Interestingly, the number fraction of Sr-rich units increases with milling time (*vide infra*).

In Fig. 6 the ^{19}F MAS NMR spectra of samples with different compositions are shown which were prepared at a milling time of 20 h. At very small x the spectrum is dominated by the NMR signal of $[Ba]_4$ at 66 ppm. With increasing x the intensity of this resonance decreases and the signal shifts towards $\delta_{iso} = 70$ ppm. Simultaneously, the intensities of the NMR signals attributed to the mixed configurations continuously increase when x values up to 0.3 are regarded. The corresponding area fractions of the different NMR lines are shown in Fig. 7. Of course, the relative populations of the structural units depend on milling time.

The assignment shown in Fig. 5 (as well as in Fig. 6) is also reasonable when the empirical superposition model of Bureau *et al.*[50] developed for ^{19}F NMR isotropic chemical shifts is considered. By using experimental δ_{iso} values of binary fluorides such as LiF, KF, BaF_2, SrF_2 it is possible to estimate isotropic shifts of structurally more complex as well as mixed fluorides in a qualitative manner.[50,51] Here, only the first shell of next nearest neighbours of one fluorine ion is taken into account. The ^{19}F NMR isotropic chemical shift δ_{iso} (with respect to that of C_6F_6) is expressed as the sum of a constant diamagnetic and a paramagnetic term comprising the contributions from neighbouring cations l such as Ba, Sr and Li: $\delta_{iso,calc.} = -127.1\text{ppm} - \sum_l n_l\sigma_l$ where n_l is the coordination number of the fluorine ion and σ_l is given by $\sigma_l = \sigma_{l,0}\exp(-\alpha_l(d - d_0))$. The pre-factor $\sigma_{l,0}$ of the paramagnetic shielding term can be obtained from experimental NMR chemical shifts $\delta_{iso,basic}$ of the so-called basic, *i.e.*, binary, fluorides (*vide supra*) according to $\sigma_{l,0} = -(\delta_{iso,basic} + 127.1\text{ ppm})/n_l$. For BaF_2, SrF_2 and LiF the following $\sigma_{l,0}$ values[50,51] are obtained −70 ppm, −52 ppm and −15 ppm, respectively. While d (*vide supra*) is the distance between the cation and the F anion in the fluoride whose chemical shift has to be calculated, d_0 represents the distance between the cation and the F anion in the related basic fluoride, see ref. 50,51. The (empirical) parameter α_l is given by $\alpha_l = -0.806r_l + 4.048$ where r_l is the ionic radius of the ligand l.[50,51] Here, we used $r_{Li} = 0.078$ nm, and $r_{Ba} = 0.143$ nm.[42] The value of d, which most likely depends on the Ba-Sr-configuration regarded, plays a crucial role in the calculation. In the

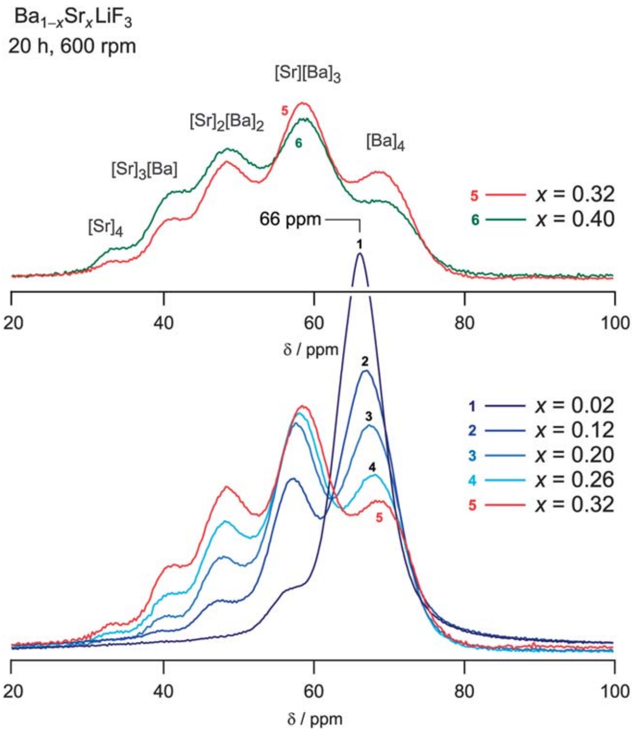

Fig. 6 Solid-state ^{19}F MAS NMR spectra of mechanosynthesized $Ba_{1-x}Sr_xLiF_3$ with different compositions. Data were recorded at 471 MHz and a spinning speed of 60 kHz. The spectra are referenced to C_6F_6. The milling time was set to 20 h; in that case x values of up to 0.4 are accessible. The area fractions of the distinct NMR lines are shown as a function of x in Fig. 7. See text for further details.

This journal is © The Royal Society of Chemistry 2011

View Article Online

Published on 24 March 2011. Downloaded by TIB und Universitaetsbibliothek Hannover on 24/03/2014 19:27:28.

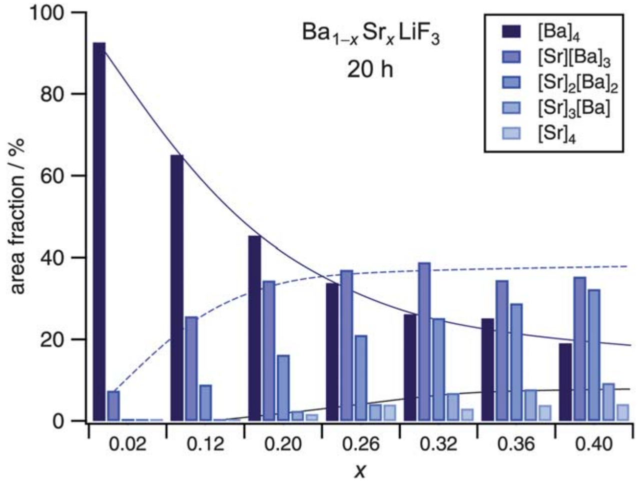

Fig. 7 Area fractions of the distinct ^{19}F NMR lines of $Ba_{1-x}Sr_xLiF_3$ which was prepared by mechanical treatment of the corresponding binary fluorides for 20 h. The lines are to guide the eye. Whereas the number of $[Ba]_4$ units continuously decreases with increasing x, those of the other species, except that of $[Sr][Ba]_3$ possibly passing through a shallow maximum at $x \approx 0.3$ (not indicated), show an increase.

present case we have simply used the lattice constants a of the pure end members $BaLiF_3$ and "$SrLiF_3$" to calculate d (Ba-F) and d (Sr-F). While for $BaLiF_3$ an experimental value can be used; the one calculated by Ouenzerfi *et al.*[43] is taken for "$SrLiF_3$". The Li-F distance is calculated using the mean lattice constant probed for $Ba_{0.74}Sr_{0.26}LiF_3$. Thus, assuming a mean Li-F distance d of 0.198 nm and Ba-F and Sr-F distances of about 0.283 nm and 0.266 nm, respectively, the results shown in Table 1 are obtained.

Let us emphasize that the $\delta_{iso,calc.}$ values obtained have to be regarded as a very rough estimate to understand the experimentally obtained ^{19}F NMR chemical shifts in structurally disordered, mixed $(Ba,Sr)LiF_3$. Nevertheless, the estimation clearly reveals that $\delta_{iso,calc.}$ decreases the more Sr cations are located in the direct neighbourhood of the F anion. Within this superposition model small variations of d can have a very large effect on the resulting chemical shifts. For example, using $a = 0.3875$ nm which is the value found after extrapolation of the fit shown in Fig. 2 (*vide supra*) to calculate $d(\text{Sr-F}) = 0.274$ nm, the following ppm values are obtained: 91, 71, 51, 31, and 10 ppm, respectively. By estimating the specific d values directly from the ionic radii of Ba, Sr and F (0.133 nm), the resulting $\delta_{iso,calc.}$ are very similar to those shown in Table 1. Quite recently, δ_{iso} of pure $BaLiF_3$ was precisely calculated on the basis of DFT calculations.[52] The theoretically predicted value of 68.9 ppm obtained by using a periodic structure model[52] is in good agreement with the experimental one found here (66 ppm) which is identical to that probed by Bureau *et al.*[50] For comparison, the value calculated for $BaLiF_3$ using the empirical superposition model turned out to be 91 ppm indicating the uncertainty of the estimated values.

Interestingly, a slight shift of δ_{iso} is observed (Fig. 8) when the composition is changed from $x = 0.02$ to $x \geq 0.3$ (Fig. 6), *i. e.*, when a decreases. For example, the signal attributed to $[Sr][Ba]_3$ shifts from about 56.5 ppm at $x = 0.02$ to approximately 59.4 ppm when x reaches a value of 0.4 (Fig. 8). Note that phase-pure samples with x values larger than 0.3 are only obtained when t_{mill} exceeds 3 h. The same trend of δ_{iso} has been recently found for the above mentioned single-crystalline $(Ca,Sr)F_2$ and is discussed in detail in ref. 49.

As mentioned above besides x (see Fig. 6) an increase of t_{mill} also affects the ratio of the line intensities of the NMR spectra shown in Fig. 5 and 6. Investigating this observation in detail one might find out whether any of the five environments are energetically more preferred than others. An attempt is presented in Fig. 9 where the area fractions of the distinct ^{19}F NMR lines of Fig. 5 are plotted as a function of milling time t_{mill}. For comparison, the corresponding spectra of $Ba_{1-x}Sr_xLiF_3$ with $x = 0.26$ are also shown. At the early stages of milling, *i.e.*, at $t_{mill} \approx 30$ min, the most intense signal is that of $BaLiF_3$ being located at 66(1) ppm. With increasing milling time its intensity decreases and δ_{iso} shifts towards 70 ppm. The other NMR signals show a negligible shift with increasing t_{mill}. Thus, besides a small amount of $(Ba,Sr)LiF_3$, the Sr-free inverse perovskite $BaLiF_3$ seems to be the initial product into which Sr is progressively introduced during mechanical treatment (see bottom of Fig. 9).

Table 1 Experimental (±2 ppm) and estimated ^{19}F NMR isotropic chemical shifts of $Ba_{0.74}Sr_{0.26}LiF_3$ by using the empirical superposition model introduced by Bureau *et al.*, see ref. 50

Structural unit	δ_{iso}/ppm	$\delta_{iso,calc.}$/ppm	$\delta_{iso} - \delta_{iso,calc.}$/ppm
$[Ba]_4$	70	92	22
$[Sr][Ba]_3$	58	79	21
$[Sr]_2[Ba]_2$	47	66	19
$[Sr]_3[Ba]$	39	53	14
$[Sr]_4$	32	39	7

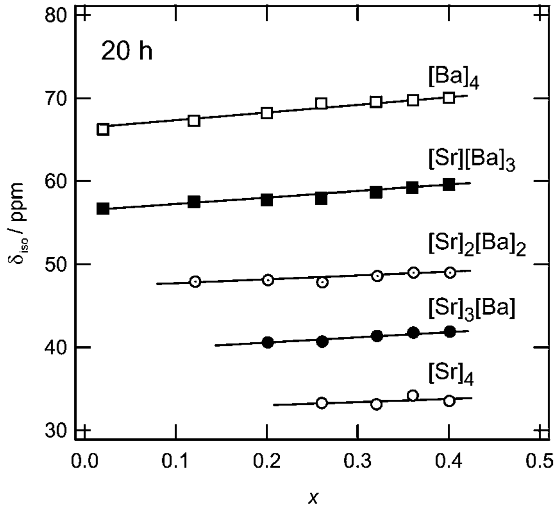

Fig. 8 Variation of the ^{19}F NMR chemical shift of the five distinct F environments in $Ba_{1-x}Sr_xLiF_3$ as a function of composition x. The milling time t_{mill} was 20 h. Note, slightly different results are obtained for $Ba_{0.74}Sr_{0.26}LiF_3$ when t_{mill} is restricted to 3 h (see Fig. 5 for comparison). This indicates that δ_{iso} depends on both composition as well as milling time. The spectra do not show any evidence for residual amounts of the starting materials or the formation of other phases such as $(Ba,Sr)F_2$ (see text for further details).

View Article Online

Published on 24 March 2011. Downloaded by TIB und Universitaetsbibliothek Hannover on 24/03/2014 19:27:28.

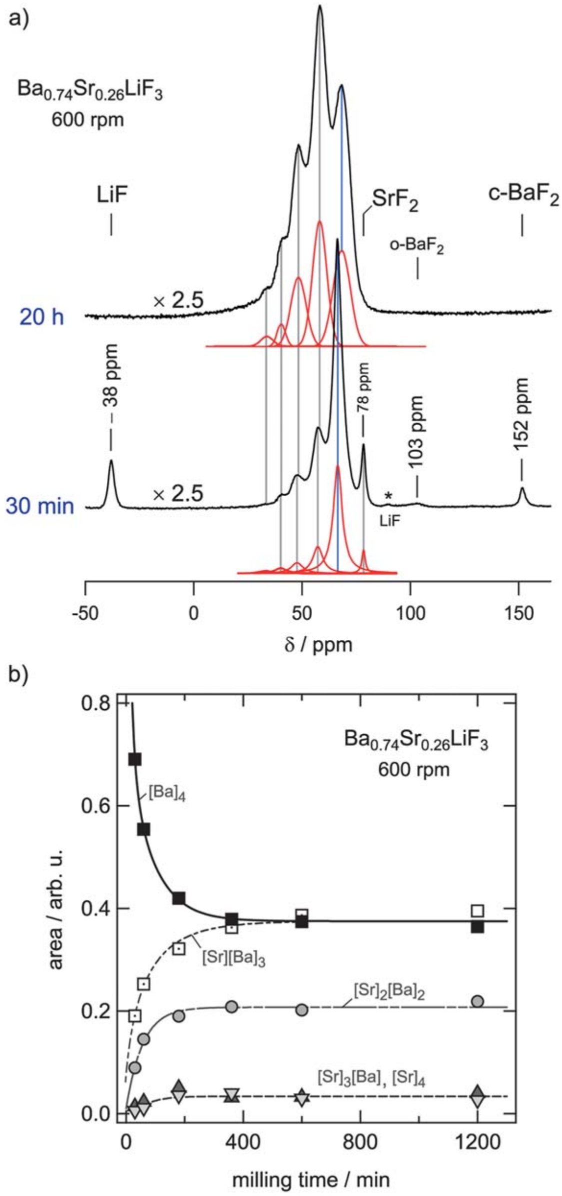

Fig. 9 (a) Solid-state ^{19}F MAS NMR spectra (471 MHz, spinning speed of 60 kHz) of a mixture of cubic-BaF_2, SrF_2, and LiF milled for 30 min and 20 h, respectively, to give $(Ba,Sr)LiF_3$ of the nominal composition $Ba_{0.74}Sr_{0.26}LiF_3$. (b) Area fraction of the distinct ^{19}F MAS NMR lines of Fig. 5; for comparison, see the ^{19}F MAS NMR spectra displayed in Fig. 9a.

If t_{mill} is chosen to be larger than or equal to 180 min the transformation into $(Ba,Sr)LiF_3$ is completed and no NMR signals arising from the source materials (LiF, cubic-BaF_2, SrF_2) are detected any more. For t_{mill} larger than 6 h the area fractions of the five NMR lines do not change any longer reaching an equilibrium state.

The NMR signal at 103(1) ppm (Fig. 9a) reveals a small amount of orthorhombic BaF_2, see also ref. 23, being a high-pressure modification of barium fluoride[53–55] whose cubic form was used for mechanosynthesis here. The formation of the orthorhombic form is seen clearest at short milling times. As an example, in Fig. 10a the ^{19}F MAS NMR spectrum of mechanosynthesized $Ba_{1-x}Sr_xLiF_3$ with $x = 0.12$ is presented which gives direct insights into the composition of the reaction mixture at the beginning of the mechanically driven solid-state reaction. In particular, $BaLiF_3$ and orthorhombic BaF_2 can be clearly identified as the initial products formed. In orthorhombic BaF_2 two magnetically inequivalent fluorine positions exist for which two different chemical shift values are expected. These two signals show up at approximately 103 and 174 ppm, respectively (see also ref. 23). To some extent orthorhombic BaF_2 is also produced when cubic BaF_2 is mechanically treated alone or together with LiF to form $BaLiF_3$ (see the ^{19}F MAS NMR spectra of Fig. 10b).

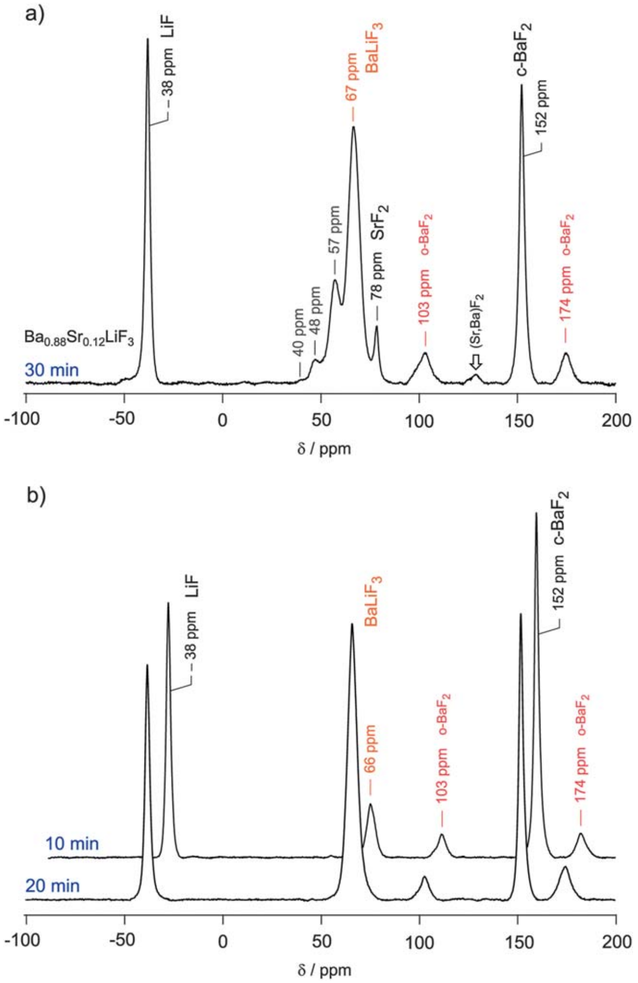

Fig. 10 (a) ^{19}F MAS NMR spectra (471 MHz, 60 kHz spinning speed) of a mixture of cubic BaF_2, SrF_2 and LiF which was mechanically treated for only 30 min to enlighten the early stages of milling. Chemical shift values presented are referenced to C_6F_6. Increasing t_{mill} to 180 min results in phase-pure $(Ba,Sr)LiF_3$ and the NMR signals of the source materials (LiF: −38(1) ppm, cubic BaF_2: 152(1) ppm, SrF_2: 78(1) ppm) as well as those of orthorhombic BaF_2 (103(1) and 175(1) ppm, respectively) cannot be detected any longer (for comparison, see the NMR spectra presented in Fig. 9). (b) Stacked plot of two ^{19}F MAS NMR spectra of a stoichiometric mixture of LiF and BaF_2 leading to phase-pure $BaLiF_3$ at sufficiently large milling times. NMR spectra were recorded at a resonance frequency of 471 MHz and a spinning speed of 60 kHz. At very short t_{mill} a relatively large amount of orthorhombic BaF_2 is detected which is also seen in the corresponding XRPD patterns.

This journal is © The Royal Society of Chemistry 2011

Published on 24 March 2011. Downloaded by TIB und Universitaetsbibliothek Hannover on 24/03/2014 19:27:28.

One might suppose that the intermediate formation of orthorhombic BaF_2 is a necessary pre-step for the successful mechanosynthesis of $BaLiF_3$ which, in the presence of SrF_2, then transforms into $(Ba,Sr)LiF_3$. Note that the crystallographic structure of orthorhombic BaF_2 resembles the inverse-perovskite structure of $BaLiF_3$. For comparison, by means of high-energy ball milling the synthesis of $SrLiF_3$ and $CaLiF_3$, expected to crystallize with a highly distorted perovskite structure if at all, has not been observed yet. This fact might be due to the circumstance that the corresponding orthorhombic modifications of SrF_2 and CaF_2 as well require much higher pressures to be formed.[53] Even when SrF_2 or CaF_2 are mechanically treated under the milling conditions as described here, there are no indications that the orthorhombic phase is created.

Finally, concerning Fig. 10a, the NMR intensity showing up at approximately 128 ppm (marked by a small arrow) presumably reflects the unresolved ^{19}F MAS NMR lines of a small amount of $(Ba,Sr)F_2$ (*vide infra*).

B. Decomposition of mechanosynthesized $(Ba,Sr)LiF_3$ as followed by XRD and ^{19}F MAS NMR

The metastable character of mechanosynthesized, nanocrystalline $(Ba,Sr)LiF_3$ comes to the fore when the phase-pure product is exposed to elevated temperatures for several hours. As an example, in Fig. 11 the XRPD patterns of $Ba_{0.74}Sr_{0.26}LiF_3$ are shown which was annealed for 3 h at 493 K and 1030 K, respectively. After exposing the sample at 1030 K the Sr-containing inverse perovskite is largely decomposed. In fact, the decomposition process starts already at lower temperatures; annealing $Ba_{0.74}Sr_{0.26}LiF_3$ for 3 h at 393 K leads to the emergence of SrF_2 peaks of very low intensity (see Fig. 11). The XRPD peaks of LiF partly overlap with those of $BaLiF_3$ as well as BaF_2 (Fig. 1) and, thus, are hardly detectable. Interestingly, no oxides are formed during the decomposition process which was carried out in air; this was also verified using *in situ* X-ray diffraction (Fig. S1, ESI†). Much more surprising is the fact that no BaF_2 can be seen after heat treatment. This is also confirmed by an *in situ* XRPD measurement carried out up to 973 K (Fig. S1, ESI†). Thus, $BaLiF_3$, from which SrF_2 as well as LiF are removed, is the main decomposition product.

Interestingly, the 2θ values of the new peaks showing up are slightly shifted towards smaller diffraction angles. Most probably, a very small amount of Ba is incorporated into SrF_2 leading to a mixed $(Sr,Ba)F_2$ phase. Indeed, mechanical treatment of SrF_2 together with BaF_2, but in the absence of LiF, unequivocally leads to the formation of structurally disordered $(Sr,Ba)F_2$ (see Fig. 12). The other way round, $SrF_2 + BaF_2 \rightarrow 2(Sr,Ba)F_2$ might be regarded as a competitive reaction with respect to the formation of $(Ba,Sr)LiF_3$ as well as $BaLiF_3$. The presence of SrF_2 seems to hinder the reaction $BaF_2 + LiF \rightarrow BaLiF_3$ since non-reacted BaF_2 is detected in the XRPD pattern of Fig. 1f when x is chosen to be large enough and t_{mill} set to 3 h. Moreover, increasing x to about 0.5 clearly leads, besides $(Ba,Sr)LiF_3$, to the formation of $(Sr,Ba)F_2$ if $t_{mill} > 10$ h. Even when the milling time is increased to 48 h or a vial set of tungsten carbide (WC), having a density (14.95 g cm^{-3}) much larger than that of ZrO_2 (6.06 g cm^{-3}), is used, residual $(Sr,Ba)F_2$ is detected by XRPD. This also shows that even under these extreme milling conditions large

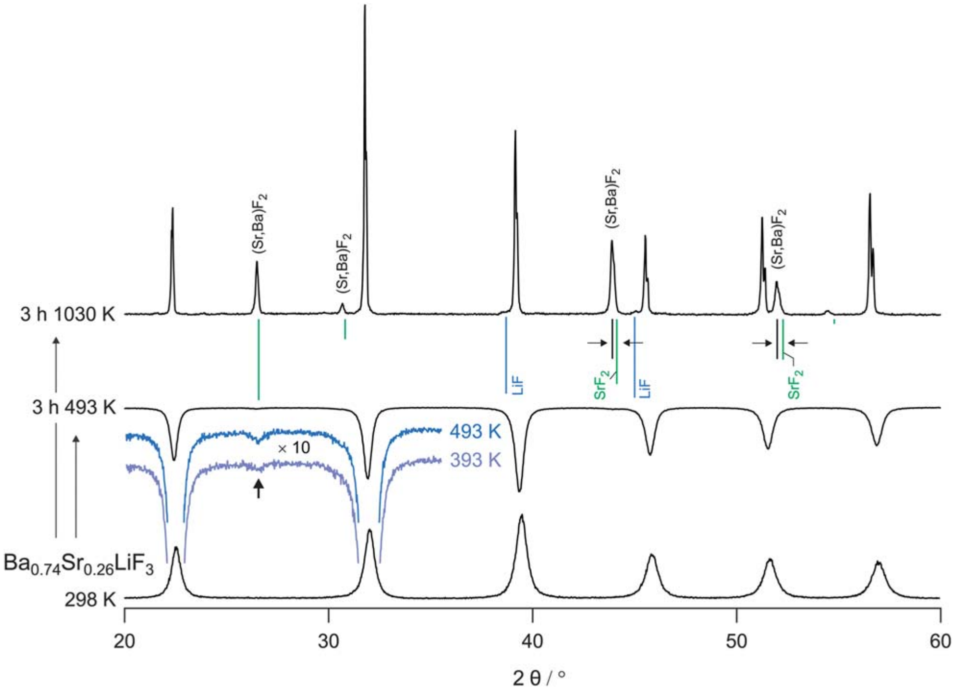

Fig. 11 XRPD pattern of mechanosynthesized $Ba_{0.74}Sr_{0.26}LiF_3$ which was annealed for 3 h at the temperatures indicated. Decomposition of the sample starts when it is exposed to 393 K. The new XRPD peaks emerging (see pattern at the top) can be attributed to a mixed $(Sr,Ba)F_2$ phase because the peaks at large diffraction angles, in particular, shift towards lower 2θ values. This indicates lattice expansion due to the incorporation of larger Ba^{2+} cations into the cubic structure of SrF_2. Narrowing of the XRPD peaks results from grain growth of the initially nm-sized crystallites. The same features were observed by *in situ* X-ray diffraction (see Fig. S1, ESI†).

Published on 24 March 2011. Downloaded by TIB und Universitaetsbibliothek Hannover on 24/03/2014 19:27:28.

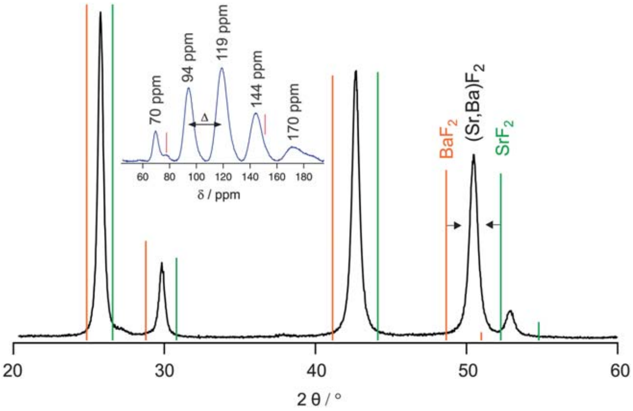

Fig. 12 XRPD pattern of (Sr,Ba)F_2 which was prepared by ball milling of SrF_2 with an equimolar amount of BaF_2 in a planetary mill for 3 h at 600 rpm. Whereas the XRPD peaks of SrF_2 shift towards smaller angles, those attributed to BaF_2 appear at larger 2θ values which clearly indicates the formation of a new phase with mixed cations. Inset: Corresponding ^{19}F MAS NMR spectrum recorded at a spinning speed of 60 kHz and a resonance frequency of 471 MHz. The five nearly equidistant NMR signals ($\Delta \approx 25$ ppm) represent the different cation environments the F ions are exposed to in the structurally disordered mixed phase. Vertical lines in the inset point to NMR intensities of residual SrF_2 and BaF_2, respectively.

amounts of Sr cannot be incorporated into $BaLiF_3$ completely. In contrast, if SrF_2 is absent, the formation of $BaLiF_3$ by high-energy ball milling of LiF together with BaF_2 is clearly finished after 3 h.[40]

Let us note that mechanical treatment of SrF_2 with CaF_2 instead of BaF_2 also leads to the formation of (Ca,Sr)F_2 solid solutions. See ref. 38 and 23 where the ionic direct current (dc) conductivity of metastable (Ba,Ca)F_2 is studied which was prepared by mechanical treatment in a very similar way. Similarly to the situation in (Ba,Sr)LiF_3, in mixed (Sr,Ba)F_2 (as well as in (Ca,Sr)F_2 as mentioned above[49]) the NMR chemical shift of fluorine depends on the number of different earth alkali cations in the (direct) neighbourhood of the nuclei. The inset of Fig. 12 shows the ^{19}F MAS NMR spectrum of mechanosynthesized (Sr,Ba)F_2. Despite the structural disorder of the nanocrystalline material different NMR signals are clearly resolved. The main signals are labeled by their chemical shift values. Vertical lines indicate the position of the NMR signals of the source materials SrF_2 (78(1) ppm) and cubic BaF_2 (152(1) ppm), respectively. Most probably, the NMR lines showing up at about 94, 119, and 144 ppm represent the mixed configurations [Sr]$_3$[Ba], [Sr]$_2$[Ba]$_2$, and [Sr][Ba]$_3$, respectively. Expectedly, the signal attributed to [Sr]$_2$[Ba]$_2$ shows the highest intensity. Interestingly, the NMR signals show up in an almost equidistant manner; beginning from about 70 ppm the ^{19}F NMR chemical shift continuously increases in steps of 25 ppm. This is very similar to the situation in (Ca,Sr)F_2.[49] The NMR signal attributed to F in the neighbourhood of a [Sr]$_2$[Ba]$_2$ configuration appears at $(\delta_{\mathrm{iso}}(\mathrm{SrF_2}) + \delta_{\mathrm{iso}}(\mathrm{BaF_2}))/2$. In agreement with Vegard's law the lattice constant a of $Sr_{0.5}Ba_{0.5}F_2$ turns out to be 0.60 nm. This is exactly the average of the lattice constants a of the two source materials, BaF_2 (0.62 nm) and SrF_2 (0.58 nm).

The decomposition of (Ba,Sr)LiF_3 can also be followed by ^{19}F MAS NMR. In Fig. 13 NMR spectra of $Ba_{0.74}Sr_{0.26}LiF_3$ (see Fig. 5) which was heated for 3 h at 393 K and 493 K, respectively, are shown. Note that the NMR spectra were recorded on the same samples after they were kept under air atmosphere for several weeks. They clearly show the re-formation of the binary fluorides LiF, SrF_2 and cubic BaF_2 which can be unambiguously identified by their specific ^{19}F NMR chemical shifts (Fig. 13b). Interestingly, as also verified by XRPD patterns, which are not shown here for brevity, the long-term exposition of the material to air does not lead to the formation of any detectable oxides or oxofluorides although this might be expected in the case of nanocrystalline materials characterised by an extremely large surface area. As indicated by TEM

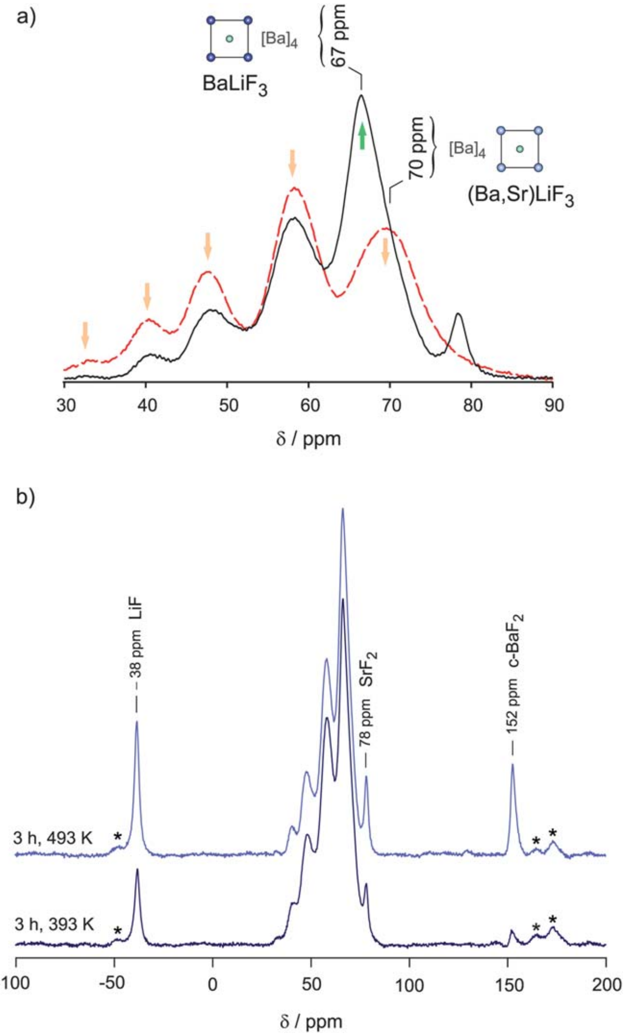

Fig. 13 ^{19}F MAS NMR spectra of $Ba_{1-x}Sr_xLiF_3$ with $x = 0.26$ which was annealed at the temperatures indicated (see text for further details). Data were recorded at a spinning speed of 60 kHz and a resonance frequency of 471 MHz. (a) Comparison of the NMR spectrum of the sample annealed at 493 K with that of the as prepared one (see Fig. 5). The signal at about 67 ppm reflects F in $BaLiF_3$ which is re-formed. The intensity at approximately 78 ppm is due to SrF_2 which is almost free of any Ba. (b) NMR spectra showing the re-formation of LiF and cubic BaF_2. Any significant amount of orthorhombic BaF_2 cannot be detected. The shallow NMR signal at about 130 ppm shows a very small amount of mixed (Ba,Sr)F_2.

This journal is © The Royal Society of Chemistry 2011

View Article Online

Published on 24 March 2011. Downloaded by TIB und Universitaetsbibliothek Hannover on 24/03/2014 19:27:28.

micrographs (see above), the surface of the nm-sized crystallites partly reveals structural disorder. Thus, it is expected to be highly reactive. However, it becomes evident from Fig. 13b that (Ba,Sr)LiF$_3$, in contrast to its behaviour at high temperature, decomposes in such a way that also BaF$_2$ is re-formed. In agreement with the NMR results the corresponding XRPD pattern reveals the formation of cubic BaF$_2$. Most probably, the (Ba,Sr)LiF$_3$ left after heat treatment, which is largely depleted or almost free of Sr (see the following paragraph), might be much more sensitive to moisture than a sample directly prepared from the binary fluorides.

The reappearance of the NMR signals of the binary fluorides at −38(1), 78(1) and 152(1) ppm, respectively, is accompanied by a decrease of those lines which are attributed to (Ba,Sr)LiF$_3$ (Fig. 13a). In accordance with the conclusion drawn from the XRPD measurements, the signal at 66(1) ppm unequivocally shows that BaLiF$_3$ almost free of Sr is (partly) re-formed while the signal at about 70 ppm is attributed to an F environment characterised by [Ba]$_4$ in mixed (Ba,Sr)LiF$_3$ (see Fig. 13a). Orthorhombic BaF$_2$ does not seem to belong to the main decomposition products observed after exposing the sample to air.

Let us mention that our attempts to prepare phase-pure Ba$_{1-x}$Sr$_x$LiF$_3$ with Sr contents of $x = 0.3$ by solid state reaction failed. A mixture of well ground source materials and a mechanosynthesized (Ba,Sr)LiF$_3$ sample were both heated at 973 K for several hours and then rapidly quenched to room temperature. The corresponding XRPDs (see Fig. S2, ESI†) clearly show the presence of BaLiF$_3$ and SrF$_2$ as well as a small amount of Sr-rich (Ba,Sr)F$_2$. The amount of Sr successfully incorporated into BaLiF$_3$ turns out to be approximately 10% at most.

C. Ion transport properties

Ion transport parameters for various freshly prepared samples of Ba$_{1-x}$Sr$_x$LiF$_3$ were studied by impedance spectroscopy.[56] Exemplarily, in Fig. 14 the impedance spectra, *i. e.*, the real part of the complex conductivity σ' *versus* frequency ν, of Ba$_{1-x}$Sr$_x$LiF$_3$ with $x = 0.26$ are shown. The isotherms are typically composed of a well-defined dc-plateau and a dispersive region showing up at low temperatures and high frequencies.[57] Dc-conductivity values σ_{dc} are obtained by extrapolating the real part σ' of the complex conductivity to $\nu \rightarrow 0$. In our case this is possible for temperatures higher than room temperature. At lower T the dispersive part of $\sigma'(\nu)$ dominates the spectra. Note that electrode polarization effects show up at higher T affecting the impedance data at low frequencies. These blocking effects have to be taken into account when σ_{dc} is read out from the impedance spectra. Alternatively, complex plane representations can be analyzed to obtain conductivity data. In the present case this yields the same results.

The isotherms shown in Fig. 14 represent those of a second run of measurements. After drying the sample, which was prepared in air, for 24 h at 333 K under vacuum, the first impedance spectrum was recorded at 323 K. Measurements were strictly carried out in nitrogen atmosphere. For the first run, the temperature was decreased to 233 K and then increased up to 473 K in steps of 20 K. Immediately after that, a second run of measurements was started for which the temperature was at first decreased from 473 K back to 233 K and after that increased once again to 473 K in steps of 20 K. In each case the sample was kept at 473 K for less than 10 min in order to prevent substantial decomposition during heating. The whole procedure is illustrated in Fig. 15, where the dc-conductivity values are plotted as $\sigma_{\mathrm{dc}}T$ *versus* the inverse temperature. Obviously, whereas the data of the first run are still affected by traces of water that might be absorbed during the synthesis process, the σ_{dc} values of the second run reflect the ionic conductivity of (Ba,Sr)LiF$_3$. This is corroborated by the observation that σ_{dc} values recorded at temperatures up to 550 K with the HP impedance analyzer fit to the data sampled at lower temperature utilizing the Novocontrol system. Thus, any further changes of σ_{dc} do not occur. Certainly, exposing the sample to higher temperatures for much longer times causes the beginning of decomposition as described above.

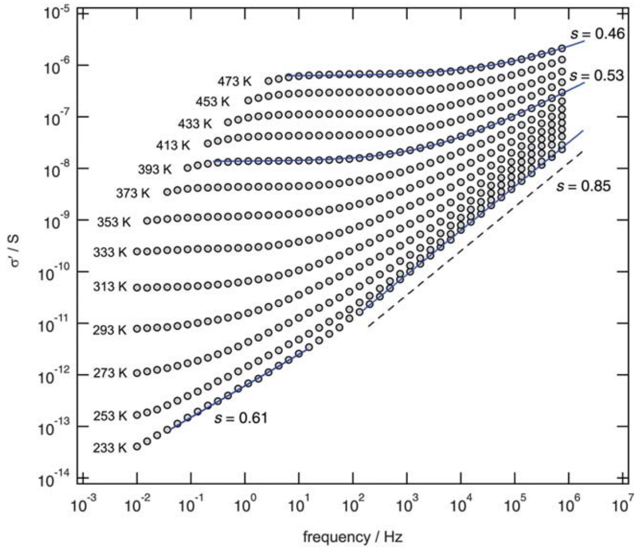

Fig. 14 Conductivity σ' of mechanosynthesized Ba$_{0.74}$Sr$_{0.26}$LiF$_3$ plotted double-logarithmically *versus* the measuring frequency. At elevated temperatures the impedance spectra are each composed of a dc-plateau and a dispersive region. At low frequencies and high temperatures distortions show up which are due to space charges accumulating near the blocking Au electrodes leading to a spurious decrease of σ'. A $\sigma' \propto \nu$ frequency dependence would represent constant loss behaviour. The spectrum recorded at the lowest temperature (233 K) is still affected by both dc and ac conductivities. The values indicated represent exponents s of a power law fit using $\sigma' = \sigma_{\mathrm{dc}} + A_0\nu^s$.

The data of the second run of measurements follow Arrhenius behaviour and yield an activation energy of about 0.76 eV. This value is very similar to that observed for mechanosynthesized, nanocrystalline BaLiF$_3$, recently.[40] Interestingly, the initial impedance spectra of the first run lead to conductivity values which show the same activation energy. The difference of the absolute conductivity values is about one order of magnitude. If this relatively small enhancement is not caused by traces of water as proposed above, it might also be explained by a structural effect. A higher density of defects due to increased structural disorder would cause an enhancement of the pre-exponential factor of the corresponding Arrhenius law for σ_{dc}. The pre-factor depends on the number of available charge carriers as well as an entropy term reflecting the degree of disorder. In a non-annealed mechanosynthesized sample the ion conductivity might be

View Article Online

Published on 24 March 2011. Downloaded by TIB und Universitaetsbibliothek Hannover on 24/03/2014 19:27:28.

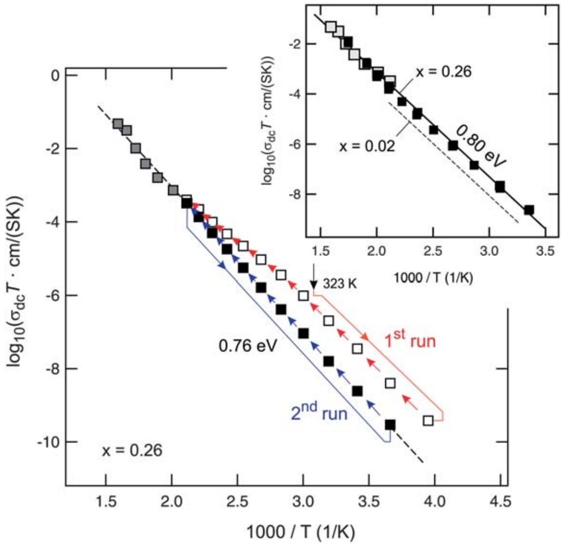

Fig. 15 Arrhenius plot for the dc conductivity ($\sigma_{dc}T$) of mechanosynthesized $Ba_{1-x}Sr_xLiF_3$ with $x = 0.26$ obtained by extrapolating σ' to $\nu \rightarrow 0$ (see Fig. 14). Uncertainties are within the size of the symbols. The dashed line is calculated using an Arrhenius law for $\sigma'_{dc}T$ with an activation energy E_a of about 0.76 eV. The arrows illustrate the chronological order of the measurements. The data of the first (□) and second (■) runs of measurements are obtained with the Novocontrol setup; the other data points (grey-filled squares) are measured by using an HP analyzer (see section II). The latter are also included in the inset and compared with those which were obtained on a $Ba_{0.74}Sr_{0.26}LiF_3$ sample prepared under argon atmosphere. See text for further details. The dashed line shown in the inset represents $\sigma_{dc}T$ of a sample with $x = 0.02$.

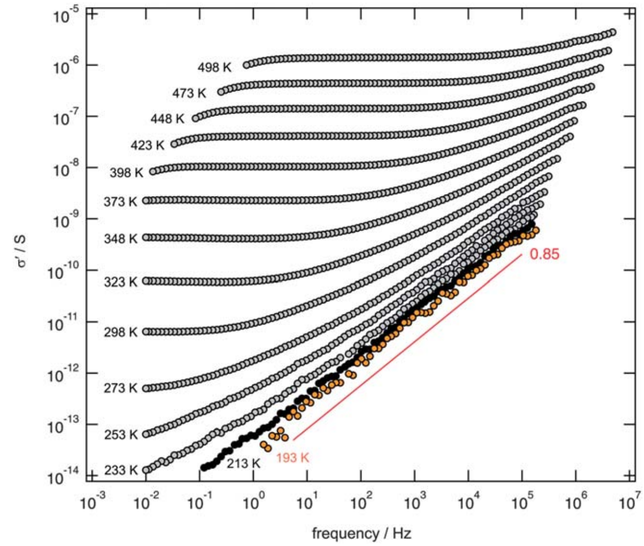

Fig. 16 Impedance spectra of $Ba_{0.74}Sr_{0.26}LiF_3$ which was mechanosynthesized in Ar atmosphere. At very low temperatures the real part of the complex conductivity follows $\sigma' = \nu^{0.85}$ (solid line) when frequencies ranging from 10^0 to 10^5 Hz are regarded. The spectra are very similar to those shown in Fig. 14. However, changes at very low temperatures and high frequencies might be attributed to localized structural relaxation occurring during annealing the sample at 500 K for about 40 min.

controlled by these frozen-in structural features. Annealing at elevated temperatures might cause structural relaxation and thus a slight decrease of σ_{dc}.

In order to enlighten the influence of the preparation atmosphere on ionic conductivity we have examined a sample which was mechanosynthesized and handled in inert gas atmosphere (Fig. 15 and 16). The inset of Fig. 15 shows σ_{dc} values of a sample with the same composition as that in the main figure but which was prepared in Ar atmosphere instead of milling the binary fluorides in air. Prior to the electrical measurements the sample was additionally dried at 500 K for about 40 min under nitrogen atmosphere inside the sample cell. Subsequently, impedance spectra were recorded in steps of 25 K down to 193 K. The corresponding isotherms are shown in Fig. 16. A second run including an initial drying period of 30 min at 573 K does not lead to any further changes of σ_{dc}. Conductivity values were readily reproduced through subsequent heating and cooling cycles. For comparison, in the inset of Fig. 15 also the high-temperature conductivity values of the sample prepared in air are included.

The solid lines shown in Fig. 14 represent fits according to a simple power law:[58] $\sigma' = \sigma_{dc} + A_0\nu^s$ with A_0 being the dispersion parameter. The exponent s usually ranges from 0 to 1. $s = 0$ is expected for uncorrelated motion of the ions which is usually expected for ionic conductors with a very low concentration of mobile charge carriers. $s = 1$ represents the so-called nearly constant loss (NCL)[57] being often observed at low temperatures. There are many studies which show that the NCL might be ascribed to caged, *i.e.*, highly localized dynamics which does not contribute to long-range transport.[57] However, a clear understanding of this phenomenon is still missing. It can be seen from Fig. 14 that the impedance spectrum recorded at 233 K can be divided into two regions obeying different power laws. At low frequencies the σ' values are influenced by both dc and ac conductivities. The slight dependence of s on temperature (see the values given in Fig. 14) vanishes after annealing the sample softly at higher T. For comparison, see the impedance spectra shown in Fig. 16 of the sample prepared in Ar atmosphere. As mentioned above this sample was exposed to 573 K yielding conductivity isotherms being similar in shape in the high frequency regime. Recently, similar observations were made for mechanosynthesized $BaLiF_3$ and ascribed to thermally-induced structural relaxation processes affecting the transport characteristics on short length scales only.[40]

For the sake of completeness, the dotted line of the inset of Fig. 15 marks the conductivity values of a sample with $x = 0.02$. The ion transport characteristics of $(Ba_{0.98}Sr_{0.02})LiF_3$ are very similar to those observed for the sample with $x = 0.26$. Careful inspection of the conductivity data shows that starting from $x = 0$ the ion conductivity first decreases by about a factor of about five. Increasing x to 0.12 leads to a small increase of σ_{dc} until the ionic conductivity reaches the σ_{dc} values of pure $BaLiF_3$ whose ionic dc conductivity almost coincides with that of a sample with $x = 0.26$. Thus, varying x in the range from $x = 0$ to $x = 0.26$ does not exhibit a great influence of the Ba:Sr ratio on the conductivity of the inverse perovskites studied.

D. Conclusions and outlook

(Ba,Sr)LiF_3 turns out to be a highly metastable quaternary fluoride crystallizing with the inverse perovskite structure. It can

This journal is © The Royal Society of Chemistry 2011

Published on 24 March 2011. Downloaded by TIB und Universitaetsbibliothek Hannover on 24/03/2014 19:27:28.

be prepared in high purity by taking advantage of room-temperature high-energy ball milling being a soft synthesis route avoiding high synthesis temperatures. A quasi *in situ* characterization of the mechanosynthesis of (Ba,Sr)LiF_3 is possible since the reaction can abruptly be stopped by switching off the mill. ^{19}F MAS NMR spectroscopy was used to elucidate both the formation mechanisms including possible side reactions as well as decomposition processes clearly starting when the material is exposed to elevated temperatures for many hours. The latter was verified by *ex* as well as *in situ* XRPD measurements. Despite the structural disorder of the material five magnetically inequivalent fluorine sites can be well resolved with the help of ultrafast ^{19}F MAS NMR. The technique helps to understand the mechanically driven solid state reactions from an atomic-scale point of view. NMR spectra reveal the structural changes with both increasing Sr content as well as milling time, *i.e.*, with increasing progress of the reaction. Obviously, $BaLiF_3$ is initially formed into which Sr is increasingly incorporated during milling. The relatively high ionic conductivity of the metastable perovskites studied so far might be further improved by replacement of Ba with other di- as well as trivalent cations using convenient one-step mechanochemical preparation techniques.

Acknowledgements

We thank the workgroup of Prof. Caro (Hannover) for access to the X-ray diffractometers as well as the Edwards evaporator and Prof. Freude (Leipzig) for recording the ^6Li MAS NMR spectrum. Financial support by the Deutsche Forschungsgemeinschaft (DFG) within the frame of the Priority Program SPP 1415 is highly acknowledged. M.W. acknowledges a research grant of the Leibniz University Hannover within in the project DYNAMA (Wege in die Forschung II).

References

1 H. L. Tuller, in *Springer Handbook of Electronic and Photonic Materials*, ed. S. Kasap and P. Capper, Springer, Berlin, 2006, ch. 11, *Ionic Conduction and Applications*, pp. 213–228.
2 E. Kendrick and P. Slater, *Annu. Rep. Prog. Chem., Sect. A*, 2010, **106**, 429.
3 P. Knauth, *Solid State Ionics*, 2009, **180**, 911.
4 A. V. Chadwick, *Phys. Status Solidi A*, 2007, **204**, 631.
5 C. S. Sunandana and P. S. Kumar, *Bull. Mater. Sci.*, 2004, **27**, 1.
6 L. Malavasi, C. A. J. Fisher and M. S. Islam, *Chem. Soc. Rev.*, 2010, **39**, 4370.
7 P. Knauth and J. Schoonman, *Nanocomposites – Ionic Conducting Materials and Structural Spectroscopies*, Springer, New York, 2007.
8 P. G. Bruce, B. Scrosati and J.-M. Tarascon, *Angew. Chem., Int. Ed.*, 2008, **47**, 2930.
9 T. Brezesinski, J. Wang, S. H. Tolbert and B. Dunn, *Nat. Mater.*, 2010, **9**, 146.
10 S. Hull, *Rep. Prog. Phys.*, 2004, **67**, 1233.
11 A. S. Aricó, P. G. Bruce, B. Scrosati, J.-M. Tarascon and W. V. Schalkwijk, *Nat. Mater.*, 2005, **4**, 366.
12 M. Whittingham, *Chem. Rev.*, 2004, **104**, 4271.
13 P. Knauth and H. Tuller, *J. Am. Ceram. Soc.*, 2004, **85**, 1654.
14 J. Maier, *Nat. Mater.*, 2005, **4**, 805.
15 J. Garcia-Barriocanal, A. Rivera-Calzada, M. Varela, Z. Sefrioui, M. R. Diaz-Guillen, K. J. Moreno, J. A. Diaz-Guillen, E. Iborra, A. F. Fuentes and S. J. Pennycook, *et al.*, *ChemPhysChem*, 2009, **10**, 1003.
16 P. Heitjans and M. Wilkening, *MRS Bull.*, 2009, **34**, 915.
17 M. Wilkening, V. Epp, A. Feldhoff and P. Heitjans, *J. Phys. Chem. C*, 2008, **112**, 9291.
18 P. Heitjans, S. Indris, and M. Wilkening, in *Nanocomposites – Ionic Conducting Materials and Structural Spectroscopies*, edited by P. Knauth and J. Schoonman, Springer, New York, 2007, p. 227.
19 P. Heitjans, M. Masoud, A. Feldhoff and M. Wilkening, *Faraday Discuss.*, 2007, **134**, 67.
20 P. Heitjans and S. Indris, *J. Phys.: Condens. Matter*, 2003, **15**, R1257.
21 M. Wilkening, S. Indris and P. Heitjans, *Phys. Chem. Chem. Phys.*, 2003, **5**, 2225.
22 N. Sata, K. Ebermann, K. Eberl and J. Maier, *Nature*, 2000, **408**, 946.
23 B. Ruprecht, M. Wilkening, A. Feldhoff, S. Steuernagel and P. Heitjans, *Phys. Chem. Chem. Phys.*, 2009, **11**, 3071.
24 A. F. Fuentes, K. J. Moreno, J. Santamaría, C. Léon, and U. Amador, in Solid-State Ionics-2006, edited by T. R. Armstrong and C. Masquelier and Y. Sadaoka, 2007, vol. 972 of *Mater. Res. Soc. Symp. Proc.*, p. 97.
25 K. J. Moreno, A. F. Fuentes, M. Maczka, J. Hanuza, U. Amador, J. Santamaría, and C. Léon, *Phys. Rev. B*75 (2007).
26 M. Jansen, K. Doll and J. C. Schön, *Acta Crystallogr., Sect. A: Found. Crystallogr.*, 2010, **66**, 518.
27 C. Mellot-Draznieks, S. Girard, G. Férey, J. C. Schön, Z. Čančarević and M. Jansen, *Chem.–Eur. J.*, 2002, **8**, 4103.
28 M. Wevers, J. Schön and M. Jansen, *J. Phys.: Condens. Matter*, 1999, **11**, 6487.
29 G. Golubkova, E. Belyaev and O. Lomovsky, *J. Alloys Compd.*, 1998, **270**, 224.
30 V. Šepelák, I. Bergmann, A. Diekmann, P. Heitjans and K. D. Becker, *Rev. Adv. Mater. Sci.*, 2008, **18**, 349.
31 V. Šepelák, S. Indris, I. Bergmann, A. Feldhoff, K. D. Becker and P. Heitjans, *Solid State Ionics*, 2006, **177**, 2487.
32 M. Nagumo, T. Suzuki, and K. Tsuchida, in Metastable, mechanically alloyed and nanocrystalline materials, edited by R. Schulz, 1996, vol. 225 of *Mater. Sci. Forum*, p. 581.
33 V. Šepelák, K. D. Becker, I. Bergmann, S. Suzuki, S. Indris, A. Feldhoff, P. Heitjans and C. P. Grey, *Chem. Mater.*, 2009, **21**, 2518.
34 V. Šepelák, I. Bergmann, A. Feldhoff, P. Heitjans, F. Krumeich, D. Menzel, F. J. Litterst, S. J. Campbell and K. D. Becker, *J. Phys. Chem. C*, 2007, **111**, 5026.
35 V. Šepelák, A. Feldhoff, P. Heitjans, F. Krumeich, D. Menzel, F. Litterst, I. Bergmann and K. Becker, *Chem. Mater.*, 2006, **18**, 3057.
36 V. V. Boldyrev, *Russ. Chem. Rev.*, 2006, **75**, 177.
37 E. Avvakumov, M. Senna, and N. Kosova, *Soft Mechanochemical Synthesis: A Basis for New Chemical Technologies*, Kluwer Academic Publishers, Boston, 2001.
38 B. Ruprecht, M. Wilkening, S. Steuernagel and P. Heitjans, *J. Mater. Chem.*, 2008, **18**, 5412.
39 A. Boumriche, J. Y. Gesland, A. Bulou, M. Rousseau, J. L. Fourquet and B. Hennion, *Solid State Commun.*, 1994, **91**, 125.
40 A. Düvel, M. Wilkening, R. Uecker, S. Wegner, V. Šepelák and P. Heitjans, *Phys. Chem. Chem. Phys.*, 2010, **12**, 11251.
41 H. Swanson, H. McMurdie, M. Morris and E. Evans, *Natl. Bur. Stand. (U.S.), Monogr*, 1967, **25**, 35.
42 V. Goldschmidt, *Skr. Norske Vidensk.-Akad. (Math.-Naturw. Kl.)*, 1926, **2**.
43 R. El Ouenzerfi, S. Ono, A. Quema, M. Goto, N. Sarukura, T. Nishimatsu, N. Terakubo, H. Mizuseki, Y. Kawazoe, A. Yoshikawa, *et al.*, *Jpn. J. Appl. Phys.* 43, L 1140 (2004).
44 P. Scherrer, *Göttinger Nachrichten*, 1918, **2**, 98.
45 G. K. Williamson and W. H. Hall, *Acta Metall.*, 1953, **1**, 22.
46 G. Chin, M. Green, L. van Uitert and W. Hargreaves, *J. Mater. Sci.*, 1973, **8**, 1421.
47 A. Düvel, M. Wilkening, S. Wegner, A. Feldhoff, V. Šepelák and P. Heitjans, *Solid State Ionics*, 2011, **184**, 65.
48 A. Picinin, R. R. Deshpande, A. S. S. de Camargo, J. P. Donoso, J. P. Rino, H. Eckert and M. A. P. Silva, *J. Chem. Phys.*, 2008, **128**, 224705.
49 R. E. Youngman and C. M. Smith, *Phys. Rev. B: Condens. Matter Mater. Phys.*, 2008, **78**, 014112.
50 B. Bureau, G. Silly, J. Buzaré and J. Emery, *Chem. Phys.*, 1999, **249**, 89.
51 M. Body, G. Silly, C. Legein and J. Buzaré, *Inorg. Chem.*, 2004, **43**, 2474.
52 A. Zheng, S.-B. Liu and F. Deng, *J. Phys. Chem. C*, 2009, **113**, 15018.

Published on 24 March 2011. Downloaded by TIB und Universitaetsbibliothek Hannover on 24/03/2014 19:27:28.

53 S. Dorfman, F. Jiang, Z. Mao, A. Kubo, Y. Meng, V. Prakapenka and S. Duffy, *Phys. Rev. B: Condens. Matter Mater. Phys.*, 2010, **81**, 174121.
54 J. M. Leger, J. Haines, A. Atouf, O. Schulte and S. Hull, *Phys. Rev. B: Condens. Matter*, 1995, **52**, 13247.
55 V. Kanchana, G. Vaitheeswaran and M. Rajagopalan, *J. Alloys Compd.*, 2003, **359**, 66.
56 E. Barsoukov and J. R. MacDonald, *Impedance Spectroscopy – Theory, Experiment and Applications*, Wiley & Sons Hoboken, New Jersey, 2005.
57 K. Funke, C. Cramer, and D. Wilmer, in *Diffusion in Condensed Matter – Methods, Materials, Models*, ed. P. Heitjans and J. Kärger, Springer, Berlin, 2005, chap. 9, pp. 857–893.
58 A. Jonscher, *Nature*, 1977, **267**, 673.

12 Mechanosynthesis of $BaMgF_4$, $BaZnF_4$ and $BaMg_{0.5}Zn_{0.5}F_4$

12.1 Introduction

$BaMgF_4$ crystallizes in the orthorhombic $BaZnF_4$ structure (space group $Cmc2_1$).[1] It melts at about 1190 K in CF_4 atmosphere[2] but decomposes in N_2 atmosphere at temperatures higher than 820 K[3]. $BaMgF_4$ (as well as $BaZnF_4$) is a ferroelectric material.[3,4] The polarization of $BaMgF_4$ (and $BaZnF_4$) established along the *a* axis is due to the displacement of the Ba ions along the *c* axis accompanied by a rotation of the MF_6 octahedra in the *ab* plane.[5,6] See Fig. 53 for the crystal structure of $BaMgF_4$ based on the data of Gingl[1].

A ferroelectric material is a material in which a permanent electrical polarization can be switched by applying an electric potential. This polarization is caused by the shift of ions inside the material. Thus, a ferroelectric material is always also pyroelectric (polarization changes with temperature) and piezoelectric (polarization caused by elastic deformation) but a pyroelectric or piezoelectric material not necessarily a ferroelectric material.

Since the polarization of ferroelectrics can be switched and is retained when no electrical field is applied it is an interesting class of materials to be used in random access memory (RAM) to obtain ferroelectric random access memory (FRAM) in which the dielectric of the capacitor used to store the information 1 or 0 (represented by the two possible directions of the polarization) is substituted by a ferroelectric material.[7] Thus, FRAM preserves the information saved in it when the electric potential is taken away while in conventional, dielectric RAM the information is lost in this case. The advantage of FRAM compared to magnetic storage devices and other non-volatile storage devices is its much shorter write and read cycle time (< 100 ns).[7] The slow read and write cycle times of established non-volatile storage devices would drastically slow down a computer. Therefore, a personal computer has to boot, i. e. the operating system stored on the magnetic storage device (or flash memory) is transferred into the much faster RAM. Thus, by using FRAM instead of RAM no booting would be necessary. However, although already in use for specialized applications FRAM is still in development to increase its performance, by decreasing the thickness of the thin films of the ferroelectrics to decrease the necessary electric potential for switching by maintaining retention and cycling enduring.[7] In addition to the use in FRAM and for many other applications ferroelectric materials are also discussed for their application in mass storage systems.[7] This is due to their much higher potential packing density compared to magnetic systems since the walls between differently directed domains (magnetization or polarization) are much broader (> 10 nm) in case of ferromagnetic materials than in case of ferroelectrics (≈ 1 nm).[7]

$BaMgF_4$ is also discussed as an optical frequency converter by second harmonic generation of radiation in the UV and VUV region due to its transparency for wavelengths < 140 nm.[3,8] Another interesting property found for $BaMgF_4$ is a quasi-one-dimensional ionic conduction along the c-axis.[9] This makes $BaMgF_4$ an interesting model system for the investigation of the fluoride ion mobility as well as the polarization properties of polycrystalline material compared to the mechanosynthesized, nano-crystalline material.

The synthesis of $BaMgF_4$ and analogous compounds like $BaMnF_4$, $BaCoF_4$, $BaNiF_4$ and $BaZnF_4$ is commonly done thermally from the melt of BaF_2 and the respective other binary fluoride at temperatures above 1073 K in an CF_4 or HF atmosphere.[3] There were also attempts to synthesize them by sol-gel methods. Fujihara et al. reported on the synthesis of $BaMgF_4$ contaminated with small amounts of the starting materials and an unknown impurity by heat treatment at 1073 K of a sol made from $Ba(CH_3COO)_2$ and $Mg(CH_3COO)_2{\cdot}4H_2O$ in trifluoroacetic acid.[10] Some years later Groß et al. reported on the sol-gel synthesis of $BaMgF_4$ contaminated by small amounts of BaF_2 by using HF as reagent.[11] In 2010 Kim et al. reported on a hydrothermal synthesis routine for the synthesis of single phase $BaMF_4$ with M = Mg, Mn, Co, Ni and Zn from the binary fluorides in trifluoroacetic acid and water.[3] However, to the knowledge of the author there are no synthesis

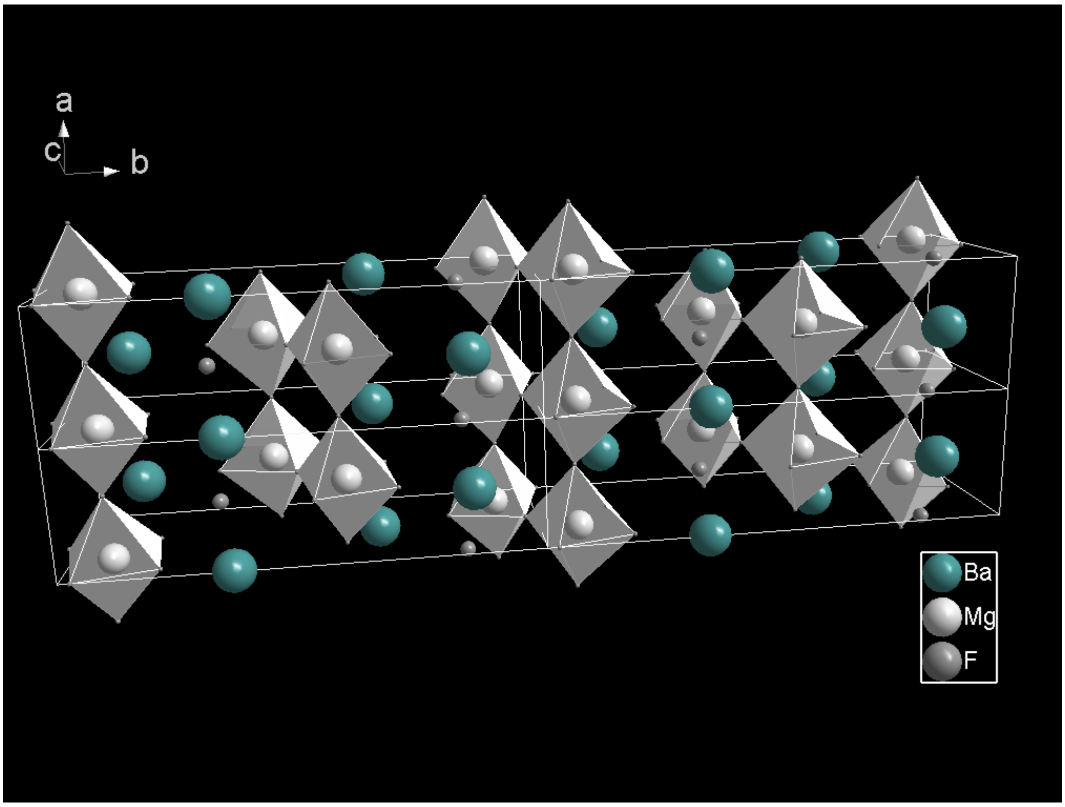

Figure 53: Crystal structure of $BaMgF_4$. Four unit cells of the structure are shown. The Mg ions are octahedrally coordinated by fluoride ions while the Ba ions are coordinated by four fluoride ions.

routines for nano-crystalline $BaMF_4$ compounds. Here the solvent-free mechanosynthesis of nano-crystalline $BaMgF_4$, $BaZnF_4$ and a mixed phase, $BaMg_{0.5}Zn_{0.5}F_4$, and its characterization by XRPD and ^{19}F MAS NMR is reported.

12.2 Experimental

Mixtures of micro-crystalline BaF_2 (99.99%, Alfa Aesar), MgF_2 (99.99%, Alfa Aesar) and ZnF_2 (99.995%, Alfa Aesar) were high-energy ball milled employing a Fritsch Pulverisette 7 premium line planetary mill at a rotational speed of 600 rpm. For the milling procedure vial sets made of tungsten carbide (45 mL) and 100 milling balls with a diameter of 5 mm made of the same material were used. The mixtures containing only BaF_2 and MgF_2 were milled under air while the mixtures including the hygroscopic ZnF_2 were milled under Argon.

The XRPD measurements were done with a Bruker Advance 8 diffractometer using Cu-K_α radiation at 40 kV leading to $\lambda_{XRD} = 0.154$ nm. ^{19}F MAS NMR spectra were recorded with a Bruker Avance III spectrometer operating at 565 MHz employing a 1.3 mm MAS probe (Bruker) with a spinning speed of 60 kHz. The NMR spectra were acquired using a single $\frac{\pi}{2}$ excitation pulse with a length of approximately 2 μs and an accumulation number of 32 scans.

12.3 Results and Discussion

12.3.1 X-ray powder diffraction

In Fig. 54 XRPD patterns of mixtures of BaF_2 and MgF_2 to give $BaMgF_4$ after various times of high-energy ball milling are shown. As can be seen, even after 30 minutes of milling, peaks which

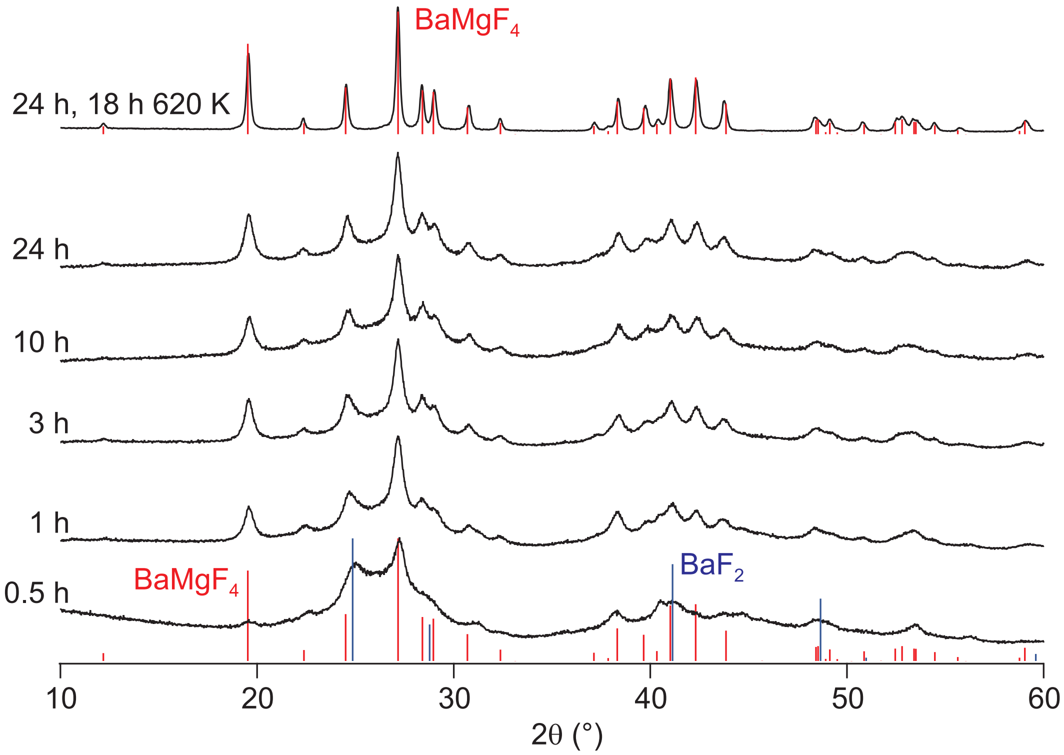

Figure 54: XRPD patterns of a mixture of BaF_2 and MgF_2 to give $BaMgF_4$ milled for different times.

can be assigned to $BaMgF_4$[1] (red bars) can be observed besides peaks of BaF_2 (blue bars) and MgF_2 (green bars). There are no other peaks visible in the XRPD patterns. Thus the $BaMgF_4$ seems to be formed directly from the binary fluorides. With increasing milling time the peaks of the binary fluorides vanish until after about 10 h of milling only peaks of $BaMgF_4$ can be observed. Milling for 24 h does not change the diffractogram in a pronounced way although the peaks seem to become more distinct.

By using the formula introduced by Williamson and Hall (equation (97)) the average crystallite diameter $\langle d \rangle$ and the lattice strain $\varepsilon = (d_{\mathrm{hkl}} - d_{\mathrm{hkl},0})/d_{\mathrm{hkl},0}$, whereby $d_{\mathrm{hkl},0}$ are distances between atomic planes in the non-strained system, and d_{hkl} the respective ones in the strained system, can be calculated.

$$\frac{\beta_r cos(\theta)}{\lambda_{\mathrm{XRD}}} = 4\varepsilon\frac{sin(\theta)}{\lambda_{\mathrm{XRD}}} + \frac{1}{\langle d \rangle}. \tag{97}$$

Thereby β_r denotes the difference of the full linewidth at half maximum (fwhm) of the XRPD peaks measured and the instrumental peak broadening (which is assumed to be 0.1° 2θ, estimated from the XRPD pattern of a ground $BaLiF_3$ single crystal). The wavelength λ of the X-ray radiation used was 0.154 nm. For the sample milled for 24 h giving $BaMgF_4$ an average crystallite size $\langle d \rangle = 35(5)$ nm and $\varepsilon = 0.005(2)$ was calculated.

In Fig. 55 the XRPD patterns of equimolar mixtures of BaF_2 and MgF_2 mechanically treated for 24 h and after heat treatment for 18 h at 620 K are shown. After heat treatment the XRPD peaks are clearly narrowed which indicates growth of the crystallites or decreased lattice strain. The peaks of the heat treated sample are in good agreement with the ones of $BaMgF_4$ from the literature[1]. The material is single phase without any traces of abraded WC.

In Fig. 56 the XRPD patterns of mixtures to give $BaMgF_4$, $BaZnF_4$ and $BaMg_{0.5}Zn_{0.5}F_4$ after milling for 24 h are shown. The XRPD pattern of the $BaZnF_4$ is in good agreement with the one

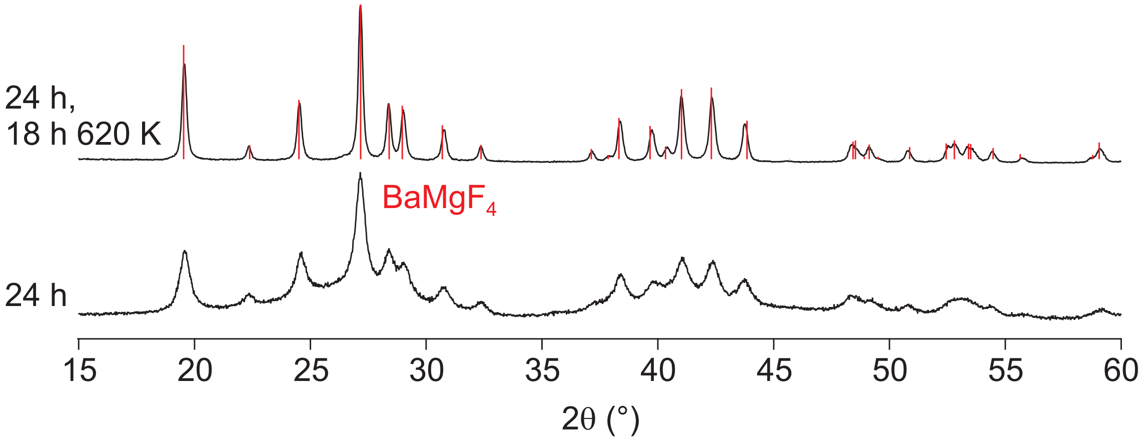

Figure 55: XRPD patterns of a mixture of BaF_2 and MgF_2 to give $BaMgF_4$ milled for 24 h and after annealing for 18 h at 620 K.

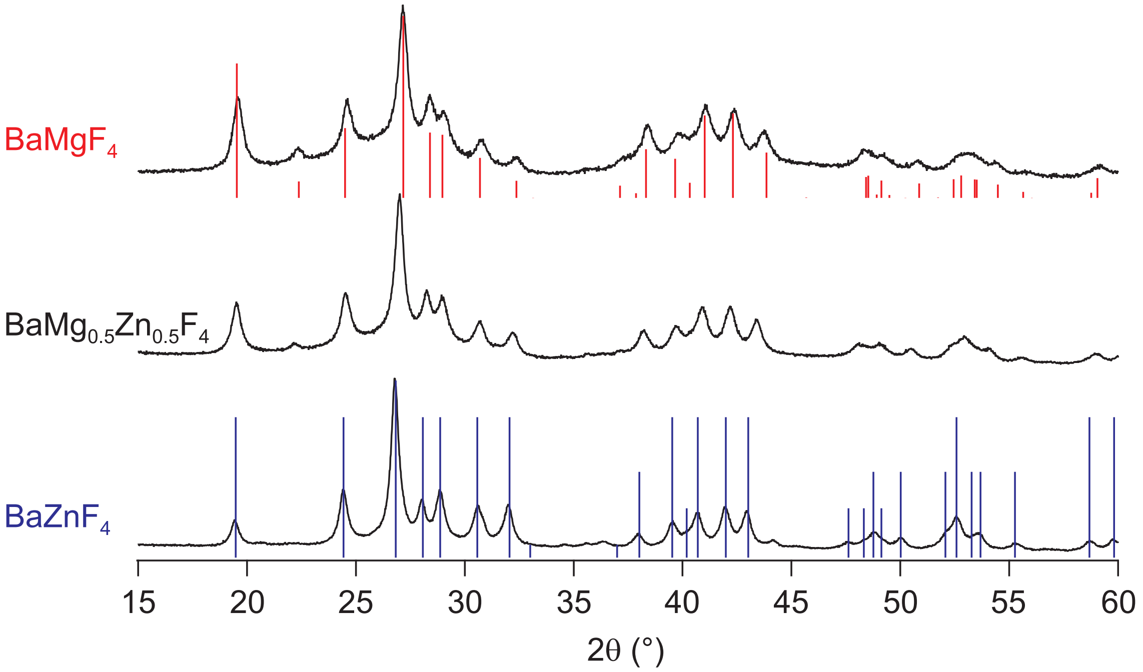

Figure 56: XRPD patterns of mixtures of the respective binary fluorides to give $BaMgF_4$ and $BaZnF_4$ as well as a mixture to give $BaMg_{0.5}Zn_{0.5}F_4$ after 24 h of milling.

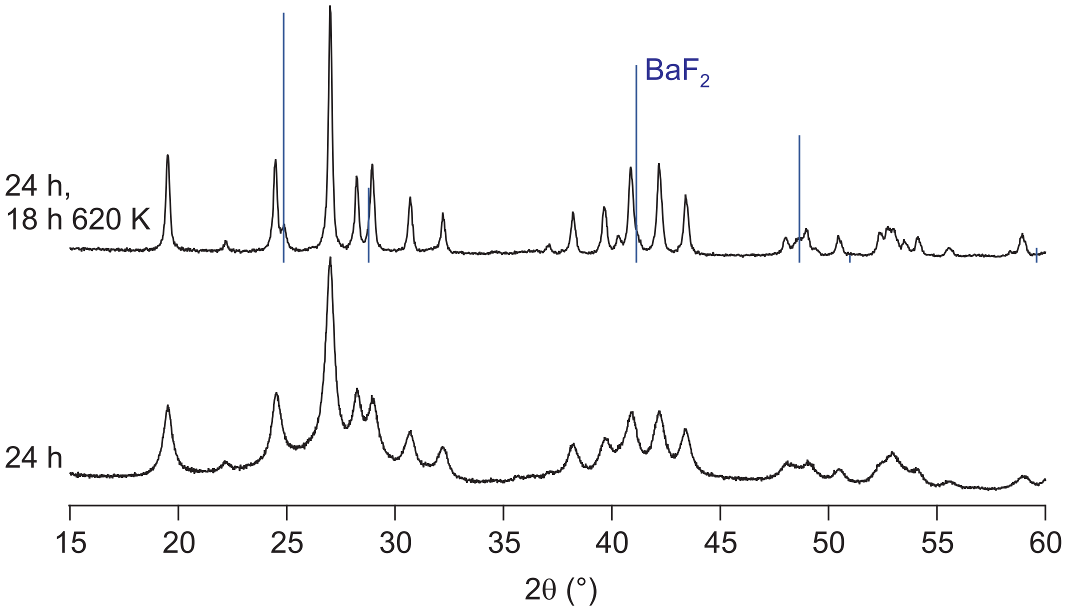

Figure 57: XRPD patterns of the mixture of the binary fluorides to give $BaMg_{0.5}Zn_{0.5}F_4$ after 24 h of milling and after heat treatment for 18 h at 620 K.

from the literature[12], although there are some additional small peaks around 35° 2θ and at 44° 2θ which cannot be assigned to the $BaZnF_4$ phase, to one of the educts used, a known $(Ba,Zn)F_z$ phase or abraded WC. The low intensities of the peaks makes the identification of the phase even more difficult.

The XRPD pattern of the mixture to give $BaMg_{0.5}Zn_{0.5}F_4$ expectedly resembles the ones of the $BaMgF_4$ and $BaZnF_4$ and shows no additional peaks of another phase. The reflex positions are in between those of $BaZnF_4$ and $BaMgF_4$. Thus, it seems plausible to assume that single phase $BaMg_{0.5}Zn_{0.5}F_4$ was prepared (ignoring the possibility of amorphous material being present in the sample) for the first time since it could not be found in the literature. In Fig. 57 the XRPD pattern of the mechanosynthesized $BaMg_{0.5}Zn_{0.5}F_4$ before and after heat treatment for 18 h at 620 K is shown. The structure of the compound is retained but there are additional XRPD peaks of cubic BaF_2. Thus, the $BaMg_{0.5}Zn_{0.5}F_4$ is reduced in Ba. Perhaps it tends towards a system in which the cations are equally represented like $Ba_{0.34}Mg_{0.33}Zn_{0.33}F_4$. Hence, it seems that $BaMg_{0.5}Zn_{0.5}F_4$ is a metastable compound. Further investigations of the mixing behavior of the three binary fluorides will be performed in the future.

The thermal lability of the $BaZnF_4$ can be seen in Fig. 58. After heat treatment for 18 h at 620 K the prominent phase is Ba_2ZnF_6 in addition to a smaller amount of $BaZnF_4$ and a small amount of cubic BaF_2. The intensity of the peaks of the unknown phase already visible in the non-heat treated material grow (black arrows in the figure) during heat treatment. In upcoming investigations the thermal stability of the mechanosynthesized $BaZnF_4$ will be tested in more detail.

12.3.2 ^{19}F MAS NMR spectroscopy

In Fig. 59 ^{19}F MAS NMR spectra of mixtures of BaF_2 and MgF_2 to give $BaMgF_4$ milled for the times indicated are shown. After 30 minutes of milling the spectrum is dominated by an intense and narrow NMR line with a chemical shift of -32 ppm which can be assigned to MgF_2[13]. The NMR line of BaF_2 is visible at 152 ppm which is also in good agreement with the value from the literature[13]. Interestingly, the NMR line of the BaF_2 is much less intense and clearly broader than the one of the MgF_2. The fitting of these two NMR lines gives a BaF_2 to MgF_2 ratio of about 1 to 5.

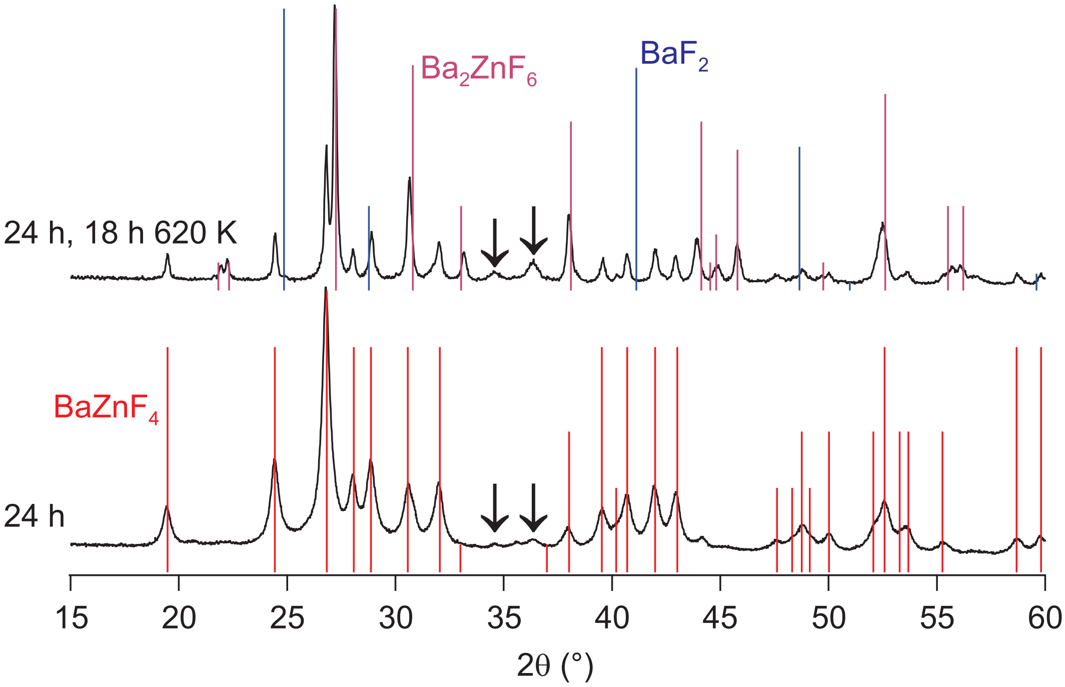

Figure 58: XRPD patterns of the sample prepared from an equimolar mixture of BaF_2 and ZnF_2 after milling for 24 h and after heat treatment for 18 h at 620 K.

Since equimolar amounts of BaF_2 and MgF_2 were milled and since after 30 minutes of high-energy ball milling the material should be well intermixed this means that a large part of the BaF_2 must have lost its chemical identity. A small part of the cubic BaF_2 transformed to orthorhombic BaF_2 which is, as was already discussed in the chapter dealing with the $Ba_{1-x}Ca_xF_2$, a high pressure polymorph of BaF_2. Its NMR lines show up at 104 ppm and 176 ppm which is in good agreement with the values found by Ruprecht et al.[14]. The rest of the BaF_2 has to be found in the other NMR lines. If the NMR line at 168 ppm which cannot be assigned to a known phase (maybe a small amount of $Ba_{1-x}Mg_xF_2$ with small or large x) is integrated and when hypothetically assuming that it is an unknown polymorph of BaF_2 (which is very unlikely) then the ratio of MgF_2 to BaF_2 would change to 2 : 1. Thus, it seems plausible to assume that the broad NMR line in between the NMR lines which can be assigned to $BaMgF_4$ is due to BaF_2 coordinated to or in reactive contact with MgF_2. Due to the different hardness of MgF_2 (according to CrysTec GmbH: 6 (Mohs scale) and BaF_2 (according to CrysTec GmbH: 3 (Mohs scale)) it is plausible to assume that very small BaF_2 crystallites surround larger MgF_2 crystallites which would explain the differences in broadness (MgF_2 is more ordered than the BaF_2 due to its larger crystallite size which leads to a narrower NMR line) and abundance of the two bulk binary fluorides in the milled mixture (loss of the chemical identity of the BaF_2 when coordinated to the MgF_2 in the grain boundary regions of the MgF_2). Hence, the large width of the NMR line located between the NMR lines of the $BaMgF_4$ is probably due to a superposition of many NMR lines with slightly different chemical shifts. This is expected if one of the fluorides is distributed in the grain boundary affected regions of the other fluoride. A similarly broad ^{19}F MAS NMR line was observed for CaF_2 distributed in the grain boundary regions of γ-Al_2O_3.[15]

With increasing milling time the broad NMR line decreases in intensity as well as the NMR lines of the binary fluorides while the intensity of the NMR lines of the $BaMgF_4$ increases, thus, the reaction progresses. As was already observed from the XRPD patterns the reaction seems to be almost finished after 10 h since no other NMR lines than the ones of the product can be observed. However, analogous to the observations from the XRPD patterns, the intensity of the broad shoulders

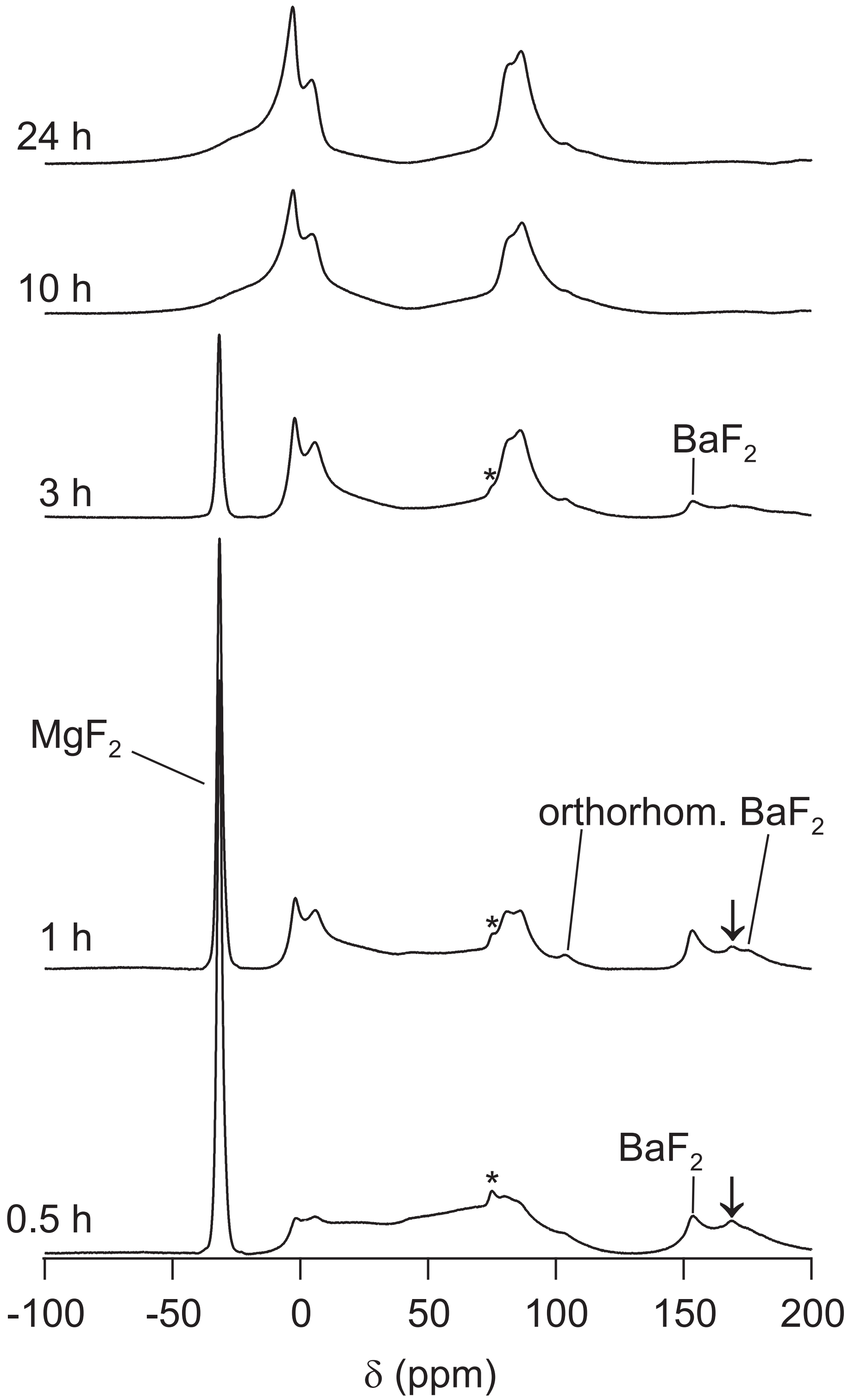

Figure 59: ^{19}F MAS NMR spectra of equimolar mixtures of BaF_2 and MgF_2 milled for the times indicated. The spectra were recorded with a spectrometer frequency of 565 MHz and an MAS spinning rate of 60 kHz. The arrows point to an unknown phase. Spinning sidebands are marked with asterisks.

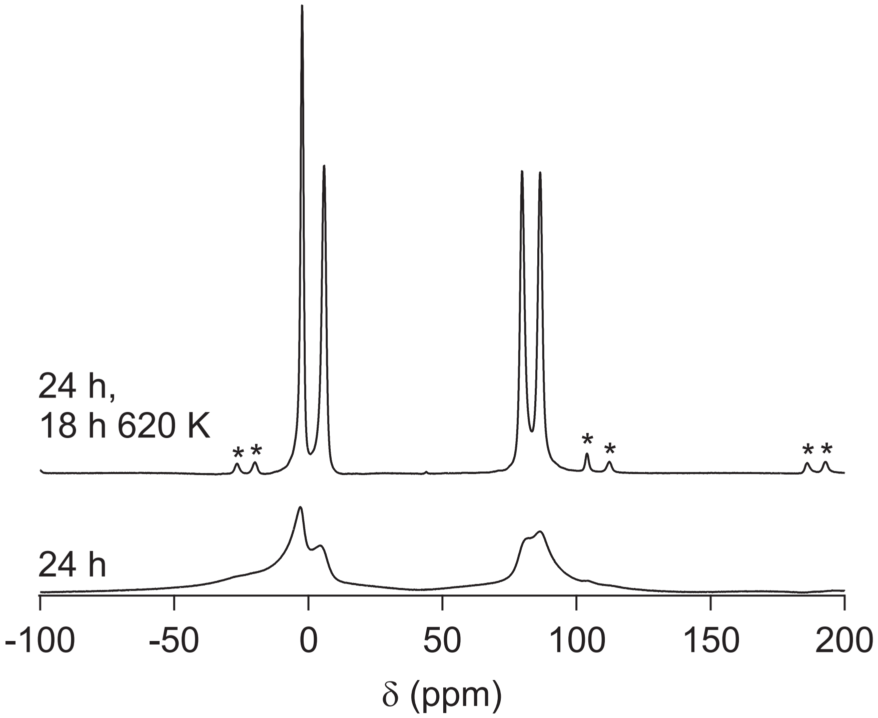

Figure 60: ^{19}F MAS NMR spectra of an equimolar mixture of BaF_2 and MgF_2 milled for 24 h, and after heat treatment for 18 h at 620 K of the milled material. The spectra were recorded with a spectrometer frequency of 565 MHz and an MAS spinning rate of 60 kHz. Spinning sidebands are marked with asterisks.

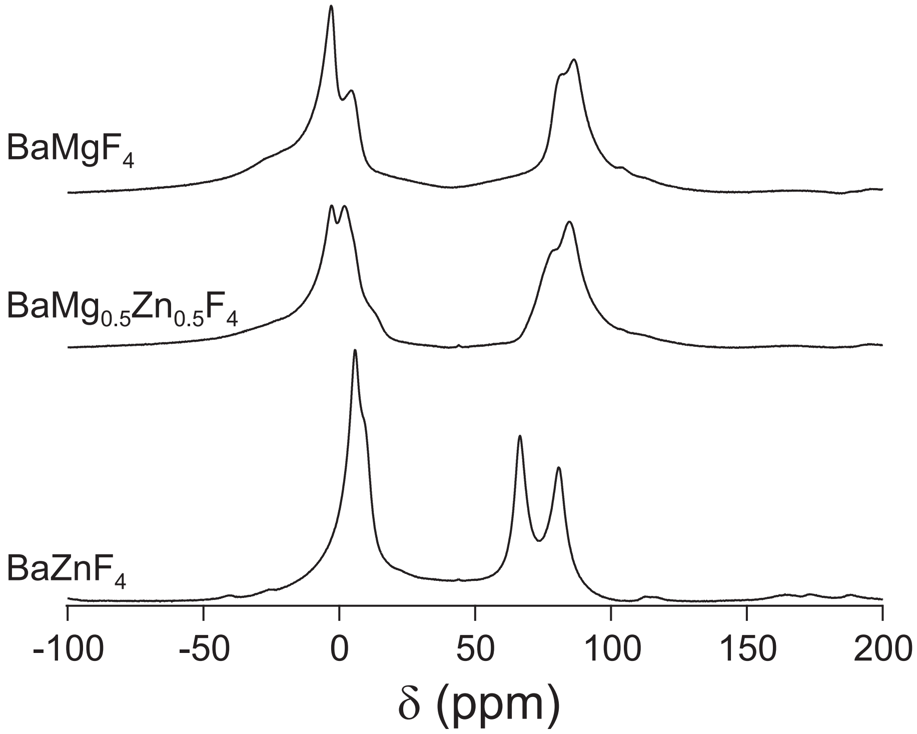

Figure 61: ^{19}F MAS NMR spectra of an equimolar mixture of BaF_2 and MgF_2, a mixture of BaF_2, MgF_2 and ZnF_2 to give $BaMg_{0.5}Zn_{0.5}F_4$, and an equimolar mixture of BaF_2 and ZnF_2, all milled for 24 h. The spectra were recorded with a spectrometer frequency of 565 MHz and an MAS spinning rate of 60 kHz.

in between the NMR lines of the $BaMgF_4$ still decreases, when going from 10 h to 24 h of milling while the NMR lines of the products become a more defined. Thus, the reaction still progresses after 10 h of milling. The chemical shift of the NMR lines are -3 ppm, 4 ppm, 82 ppm and 86 ppm and thus in quite good agreement with the ones found in the literature (-5 ppm, 4 ppm, 77 ppm, 85 ppm according to ref. 13 or -2 ppm, 6 ppm 80 ppm and 86 ppm according to ref. 16). The four NMR lines correspond to the four different sites[1] of the fluoride ions in the $BaMgF_4$ lattice as shown by Kowalczyk et al.[16] After heat treatment for 18 h at 620 K the chemical shift changes to -2 ppm, 6 ppm, 80 ppm and 86 ppm being in perfect agreement with the chemical shift values reported by Kowalczyk et al.[16] Furthermore the NMR lines are much narrower and clearly separated giving a spectrum very similar to the one recorded for single crystalline $BaMgF_4$[16], see Fig. 60. The differences in chemical shift, although rather small, exhibit structural differences between the heat treated and, thus, micro-crystalline $BaMgF_4$ and the nanocrystalline $BaMgF_4$. Since the NMR lines of the similarly coordinated fluoride ions leading to chemical shift of -2 ppm and 4 ppm, as well as 82 ppm and 86 ppm are closer to each other than for the heat treated sample the microstructure seems to become slightly more symmetric. However, the structural changes should affect the polarization behavior and probably also the conductivity behavior as will be tested in the future.

In Fig. 61 the ^{19}F MAS NMR spectra of the mixtures of the respective binary fluorides to give $BaMgF_4$, $BaZnF_4$ and $BaMg_{0.5}Zn_{0.5}F_4$ after mechanical treatment for 24 h are shown. The line shape of $BaMg_{0.5}Zn_{0.5}F_4$ differs from the line shapes of $BaMgF_4$ and $BaZnF_4$ regarding the chemical shifts and intensities of the NMR lines. There are no NMR lines of $BaMgF_4$ or $BaZnF_4$ visible in the spectrum of $BaMg_{0.5}Zn_{0.5}F_4$. This supports the assumption of the formation of this cation mixed phase. The chemical shifts of the NMR lines of the mechanosynthesized $BaMg_{0.5}Zn_{0.5}F_4$ are -2.8 ppm, 1.9 ppm, 80 ppm and 85 ppm. There seems to be an NMR line at about 6 ppm, too.

The chemical shifts of the mechanosynthesized $BaZnF_4$ (5.8 ppm, $\sim$9 ppm, 66.5 ppm and 80.7 ppm) are in good agreement with the ones reported in the literature (3 ppm, 7 ppm, 65 ppm and 80 ppm according to ref. 13 or 6.3 ppm, 9.6 ppm, 66.1 ppm and 80.7 ppm according to ref. 16) although the two NMR lines at about 6 ppm and 9 ppm, respectively, overlap. There is one additional NMR line of low intensity at about -40 ppm visible which cannot be assigned to a known compound.

After heat treatment of $BaMg_{0.5}Zn_{0.5}F_4$ for 18 h at 620 K the ^{19}F MAS NMR spectrum reveal seven clearly separated NMR lines with the chemical shifts -2.3 ppm, 2.7 ppm, 5.7 ppm, 13.6 ppm, 74.6 ppm, 77.2 ppm and 84.4 ppm in addition to the NMR line of BaF_2 at 152 ppm which was also observed in the XRPD pattern (Fig. 57), see Fig. 62. There seem to be two more NMR lines at about 9 ppm and 70 ppm. This large number of NMR lines reveal the cation mixing in the compound creating different cationic environments for the fluoride ions. The chemical shifts are different from the ones of $BaMgF_4$ and $BaZnF_4$ and, thus, a mixture of this both compounds creating this spectrum can be excluded.

As already revealed by XRPD the heat treatment of pure $BaZnF_4$ leads to the formation of Ba_2ZnF_6 which can also be seen in the ^{19}F MAS NMR spectrum of this compound where the diagnostic NMR lines of this phase appear at 16.5 ppm, 28 ppm and 166.5 ppm which is in good agreement with the values from the literature (15 ppm, 30 ppm, 167 ppm)[13]. The NMR lines at 15 ppm and 30 ppm can also be seen in the ^{19}F MAS NMR spectrum of single crystalline $BaZnF_4$ recorded by Kowalczyk et al.[16], from which they denoted only the NMR line at 30 ppm as an impurity and assumed the NMR line at 15 ppm being a spinning sideband, exhibiting the difficulties in preparing phase pure $BaZnF_4$.

12.4 Conclusions and Outlook

Single phase nano-crystalline $BaMgF_4$ was synthesized by high-energy ball milling. It showed slightly different chemical shifts compared with the also phase pure $BaMgF_4$ after heat treatment.

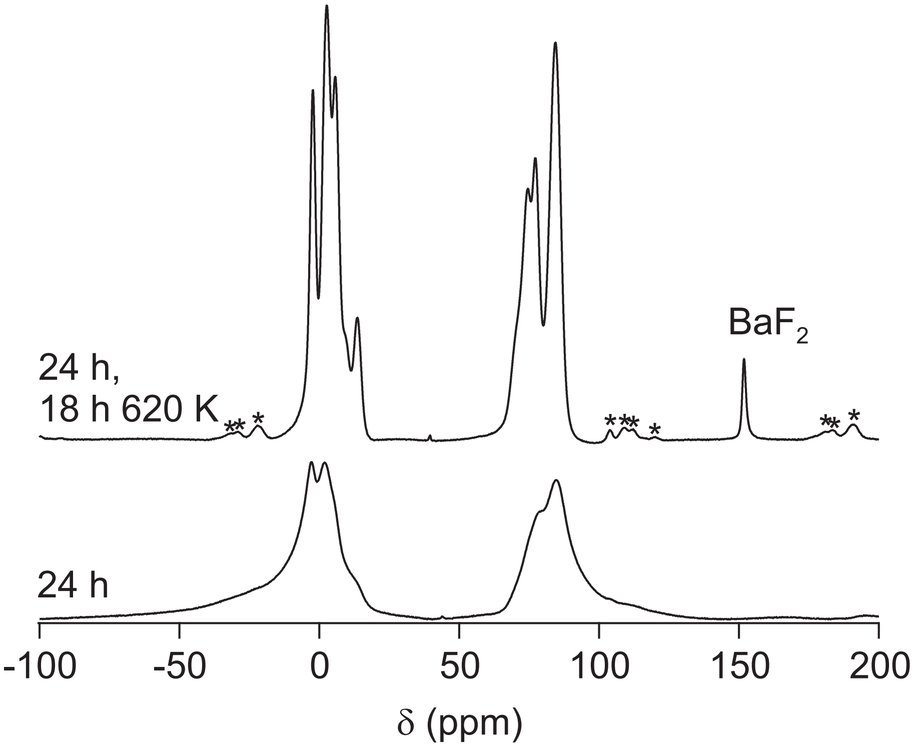

Figure 62: ^{19}F MAS NMR spectra of the mixture of BaF$_2$, MgF$_2$ and ZnF$_2$ to give BaMg$_{0.5}$Zn$_{0.5}$F$_4$ after milling for 24 h and after heat treatment for 18 h at 620 K.

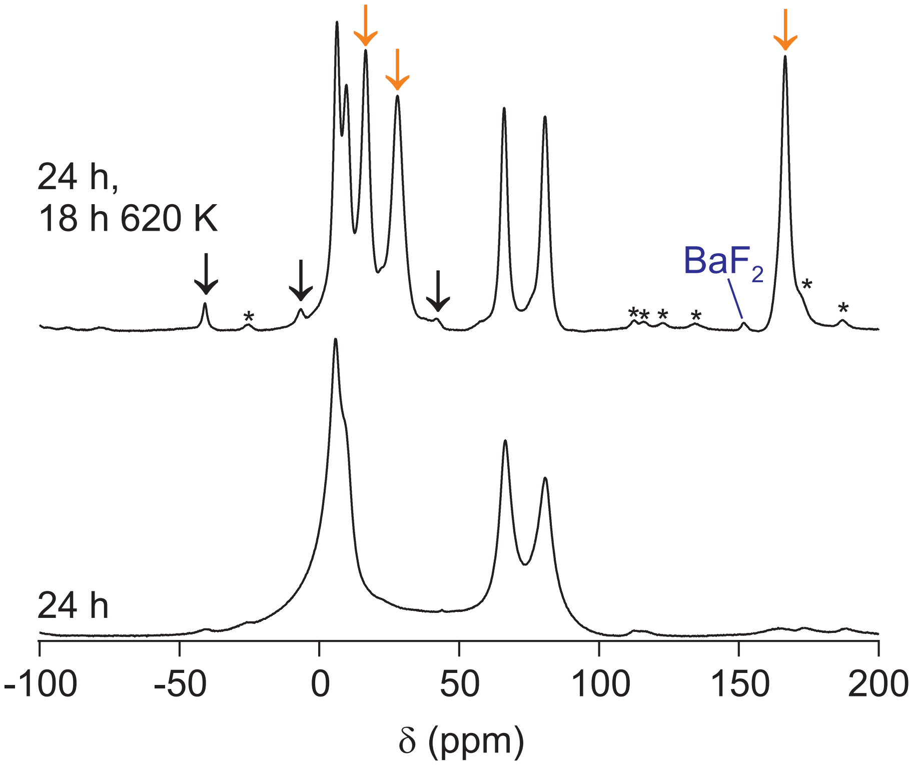

Figure 63: ^{19}F MAS NMR spectra of the equimolar mixture of BaF$_2$ and ZnF$_2$ after milling for 24 h and after heat treatment for 18 h at 620 K. The orange arrows mark the NMR lines of Ba$_2$ZnF$_6$ while the black arrows mark the NMR lines of an unknown impurity. Spinning sidebands are marked by asterisks.

This indicates a different, probably slightly more symmetric microstructure of the mechanosynthesized material. In case of $BaZnF_4$ almost single phase material was gained this way which, however, is contaminated by a small amount of an unknown impurity. Heat treatment of this material leads to the formation of Ba_2ZnF_6 and BaF_2 in addition to $BaZnF_4$. The mechanosynthesis of $BaMg_{0.5}Zn_{0.5}F_4$ was reported which loses some BaF_2 when heat treated at 620 K and, therefore, seems to be metastable. Evidence for the formation of this compound was shown by XRPD and more strikingly by ^{19}F MAS NMR revealing the mixed cationic environments of the fluoride ions in the $BaMg_{0.5}Zn_{0.5}F_4$ as well as in the in BaF_2 reduced compound after heat treatment.

In upcoming studies the heat stability of $BaMg_{0.5}Zn_{0.5}F_4$ and $BaZnF_4$ will be investigated in more detail. Furthermore, it will be tested if other stoichiometries of the quarternary fluoride can be prepared by high energy ball milling. The investigation of the ionic conductivity and polarization behavior of the mechanosynthesized and heat treated compounds will also be in the main focus in the future.

Acknowledgement. The author thanks A.-T. Duong for her support in preparation of the samples. Financial support by the Deutsche Forschungsgemeinschaft (DFG) within the frame of the Priority Program 1415, Kristalline Nichtgleichgewichtsphasen, is highly appreciated.

References

[1] F. Gingl, Z. anorg. allg. Chem. 623 (1997) 705.

[2] K. Shimamura, E. G. Villora, K. Muramatsu, N. Ichinose, J. Cryst. Growth 275 (2005) 128.

[3] S. W. Kim, H. Y. Chang, P. S. Halasyamani, J. Am. Chem. Soc. 132 (2010) 17684.

[4] M. Eibschütz, H. J. Guggenheim, S. H. Wemple, I. Camlibel, M. DiDomenico, Phys. Lett. 29A (1969) 409.

[5] A. R. Akbashev, A. R. Kaul, Russ. Chem. Rev. 80 (2011) 1159.

[6] J. Ravez, J. Phys. III 7 (1997) 1129.

[7] N. Setter, D. Damjanovic, L. Eng, G. Fox, S. Gevorgian, S. Hong, A. Kingon, H. Kohlstedt, N. Y. Park, G. B. Stephenson, I. Stolitchnov, A. K. Taganstev, D. V. Taylor, T. Yamada, S. Streiffer, J. Appl. Phys. 100 (2006) 051606.

[8] H. R. Zeng, K. Shimamura, C. V. Kannan, E. A. G. Villora, S. Takekawa, K. Kitamura, Appl. Phys. A 85 (2006) 173.

[9] C. V. Kannan, K. Shimamura, H. R. Zeng, H. Kimura, E. G. Villora, K. Kitamura, J. Appl. Phys. 104 (2008) 114113.

[10] S. Fujihara, S. Ono, Y. Kiskiki, M. Tada, T. Kimura, J. Fluor. Chem. 105 (2000) 65.

[11] U. Groß, S. Rüdiger, E. Kemnitz, Solid State Sci. 9 (2007) 838.

[12] M. Samouel, A. de Kozak, Cr. Acad. Sci. C Chim. 268 (1969) 2312.

[13] B. Bureau, G. Silly, J. Y. Buzaré and J. Emery, Chem. Phys. 249 (1999) 89.

[14] B. Ruprecht, M. Wilkening, A. Feldhoff, S. Steuernagel and P. Heitjans, Phys. Chem. Chem. Phys. 11 (2009) 3071.

[15] A. Düvel, E. Romanova, M. Sharifi, D. Freude, M. Wark, P. Heitjans, M. Wilkening, J. Phys. Chem. C 115 (2011) 22770.

[16] M. R. Kowalczyk, T. F. Kemp, D. Walker, K. J. Pike, P. A. Thomas, J. Kreisel, R. Dupree, M. E. Newton, J. V. Hanna, M. E. Smith, J. Phys.: Condens. Matter 23 (2011) 315402.

13 The fast fluoride ion conducting system LaF_3-SnF_2 and first investigations of the electrochemical stability of mechanosynthesized fluorides

The commonly used secondary battery systems today are, in addition to lead accumulators, mainly Li ion batteries. However, starting in the late seventies of the 20th century there were also attempts to build fluoride ion batteries based on the conversion reaction: MF_y + M' $\rightleftharpoons$ M + M'F_z.[1–12] Thus, fluoride ions serve as charge carriers between the electrodes consisting of a metalfluoride and a metal, respectively. The electrolytes used till now are ceramic fluoride ion conductors. These only show sufficiently high ionic conductivities at high temperatures. The main advantage of a fluoride ion battery is the fact that per metal cation at least one fluoride ion can be stored in the electrode leading to a very high theoretical specific capacitance of such a battery system. However, the metalfluoride as well as the countering metal has to be combined with a material that conducts electrons as well as fluoride ions.

In case of a complete discharge of the battery the following reaction should take place: MF_y + M' $\rightarrow$ M + M'F_z. For the reduction of MF_y to M the fluoride ions have to be transported from the interior of the MF_y grains to their surfaces and, thus, to the ion conducting material transporting the fluoride ions eventually to M' to form M'F_z. Therefore, the MF_y structure should change to the structure of the metal M starting from the middle of the grain in case MF_y is a fluoride ion conductor. It is not clear if the fluoride ions can work their way into the grains of the metal M' instead of just fluorinating the surfaces. This problem may be overcome if a larger amount of the metal M' is used or if M' has a higher valence than M. However, if this battery shall be charged again, the same problem should arise with the metal M. Thus, both, the metal as well as the metalfluoride should be nano-crystalline such that a large amount of the material is located in the grain boundary regions. Another solution could be the use of high surface geometries like nanorods. However, due to the oxidation of the metal and the reduction of the metalfluoride the volume of the grain (or nanorod) will change which should lead to contact-problems with the fluoride ion and electron conductor. A redox stable viscous liquid (maybe an ionic liquid) in which the metal and the metalfluoride particles are dispersed (like soggy sand) which conducts the fluoride ions as well as the electrons while keeping the nanoparticles well separated could be a solution to this problem. However, such a liquid was not found until now. Furthermore, the fluorination of the surfaces of the metal will in many cases interrupt the electron transport from the metal to the charge collector. Thus, another solution should be found which could be the one used for Li ion batteries: insertion compounds. These compounds retain their structure and the volume changes are sufficiently small. In Li ion batteries graphite acts as the anode material by incorporating Li (which gives its electron to the graphite and becomes Li^+, giving the battery its name). Graphite, however, will most probably not incorporate negatively charged ions in between its layers but react to CF_x. Therefore other materials, maybe containing metal ions which can change their valence without changing the structure in a pronounced way, have to be found.

Another problematic piece of a fluorine battery is, as was already mentioned, the electrolyte. The fastest fluoride ion conductors known are $PbSnF_4$ followed by $KSnF_4$ and $BaSnF_4$[13], thus Sn containing compounds. Here first results on a new system exhibiting very high ionic conductivities shall be briefly shown. In Fig. 64 a) the admittance spectra of a mixture of LaF_3 (99.9%, Fluka) and SnF_2 ("for synthesis", Chempur) with $x(SnF_2) = 0.60$ are shown. The samples were prepared by high-energy ball milling the mixtures for 6 h in a Fritsch Pulverisette 7 premium line planetary mill employing a milling beaker (45 mL) made of stabilized ZrO_2 and 140 milling balls (diameter: 5 mm) of the same material. The conductivity measurements were done with a Novocontrol Concept 80 broadband dielectric spectrometer at pellets cold-pressed from the powders at an uniaxial pressure of about 1 GPa. The measurements were done by slowly heating the samples up to a temperature of 513 K (for some samples only 473 K) and then decreasing the temperature in steps of 20 K except for SnF_2 where the sample was heated from 373 K up to 473 K to prevent sintering of the crystallites. The measurements were done in N_2 atmosphere which was evaporated from liquid nitrogen. Therefore, the pellets should be free of any water and, thus, there should be no pronounced contribution of proton-conduction to the overall conductivity. As can be seen a well developed dc plateau can already be seen at a temperature of 233 K. Starting at a temperature of 253 K, electrode polarization effects can be clearly

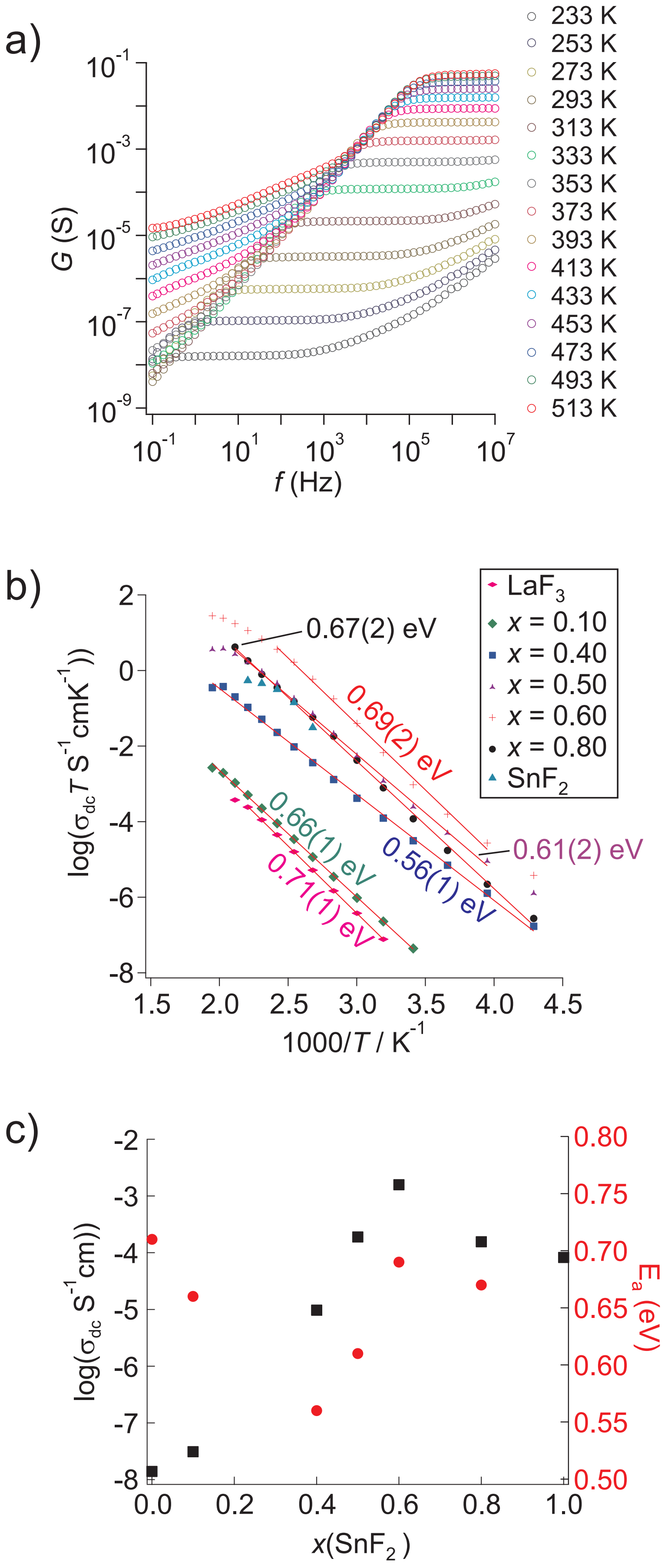

Figure 64: a) Admittance spectra of a milled mixture of LaF_3 and SnF_2 with $x(SnF_2) = 0.60$. b) Arrhenius plots of the high-energy ball milled LaF_3-SnF_2 mixtures. c) Logarithmic plot of the dc conductivities and activation energies of the LaF_3-SnF_2 mixtures as a function of composition x at 373 K.

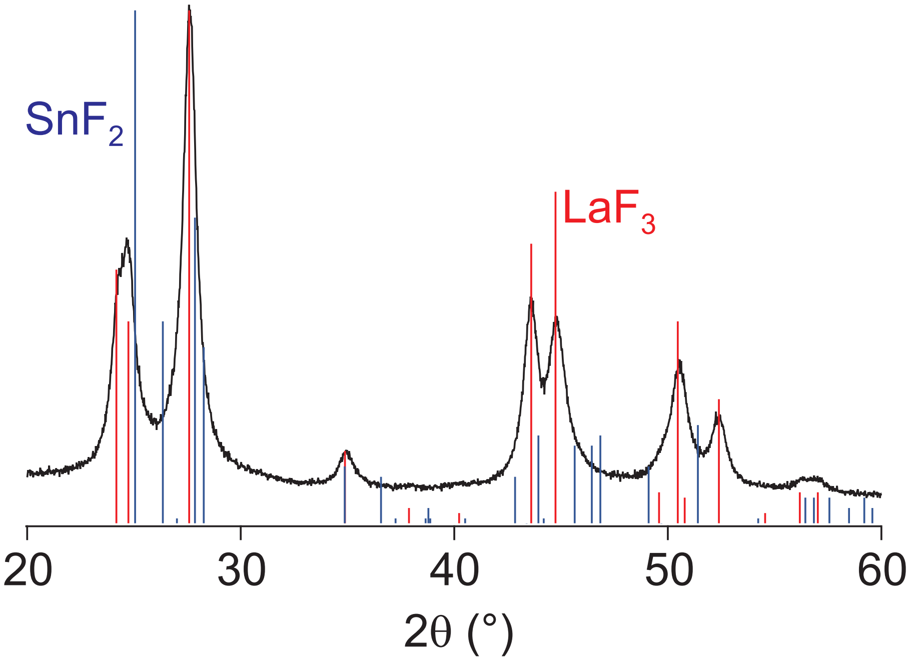

Figure 65: XRPD pattern of the sample with $x = 0.50$. The peak positions of LaF_3 and SnF_2 are shown by red (LaF_3) and blue (SnF_2) bars.

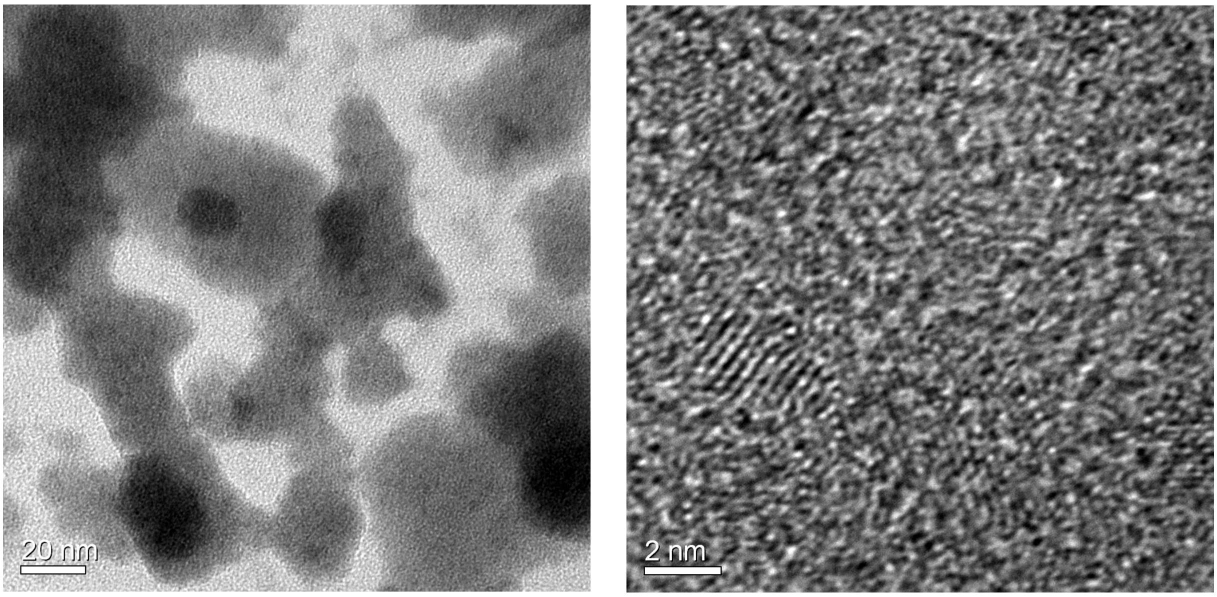

Figure 66: HRTEM micrographs of the sample with $x = 0.60$. In the picture on the left the reference bar has a length of 20 nm, in the picture on the right it is 2 nm.

seen at low frequencies shifting the dc plateau to higher frequencies with increasing temperature due to the ion blocking electrodes. Thus, the conductivity is probably mainly ionic. At 513 K the transfer number of the electrons, being the fraction of charge carried by them, can be estimated to be smaller than 10^{-4} from the difference of admittance at the dc plateau and the admittance measured at the lowest frequency. However, since a conductivity plateau at low frequencies (caused by the electron conduction) is not visible, polarization measurements will be done in the future to separate the ionic from the electronic conductivity more accurate. Arrhenius behavior is observed for all the samples, see Fig. 64 b). The activation energies seem to follow the dc conductivities for the samples with $x \geq 0.40$, i. e. a high conductivity comes along with a high activation energy. Thus, since the ionic conductivity is in general dominated by the height of the migration barriers and the number of mobile ions it seems that the ionic conductivities scale with the number of mobile ions at least for the samples with $x \geq 0.40$. The Arrhenius plot of the sample with $x = 0.60$ shows a change of its slope at high temperatures exhibiting a decrease of the activation energy. Since the measurements were done starting from high temperatures and going to low temperatures this is not due to grain growth but indicates a change of the conduction mechanism which may be caused by structural changes in this temperature regime.

Plotting the conductivity of the investigated samples, measured at $T = 373$ K, as a function of composition x, Fig. 64 c) is obtained. The samples with $x = 0.20$ and $x = 0.30$ are missing since the mechanical treatment of these mixtures reproducibly lead to a product which generated an intense, moldy stench of which the origin remains unclear (HF and F_2 are described as having a keen smell; organo-tin compounds are described as having a moldy smell whereby their formation seems to be actually impossible). However, since it is not unlikely that the gaseous substance is (highly) toxic or (highly) corrosive the conductivities of these samples were not measured, yet. As can be seen the sample with $x = 0.60$ shows the highest dc conductivity which is higher than the one of $BaSnF_4$[13] and just about one order of magnitude smaller than the one of $PbSnF_4$[13] being the fastest known fluoride ion conductor. The reason for this high ion conductivity could be the nanostructuring of the SnF_2. In case of the pure high-energy ball milled SnF_2 the dc conductivity is very comparable to the one of the sample with $x = 0.50$ exhibiting the second highest dc conductivity of the samples investigated and being also higher than the conductivity of the high-energy ball milled SnF_2 reported in ref. 14. This would also explain the change of the activation energy at high temperatures since SnF_2 itself shows a similar behavior for temperatures larger than about 433 K which is not far from its melting point of 468 K[15] and, thus, probably related with the beginning of structural changes. However, since the measurements started at 513 K the SnF_2 should have been molten in the beginning such that the nanostructuring should have no effect anymore. Thus, the LaF_3 may somehow stabilize the nano-crystalline SnF_2. Structural investigations of heat treated samples will be done in the future.

In Fig. 65 the XRPD pattern (recorded with a Bruker Advance D8 diffractometer by using Cu-Kα radiation at 40 kV) of the sample with $x = 0.50$ is shown. The XRPD peaks of the LaF_3 can clearly be identified but there are no peaks of the SnF_2 visible. The LaF_3 peaks however are not shifted which indicates that there was no or at least almost no substitution of La ion by Sn ions. Thus, the SnF_2 seems to be amorphous or its crystallites are extremely small. In Fig. 66 two high resolution transmission electron microscopy (HRTEM) images of the sample with $x = 0.60$ are shown. The measurements were done in Hannover by Prof. Armin Feldhoff using a JEOL JEM-2100F. In the image on the left crystallites with diameters of about 40 nm can be seen which is probably the LaF_3. In the image on the right the atomic planes of a grain with a diameter of about 2-3 nm can be observed which is surrounded by material which exhibits no atomic planes. Thus, the residual material surrounding this crystallite seems to be amorphous. However, it should be noted that only the atomic planes which are orientated parallel to the electron beam can be seen. Therefore, it seems likely that the SnF_2 is nano-crystalline with crystallite sizes of a few nanometers which is, therefore, X-ray amorphous. It should be noted that EDX measurements were not done at high resolution due to technical problems with the device such that the chemical identity of the differently sized crystallites were not determined. Thus, at first glance the high ionic conductivity observed may be due to highly mobile fluoride ions in the grain boundary regions of the SnF_2 of which this material exhibits a large amount. The LaF_3 could act as tiny milling balls efficiently reducing the size of the SnF_2 crystallites. However, further investigations of the (micro) structure as well as of the ionic diffusivity are needed for a better understanding of this system.

The simple preparation and the fact that no PbF_2 is needed but less toxic LaF_3 for this fast fluoride ion conductor might be interesting for some applications. However, coming back to the fluoride ion battery it has to be considered that the specific energy of a battery is the product of the specific capacity and the working voltage. Thus, the larger the potential difference between anode and cathode the larger the possible specific energy of a battery can be. SnF_2[16], PbF_2[17] and $PbSnF_4$[18] turned out to be stable only in a narrow voltage range. Thus it seems likely that this is also true for the LaF_3-SnF_2 compounds prepared within this study (as well as for $BaSnF_4$). Maybe it can be used as an electrode material. However, the electrochemical stability of these compounds will be tested in the future as it was already done for $Ba_{0.50}Ca_{0.50}F_2$ and $Ba_{0.40}La_{0.60}F_{2.60}$ for which cyclovoltammograms were recorded in a cooperation with Dr. Ilie Hanzu, see the abstract titled "Evaluation of the electrochemical window of fast fluoride conductors by solid-state voltammetry" for the SSI 19 which was held in Kyoto (Japan) in 2013 attached to this chapter. It was found that in contrast to $Ba_{0.50}Ca_{0.50}F_2$ the $Ba_{0.40}La_{0.60}F_{2.60}$ is stable in a broad voltage range of about 3.2 - 3.5 V which makes this material interesting as an electrolyte in a fluoride ion battery when operated at high temperatures (due to its rather low fluoride ion conductivity). Perhaps a battery with a $Ba_{1-x}La_xF_{2+x}$ electrolyte could be operated at temperatures close to ambient temperature when thin films are used for which the ball milled material could be dispersed in a liquid and applied to the electrode material by spin coating (see e. g. ref. 19 for a short explanation of this technique).

Acknowledgement. The author thanks A. Feldhoff for the TEM measurements and W. Y. Tsang for her support in preparation of the samples. Financial support by the Deutsche Forschungsgemeinschaft (DFG) within the frame of the Priority Program 1415, Kristalline Nichtgleichgewichtsphasen, is highly appreciated.

References

[1] J. G. Kennedy, C. Hunter, J. Electrochem. Soc., **1976**, 123, 10-14.

[2] J. Schoonman, J. Electrochem. Soc., **1976**, 123, 1772-1775.

[3] Y. Danto, G. Punjade, J. D. Pistré, C. Lucat, J. Salardenne, Thin Solid Films, **1978**, 55, 347-354.

[4] J. Schoonman, K. E. D. Wapenaar, G. Oversluizen, G. J. Dirksen, J. Electrochem. Soc., **1979**, 126, 709-713.

[5] P. Hagenmuller, J.-M. Réau, C. Lucat, S. Matar, G. Villeneuve, Solid State Ionics, **1981**, 3/4, 341-345.

[6] J. Schoonman, A. Wolfert, Solid State Ionics, **1981**, 3/4, 373-379.

[7] I. Kosacki, Appl. Phys. A, **1989**, 49, 413-424.

[8] M. Shareefuddin, M. Jamal,. M. N. Chary, J. Phys. D: Appl. Phys., **1995**, 28, 440-442.

[9] G. G. Amatucci, N. Prereira, J. Fluorine Chem., **2006**, 128, 243-262.

[10] N. I. Sorokin, Russ. J. Electrochem., **2006**, 42, 744-759.

[11] W. West, J. Whitacre and L. Del Castillo, "Solid State Fluoride Battery for High Temperature Applications", Electrochemical Society Meeting Proceedings, May **2007**, Chicago, IL.

[12] M. Anji Reddy, M. Fichtner, J. Mater. Chem. 21 (2011) 17059.

[13] L. N. Patro, K. Hariharan, Solid State Ionics 239 (2013) 41.

[14] L. N. Patro, K. Hariharan, Mater. Lett. 80 (2012) 26.

[15] A. F. Hollemann, E. Wiberg, "Lehrbuch der Anorganischen Chemie", ed. 101, Walter de Gruyter, Berlin, New York 1995, S. 965.

[16] S. Bouazza, A. Saberi, M. Willert-Porada, Mater. Lett., **2011**, 65, 1334-1336.

[17] R. W. Bonne, J. Schoonman, J. Electrochem. Soc., **1978**, 125, 1628-1632.

[18] I. C. Stefan, C. P. Jacobson, S. J. Visco, L. C. De Jonghe, "Solid-state electrochemistry of fluoride ionic conductive materials", Abs. 1707, 206th Meeting, **2004**, The Electrochemical Society, Inc.

[19] F. E. Bulette, J. Appl. Phys. 25 (1954) 810.

EVALUATION OF THE ELECTROCHEMICAL WINDOW OF FAST FLUORINE ION CONDUCTORS BY SOLID-STATE VOLTAMMETRY

Ilie Hanzu[1], Andre Düvel[2], Florian Preishuber-Pflügl[1], Paul Heitjans[2] and Martin Wilkening[1]

[1] Technische Universität Graz, Institut für Chemische Technologie von Materialien
Stremayrgasse 9, 8010 Graz, Austria
[2] Gottfried Wilhelm Leibniz Universität Hannover, Institut für Physikalische Chemie und Elektrochemie
Callinstraße 3a, 30167 Hannover, Germany
E-mail: hanzu@tugraz.at

Keywords: fluorine-ion batteries, mechanochemistry, solid electrolytes, solid-state voltammetry

Introduction

Today, energy and environment related issues are undoubtedly of tremendous importance. Thus, many of the current research efforts are focused on prospecting and evaluating new materials with applications in the field of electrochemical energy storage.

Fluorine ion conductors have already been pioneered as solid electrolytes in full solid-state electrochemical systems. Systems such as Pb-CuF_2, Pb-BiF_3 or Sn-SnF_2 have been proposed and investigated [1]. Unfortunately, the choice of materials usable as solid electrolytes is somehow limited by the low mobility of F^-. Nevertheless, nanocrystalline fluorides with the fluorite-type structure exhibit an order-disorder transition accompanied by an increase in ionic conductivity and have been shown to have competitive conductivities. More recently, the preparation of materials with high defect concentrations by high-energy ball-milling has further improved the performances of the fluorides in terms of F^- conductivity [2].

However, in order to evaluate the stability and reliability of a full electrochemical cell based on fluorine ion conductors, the stability of the electrolyte with respect to the operating potentials of the electrodes has to be studied. Here, we report first results on the determination of the electrochemical window of two selected fluorine ion conductors.

Experimental

Nanocrystalline fluorine ion conductors were prepared by high-energy ball milling the binary fluorides (CaF_2: 99.99%, Alfa; BaF_2: 99.99%, Sigma; LaF_3: 99.9%, Fluka) in a Fritsch Pulverisette 7 (premium line) planetary mill. The mechanosynthesis was carried out in a zirconia milling beaker with 140 Y-stabilized ZrO_2 balls with a diameter of 5 mm. The mixtures were milled for 360 min at 600 rpm under air. After optimization the procedure, two fluoride conducting phases were obtained *viz* $Ba_{0.5}Ca_{0.5}F_2$ [2] and $Ba_{0.4}La_{0.6}F_{2.6}$. Pellets were assembled and pressed with a platinum grid in the middle. The Pt grid served as a pseudo-reference electrode for the cyclic voltammetry measurements. The use of Pt as a reference electrode has been already well documented in the literature [3]. The diameter of the pressing tool was 7 mm and the pressure used was 2 Mp. Gold contacts were applied to both sides of the pellets and they were fitted between the platinum contacts of a laboratory made measuring cell. Cyclic voltametry experiments were carried out under nitrogen protective atmosphere at 573 K with a VMP3 potentiostat (BioLogic Science Instruments).

Results and Discussion

First results show that the stability of ternary $Ba_{0.5}Ca_{0.5}F_2$ is relatively poor when compared to $Ba_{0.4}La_{0.6}F_{2.6}$ (see Fig. 1). $Ba_{0.5}Ca_{0.5}F_2$ reveals a sharp rise in current around 0.5 V (*vs* Pt reference) and thus seems to be considerably less stable with respect to oxidation. It also presents multiple peaks when scanning is performed in the cathodic direction. Most likely, this unexpected behavior is caused by the high concentration of point defects in combination with an inert (and thus reducing) atmosphere.

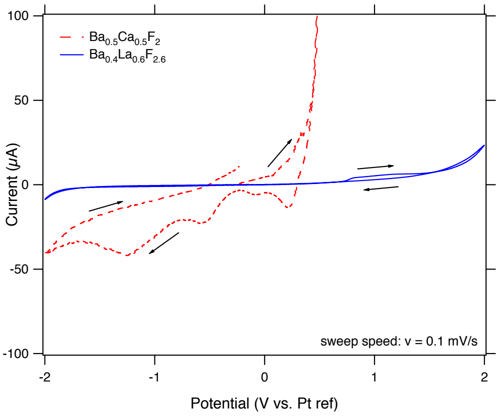

Fig 1. Solid-state cyclic voltammetry of two selected fluorine ion conductors. $Ba_{0.4}La_{0.6}F_{2.6}$ shows a better stability and a wider electrochemical window as compared to $Ba_{0.5}Ca_{0.5}F_2$.

On the other hand, $Ba_{0.4}La_{0.6}F_{2.6}$ appears to be significantly more stable and its electrochemical window can be estimated to 3.2 – 3.5 V. The almost absent current hysteresis points towards a stable system with promising applications to fluorine-ion batteries.

References

[1] M. A. Reddy and M. Fichtner, *J. Mater. Chem.* **21** (2011) 17059
[2] A. Düvel, B. Ruprecht, P. Heitjans, and M. Wilkening, *J. Phys. Chem. C* **115** (2011) 23784
[3] K. K. Kasem and S. Jones, *Platin. Met. Rev.* **52** (2008) 100

14 Mechanosynthesis of a new polymorph of SnF_2?

In the course of the work on the LaF_3-SnF_2 system it was found that high-energy ball milling of pure SnF_2 ("for synthesis", Chempur) leads to a change of its XRPD pattern instead of an amorphization as found in case of the LaF_3-SnF_2 system. The first clear changes of the XRPD patterns occurred after about 30 h of milling 2 g of SnF_2 in a milling beaker (45 mL) made of stabilized ZrO_2 equipped with 140 milling balls made of the same material (5 mm in diameter) in a Fritsch P7 premium line planetary mill at 600 rpm. Most noticeable is a new peak at about 24.7° 2θ next to the peak of the stable α-SnF_2 (at 25.05° 2θ).

After about 50 h of milling the XPRD pattern clearly differs from the one of α-SnF_2. Increasing the milling time further led to further changes of the XRPD pattern. It should be noted that this change of the structure due to ball milling does not depend on the milling atmosphere since it can be observed after milling in air as well as after milling in argon atmosphere. Therefore, it seems very unlikely that these changes are caused by the formation of oxides or oxyfluorides. The investigation of the structure is currently in progress in cooperation with Dr. Lars Robben (Uni Bremen). The new pattern cannot be matched with any of the known polymorphs of SnF_2 like β-SnF_2 and γ-SnF_2[1,2]. It seems plausible to assume the formation of a high-pressure polymorph of SnF_2. The high pressure phase of SnF_2 reported by Ghedia[3] in his thesis, however, differs from the phase prepared within this study. Furthermore, the XRPD patterns of other Sn_xF_y compounds or elemental Sn (which might form by a disproportionation reaction $SnF_2 \rightarrow Sn + SnF_4$) also showed no agreement with the pattern of the prepared material. The XRPD pattern of the sample milled for 50 h employing Mo Kα radiation ($\lambda \approx 0.07107$ nm) could be indexed to a tetragonal lattice with $a = b = 1.27$ nm and $c = 1.31$ nm by L. Robben. However, a high resolution X-ray scattering measurement conducted at Deutsches Elektronen Synchrotron (DESY) by Dr. Jozef Bednarcik, with $\lambda = 0.02073$ nm, lead to a more complex pattern, see Fig. 67. It was indexed to a monoclinic system with $a = 1.25767$ nm, $b = 0.61187$ nm and $c = 1.12058$ nm by L. Robben. A pair distribution function (PDF) was calculated from another pattern recorded over a larger q-range ($q = 4\,\pi\,\sin(\theta)/\lambda$) of up to 20 Å^{-1}, see Fig. 67. The interpretation of the data is still in progress.

The change of the structure was also investigated by ^{19}F MAS NMR spectroscopy conducted with an Avance III 600 MHz spectrometer (Bruker). The measurements were done at $\nu_L(^{19}F) = 565$ MHz ($B_0 = 14.1$ T) employing a 1.3 mm MAS probe (Bruker) at a spinning rate of 60 kHz. The NMR lines were referenced to C_6F_6. The NMR spectrum of the non-milled α-SnF_2 reveals four NMR lines with the chemical shifts 112 ppm, 115 ppm, 119 ppm and 124 ppm which can be assigned to the four different sites of the fluoride ions in the α-SnF_2 structure[4]. In table 1 the number of neighboring tin ions and their distances to the fluoride ion at the respective sites are listed. The ^{19}F MAS NMR spectrum is similar to the one reported by Bräuniger et al.[5] for α-SnF_2 (99%, Sigma Aldrich) although they were not able to resolve four but only two NMR lines located at 112 ppm and 121 ppm albeit they used a spinning rate of 60 kHz. This difference is probably due to the smaller field-strength of the magnet they used ($B_0 = 9.4$ T) for their measurements. Interestingly, in the ^{19}F MAS NMR spectrum of Bräuniger et al.[5] an additional, narrow NMR line was observed at about 50 ppm. They assigned it to an impurity. Thus, the batch of SnF_2 sold by Chempur seems to be less contaminated with other fluorides than the one from Sigma Aldrich.

As already discussed in the chapter "Increase of the fluoride ion conductivity in cation-mixed alkaline earth fluorides: mechanosynthesis and characterization of metastable $Ba_{1-x}Ca_xF_2$" the ^{19}F NMR chemical shift is a function of the distance between the cations and the fluoride ions, and the number of neighboring cations. The larger the number of neighbors and the smaller the distance between fluoride ion and cation, the larger the chemical shift. It should be recalled that the deshielding decreases exponentially with d(Sn-F). Thus, it seems plausible to assign the NMR line with the smallest chemical shift of approximately 112 ppm to the fluoride ions on F4 sites. In case of the fluoride ions on the other sites the assignment is difficult without knowing the exponential function of the shielding: Is the deshielding of the fluoride ions on F1 sites larger since it is characterized by the smallest d(Sn-F) of all sites than in case of F2 where the distance of the second Sn ion is clearly smaller than in case of the F1 site? How large is the additional deshielding caused by the Sn ion located in a distance of 0.26753 nm in case of the F3 site? Thus, an assignment can only be guessed. Furthermore, Sn has an electronegativity of about 1.7. Thus, the bonds between the Sn and fluoride ions will have a non-negligible covalent part which also affects the deshielding of the fluoride ions.

After 10 h of milling the SnF_2 its NMR lines start to coalesce, eventually forming a single, broad NMR

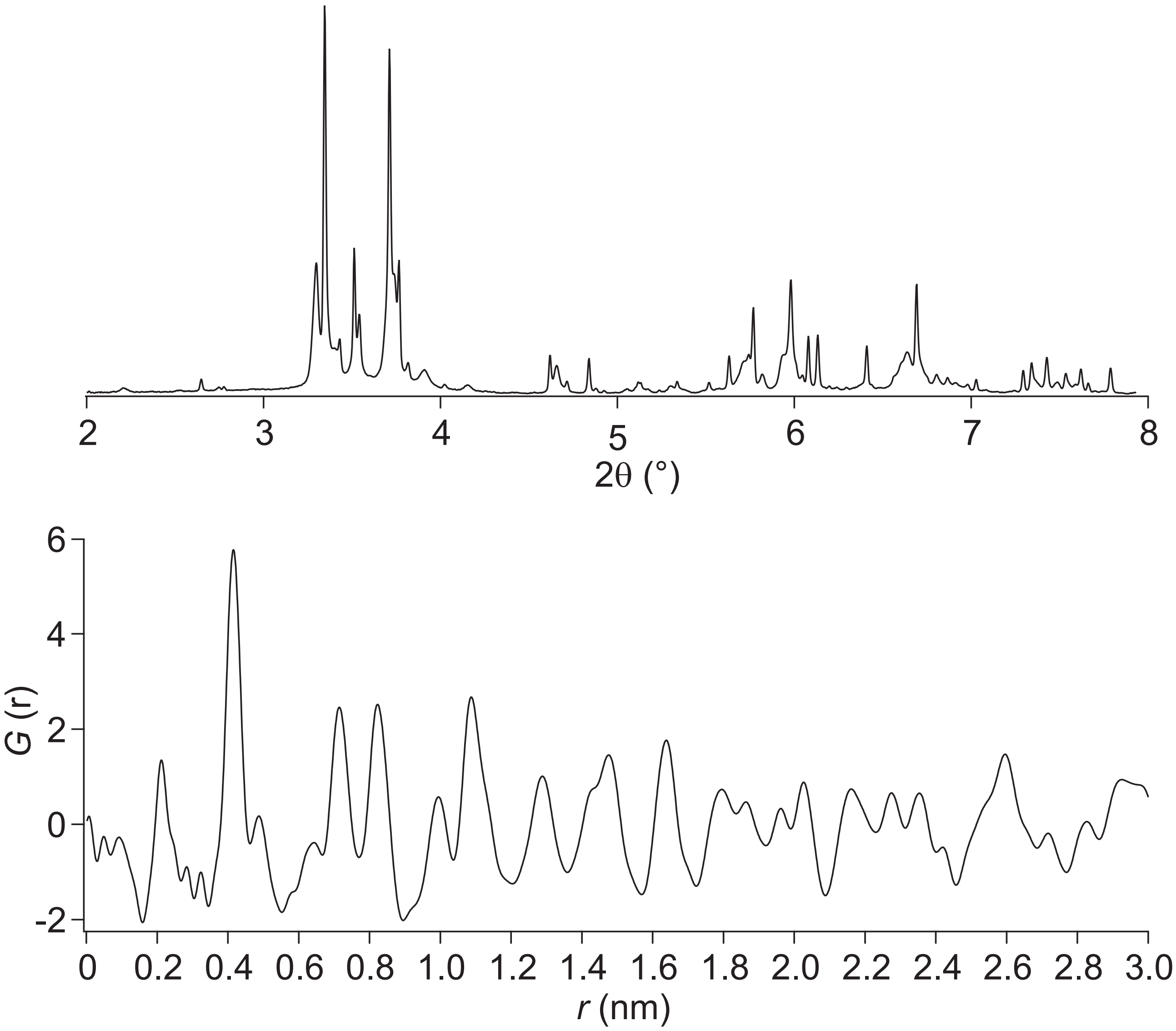

Figure 67: Top: XRPD pattern of SnF_2 milled for 50 h recorded at DESY with λ = 0.02073 nm. Bottom: PDF pattern of the same sample calculated from a XRPD pattern with larger q-range also recorded at DESY.

Table 4: Number of next nearest neighbors of the fluoride ions on the four different sites and their distances d(Sn-F) in accordance with ref. 4

site	d(Sn-F) in nm
F1	0.20266 0.24007
F2	0.20981 0.22037
F3	0.20678 0.24740 0.26753
F4	0.2182 0.2734 0.28439

line located at about 125 ppm in the spectra of the SnF_2 milled for 50 h. This chemical shift is very similar to the largest chemical shift in the ^{19}F NMR spectrum of the non-milled α-SnF_2. Furthermore, an additional narrow NMR line emerges at about 65 ppm. Increasing the milling time to 80 h the intensity of the narrow NMR line is increased and the broad NMR line exhibits a shoulder indicating an additional NMR line at about 130 ppm. Thus, it seems plausible to assume that the structure of the milled SnF_2 leads to an increase of the coordination number of the fluoride ions or a decrease of the average d(Sn-F) leading to an increase of the average chemical shift. However, the broad single NMR line might also be due to a beginning coalescence caused by a high jump rate of the fluoride ions in the milled SnF_2. ^{19}F MAS NMR measurements at lower temperatures planned for the future will allow a discrimination between structural and dynamic effects. The NMR line at about 65 ppm points to a small coordination number or a large Sn-F distance. It might also be a side-product of the reaction (like HF, which chemical shift strongly depends on its chemical environment[5]).

If the sample milled for 50 h is stored for some weeks, its XRPD pattern changes back to the one of α-SnF_2. Storage under air and storage in Argon atmosphere lead to very similar results. Thus, the decomposition is probably thermally induced rather than due to moisture or oxygen. This will be tested by in situ XRPD measurements in the future. However, the low stability of the material probably impedes conductivity measurements since the material has to be dried at temperatures larger than 373 K to get rid of the proton conductivity. The applicability of non-thermal drying techniques (drying in vacuum, or storage in the presence of P_2O_5) for this purpose will be tested in the future.

To get more information about the structure high resolution transmission electron microscopy (HRTEM) measurements were performed by Dr. Di Wang at Karlsruhe Institute of Technology (KIT) using a FEI Titan 80-300 with CEOS image Cs correction. The micrographs showed a fast structural change of the material caused by the electron beam, see Fig. 68. The change is accompanied by a decrease of the volume. Thus, the new phase seems to be rather a high-temperature than a high-pressure phase. The electron diffraction patterns, however, could not be interpreted due to insufficient data. Therefore, additional TEM measurements were done by Prof. Dr. Armin Feldhoff in Hannover. Strangely, although the sample investigated exhibited the XRPD pattern of a crystalline solid no crystalline material was observed by TEM and HRTEM. To rule out a decomposition by the solvent (isopropyl alcohol) used to disperse the SnF_2, additional measurements by simply scattering the dry material onto the grid were carried out. In that case again no crystalline material was observed. Therefore, no useful electron diffraction patterns are available for the milled SnF_2.

Planned ^{119}Sn Mößbauer spectroscopic measurements at KIT by Dr. habil. Vladimir Šepelák as well as by Prof. Franz Renz (Hannover) could not be done since no active Sn-source was available at the moment. That way information about the valence of the Sn and its coordination in the lattice could have been obtained. Maybe synchrotron radiation could be used for this purpose in the future. Also Raman-spectroscopic measurements are planned. However, the system is highly complex since its structure seems to change with prolonged milling. Furthermore, there are some difficulties concerning the reproducibility of the structural

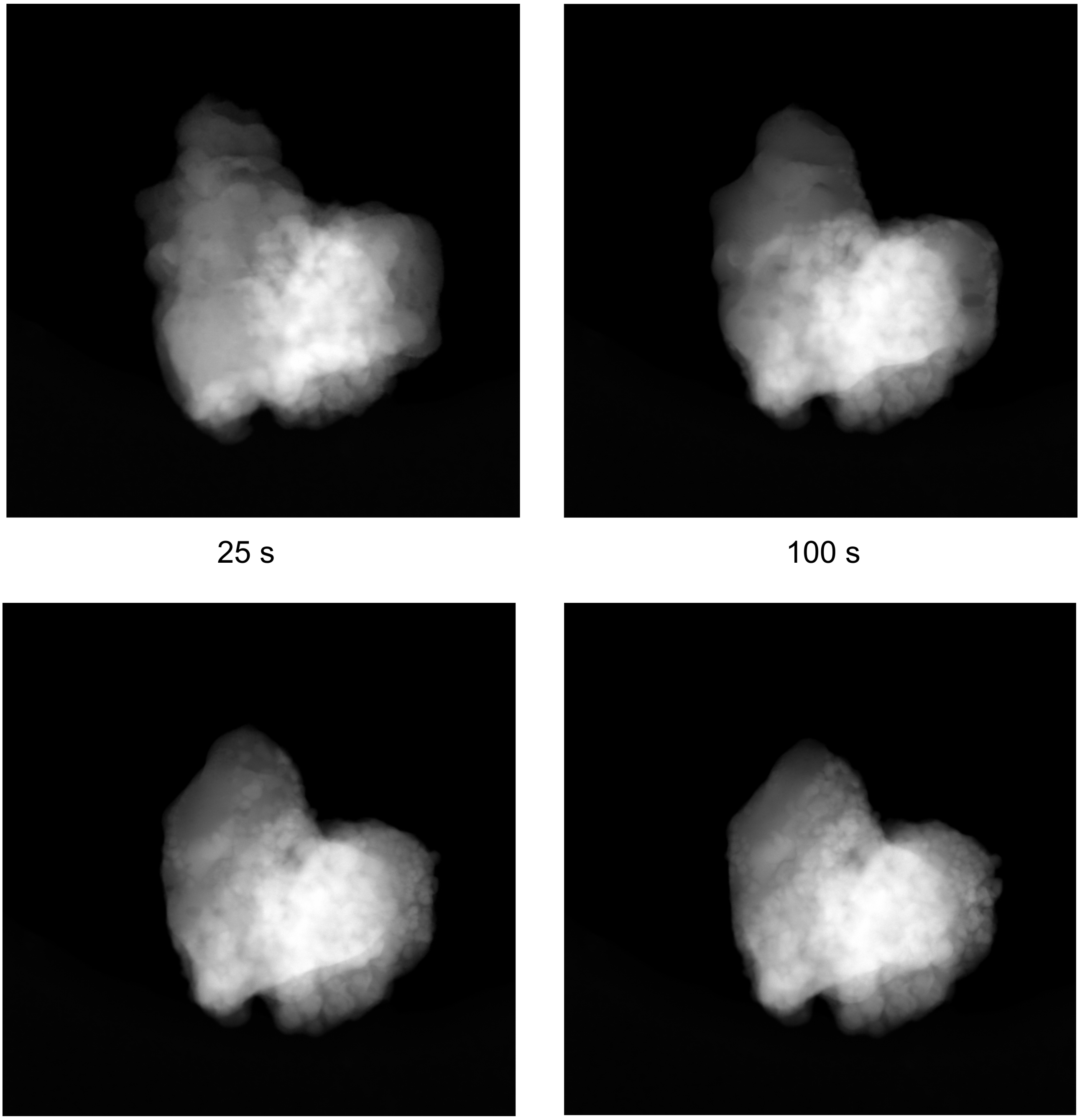

25 s

100 s

175 s

250 s

Figure 68: The change of a crystallite of SnF_2 milled for 50 h observed by scanning TEM microscopy.

changes which seem not to be related with the ball to powder mass ratio. Thus, other factors like, for instance, the air humidity at the moment the SnF_2 is put into the milling beakers may play a role. Another problem could be the purity of the α-SnF_2 used for this study. All this will be investigated in the future.

The preliminary results discussed here were exhibited on a poster at the 10th International Conference Solid State Chemistry (SSC) in Pardubice (CZ) which is shown in the following.

References

[1] G. Denes, J. Pannetier, J. Lucas, J. Solid State Chem. 33 (1980) 1.

[2] G. Denes, J. Solid State Chem. 78 (1989) 52.

[3] Stefan Anil Ghedia, "High Pressure - High Temperature Investigations of Solid Oxides and Fluorides", Dissertation, 2010, pp. 69-84.

[4] R. C. McDonald, H. Ho-Kuen Hau, K. Eriks, Inorg. Chem. 15 (1976) 762.

[5] T. Bräuniger, S. Ghedia, M. Jansen, Z. Anorg. Allg. Chem. 636 (2010) 2399.

Mechanosynthesis of a new metastable polymorph of SnF_2

A. Düvel[a], L. Robben[b], V. Šepelák[c], M. Wilkening[a,d], P. Heitjans[a]

[a)]Leibniz University of Hannover, [b)]University of Bremen, [c)]Karlsruher Institute of Technology, [d)]TU Graz

Mechanosynthesis of non-equilibrium fluorides

- the discovery of new materials is a mainspring for progress in many scientific and technological areas
- many interesting (regarding *e. g.* electrical, magnetic, mechanic and optical properties) materials are metastable which makes their synthesis a difficult task
- high-energy ball milling performed at ambient temperature was found to be a powerful technique for the preparation of highly metastable compounds

A new polymorph of SnF_2?

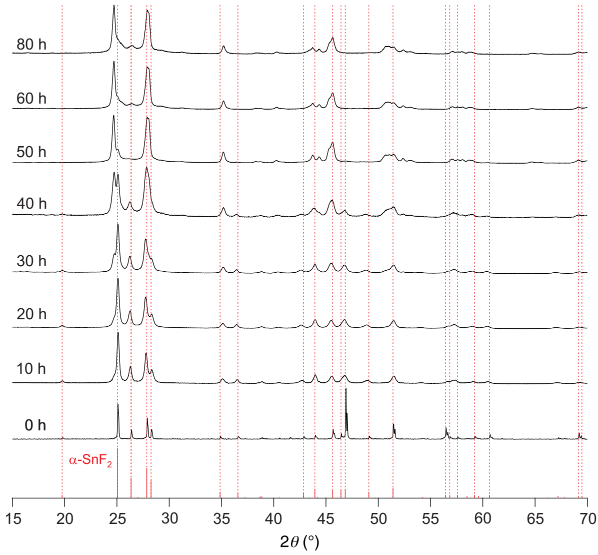

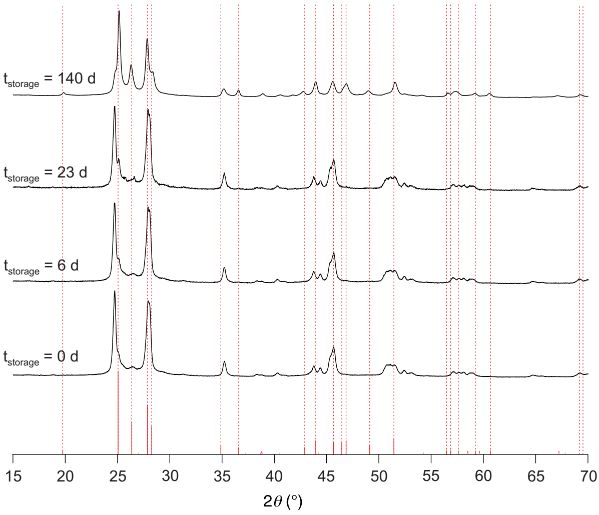

- SnF_2 is known to crystallize in different modifications (monocl. α-SnF_2, orthorh. β-SnF_2, tetrag. γ-SnF_2)
- broadening of peaks after several hours of milling
- after 10 h a new peak at ≈ 24.7 °2θ appears increasing in intensity with increasing milling time
- after 50 h of milling the XRPD pattern is different from the ones of SnF_2 polymorphs in the literature
- the pattern obtained after 50 h of milling can be indexed with a tetragonal lattice with a = b = 1.27 nm and c = 1.31 nm → tetragonally distorted cubic cell
- for longer milling times than 50 h an additional peak at 26.5 °2θ shows up
- ^{19}F MAS NMR line at 115 ppm of the α-SnF_2 shifts to larger values with increasing milling time; after 50 h: broad single NMR line with δ_{iso} = 124 ppm (reference = C_6F_6)

  → combination of higher symmetry and nanostructuration

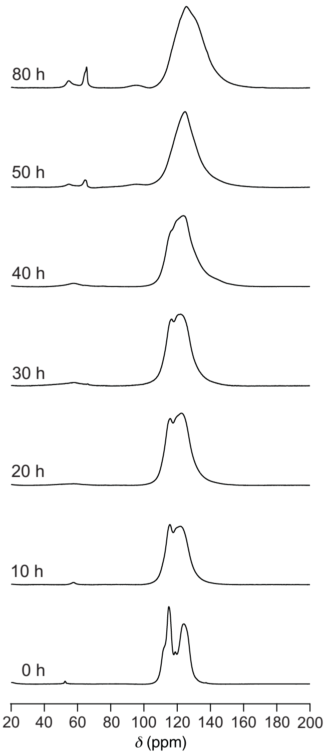

^{19}F MAS NMR spectra (spinnig rate = 60 kHz, $\omega_0/2\pi$ = 565 Mhz)

- samples milled for 50 h: storage in air or argon atmosphere leads to a retransformation of the new polymorph to α-SnF_2 → metastability
- questions: NMR lines showing up at 65 ppm, 55 ppm and 131 ppm?
  After 50 h of milling: another polymorph?
- investigations to elucidate the structure of the SnF_2 polymorph(s) in more detail are on the way (TEM, Mössbauer, ^{119}Sn NMR), magnetic and dynamic properties will be investigated by SQUID and static ^{19}F NMR techniques, respectively

Acknowledgments

We thank J. Caro and A. Feldhoff for access to the X-ray diffraction device (Bruker D8 Advance). Many thanks to E. Merzlyakova for their help with sample preparation.

SPP 1415

Financial support by the DFG (SPP 1415) is gratefully acknowledged.

DFG

15 Mechanosynthesis and characterization of the garnet-type fast Li ion conductor Al-doped $Li_7La_3Zr_2O_{12}$

Fast ceramic Li ion conductors are interesting for the use as electrolytes in all solid state Li ion batteries. In common Li ion batteries liquids or polymers are used as electrolytes such that they are not stable at elevated temperatures. Furthermore, these liquids are often toxic and flammable. Thus, the use of ceramic electrolytes should improve the performance and safety of a Li ion battery.[1] However, such an electrolyte needs to have an ionic conductivity of at least 10^{-4} S/cm at ambient temperature combined with a negligible electronic conductivity. Apart from this, it has to have a high (electro-)chemical stability.[1]

In 2007 Murugan et al.[1] reported on the synthesis of a ceramic Li ion conductor exhibiting ionic conductivities higher than 10^{-4} S/cm at ambient temperature. The compound prepared by them with the assumed composition $Li_7La_3Zr_2O_{12}$ (LLZ) crystallizes in a cubic garnet-type structure. The material exhibited a high mechanical and chemical stability. However, the first attempts of other groups to prepare this compound failed. Instead of the cubic garnet with the high ionic conductivity, LLZ with a tetragonal garnet structure was obtained which exhibited a conductivity of about 10^{-6} S/cm at ambient temperature[2,3]. Later it was found that the cubic phase can be stabilized by Al ions.[4–7] Thus it seems likely that they were accidentally introduced into the $Li_7La_3Zr_2O_{12}$ during the high-temperature synthesis from the corundum crucibles used by Murugan et al. This result raised several questions regarding the role of the Al in the LLZ. Which sites does the Al occupy? How does the Al affect the Li ion conductivity? Which amounts of Al can be introduced into the LLZ structure? Is there an optimal concentration of Al regarding the Li ion conductivity?

In the present study which was a collaborative work with Dr. Alexander Kuhn (a phd student of Prof. Heitjans at that time) a mechanochemical synthesis routine for the LLZ was created. It turned out that LLZ can be prepared directly from the oxides (Li_2O, Al_2O_3, La_2O_3 and ZrO_2) by high-energy ball milling employing a tungsten carbide milling vial set. However, subsequent heat treatment of the product at 873 K for 6 h was needed to obtain the phase pure LLZ. At these low temperatures there is almost no loss of the volatile Li and Al which was tested by elemental analysis before and after heat treatment employing inductive coupled plasma (ICP) optical emission spectroscopy (OES). Furthermore, the introduction of impurities from the crucibles can be impeded in this manner. Thus, a systematic study of the effect of the variation of the composition on structure and Li ion dynamics was possible. Since in case of the conventional solid state synthesis overstoichiometric amounts of Li were used, three different batches of LLZ were prepared differing in the amount of Li_2O in the starting mixture. In each batch the Al content of the mixtures was varied. The structure of the samples prepared was investigated by XRPD and ^{27}Al MAS NMR spectroscopy. The Li ion dynamics were investigated by several ^{7}Li NMR spectroscopy techniques and impedance measurements.

Interestingly, it was possible to synthesize an Al-free compound which seems to crystallize in an only slightly distorted cubic garnet structure. It seems that the low synthesis temperature allowed a stabilization of this, probably metastable, distorted cubic structure against the stable tetragonal structure. The introduction of Al leads to samples exhibiting XRPD patterns of the cubic garnet LLZ which are in excellent agreement with the diffractograms reported in the literature. With increasing amounts of Al the widths of the XRPD peaks were reduced indicating larger crystallites and less strain, thus, a better crystallinity of the samples. In case of the samples doped with small amounts of A the phase pure samples showed an ^{27}Al MAS NMR line at about 64 ppm (referenced versus an aqueous solution of $AlNO_3$), thus, tetrahedrally coordinated Al which probably occupies a vacant Li site in the garnet structure as first proposed by Geiger et al.[6] With increasing amount of Al in the LLZ two additional NMR lines emerged at about 78 ppm and 82 ppm. According to their chemical shift, also these Al were tetrahedrally coordinated by oxygen. The emergence of these NMR lines was accompanied by the formation of $La_2Zr_2O_7$. A Rietveld refinement of a LLZ sample with high Al content done by Dr. Lars Robben (Universität Bremen) showed a decreased electron density at the La and Zr sites. Therefore, the two ^{27}Al NMR lines at 78 ppm and 82 ppm were assigned to the substitution of La and Zr by Al, although the Al does not occupy their sites since the Zr is octahedrally coordinated by oxygen and the La dodecahedrally. If the Al would have occupied these sites the ^{27}Al NMR chemical shifts were clearly different (octahedrally by oxygen coordinated Al can be found at chemical shift values of around 6 ppm to 20 ppm). Furthermore, if the amounts of La_2O_3 and ZrO_2 are reduced in the starting mixtures, large amounts of Al can be introduced into the garnet-structure without the emergence of any side products. The same effect was observed when the Li_2O content of the starting mixtures was increased. If all the Li is introduced into the LLZ this automatically leads to a reduction of the amounts of the other cations in the LLZ. Thus, the use of overstoichiometric amounts of Li_2O imitates the reduction of La and Zr in the LLZ. Based on this results the following chemical formula for the Al-doped LLZ was suggested: $\mathrm{Li}^{+}_{7-3x+z}\mathrm{Al}^{3+}_{x}[\mathrm{La}_{3-y}\mathrm{Al}_{y}\mathrm{Zr}_{2-z}\mathrm{Al}_{z}\mathrm{O}_{12}]^{z-7}$. The structure of the LLZ can be seen as build up by the La- and Zr-units and stuffed with Li for charge compensation. Thus, as observed, the substitution of Li by Al should not have a large impact on the structure. In contrast, the substitution of La and Zr by Al should clearly affect the structure as observed within this study. These structural changes are probably also responsible for the different Li ion mobilities due to the change of the potential landscape. The structural changes due to the La and Zr substitution by Al seems to decrease the jump barriers for the Li ions.

The ionic mobility of the samples was studied mainly by ^{7}Li NMR line shape analysis. The onset temperature for the motional narrowing gives the jump frequency of the Li ions at that temperature being the full width at half maximum of the non-narrowed ^{7}Li NMR line. No clear dependence of the ionic mobility from the Al amount of the Al-doped LLZ was found. However, very small amounts as well as very large amounts of Al seem to be not beneficial for the Li ion mobility. Interestingly, the ratio of by Al substituted La to the by Al substituted Zr ions seems to play an important role regarding the ionic mobility and the structure of the LLZ.

The ^{7}Li NMR spin lattice relaxation measurements gave rate maxima in the range from 573 K to 623 K for the samples prepared. For a few samples field gradient measurements were carried out by A. Kuhn. With this technique the measurement of the long range (= several μm) diffusion of the Li ions is accessible. For the measurements the sample was put in a commercial probe (Bruker) and put into the magnet but not in its usual place where a homogeneous magnetic field is present but beneath this place such that the sample experiences a magnetic field gradient. Thus, the sample experiences different magnetic field strengths along the z-axis (= parallel to the field direction). Therefore, the Li ions of a thin layer (in the order of one μm) in the sample perpendicular to the magnetic field B_0 are marked with their Larmor Frequency. The magnetization build up by the Li ions in this layer can be turned from the z-axis into the xy-plane by a $\pi/2$-pulse. Staying there the magnetization defocusses due to spin-spin relaxation. A π-pulse after a waiting time leads to a refocussing of the magnetization such that the signal can be detected. However, the refocussing does only work for the Li ions staying in the layer. Thus, if Li ions leave the layer during the waiting time the intensity of the signal is decreased. This way the diffusion coefficient of the Li ions in the material is directly accessible (in case of sufficiently long spin-spin relaxation times). For a more detailed description of this technique, see ref. 8.

The low synthesis temperatures created polycrystalline LLZ which exhibited a large amount of blocking grain boundaries. Therefore, the samples heat treated at 873 K showed very low dc conductivities. However, a high-frequency plateau was observed exhibiting the Li ion conductivity in the bulk. For completeness an Li_2O enriched starting mixture was heat treated after the milling process at about 1500 K for 15 h. For this sample a dc conductivity of about 1 x 10^{-4} S/cm at ambient temperature was observed giving an activation energy of about 0.33 eV for the sample with $n(\mathrm{Al}) = 0.30$ ($n(\mathrm{Al}) = x+y+z$).

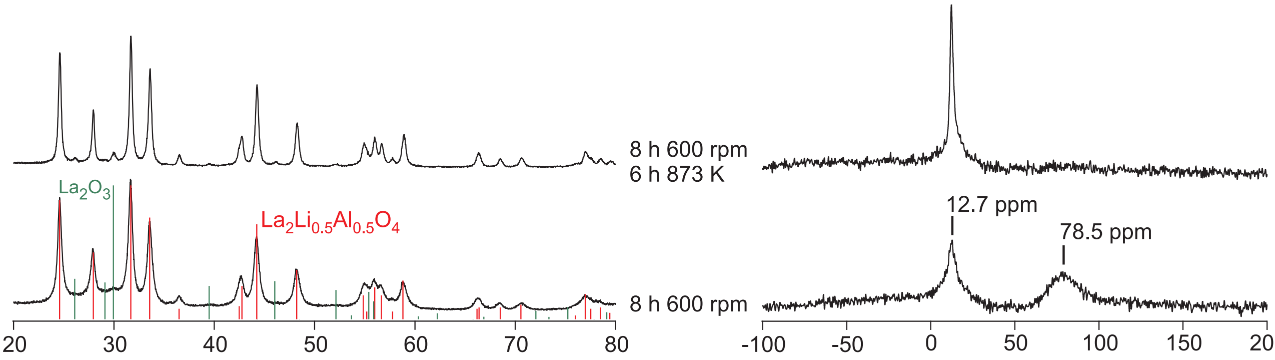

Figure 69: XRPD patterns and ^{27}Al MAS NMR spectra of mechanosynthesized $La_2Li_{0.5}Al_{0.5}O_4$ before and after heat treatment at 873 K for 6 h.

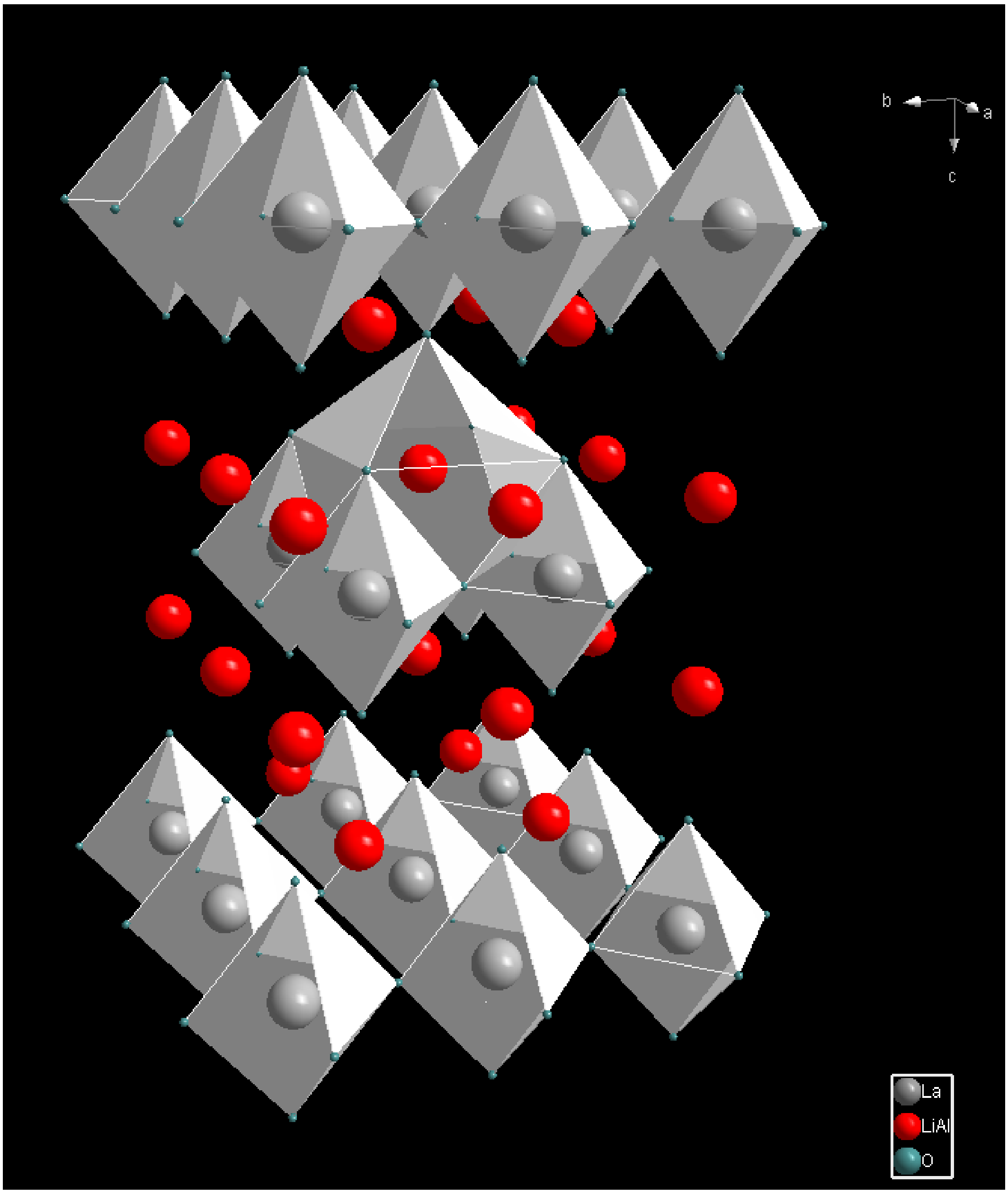
b
a
c
La
LiAl
O

Figure 70: Crystal structure of $La_2Li_{0.5}Al_{0.5}O_4$.

From the different experiments giving jump rates (line shape analysis, spin lattice relaxation rates) or diffusion coefficients (static field gradient measurements) as well as from the impedance measurements the jump rates of the Li ions were calculated. In a plot of the logarithmic jump rate versus the inverse temperature for a sample with $n(\mathrm{Al}) = 0.40$ a straight line was obtained giving an activation energy of about 0.33 eV.

Several questions remain to be answered, for example: What are the exact positions of the Al ions introduced into the LLZ? Which substitution ratio is optimal for a high ionic conductivity? How to control the reaction to be more reproducible regarding the Li ion mobility properties?

Some of the questions might be answered by the investigation planned for the near future. Furthermore, it will be tested if the sintering temperature can be reduced from the 1500 K used for the highly conducting LLZ pellet. This would ease the use of the LLZ for applications. Especially the preparation of thin films of the LLZ to be used as electrolytes in all solid state batteries is of large interest. To the knowledge of the author, the mechanosynthesis routine presented in this work is currently used by several research groups to prepare thin films of LLZ for application in micro batteries.

The results were presented in a paper written by A. Kuhn and the author, published in J. Phys. Chem. C (shown below). It should be noted that some of the main results of this work are also shown in a tutorial review about the mechanosynthesis of oxides.[9]

Another interesting result from that study was the synthesis of $La_2Li_{0.5}Al_{0.5}O_4$ as a side phase. Only a single publication written by Abbattatista et al.[10] dealing with the preparation of this compound could be found by the author. According to this publication, the compound crystallizes in the tetragonal K_2NiF_4 structure (space group: $I4/mmm$). Thereby, the La ions occupy sites coordinated by nine oxygen ions (4e) (4 oxygen ions forming a square beneath a larger "oxygen-square" twisted by 45° to the first one almost even with the La ion and another oxygen ion forming a pyramid with the large square) while the Al and Li ions are statistically distributed over the octahedrally coordinated site (2a). First attempts to prepare $La_2Li_{0.5}Al_{0.5}O_4$ by high-energy ball milling a mixture of Li_2O, Al_2O_3 and La_2O_3 for 8 h under the same conditions as already reported for the synthesis of the LLZ, resulted in almost phase pure material exhibiting a small amount of residual La_2O_3, see Fig. 70. It will be tested in the future if phase pure $La_2Li_{0.5}Al_{0.5}O_4$ can be prepared (e. g., by enhancing the milling time). Also a doping with other elements will be tried. Interestingly, the ^{27}Al MAS NMR spectrum of the mechanosynthesized $La_2Li_{0.5}Al_{0.5}O_4$ exhibits two NMR lines with chemical shifts of 12.7 pm and 78.5 ppm pointing to octahedrally and tetrahedrally by oxygen coordinated Al, respectively, see Fig. 70. After heat-treatment of the sample only a single NMR line representing Al ions with octahedral coordination can be seen, as expected for the structure. The XRPD pattern of the heat-treated sample exhibits a narrowing of the peaks due to grain growth and reduction of strain. Also the peaks of La_2O_3 are still visible. Since the XRPD pattern of the mechanosynthesized material clearly shows the structure of $La_2Li_{0.5}Al_{0.5}O_4$, it seems likely that the mechanosynthesized $La_2Li_{0.5}Al_{0.5}O_4$ is characterized by a distribution of Al ions over the 2e and 4e sites (although the 4e sites are not tetrahedrally, but at least asymmetrically coordinated). This might affect properties of this material like its ionic conductivity[11] or dielectric behavior[12]. This shall be tested in the future. A distribution of cations on the sites of the structure of a compound prepared by high-energy ball milling differing with the one in the structure of the same compound prepared by a conventional solid state synthesis is inter alia known for compounds crystallizing in the spinel structure.[13,14]

References

[1] R. Murugan, V. Thangadurai, W. Weppner, Angew. Chem. Int. Ed. 46 (2007) 7778.

[2] J. Awaka, N. Kijima, H. Hayakawa, J. Akimoto, J. Solid State Chem. 182 (2009) 2046.

[3] A. Kuhn, S. Narayanan, L. Spencer, G. Goward, V. Thangadurai, M. Wilkening, Phys. Rev. B 83 (2011) 094302.

[4] K. Kanamura, A. Kaeriyama, A. Honda, T. Yoshida, Y. Sato, US patent application number 20110053000.

[5] H. Buschmann, J. Dolle, S. Berendts, A. Kuhn, P. Bottke, M. Wilkening, P. Heitjans, A. Senyshyn, H. Ehrenberg, A. Lottnyk, V. Duppel, L. Kienle, J. Janek, Phys. Chem. Chem. Phys. 13 (2011) 19378.

[6] C. A. Geiger, E. Alekseevm, B. Lazic, M. Fisch, T. Armbruster, R. Langner, M. Fechtelkord, N. Kim, T. Pettke, W. Weppner, Inorg. Chem. 50 (2011) 525.

[7] E. Rangasamy, J. Wolfenstine, J. Sakamoto, J. Solid State Ionics 206 (2012) 28.

[8] A. Kuhn, "Fundamental Studies on Li Diffusion in Materials Considered for Battery Applications", Dissertation, 2012.

[9] V. Šepelák, A. Düvel, M. Wilkening, K.-D. Becker, P. Heitjans, Chem. Soc. Rev. 42 (2013) 7507.

[10] F. Abbattatista, M. Vallino, D. Mazza, Inorg. Chim. Acta 140 (1987) 147.

[11] R. Sayers, J. Liu, B. Rustumji, S. J. Skinner, Fuel Cells 08 (2008) 338.

[12] C.-Y. Shi, Z.-B. Hu, Y.-M. Hao, J. Alloy Compd. 509 (2011) 1333.

[13] V. Šepelák, S. M. Becker, I. Bergmann, S. Indris, M. Scheuermann, A. Feldhoff, C. Kübel, M. Bruns, N. Stürzl, A. S. Ulrich, M. Ghafari, H. Hahn, C. P. Grey, K. D. Becker, P. Heitjans, J. Mater. Chem. 22 (2012) 3117.

[14] V. Šepelák, K. D. Becker, J. Korean Ceram. Soc. 49 (2012) 19.

Reproduced with permission from A. Düvel, A. Kuhn, L. Robben, M. Wilkening, P. Heitjans, J. Phys. Chem. C 116 (2012) 15192. Copyright 2014 American Chemical Society.
http://pubs.acs.org/doi/abs/10.1021/jp301193r?journalCode=jpccck&quickLinkVolume=116&quickLinkPage=15192&selectedTab=citation&volume=116

THE JOURNAL OF PHYSICAL CHEMISTRY C
Article
pubs.acs.org/JPCC

Mechanosynthesis of Solid Electrolytes: Preparation, Characterization, and Li Ion Transport Properties of Garnet-Type Al-Doped $Li_7La_3Zr_2O_{12}$ Crystallizing with Cubic Symmetry

Andre Düvel,*[†] Alexander Kuhn,*[†,⊥] Lars Robben,[‡,§] Martin Wilkening,[†,∥] and Paul Heitjans[†]

[†]Institute of Physical Chemistry and Electrochemistry, and ZFM – Center for Solid State Chemistry and New Materials, Leibniz University Hannover, Callinstr. 3a, D-30167 Hannover, Germany

[‡]Institute of Mineralogy, Leibniz University Hannover, Callinstr. 3, D-30167 Hannover, Germany

Supporting Information

ABSTRACT: Various polycrystalline samples of Al-doped garnet-like $Li_7La_3Zr_2O_{12}$ crystallizing with cubic symmetry were synthesized from the binary oxides Li_2O, ZrO_2, Al_2O_3, and La_2O_3. The synthesis of phase pure samples was carried out following a two-step preparation route. It consists of an activation step by high-energy ball milling and a subsequent annealing step at elevated temperatures. The synthesis route chosen allows the precise adjustment of the cationic ratios, leading to a garnet which is best described by the formula $Li_{7-3x+z}Al_{x+y+z}La_{3-y}Zr_{2-z}O_{12}$. As confirmed by X-ray powder diffraction and ^{27}Al magic angle spinning nuclear magnetic resonance (NMR), at low Al concentrations the incorporated Al^{3+} ions act as an aliovalent dopant by replacing three Li^+ ions. However, with increasing Al content, La^{3+} and Zr^{4+} ions are progressively replaced by Al ions. It turned out that, in particular, the substitution of La^{3+} and Zr^{4+} with Al^{3+} ions stabilizes the cubic modification of the garnet and greatly affects the corresponding Li ion dynamics. The latter has been probed by both impedance and ^7Li NMR spectroscopy. The high ion conductivity (10^{-4} S cm^{-1} at 293 K) found does not only depend on the stoichiometry and the annealing conditions chosen but also on the exact kind of Al distribution on the different sites in $Li_7La_3Zr_2O_{12}$.

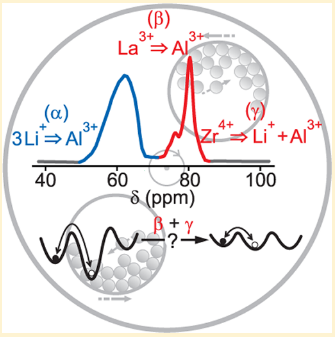

I. INTRODUCTION

Li-containing garnet-type oxides are considered to act as promising fast ion-conducting electrolytes in, e.g., all-solid-state lithium-ion batteries. These are expected to be one of the key technologies to store electrical energy in the next years.[1−7] Hence, previously a number of studies have been published which are concerned with profound investigations of the structure−property relations of crystalline garnet-type oxides (see, e.g., refs 6 and 8−14). In particular, the garnet with the nominal composition "$Li_7La_3Zr_2O_{12}$" (LLZ) crystallizing with cubic symmetry attracted large interest. In contrast to the tetragonal counterpart, which is characterized by an ionic bulk conductivity in the order of 10^{-6} S cm^{-1} (300 K),[16,22] some of the samples with cubic symmetry investigated so far show an extraordinarily high Li^+ conductivity in the order of 10^{-4} S cm^{-1} (300 K).[1,7,14−21] Currently, much work is in progress to identify the origins causing the high lithium ion conductivity.

The results of recently published studies provide strong evidence that Al^{3+} ions, which were unintentionally incorporated into LLZ during the high-temperature synthesis procedure using alumina crucibles, at least stabilize the cubic modification against the tetragonal one.[14,17,20,23] For comparison, the preparation of Al-free LLZ usually leads to the formation of the tetragonally distorted garnet.[17,19,23] It is worth noting that Al-free tetragonal LLZ transforms into the cubic modification at elevated temperatures.[23] However, as some of us showed quite recently, the phase transformation is not accompanied by a significant enhancement of the ionic conductivity.[16] Obviously, merely increasing the symmetry does not lead to the enhancement of the Li^+ conductivity observed for some of the samples studied (see also ref 24). As already discussed by Geiger et al., at low dopant levels the incorporation of Al may influence the number fraction of Li vacancies and, thus, the Li ion conductivity. Further investigations focusing on the role Al plays in influencing the Li ion dynamics parameters might be useful to understand and, in the best case, to improve Li ion transport in LLZ.

Here, we present a systematic study addressing in depth the effects of Al incorporation on both structural and dynamic properties of LLZ. For this purpose we developed a soft synthesis route avoiding high temperatures and enabling the precise adjustment of the contents of all cations in LLZ. Alternatively, sol−gel procedures[25−28] may certainly be used for similar investigations. However, the necessary temperatures for the latter procedures are still higher than the temperatures needed for the synthesis routine described here.

In the present study, various polycrystalline samples of cubic LLZ with different amounts of Al were prepared from mixtures

Received: February 6, 2012
Revised: June 18, 2012
Published: June 25, 2012

ACS Publications © 2012 American Chemical Society

of the binary oxides Li_2O, ZrO_2, La_2O_3, and Al_2O_3 by high-energy ball milling[29−32] and subsequent annealing of the mechanically activated mixtures. While the final composition of the samples can easily be controlled by precisely adjusting the amounts of the starting materials used, a low annealing temperature prevents Li loss usually taking place when LLZ is prepared according to high-temperature ceramic synthesis routes. Sample characterization was carried out by X-ray powder diffraction (XRPD) and ^{27}Al magic angle spinning (MAS) nuclear magnetic resonance (NMR) spectroscopy. In particular, ^{27}Al NMR spectroscopy has been used to roughly correlate the distinct NMR lines of Al-doped LLZ[17,23] with the doping mechanisms identified. Ion transport properties were probed by variable-temperature ^{7}Li NMR line shape measurements as well as impedance spectroscopy. The latter take advantage of measurements carried out at frequencies up to the gigahertz range.

II. EXPERIMENTAL DETAILS

A series of polycrystalline samples with the nominal composition $Li_{7-3x+z}Al_{x+y+z}La_{3-y}Zr_{2-z}O_{12}$ were prepared by high-energy ball milling from the corresponding binary oxides, viz. dry Li_2O (99.5%, Sigma-Aldrich), γ-Al_2O_3 (99.997%, Alfa Aesar), La_2O_3 (99.99%, Fluka), and ZrO_2 (99.99%, Sigma-Aldrich).

For the conventional solid-state synthesis routines reported in the literature an excess of Li is used (*vide supra*). To elucidate the effect of the Li_2O ratio on the structure as well as on the ion dynamics, three series of samples with different Li_2O ratios were prepared. The first one, labeled series A, has the nominal stoichiometry $Li_{7-3x}Al_xLa_3Zr_2O_{12}$. Series B, which is $Li_{7-3x}Al_xLa_3Zr_2O_{12} + 0.75x(Li_2O)$ and series C ($Li_{7-3x}Al_xLa_3Zr_2O_{12} + 1.25x(Li_2O)$) were preapred with a slight excess of Li_2O.

Here, mixtures with a total mass of 2 g were high-energy ball milled in an argon atmosphere using a planetary mill P7 premium line (Fritsch) in combination with a vial set made of tungsten carbide (45 mL beaker, 100 balls with a diameter of 5 mm each). The mixtures were milled at a rotational speed of 600 rpm for 8 h at ambient temperature. Afterward, a pellet (8 mm in diameter and ~1 mm in thickness) was prepared from each of the milled powders by cold-pressing at ~1 GPa. The pellet and the residual powder were placed in quartz shuttles and annealed at 873 K using a constant flow of synthetic air (Linde). After 6 h, the samples were cooled down to a temperature of about 773 K. After that, the shuttles were removed from the oven and quenched to ambient temperature by putting them on a fire brick. For comparison, for one of the samples the annealing step was replaced by a reaction step; i.e., the powder was kept for 15 h at 1500 K in a corundum crucible.

The obtained powders were characterized by XRPD using a D8 Advance diffractometer (Bruker) operating with Cu Kα radiation at 40 kV. Further characterization was carried out by ^{27}Al MAS NMR spectroscopy using a Bruker Avance III spectrometer connected to an Ultrashield Plus 600 MHz magnet (Bruker) with a nominal field of 14.1 T. NMR spectra were acquired with a Bruker 2.5 mm double-resonance MAS probe using a single excitation pulse with a length of ~2 μs. The spinning rate ν_{rot} was set to 30 kHz using room-temperature bearing gas. Chemical shift values δ_{iso} were referenced to an aqueous solution of aluminum nitrate.

Variable-temperature ^{7}Li NMR measurements, including the acquisition of (i) line shapes under nonrotating, i.e., static conditions, and (ii) spin−lattice relaxation (SLR) rates, were performed with an MSL 400 spectrometer (Bruker) in combination with a 9.4 T cryomagnet (Oxford). Prior to these measurements the samples were dried at 373 K for at least 12 h in vacuum and then heat-sealed in glass ampulla. The resonance frequency was 155.4 MHz. For the measurements presented a standard high-temperature probe (Bruker) was used. The $\pi/2$ pulse length was 2 μs. SLR NMR rates were measured with the saturation recovery pulse sequence where a comb of closely spaced $\pi/2$ pulses was used to destroy any longitudinal magnetization $M(t)$.[33,34] The subsequent recovery of $M(t)$ was probed with a single $\pi/2$ pulse as a function of waiting time. Additionally, some preliminary solid echo NMR measurements were recorded by taking advantage of the static field-gradient of a cryomagnet (14.1 T of an Avance III spectrometer (Bruker)). Macroscopic lithium diffusion coefficients were estimated from the obtained echo decay curves.

Additionally, ac impedance spectra (0.05 Hz to 20 MHz) were measured with a Novocontrol Concept 80 broadband dielectric spectrometer which is equipped with an Alpha-AN analyzer in connection with a ZGS active sample cell test interface (Novocontrol). The sample temperature was controlled (±0.1 K) with a Novocontrol QUATRO using a gas-flow of heated nitrogen which was freshly evaporated. After annealing the impedance pellets as mentioned above electrodes were applied by Au evaporation using an Edwards 306 evaporator. In order to remove any residual moisture, prior to the measurements all pellets were kept several hours inside the sample cell at 390 K under a constant flow of nitrogen gas. The ac impedance data, recorded at frequencies up to 3 GHz, were measured using a (microwave) rf extension line (Novocontrol) connected to an Agilent 4991 rf analyzer.

For selected samples the amount of Al and Li was measured by inductive coupled plasma (ICP) optical emission spectroscopy (OES) using a Varian 715 spectrometer. Here, 25 mg of the samples was mixed with an equimolar solution of 3 mL of concentrated nitric acid and concentrated phosphoric acid. The mixture was placed in a Teflon autoclave which was heated inside a microwave oven at 523 K for about 25 min. Calibration curves were measured using LiOH and Al_2O_3. It turned out that the losses of Li and Al, occurring during annealing at 873 K for 6 h after mechanical activation, were as low as ca. 1 and 2 wt %, respectively.

III. RESULTS AND DISCUSSION

A. Mechanosynthesis of Al-Doped $Li_7La_3Zr_2O_{12}$.

Exemplarily, in Figure 1 the XRPD patterns of mechanosynthesized Al-doped LLZ with $x = 0.3$ (series B) before and after the annealing step are shown. Judging from XRPD the two-step synthesis route yields phase-pure LLZ crystallizing with cubic symmetry. Directly after high-energy ball milling, the polycrystalline powder is composed of nanometer-sized crystallites of LLZ as well as ZrO_2. The XRPD pattern of ZrO_2 (Joint Committee on Powder Diffraction Standards (JCPDS) number 37-1484) is indicated in Figure 1a by vertical bars. The broad humps detected point to amorphous milling products. Thermal annealing of the activated powder for 6 h at 873 K completes the mechanically initiated reaction. The pattern obtained for the final product (Figure 1b) is in perfect agreement with the data reported by Geiger et al.[23]

Without the assistance of thermal annealing, merely by increasing the milling time (up to 48 h) no complete conversion of the starting materials has been observed. Thus,

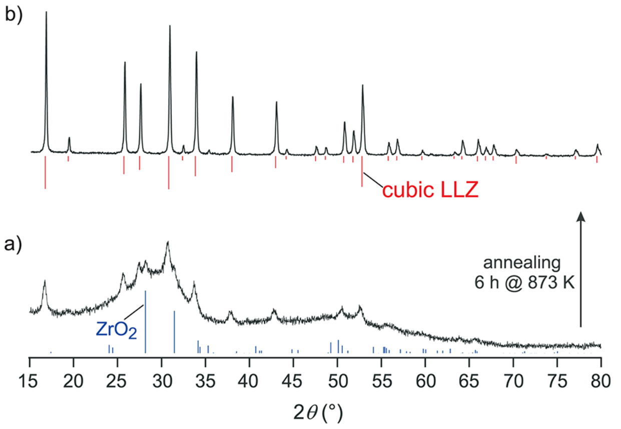

Figure 1. XRPD patterns of a mechanosynthesised sample of LLZ with $x = 0.30$ (series B, see text for further details): (a) XRPD directly recorded after 8 h of mechanical treatment in a high-energy ball mill; (b) final XRPD pattern of phase-pure cubic LLZ which was obtained after annealing the material for 6 h at 873 K.

soft annealing is a necessary preparation step in the synthesis of cubic LLZ. Here, the complete transformation of a mechanically activated mixture advantageously occurs at a significantly lower temperature as compared to conventional synthesis routes (see also ref 29).

B. Aliovalent Doping: Replacement of $3Li^+$ with Al^{3+}.

It is assumed that a replacement of Li with Al according to $3Li^+ \Rightarrow Al^{3+}$, which leads to LLZ with the composition $Li_{7-3x}Al_xLa_3Zr_2O_{12}$, takes place. This doping mechanism, in the following denoted by (α), was already discussed by Geiger et al.[23] (*vide supra*). At first glance, one might assume that the substitution of Al^{3+} for $3Li^{3+}$ could explain the enhanced conductivity usually observed for cubic "$Li_7La_3Zr_2O_{12}$". However, it seems questionable whether the associated formation of additional vacancies on the lithium sites further facilitates Li transport since, from the outset, the regular Li sites are only partially occupied in cubic LLZ.

In order to get further insight into the role that Al plays, in a first approach we prepared aliovalently exchanged LLZ samples with the nominal composition of $Li_{7-3x}Al_xLa_3Zr_2O_{12}$ ($0 \leq x \leq 1.2$) by using the exact stoichiometric ratios of the starting materials (series A, *vide supra*). Figure 2a shows the corresponding XRPD patterns recorded with the Al contents x as indicated. For all values of x, LLZ is obtained as a major phase. Up to an Al amount of $x = 0.25$, the products are phase-pure on the XRD level, and the aliovalent exchange turns out to be successful.

For $x < 0.20$ the obtained powders do not crystallize well with cubic symmetry. This is in good agreement with the results of Rangasamy et al.[14] The patterns show broad and asymmetric peaks presumably caused by very small crystallites and/or increased lattice strain. Moreover, a partial reduction of the crystal symmetry might be responsible for the broadening observed. In Figure 5, the width of the most intense XRPD peak, showing up at $2\theta \approx 17°$, of the three series is shown as a function of x. Except for a few samples (notably the ones with $x = 0.60$ of series A and C), the peak width almost continuously decreases with increasing Al content. Obviously, the relevant substitution processes taking place (see below) stabilize the cubic crystal structure.

The aliovalent exchange goes along with the emergence of a ^{27}Al MAS NMR line around 64 ppm (see Figure 2b). With increasing Al content several impurity phases such as $La_2Zr_2O_7$ (JCPDS 17-450), $LaAlO_3$ (JCPDS 31-22), γ-$LiAlO_2$ (JCPDS

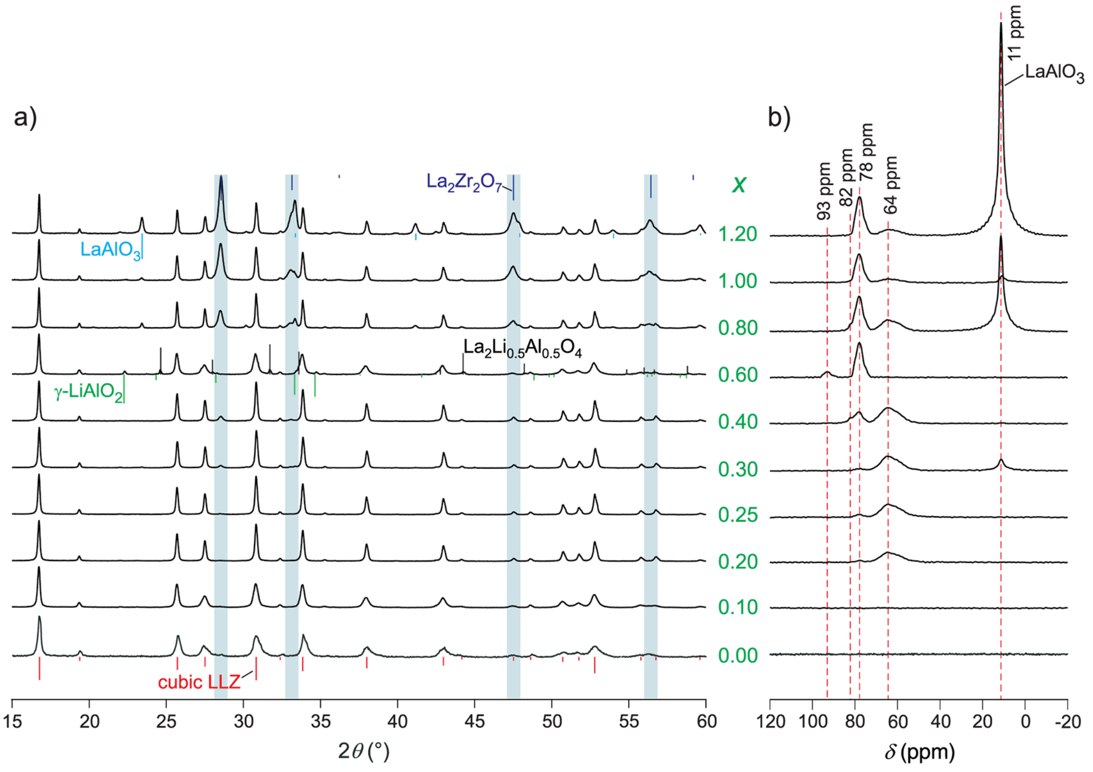

Figure 2. (a) XRPD patterns of a series of $Li_{7-3x}Al_xLa_3Zr_2O_{12}$ samples (series A) with the nominal Al contents x as indicated. (b) Corresponding ^{27}Al MAS NMR spectra which were recorded at a magnetic field of 14.1 T and an MAS spinning rate of 30 kHz. See text for further explanation.

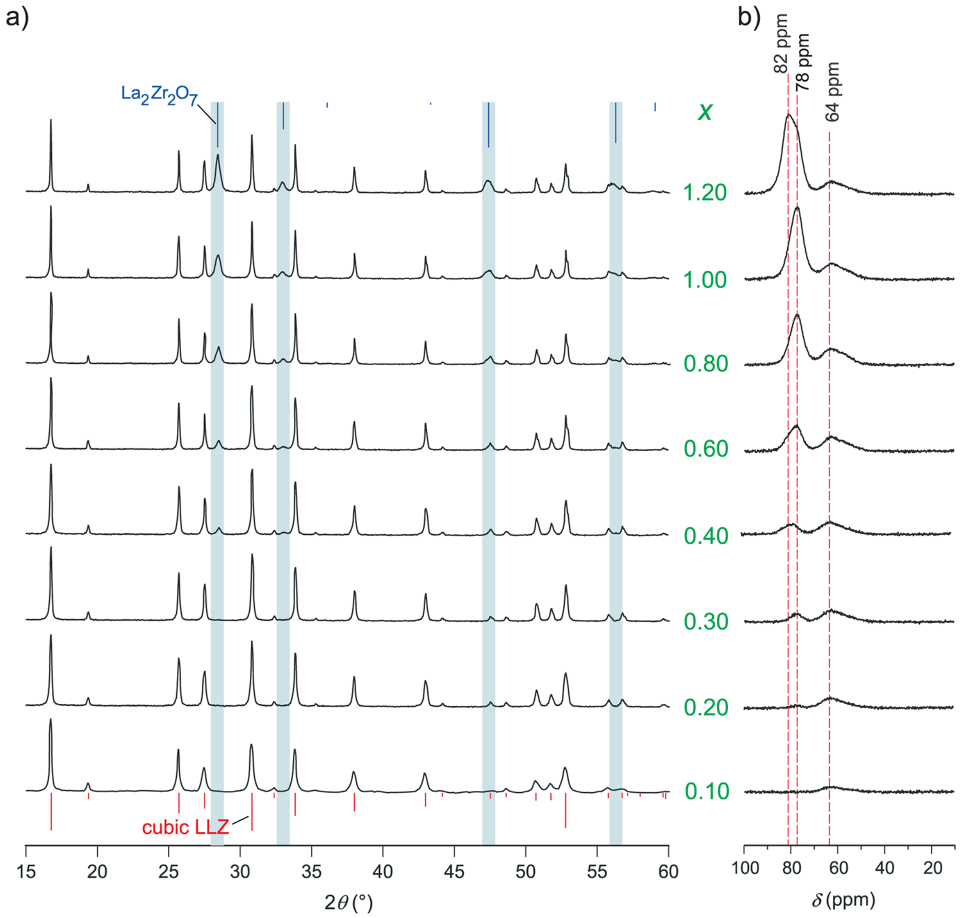

Figure 3. (a) XRPD patterns of a series of $Li_{7-3x}Al_xLa_3Zr_2O_{12}$ + 0.75 $x(Li_2O)$ samples (series B) with the nominal Al contents x as indicated. (b) Corresponding ^{27}Al MAS NMR spectra which were recorded at a magnetic field of 14.1 T and an MAS spinning rate of 30 kHz. See text for further explanation.

38-1464) and $La_2Li_{0.5}Al_{0.5}O_4$ (JCPDS 40-1167) show up. However, no clear trend in the formation of these phases is observed. At least for $x > 0.6$, $La_2Zr_2O_7$ seems to be the main side product formed. An important consequence is that the stoichiometry of the LLZ phase is altered. For example, when $La_2Zr_2O_7$ is formed, the garnet phase contains less La and Zr. Accordingly, when $LaAlO_3$ shows up, LLZ is reduced in Al and La. Obviously, Al replaces not only Li but also La and Zr.

The corresponding ^{27}Al MAS NMR spectra of the samples (Figure 2b) comprise several lines viz. at 11, 64, 78, 82, and 93 ppm. The signal at 11 ppm shows up when $LaAlO_3$ is formed. The associated isotropic chemical shift value δ_{iso} is in accordance with literature data for pure $LaAlO_3$.[23,35] The corresponding chemical shift of γ-$LiAlO_2$ can be calculated from the quadrupolar and isotropic shift values given in the literature.[39] It turns out to be ~75 ppm at 14.1 T. Here, a slight shoulder is indeed observed at 75 ppm when $LiAlO_2$ is formed. However, it is covered by the intense NMR line at 78 ppm which represents Al in the LLZ phase. Interestingly, the line at 78 ppm is observed in La or Zr deficient LLZ. Therefore, it might represent Al residing on the La and/or Zr sites in the garnet. This assumption will be checked in detail below. Interestingly, some of the samples investigated by ^{27}Al MAS NMR reveal a slight shoulder at 82 ppm. Probably, this NMR line also represents Al in LLZ (see also below).

The NMR line at 93 ppm is only observed for $x = 0.6$. At first glance it might be assigned to Al ions in $La_2Li_{0.5}Al_{0.5}O_4$ wherein Al is assumed to be coordinated by oxygen forming an elongated octahedron.[36] Because there are no NMR data in the literature available, we prepared almost phase pure $La_2Li_{0.5}Al_{0.5}O_4$ by mechanosynthesis. The corresponding ^{27}Al MAS NMR spectrum of an annealed sample (6 h at 873 K) is composed of a single line at 12 ppm which shows a relatively low intensity. This might explain the absence of such an NMR line with this chemical shift in the ^{27}Al MAS NMR spectrum of the LLZ sample with $x = 0.60$ (see Figure S1, Supporting Information). Thus, the NMR intensity located at 93 ppm seems to represent Al on an unknown site in the garnet (see also ref 37).

The effect that incorporated Al does stabilize the cubic modification over the tetragonal one has already been discussed in refs 17 and 23. In the present study, this effect can also be monitored via the change of the XRPD peak widths with increasing x. The peak widths are significantly reduced with the incorporation of Al (see Figure 5). Certainly, when impurity phases are present (series A), the trend is less clearly visible. The samples of series B and C, which were prepared with an excess of Li_2O, proved to be more suitable to show the effect. The additional amount of Li_2O seems to provide a reaction medium where the growth of the LLZ phase is favored. For example, this might be due to an improved contact between crystallites in the ball-milled precursor material. However, in the case of series B and C, the only significant minority phase found is $La_2Zr_2O_7$.

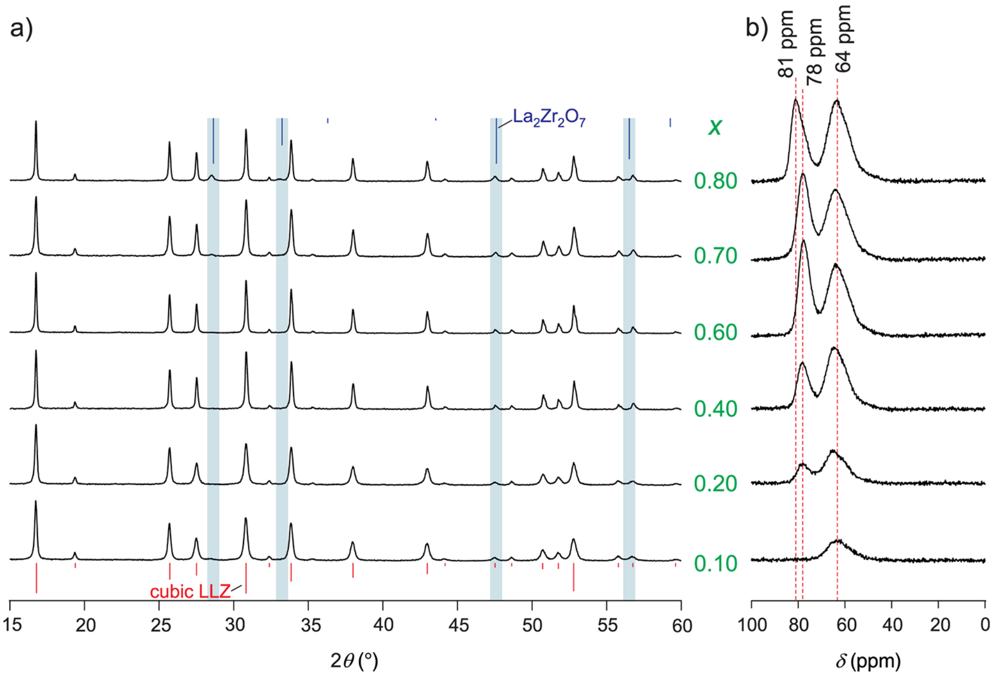

Figure 4. (a) XRPD patterns of a series of $Li_{7-3x}Al_xLa_3Zr_2O_{12}$ + 1.25x(Li_2O) samples (series C) with the nominal Al contents x as indicated. (b) Corresponding ^{27}Al MAS NMR spectra which were recorded at a magnetic field of 14.1 T and an MAS spinning rate of 30 kHz. See text for further explanation.

The corresponding XRPD patterns and ^{27}Al MAS NMR spectra of series B are shown in Figure 3. The XRPD data point to phase-pure LLZ up to a value of about x = 0.3. The incorporation of small amounts of Al in the LLZ phase goes along with the emergence of a ^{27}Al MAS NMR line at 64 ppm, which again represents the aliovalent exchange of Al for Li. At higher Al levels, XRPD peaks of a second phase, viz. $La_2Zr_2O_7$, are observed. Again, this results in a garnet phase depleted in La and Zr. Concomitantly, the NMR line at 78 ppm emerges with both increasing x and the formation of $La_2Zr_2O_7$ (see above). Exemplarily, a Rietveld refinement of the sample with x = 1.2 revealed that it is composed of ~33 wt % $La_2Zr_2O_7$ and ~66 wt % Al-doped LLZ. With these values the actual stoichiometry $Li_{7-3x+z}Al_{x+y+z}La_{3-y}Zr_{2-z}O_{12}$ of the sample can be determined to be $Li_{6.68}Al_{1.54}La_{2.55}Zr_{1.26}O_{12}$ with $x \approx 0.35$, $y \approx 0.45$, and $z \approx 0.74$. These values are in good agreement with those estimated from ^{27}Al MAS NMR: the three distinct NMR lines showing up at 64, 78, and 82 ppm are assumed to be related to three distinct doping mechanisms (α), (β), and (γ). While (α) denotes aliovalent doping (see above), (β) is described by $La^{3+} \Rightarrow Al^{3+}$ and (γ) denotes $Zr^{4+} \Rightarrow Li^+ + Al^{3+}$. Assuming $x + y + z = 1.54$, as calculated from Rietveld analysis, a rough deconvolution of the corresponding ^{27}Al MAS NMR spectrum of the sample with x = 1.2 (series B) yields x = 0.33, y = 0.42, and z = 0.80.

It should be mentioned that ^{27}Al MAS NMR signals around 80 ppm were also observed by Geiger et al.[23] From their ^{27}Al MQMAS NMR measurements they concluded that these signals result from a single NMR line which is perturbed by second-order quadrupolar effects. However, judging from the ^{27}Al MAS NMR spectra of some of our samples (see below), we may not rule out that these signals could also originate from two separate NMR lines representing different crystallographic sites in the structure of the garnet.

Compared with series B, the samples of series C show very similar results (see Figure 4a): phase-pure LLZ is obtained but up to Al levels of x = 0.6; at even higher values of x the formation of $La_2Zr_2O_7$ is observed. Interestingly, the ^{27}Al MAS NMR line at 78 ppm (and 82 ppm) emerges with significant intensity although the XRPD patterns do not reveal any indications for the formation of $La_2Zr_2O_7$, see Figure 4b. This might be considered as an argument against the above-given assignment that this NMR line reflects the replacement of Zr and La with Al. It is worth noting that no residual Li_2O can be detected by XRPD which does not rule out that it may be X-ray amorphous. However, assuming that the excess of Li_2O has been incorporated into the garnet and disregarding the formation of oxygen vacancies, the LLZ formed should be characterized by smaller ratios of Al, La, and Zr. In the case of series C with $Li_{7-3x}Al_xLa_3Zr_2O_{12}$ + 1.25x(Li_2O) this would lead to $[(12 + 1.25x)/12]Li_{(7-0.5x)[12/(12+1.25x)]}Al_{x[12/(12+1.25x)]}\cdot La_{3[12/(12+1.25x)]}Zr_{2[12/(12+1.25x)]}O_{12}$. This assumption would explain why for series C garnet-type LLZ is obtained phase pure up to higher Al contents (x = 0.60) than for series A (x = 0.25) and B (x = 0.30) as well as for series B compared to series A. This might be considered as another argument for the existence of the doping mechanisms $La^{3+} \Rightarrow Al^{3+}$ and $Zr^{4+} \Rightarrow Al^{3+} + Li^+$, respectively.

C. Mixed Doping Mechanisms. In order to check the assumption that Al replaces La and Zr in LLZ as mentioned above, we synthesized several LLZ samples with very high Al contents, which can be described with the formula $Li_{7-3x+z}Al_{x+y+z}La_{3-y}Zr_{2-z}O_{12}$. Indeed, it is possible to synthesize nearly phase-pure LLZ with nominal Al contents up to $n(Al) = x + y + z \approx 2$ whereby considerable amounts of La and Zr are replaced by Al. Selected results are shown in Figure 6.

In Figure 7 three different compositions with very high Al contents are presented. Interestingly, both the XRPD pattern and ^{27}Al MAS NMR spectrum of a sample with the nominal

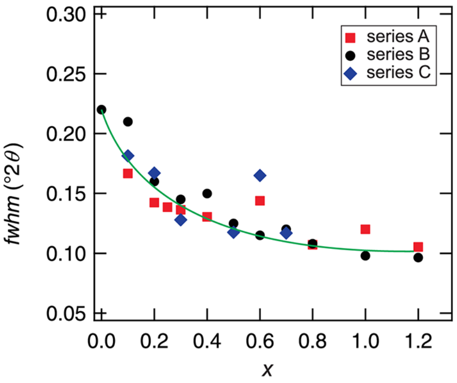

Figure 5. Width of the XRPD peak (full width at half-maximum (fwhm)) at $2\theta \approx 17°$ (see Figures 2a, 3a, and 4a) as a function of Al content x. The solid line is drawn to guide the eye.

composition "$Li_{6.95}Al_2La_{2.15}Zr_{1.15}O_{12}$" are very similar to those of the sample with $x = 0.60$ of series A. However, in the case of $Li_{6.36}Al_{1.78}La_{2.26}Zr_{1.38}O_{12}$ besides a small amount of γ-$LiAlO_2$ almost phase pure LLZ is obtained. The corresponding ^{27}Al MAS NMR spectrum reveals a signal with a very low intensity at 11 ppm (see inset in Figure 7). It probably indicates the formation of a small amount of $LaAlO_3$. Increasing the nominal amounts of La and Zr up to a composition of approximately $Li_{5.73}Al_{1.78}La_{2.36}Zr_{1.47}O_{12}$, the formation of $La_2Zr_2O_7$ can be observed. Hence, the maximum amount of Al which can substitute La and/or Zr in the LLZ seems to be $n(\text{Al}) \approx 1.78$ while $n(\text{Al}) = 2$ leads to the formation of, e.g., γ-$LiAlO_2$ and $La_2Li_{0.5}Al_{0.5}O_4$. Interestingly, the XRPD peaks of these three samples are considerable broader than those found for the other LLZ samples with a large Al content. Therefore, it seems plausible to assume a characteristic Al content at which the stabilization of the cubic LLZ is at its maximum. If the amount of Al is increased further, the cubic LLZ is destabilized once again.

For comparison, the aliovalently Al-doped sample (mechanism (α) assumed) with $x = 1.20$ (series B) is also shown in Figure 6. Note that the intensity of the NMR line at 82 ppm of this sample is higher than those found for the other samples (see Figure 6). Assuming that the signal at 82 ppm reflects mechanism (γ) $Zr^{4+} \Rightarrow Li^{+} + Al^{3+}$, a very large amount of Al has been substituted for Zr, which is in agreement with the calculated chemical formula $Li_{6.68}Al_{1.54}La_{2.55}Zr_{1.26}O_{12}$ (*vide supra*). However, this seems to be an exception since generally we observed a preference of the substitution mechanism connected to the ^{27}Al NMR line at 78 ppm over that one ascribed to the signal at 82 ppm.

From the results presented up to here, two main conclusions can be drawn: (i) the doping mechanisms $La^{3+} \Rightarrow Al^{3+}$ and $Zr^{4+} \Rightarrow Al^{3+} + Li^{+}$ do take place, and (ii) the ^{27}Al NMR lines showing up at 64, 78, and 82 ppm result from Al residing on different crystallographic sites in the garnet. Hereby, the line at 64 ppm represents the replacement of Li by Al while the other lines reflect the replacement of La and Zr. NMR chemical shifts of the three signals lie in the range being typical of tetrahedral coordination. The signal at 64 ppm might well be Al on the tetrahedral Li1 position. For the substitution of Al for La and Zr the situation is probably different. In garnet-type LLZ La resides in a dodecahedral site and Zr in an octahedral site. The ^{27}Al NMR lines with chemical shifts of 78 and 82 ppm, which emerge with the exchange of La and Zr by Al, rather point to 4-fold oxygen coordination.[40] Therefore, Al probably does not occupy the La or Zr sites but resides on tetrahedral sites next to a vacancy created. So far, the correct assignment of the various NMR signals turns out to be a difficult task because no clear relation between isotropic ^{27}Al MAS NMR chemical shifts and both the coordination number and the Al−O distance d can be found in the literature.[38]

By comparing the different doping mechanisms, there is a qualitative difference between the aliovalent doping mechanism and the mixed doping mechanism. This can be rationalized by considering the structure of the garnets stuffed with Li. $Li_7La_3Zr_2O_{12}$ should be understood as $Li_7^{+}[La_3Zr_2O_{12}]^{7-}$, i.e., a negatively charged garnet network being filled with Li ions compensating for the negative charge. The aliovalent doping mechanism then leads to $Li_{7-3x}^{+}Al_x^{3+}[La_3Zr_2O_{12}]^{7-}$. In this case, the stoichiometry of the garnet network is not affected by

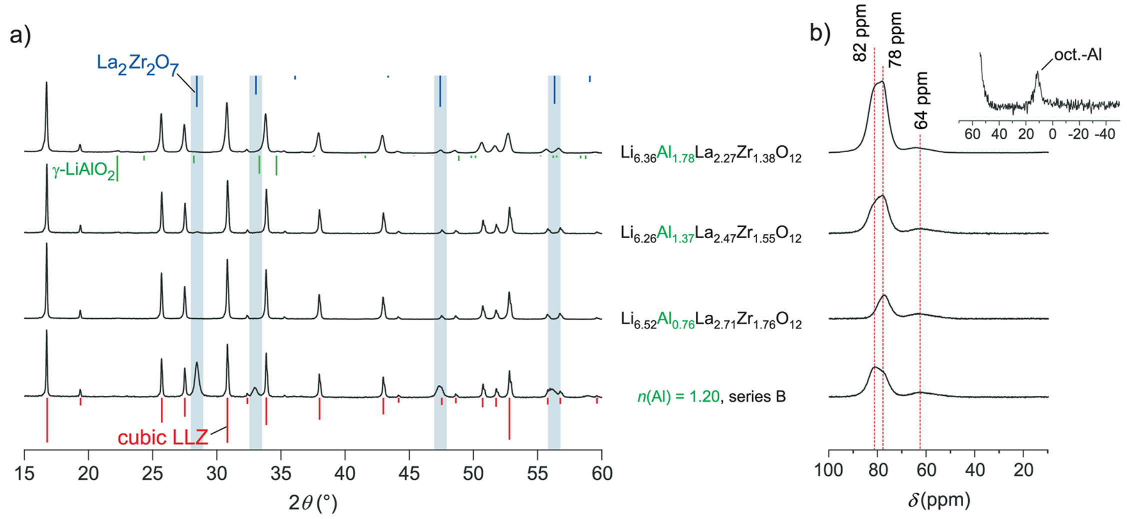

Figure 6. (a) XRPD patterns of a sample of series B with $x = 1.2$ as well as of selected samples systematically reduced in La and Zr. (b) Corresponding ^{27}Al MAS NMR spectra recorded at a field of 14.1 T and an MAS spinning rate of 30 kHz. The inset shows a magnification of a part of the NMR spectra of the sample with the composition $Li_{6.36}Al_{1.78}La_{2.27}Zr_{1.36}O_{12}$. It exhibits a small amount of octahedrally coordinated Al (see text).

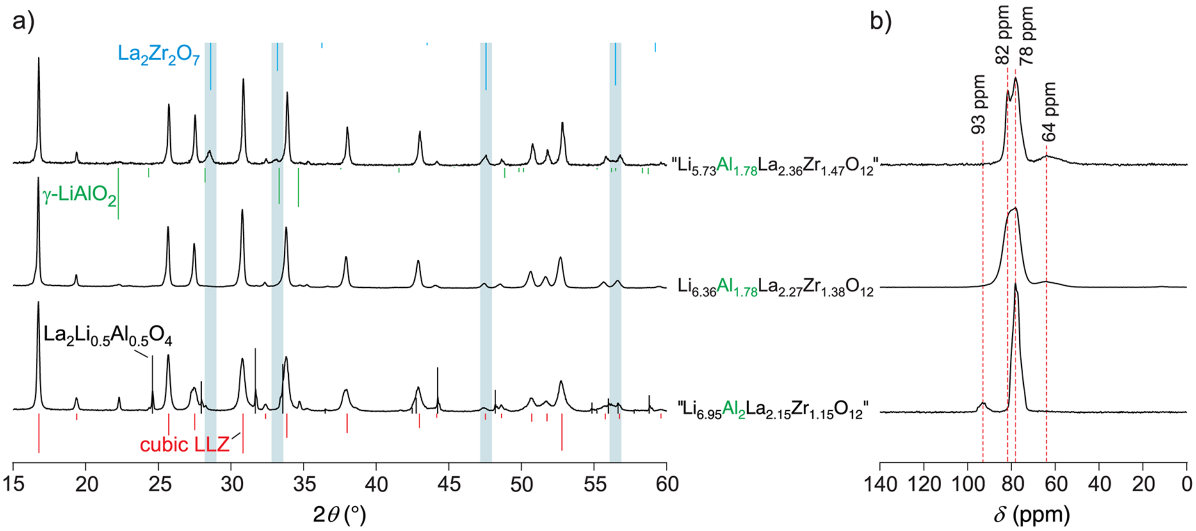

Figure 7. (a) XRPD patterns of three samples systematically reduced in La and Zr but with a very high Al content. (b) Corresponding ^{27}Al MAS NMR spectra recorded at a field of 14.1 T and an MAS spinning rate of 30 kHz.

doping, and a significant impact on the Li dynamics is not to be expected. The replacement of La and Zr by Al, however, directly affects the garnet network itself, leading to $Li_{7-3x+z}{}^{+}Al_x{}^{3+}[La_{3-y}Al_yZr_{2-z}Al_zO_{12}]^{z-7}$. It is obvious that this kind of doping will more likely have a significant impact on the garnet structure as well as on the Li ion dynamics.

D. Li Ion Dynamics As Probed by NMR and Impedance Spectroscopy. *1. NMR Line Narrowing.* Li ion dynamics of the samples were roughly characterized by static ^{7}Li NMR line narrowing measurements. Such measurements are useful when short-ranged dynamics have to be studied. As an example, in Figure 8a the ^{7}Li NMR lines of the sample with $x = 0.30$ of series B are shown. At low T the NMR line is dipolarly broadenend and can be described with a Gaussian line shape. At higher temperatures, as the jump rate of the Li spins exceeds the dipolar coupling constant, the dipole−dipole interactions are averaged, resulting in a motionally narrowed NMR line.[41] Here, a two-step narrowing is observed pointing to a hetergeneous Li ion dynamics.[11,17]

By plotting the line width (full width at half-maximum, fwhm) vs T, a so-called motional narrowing (MN) curve is obtained which can be used to roughly estimate the Li$^+$ diffusivity. In Figure 8b, the corresponding narrowing curve of cubic LLZ (series B, $x = 0.30$) is shown together with those of the previously studied tetragonal[16] and cubic[17] LLZ prepared by conventional solid-state synthesis. The Li diffusivity of the mechanosynthesized material is nearly as high as that of cubic LLZ synthesized conventionally but significantly higher than that of the Al-free LLZ crystallizing with tetragonal symmetry.

At the inflection point ($T = T_{MN}$) of the NMR MN curve the mean Li jump rate τ_{MN}^{-1} is approximately given by the relation $\tau_{MN}^{-1} \approx \Delta\omega_{rl}$, where $\Delta\omega_{rl}$ denotes the rigid lattice line width in radians. Here, $\Delta\omega_{rl}(T \rightarrow 0)$ is approximately 5.7×10^4 s^{-1}. In Figure 8b, the temperature T_{MN} is marked by a vertically drawn dashed line. To compare the dynamic properties of the samples prepared, in Figure 8c T_{MN} is shown as a function of $n(Al)$ (which is x for series A, B, and C) together with the T_{MN} values of both cubic LLZ[17] and Al-free tetragonal LLZ[16] prepared via high-temperature solid-state synthesis. Most of the samples prepared exhibited T_{MN} values ranging from 235 to 315 K and,

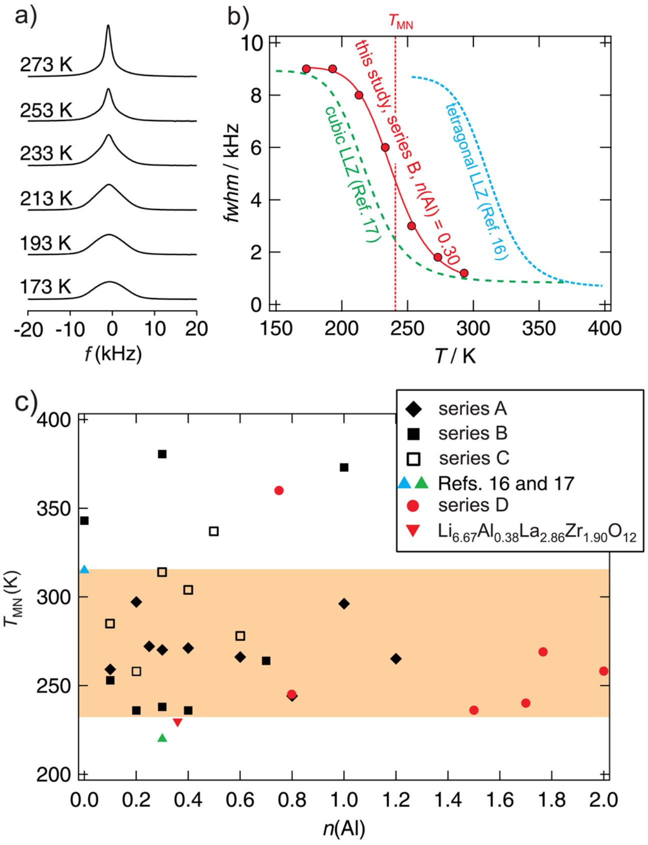

Figure 8. (a) ^{7}Li NMR lines of mechanosynthesized, aliovalently doped LLZ with $x = 0.30$ (series B). Data were recorded under static conditions at $\omega_0/2\pi = 155.4$ MHz. (b) Motional narrowing (MN) of the corresponding line width (red data points). For comparison, the MN curves of cubic (dashed black line, data taken from ref 17) and tetragonal (dashed blue line, data taken from ref 16) LLZ prepared by conventional solid-state syntheses are included as well. (c) T_{MN} (deduced from the curves shown in (b)) as a function of the nominal composition n(Al). Series D marks the samples systematically reduced in La and Zr. The data point at $n(Al) = 1.78$ refers to the sample $Li_{6.36}Al_{1.78}La_{2.26}Zr_{1.38}O_{12}$. The green and blue triangles mark the inflection points of cubic and tetragonal LLZ.[16,17]

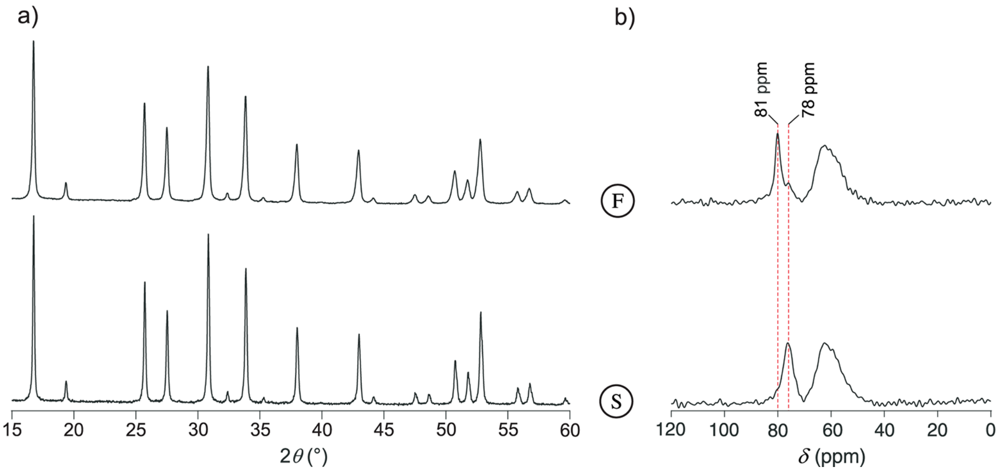

Figure 9. (a) XRPD patterns of two different samples of series B with $x = 0.30$. The XRPD peak widths of the sample labeled as "F" are broader than those found for the sample labeled as "S". (b) ^{27}Al MAS NMR spectra of the two materials which were recorded at a field of 14.1 T and a spinning rate of 30 kHz.

thus, show higher diffusivities than the samples free of Al (see Figure 8c).

Regarding $T_{MN}(n(\mathrm{Al}))$, the characteristic temperature seems to pass through a broad minimum located between $n(\mathrm{Al}) = 0.20$ and $n(\mathrm{Al}) = 0.60$ for the samples of series A and B. It points to a maximum Li ion diffusivity for samples with these compositions. At $n(\mathrm{Al}) \approx 1.00$ there seems to be a minimum of the Li diffusivity for these two series. Interestingly, the Li diffusivity increases once more when the Al content is increased further. For comparison, the value of a very fast sample with a nominal composition of $Li_{6.67}Al_{0.38}La_{2.86}Zr_{1.90}O_{12}$ is also shown.

Obviously, the Al content itself is not the only parameter determining the Li ion dynamics. Possible explanations could be (i) a correlation with the Li concentration,[42] (ii) the occurrence of oxygen vacancies as presumed by Murugan et al.,[42] or (iii) a strong influence of the relative contributions of the different doping mechanisms. As to (i), we did not observe a clear correlation between the Li content and the ion diffusivity of the samples prepared which was evaluated by comparing the integrals of the ^{7}Li NMR lines. Concerning (ii), with the analytical tools available we are not able to decide whether oxygen vacancies, which have been assumed in, e.g., refs 26 and 42, are present to a significant extent. As to (iii), it is important to consider the different types of doping which definitely have a different impact on the garnet structure as pointed out above.

It is worth mentioning that some of the samples were prepared several times in different batches to check the reproducibility of the results. It turned out that T_{MN} varied by up to ~140 K for some equally prepared samples. Exemplarily, in Figure 9a the XRPD patterns of two samples with $x = 0.30$ of series B are shown.

The sample labeled as "F" (fast) is characterized by $T_{MN} = 240$ K while the slower one labeled as "S" is shifted toward higher T, yielding $T_{MN} = 380$ K (see Figure 8c). Interestingly, the XRPD peak widths of sample "F", which is also included in Figure 5, are larger than those obtained for sample "S". In Figure 9b, the corresponding ^{27}Al MAS NMR spectra are shown to check for any differences of the two samples. Whereas the NMR spectrum of sample "S", which has already been included in Figure 3b, reveals a distinct signal at 78 ppm presumably reflecting the doping mechanism (β), in the corresponding NMR spectrum of sample "F" a signal at 81 ppm shows up. Tentatively, the latter can be ascribed to doping mechanism (γ). Independently of these differences, the two spectra show very similar NMR intensities at 64 ppm ascribed to the aliovalent doping (α). Thus, as already proposed above, the relative contributions of the different doping mechanisms (β) and (γ) seem to significantly affect Li ion dynamics in LLZ.

However, it should be mentioned that there are also some samples with a similar composition prepared more than one time which revealed besides similar XRPD patterns very comparable dynamic properties.

Since some of the samples of series B reveal the highest Li diffusivities observed in this study, only samples of these series were chosen for additional conductivity measurements and NMR experiments.

2. ^{7}Li NMR Spin–Lattice Relaxation Rates. When plotted as a function of inverse temperature, the ^{7}Li NMR spin–lattice relaxation (SLR) rate R_1 passes through a maximum at the temperature at which the Li jump rate τ^{-1} is in the order of the Larmor frequency: $\tau^{-1} \approx \omega_0$. Exemplarily, in Figure 10 the SLR

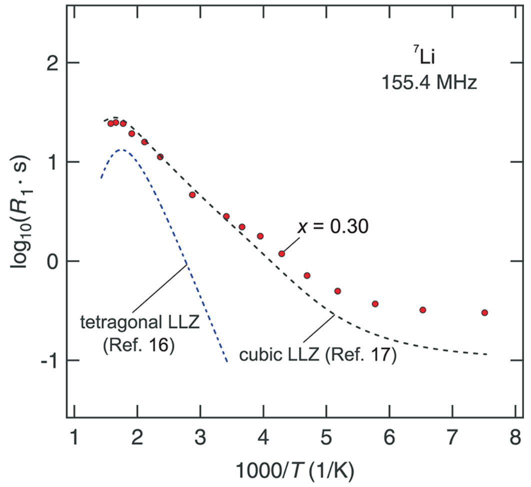

Figure 10. ^{7}Li NMR SLR rates R_1 of LLZ with $x = 0.30$ (series B) recorded at $\nu_0 = \omega_0/2\pi = 155.4$ MHz. For comparison, those of cubic and tetragonal LLZ prepared by a solid-state synthesis are also included (data were taken from refs 16 and 17).

rates R_1 of LLZ with x = 0.30 (series B) are shown. The diffusion-induced NMR SLR rates are very similar to those of conventionally synthesized cubic LLZ which has been studied by some of us quite recently (see ref 17). For comparison, the corresponding data are indicated in Figure 10 by a dashed line. Below 180 K the rate R_1 is governed by nondiffusion induced background relaxation, which is characterized by a very weak temperature dependence. At elevated temperatures the low-T flank of the diffusion-induced rate peak $R_1(1/T)$ is visible. For the sake of completeness also the NMR SLR rates recently obtained for Al-free LLZ crystallizing with tetragonal symmetry[16] are included (see dashed-dotted line).

Independent of n(Al), diffusion-induced rate maxima show up between 573 and 623 K pointing to jump rates in the order of 10^9 s^{-1} (see the Arrhenius plot of Figure 12 where τ^{-1} is plotted vs $1/T$). Taking into account the estimated jump rate from NMR motional narrowing measurements, which has also been included in Figure 12, an activation energy E_a of 0.33(2) eV can be deduced. This value is in good agreement with the results from recently published studies on cubic LLZ.[1,17] For comparison, the corresponding Arrhenius lines of cubic and Al-free tetragonal LLZ are also shown in Figure 12 (see the dashed lines).

3. Static Field-Gradient NMR Measurements. The Li jump rate deduced from ^{7}Li SLR NMR is very similar to that extracted from preliminary static field-gradient (SFG) NMR measurements which were exemplarily carried out using the mechanosynthesized sample with x = 0.30 (series B). In general, SFG NMR probes macroscopic Li diffusion coefficients D in the micrometer range.[43−46] In order to compare D with the Li jump rates probed by SLR NMR, the diffusion coefficients recorded at various temperatures were converted into τ^{-1} values with the help of the Einstein−Smoluchowski equation. Here, we assumed uncorrelated motion and a jump distance of ~0.25 nm. Although the absolute value of the so-obtained rates included in Figure 12 is fraught with an uncertainty of up to a factor of ~5, good agreement is found with the data obtained from motional narrowing and SLR NMR (see, e.g., ref 47 for comparison with other studies).

For the sake of completeness, additional SFG NMR measurements were carried out on cubic and Al-free tetragonal LLZ studied in refs 17 and 16, respectively. Once again, the values probed are in very good agreement with the corresponding Arrhenius lines of Figure 12.

4. Impedance Measurements. Impedance spectroscopy measurements were carried out at room temperature for selected samples. In Figure 11, the real part σ' of the complex impedance of the sample with x = 0.30 (series B) is shown as a function of frequency f. While at low frequencies σ' is influenced by the effects of ion-blocking electrodes, at f = 1 Hz the conductivity reaches a plateau which passes into a dispersive regime. At even higher frequencies (f > 10 MHz) a second plateau shows up which reflects the bulk conductivity being in the order of 10^{-5}−10^{-4} S cm^{-1}. The exact value of σ' associated with this shallow plateau turns out to depend on n(Al) as well as the synthesis conditions chosen. A similar behavior of σ' was found for all the samples prepared by sintering the high-energy ball milled powders at 873 K for 6 h.

Most likely, the low-frequency plateau observed is governed by grain boundary effects significantly blocking long-range ion transport in LLZ. This can be easily verified by sintering the samples at temperatures much higher than 873 K. As an example, in Figure 11 the impedance spectrum of a mechanosynthesized sample of LLZ with x = 0.40 is shown which was annealed at 873 K for 6 h. For comparison, the electrical response of a sample with n = 0.40 is included which has been annealed at 1500 K for 15 h. Its composition is "$Li_{7.75}Al_{0.40}La_3Zr_2O_{12}$", i.e., an excess of Li was intentionally added to compensate for Li loss during annealing (see Figure S2 in the Supporting Information for the XRPD pattern and the corresponding ^{27}Al MAS NMR spectrum). As can be clearly seen in Figure 11, sintering drastically changes the impedance response: the plateau associated with the bulk conductivity is significantly shifted toward higher frequencies dominating σ' in the range from 10 kHz to 10 MHz. $\sigma'(T)$ of the bulk response follows Arrhenius behavior with an activation energy of 0.28(3) eV (see Figure S3, Supporting Information), which is in fair agreement with literature data.[1,17] Conversely, when the pellet sintered at 1500 K is thoroughly ground in an agate mortar and the obtained powder is cold pressed to a new pellet, a conductivity spectrum very similar to the original one is obtained. For comparison, samples which were not annealed after mechanical activation show a rather low Li diffusivity and conductivity, respectively.

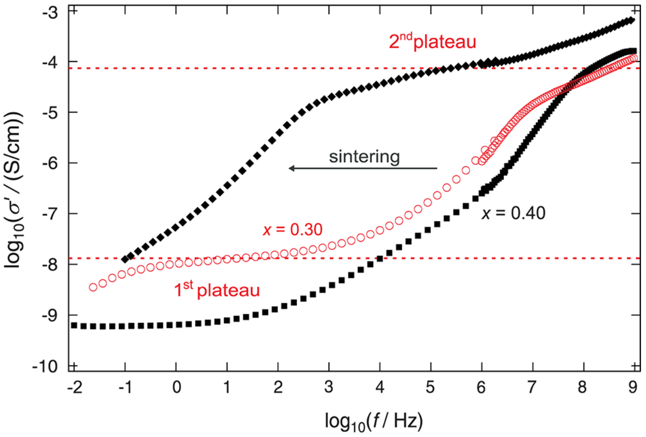

Figure 11. Impedance spectra of mechanosynthesized LLZ with x = 0.30 (red circles) measured at ambient temperature. For comparison, the black squares represent two impedance spectra of a sample with a nominal Al content of x(Al) = 0.40. As indicated by the arrow, sintering at 1500 K for 15 h, which was immediately carried out after the milling step, significantly affects the electrical response.

Finally, coming back to the sample with an Al content of n(Al) = 0.30, in analogy to ref 16, the conductivity values of the two plateaus seen in Figure 11 have been converted into Li jump rates using the Nernst−Einstein equation and the Einstein−Smoluchowski equation. The values calculated are included in the Arrhenius plot of Figure 12. It is evident that the plateau showing up at higher frequencies reflects the fast transport process. The solid line included in the figure represents a least-squares fit taking into account also NMR data. The activation energy turned out to be ~0.33 eV.

IV. CONCLUSIONS

Phase pure Al-doped $Li_7La_3Zr_2O_{12}$ crystallizing with cubic symmetry with an Al content of almost up to n(Al) = 1.78 can easily be prepared by high-energy ball milling and subsequent annealing carried out at rather low temperatures. In contrast to conventional high-temperature solid-state synthesis the low-temperature mechanosynthesis avoids Li loss and allows the precise adjustment of the samples' stoichiometry. This turned out to be beneficial to study the effect of various kinds of

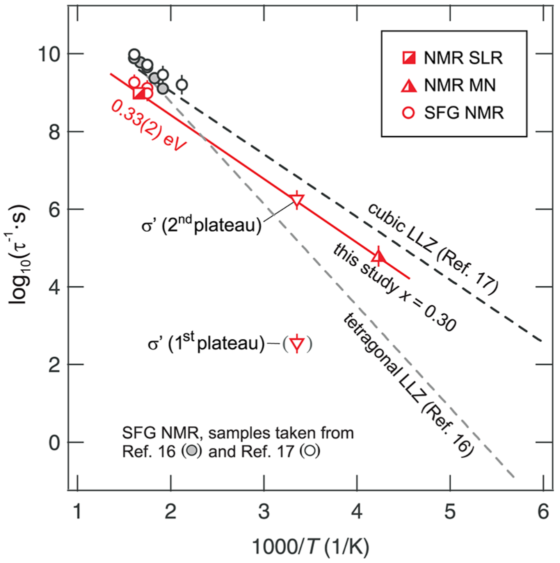

Figure 12. Arrhenius plot of the Li jump rates of the mechanosynthesized sample with $x = 0.30$ (series B). The rates were obtained from various NMR methods, including ^{7}Li SLR NMR, SFG NMR, and line shape measurements (see key) as well as deduced from the impedance spectrum $\sigma'(f)$ shown in Figure 11. For comparison, the Arrhenius lines of cubic,[17] and Al-free tetragonal LLZ,[16] prepared by solid-state synthesis are also included. See text for further explanation.

doping on both structural and dynamic properties of garnet-type LLZ. The comprehensive structural investigation of various Al-doped LLZ samples by XRPD and ^{27}Al MAS NMR reveals that the three distinct NMR lines showing up appear to be connected to three different doping mechanisms whereby Al replaces Li (preferred at low dopant concentrations), La, and Zr. The impact of the Al dopant on the stuffed garnet $\mathrm{Li_7}^+[\mathrm{La_3Zr_2O_{12}}]^{7-}$ is not restricted to the Li sublattice but does directly affect the garnet network itself, leading to $\mathrm{Li}_{7-3x+z}{}^+\mathrm{Al}_x{}^{3+}[\mathrm{La}_{3-y}\mathrm{Al}_y\mathrm{Zr}_{2-z}\mathrm{Al}_z\mathrm{O}_{12}]^{z-7}$ or $\mathrm{Li}_{7-3x}{}^+\mathrm{Al}_x{}^{3+}[\mathrm{La}_{3-y}\mathrm{Al}_y\mathrm{Zr}_{2-z}\mathrm{Al}_z\mathrm{O}_{12-2z}]^{7-}$. This rationalizes the large impact of Al doping on the Li ion diffusivity as well as ion conductivity of cubic LLZ.

Appropriate Al doping results in highly conducting LLZ with a bulk conductivity in the order of 10^{-4} S cm^{-1} similar to that reported by Murugan et al.[1] Using an LLZ sample with $n(\mathrm{Al}) = 0.30$ (series B), the fast Li diffusion process was exemplarily probed by various NMR techniques and impedance spectroscopy altogether covering a dynamic range of many decades. In agreement with recent investigations, the activation energy turned out to be ~0.3 eV. Impedance spectroscopy measurements revealed that the grain boundaries of a cold-pressed nonsintered powder sample have a significant blocking effect on Li ion transport. This can be overcome by appropriate high-temperature sintering of the garnets.[48]

Certainly, further studies are needed to investigate the relationship between synthesis conditions and the relative contributions of the various doping mechanisms taking place. Small variations of the preparation parameters seem to have a significant effect on this ratio which, in turn, is expected to affect Li ion transport.

■ ASSOCIATED CONTENT

Supporting Information

Additional figures showing XRPD patterns and ^{27}Al MAS NMR spectra of some of the samples as well as the dc conductivity in an Arrhenius representation of one of the samples studied. This material is available free of charge via the Internet at http://pubs.acs.org.

■ AUTHOR INFORMATION

Corresponding Author

*E-mail: duevel@pci.uni-hannover.de; Alexander.Kuhn@pci.uni-hannover.de.

Present Addresses

§Solid State Chemical Crystallography/FB02, University of Bremen, Leobener Straße/NW2, D-28359 Bremen, Germany.
‖Institute for Chemistry and Technology of Materials, Graz University of Technology, Stremayrgasse 9, A-8010 Graz, Austria.
⊥Max Planck Institute for Solid State Research, Heisenbergstr. 1, D-70569 Stuttgart, Germany.

Notes

The authors declare no competing financial interest.

■ ACKNOWLEDGMENTS

We thank E. Merzlyakova for her help in sample preparation and M. Krey and M. Binnewies for the ICP OES measurements. We thank J. Caro and A. Feldhoff for access to the Edwards 306 evaporater as well as to the D8 Advance diffractometer. We are indebted to H. Buschmann, S. Berendts, J. Janek (University of Gießen), V. Thangadurai (University of Calgary), and F. Tietz (Forschungszentrum Jülich) for valuable discussions. In particular, we are grateful to J. Janek and V. Thangadurai for leaving us the samples of refs 16 and 17 for the preliminary SFG NMR measurements included here. Financial support by the Federal Ministry of Education and Research (BMBF) in the frame of the project "Kompetenzverbund Nord (KVN)" is highly appreciated. We further acknowledge financial support by the Deutsche Forschungsgemeinschaft (DFG) in the frame of the Research Unit 1277 molife (mobility of lithium ions in solids).

■ REFERENCES

(1) Murugan, R.; Thangadurai, V.; Weppner, W. *Angew. Chem., Int. Ed.* **2007**, *46*, 7778−7781.
(2) Thangadurai, V.; Kaack, H.; Weppner, W. *J. Am. Ceram. Soc.* **2003**, *86*, 437−440.
(3) Liu, Z.; Huang, F.; Yang, J.; Wang, Y.; Sun, J. *Solid State Sci.* **2008**, *10*, 1429−1433.
(4) Etacheri, V.; Marom, R.; Elazari, R.; Salitra, G.; Aurbach, D. *Energy Environ. Sci.* **2011**, *4*, 3243−3262.
(5) Kumar, B.; Kumar, J.; Leese, R.; Fellner, J. P.; Rodrigues, S. J.; Abraham, K. M. *J. Electrochem. Soc.* **2010**, *157*, A50−A54.
(6) Ramzy, A.; Thangadurai, V. *Appl. Mater. Interfaces* **2010**, *2*, 385−390.
(7) Kotokubi, M.; Munakata, H.; Kanamura, K.; Sato, Y.; Yoshida, T. *J. Electrochem. Soc.* **2010**, *157*, A1076−A1079.
(8) Thangadurai, V.; Weppner, W. *Adv. Funct. Mater.* **2005**, *15*, 107−112.
(9) Thangadurai, V.; Weppner, W. *J. Power Sources* **2005**, *142*, 339−344.
(10) Wuellen, L. v.; Echelmeyer, T.; Meyer, H.-W.; Wilmer, D. *Phys. Chem. Chem. Phys.* **2007**, *9*, 3298−3303.
(11) Koch, B.; Vogel, M. *Solid State Nucl. Magn. Reson.* **2008**, *34*, 37−43.
(12) Cussen, E. J. *Chem. Commun.* **2006**, 412−413.
(13) Cussen, E. J. *J. Mater. Chem.* **2010**, *20*, 5167−5173.
(14) Rangasamy, E.; Wolfenstine, J.; Sakamoto, J. *Solid State Ionics* **2012**, *206*, 28−32.

(15) Weppner, W. German patent number DE102004010892-B3.
(16) Kuhn, A.; Narayanan, S.; Spencer, L.; Goward, G.; Thangadurai, V.; Wilkening, M. *Phys. Rev. B* **2011**, *83*, 094302−1−094302−11.
(17) Buschmann, H.; Dolle, J.; Berendts, S.; Kuhn, A.; Bottke, P.; Wilkening, M.; Heitjans, P.; Senyshyn, A.; Ehrenberg, H.; Lottnyk, A.; et al. *Phys. Chem. Chem. Phys.* **2011**, *13*, 19378−19392.
(18) Kim, K. H.; Iriyama, Y.; Yamamoto, K.; Kumazaki, S.; Asaka, T.; Tanabe, K.; Fisher, C. A. J.; Hirayama, T.; Murugan, R.; Ogumi, Z. *J. Power Sources* **2011**, *196*, 764−767.
(19) Kumazaki, S.; Iriyama, Y.; Kim, K.-H.; Murugan, R.; Tanabe, K.; Yamamoto, K.; Hirayama, T.; Ogumi, Z. *Electrochem. Commun.* **2011**, *13*, 509−512.
(20) Kanamura, K.; Kaeriyama, A.; Honda, A.; Yoshida, T.; Sato, Y. US patent application number 20110053000.
(21) Kotobuki, M.; Kanamura, K.; Sato, Y.; Yoshida, T. *J. Power Sources* **2011**, *196*, 7750−7754.
(22) Awaka, J.; Kijima, N.; Hayakawa, H.; Akimoto, J. *J. Solid State Chem.* **2009**, *182*, 2046−2052.
(23) Geiger, C. A.; Alekseev, E.; Lazic, B.; Fisch, M.; Armbruster, T.; Langner, R.; Fechtelkord, M.; Kim, N.; Pettke, T.; Weppner, W. *Inorg. Chem.* **2011**, *50*, 1089−1097.
(24) Kuhn, A.; Choi, J.-Y.; Robben, L.; Tietz, F.; Wilkening, M.; Heitjans, P. *Z. Phys. Chem.* **2012**, *226*, 525−537.
(25) Kokal, I.; Somer, M.; Notten, P. H. L.; Hintzen, H. T. *Solid State Ionics* **2011**, *185*, 42−46.
(26) Shimonishi, Y.; Toda, A.; Zhang, T.; Hirano, A.; Imanishi, N.; Yamamoto, O.; Takeda, Y. *Solid State Ionics* **2011**, *183*, 48−53.
(27) Xie, H.; Alonso, J. A.; Li, Y.; Fernández-Díaz, M. T.; Goodenough, J. B. *Chem. Mater.* **2011**, *23*, 3587−3589.
(28) Janani, N.; Ramakumar, S.; Dhivya, L.; Deviannapoorani, C.; Saranya, K.; Murugan, R. *Ionics* **2011**, *17*, 575−580.
(29) Kosova, A. *Ann. Chim.* **2009**, *34*, 401−413.
(30) Plesingerova, B.; Buchal, A.; Šepelák, V.; Tkacova, K. *Ceram.-Silik.* **1996**, *40*, 131−136.
(31) Da Silva, K. L.; Šepelák, V.; Paesano, A., Jr.; Litterst, F. J.; Becker, K. D. *Z. Anorg. Allg. Chem.* **2010**, *636*, 1018−1025.
(32) Da Silva, K. L.; Šepelák, V.; Düvel, A.; Paesano, A., Jr.; Hahn, H.; Litterst, F. J.; Heitjans, P.; Becker, K. D. *J. Solid State Chem.* **2011**, *184*, 1346−1352.
(33) *Diffusion in Condensed Matter − Methods, Materials, Models*; Heitjans, P.; Kärger, J., Eds.; Springer: Berlin, 2005.
(34) Fukushima, E.; Roeder, S. B. W. *Experimental Pulse NMR*; Addison-Wesley: Reading, MA, 1981.
(35) Blanc, F.; Middlemiss, D. S.; Buannic, L.; Palumbo, J. L.; Farnan, I.; Grey, C. P. *Solid State Nucl. Magn. Reson.* **2012**, *42*, 87−97.
(36) Abbattista, F.; Vallino, M.; Mazza, D. *Inorg. Chim. Acta* **1987**, *140*, 147−149.
(37) Narayanan, S.; Epp, V.; Wilkening, M.; Thangadurai, V. *RSC Adv.* **2012**, *2*, 2553−2561.
(38) Choi, M.; Matsunaga, K.; Oba, F.; Tanaka, I. *J. Phys. Chem. C* **2009**, *113*, 3869−3873.
(39) Müller, D.; Gessner, W. *Polyhedron* **1983**, *11*, 1195−1198.
(40) Müller, D.; Gessner, W.; Behrens, H.-J.; Scheler, G. *Chem. Phys. Lett.* **1981**, *79*, 59−62.
(41) Bloembergen, N.; Purcell, E.; Pound, R. *Phys. Rev.* **1948**, *73*, 679−712.
(42) Murugan, R.; Thangadurai, V.; Weppner, W. *Appl. Phys. A: Mater. Sci. Process.* **2008**, *91*, 615−620.
(43) Stilbs, P. *Progr. NMR Spectrosc.* **1986**, *19*, 1−45.
(44) Karlicek, R. F., Jr.; Lowe, I. J. *J. Magn. Reson.* **1980**, *37*, 75−91.
(45) Fischer, D. M.; Duwe, P.; Indris, S.; Heitjans, P. *Solid State Nucl. Magn. Reson.* **2004**, *26*, 74−83.
(46) Gutsze, A.; Masierak, W.; Geil, B.; Kruk, D.; Pahlke, H.; Fujara, F. *Solid State Nucl. Magn. Reson.* **2005**, *28*, 244−249.
(47) Heitjans, P.; Indris, S. *J. Phys.: Condens. Matter* **2003**, *15*, R1257−R1289.
(48) Wolfenstine, J.; Rangasamy, E.; Allen, J. L.; Sakamoto, J. *J. Power Sources* **2012**, *208*, 193−196.

16 Investigations of the mechanically induced phase transformation of γ-Al_2O_3 to α-Al_2O_3

The thermally induced phase transformation of γ-Al_2O_3 was investigated in the early 1980s. It was found that it starts from unsaturated Al on the surface of the γ-Al_2O_3 crystallites from which the α-Al_2O_3 crystallites grows into the γ-Al_2O_3 crystallites.[1–8] This unsaturated Al was identified as fivefold by oxygen coordinated Al by employing ^{27}Al magic angle spinning (MAS) nuclear magnetic resonance (NMR) spectroscopy.[9] In γ-Al_2O_3 Al is typically coordinated by four or six oxygen atoms. About one decade later the mechanically induced γ-Al_2O_3 to α-Al_2O_3 phase transformation came into focus due to the attempts of producing nanocrystalline alumina to increase its surface area (e. g. for catalysis) or improve its sintering behavior to obtain denser, stiffer and harder corundum.[10–12] Some of the groups investigating the mechanically induced phase transformation observed a transformation from the γ-phase to the α-phase, but some did not, see ref. 12 for an overview. In 2005 Wang et al.[12] published a study in which they proposed that this phase transformation can only occur in the presence of seed crystals of α-Al_2O_3. Three years later a very similar study was published by Bodaghi et al.[13] with the same result.

In the current study which is presented in the following paper entitled "Mechanically Induced Phase Transformation of γ-Al_2O_3 into α-Al_2O_3. Access to Structurally Disordered γ-Al_2O_3 with a Controllable Amount of Pentacoordinated Al Sites", written by the author and Prof. M. Wilkening, this assumption was tested. Three γ-Al_2O_3 distributed by different companies (Alfa Aesar, Merck and Dalian Luming Nanometer Material Ltd.) exhibiting different crystallite sizes and BET surface areas (measured by Dr. Monir Sharifi being a phd student of Prof. Michael Wark that time) were investigated. The phase transformation was followed by ^{27}Al MAS NMR spectroscopy since XRPD patterns of γ-Al_2O_3 and transition aluminas are often very noisy and hard to interpret. The ^{27}Al MAS NMR spectra of the two polymorphs are, however, very easily distinguishable since the γ-phase shows octahedrally as well as tetrahedrally coordinated Al, while in the α-phase only octahedrally coordinated Al occurs.[9] The ^{27}Al MAS NMR spectra for this study were recorded by Dr. Ekaterina Romanova using a cryomagnet with a nominal field of 17.6 T in Leipzig. The high magnetic field increases the resolution of the spectra compared to average or low magnetic fields (increased signal intensity, larger frequency range for the spectrum, reduced second order quadrupolar interactions (^{27}Al: $I = 5/2$)). It was found that the phase transformation of the γ-phase to the α-phase occurred in one sample after 5 h of milling (sample A), whereas the other two samples (samples D and M) showed a much slower transformation behavior. The reason for these differences were identified to be the size of the surface area of the γ-Al_2O_3 crystallites. For very small crystallites which, therefore, are characterized by a large surface area the γ-phase is stabilized due to the lower surface-energy of this polymorph compared to the one of the α-phase.[14] Thus, if γ-Al_2O_3 with small crystallite sizes and, therefore, a large surface area is milled, the transformation does not occur but a further comminution of the crystallites stabilizing the γ-phase even more. If the unmilled samples D and M which did not transform by mechanical treatment are heat treated at temperatures clearly smaller than necessary for the thermally induced phase transformation, grain growth can be observed. When these samples are high-energy ball milled afterwards they transform to the α-phase almost as fast as observed for sample A. However, by increasing the amount of energy introduced by ball milling by changing the milling vial set material from ZrO_2 to WC, which is harder and much denser, also the high-surface area γ-Al_2O_3 can be transformed by milling for 5 h. Under these conditions the reaction can probably be performed endothermal.

Furthermore, it was found that the pentagonally coordinated Al (penta-Al) plays a crucial role for the mechanically induced γ-Al_2O_3 to α-Al_2O_3 phase transformation. If γ-Al_2O_3 is high-energy ball milled the penta-Al forms most probably due to the breakage of Al-O bonds when a crystallite is mechanically cracked. By adding fluorides like either CaF_2, BaF_2 or an oxide like La_2O_3 to sample A the phase transformation does not take place or is clearly slowed down. This is accompanied by a strong reduction of the amount of penta-Al which can be observed by ^{27}Al MAS NMR since the fluoride of the CaF_2 or BaF_2 or the oxygen of the La_2O_3 coordinates to the unsaturated penta-Al. Thus, the mechanically induced γ-Al_2O_3 to α-Al_2O_3 phase transformation seems to be very similar to the thermally induced phase transformation described before.

Another very interesting result is the possibility to produce large amounts of penta-Al in case of the aluminas that do not or only very slowly transform to the α-phase. T_1 measurements of the three Al sites

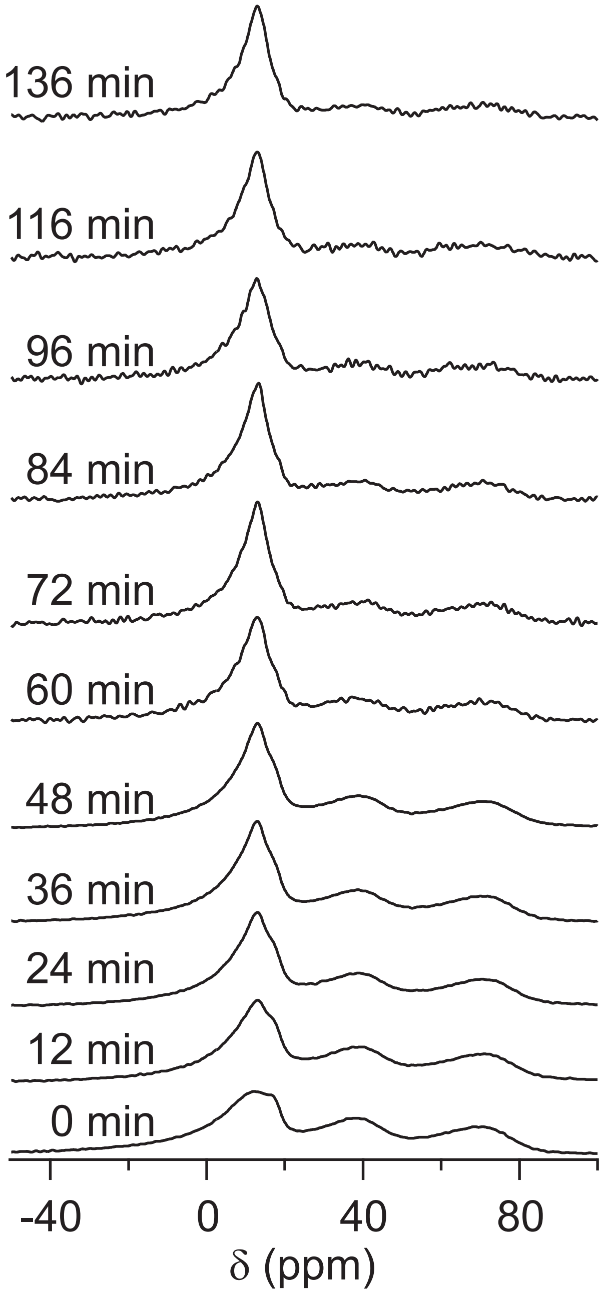

Figure 71: ^{27}Al MAS NMR spectra of a mixture of γ-Al_2O_3 milled for 10 h and deionized water. The mixture was put into the rotor and measured several times in a row. The spinning frequency of the rotor was 30 kHz. See text for further explanations.

in the high-energy ball milled γ-Al_2O_3 indicated that the penta-Al is probably mainly located in the surface regions of the crystallites. Penta-Al at the surface of aluminas is an anchoring site for catalytically active materials like Pt or V_2O_5.[15] The bonding occurs via the oxygen delivered by the catalytically active material like it was also shown within this study for La_2O_3 and the fluorides. Consequently, bonds like O_5Al-O-Pt_x or O_5Al-O-$V_2O_4(V_2O_5)_x$ are created. Hence, "a substantial challenge remains to develop synthesis methods that allow for the systematic and controllable variation of the number of Al^{3+}_{penta} sites, ultimately enabling us to tailor the dispersion and morphology and, therefore, catalytic activity of active metals on the commonly used γ-Al_2O_3 support material."[15] This is possible with the method introduced here. A large amount of penta-Al is accessible by high-energy ball milling of γ-Al_2O_3 characterized by a large specific surface area. This amount can be tailored by the milling time as well as through subsequent annealing as demonstrated in the paper. Catalytic active materials are commonly brought onto a supporting material by wet impregnation technique, i. e. salts containing the metal to be brought onto the support are dissolved in water. The solution obtained is brought into contact with the support material.

However, it was found that the high-energy ball milled γ-Al_2O_3 transforms to γ-AlOOH (boehmite) when in contact with water and heat-dried. This can be seen in Fig. 71 where ^{27}Al MAS NMR spectra of a mixture of 10 h milled γ-Al_2O_3 (sample D) and distilled water are shown for different measuring times. The rotation of the rotor leads to an increase of the temperature of the rotor which can be measured directly by the change of the chemical shift of the ^{79}Br NMR line of KBr. The change of the distances between the Br and K ions due to the temperature change leads to a change of the chemical shift. These measurements were done for several rotational speeds with the probes and rotors present in the group by Kai Volgmann who was a phd student of Prof. Paul Heitjans that time. He found a temperature of about 327 K at a spinning frequency of 30 KHz. This spinning frequency was also used for the measurements here. As can be seen in Fig. 71 the spectrum changed after already 12 minutes of rotation. A sharp NMR line becomes visible at about 12 ppm while the intensities of the NMR lines of the penta-Al at about 35 ppm and the one of the tetrahedrally coordinated Al at about 68 ppm decrease with increasing measuring time. Thus, the transformation can be followed in situ. However, since the water is consumed by the reaction, the reaction slows down after a while such that the measurements had to be stopped. After 48 min of measuring the dried powder was removed from the rotor, mixed with water again, and put back into the rotor. Since the amount of powder was reduced due to this procedure and the amount of Al per formula unit decreased from two to one the quality of the spectra is reduced. After 84 min the procedure has to be repeated which again leads to a decrease of the intensity such that the measuring time had to be doubled. The reaction kinetics are not accessible this way since the amount of water which can be added to the mixture is too small for an unimpeded reaction. This is due to the fact that the rotor cannot be spun up to 30 kHz when mainly filled with water.

However, the transformation of the high-energy ball milled γ-Al_2O_3 exhibiting a large amount of penta-Al to boehmite does not happen to a significant extent if the water is removed from the mixture at low temperatures under reduced pressure since the transformation does not happen at ambient temperature. This was done for a study of the catalytic activity of Al_2O_3 supported V_2O_5 for the oxidative dehydrogenation of ethane to ethylene for which the effect of different alumina supports was tested. For that study which was done by Ai-Ling Qiao et al. at the Leibniz-Institut für Katalyse (LIKAT, Rostock, Germany) the catalysts were prepared by wet impregnation technique. NH_4VO_3 being the precursor of V_2O_5 was dissolved in deionized water together with oxalic acid. This solution was impregnated onto the aluminas. After that the solvent was removed under reduced pressure with a rotavapor. The solid remainings were dried at 393 K and eventually calcined at 873 K for 6 h. It was found that the catalytic activity and more important the product selectivity of the catalyst based on the high-energy ball milled γ-Al_2O_3 (sample D, milled 10 h at 600 rpm employing a ZrO_2 vial set with 140 balls with a diameter of 5 mm of the same material) was very similar to the ones of the two best performing samples. The latter ones were γ-Al_2O_3 samples with surface areas larger than 200 m^2/g while the surface area of the mechanically treated alumina was only 5.8 m^2/g. Expectedly, by UV-vis spectroscopy and transmission electron microscopy evidence was found for the presence of very small V_2O_5 clusters homogeneously distributed on the surface of the mechanically treated alumina crystallites. Thus, if the activity and selectivity could be increased further or if a similar catalytic activity could be achieved by using less V_2O_5 (here 10 wt% was used) the use of mechanically treated γ-Al_2O_3 would be an alternative to the usage of non-milled aluminas. In addition to this, the long term stability of the catalysts should be investigated since the sintering tendency of the V_2O_5 at the surface of the ball milled alumina might be reduced compared to V_2O_5 at the surface of conventional aluminas. Perhaps the surface area of the ball milled alumina can be increased without decreasing the amount of the penta-Al which should lead to a better performance of the catalyst. Furthermore, the catalytic performance of co-milled γ-Al_2O_3 and V_2O_5 (as well as that of a milled mixture of sample D, PtO and Pt) is currently investigated at LIKAT. A manuscript dealing with the results gained at LIKAT was submitted to Industrial & Engineering Chemistry Research.[16]

It should be noted that some of the main results of the work published in J. Phys. Chem. C are also shown in a tutorial review about the mechanosynthesis of oxides.[17]

References

[1] P. Burtin, J. P. Brunelle, M. Pijolat, M. Soustelle, Appl. Catal. 34 (1987) 225.

[2] P. Burtin, J. P. Brunelle, M. Pijolat, M. Soustelle, Appl. Catal. 34 (1987) 239.

[3] D. S. Tucker, J. Hren, J. Mater. Res. Soc. Symp. Proc. 31 (1984) 337.

[4] D. S. Tucker, J. Am. Ceram. Soc. 68 (1985) C163.

[5] D. S. Tucker, E. J. Jenkins, J. H. Hren, J. Electron Microsc. Tech. 2 (1985) 29.

[6] F. W. Dynis, J. W. Halloran, J. Am. Ceram. Soc. 65 (1982) 442.

[7] R. B. Bagwell, G. L. Messing, P. R. Howell, J. Mater. Sci. 36 (2001) 1833.

[8] B. Béguin, E. Garbowski, M. Primet, Appl. Catal. 75 (1991) 119.

[9] J. H. Kwak, J. Hu, A. Lukaski, D. H. Kim, J. Szanyi, C. H. F. Peden, J. Phys. Chem. C 112 (2008) 9486.

[10] P. A. Zieliński, R. Schulz, S. Kaliaguine, A. Van Neste, J. Mater. Res. 8 (1993) 2985.

[11] S. Cava, S. M. Tebcherani, I. A. Souza, S. A. Pianaro, C. A. Paskocimas, E. Longo, J. A. Varela, Mater. Chem. Phys. 103 (2007) 394.

[12] Y. Wang, A. Suryanarayana, L. An, J. Am. Ceram. Soc. 88 (2005) 780.

[13] M. Bodaghi, A. R. Mirhabibi, H. Zolfonum, M. Tahriri, M. Karimi, Phase Transform. 81 (2008) 571.

[14] J. M. McHale, A. Auroux, A. J. Perrotta, A. Navrotsky, Science 277 (1997) 788.

[15] J. H. Kwak, J. Hu, D. Mei, C.-W. Yi, D. H. Kim, C. H. F. Peden, L. F. Allard, J. Szanyi, Science 325 (200) 1670.

[16] A. Qiao, V. N. Kalevaru, J. Radnik, A. Düvel, P. Heitjans, A. Sri Hari Kumar, P. S. Sai Prasad, N. Lingaiah, A. Martin, submitted to ind. Eng. Chem. Res.

[17] V. Šepelák, A. Düvel, M. Wilkening, K.-D. Becker, P. Heitjans, Chem. Soc. Rev. 42 (2013) 7507.

Reproduced with permission from A. Düvel, E. Romanova, M. Sharifi, D. Freude, M. Wark, P. Heitjans, M. Wilkening, J. Phys. Chem. C 115 (2012) 22770.
Copyright 2014 American Chemical Society.
http://pubs.acs.org/doi/abs/10.1021/jp206077r?journalCode=jpccck&quickLinkVolume=115&quickLinkPage=22770&selectedTab=citation&volume=115

THE JOURNAL OF PHYSICAL CHEMISTRY C
ARTICLE
pubs.acs.org/JPCC

Mechanically Induced Phase Transformation of γ-Al_2O_3 into α-Al_2O_3. Access to Structurally Disordered γ-Al_2O_3 with a Controllable Amount of Pentacoordinated Al Sites

A. Düvel,[*,†] E. Romanova,[†] M. Sharifi,[†] D. Freude,[‡] M. Wark,[†] P. Heitjans,[†] and M. Wilkening[*,†]

[†]Institute of Physical Chemistry and Electrochemistry, and Center for Solid State Chemistry and New Materials (ZFM), Leibniz University Hannover, Callinstr. 3a, D-30167 Hannover, Germany

[‡]Institute for Experimental Physics, University of Leipzig, Linnéstr. 5, 04103 Leipzig, Germany

Supporting Information

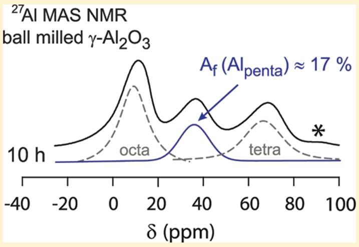

ABSTRACT: One of the most important goals in materials science is the modification and design of solids to obtain functionalized materials with tailored properties. However, in many cases the structure—property relationships are unknown or turn out to be highly complex and difficult to bring under control. In the present paper we show how the atomic-scale structure of a technically important oxide can be modified by mechanical rather than by chemical treatment. We comprehensively investigated the phase transformation of γ-Al_2O_3 into α-Al_2O_3 which was mechanically initiated by treatment of various samples in a high-energy ball mill. The progress of the transformation is followed on an atomic scale by ^{27}Al MAS NMR spectroscopy carried out at a very high magnetic field of 17.6 T. Depending on the kind of milling, unsaturated, i.e., pentacoordinated, Al ions are formed to an unexpectedly large number fraction as high as 20%. The progress of the phase transformation turns out to depend on a number of parameters such as the initial morphology and surface area of the samples as well as the milling conditions. By systematically evaluating and varying these parameters, several ways have been found to easily manipulate the phase transformation and, more importantly, to ultimately control both the formation and amount of pentacoordinated Al centers. These have been shown to act as anchoring sites for catalytically active materials such as widely used Pt. Finally, the mechanical preparation route found might establish a basis for the design of catalysts whose activity can be thoroughly tailored.

I. INTRODUCTION

The study of solid state reactions as well as phase transformations from a microscopic point of view is of great importance to uncover the details of the underlying formation mechanisms. The information gained is highly useful to vary the preparation conditions in order to synthesize materials with tailored properties in a knowledge-based way. In particular, with nonconventional preparation techniques such as mechanosynthesis, in many cases nonequilibrium, metastable compounds are accessible. Understanding their formation processes might help improve their properties so that highly functionalized materials can be made available. In this study, we show in detail by using ^{27}Al magic angle spinning (MAS) nuclear magnetic resonance (NMR) spectroscopy, in particular, by which parameters the mechanically induced phase transformation from γ-Al_2O_3 to its α-modification is influenced. It turned out that the transformation highly depends on the properties of the starting materials as well as the various milling conditions applied. The present study is closely entangled with the preparation of nanocrystalline γ-Al_2O_3 by high-energy ball milling.

Besides the α-modification and γ-phase, six polymorphs of Al_2O_3 are known, viz., δ, η, θ, κ, ρ, and χ. Whereas the α-phase is the thermodynamically stable one, the other polymorphs are metastable at room temperature. α-Al_2O_3 is a well-known multipurpose material with applications in many industries. For instance, besides its prevailing use as abrasive it represents a universally applicable high-temperature ceramic due to its hardness and resistance against corrosive materials.[1−7] Furthermore, transition metal doped alumina such as Cr:Al_2O_3, see ref 8, and Ti:Al_2O_3 belong to the very first lasing media and continue to be of great importance in this field.[9,10]

The γ-phase of Al_2O_3 is commonly used as a catalyst support material in practical applications.[11−14] Many studies are concerned with the investigation of the so-called metal—support interactions; see, e.g., refs 15−17. Understanding these interactions from an atomic-scale point of view might be very helpful for the target-oriented design of new catalysts as well as improved support materials. Quite recently, it has been proven by high-resolution ^{27}Al NMR that coordinatively unsaturated, i.e., 5-fold, coordinated Al^{3+} centers on the γ-Al_2O_3 surfaces act as binding sites for active catalyst phases such as widely used PtO being the precursor for metallic Pt.[15] Interestingly, 5-fold Al ions[13,18] also show up during the thermally induced irreversible $\gamma \longrightarrow \alpha$ phase transformation which has been the topic of numerous studies.[12,19−22]

Received: June 28, 2011
Revised: September 30, 2011
Published: October 05, 2011

It occurs according to the following transformation sequence involving the δ and θ phase of aluminum oxide[23]

$$\gamma\text{-Al}_2\text{O}_3 \xrightarrow{1023\ \text{K}} \delta\text{-Al}_2\text{O}_3$$

$$\delta\text{-Al}_2\text{O}_3 \xrightarrow{1173\ \text{K}} \theta\text{-Al}_2\text{O}_3 \xrightarrow[1050\ \text{K see refs 12, 24}]{1373-1473\ \text{K}} \alpha\text{-Al}_2\text{O}_3$$

The thermally induced phase transformation is assumed to be a surface-controlled reaction: α-Al_2O_3 is reported to grow from the γ-Al_2O_3 surface toward the interior of the grain; unsaturated Al centers located on the surface are assumed to act as starting points.[12,19,20,22,25−28] The formation and the role of 5-fold coordinated Al ions in the thermally induced transformation have been studied in detail by Kwak et al. by ^{27}Al MAS NMR spectroscopy making use of the advantages[29] of measurements carried out at ultrahigh magnetic fields.[13,18] In accordance with previous assumptions they found strong evidence that this species is exclusively located on the surface of the micrometer-sized γ-Al_2O_3 crystallites. This view is strongly supported by the observation that the phase transformation can be inhibited by adding suitable hydroxides or oxides such as La_2O_3 and BaO which bond to the unsaturated Al ions.[12,13,18,30] Consequently, bonded oxides reduce the number of nucleation sites needed for the phase transformation. It is worth mentioning in this context that, quite recently, Lee et al. detected large amounts of four- and five-coordinated Al sites in a thin film of amorphous Al_2O_3.[31,32] In an impressive study they used 2D MAS NMR spectroscopy[31] to characterize the structure of a fully X-ray amorphous Al_2O_3 sample.

Besides heat treatment, it is known that the $\gamma \rightarrow \alpha$ phase transformation can also be initiated mechanically by ball milling at ambient temperature. Zieliński et al.[33] reported on a virtually complete transformation by milling of γ-Al_2O_3 for 8 h in a high-energy ball mill. They used vial sets made of either tungsten carbide or hardened steel. While some of the subsequent studies could reproduce this result,[23,34,35] others, however, could not confirm the initiation of the $\gamma \rightarrow \alpha$ phase transformation.[36,37] Wang et al. suggested that the phase transformation can only be initiated mechanically if a small amount of α-Al_2O_3 particles, acting as seed crystals, is already present from the beginning which is well-known when the phase transformation is thermally induced.[36] Later Bodaghi et al. came up with the same assumption.[37]

As we illustrate below, reactive 5-fold coordinated Al sites also show up during the mechanically induced $\gamma \rightarrow \alpha$ phase transformation. The transformation is initiated by high-energy ball milling of polycrystalline γ-Al_2O_3 in a planetary mill at ambient temperature. This leads to nanostructured materials characterized by a large surface area and an increased volume fraction of interfacial regions which are anticipated to show structural disorder, see also refs 31 and 32. The crucial role of nanomaterials in catalytic processes has been outlined previously.[38]

Here, the progress of the phase transformation is comprehensively followed by both X-ray powder diffraction (XRPD) as well as ^{27}Al MAS NMR spectroscopy as mentioned above. NMR measurements were carried out at a high magnetic field of 17.6 T. Magnetically inequivalent Al species can be well distinguished by ^{27}Al MAS NMR due to their distinct isotropic chemical shifts δ_{iso}.[39] Whereas NMR lines showing up in the range from 12 to 16 ppm indicate Al species being coordinated by six oxygen anions, signals at 35 ppm can be assigned to 5-fold and those at approximately 70 ppm to 4-fold coordinated Al ions.[31,32,40,41] In α-Al_2O_3 crystallizing with space group $R\bar{3}c$ all of the Al ions are octahedrally coordinated by oxygen. This is in contrast to the crystal structure of the γ-phase where the Al cations are distributed among distinct tetrahedral and octahedral sites.[42] Thus, the $\gamma \rightarrow \alpha$ phase transformation can directly be tracked on an atomic-scale level by following the changes of the ^{27}Al MAS NMR spectra of the corresponding γ-Al_2O_3 powders mechanically treated for different milling times, t_{mill}.

Depending on both the initial morphology of the sample and the kind of milling, the phase transformation can be successfully suppressed and nanostructured γ-Al_2O_3 is produced. Surprisingly, under certain milling conditions pentacoordinated Al species (Al_{penta}) are formed to an unexpectedly large number fraction as high as 20%. The role of unsaturated Al sites during the phase transformation as well as the influence of milling conditions, thermal pretreatment, and surface area of the starting materials are comprehensively and systematically evaluated. In particular, the above-mentioned assumption[36,37] concerning the important role of α-Al_2O_3 seed crystals for the mechanically induced transformation will be reviewed.

Within this study we present the guidelines allowing one to definitely influence both the initialization and inhibition of the phase transformation as well as the number fraction of pentacoordinated Al ions formed. Controlling the latter is a key requirement to design support materials for catalytically active materials which bind on the unsaturated Al sites of the γ-Al_2O_3 particles.

Table 1. Sample Purities and Initial Surface Areas of the γ-Al_2O_3 Powders Investigated

	supplier	purity (%)	BET surface area measured ($m^2\ g^{-1}$)
A	Alfa Aesar	99.997	60
D	Dalian Luming Nanometer Material Ltd.	99.99	144
M	Merck	>99.5	126

II. EXPERIMENTAL DETAILS

Three different samples of γ-Al_2O_3 (labeled A, D, and M) were investigated which were purchased from Alfa Aesar (A), Dalian Luming Nanometer Material, Ltd. (D), and Merck (M), respectively (see Table 1). α-Al_2O_3 (99.99%) used as seed crystals was obtained from Alfa Aesar.

In order to initiate the phase transformation, 2 g of γ-Al_2O_3 was milled under air in a Fritsch P7 planetary mill (premium line) at a rotational speed of 600 rpm. If not stated otherwise a 45 mL zirconia (ZrO_2, Mohs' hardness 8.5) vial set equipped with 140 balls of the same material was employed leading to a ball-to-powder mass ratio of approximately 27:1.

The samples were characterized by XRPD (see Figure 1) using either a Philips X'Pert or a Bruker Advance D8 X-ray diffractometer both operating with Cu Kα radiation ($\lambda \approx 0.154$ nm). XRPD measurements were carried out in air atmosphere at ambient temperature. For supplementary transmission electron microscope (TEM) investigations, a powder specimen was dispersed in ethanol, and a drop of 10 μL of suspension was dried on a copper-supported holey carbon film. (Scanning) transmission electron microscopy (S)TEM was made at 200 kV

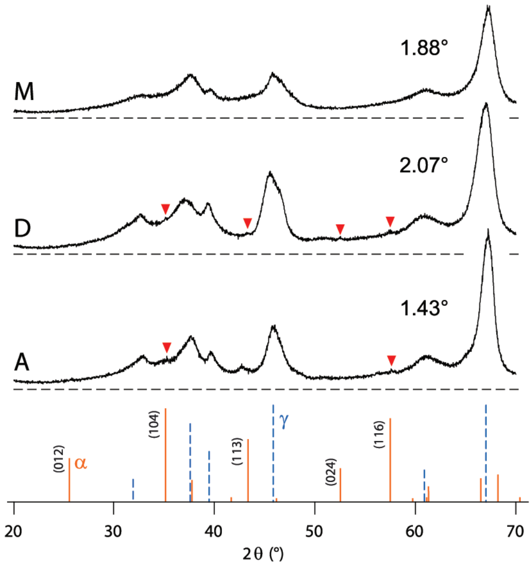

Figure 1. X-ray diffraction pattern of the γ-Al_2O_3 powders used as starting materials. The patterns of samples A and D reveal a small amount of α-Al_2O_3 highlighted by red arrows. Solid lines show the expected XRPD pattern of α-Al_2O_3. The diffraction peaks of γ-Al_2O_3 are represented by dashed lines. The values given represent the widths Δ_{fwhm} (full width at half-maximum) of the peak with the highest intensity. They might be used for a rough comparison of the mean crystallite sizes of the starting materials used. The trend of the peak width agrees well with that revealed by the SEM images shown in Figure 2.

on a field-emission instrument of the type JEOL JEM-2100F-UHR in bright-field, dark-field, and phase contrast. Additional TEM measurements were carried out on a JEOL JEM-2010 at 200 kV.

^{27}Al MAS NMR measurements were carried out using an Avance 750 NMR spectrometer (Bruker) connected to a wide-bore cryomagnet providing a field of 17.6 T. This external magnetic field corresponds to a ^{27}Al NMR resonance frequency of 195.25 MHz. A commercial 4 mm MAS probe (Bruker) in combination with high-speed 4 mm rotors with an inner diameter of 2.5 mm were used. The spinning speed was set to 15 kHz. NMR spectra were recorded with a single pulse sequence. The $\pi/2$-pulse length was 16 μs, and the recycle delay was about 5 s ensuring full spin−lattice relaxation. Up to 1000 scans were accumulated for each spectrum. NMR spectra recorded were referenced to an aqueous solution of $Al(NO_3)_3$. For comparison, an Avance 600 spectrometer in connection to a 14.1 T magnet was employed to record ^{27}Al MAS NMR spectra at spinning speeds of 15 and 30 kHz. The excitation pulse length was 2 μs ($\pi/2$-pulse); the recycle delay was at least 5 s (see above). Shorter or longer excitation pulses do not influence the resulting NMR spectra. For the measurements carried out at 14.1 T a standard MAS NMR probe in combination with ZrO_2 rotors (2.5 mm in outer diameter) was used. ^{27}Al NMR spin−lattice relaxation (SLR) rates were measured using the well-known saturation recovery pulse sequence.[43] In order to obtain signal-specific NMR SLR rates, the free induction decays were Fourier transformed and the individual signal intensities plotted as a function of delay time afterward. Supplemental ^{19}F MAS NMR spectra (see Figure S2, Supporting Information) were recorded with the Avance 600 spectrometer at a resonance frequency of 565 MHz. The rotation frequency was 60 kHz. A single-pulse sequence was used for data acquisition; the $\pi/2$-pulse length was 2 μs.

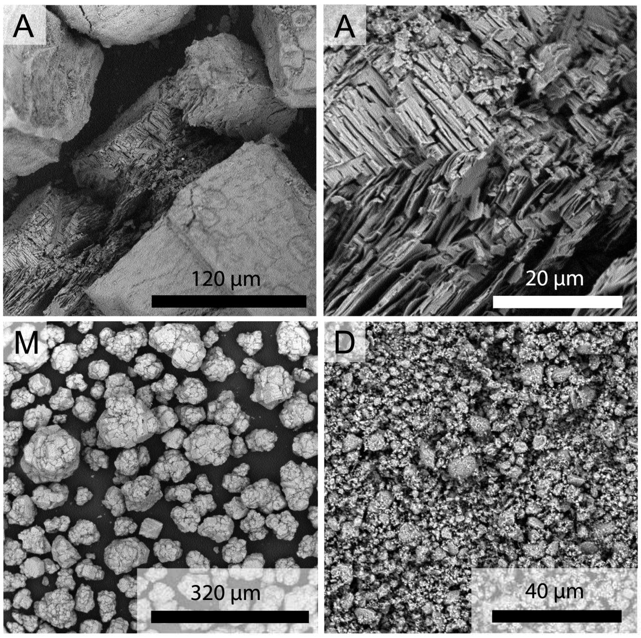

Figure 2. SEM micrographs of sample A (top) as well as samples M and D (bottom).

Nitrogen adsorption isotherms at 77 K were determined with a Quantachrome Autosorb 3 apparatus. Prior to each adsorption measurement, the samples were outgassed at 473 K for 24 h. The Brunauer−Emmett−Teller (BET) method was used to determine the specific surface area.

It is important to note that Wang et al.[36] and Bodaghi et al.[37] have also investigated samples D and M from the same suppliers. However, they examined batches which had been delivered some years ago. Provided the synthesis conditions have remained the same during the last years, a comparison of our results with those found earlier can be made (see below).

III. RESULTS AND DISCUSSION

A. Characterization of the γ-Al_2O_3 Samples. The XRPD patterns of the starting materials reveal the typical signature of γ-Al_2O_3. However, the first peak showing up at $2\theta = 33°$ does not match exactly with the pattern of γ-Al_2O_3 typically found in the literature;[44,45] see Figure 1. A small amount of α-Al_2O_3, not exceeding more than 5%, shows up in samples D and A. The XRPD pattern of sample A exhibits an additional peak at about $2\theta = 41°$ which cannot clearly be attributed to any of the known phases of Al_2O_3. In contrast to A and D, sample M seems to be free of α-Al_2O_3. Let us note that traces of α-Al_2O_3 are hardly detected by XRPD.

The full width at half-maximum, Δ_{fwhm}, of the most intense peak located at $2\theta = 67°$ (see Figure 1), which is inversely proportional to the mean crystallite size $\langle d \rangle$, cf. ref 46, increases in the following manner: $\Delta_{fwhm}(A) < \Delta_{fwhm}(M) < \Delta_{fwhm}(D)$. In the case of γ-Al_2O_3 estimation of mean crystallite size on the basis of the XRPD pattern shown in Figure 1 is fraught with large uncertainties. Thus, the values presented here are just used for a qualitative comparison: at the beginning, sample A consists of larger crystallites than the other two samples. This is well corroborated by the SEM images shown in Figure 2 (see below) giving a much clearer insight into mean particle sizes of the oxides investigated. Let us note that usually samples of Al_2O_3, as well as other oxide ceramics,[47] milled for many hours reveal crystallite sizes on the order of 20 nm.[48] TEM micrographs taken, which are not shown here for the sake of brevity, revealed that after a few hours of milling the powders consist of cluster-assembled particles of 200−300 nm which are themselves composed of much smaller and agglomerated nanocrystals with diameters ranging from 20 to 50 nm. Instability of the milled samples under the conditions of TEM measurement made it very difficult to distinguish between crystalline and amorphous regions in the samples. It is worth noting that Lee et al. used 2D ^{27}Al NMR to show that a thin film of amorphous Al_2O_3 was dominated by 4- and 5-fold coordinated Al ions while 6-fold Al ions appear to be the minor species.[31,32]

The BET surface area a_{BET} of sample A is 60 m^2 g^{-1} while those of samples D and M are 144 and 126 m^2 g^{-1}, respectively. On the basis of molecular dynamics simulations Blonski and Garofalini predicted that γ-Al_2O_3 becomes the stable modification when its specific surface area exceeds approximately 125 m^2 g^{-1}.[49] The stabilization stems from the lower surface energy of γ-Al_2O_3 playing a decisive role in the case of nanometer-sized crystallites. Later McHale et al. verified this prediction experimentally by means of absorption microcalorimetry measurements.[50]

Hence, comparing these results with the properties of the samples studied here, only sample A is expected to undergo the $\gamma \rightarrow \alpha$ phase transformation easily if the initial properties of the material play a crucial role for the phase transformation to be initialized. Regarding its morphology before milling, material A is characterized by the smallest BET surface area and the largest mean crystallite diameter. In the earlier studies on the samples D and M mentioned above[36,37] the a_{BET} values of the samples had not been measured. The surface areas were roughly estimated from the average grain sizes to be smaller than 125 m^2 g^{-1}. According to the SEM micrographs shown in Figure 2 the mean particle size of sample M approximately ranges from 20 to 160 μm while that of sample D lies in the range from 1 to 20 μm. As can be clearly seen, the particles of sample M initially consist of agglomerated smaller crystallites (Figure 2). Certainly, for the stabilization of the γ phase of Al_2O_3 (see above) the crystallite rather than the particle size is relevant.

B. Mechanically Induced $\gamma \rightarrow \alpha$ Phase Transformation.

1. Sample A. The ^{27}Al MAS NMR spectrum of sample A (Figure 3) is composed of two distinct lines at δ_{iso} = 12 ppm and δ_{iso} = 70 ppm.

These isotropic chemical shifts can be attributed to Al octahedrally and tetrahedrally coordinated by oxygen, respectively (see above). After 2 h of milling the intensity of the latter resonance line decreases and an additional signal concomitantly emerges at approximately 37 ppm. It can be attributed to 5-fold coordinated Al generated during milling as already assumed by Zieliński et al.[33] Most probably, the unsaturated Al centers are located on or near the surface of the particles being expected to show structural disorder. Indeed, strong evidence for this assumption was found by Kwak et al. who investigated the thermally induced $\gamma \rightarrow \alpha$ phase transformation of micrometer-sized Al_2O_3 particles by ^{27}Al MAS NMR spectroscopy.[13,18] Here, it turns out that any penta-coordinated Al ions (of the order of 1−2%, see ref 13) of the starting material are difficult to detect when a 17.6 T magnet is used. Since pentacoordinated Al ions are generated during milling, the mechanism of the mechanically driven transformation might be very similar to that observed when γ-Al_2O_3 is exposed to high temperatures. This means that coordinatively unsaturated Al centers serve as nuclei for the growth of α-Al_2O_3. Indeed, the results presented below give strong evidence for this assumption.

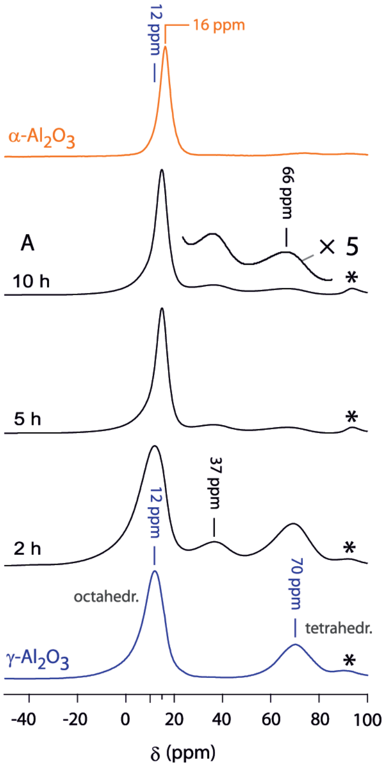

Figure 3. ^{27}Al MAS NMR spectra of sample A treated for the milling times as indicated. The spectra were recorded at a resonance frequency of 195.25 MHz and a spinning speed of 15 kHz. Spinning sidebands are marked with asterisks.

After 5 h of milling the phase transformation is almost finished and the corresponding NMR spectrum is dominated by a single line located at 15 ppm. For comparison, that of pure α-Al_2O_3, which is also included in Figure 3, solely consists of a diagnostic NMR line located at 16−17 ppm. Increasing t_{mill} to 10 h does not lead to any further changes of the NMR spectrum. The XRPD of a sample milled for 10 h reveals the typical pattern expected for α-Al_2O_3 (Figure 4).

However, although the NMR signal at 37 ppm has drastically decreased in intensity after 5 h of milling, there is still a small number fraction of 5-fold as well as 4-fold coordinated Al ions detectable by NMR (see the magnification of the corresponding NMR spectrum in Figure 3). The shallow NMR line at 70 ppm points to nanometer-sized Al_2O_3 crystallites which have not been transformed into the α-modification. As mentioned above, the γ-modification is reported to get stabilized at a sufficiently small crystallite size (see below for further details).[50] In contrast to NMR, such detailed features cannot be observed by XRPD. The corresponding powder patterns do not reveal any significant indications of residual (crystalline) γ-Al_2O_3 (see Figure 4) demonstrating the well-known difficulties to study (inherently) structurally disordered materials by X-ray diffraction. Certainly, the residual number fraction of 4- and 5-fold Al ions might point to a small amount of X-ray amorphous Al_2O_3.[31,32]

Remarkably, the transformation can almost be inhibited when a certain amount of CaF_2 or a small amount of La_2O_3 is added. The ^{27}Al MAS NMR spectrum of a mixture of CaF_2 and γ-Al_2O_3

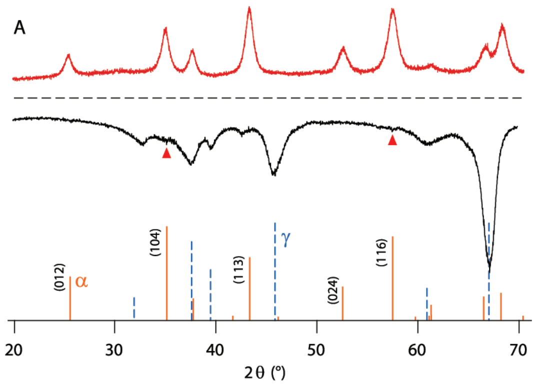

Figure 4. XRPD pattern of sample A which was milled for 10 h (top). No significant amounts of residual crystalline γ-Al_2O_3 can be detected. For comparison, the XRPD pattern of the starting material (see Figure 1) is also shown.

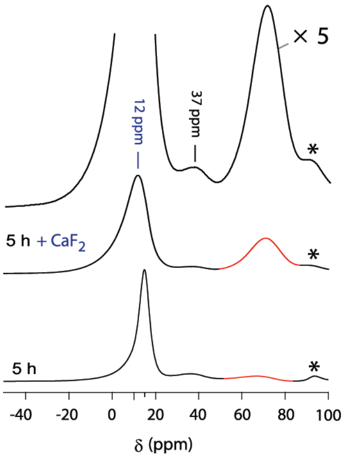

Figure 5. ^{27}Al MAS NMR spectra of sample A which was mechanically treated for 5 h in a high-energy ball mill together with an equimolar amount of CaF_2. For comparison, the corresponding NMR spectrum of the sample treated without the fluoride (see Figure 3) is also shown. Spinning sidebands are marked with asterisks.

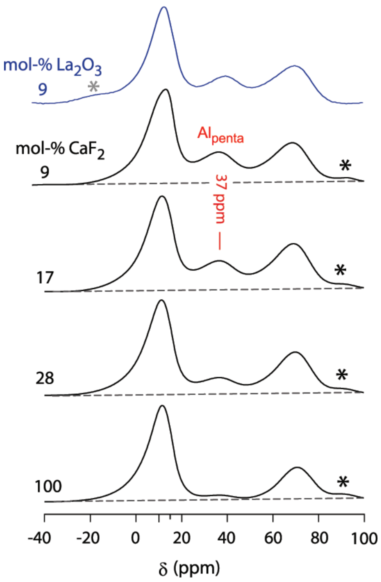

Figure 6. ^{27}Al MAS NMR spectra of mixtures of sample A and CaF_2 (as well as La_2O_3) milled for 5 h in order to influence the phase transformation and the amount of pentacoordinated Al ions formed. Spinning sidebands are marked with asterisks. (100 mol % means a stoichiometric mixture (1:1) of CaF_2 and Al_2O_3.)

(molar ratio of 1:1), which was treated for 5 h in the planetary mill, is shown in Figure 5. In contrast to pure γ-Al_2O_3 (see also Figure 3) the formation of pentacoordinated Al ions is significantly suppressed. The NMR signals at δ_{iso} = 12 ppm and particularly that at δ_{iso} = 67 ppm clearly show that the $\gamma \rightarrow \alpha$ phase transformation has been greatly suppressed. The magnification of the corresponding NMR spectrum (shown at the top of Figure 5) reveals only a very small number fraction of Al_{penta} centers. It was verified by XRPD (see Figure S3, Supporting Information) as well as ^{19}F MAS NMR that no mechanochemical reaction between the fluoride and Al_2O_3 took place which means that no new (bulk) phase has been formed. The relevant NMR spectra, which are not shown here for the sake of brevity, are included in the Supporting Information section (Figure S2). Obviously, as in the case of BaO and La_2O_3, see refs 12 and 30, F anions of CaF_2 coordinate to the unsaturated Al sites (located on the surface) and, thus, prevent the phase transformation from taking place. Interestingly, when the amount of CaF_2 is reduced and only 9 mol % of the fluoride is added, the phase transformation is still largely suppressed and, additionally, a significant amount of pentacoordinated Al ions is formed (see Figure 6); the same holds for a mixture of a sample with 9 mol % La_2O_3. The important effect of these additives is discussed in detail in the next section relating the initial morphologies of the samples with the initialization of the transformation and the role of pentacoordinated Al ions.

2. Samples D and M. In Figure 7 the ^{27}Al MAS NMR spectra of sample D and M are shown. As in the case of sample A, with increasing t_{mill} the intensity of the signal at 70 ppm decreases and 5-fold coordinated Al shows up at approximately 37 ppm. Simultaneously, a second NMR line emerges at 14 ppm finally shifting to 15 ppm when t_{mill} is increased to 20 h (sample D). This clearly indicates that the microstructure of the sample has been changed and that the $\gamma \rightarrow \alpha$ phase transformation has been, at least partly, initiated. For comparison, the corresponding XRPD pattern reveals a very small amount of crystalline α-Al_2O_3 (Figure 8). In contrast to the behavior of sample A, the phase transformation is largely suppressed when D or M are mechanically treated. However, in compensation for the absent phase transformation, a large amount of pentacoordinated Al ions shows up (cf. the discussion below).

For comparison, the same samples were mechanically treated in refs 36 and 37 and studied by XRPD as mentioned above. However, no phase transformation could be detected at all. Certainly, a straightforward comparison with earlier results is difficult because in previous studies[36,37] different milling techniques and vial sets were used. Keeping in mind that the milling conditions might greatly affect the initiation of the transformation (as will be shown in detail below), the local changes made visible by NMR are obviously hard to detect by XRPD. This disadvantage is further increased due to the additional disorder expected to be introduced during milling. Let us note that ^{27}Al MAS NMR spectra recorded at 14.1 T and a spinning speed of 30 kHz are very similar to those recorded at higher magnetic field (see the corresponding spectrum in Figure 7). Thus, the smaller

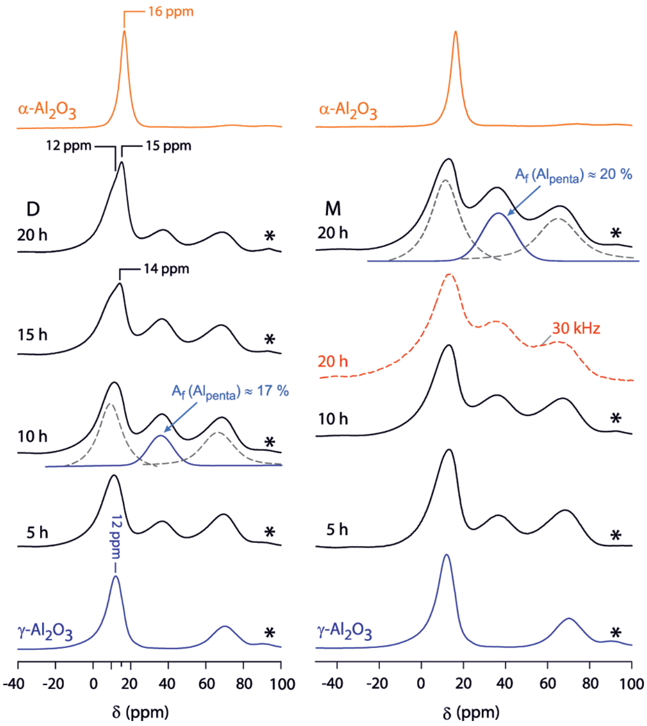

Figure 7. ^{27}Al MAS NMR spectra recorded on samples D (left) and M (right) after the materials were milled for several hours in a high-energy ball mill. Data were recorded at a resonance frequency of 195.25 MHz (17.6 T) and a spinning speed of 15 kHz. Spinning sidebands are marked with asterisks. The spectrum represented by a dashed line (see right-hand side of the figure) has been recorded at 14.1 T and a spinning speed of 30 kHz. See text for further details.

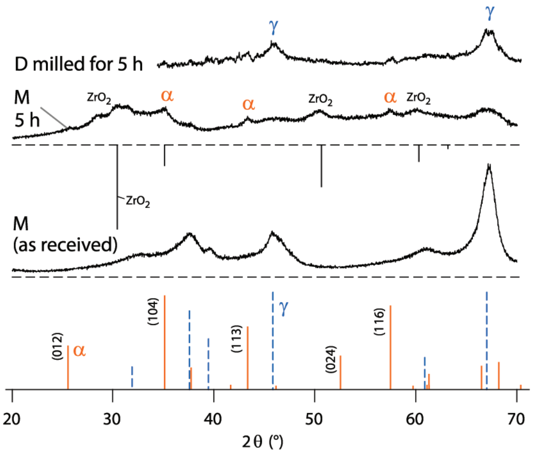

Figure 8. The XRPD pattern of samples M and D which were each milled for 5 h (top). In the case of sample M strong abrasion of ZrO_2 (see vertical bars) can be detected. For comparison, the XRPD of the as-received sample M is also shown (bottom).

rotation frequency of 15 kHz, mainly used for the NMR experiments presented here, has negligible effects on the spectral features observed at 17.6 T.

In the present case, milling of sample M leads to abrasion of ZrO_2 (Figure 8). This might be due to the sharp-edged morphology of sample M. Since abrasion is not observed when sample D (as well as A) is milled, it can be clearly ruled out that abrasion originating from the vial set significantly prevents (or inhibits) the transformation. This can be corroborated when sample A is intentionally jointly milled with ZrO_2 (see Figure S5 presented in the Supporting Information section).

In contrast to sample A, at comparable milling times an unexpectedly large amount of pentagonal coordinated Al shows up in the NMR spectra of samples D and M. At milling times being equal or larger than 10 h, the number fraction A_f of 5-fold coordinated Al ions, Al_{penta}, reaches a value of approximately 20%. In Figure 7 the ^{27}Al MAS NMR spectra were roughly fitted with a combination of Gaussian- and Lorentzian-shaped functions to estimate the area fraction A_f of the NMR line showing up at 37 ppm.

Since the transformation of sample D as well as M is much slower than that observed for sample A, the coordinatively unsaturated Al centers seem to be hindered to serve as starting points for the growth of α-Al_2O_3. Furthermore, traces of α-Al_2O_3, which are particularly seen in the XRPD pattern of sample M (Figure 8), do not promote the transformation of γ-Al_2O_3 into α-Al_2O_3 as expected. Thus, α-Al_2O_3 seed crystals seem to not play the crucial role assumed for the same sample previously.[36,37]

This might be explained by the fact that at the very early stages of milling the mean crystallite sizes of samples M and D are smaller than that of sample A. For small Al_2O_3 crystallites with diameters in the nanometer range the γ-modification becomes the thermodynamically stable form.[50] Obviously, further mechanical treatment simply causes the reduction of the crystallite size or the formation of amorphous Al_2O_3 but does not lead to a completion of the partly initialized phase transformation. This might also explain the features of the ^{27}Al MAS NMR spectrum of sample A showing a small amount of nanometer-sized γ-Al_2O_3 (see the NMR spectrum of sample A which was treated for 10 h in a planetary mill (Figure 3)). This result leads to an important conclusion: a large amount of unsaturated Al ions can be generated if sufficiently small γ-Al_2O_3 crystallites are used as starting material. For comparison, nanocrystalline γ-Al_2O_3 prepared in ways other than ball-milling is not expected to show such a large amount of Al_{penta} ions which are located, most likely, in the structurally disordered interfacial regions.

According to this explanation the role of the additives such as La_2O_3 and CaF_2, when treated together with sample A (see above), can also be understood: Presumably, if jointly milled from the beginning, they immediately coordinate to the initially formed unsaturated Al centers and prevent the phase transformation from being induced. This indicates that the initially generated Al_{penta} ions might be located on the surfaces of the crystallites or, more precisely, located in the surface-influenced volume. Assuming a surface layer of 0.5 nm thickness, which is reasonable for the sample studied here, and taking into account a mean crystallite size of approximately 10 nm (20 nm, see above), up to 30% (15%) of the ions might be located in such areas.[51] Simultaneously with the coordination process, increasing of t_{mill} causes the mean crystallite size to be progressively reduced so that nanocrystalline γ-Al_2O_3 is obtained. Because of the large surface area such a sample turns out to be resistant against transforming into α-Al_2O_3. If the amount of additives remains below a certain limit, the nanostructured powder obtained will be additionally characterized by a large number fraction of pentacoordinated Al ions. These are continuously formed with increasing milling time until a certain (controllable) limit is reached.

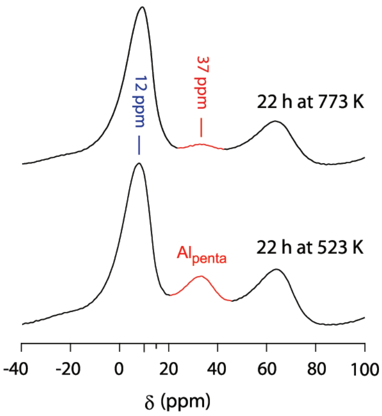

Figure 9. ^{27}Al MAS NMR spectra of sample D which was treated in a planetary mill for 10 h (see the corresponding spectrum shown in Figure 7) and then heat treated for the durations and temperatures indicated. Interestingly, even after a rude heat treatment at 523 K, the number fraction of pentacoordinated Al sites (Al$_{penta}$) of the sample remains very high. The corresponding NMR line takes about 11% of the total area.

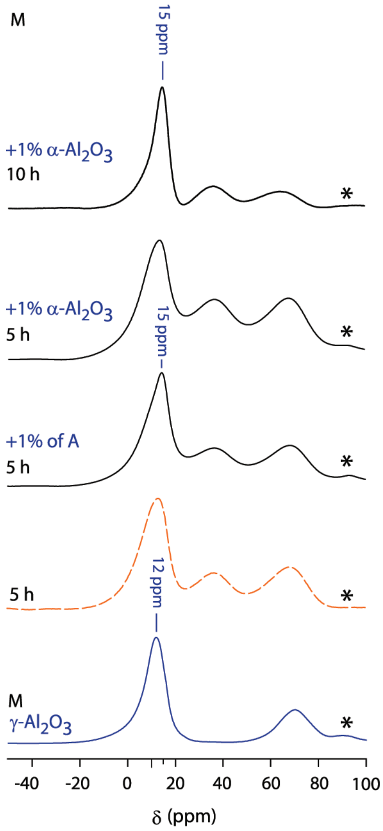

Figure 10. ^{27}Al MAS NMR spectra of sample M which were recorded after the material had been milled for the times indicated. Intentionally, pure α-Al$_2$O$_3$ or a small amount of sample A was added. For comparison, the corresponding NMR spectrum of Figure 7 (no seed crystals) is also shown. The spectra were recorded at a resonance frequency of 195.25 MHz and a spinning speed of 15 kHz. Spinning sidebands are marked with asterisks.

Interestingly, the 5-fold coordinated Al species of sample M treated for 20 h in a ZrO$_2$ vial (see Figure 7) are characterized by a (room temperature) ^{27}Al MAS NMR SLR rate ($1/T_{1,5\text{-fold}} = R_{1,5\text{-fold}} = 2.6(1)$ s^{-1}) which is by a factor of 2 larger than those of the 4- and 6-fold coordinated species ($R_{1,4\text{-fold}} = R_{1,6\text{-fold}} = 1.4(1)$ s^{-1}). This is in agreement with the observation of Kwak et al. regarding a short NMR relaxation time as being diagnostic of Al sites located on the surface of micrometer-sized crystallites.[13,18] Let us note that irrespective of the coordination number the corresponding magnetization transients $M(t)$ follow stretched exponential $M(t) \propto 1 - \exp(-(t/T_1)^{\gamma})$ time behavior with $\gamma \approx 0.6$ (see Figure S5, Supporting Information). Pentacoordinated Al ions located on or near the surface are exposed to a quite different electrical environment than Al in 4- and 6-fold coordination in the bulk structure. Consequently, these are expected to show a different NMR SLR behavior due to an enhanced electric quadrupole relaxation mechanism. However, in the case of structurally disordered nanometer-sized crystallites prepared by ball milling this interpretation does not rule out the possibility of unsaturated Al ions being also present in the bulk regions of the nanocrystallites which are expected to show a high defect density. Nevertheless, at least those residing in the structurally disordered areas on the surface of the particles might coordinate to suitable fluorides or oxides added to the starting material (see above and Figures 5 and 6). Thus, the number fraction A_f of pentacoordinated Al ions available to act as anchoring sites for catalytically active materials can be easily adjusted in these cases. Apart from varying the milling conditions and morphologies of the starting materials (see below), this represents an easy to handle strategy to purposefully design γ-Al$_2$O$_3$ substrate materials useful in catalysis.

The pentacoordinated Al ions formed turned out to be remarkably stable against heat treatment. Even when the nanocrystalline samples were kept at 523 K for more than 20 h still a large amount of pentacoordinated Al is detectable by ^{27}Al MAS NMR (Figure 9). Finally, the metastability of sample D (as well as M) mechanically treated for 10 h shows up when the material has been exposed to 773 K for 22 h. However, even after this rather crude annealing step, the ^{27}Al MAS NMR spectrum recorded still reveals an easily detectable amount of pentacoordinated Al sites. Interestingly, sample D when milled for 10 h transforms almost completely into γ-AlO(OH) (boehmite) when heated in water at temperatures above 320 K for several hours. This is not observed for an unmilled sample (not shown for the sake of brevity). However, storing the samples in air for several weeks does not lead to decomposition of the metastable products as verified by ^{27}Al MAS NMR and XRPD as well.

C. Influence of Seed Crystals on the Phase Transformation. When sample M is intentionally contaminated with a small amount of α-Al$_2$O$_3$, the phase transformation is promoted to a certain degree; however, even after 10 h of milling, a complete transformation is not observed. In Figure 10 ^{27}Al MAS NMR spectra of sample M are shown which was intentionally contaminated with 1 mol % α-Al$_2$O$_3$ and 1 mol % of sample A, respectively.

Similarly to the observations discussed above, after 5 h of milling a large amount of 5-fold coordinated Al is formed and an additional NMR line at approximately 15 ppm emerges which can be ascribed to Al in α-Al$_2$O$_3$. As expected, the amount of γ-Al$_2$O$_3$ decreases with increasing t_{mill}. Obviously, the γ-Al$_2$O$_3$ crystallites of sample A, which easily convert into α-Al$_2$O$_3$ (vide supra), additionally promote the phase transformation. However, compared to sample A (see Figure 3) the extent of the phase transformation is still largely reduced. This is also verified by

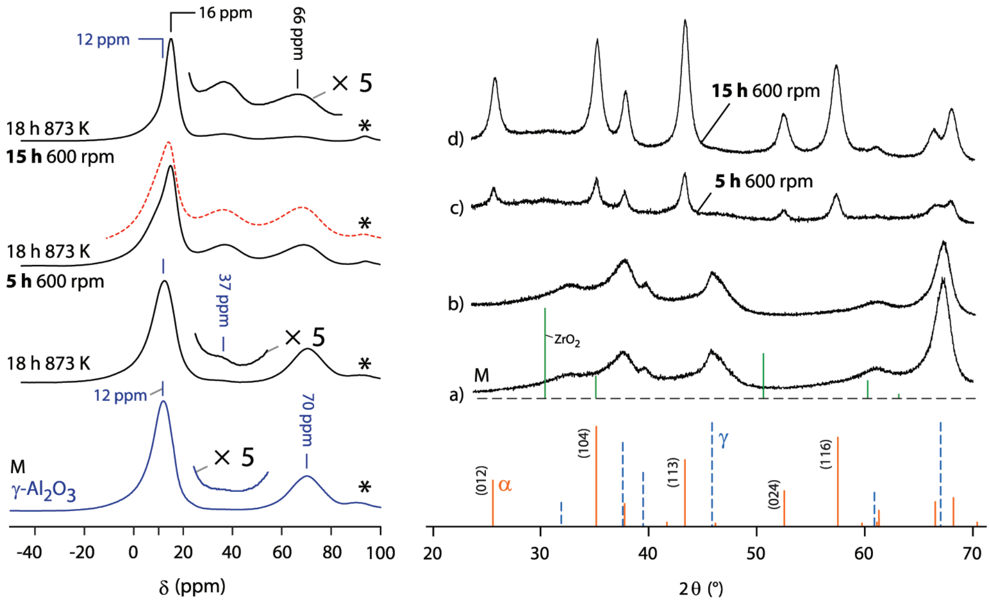

Figure 11. (Left) ^{27}Al MAS NMR spectra of sample M after annealing at 873 K for approximately 18 h. For comparison, the corresponding spectrum of the as obtained material is also shown. Ball milling for several hours initializes the phase transformation: pentacoordinated Al species show up and the NMR line at approximately 70 ppm decreases. The corresponding NMR spectrum of sample M contaminated with sample A is shown for comparison (dotted line, see Figure 10). Spinning sidebands are marked with asterisks. (Right) (a, b) XRPD pattern of sample M before and after heat treatment. (c, d) XRPD pattern of the same material treated for the milling times indicated.

XRPD; the corresponding pattern of sample M mixed with a small amount of A and milled for 5 h is very similar to that which is obtained without contaminating the material. In conclusion, although a large number fraction of 5-fold coordinated Al ions is generated (see Figures 7 and 11), even seed crystals, whether initially formed (see the XRPD pattern of sample M in Figure 8) or intentionally added, seem to be more and more ineffective to promote the $\gamma \rightarrow \alpha$ phase transformation at long milling times.

D. Influence of Annealing on the Phase Transformation. Sample M converts almost completely into α-Al_2O_3 after 15 h of milling when the starting material was annealed at 873 K for 18 h (see Figure 11). Even after 5 h of milling the $\gamma \rightarrow \alpha$ phase transformation is almost finished. The corresponding NMR spectrum reveals only a very small amount of residual γ-Al_2O_3 (Figure 11).

Let us note that the milling conditions remained exactly the same. Furthermore, the temperature chosen is much below that being necessary for a thermally induced $\gamma \rightarrow \alpha$ phase transformation. Accordingly, the XRPD pattern and the ^{27}Al MAS NMR spectrum of the annealed material nearly coincide with those of the thermally untreated sample (Figure 11). Grain growth is reflected by a slight decrease of the XRPD peak widths. Thus, the average crystallite size of sample M increases during annealing. However, the peak widths are still broader than those found for sample A. In order to probe whether this is a special feature of sample M, sample D was also tested in the same way. Annealing sample D for 15 h at 823 K also promotes the mechanically induced $\gamma \rightarrow \alpha$ phase transformation significantly (see Figure 12).

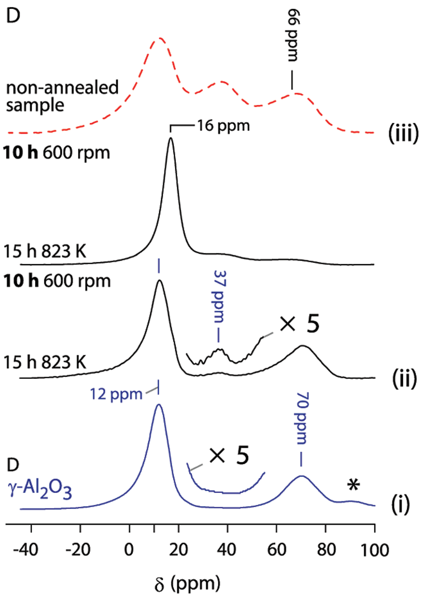

Figure 12. ^{27}Al MAS NMR spectra of sample D which was annealed at 823 K for 15 h and then mechanically treated at 600 rpm in a planetary mill for 10 h. For comparison, the NMR spectrum of the starting material (i), the spectrum of the unmilled but heat-treated sample (ii) as well as the NMR spectrum of nonannealed γ-Al_2O_3 (sample D) treated for 10 h (iii) are shown. Note that those of the sample annealed at elevated T were recorded at 14.1 T at a spinning speed of 15 kHz. Spinning sidebands, if visible, are marked with an asterisk.

Compared to the nonannealed powder the initial surface area a_{BET} of sample M, which was exposed to 873 K, decreased from 126 to 108 m^2 g^{-1}. Therefore, a significant amount of the initial γ-Al_2O_3 crystallites should have a surface area smaller than about 125 m^2 g^{-1}. Interestingly, only a rather small amount of 5-fold coordinated Al shows up after mechanical treatment. This observation and the extent of the phase transformation are very similar to those observed for sample A being characterized by a_{BET} = 60 m^2 g^{-1} and most probably even larger crystallites. This result is

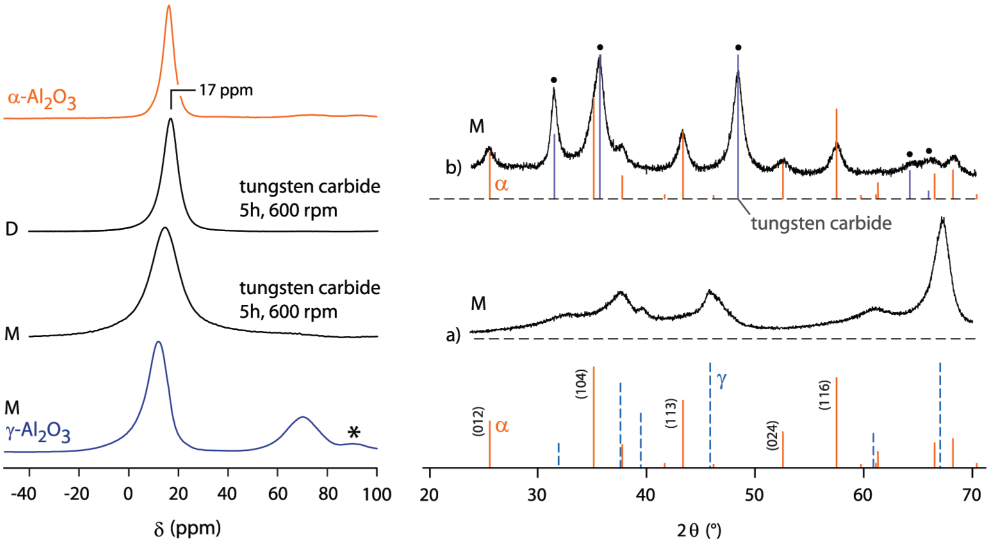

Figure 13. (Left) ^{27}Al MAS NMR spectra of sample M (as well as D) after mechanical treatment for 5 h in a WC vial using 100 balls of the same material. Spectra were acquired at 14.1 T with a spinning speed of 15 kHz. For comparison, the NMR spectrum of the starting material (bottom) and that of pure α-Al_2O_3 (top) are shown, too. (Right) Corresponding XRPD pattern of sample M. Besides the strong peaks belonging to α-Al_2O_3 the pattern reveals massive abrasion of tungsten carbide (corresponding peaks are marked by black dots). However, this obviously does not hinder the phase transformation from taking place.

in good agreement with the prediction of McHale et al.[50] that the γ modification is stabilized for crystallites with surface areas exceeding approximately 125 m^2 g^{-1}. However, the observation here is in contradiction to the explanation of Wang et al. as well as Bodaghi et al. (see above)[36,37] claiming that the phase transformation can solely be induced by α-Al_2O_3 seed crystals. Despite the change in initial surface area as well as crystallite size, which is an easy to prove and obvious experimental fact, we analyzed the ^{27}Al MAS NMR spectra of the annealed sample M (as well as D) in more detail to reveal any structural changes on an atomic-scale level. Such changes might also facilitate the $\gamma \rightarrow \alpha$ phase transformation. Indeed, a small number fraction of Al_{penta} ions form upon calcination (see the corresponding magnification in Figure 11). This has already been observed by Kwak et al.[15,18] One might assume that the reduction in surface area in combination with the generation of 5-fold coordinated Al ions is responsible for the $\gamma \rightarrow \alpha$ phase transformation observed after annealing.

E. Variation of the Milling Conditions. The results presented so far were obtained by milling the γ-Al_2O_3 samples employing a ZrO_2 vial set under the conditions stated in section II. Changing these conditions (Figure 13) toward a higher mechanical impact by using vials made of materials with a higher hardness and density has a drastic effect on the initialization as well as progress of the phase transformation. For example, when sample M is treated in a vial set made of tungsten carbide (WC) together with 100 balls made of the same material, the $\gamma \rightarrow \alpha$ phase transformation is completed already after 5 h of milling. The same is observed for sample D (Figure 13). Note that Mohs' hardness of WC is 9.5 whereas that of ZrO_2 is 8.5. As in the case of sample A, which was milled using the ZrO_2 vial, the corresponding ^{27}Al MAS NMR spectrum solely consists of an NMR line at 15 ppm. It is noteworthy that large amounts of abraded tungsten carbide show up in the XRPD of sample M (Figure 13). However, these do not hinder the phase transformation from taking place.

Obviously, in the case of sample M, a sufficiently large mechanical impact, which can be controlled by the kind of vial set and the number of balls used, is needed to initialize the phase transformation. Depending on the properties of the sample under study, below a certain limit, mechanical treatment may simply lead to the formation of (stable) structurally disordered nanostructured γ-Al_2O_3 with a large amount of pentacoordinated Al atoms. At an even lower mechanical impact, which can be adjusted by decreasing the number of balls from 140 to 100, the formation of 5-fold coordinated Al ions is almost completely suppressed when, for example, sample D is treated in the planetary mill. For comparison, using a shaker (Spex 8000 M) instead of a planetary mill in combination with a ZrO_2 vial and a single ball of 4 g (10 mm in diameter) the transformation observed for sample A (see above) can also be suppressed to a great extent. Even after 32 h of milling only a small amount of pentacoordinated Al is found. This manipulation works also in the direction of promoting the phase transformation: Using a ZrO_2 vial, the $\gamma \rightarrow \alpha$ phase transformation of sample M can be pushed on by increasing the number as well as the weight of the ZrO_2 balls used. Thus, the $\gamma \rightarrow \alpha$ phase transformation as well as the formation of 5-fold coordinated Al centers turn out to be very sensitive to the (initial) milling conditions used. In summary, soft mechanical treatment, which can be adjusted by changing the type of mill, the vial, and the rotational speed as well as the kind and number of milling balls, might be very useful to isolate (metastable) Al_2O_3 showing a large number fraction of pentacoordinated Al ions.

IV. CONCLUSIONS AND OUTLOOK

Several samples of γ-Al_2O_3, which were purchased from different suppliers, were mechanically treated in a planetary mill to initiate the $\gamma \rightarrow \alpha$ phase transformation. The latter is known to take place when γ-Al_2O_3 is heated up or mechanically treated in high-energy ball mills. In the present study, structural changes during milling were observed by both X-ray powder diffraction and high-field ^{27}Al MAS NMR spectroscopy. While X-ray diffraction measurements suffer from structural disorder present, local coordination spheres of the Al cations can be well-resolved by NMR techniques particularly when carried out at high magnetic fields. In all cases the formation of pentacoordinated Al ions was found indicating that the transformation mechanism is similar to the one reported for the thermally induced $\gamma \rightarrow \alpha$ phase transformation, i.e., the growth of α-Al_2O_3 starts from the unsaturated Al centers on the, presumably structurally disordered, surface of a metastable γ-Al_2O_3 crystallite and propagates into the inner regions.[13] Noteworthy, when the initially formed pentacoordinated Al centers are promptly trapped by, e.g., adding CaF_2 as shown here (cf. the behavior of sample A), the initialization of the phase transformation can be largely suppressed. This might illustrate the crucial role of unsaturated Al ions during the mechanically induced phase transformation.

Furthermore, it turned out that the presence of α-Al_2O_3 seed crystals seem to play neither the major nor the only role in initializing the phase transformation. The main reasons for a complete phase transformation have to be looked for in the very early stages of milling. Obviously, the initial surface area of the starting material takes a decisive part. The smaller the surface area of the crystallites the easier the phase transformation takes place. Presumably, this is due to the fact that the γ-modification of Al_2O_3 becomes stabilized when the mean crystallite size falls below a certain limit.[50] Thus, at least two competitive processes may explain the different results obtained: mechanical treatment induces the formation of α-Al_2O_3 and simultaneously causes nanostructuring of the material. The various milling conditions can be adjusted by changing the type of mill, the milling vial, and the ball-to-powder weight ratio. This enables influence on the result of the milling process in a directed way.

Depending on the (initial) properties and composition of a phase-pure sample, being modifiable by preannealing or by adding seed crystals, respectively, mechanical treatment can, when just the limiting cases are regarded, lead either to a complete phase transformation or to the formation of nanocrystalline, structurally disordered γ-Al_2O_3. More importantly, milling conditions can be chosen such that the final product is provided with an exceptionally large number fraction of 5-fold coordinated Al ions located in the surface-influenced volume which is most likely characterized by structural disorder. In particular, this holds when nanometer-sized γ-Al_2O_3 crystallites serve as starting material. The so prepared oxide, which is in this case free of any additives, might be of large interest for the preparation of catalysts since the unsaturated Al centers act as anchoring sites for catalytically active materials, see refs 13−15.

Altogether, the mechanically induced phase transformation investigated is controlled by a complex interplay of the materials properties and the external milling conditions. Besides the details of the present study, the investigation clearly shows that high-energy ball milling represents an highly effective tool to isolate (metastable) compounds which are not available by conventional synthesis routes.

■ ASSOCIATED CONTENT

Supporting Information. Additional figures showing electron diffraction patterns, ^{19}F MAS NMR spectra, XRPD patterns, magnetization transients, and ^{27}Al MAS NMR spectra of some of the samples studied. This material is available free of charge via the Internet at http://pubs.acs.org.

■ AUTHOR INFORMATION

Corresponding Author

*E-mail: duevel@pci.uni-hannover.de; wilkening@pci.uni-hannover.de; wilkening@tugraz.at.

■ ACKNOWLEDGMENT

We gratefully acknowledge the group of Professor J. Caro for access to the BET surface analyzer as well as the X-ray diffractometer. We thank Professor J. Haase for access to the 750 MHz NMR spectrometer in Leipzig. We thank V. Becker for the SEM micrographs and A. Feldhoff, G. Gershteyn, and F. Steinbach for the supplementary TEM images. Financial support by the Deutsche Forschungsgemeinschaft (DFG) is highly appreciated (DFG priority program 1415, Kristalline Nichtgleichgewichtsphasen).

■ REFERENCES

(1) Makarov, N. A.; Sidorin, V. A.; Lukin, E. S. *Glass Ceram.* **2004**, *61*, 228.

(2) Lukin, E. S.; Tarasova, S. V.; Korolev, A. V. *Glass Ceram.* **2001**, *58*, 228.

(3) Lukin, E. S.; Makarov, N. A.; Pershikova, E. M.; Popova, N. A.; Kuteinikova, A. L.; Anufrieva, E. V.; Tarasova, S. V.; Kozlov, A. I.; Zhirnov, R. V.; Zonin, A. V. *Phys. Rev. B* **1996**, *55*, 4285.

(4) Schrewelius, N. G. *J. Am. Ceram. Soc.* **1948**, *31*, 228.

(5) Jackman, E. A.; Roberts, J. P. *Philos. Mag.* **1955**, *46*, 809.

(6) White, E. A. *Nature* **1961**, *191*, 901.

(7) Golubev, B. P.; Vasileva, G. A.; Kalitin, P. P.; Smirnov, S. N.; Khariton, F. Y. *High Temp.* **1965**, *3*, 233.

(8) Maiman, T. H. *Nature* **1960**, *187*, 493–494.

(9) Moulton, P. F. *Proc. IEEE* **1992**, *80*, 348.

(10) Huber, G.; Kränkel, C.; Petermann, K. *J. Opt. Soc. Am. B* **2010**, *27*, B93.

(11) Wang, S.; Borisevich, A.; Rashkeev, S.; Glazoff, M.; Sohlberg, K.; Pennycook, S.; Pantelides, S. *Nat. Mater.* **2004**, *3*, 143.

(12) Béguin, B.; Garbowski, E.; Primet, M. *Appl. Catal.* **1991**, *75*, 119.

(13) Kwak, J. H.; Hu, J. Z.; Kim, D. H.; Szanyi, J.; Peden, C. H. F. *J. Catal.* **2007**, *251*, 189.

(14) Mei, D.; Kwak, J. H.; Cho, S. J.; Szanyi, J.; Allard, L. F.; Peden, C. H. F. *J. Phys. Chem. Lett.* **2010**, *1*, 2688.

(15) Kwak, J. H.; Hu, J.; Mei, D.; Yi, C.-W.; Kim, D. H.; Peden, C. H. F.; Allard, L. F.; Szanyi, J. *Science* **2009**, *325*, 1670.

(16) Nellist, P.; Pennycook, S. *Science* **1996**, *274*, 413.

(17) Sohlberg, K.; Rashkeev, S.; Borisevich, A.; Pennycook, S.; Pantelides, S. *Chem. Phys. Chem.* **2004**, *5*, 1893.

(18) Kwak, J. H.; Hu, J.; Lukaski, A.; Kim, D. H.; Szanyi, J.; Peden, C. H. F. *J. Phys. Chem. C* **2008**, *112*, 9486.

(19) Burtin, P.; Brunelle, J. P.; Pijolat, M.; Soustelle, M. *Appl. Catal.* **1987**, *34*, 225.

(20) Burtin, P.; Brunelle, J. P.; Pijolat, M.; Soustelle, M. *Appl. Catal.* **1987**, *34*, 239.

(21) Oudet, F.; Courtine, P.; Vejux, A. *J. Catal.* **1988**, *114*, 112.

(22) Bagwell, R. B.; Messing, G. L.; Howell, P. R. *J. Mater. Sci.* **2001**, *36*, 1833.

(23) Tonejc, A.; Stubičar, M.; Tonejc, A. M.; Kosanović, K.; Subotić, B.; Smit, I. *J. Mater. Sci. Lett.* **1994**, *13*, 519.

(24) Cava, S.; Tebcherani, S. M.; Souza, I. A.; Pianaro, S. A.; Paskocimas, C. A.; Longo, E.; Varela, J. A. *Mater. Chem. Phys.* **2007**, *103*, 394.

(25) Tucker, D. S.; Hren, J. J. *Mater. Res. Soc. Symp. Proc.* **1984**, *31*, 337.

(26) Tucker, D. S. *J. Am. Ceram. Soc.* **1985**, *68*, C163.

(27) Tucker, D. S.; Jenkins, E. J.; Hren, J. H. *J. Electron Microsc. Tech.* **1985**, *2*, 29.

(28) Dynis, F. W.; Halloran, J. W. *J. Am. Ceram. Soc.* **1982**, *65*, 442.

(29) Stebbins, J.; Du, L.; Kroeker, S.; Neuhoff, P.; Rice, D.; Frye, J.; Jakobsen, H. *Solid State Nucl. Magn. Reson.* **2002**, *21*, 105.

(30) Matsuda, S.; Kato, A.; Mizumoto, M.; , Yamashita, H. *8th International Congress on Catalysis*; Verlag Chemie: Weinheim, Dechema, 1984; Vol. IV, p 879.

(31) Lee, S. K.; Park, S. Y.; Yi, Y. S.; Moon, J. *J. Phys. Chem. C* **2010**, *114*, 13890.

(32) Lee, S. K.; Park, S. Y.; Yi, Y. S.; Ahn, C. W. *Phys. Rev. Lett.* **2009**, *103*, 095501.

(33) Zieliński, P. A.; Schulz, R.; Kaliaguine, S.; Van Neste, A. *Mater. Res. Soc.* **1993**, *8*, 2985.

(34) Kostić, E.; Kiss, S. J.; Zec, S.; Bošković, S. *Powder Technol.* **2000**, *107*, 48.

(35) Li, P.; Xi, S.; Zhou, J. *Ceram. Int.* **2009**, *35*, 247.

(36) Wang, Y.; Suryanarayana, A.; An, L. *J. Am. Ceram. Soc.* **2005**, *88*, 780.

(37) Bodaghi, M.; Mirhabibi, A. R.; Zolfonum, H.; Tahriri, M.; Karimi, M. *Phase Transform.* **2008**, *81*, 571.

(38) Bell, A. T. *Science* **2003**, *299*, 1688.

(39) Müller, D.; Gessner, W.; Behrens, H.-J.; Scheler, G. *Chem. Phys. Lett.* **1981**, *79*, 59.

(40) Morris, H. D.; Ellis, P. D. *J. Am. Chem. Soc.* **1989**, *111*, 6045.

(41) Chen, F. R.; Davis, J. G.; Fripiat, J. J. *J. Catal.* **1992**, *133*, 263.

(42) Menéndez-Proupin, E.; Gutiérrez, G. *Phys. Rev. B* **2005**, *72*, 035116.

(43) Fukushima, E.; Roeder, S. *Experimental Pulse NMR*; Addison-Wesley: Reading, MA, 1981.

(44) Rooksby, H. P. *X-Ray Identification and Crystal Structures of Clay Materials*; Brindley, G. W., Ed.; The Mineralogical Society: London, 1951.

(45) Smrčok, L.; Langer, V.; Křestan, J. *Acta Crystallogr.* **2006**, *C62*, i83.

(46) Scherrer, P. *Göttinger Nachr.* **1918**, *2*, 98.

(47) Indris, S.; Bork, D.; Heitjans, P. *J. Mater. Synth. Process.* **2000**, *8*, 245.

(48) Wilkening, M.; Indris, S.; Heitjans, P. *Phys. Chem. Chem. Phys.* **2003**, *5*, 2225.

(49) Blonski, S.; Garofalini, S. H. *Surf. Sci.* **1993**, *295*, 263.

(50) McHale, J. M.; Auroux, A.; Perrotta, A. J.; Navrotsky, A. *Science* **1997**, *277*, 788.

(51) Vollath, D. *Nanomaterials—An Introduction to Synthesis, Properties and Applications*; Wiley-VCH: Weinheim, 2008.

Curriculum Vitae

Personal details

Name	Andre Düvel
Date of Birth	28.10.1981
Place of Birth	Hannover, Germany
Nationality	German

Education

2009-2013	PhD student in the group of Prof. Dr. P. Heitjans, Institute of Physical Chemistry and Electrochemistry, Leibniz University Hannover, Germany. Topic: "NMR- und impedanzspektroskopische Untersuchungen zur Dynamik und lokalen Struktur in mechanochemisch dargestellten Nichtgleichgewichtsphasen"
2008	diploma degree in chemistry, Leibniz University of Hannover, Germany; diploma thesis: "NMR-Messungen zur Diffusion und lokalen Struktur in nanokristallinen Fluorionenleitern"
2006	first diploma, Leibniz University Hannover, Germany
2001	Abitur
1994-2001	Gymnasium Goetheschule, Hannover, Germany
1992-1994	Orientierungsstufe Meldaufstraße, Hannover, Germany
1988-1992	Grundschule Fuhsestraße, Hannover, Germany

Teaching

2011-2013	in charge of the "Physikalisch-Chemisches Praktikum I"
2008-2012	teaching in the "Physikalisch-Chemisches Praktikum I"

List of Publications

A. Düvel, J. Bednarcik, V. Šepelák, P. Heitjans, "Mechanosynthesis of the Fast Fluoride Ion Conductor $Ba_{1-x}La_xF_{2+x}$ – From the Fluorite to the Tysonite Structure", J. Phys. Chem. C 118 (2014) DOI 10.1021/jp410018t.

M. Senna, A. Düvel, V. Šepelák, J. Shi, K. L. da Silva, V. Laporte, S. Lebedkin, C. Kübel, D. Wang, D. Schünemann, K.-D. Becker, P. Heitjans, "Transfer and State Changes of Fluorine at Polytetrafluoroethylene/Titania Boundaries by Mechanical Stressing and Thermal Annealing", J. Phys. Chem. C 117 (2013) 15272.

G. Scholz, K. Meyer, A. Düvel, P. Heitjans, E. Kemnitz, "Fast Ion Conducting Nanocrystalline Alkaline Earth Fluorides Simply Prepared by Mixing or Manual Shaking", Z. Anorg. Allg. Chem. 639 (2013) 960.

V. Šepelák, A. Düvel, M. Wilkening, K.-D. Becker, P. Heitjans, "Mechanochemical reactions and syntheses of oxides", Chem. Soc. Rev. 42 (2013) 7507.

A. Düvel, A. Kuhn, L. Robben, M. Wilkening, P. Heitjans, "Mechanosynthesis of solid electrolytes: preparation, characterization, and Li ion transport properties of garnet-type Al-doped $Li_7La_3Zr_2O_{12}$ crystallizing with cubic symmetry", J. Phys. Chem. C 116 (2012) 15192.

A. Düvel, B. Ruprecht, P. Heitjans, M. Wilkening, "Mixed alkaline-earth effect in the metastable anion conductor $Ba_{1-x}Ca_xF_2$ ($0 \leq x \leq 1$): Correlating long-range ion transport with local structures revealed by ultrafast ^{19}F MAS NMR", J. Phys. Chem. C 115 (2011) 23784.

A. Düvel, E. Romanova, M. Sharifi, D. Freude, M. Wark, P. Heitjans, M. Wilkening, "Mechanically Induced Phase Transformation of γ-Al_2O_3 into α-Al_2O_3. Access to Structurally Disordered γ-Al_2O_3 with a Controllable Amount of Pentacoordinated Al Sites", J. Phys. Chem. C 115 (2011) 22770.

K. L. da Silva, V. Šepelák, A. Düvel, A. Paesano, H. Hahn, F. J. Litterst, P. Heitjans, K. D. Becker, "Mechanochemical preparation and structural studies of mullite-type $Bi_2(Ga_xAl_{1-x})_4O_9$ solid solutions", J. Solid State Chem. 184 (2011) 1346.

K. L. da Silva, D. Menzel, A. Feldhoff, C. Kübel, M. Bruns, A. Paesano, A. Düvel, M. Wilkening, M. Ghafari, H. Hahn, F. J. Litterst, P. Heitjans, K. D. Becker, V. Šepelák, "Mechanosynthesized $BiFeO_3$ nano particles with highly reactive surface and enhanced magnetization", J. Phys. Chem. C 115 (2011) 7209.

A. Düvel, M. Wilkening, S. Wegner, A. Feldhoff, V. Šepelák, P. Heitjans, "Ion conduction and dynamics in mechanosynthesized nanocrystalline $BaLiF_3$", Solid State Ionics 184 (2011) 65.

A. Düvel, S. Wegner, K. Efimov, A. Feldhoff, P. Heitjans, M. Wilkening, "Access to metastable complex ion conductors via mechanosynthesis: preparation, microstructure and conductivity of $(Ba,Sr)LiF_3$ with inverse perovskite structure", J. Mater. Chem. 21 (2011) 6238.

A. Düvel, M. Wilkening, R. Uecker, S. Wegner, V. Šepelák, P. Heitjans, "Mechanosynthesized nanocrystalline $BaLiF_3$: The impact of grain boundaries and structural disorder on ionic transport", Phys. Chem. Chem. Phys. 12 (2010) 11251.

A. Düvel, M. Wilkening, R. Uecker, P. Heitjans, "Ion transport properties of the inverse perovskite $BaLiF_3$ prepared by high-energy ball milling", Diffusion Fundamentals 12 (2010) 104.

A. Düvel, M. Wilkening, P. Heitjans, "Ionic Transport in Mechanosynthesized Nanocrystalline $BaLiF_3$", Diffusion Fundamentals 11 (2009) 46.

Acknowledgment

I would like to express my gratitude to my family, friends, colleagues, supervisors and cooperation partners.

First of all I would like to thank Prof. Dr. P. Heitjans and Prof. Dr. M. Wilkening for their support during the last years and the opportunity to profit from a free and open research atmosphere.

I would like to thank Vladimir Šepelák for all the support, the discussions and the good times we had at several conferences and meetings.

Thanks to Dr. Alexander Kuhn and Dr. Ilie Hanzu for a fruitful cooperation and the good time. I am thankful for many scientific discussions with Alexander Kuhn, Benjamin Ruprecht and Viktor Epp and their support. Thanks to Kai Volgmann, Elena Witt and Katharina Bösebeck and the rest of the group for their support.

Thanks to Prof. Dr. Caro, Prof. Dr. A. Feldhoff, Prof. Dr. P. Behrens, Prof. Dr. M. Binnewies and Prof. Dr. C. Vogt for helping out with XRD, REM and TEM, IR, ICP-OES and access to the REM. Thanks to the whole Institute for the good atmosphere and cooperation.

Many thanks to Prof. Dr. Alan Chadwick, Dr. Dean Sayle and Dr. Silvia Ramos for enabling the EXAFs measurements. It was great time with you. Thanks to Dr. Lars Robben for all his help finding the correct XRPD patterns, the discussions and the fruitful cooperation. Thanks to Dr. Di Wang, Dr. Andriy Lotnik and Dr. Grygoriy Gershteyn for several TEM measurements. Many thanks also to Jozef Bednarcik for the measurements at DESY, Reinhard Uecker for the preparation of single crystals of $BaLiF_3$, $Ba_{0.50}Sr_{0.50}F_2$ and $Ba_{0.67}Sr_{0.33}F_2$, Malte B. Rücker for the programming of the lattice simulator, Dr. Sebastian Wegner for many ^{19}F MAS NMR measurements, Elena Merzlyakova, Anh-Thu Duong, Wing-Yang Tsan and Kave Partovi for their support in preparation of, and some measurements at, the samples. Thanks to Martin Hesse and Tim Smolinsky for the great time.

Many thanks to Alexander Kuhn and Kai Rohmann for proof-reading this manuscript. And my deepest gratitude to Elena for her support especially in the last months.